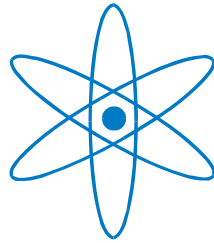


**PHYSIK-DEPARTMENT**



**Flue gas fired absorption chillers**

**Christoph KREN**

**Dissertation**



**TECHNISCHE UNIVERSITÄT**

**MÜNCHEN**



Technische Universität München – TUM  
Physik Department, Lehrstuhl für Physik E19

# **Flue gas fired absorption chillers**

Dipl.-Phys. (Univ.) Christoph KREN

Vollständiger Abdruck der von der Fakultät für Physik der Technischen Universität München  
zur Erlangung des akademischen Grades eines

*Doktors der Naturwissenschaften (Dr. rer. nat.)*

genehmigten Dissertation.

Vorsitzender: Univ.-Prof. Dr. P. Vogl

Prüfer der Dissertation:

1. Univ.-Prof. Dr. U. Stimming

2. Univ.-Prof. Dr. F. Ziegler (Technische Universität Berlin)

Die Dissertation wurde am 28.11.2006 bei der Technischen Universität München  
eingereicht und durch die Fakultät für Physik am 18.02.2008 angenommen.



# Executive summary

## Summary in English

The development of direct-fired and exhaust-fired absorption chillers, with optimized cycles and multi-stage utilization of the flue gas enthalpy, is a key step towards improved energy efficiency in absorption refrigeration and in CCHP applications. Fundamental thermodynamic relations and boundary conditions are discussed with regard to promising cycle concepts and recent developments. A generally valid approach for the optimization of flue gas heat exchangers is presented and consequently applied in a numerical parameter study at typical boundary conditions for regenerators in such absorption chillers. Experimental results from laboratory tests on a novel regenerator prototype, built as a natural convection boiler with vertical boiling tubes, are given. The heat transfer and pressure drop at the flue gas side are discussed, as well as the boiling heat transfer and solution circulation inside the tubes. The agreement of the experimental results and theoretical predictions is shown.

(996 characters including blanks)

## Zusammenfassung auf Deutsch

Die Entwicklung direktbefeuertter und abgasbeheizter Absorptionskaltwassersätze mit optimierten Kreisläufen und mehrstufiger Rauchgaswärmenutzung ist ein wesentlicher Schritt zu besserer Energieeffizienz in Absorptionskälteanlagen und KWKK-Anwendungen. Grundlegende thermodynamische Zusammenhänge und Randbedingungen werden im Hinblick auf aussichtsreiche Kreislaufkonzepte und aktuelle Entwicklungen diskutiert. Ein allgemeiner Ansatz zur Optimierung von Rauchgaswärmetauschern wird dargestellt und in einer numerischen Parameterstudie unter typischen Randbedingungen für Austreiber solcher Kältemaschinen angewandt. Experimentelle Ergebnisse von Labortests am Prototyp eines neuartigen Naturumlauf-Austreibers mit stehenden Siederohren werden dargestellt. Wärmeübergang und Druckverlust auf der Rauchgasseite sowie der siedende Wärmeübergang und der Lösungsumlauf innerhalb der Rohre werden diskutiert. Die Übereinstimmung von experimentellen Ergebnissen mit theoretischen Berechnungen wird gezeigt.

(1000 characters including blanks)



# Preface and acknowledgements

The present thesis has been created during my work at the Garching department of the Bavarian Center for Applied Energy Research (ZAE Bayern - Bayerisches Zentrum für Angewandte Energieforschung e.V.). The experimental part mainly relies on work that has been conducted in the course of the joint European research project “LiBrAC” by the project partners ZAE Bayern e.V. (Germany), Weir ENTROPIE S.A (France), Gas Natural SDG S.A. (Spain), and BG Technology Ltd. / Advantica (UK) with funding by the European Commission.

This thesis would not have been possible without the continued inspiration and support from my teacher and supervisor Felix Ziegler, who was always available for many enlightening discussions, not only during his time as head of the division of the ZAE Bayern in Garching but also at his later position as full professor at the TU Berlin. I also want to express my gratitude to Wolfgang Schölkopf, present head of the division, who provided me a lot of valuable guidance and personal assistance for finalizing my thesis although having not been involved in the origins of this work. In addition, I really have to acknowledge the patience and the support of Prof. Stimming, scientific director of the division, who always provided me the suitable environment for my studies although they were not in the focus of his main area of research and although they took way too much time to get finished.

I want to say “thank you” to all the partners in the “LiBrAC” project for the good cooperation and for a lot of personal positive experiences with interational collaboration: Marie-Helene Fulachier, Christophe Larger, and Jürgen Scharfe from Weir ENTROPIE, Jose Sahun from Gas Natural, Dave Clark, Aik Lua, Jeff Sadler, and Bob Tucker from BGT. And, of course, my thanks go to all the members of the “LiBrAC” team at the ZAE Bayern over the years: Tobias Dantele, Herbert Reithmeier, Christian Keil, Dominik Neidinger, Martin Scholz, Tom Jelinek, Gerhard Eberl, and to all others that I might have forgotten here. Additionally, I want to express my thanks to all my former colleagues at the ZAE Bayern for the friendship and for the good times – without mentioning names because any listing would be incomplete.

Finally, I want to to say thank you to my wife for her love and her patience throughout all the years.





# Contents

|  |           |
|--|-----------|
| <b>Flue gas fired absorption chillers .....</b>  | <b>i</b>  |
| Executive summary .....  | iii       |
| Preface and acknowledgements .....   | v         |
| Contents .....   | vii       |
| Nomenclature .....   | xi        |
| List of figures .....  | xvii      |
| List of tables .....   | xxi       |
| <br>   |           |
| <b>1 Introduction .....</b>  | <b>1</b>  |
| <b>1.1 Absorption refrigeration .....</b>  | <b>1</b>  |
| <b>1.2 Work outline.....</b>   | <b>2</b>  |
| <br>   |           |
| <b>2 State of the art of absorption refrigeration .....</b>                                      | <b>4</b>  |
| <b>2.1 Fundamentals and terminology .....</b>  | <b>4</b>  |
| 2.1.1 Thermodynamic fundamentals .....   | 4         |
| 2.1.2 Basic absorption cycle .....   | 7         |
| 2.1.3 Multi-stage absorption cycles .....  | 11        |
| 2.1.4 Solution cycle design .....  | 13        |
| 2.1.5 Commercially available types of absorption chillers .....                                  | 15        |
| 2.1.6 Reference operating conditions .....   | 16        |
| <b>2.2 Thermal efficiency of indirect-fired absorption chillers.....</b>                         | <b>17</b> |
| 2.2.1 Thermal efficiency of an ideal/reversible thermodynamic process for<br>refrigeration ..... | 17        |
| 2.2.2 The endoreversible model for absorption chillers .....                                     | 18        |
| 2.2.3 Internal loss mechanisms in single-effect cycles .....                                     | 24        |
| 2.2.4 Efficiency of indirect-fired double-effect chillers.....                                   | 29        |
| 2.2.5 Triple-effect and quadruple-effect chillers.....   | 31        |
| 2.2.6 Integrated multi-stage chillers.....   | 32        |
| <b>2.3 Flue gas fired absorption chillers .....</b>  | <b>33</b> |
| 2.3.1 Terminology .....  | 33        |
| 2.3.2 Common design .....  | 33        |
| 2.3.3 Thermal efficiency .....   | 34        |
| <br>   |           |
| <b>3 Basic concepts for highly efficient flue gas fired chillers .....</b>                       | <b>37</b> |
| <b>3.1 General settings .....</b>  | <b>37</b> |
| 3.1.1 Terminal temperature difference for flue gas heat exchangers.....                          | 37        |
| 3.1.2 Lower temperature limit of flue gas utilization .....                                      | 37        |
| 3.1.3 Upper internal temperature limit for driving heat input.....                               | 38        |

|            |  |            |
|------------|--|------------|
| <b>3.2</b> | <b><i>Cycle analysis</i></b> .....   | <b>38</b>  |
| 3.2.1      | Flow scheme and equilibrium states .....   | 38         |
| 3.2.2      | Internal losses and internal heat recovery .....   | 42         |
| <b>3.3</b> | <b><i>Multi-stage utilization of flue gas enthalpy</i></b> .....                           | <b>46</b>  |
| 3.3.1      | Basic considerations .....   | 46         |
| 3.3.2      | Technical options for external heat input in absorption chillers .....                     | 50         |
| <b>3.4</b> | <b><i>Examples of recent developments</i></b> .....  | <b>56</b>  |
| 3.4.1      | Advanced direct-fired absorption chillers .....  | 56         |
| 3.4.2      | Novel exhaust-fired absorption chillers .....  | 58         |
| <b>3.5</b> | <b><i>Conclusions for chiller design</i></b> .....   | <b>61</b>  |
| <b>4</b>   | <b>Fundamentals - Heat transfer and pressure drop in flue gas fired regenerators</b> ..... | <b>62</b>  |
| <b>4.1</b> | <b><i>Basic design considerations on flue gas fired regenerators</i></b> .....             | <b>62</b>  |
| 4.1.1      | Heat exchanger concepts .....  | 62         |
| 4.1.2      | Typical heat transfer settings .....   | 65         |
| <b>4.2</b> | <b><i>General definitions for heat transfer and pressure drop calculations</i></b> .....   | <b>68</b>  |
| 4.2.1      | Heat transfer coefficients at circular tubes .....   | 68         |
| 4.2.2      | Dimensionless numbers and property data .....  | 68         |
| 4.2.3      | Reversible and non-reversible pressure drops .....   | 70         |
| <b>4.3</b> | <b><i>Forced single phase flow inside circular tubes</i></b> .....                         | <b>71</b>  |
| 4.3.1      | Definition of the Reynolds number .....  | 71         |
| 4.3.2      | Heat transfer .....  | 71         |
| 4.3.3      | Frictional pressure drop .....   | 74         |
| <b>4.4</b> | <b><i>Forced convection flow across tube bundles</i></b> .....                             | <b>76</b>  |
| 4.4.1      | Definition of dimensionless numbers .....  | 76         |
| 4.4.2      | Heat transfer .....  | 79         |
| 4.4.3      | Frictional pressure drop .....   | 83         |
| <b>4.5</b> | <b><i>Boiling heat transfer</i></b> .....  | <b>86</b>  |
| 4.5.1      | Boiling regimes .....  | 86         |
| 4.5.2      | Convective heat transfer in two-phase flows inside tubes .....                             | 89         |
| 4.5.3      | Onset of nucleate boiling in saturated and subcooled liquids .....                         | 91         |
| 4.5.4      | Nucleate pool boiling of saturated liquids .....   | 94         |
| 4.5.5      | Nucleate boiling in upward tube flow .....   | 100        |
| 4.5.6      | Calculation of overall heat transfer in flow boiling .....                                 | 102        |
| 4.5.7      | Boiling of aqueous salt solutions .....  | 104        |
| <b>4.6</b> | <b><i>Natural-convection boilers with vertical boiling tubes</i></b> .....                 | <b>108</b> |
| 4.6.1      | Common fields of application .....   | 108        |
| 4.6.2      | General aspects of modeling of natural-convection boilers .....                            | 108        |
| 4.6.3      | Steam boilers for power generation .....   | 110        |
| 4.6.4      | Steam-heated thermosiphon reboilers .....  | 111        |
| 4.6.5      | Laboratory experiments with unconventional designs .....                                   | 116        |

|            |   |            |
|------------|---|------------|
| <b>5</b>   | <b>Optimized flue gas heat exchanger design.....</b>  | <b>119</b> |
| <b>5.1</b> | <b>General settings .....</b>   | <b>119</b> |
| 5.1.1      | Definition of the optimization problem .....  | 119        |
| 5.1.2      | Considered types of heat exchangers .....   | 119        |
| 5.1.3      | Free parameters for design optimization .....   | 120        |
| <b>5.2</b> | <b>Theoretical analysis: Fundamental relations for optimization of heat exchanger design.....</b> | <b>121</b> |
| 5.2.1      | Basic assumptions.....  | 121        |
| 5.2.2      | Relations between geometric and operational parameters .....                                      | 123        |
| 5.2.3      | Formal optimization approach .....  | 125        |
| 5.2.4      | Welding effort.....   | 126        |
| 5.2.5      | Power-law relations for different configurations and regimes.....                                 | 128        |
| 5.2.6      | Overview and discussion of the resulting relations.....   | 129        |
| <b>5.3</b> | <b>Numerical determination of promising configurations .....</b>                                  | <b>132</b> |
| 5.3.1      | Method.....   | 132        |
| 5.3.2      | Basic assumptions.....  | 133        |
| 5.3.3      | Calculation results for exhaust-fired regenerators .....  | 136        |
| 5.3.4      | Calculation results for direct-fired regenerators.....  | 147        |
| 5.3.5      | Comparison and discussion of the numerical results .....  | 152        |
| <b>5.4</b> | <b>Conclusions for regenerator design.....</b>  | <b>157</b> |
| <br>       |   |            |
| <b>6</b>   | <b>Laboratory testing of a direct-fired regenerator prototype .....</b>                           | <b>159</b> |
| <b>6.1</b> | <b>Heat exchanger design .....</b>  | <b>159</b> |
| <b>6.2</b> | <b>Test rig and experimental setup.....</b>   | <b>160</b> |
| 6.2.1      | Overview.....   | 160        |
| 6.2.2      | Instrumentation .....   | 162        |
| <b>6.3</b> | <b>Evaluation of measured data.....</b>   | <b>168</b> |
| 6.3.1      | Data recording and selection of stationary operational states .....                               | 168        |
| 6.3.2      | Calculation of process variables from measured data.....  | 168        |
| 6.3.3      | Range of experimental data from stationary states .....   | 172        |
| 6.3.4      | Estimation of radiative heat transfer .....   | 174        |
| 6.3.5      | Determination of specific numbers .....   | 179        |
| <b>6.4</b> | <b>Experimental results .....</b>   | <b>183</b> |
| 6.4.1      | Flue gas side heat transfer .....   | 183        |
| 6.4.2      | Flue gas side pressure drop .....   | 190        |
| 6.4.3      | Natural convection in thermosyphon tubes .....  | 194        |
| 6.4.4      | Solution side heat transfer .....   | 199        |
| <br>       |   |            |
| <b>7</b>   | <b>Conclusion and outlook.....</b>  | <b>214</b> |
| <b>7.1</b> | <b>Conclusions from this work .....</b>   | <b>214</b> |
| <b>7.2</b> | <b>Unresolved issues and further work.....</b>  | <b>216</b> |

|   |                |
|---|----------------|
| <b>Appendix.....</b>  | <b>219</b>     |
| <b>A.1 Endoreversible efficiency and loss mechanisms .....</b>  | <b>219</b>     |
| A.1.1 Endoreversible efficiency according to internal temperatures .....  | 219            |
| A.1.2 Endoreversible efficiency assuming an ideal working pair.....   | 220            |
| A.1.3 Endoreversible efficiency for real working pairs.....   | 221            |
| A.1.4 Efficiency limits for real water/lithium bromide chillers .....   | 225            |
| <b>A.2 The “square-root criterion” revised .....</b>  | <b>229</b>     |
| A.2.1 Basic assumptions .....   | 229            |
| A.2.2 Optimization approach.....  | 231            |
| A.2.3 Discussion .....  | 233            |
| <b>A.3 Raw data from stationary operational states.....</b>   | <b>235</b>     |
| <b>A.4 Raw data from pressure drop measurements and employed<br/>        interpolations for data evaluation .....</b> | <b>238</b>     |
| <br><b>Literature .....</b>   | <br><b>241</b> |
| List of referenced literature.....  | 241            |
| Declaration of prior publication .....  | 252            |

# Nomenclature

## Latin Variables

|                  |                               |  |
|------------------|-------------------------------|--|
| $A$              | $m^2$                         | area   |
| $A_D$            | -                             | Dühring gradient   |
| $A_{PLAIN}$      | $m^2$                         | outer surface area of a plain tube w/o fins                                  |
| $A_{TOT}$        | $m^2$                         | total outer surface area of a finned tube                                    |
| $AFR$            | -                             | air/fuel-ratio   |
| $a$              | $m^2/s$                       | thermal diffusivity or temperature conductivity                              |
| $B_D$            | $K$                           | Dühring intercept  |
| $b$              | $W \cdot s^{1/2}/m^2 \cdot K$ | thermal effusivity   |
| $C$              | -                             | constant factor an a correlation   |
| $COP$            | -                             | coefficient of performance, thermal efficiency                               |
| $COP_C$          | -                             | coefficient of performance of a heat pump/chiller in cooling mode            |
| $COP_H$          | -                             | coefficient of performance of a heat pump/chiller in heat pump mode          |
| $c, c_p$         | $J/kg \cdot K$                | specific (isobaric) heat capacity  |
| $d$              | $m$                           | diameter, tube diameter  |
| $F_{2P}$         | -                             | enhancement factor for convective heat transfer in two-phase flow            |
| $f$              | -                             | specific solution flow rate, solution/refrigerant circulation ratio          |
| $g$              | -                             | thermodynamic quality factor, ratio of real to ideal efficiency              |
| $g$              | $m^2/s$                       | gravity  |
| $H$              | $J$                           | enthalpy   |
| $h$              | $J/kg$                        | specific enthalpy  |
| $\Delta h_{CV}$  | $J/kg$                        | calorific value of combustion  |
| $\Delta h_{SOL}$ | $J/kg$                        | specific heat of solution  |
| $\Delta h_{VAP}$ | $J/kg$                        | specific heat of vaporization  |
| $k_W$            | $W/m^2 \cdot K$               | heat transmission coefficient for heat conduction through a wall             |
| $L$              | $m$                           | characteristic length for definition of dimensionless numbers                |
| $LMTD$           | $K$                           | logarithmic mean temperature difference                                      |
| $l$              | $m$                           | tube length  |
| $l_{Lo}$         | $m$                           | length of the tube bundle in longitudinal direction                          |
| $\dot{M}$        | $kg/s$                        | absolute mass flow rate  |
| $\dot{m}$        | $kg/s \cdot m^2$              | mass flux density, mass flow rate per unit cross-sectional area <sup>1</sup> |
| $N$              | -                             | integer number   |
| $NNU$            | -                             | exponent for dependency of $Nu$ on $Re$                                      |
| $Nu$             | -                             | dimensionless Nusselt number   |
| $NZ$             | -                             | exponent for dependency of $\zeta$ on $Re$                                   |
| $Pr$             | -                             | dimensionless Prandtl number   |

<sup>1</sup> Also frequently denoted  $G$  in literature.

|                 |                 |  |
|-----------------|-----------------|--|
| $p$             | $Pa, mbar$      | (absolute) pressure  |
| $\Delta p_{FR}$ | $Pa$            | frictional pressure drop   |
| $p^*$           | -               | reduced pressure   |
| $\dot{Q}$       | $W$             | heat duty, thermal capacity, refrigerating capacity                                    |
| $q$             | $W/(kg/s)$      | specific heat flux per circulating (refrigerant) mass flow, spec. energy               |
| $\dot{q}$       | $W/m^2$         | heat flux density, heat flux per unit area   |
| $R$             | $J/kg \cdot K$  | specific gas constant for water, $R = 0.461526 \text{ kJ/kg} \cdot K$                  |
| $R_A$           | $m$             | arithmetic mean surface roughness  |
| $R_D$           | -               | slope in Dühring plot, inverse Dühring gradient  |
| $R_F$           | $m$             | fin height   |
| $Re$            | -               | dimensionless Reynolds number  |
| $r$             | $m$             | radius   |
| $S$             | $J/K, kJ/K$     | entropy  |
| $T$             | $K, ^\circ C$   | temperature, internal/cycle temperature  |
| $\bar{T}$       | $K, ^\circ C$   | entropic mean internal/cycle temperature   |
| $T_F$           | $m$             | fin thickness  |
| $t$             | $K, ^\circ C$   | external heat carrier/coolant temperature  |
| $\bar{t}$       | $K, ^\circ C$   | entropic mean external heat carrier/coolant temperature                                |
| $TTD$           | $K$             | terminal temperature difference, i.e. minimum approach temperature in a heat exchanger |
| $TTD_{SHX}$     | $K$             | terminal temperature difference of the recuperative solution heat exchanger            |
| $U$             | $W/m^2 \cdot K$ | overall heat-transfer coefficient  |
| $u$             | $m/s$           | fluid velocity   |
| $v$             | $m^3/kg$        | specific volume  |
| $w$             | $m$             | width  |
| $X$             | $wt. \%$        | salt concentration in solution in terms of kg salt per kg solution                     |
| $x$             | $m$             | position in flow direction   |
| $Y$             | $m$             | tube pitch   |
| $Y_F$           | $m$             | fin pitch  |
| $y$             | -               | tube pitch ratio (with respect to tube diameter)                                       |

### Greek Variables

|           |                 |  |
|-----------|-----------------|--|
| $\alpha$  | $W/m^2 \cdot K$ | heat-transfer coefficient (HTC)            |
| $\beta_F$ | -               | surface enhancement factor of finned tubes |
| $\gamma$  | -               | ratio                                      |
| $\zeta$   | -               | friction factor                            |
| $\eta$    | -               | efficiency                                 |
| $\lambda$ | $W/m \cdot K$   | thermal conductivity                       |

|                     |                 |  |
|---------------------|-----------------|--|
| $\lambda_{EXC.AIR}$ | -               | excess combustion air coefficient, ratio of combustion air to stoichiometric air |
| $\mu$               | $N \cdot s/m^2$ | dynamic or absolute viscosity  |
| $\nu$               | $m^2/s$         | kinematic viscosity  |
| $\rho$              | $kg/m^3$        | specific density   |
| $\sigma$            | $N/m$           | surface tension  |
| $\dot{\chi}$        | -               | steam quality of a two-phase flow, vapor mass fraction                           |
| $\psi$              | -               | void ratio of a tube bank  |

Note: SI units are employed for all formulas given unless otherwise mentioned in the text. In diagrams and tables, the applied units are explicitly specified for all values given to avoid ambiguities.

**Superscripts**

|   |   |
|---|---|
| ' | liquid phase in general, liquid in saturation   |
| " | gas/vapor phase in general, vapor in saturation |

**Subscripts**

|                |  |
|----------------|--|
| <i>0</i>       | lowest temperature or pressure level of a thermodynamic cycle, refrigeration temperature of a chiller        |
| <i>1</i>       | intermediate temperature or pressure level of a thermodynamic cycle, heat rejection temperature of a chiller |
| <i>2</i>       | highest temperatures or pressure level of a thermodynamic cycle, driving heat temperature                    |
| <i>2P</i>      | two-phase flow   |
| <i>A</i>       | absorber   |
| <i>ACC</i>     | acceleration (pressure drop)   |
| <i>AMB</i>     | ambient  |
| <i>AVAIL</i>   | available  |
| <i>B</i>       | nucleate boiling   |
| <i>BPE</i>     | boiling point elevation  |
| <i>C</i>       | condenser  |
| <i>C</i>       | property at critical point of a fluid  |
| <i>CS</i>      | cross section  |
| <i>CV</i>      | convective   |
| <i>CV</i>      | calorific value  |
| <i>CYC</i>     | cycle (efficiency)   |
| <i>D</i>       | Dühring parameter  |
| <i>D</i>       | with reference to tube diameter  |
| <i>DE</i>      | double-effect  |
| <i>DIAG</i>    | diagonal   |
| <i>E</i>       | evaporator   |
| <i>ENDOREV</i> | endo-reversible, internally reversible   |
| <i>ENTER</i>   | entering a heat exchanger  |
| <i>EQ</i>      | equilibrium  |
| <i>EXC.AIR</i> | excess air (of a combustion process)   |
| <i>F</i>       | fin, finned  |
| <i>FI</i>      | section of finned tubes in the regenerator heat exchanger  |
| <i>FC</i>      | free channel   |
| <i>FG</i>      | flue gas   |
| <i>FGF</i>     | flue gas fired   |
| <i>FGU</i>     | flue gas utilization   |
| <i>FR</i>      | frictional   |
| <i>G</i>       | (re-)generator   |
| <i>G</i>       | gas, gas side of a wall  |



|               |  |
|---------------|--|
| <i>GAS</i>    | natural gas (combustion related properties)  |
| <i>GO</i>     | gas-only; assuming a two-phase flow was completely in gas phase  |
| <i>GRAV</i>   | gravitational (pressure drop)  |
| <i>HH</i>     | half-height  |
| <i>HT</i>     | high-temperature   |
| <i>HTG</i>    | high-temperature (re-)generator in a multistage absorption cycle   |
| <i>I</i>      | inner diameter, inner side of a tube   |
| <i>IN</i>     | inline arrangement of tubes in a bundle  |
| <i>IN</i>     | inlet  |
| <i>INT</i>    | internal   |
| <i>L</i>      | liquid, liquid side of a wall  |
| <i>L</i>      | with reference to a characteristic length in general, with reference to a characteristic length other than tube diameter |
| <i>LT</i>     | low-temperature  |
| <i>LO</i>     | liquid-only, assuming a two phase flow was completely in liquid phase  |
| <i>LO</i>     | longitudinal, in flow direction  |
| <i>LOC</i>    | local (heat transfer)  |
| <i>LTG</i>    | low-temperature (re-)generator in a multistage absorption cycle  |
| <i>MN</i>     | mean   |
| <i>N</i>      | dependent on the number of tube rows   |
| <i>O</i>      | outer diameter, outer side of a tube   |
| <i>ONB</i>    | onset of nucleate boiling  |
| <i>OUT</i>    | outlet   |
| <i>P</i>      | passes in a heat exchanger   |
| <i>PL</i>     | section of plain tubes in the regenerator heat exchanger   |
| <i>Q</i>      | constant heat flux density   |
| <i>QE</i>     | quadruple-effect   |
| <i>RE</i>     | dependent on the Reynolds number   |
| <i>REFR</i>   | refrigerant  |
| <i>REV</i>    | reversible   |
| <i>SAT</i>    | saturation   |
| <i>SHX</i>    | recuperative solution heat exchanger   |
| <i>SOL</i>    | solution   |
| <i>ST</i>     | staggered arrangement of tubes in a bundle   |
| <i>STOIC</i>  | stoichiometric   |
| <i>STRONG</i> | strong solution  |
| <i>T</i>      | constant wall temperature  |
| <i>TB</i>     | tubes  |
| <i>TE</i>     | triple-effect  |
| <i>TOT</i>    | total outer surface of a finned tube   |
| <i>TR</i>     | transversal, normal to flow direction  |
| <i>V</i>      | vapor  |
| <i>W</i>      | wall, tube wall  |

---

|             |   |
|-------------|---|
| <i>WS</i>   | weld seams (for welding heat exchanger tubes into tubesheets) |
| <i>WEAK</i> | weak solution   |

# List of figures

|  |    |
|--|----|
| Fig. 1: Dühring chart for aqueous lithium bromide solutions.....   | 5  |
| Fig. 2: Basic flow scheme of a simple single-effect absorption chiller based on lithium bromide/water.....   | 8  |
| Fig. 3: Flow scheme (top) and component identification (bottom) of a state-of-the-art commercially available steam-fired absorption chiller (Trane Horizon™).....  | 11 |
| Fig. 4: Flow scheme of an integrated single-effect/double-effect (SE/DE) absorption chiller.....   | 13 |
| Fig. 5: Conventional flow schemes (top) and sample temperatures and concentrations of the LiBr solution (bottom) of double-effect chillers comprising series-flow (left) and parallel-flow (right) cycle layouts.....  | 14 |
| Fig. 6: Ideal model for heat driven chillers with three temperature levels.....  | 18 |
| Fig. 7: Endoreversible model for heat driven chillers.....   | 20 |
| Fig. 8: Visualization of equilibrium states and internal mass flows of a sample single-effect chiller (cp. Tab. 4) in a Dühring chart.....   | 25 |
| Fig. 9: Examples for recently installed direct exhaust-fired double-effect chillers with voluminous smoke-tube regenerators covering about half the footprint of the total plant.....  | 34 |
| Fig. 10: Visualization of equilibrium states and internal mass flows of a sample double-effect chiller (cf. Tab. 5) in a Dühring chart.....  | 39 |
| Fig. 11: Relative share of useful flue gas heats in temperature ranges above 190°C, between 110°C and 190°C, and between 90°C and 110°C in dependence on the flue gas entering temperature in exhaust-fired chillers or the adiabatic flame temperature in direct-fired chillers respectively.....                                   | 46 |
| Fig. 12: Comparison of available flue gas heat and heating demand in temperature range 110...190°C.....  | 48 |
| Fig. 13: Flow scheme of a flue-gas fired SE/DE absorption chiller.....   | 50 |
| Fig. 14: Cooling produced from exhaust gas waste heat per total exhaust gas heat capacity $COP_{FGF}$ with reference to the exhaust gas entering temperature.....  | 51 |
| Fig. 15: Flue gas utilization in direct-fired chiller with split/series-flow cycle layout.....   | 52 |
| Fig. 16: Thermodynamic evaluation of different options for integration of a flue gas recuperator in a series-flow double-effect cycle.....   | 53 |
| Fig. 17: Flow scheme (simplified Dühring chart) showing the integration of an exhaust gas recuperator ("EGHX") in the weak solution line between low-temperature solution heat exchanger ("LSHX") and high-temperature solution heat exchanger ("HSHX") in a series-flow double-effect cycle, as suggested by Cho et al. (2005)..... | 54 |
| Fig. 18: Flow scheme of the modified parallel-flow double-effect chiller with additionally installed flue gas recuperator (rightmost device in drawing) that has been experimentally investigated by Yoon et al. (2003).....   | 55 |
| Fig. 19: Potential configuration of a direct-fired chiller with parallel-flow cycle and heat recovery from leaving flue gas and refrigerant condensate.....  | 56 |
| Fig. 20: Advanced direct-fired chiller developed by Japanese consortium.....   | 57 |
| Fig. 21: Flow scheme of a highly efficient direct-fired chiller from Sanyo Electric.....   | 58 |
| Fig. 22: Exhaust-fired SE/DE-chiller with four-stage flue gas utilization.....   | 59 |
| Fig. 23: Flow scheme of a flexible SE/DE-chiller in a CCHP system with two-stage exhaust gas utilization.....  | 60 |
| Fig. 24: Principal sketch of two basic concepts of flue gas fired regenerators: Shell boiler with horizontal smoke tubes completely immersed in the boiling liquid (left) and tube boiler with liquid inside the vertical boiling tubes (right).....   | 62 |

|   |     |
|---|-----|
| Fig. 25: <i>Folded hybrid design of a Sanyo-type direct-fired regenerator. Patent drawings from Furukawa (1988).</i> .....  | 63  |
| Fig. 26: <i>Principal sketch of tube boilers with forced convection and circulation pump (left) and with natural convection and downcomer tubes (right).</i> .....  | 64  |
| Fig. 27: <i>Principal sketch of natural convection boilers with plain and finned boiling tubes.</i> .....   | 65  |
| Fig. 28: <i>Basic settings for heat transfer from flue gas to boiling lithium bromide solution in shell boilers and tube boilers.</i> .....   | 66  |
| Fig. 29: <i>Basic configuration of tube bundles with staggered (left) and in-line (right) arrangement. Definition of transverse and longitudinal tube pitch.</i> .....  | 76  |
| Fig. 30: <i>Definition of fin height, fin thickness and fin pitch of tubes with outer circular fins.</i> .....  | 77  |
| Fig. 31: <i>Development of a two-phase flow in a vertical tube with uniform wall heat flux (not to scale).</i> .....  | 88  |
| Fig. 32: <i>The influence of heat flux on two-phase flow behavior. Cited from Lienhard &amp; Lienhard (2003).</i> .....   | 89  |
| Fig. 33: <i>Schematic visualization of incipience condition for onset of nucleate boiling assuming upward flow next to a heated surface. Cited from Kamil et al. (2005).</i> .....  | 92  |
| Fig. 34: <i>Nucleate boiling heat transfer coefficients <math>\alpha_B</math> and exponents N for water.</i> .....  | 98  |
| Fig. 35: <i>Boiling heat transfer coefficients <math>\alpha_B</math> for water in vertical tubes as predicted by the correlations of Cooper (1989) and Steiner &amp; Taborek (1992) in dependence of the reduced pressure.</i> .....              | 102 |
| Fig. 36: <i>Relative nucleate boiling heat transfer coefficient of aqueous lithium bromide solution in relation to pure water at the same saturation pressure and heat flux density.</i> .....  | 106 |
| Fig. 37: <i>Standard setup of a steam-heated vertical thermosiphon reboiler. Cited from Arneht &amp; Stichlmair (2001).</i> .....   | 111 |
| Fig. 38: <i>Schematic of a vertical thermosiphon reboiler with a single boiling tube (left) and characteristic temperature profile inside the boiling tube (right).</i> .....   | 112 |
| Fig. 39: <i>Measured temperature profiles (left) and mean heat transfer coefficients in heating and evaporation zone (right). Visualization of experimental data by Nagel (1962) and Nagel &amp; Kirschbaum (1963).</i> .....                     | 114 |
| Fig. 40: <i>Specific overall heat flux and boiling tube mass flux density in dependence on the total driving temperature difference in a thermosiphon reboiler for the boiling of water at atmospheric pressure.</i> .....                        | 115 |
| Fig. 41: <i>Measured wall temperature profiles during the atmospheric boiling of water in an electrically heated vertical thermosiphon reboiler with tube length <math>l = 1.9</math> m and inner diameter <math>d_i = 25.25</math> mm.</i> ..... | 117 |
| Fig. 42: <i>Mean convective heat transfer coefficient and frictional pressure drop at the flue gas side of boilers with gas flow inside tubes as functions of inner diameter and Reynolds number.</i> .....                                       | 136 |
| Fig. 43: <i>Mean convective heat transfer coefficient and frictional pressure drop at the flue gas side of boilers with gas flow across tube banks as functions of outer diameter and Reynolds number.</i> .....                                  | 138 |
| Fig. 44: <i>Feasible Reynolds numbers, heat transfer coefficients and pressure drops at the flue gas side of boilers with gas flow inside tubes.</i> .....  | 139 |
| Fig. 45: <i>Feasible Reynolds numbers, heat transfer coefficients and pressure drops at the flue gas side of boilers with gas flow across plain (upper two diagrams) and finned (bottom two diagrams) tube bundles.</i> .....                     | 141 |
| Fig. 46: <i>Feasible “effective” heat transfer coefficients and corresponding pressure drops in dependence on the Reynolds number for gas flow inside tubes (left) and for gas flow across finned bundles (right).</i> .....                      | 142 |
| Fig. 47: <i>Variation of tube arrangement and tube pitch ratio for flue gas flow across plain tube bundles.</i> .....   | 145 |

|   |     |
|---|-----|
| <i>Fig. 48: Variation of tube arrangement and tube pitch ratio for flue gas flow across finned tube bundles.</i>  | 146 |
| <i>Fig. 49: Ranges of feasible heat transfer coefficients and pressure drops in the fully laminar and the fully turbulent region for heat exchangers with gas flow inside tubes.</i>  | 148 |
| <i>Fig. 50: Variation of tube arrangement and tube pitch ratio for flue gas flow across plain tube bundles.</i>   | 150 |
| <i>Fig. 51: Variation of tube arrangement and tube pitch ratio for flue gas flow across finned tube bundles.</i>  | 151 |
| <i>Fig. 52: Patent drawing of the direct-fired regenerator prototype as disclosed by Tucker et al. (2000) and Tucker et al. (2001). No. 56 denotes the additional flue gas recuperator ("economizer") mounted downstream of the main regenerator.</i>   | 160 |
| <i>Fig. 53: Photograph of the regenerator test station before (left) and after (right) the installation of the evaporator/absorber unit.</i>  | 161 |
| <i>Fig. 54: Flow scheme of the initial regenerator test rig in the lab before the installation of the evaporator/absorber unit. Drawing taken from Dantele (1999).</i>  | 161 |
| <i>Fig. 55: Simplified P&amp;ID showing a subset of measuring points at regenerator prototype and test rig that has been used for the evaluations presented below.</i>  | 162 |
| <i>Fig. 56: Range of available experimental data from 13 stationary operational states with full measurement instrumentation installed (filled symbols) and 7 additional stationary states recorded prior to completion of the instrumentation (empty symbols), compared to the design values of the regenerator prototype at full load operation (enlarged symbols).</i> | 173 |
| <i>Fig. 57: Different approaches to the estimation of the radiative heat transfer over the gas burner duty.</i>   | 176 |
| <i>Fig. 58: Range of available experimental data from stationary operational states in terms of specific numbers.</i>   | 181 |
| <i>Fig. 59: Range of experimental heat fluxes at the gas side of the regenerator in comparison with the design values at full load operation.</i>   | 181 |
| <i>Fig. 60: Main influencing variables for determination of experimental heat transfer coefficients at the flue gas side of the regenerator prototype and assumed experimental uncertainties for these variables.</i>   | 184 |
| <i>Fig. 61: Overall heat transfer coefficients vs. heat flux at plain (left) and finned (right) sections of the regenerator with respect to the outer surface of plain tubes.</i>   | 185 |
| <i>Fig. 62: Effective flue gas side heat transfer coefficients with respect to the surface of plain tubes (left) and flue gas side Nusselt numbers (right) vs. the mean flue gas Reynolds numbers in plain and finned section.</i>  | 187 |
| <i>Fig. 63: Experimentally found vs. theoretically predicted Nusselt numbers (top two diagrams) and relative deviation of experimental from theoretical values (bottom two diagrams).</i>   | 189 |
| <i>Fig. 64: Experimentally found and theoretically predicted pressure drop at the flue gas side of the regenerator vs. the free-channel mass flux.</i>  | 191 |
| <i>Fig. 65: Experimental and predicted frictional pressure drops (upper two diagrams) and friction factors (bottom two diagrams) for the flue gas flow across the section of plain tubes (left two diagrams) and across the section of finned tubes (right two diagrams) vs. the mean Reynolds numbers in the respective sections.</i>                                    | 193 |
| <i>Fig. 66: Experimentally found vs. theoretically predicted pressure drops in the flue gas.</i>  | 194 |
| <i>Fig. 67: Measured and calculated differences in the solution temperature in the regenerator prototype.</i>   | 195 |
| <i>Fig. 68: Velocity of natural convection flow in downcomer tubes in dependence of various possible influencing variables.</i>   | 197 |
| <i>Fig. 69: Estimated cross-sectional mass flux in boiling tubes vs. surface heat flux at the solution side.</i>  | 198 |

|   |            |
|---|------------|
| <i>Fig. 70: Measured tube wall temperatures at the flue gas side vs. the measured temperature of the leaving strong solution. ....</i>  | <i>199</i> |
| <i>Fig. 71: Temperature differences between measuring points at the boiling tube walls (gas side) and the leaving solution temperature vs. the mean heat flux at the solution side of all boiling tubes. ....</i>                 | <i>200</i> |
| <i>Fig. 72: Temperature difference between boiling tube wall (gas side) and leaving solution temperature in dependence of the location of the wall temperature measurement. ....</i>  | <i>201</i> |
| <i>Fig. 73: Temperature difference between measured tube wall temperatures (gas side) and estimated local saturation temperatures vs. the estimated local surface heat flux at each position. ....</i>                            | <i>204</i> |
| <i>Fig. 74: Local heat flux vs. wall superheat at liquid side (Nukiyama-plot). Experimental values in comparison with various boiling correlations. ....</i>  | <i>207</i> |
| <i>Fig. 75: Boiling heat transfer coefficients vs. heat flux. Comparison of experimental values with various nucleate boiling correlations. ....</i>  | <i>209</i> |
| <i>Fig. 76: Boiling heat transfer coefficients vs. heat flux. Comparison of experimental values with various calculations for convective heat transfer in a two-phase flow regime (convective flow boiling). ....</i>             | <i>211</i> |
| <i>Fig. 77: Raw data from pressure drop measurements (empty symbols) and interpolations (colored lines) of data points from stationary operational states (filled black circles) that have been employed for evaluation. ....</i> | <i>239</i> |
| <i>Fig. 78: Interpolation of flue gas properties between individual operational states for calculation of theoretical pressure drop curves. ....</i>  | <i>240</i> |

# List of tables

|   |     |
|---|-----|
| Tab. 1: Comparison of typical operational data of indirect-fired single-effect and double-effect absorption chillers (full load operation).....   | 12  |
| Tab. 2: Standard rating conditions for absorption chillers. Leaving fluid temperatures have been calculated for ARI conditions assuming COP of 0.7 for single-effect chillers and COP of 1.2 for double-effect chillers.....  | 16  |
| Tab. 3: Driving temperature differences in main components of absorption chillers – lower technical limits and typical design values.....   | 19  |
| Tab. 4: Example calculation utilizing the endoreversible model and approximate Dühring coefficients for evaluation of a typical single-effect chiller running at ARI standard conditions.....   | 22  |
| Tab. 5: Example calculation of mean internal and external temperatures in a typical double-effect chiller running at ARI standard conditions utilizing.....   | 31  |
| Tab. 6: Arrangement constant $C_A$ for heat transfer in fluid flow across finned tube bundles, in dependence on arrangement and number of consecutive rows of tubes $N_{TB,LO}$ .....   | 81  |
| Tab. 7: Correction factors $f_{N,ST}$ and $f_{N,IN}$ for friction pressure drop across finned tube bundles in dependence on arrangement and number of consecutive rows of tubes $N_{TB,LO}$ .....   | 85  |
| Tab. 8: Coefficient $C_{REST}$ and exponent $N_{ST}$ for friction pressure drop across finned tube bundles with staggered arrangement in dependence of the magnitude of the Reynolds number $Re_D$ .....  | 85  |
| Tab. 9: Coefficient $C_{RE,IN}$ and exponent $N_{IN}$ for friction pressure drop across finned tube bundles with in-line arrangement in dependence of the magnitude of the Reynolds number $Re_D$ .....   | 86  |
| Tab. 10: Normalization values for saturated pool boiling correlation with respect to more or less typical operating conditions for technical boiling processes and typically machined copper tubes as heater.....   | 96  |
| Tab. 11: Surface roughness and thermal effusivity of steel tubes in water boilers.....  | 96  |
| Tab. 12: Normalization values for nucleate boiling in vertical tubes.....   | 101 |
| Tab. 13: Comparison of important parameters for design of tube boilers at high and low absolute pressure.....   | 110 |
| Tab. 14: Typical design and operation data of steam-fired natural convection boilers according to Arneht (1999).....  | 112 |
| Tab. 15: Approximate relations for heat transfer and pressure drop.....   | 130 |
| Tab. 16: General assumptions and boundary conditions for comparison of different heat exchanger designs.....  | 133 |
| Tab. 17: Parameter variation considered for comparison of different designs.....  | 134 |
| Tab. 18: Comparison of design data of the heat exchanger configurations yielding the largest feasible heat transfer coefficient in regenerators fired by exhaust gas under the boundary conditions of Tab. 16 and Tab. 17 for different basic regenerator designs (cf. Fig. 44 - Fig. 48 in 5.3.3)..... | 152 |
| Tab. 19: Comparison of design data of the heat exchanger configurations yielding the largest feasible heat transfer coefficient in direct-fired regenerators under the boundary conditions of Tab. 16 and Tab. 17 for different basic regenerator designs (cf. Fig. 49 - Fig. 51 in 5.3.4).....         | 153 |
| Tab. 20: Subset of the measuring points in the internal cycle and at the boiling tube walls.....  | 164 |
| Tab. 21: Subset of the measuring points in the external cooling water loops.....  | 165 |
| Tab. 22: Subset of the measuring points in the natural gas / combustion air / flue gas system.....  | 166 |
| Tab. 23: Raw data from stationary operational states no. 1-10 (mean values of measured variables).....  | 236 |
| Tab. 24: Raw data from stationary operational states no. 11-21 (mean values of measured variables).....   | 237 |





# 1 Introduction

## ***1.1 Absorption refrigeration***

Absorption chillers, unlike the more prominent vapor recompression chillers, have the capability of utilizing heat, instead of mechanical work, as the main driving power to produce usable cold. The dominant field of application in terms of total installed capacity, for this kind of technology, is the centralized air conditioning of buildings, especially in the U.S. and in various Asian countries. As this purpose requires chilled water above the freezing point, here especially absorption chillers based on the working pair water/lithium bromide are of economic importance. In this case, pure water serves as the refrigerant and aqueous lithium bromide salt solution as the absorbent. Such machines are available from series production in the range from about 50 kilowatts to several megawatts cooling capacity.

Due to the high latent heat of vaporization of the refrigerant water and the non-volatility of the lithium bromide salt, this working pair is superior to many other possible working fluids, in terms of the combination of the good thermal efficiency of the refrigeration process together with the relatively simple apparatus design. Another economically important working pair is ammonia/water; it has a long tradition in industrial refrigeration and is still the first choice where absorption refrigeration applications at temperatures below zero degrees Celsius are concerned.

The absorption heat pump is another technology that is quite similar to absorption chillers; both water/lithium bromide and ammonia/water based machines are commercially available. Concurrently, Asian manufacturers offer various types of water/lithium bromide based absorption heat pumps that are effectively slightly modified standard chillers from series production. Nevertheless, the number of absorption heat pumps produced, compared to absorption chillers, is still much lower. This work mainly focuses on water/lithium bromide based absorption chillers for standard air-conditioning applications. However, as the technology is by and large the same, the findings also apply to water/lithium bromide based absorption heat pumps.

Traditionally, standard manufacturers of water/lithium bromide absorption chillers have offered their series production units either steam-fired, hot water fired or direct-fired. The utilization of waste heat from industrial processes or power generation in steam or hot water fired chillers, either on-site or remotely – connected via a district-heating network, has always been a major field of application for absorption refrigeration technology. Competing directly with electrically driven vapor recompression chillers, absorption machines fired from fossil

fuel combustion are attractive in regions where electricity is either in short supply or expensive during the daily peak hours of cooling demand.

Recent developments in the field of hot water fired chillers, which are typically waste heat driven, aim to extend the fields of application by the better utilization of low-grade heat sources or adaptation to the needs of special applications, like solar cooling. On the other hand, in the field of direct-fired chillers, recent work has targeted an increase of the efficiency with respect to primary energy utilization. A new subtype, the direct-exhaust-fired chiller, was introduced to serve the requirements for increased energy efficiency in combined cooling heating and power (CHP/CCHP) systems. The direct utilization of hot exhaust gas from a gas turbine or a combustion engine, employed as prime movers, without an intermediate heat carrier cycle is a new field of application for absorption chillers. It has been established in recent years, following a general trend towards efficient energy utilization in decentralized power generation. Direct-exhaust-fired chillers are based on the established design of direct-fired chillers; however, some modifications are required.

## **1.2 Work outline**

This work focuses on water/lithium bromide based absorption chillers that utilize a hot flue gas stream, either from the direct combustion of fossil fuels or from a waste heat source, as the main driving energy input. The main objective is to address issues relating to the energetic and economic efficiency, which are specific to plants with direct flue gas utilization and not common to all kinds of absorption chillers.

Intentionally, neither a fundamental introduction into the basics of absorption refrigeration technology nor an in-depth discussion of the general features of highly efficient absorption chillers are provided in this work, as these topics are already sufficiently covered in the literature. Nevertheless, an introduction of the terminology and basic thermodynamic concepts to be employed in this work is provided at the beginning. Also, the typical design data that will be used as the basis for further calculations are quoted.

Actually, the efficient utilization of the flue gas heat that is available at a gliding temperature is a key issue in both direct and exhaust-fired absorption chillers. On the one hand, this affects the appropriate cycle design of the absorption refrigeration process, and on the other hand, it requires the suitable design of the respective flue gas heat exchangers, especially for the high-temperature regenerator. Therefore, this work starts with a discussion of thermodynamically promising concepts for efficient flue gas utilization in absorption chillers and their effectiveness and feasibility at different boundary conditions.

The main part of this work focuses on the design of the flue gas fired regenerator, which is a key component for thermo-economic optimization. Different heat exchanger concepts are evaluated based on fundamental relations between the heat transfer, pressure drop, and geometry parameters. Promising configurations for different applications are determined by a numerical parameter study.

Finally, experimental results from the laboratory testing of a novel regenerator prototype are presented.

## 2 State of the art of absorption refrigeration

### 2.1 Fundamentals and terminology

#### 2.1.1 Thermodynamic fundamentals

The fundamentals of absorption technology are presented in numerous literature sources; the comprehensive works of *Herold et al. (1996)*, *Ziegler (1997)*, and *Schweigler (1999)* can be given as examples, which are more recent. Therefore, within this work fundamentals and basic concepts of this technology common to all commercially available chillers will not be repeated again in detail. Nomenclature and terminology, however, may vary between different literature sources; therefore naming conventions and common abbreviations that will be used within this work shall be introduced below.

Lithium bromide based absorption chillers utilize the well-known physical effect of the boiling point elevation: the boiling point of water – which acts as the refrigerant – rises at constant absolute pressure, when a soluble salt – lithium bromide in this case – is added to the liquid phase. This process being reversed, refrigerant vapor can be absorbed by a salt solution at the same pressure level but at a higher temperature than that of a simultaneous evaporation process. Unlike the boiling of binary mixtures of two volatile components like ammonia/water that are present both in the vapor phase as well, only pure water is present in the vapor phase above boiling aqueous lithium bromide solutions. This simplifies things a lot with lithium bromide, regarding both thermodynamic framework and machinery design.

The capability of the dissolved salt to raise the boiling point of the refrigerant however is limited by its solubility at the required temperatures. For lithium bromide in aqueous solution, solubility ranges from concentrations of about  $60\text{wt.}\%$ <sup>2</sup> at room temperature to  $70\text{wt.}\%$  and more above  $100^\circ\text{C}$  liquid temperature, this is quite a lot compared to e.g. common table salt. Of course, chiller applications mainly focus on process concentrations close to the solubility limit as they allow for the greatest temperature lifts<sup>3</sup>. Mainly for applications utilizing low grade driving heat, lower salt concentrations down to  $40\text{wt.}\%$  are of technical importance, too.

Generally, the boiling point elevation between salt solution and pure refrigerant  $\Delta T_{BPE} = T_{SAT,SOL} - T_{SAT,REFR}$  is a function of both, the salt concentration in solution  $X_{SOL}$  and the temperature itself:

<sup>2</sup> i.e. 60 kg salt per 100 kg solution, following this commonly used convention

<sup>3</sup> The temperature difference between the temperature level of the reject heat dissipation and the temperature level of the generation of cooling is called “temperature lift”.

$$\Delta T_{BPE} = T_{SAT,SOL} - T_{SAT,REFR} = f(X_{SOL}, T_{SAT,REFR}) \quad (2.1)$$

Evaluation of experimentally obtained property data shows, however, that for several common working fluids the function  $\Delta T_{BPE}(X_{SOL}, T_{SAT,REFR})$  is nearly linear in the absolute refrigerant temperature; this behavior is often called *Dühring's rule*. Therefore, the relation between solution temperature  $T_{SAT,SOL}$  and refrigerant temperature  $T_{SAT,REFR}$  at the same equilibrium vapor pressure can be expressed by a linear function of the Dühring-coefficients<sup>4</sup>  $A_D(X_{SOL})$ , also known as Dühring-gradient, and  $B_D(X_{SOL})$ , also known as Dühring-intercept, both only dependent on the salt concentration:

$$T_{SAT,SOL} = A_D(X_{SOL}) \cdot T_{SAT,REFR} + B_D(X_{SOL}) \quad (2.2)$$

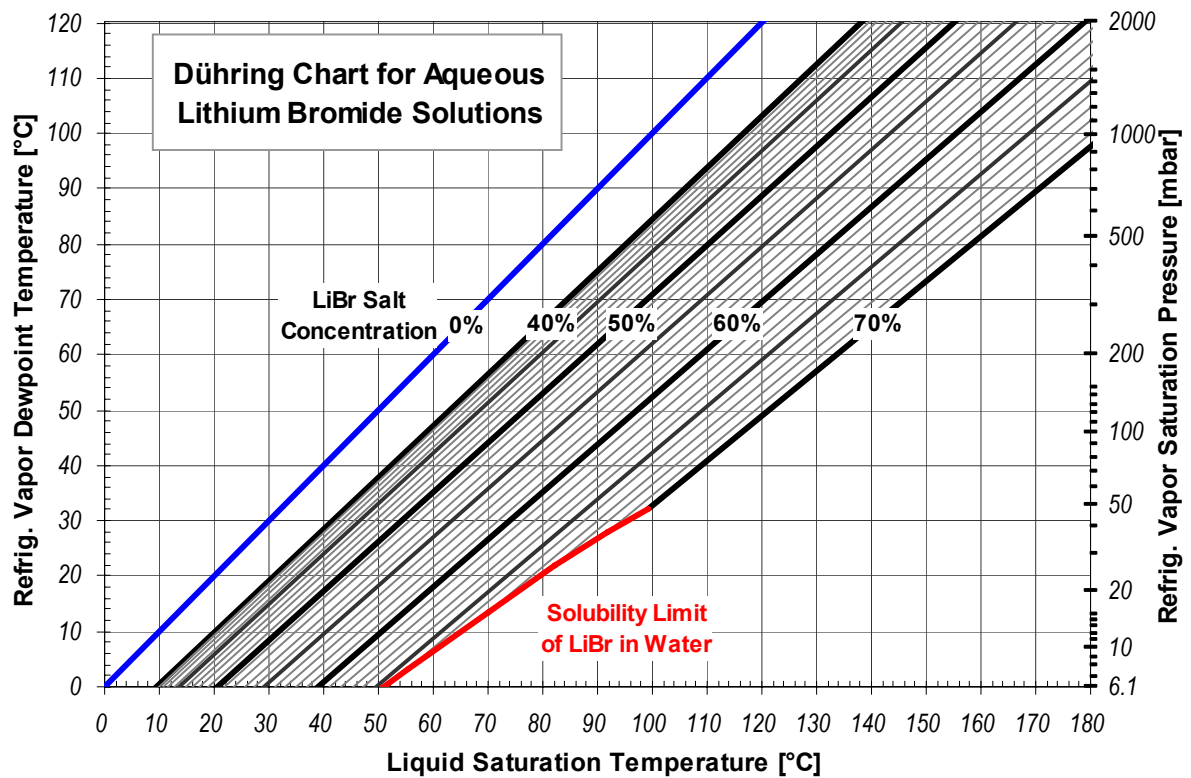


**Fig. 1: Dühring chart for aqueous lithium bromide solutions.**

For creation of this graph, proprietary property data software of the ZAE Bayern has been employed utilizing Dühring-coefficients according to [Feuerecker et al. \(1994\)](#).

Consequently, in a diagram with the x-axis displaying the boiling temperature of lithium bromide solution  $T_{SAT,SOL}$  and the y-axis giving the dewpoint temperature of the refrigerant vapor  $T_{SAT,REFR}$  (cf. Fig. 1), the equilibrium states for each salt concentration form a straight line with the slope  $R_D(X_{SOL}) = 1 / A_D(X_{SOL})$  being the inverse Dühring gradient. The linear equation for these equilibrium states reads:

$$T_{SAT,REFR} = [T_{SAT,SOL} - B_D(X_{SOL})] / A_D(X_{SOL}) = [T_{SAT,SOL} - B_D(X_{SOL})] \cdot R_D(X_{SOL}) \quad (2.3)$$

<sup>4</sup> Sometimes there is also found an alternative definition in literature where the Dühring-coefficients are exchanged:  $A^*(X)=B(X)$  and  $B^*(X)=A(X)$

This kind of diagram is commonly referenced as Dühring chart<sup>5</sup> and widely used to visualize the relation between salt concentration, boiling temperature, and vapor dewpoint of lithium bromide solutions.

For aqueous lithium bromide solutions, the slope parameter  $R_D(X_{SOL})$  turns down with increasing salt content from the value of exactly 1.0 for pure water to values of about 0.8 at the solubility limit while the intercept  $B_D(X_{SOL})$  ranges between 0 K and about -15 K<sup>6</sup>. As for aqueous lithium bromide solutions  $B_D$  is a small number compared to the applicable refrigerant temperatures of at least 273 K, the slope parameter  $R_D$  can be estimated from the quotient of the saturation temperatures of pure water  $T_{SAT,REFR}$  and salt solution  $T_{SAT,SOL}$ :

$$R_D \approx T_{SAT,REFR} / T_{SAT,SOL} \Leftrightarrow B_D \approx 0 \text{ (deviation of } R_D \leq 5\%) \quad (2.4)$$

A quite good approximation is the assumption of a mean value of -7.5 K for the intercept  $B_D$  that leads to:

$$R_D \approx T_{SAT,REFR} / (T_{SAT,SOL} + 7.5 \text{ K}) \Leftrightarrow B_D \approx 7.5 \text{ K (deviation of } R_D \leq 1.8\%) \quad (2.5)$$

For more accurate calculations least-square-fits for the Dühring-gradient  $A_D(X_{SOL})$  and the Dühring-intercept  $B_D(X_{SOL})$  in dependence of the salt concentration can be found in various literature sources, whereof especially the frequently cited work of [Feuerecker et al. \(1994\)](#) and the quite comprehensive recent work of [Chua et al. \(2000a\)](#) is to be mentioned. However, there are also authors who directly provide the refrigerant dewpoint temperature as a polynomial function of both, solution temperature and salt content without calculating Dühring-coefficients. A recent example of the latter approach is the comprehensive study of [Kaita \(2001\)](#). Unless otherwise noted for calculations within this work proprietary property data software of the ZAE Bayern has been employed utilizing Dühring-coefficients according to [Feuerecker et al. \(1994\)](#) for saturation temperature calculations.

If the functional dependence of the vapor pressure of the pure refrigerant  $p_{SAT,REFR}$  on the temperature  $T_{REFR}$  is known, then also the vapor pressure of the salt solution can be expressed as a function of solution temperature and salt content.

$$\begin{aligned} p_{SAT,SOL}(T_{SOL}, X_{SOL}) &= p_{SAT,REFR}(T_{SAT,REFR}(T_{SOL}, X_{SOL})) \\ &= p_{SAT,REFR}[(T_{SAT,SOL} - B_D(X_{SOL})) \cdot R_D(X_{SOL})] \end{aligned} \quad (2.6)$$

<sup>5</sup> Originally, the term Dühring chart indicated the inverse diagram with the x-axis showing the boiling/condensation temperature of the pure solvent and the y-axis giving the related temperature of the salt solution. Therefore also the definition  $R^*(X) = 1 / R(X) = A(X)$  can be found in literature which then indicates the slope of the straight lines of constant concentration in the original Dühring chart.

<sup>6</sup> It is also popular defining the Dühring-coefficients for temperatures in °C instead of Kelvin. For this case numerical values of the Dühring-intercept  $B$  range from 0°C to about 80°C.

According to the Clausius-Clapeyron equation for evaporation with  $\Delta h_{VAP}$  being the specific heat of evaporation and  $R$  being the specific gas constant<sup>7</sup> of the respective substance:

$$\partial \ln(p_{SAT}) / \partial (-1/T_{SAT}) \approx \Delta h_{VAP} / R, \text{ for water: } R_{H_2O} = 0.461526 \text{ kJ}/(\text{kg} \cdot \text{K}) \quad (2.7)$$

The dependence of the vapor pressure on temperature can be approximated by an exponential law:

$$p_{SAT,REFR}(T_{SAT,REFR}) \approx p_0 \cdot e^{-\Delta h_{VAP} / R \cdot T_{SAT,REF}} \quad (2.8)$$

Actually the specific heat of evaporation is not constant but also dependent on boiling temperature  $\Delta h_{VAP} = \Delta h_{VAP}(T_{SAT,REFR})$ , however, mean coefficients of  $p_{0,H_2O} \approx 8.7 \cdot 10^{10} \text{ Pa}$  and  $(\Delta h_{VAP}/R)_{H_2O} \approx 5100 \text{ K}$  give reasonable results for water at 0...3 bar and respective saturation temperatures. For calculations that are more accurate, the simple exponential law provided in (2.8) can be replaced by the normative calculation methods<sup>8</sup> IAPWS-95 and IAPWS-IF97 put down in the respective releases of the International Association for the Properties of Water and Steam *IAPWS (1996)* and *IAPWS (1997)*.

## 2.1.2 Basic absorption cycle

Every absorption chiller working with water/lithium bromide comprises at least one evaporator (E) where the refrigerant being pure water is evaporated generating usable cold, and at least one absorber (A) at the same pressure level where the refrigerant vapor is absorbed into an aqueous lithium bromide solution. At a higher pressure and temperature level, there is at least one solution (re-)generator (G) where the salt solution is concentrated by boiling off the absorbed refrigerant, and finally at least one condenser (C) where this vaporous refrigerant is condensed again before being fed back into the evaporator.

This work will follow the convention that the lithium bromide solution entering the absorber with a low refrigerant content but a high salt content is referenced as “strong” (i.e. strong absorption capability) or “concentrated” (with respect to salt concentration) while the solution leaving the absorber having a high refrigerant content is called “weak” (i.e. weak absorption capability) or “diluted”. Along with the decreasing or increasing salt concentration, the saturation temperature of the solution changes according to (2.2) within an absorber or regenerator at constant vapor pressure.

<sup>7</sup> The specific gas constant of a substance is the quotient of the universal gas constant and the molar mass of this substance. For e.g. water with  $R_U$  being the universal gas constant and  $M_{H_2O}$  being the molar mass of water, the specific gas constant yields:  $R_{H_2O} = R_U / M_{H_2O}$

<sup>8</sup> Note that the IAPWS calculation methods do not employ any exponential function at all for calculating the vapor pressure.

A single-effect (“SE”) chiller, also known as “single-stage chiller” represents the most simple type of an absorption chiller. It comprises just one of each previously mentioned component: evaporator, absorber, regenerator, and condenser; reject heat from both, absorber and condenser has to be transferred to a heat sink like e.g. a cooling tower by an external coolant loop. The schematic typically is completed by some pumps, valves, and at least one recuperative heat exchanger in the solution cycle (SHX).

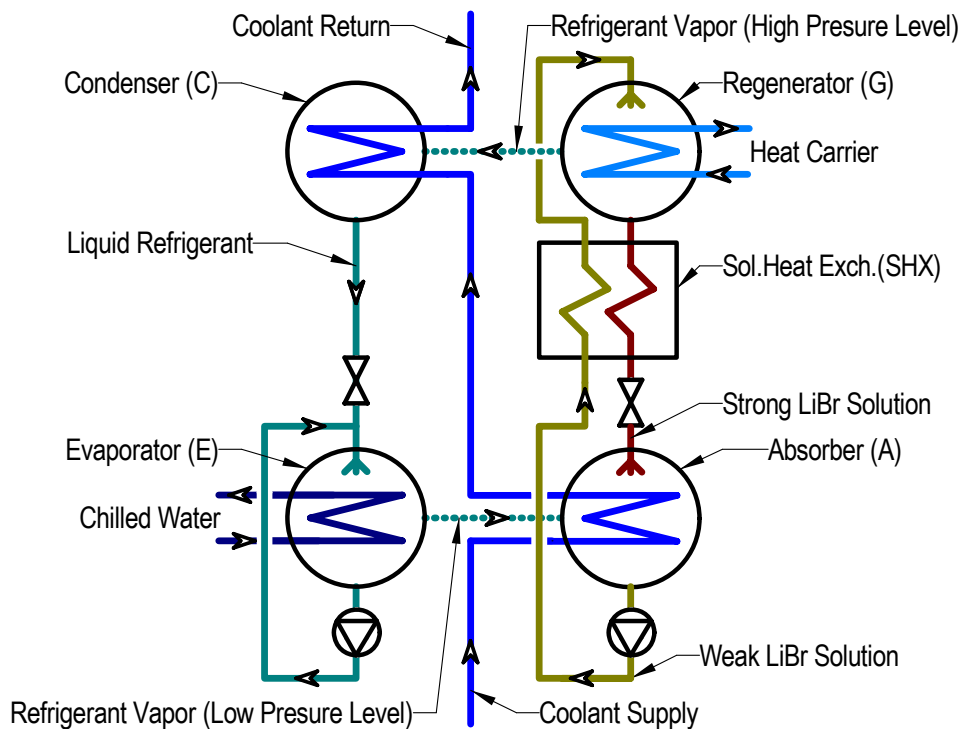


**Fig. 2: Basic flow scheme of a simple single-effect absorption chiller based on lithium bromide/water.**

Fig. 2 gives the basic flow scheme of such a simple absorption chiller, comprising all components that are active under steady-state operation. Some more valves and pipes are required in every real machine for operation control and servicing procedures (e.g. startup, shutdown, purging, crystallization prevention). Finally, in actual machines heat exchanger pairs at the same pressure level with a vapor interconnection in-between like evaporator-absorber and regenerator-condenser are typically integrated into the same pressure vessel. If this refrigerating cycle is to be utilized as heat pump, the chilled water lines have to be connected to the heat source while the coolant line shown in Fig. 2 carries the useful heat.

In all absorption chillers, the circulation rate of the absorbent is a multiple of the refrigerant mass flow. This is expressed by the specific solution flow rate  $f$  that is calculated as the ratio of solution mass flow to refrigerant mass flow. For a single-effect cycle where weak solution flow  $\dot{M}_{WEAK}$  and strong solution flow  $\dot{M}_{STRONG}$  differ by just the refrigerant mass flow  $\dot{M}_{REFR}$ , the definitions for the specific circulation rates of strong solution  $f_{STRONG}$  and weak solution  $f_{WEAK}$  read:



$$\dot{M}_{WEAK} = \dot{M}_{STRONG} + \dot{M}_{REFR} \quad (2.9)$$

$$f_{STRONG} = \dot{M}_{STRONG} / \dot{M}_{REFR} \quad (2.10)$$

$$f_{WEAK} = \dot{M}_{WEAK} / \dot{M}_{REFR} = 1 + f_{STRONG} \quad (2.11)$$

These specific circulation rates are directly linked to the concentration difference  $\Delta X_{SOL} = X_{STRONG} - X_{WEAK}$  between strong and weak solution:

$$f_{STRONG} = X_{WEAK} / (X_{STRONG} - X_{WEAK}) = X_{WEAK} / \Delta X_{SOL} \quad (2.12)$$

$$f_{WEAK} = X_{STRONG} / (X_{STRONG} - X_{WEAK}) = X_{STRONG} / \Delta X_{SOL} \quad (2.13)$$

Typical values for full load operation range from specific solution circulations of at least 7 to about 30; respective concentration differences run from up to 9 wt.% down to 2 wt.% strongly dependent on application and heat exchanger design. From Fig. 2 it is obvious that lower solution circulations are advantageous in principle as they allow for a smaller and therefore less expensive solution heat exchanger. On the other hand, there are two main factors providing a lower limit for the solution circulation: First, the solubility limit of the salt (see Fig. 1) imposes some constraints on the possible concentration difference  $\Delta X_{SOL}$  and second there is a certain solution flow required to ensure a proper wetting of the absorber heat exchanger surface. For common heat exchanger designs, a specific strong solution circulation of 7 already requires a height of the tube bundle in the absorber of at least 1 meter, which is more or less a practical limit for a compact plant design. A more detailed discussion of the impact of the solution circulation on the heat exchanger design is given by [Schweigler \(1999\)](#).

From property data for common operating conditions, a typical shift in saturation temperature of about 2 K for a change of 1 wt.% in salt content can be obtained. However, this is no constant; actually, this gradient itself varies between about 1.3 K/wt.% and 2.6 K/wt.% along with changes in temperature and salt content. Nevertheless, it can be favorable for system-level calculations to operate with a mean saturation temperature together with a mean solution concentration for an absorber or regenerator, what still is a reasonable approximation for small concentration differences of a few percent between strong and weak solution.

Utilizing this approximation, the correlation of refrigerant saturation temperature in an evaporator  $T_E$  and the corresponding mean saturation temperature  $T_A$  of a salt solution of the mean concentration in an attached absorber can be written on the lines of (2.3):

$$T_E = (T_A - B_D(\bar{X}_{SOL})) \cdot R_D(\bar{X}_{SOL}) \quad (2.14)$$

If there is a regenerator working at the same mean salt concentration  $\bar{X}_{SOL}$  as the above-mentioned absorber, the respective correlation for mean condenser temperature  $T_C$  and mean regenerator temperature  $T_G$  is:

$$T_C = (T_G - B_D(\bar{X}_{SOL})) \cdot R_D(\bar{X}_{SOL}) \quad (2.15)$$

Subtraction eliminates  $B_D(\bar{X}_{SOL})$  and leads to the Dühring-equation<sup>9</sup> of the basic absorption cycle:

$$T_C - T_E = (T_G - T_A) \cdot R_D(\bar{X}_{SOL}) \quad (2.16)$$

In contrast to vapor compression chillers driven by mechanical work where efficiency is typically expressed in units of produced refrigeration per one unit of consumed electricity, for the specification of absorption chiller efficiency the relatively small electricity consumption of pumps, control valves, etc. is typically neglected. The thermal efficiency number  $COP$  (=coefficient of performance) for cooling mode of an absorption machine is defined as ratio of refrigeration capacity to consumed driving heat:

$$COP = COP_C = \dot{Q}_E / \dot{Q}_G \quad (2.17)$$

Here  $\dot{Q}_E$  is the refrigerating capacity at the evaporator and  $\dot{Q}_G$  is the heat consumption at the externally heated regenerator. For the same machine utilized as heat pump the thermal efficiency number  $COP_H$  can be defined as ratio of absorber and condenser reject heat to consumed driving heat

$$COP_H = (\dot{Q}_A + \dot{Q}_C) / \dot{Q}_G \approx 1 + COP_C \quad (2.18)$$

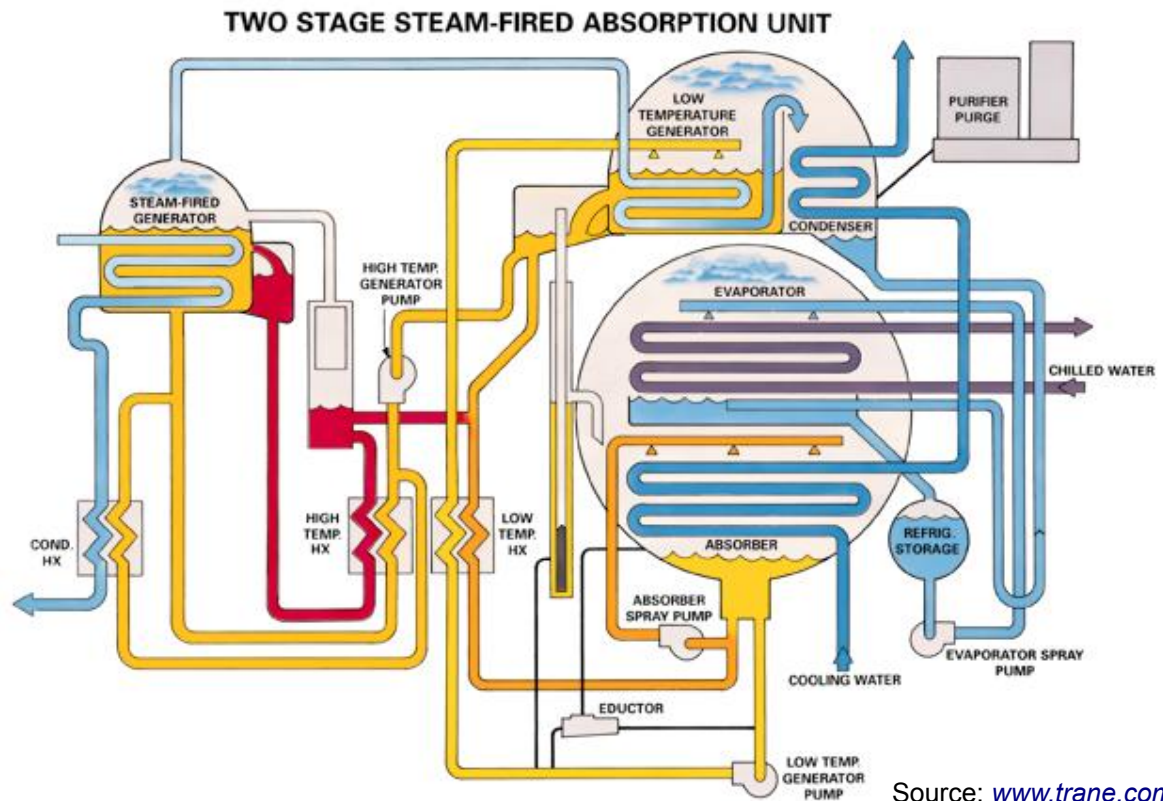
where  $\dot{Q}_G$  is the heat consumption at the externally heated regenerator, and  $\dot{Q}_A$  and  $\dot{Q}_C$  is the reject heat at absorber and condenser, respectively, which is utilized for heating purposes. If the net heat loss<sup>10</sup> of the absorption machine to ambient can be neglected the simple relation between  $COP_C$  and  $COP_H$  is valid:

$$\dot{Q}_E + \dot{Q}_G = \dot{Q}_A + \dot{Q}_C \Leftrightarrow COP_H = 1 + COP_C \quad (2.19)$$

<sup>9</sup> There also exists the alternative formulation  $T_G - T_A = (T_K - T_V) \cdot R^*(X_{SOL})$  in literature, based on the alternative definition of the Dühring-coefficient  $R^*(X_{SOL}) = 1 / R(X_{SOL})$

<sup>10</sup> Typically, there is a nonzero heat loss at components being warmer than ambient like the regenerators and simultaneously a nonzero heat gain (i.e. refrigerating capacity loss) at components colder than ambient like the evaporator. Although these effects are typically small for well-insulated commercial machines with refrigerating capacities of 100kW and above, they may affect the thermal efficiency. The net heat loss of the entire machine is always smaller than the summarized heat losses at hot parts as heat gains partly compensate for the heat losses.

### 2.1.3 Multi-stage absorption cycles



Horizon™ Two-Stage Fired or Hot Water Absorption Water Chiller Component Identification

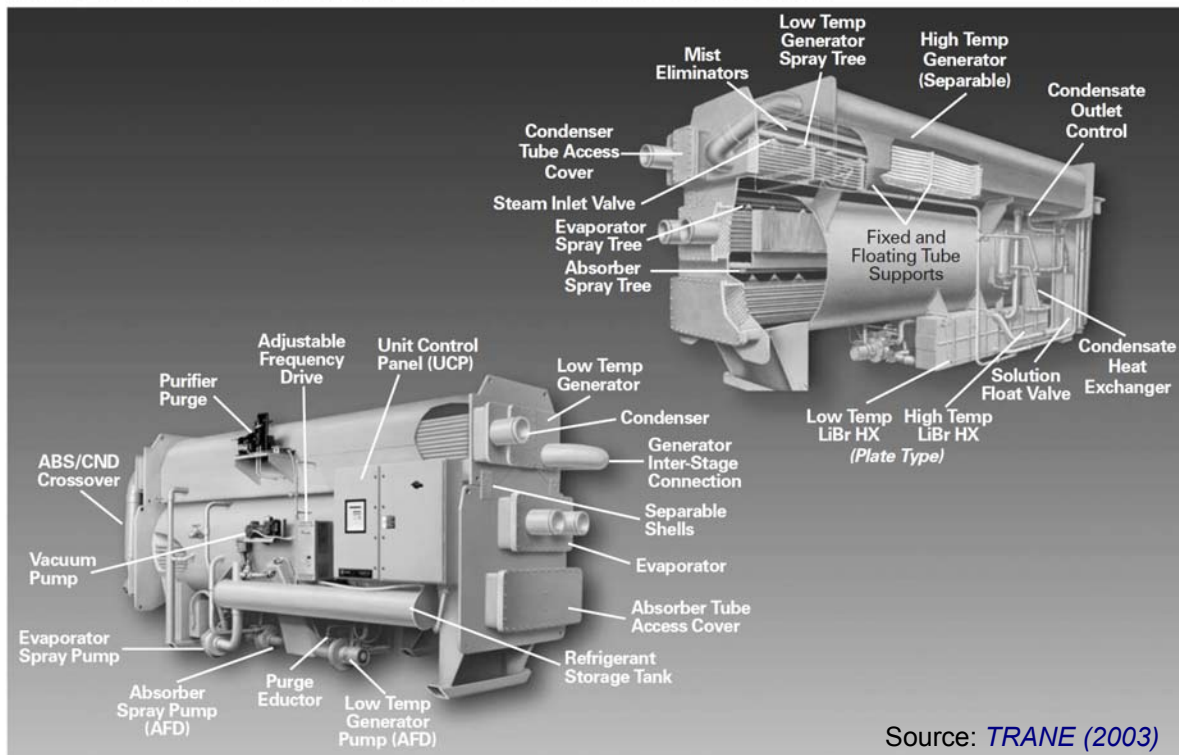


**Fig. 3: Flow scheme (top) and component identification (bottom) of a state-of-the-art commercially available steam-fired absorption chiller (Trane Horizon™).**

Displayed machine is equipped with condensate sub-cooling (“COND.HX”) and sophisticated reverse-flow solution cycle with bypass. See [TRANE \(2003\)](#) for a more detailed description.

Within a single plant, two or more basic absorption cycles can be combined in a way that there is an internal heat exchange between a main component of the one cycle and another main component of the other cycle. These absorption cycles may also share some of their main components. The theory of such multistage absorption cycles is put down in fundamental works like *Alefeld (1982)*, *Alefeld (1985)*, *Alefeld & Radermacher (1993)*, *Herold et al. (1996)*, or *Ziegler (1997)* and shall not be repeated here. Comprehensive review of various multistage cycles is also provided by *Furutera et al. (1996)* and *Kang et al. (2000)*.

The most prominent application of this principle is the so-called double-effect (“DE”) absorption chiller, also known as “two-stage” chiller. In these machines, a second regenerator (low-temperature regenerator) at an intermediate temperature level is added to the basic single-effect cycle (cf. Fig. 2). The additional regenerator is heated internally by the condensation of the refrigerant that is evaporated in the externally driven first regenerator (high-temperature regenerator). Fig. 3 shows the drawing of an commercially available double-effect chiller (again, this is a simplified scheme omitting some additional valves and pipes that are required for control and servicing purposes).

Thermodynamically, a DE-chiller is a superposition of two SE-chillers where the one is driven by reject-heat of the other, resulting in an extra amount cold production from the same amount of driving heat and thus increased thermal efficiency. The price for this boost in capacity is not only an increased complexity of the apparatus but also an increased temperature level of the driving heat source. A comparison of typical operational data of indirect-fired SE-chillers and DE-chillers is given in Tab. 1.

| Typical operational data                                   | Single-effect chiller | Double-effect chiller |
|--|-----------------------|-----------------------|
| Chilled water supply temperature (leaving)                 | 5...8°C               | 5...8°C               |
| Coolant supply temperature (entering)                      | 26...32°C             | 26...32°C             |
| Driving heat supply/condensation <sup>11</sup> temperature | 80...140°C            | 150...190°C           |
| Thermal efficiency in cooling mode ( $COP_c$ )             | 0.6...0.8             | 1.1...1.5             |

**Tab. 1: Comparison of typical operational data of indirect-fired single-effect and double-effect absorption chillers (full load operation).**

From theory, it has been shown that numerous possible configurations of absorption chillers or heat pumps of increasing complexity and number of main components can be synthesized by superposition of several basic absorption cycles. All of them – in simple words – either can be characterized by an increase in efficiency together with an increase in driving temperature (increased number of “effects”) or by a reduction in driving temperature along with

<sup>11</sup> Driving heat supply temperature applies for liquid heat carriers (e.g. water cycles) while heat carrier condensation temperature applies for steam.

with a reduction in efficiency (increased number of “lifts”). Especially the development of triple-effect (“TE”) chillers has been subject of various theoretical and experimental studies<sup>12</sup>.

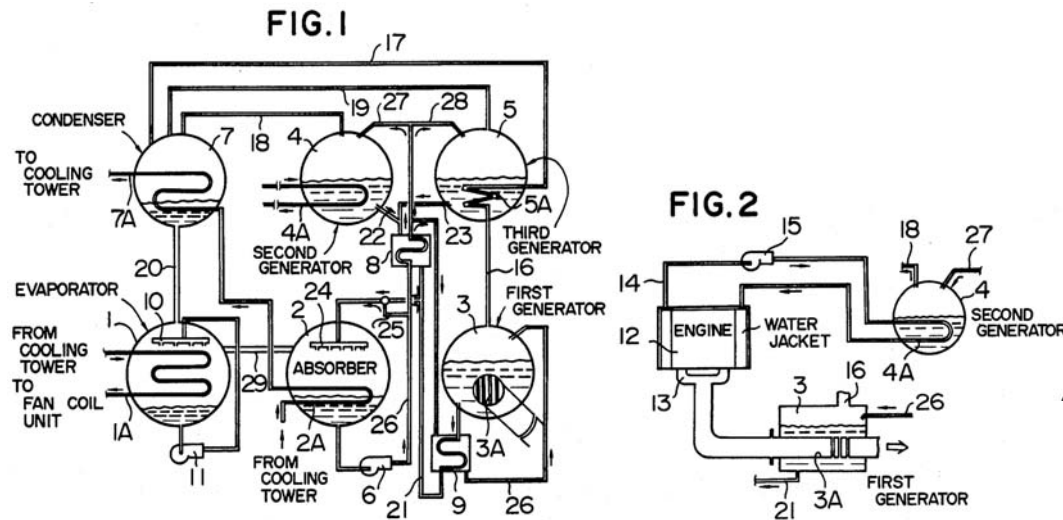


**Fig. 4: Flow scheme of an integrated single-effect/double-effect (SE/DE) absorption chiller.**

Simultaneous utilization of flue gas of a combustion engine in the high-temperature regenerator (“first generator”) and jacket cooling water in a low-temperature regenerator (“second generator”). Patent drawings from Mori et al. (1984).

Similarly, integrated machines can be synthesized by superposition that comprise two or more different cycles at the same time. Examples are integrated single-effect/double-lift (SE/DL) cycles – discussed by Schweigler (1999) – or integrated single-effect/double-effect (SE/DE) machines<sup>13</sup> that utilize external driving heat simultaneously in different regenerators at different temperature levels. An example for a simple flow scheme of an integrated SE/DE-chiller for utilization of waste heat of an internal combustion engine is shown in Fig. 4. In this scheme, the “first generator” and the “third generator” are part of a double-effect cycle, while the “second generator” belongs to the superpositioned single-effect cycle. Both low-temperature regenerators in Fig. 4 – “second generator” and “third generator” – are at the same pressure and temperature level, therefore integration into a single vessel with two independent heating coils would result in a thermodynamically equivalent design<sup>14</sup>.

### 2.1.4 Solution cycle design

As every double-effect chiller comprises one absorber and two solution regenerators between which the working solution has to be circulated, there are several possible configurations for the solution cycle of the machine. This work will follow the convention that a

<sup>12</sup> see e.g. Grossman et al. (1994), Furutera et al. (1996), Kohler & He (1999), Kang et al. (2000), Kujak & Schulz (2000), Kaita (2002), Kashiwagi et al. (2002), Inoue et al. (2003), Mori et al. (2003), Yabase et al. (2005)

<sup>13</sup> see e.g. Mori et al. (1984), Takahata et al. (1999), Katayama et al. (2002), Edera & Kojima (2002), Inoue & Endo (2004a), Inoue & Endo (2004b), Kren et al. (2004), Paul (2004), Plura et al. (2004), Plura et al. (2005), Keil et al. (2005); the basic principle has already been proposed by Alefeld (1982)

<sup>14</sup> Nevertheless, a different transient behavior might result if both regenerators were integrated into a single vessel.



solution cycle where the weak solution leaving the absorber is pumped to the high-temperature regenerator, the solution leaving the high-temperature regenerator flows to the low-temperature regenerator, and finally the strong solution from the low-temperature regenerator flows back to the absorber is referenced as “series-flow design” (see left sketch in Fig. 5). According to the same convention, the opposite case where the weak solution coming from the absorber passes the low-temperature regenerator first and the high-temperature regenerator afterwards is called “reverse-flow design” (also called “series flow type II” in some literature sources). If the solution stream leaving the absorber is split into one share passing the high-temperature regenerator and into another share passing the low-temperature regenerator, the design is commonly referenced as “parallel-flow” (see right sketch in Fig. 5). A more detailed discussion of the three basic types of solution cycles is e.g. provided by *Herold et al. (1996)*.

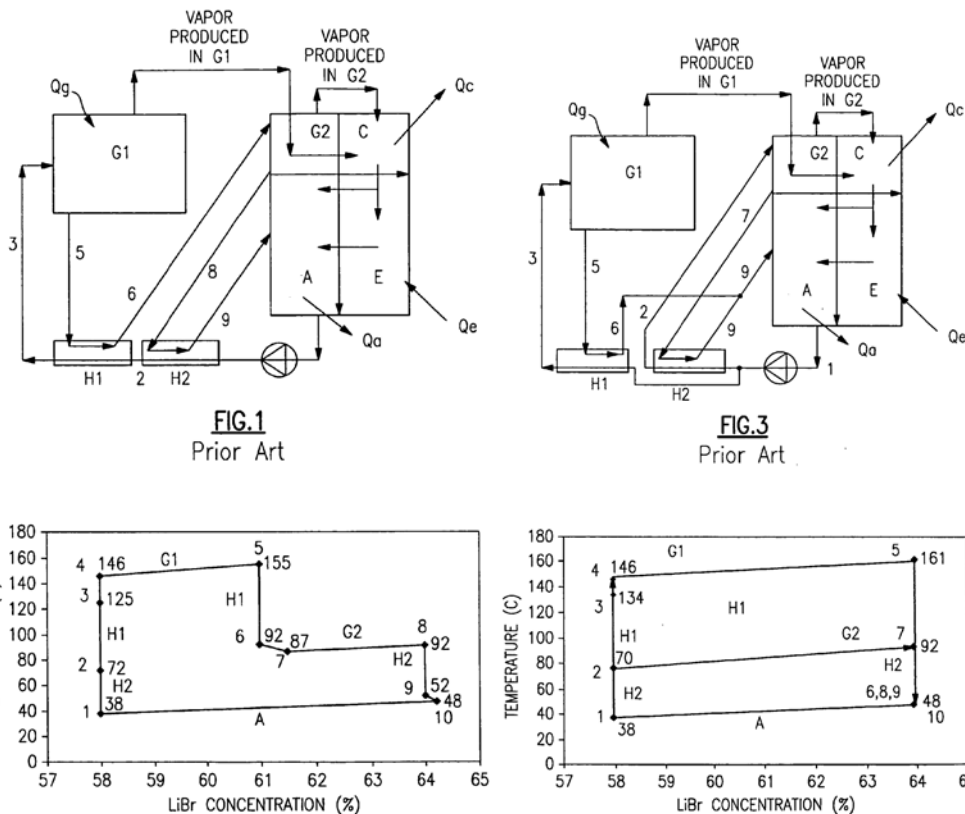


**Fig. 5: Conventional flow schemes (top) and sample temperatures and concentrations of the LiBr solution (bottom) of double-effect chillers comprising series-flow (left) and parallel-flow (right) cycle layouts.** Solution circulates between absorber (A), low-temperature solution heat exchanger (H2), low-temperature regenerator (G2), high-temperature solution heat exchanger (H1), and high-temperature regenerator (G1). Patent drawings from *Gupte (2005)*.

There are some more possible configurations of the solution cycle that all can be considered subtypes of either the “series-flow” or the “reverse-flow” cycle. The solution stream can be split and one partial flow can bypass one of the regenerators, typically the high temperature device. The commercially available machine shown in Fig. 3 is an example for a reverse solution cycle with split solution flow and partial bypass of the high-temperature regenerator.

An example for the quite rare series flow cycle with split solution flow and partial bypass of the high temperature regenerator can be found in Fig. 15 in 3.3.1 below. Further subtypes of each design can be derived by considering different configurations with respect to the positions of valves, pumps, and recuperative heat exchangers. Even more variations of the solution cycle are possible in machines with three regenerators like those shown in Fig. 4; for triple-effect chillers, a study of *Inoue et al. (2003)* lists even sixty possible patterns of the solution cycle.

The advantages and disadvantages of different solution cycle designs have subject to various studies by e.g. *Gommed & Grossman (1990)*, *Grossman et al. (1994)*, *Saito et al. (1996)*, *Shitara (2000)*, *Chua et al. (2000b)*, *Arun et al. (2001)*, *Lee & Sherif (2001)*, *Kaita (2002)*, *Mori et al. (2003)*, and *Abyaneh & Saidi (2005)*. The main difference between the various solution-cycle layouts is that a series-flow layout results in the most simple plant design while layouts with a split solution flow – only a partial flow passing the high-temperature regenerator – allow for a smaller and cheaper high-temperature solution heat exchanger (“HIGH TEMP. HX” in Fig. 3, “H1” in Fig. 5). Consequently, in studies comparing different solution cycle designs at constant heat exchanger size a better performance of the parallel-flow cycle than of the basic series-flow cycle was found.

### 2.1.5 Commercially available types of absorption chillers

Presently, all lithium bromide based absorption chillers from series production are either single-effect (SE) or of the double-effect (DE) machines; the regenerator at the highest internal temperature level is either direct-fired or driven by an external hot water or steam cycle (indirect-fired). In the meanwhile, Exhaust-fired or co-fired double-effect chillers – being modified direct-fired chillers – are commercially available from established manufacturers, too. Three basic designs of the solution cycle are deployed in standard double-effect chillers from series production: the simple series-flow design, the thermodynamically more promising parallel-flow design, and a reverse-flow design with partial bypass of the high-temperature regenerator (cf. Fig. 3).

Whereas only a few prototypes of integrated single-effect/double-effect (SE/DE) cycles utilizing external driving heat in two regenerators at different temperature levels have been shipped so far, it can be considered state-of-the-art to utilize an additional external heat source to preheat lithium bromide solution flowing into a regenerator. This is typically realized in steam-fired double-effect chillers by sub cooling the return condensate (cf. Fig. 3).

Cycles that are even more complex, like the double-lift (DL) and single-effect/double-lift (SE/DL) machines utilizing more than one absorber – as described by *Schweigler (1999)* –

have also been commercialized; however, the few shipped units are still custom-made and far away from entering series production.

Mainly due to economical considerations, so-called triple-effect (TE) cycles with increased driving temperature and efficiency compared to double-effect cycles have not been commercialized so far. Although several established manufacturers have developed and demonstrated their first prototypes as reported in *Kujak & Schulz (2000)*, *Mori et al. (2003)*, and *Yabase et al. (2005)*.

### 2.1.6 Reference operating conditions

The performance of an absorption chiller is always dependent on the chosen operating conditions, namely on the flow and return temperatures of chilled water and coolant. As already indicated in Tab. 1, these design values may differ from site to site depending on requirements, building standards and climate conditions. Especially the setpoint for cooling water temperature is dependent on the actual cooling limit temperatures, resulting in lower cooling water temperatures in areas of moderate climate and in elevated cooling water temperatures in tropical areas. In addition, temperatures may vary depending on current load and ambient temperature. Therefore, reference operating-conditions have to be specified if the performance of a chiller is to be rated. Such a set of rating conditions for full load and for part-load is provided by the American ANSI/ARI standard 560-2000 *ARI (2000)*, which is used as a reference even out of its validity area in terms of geography. An overview on the ARI conditions for full load operation in comparison to common design values for Germany is given in Tab. 2. As the ARI standard provides entering water temperatures and specific flow rates rather than leaving water temperatures, the latter have been calculated assuming *COP* of 0.7 for single-effect chillers and 1.2 for double-effect chillers.

| Standard rating conditions for absorption chillers | Single-effect chiller ANSI/ARI standard | Double-effect chiller ANSI/ARI standard | Absorption chillers Germany (typical) |
|--|---|---|---------------------------------------|
| Entering chilled water (evaporator)                | 12.2 °C                                 | 12.2 °C                                 | 12 °C                                 |
| Leaving chilled water (evaporator)                 | 6.7 °C                                  | 6.7 °C                                  | 6 °C                                  |
| Entering cooling water (absorber)                  | 29.4 °C                                 | 29.4 °C                                 | 27 °C                                 |
| Leaving cooling water (condenser)                  | (38.4 °C)                               | (35.5 °C)                               | 35 °C                                 |

*Tab. 2: Standard rating conditions for absorption chillers. Leaving fluid temperatures have been calculated for ARI conditions assuming COP of 0.7 for single-effect chillers and COP of 1.2 for double-effect chillers.*

To save installation cost for piping as well as energy cost for pump operation, however, low-flow designs with reduced cooling water flow and accordingly elevated leaving cooling water temperatures are gaining in importance.



## 2.2 Thermal efficiency of indirect-fired absorption chillers

The term indirect-fired commonly references all machines that obtain their driving heat by an intermediate heat carrier cycle which is typically hot water or condensing steam. In most cases, this is a closed-loop heat-carrier cycle with a moderate temperature difference between supply and return. For approximate thermodynamic considerations a typical liquid heat carrier cycle with small temperature difference of about 5 to 15 K between supply and return or a steam cycle without significant sub-cooling of the return condensate can be characterized as one heat source at a single temperature level. This applies similarly for typical chilled-water cycles and coolant cycles having maximum temperature differences between supply and return of about 5 to 10 K.

For exact thermodynamic calculations instead of the arithmetic mean temperature  $\bar{t}_{MN} = (t_{SUPPLY} + t_{RETURN}) / 2$  the entropic mean temperature  $\bar{t}$  is to be used:

$$\bar{t} = (t_{SUPPLY} - t_{RETURN}) / \ln(t_{SUPPLY} / t_{RETURN}) \quad (2.20)$$

For small temperature difference  $t_{SUPPLY} - t_{RETURN} \ll t_{RETURN}$  relative to the absolute temperatures, the entropic mean temperature (2.20) converges to the arithmetic mean temperature. This can easily be shown by employing the first order term of an appropriate fractional series (2.21) for approximation of the logarithm in (2.20) at arguments close to unity, i.e.  $t_{SUPPLY} / t_{RETURN} \approx 1$ :

$$\begin{aligned} \ln(x) &= 2 \cdot \left[ \frac{1}{1} \cdot \left( \frac{x-1}{x+1} \right)^1 + \frac{1}{3} \cdot \left( \frac{x-1}{x+1} \right)^3 + \dots \right] \\ &\approx 2 \cdot (x-1) / (x+1), \quad \text{deviation: } (-1/+0)\% \text{ for } x = 0.7 \dots 1.3 \end{aligned} \quad (2.21)$$

### 2.2.1 Thermal efficiency of an ideal/reversible thermodynamic process for refrigeration

As simplification, it can be assumed that an absorption chiller consumes the driving heat  $\dot{Q}_2 < 0$  at the mean heat source temperature  $t_2$  providing the refrigeration capacity  $\dot{Q}_0 < 0$  at the mean chilled water temperature  $t_0$  and rejecting the heat  $\dot{Q}_1 > 0$  at the mean coolant temperature  $t_1$  (see Fig. 6).

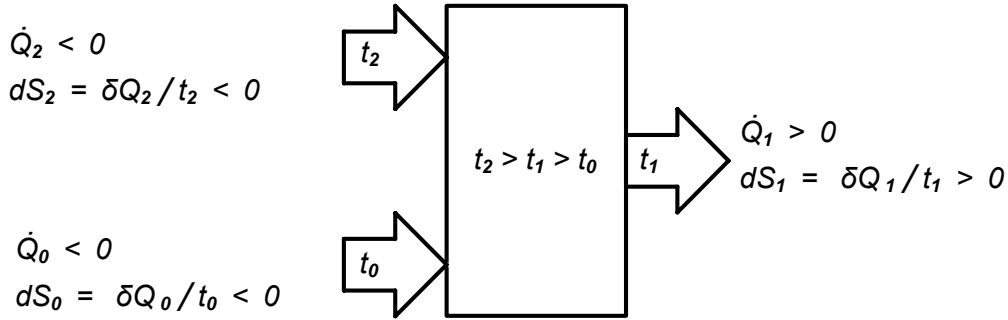


Fig. 6: Ideal model for heat driven chillers with three temperature levels.

If no significant thermal losses or gains from ambient have to be accounted for, the first and second law of thermodynamics for such an absorption chiller read:

$$\dot{Q}_0 + \dot{Q}_1 + \dot{Q}_2 = 0 \quad (2.22)$$

$$dS = dS_0 + dS_1 + dS_2 = \delta Q_0 / t_0 + \delta Q_1 / t_1 + \delta Q_2 / t_2 \geq 0 \quad (2.23)$$

Hence results the cooling efficiency  $COP_{C,REV}$  of an ideal reversible thermodynamic machine (i.e.  $dS = 0$ ), which acts as the upper limit for the actual thermal efficiency for cooling  $COP_C$  in dependence of the three temperature levels:

$$COP_{C,REV} = (t_2 - t_1) / t_2 \cdot t_0 / (t_1 - t_0) \quad (2.24)$$

$$COP_C = \dot{Q}_E / \dot{Q}_G \leq COP_{C,REV} \quad (2.25)$$

Equation (2.24) still holds true – as a special case – for the reversible efficiency of mechanically driven refrigeration like vapor recompression chillers, if the driving heat temperature  $t_2$  is set to infinite whereby the first multiplicand in (2.24) becomes unity.

## 2.2.2 The endoreversible model for absorption chillers

Actually, the efficiency  $COP_{C,REAL}$  of an actual machine is significantly lower than that of an ideal reversible thermodynamic process  $COP_{C,REV}$ . The difference can be attributed to a number of irreversible loss mechanisms that can be individually studied and minimized – if possible – to increase the overall cooling efficiency of the actual chiller. While this might be an exhausting task for technical systems in general, it has been shown by [Ziegler \(1997\)](#) that the so-called “entropy method” can be an advantageous approach for absorption chillers.

Unlike vapor recompression chillers, for absorptions chillers it actually can be shown, that the principal non-reversibility of the machine results from the heat-transfer between the external heat/cold-carrier cycles and the internal processes in the evaporator(s), absorber(s), condenser(s) and regenerator(s) of the chiller requiring a certain driving temperature difference in each heat exchanger. The design values of these temperature differences are

typically the results of an optimization in terms of size and cost of the heat exchangers and hence they are intentionally significantly larger than their technical lower limits. For evaporators and condensers of falling-film type temperature differences below 1 K are possible while absorbers and regenerators of the same type require temperature differences of at least 1–2 K to overcome mass transfer resistances. Regenerators of pool-boiling type, however, require temperature differences of at least 10–15 K for proper operation in the nucleate-boiling regime. For operation on smaller driving temperature differences than these so-called technical limits, still some heat transfer will take place but heat transfer coefficients might drop sharply and a stable and predictable operation of the cycle cannot be assured.

The freezing of the refrigerant water at temperatures below 0°C, the possible crystallization of the lithium bromide solution at salt concentrations above 64wt.%<sup>15</sup> and the actual available heat source temperature impose upper technical limits for the driving temperature differences in these heat exchangers. An overview of typical design values is given in Tab. 3.

| Driving temperature difference in main components of absorption chillers | Lower technical limit   | Design for low grade heat sources | Standard design           |
|--|-------------------------|-----------------------------------|---------------------------|
| Condenser (tube bundle/falling film)                                     | < 1 K                   | 2...5 K                           | 4...7 K                   |
| Evaporator (tube bundle/falling film)                                    | < 1 K                   | 3...5 K                           | 5...7 K                   |
| Absorber (tube bundle/falling film)                                      | 1...2 K                 | 5...10 K                          | 10...15 K                 |
| Regenerator (tube bundle/falling film)                                   | 1...2 K                 | 5...10 K                          | (10...20 K) <sup>16</sup> |
| Regenerator (immersed tube bundle)                                       | 10...15 K <sup>17</sup> | (5...10 K) <sup>18</sup>          | 10...20 K                 |

**Tab. 3: Driving temperature differences in main components of absorption chillers – lower technical limits and typical design values.**

In literature, analytic deductions for optimized distribution of heat exchange surfaces and available driving temperature differences in absorption chillers can be found. It has already been shown by *Riesch (1991)*, *Ziegler (1997)*, *Schweigler (1999)*, and *Cerkvenik et al. (2001)* that an analytical expression called “square-root criterion” can be derived for the ratio of the heat exchanger surfaces of all main components as a solution of this optimization problem. Of course, this mathematically derived surface distribution may be constrained in reality by concentration or pressure limits to avoid crystallization of freezing in the machine. As already discussed by *Schweigler (1999)*, the “square-root criterion” typically fails to predict the optimum size of evaporator and absorber in cycles where relatively high driving temperature is available while it is quite useful for design of machines utilizing low-grade driving heat. It

<sup>15</sup> at temperatures related to saturation pressures corresponding to about 0°C refrigerant temperature

<sup>16</sup> not preferable, flooded heat exchanger utilizing nucleate boiling more efficient

<sup>17</sup> onset of nucleate boiling

<sup>18</sup> operation below onset of nucleate boiling may require special design and/or increased size of the heat exchanger

has to be stated however that the formulation of this optimum surface distribution, initially derived by *Riesch (1991)* and consequently adopted by the other authors, was based on a simplified linear modeling of absorption machines; thus, it may lead to significant calculation errors. A revised derivation of a more generally valid formulation is provided in appendix A.2.

Based on the assumption of similar heat transfer coefficients and similar heat rates such a model would propagate also similar driving temperature differences for evaporator, absorber, and regenerator of falling-film type in a single-effect chiller to minimize the total required heat exchanger surface. If driving heat temperature is not that low, however, the possible temperature differences in evaporator and absorber are mainly limited by the constraints that refrigerant temperature has to keep a certain safety distance to freezing point and solution concentration has to keep a respective distance to solubility limit to ensure proper operation. Absolute numbers are mainly dependent on sophistication of design and control strategy, realistic values for the internal refrigerant temperature minimum are 2...3°C the maximum concentration for the strong solution entering the absorber of a chiller is about 63.5...64.0 wt.%, the mean concentration should not exceed 62 wt.%.

Taking into account these actual temperature differences the endoreversible model for heat driven chillers estimates a more realistic upper limit for the thermal efficiency of the cycle. It assumes that an internal refrigeration cycle which – in best case – operates reversible and without losses is coupled to the external heat carrier cycles by non-reversible heat exchange processes utilizing nonzero driving temperature differences. Thus the internal cycle operates at internal temperature levels  $T_0$ ,  $T_1$ , and  $T_2$  that differ from the mean heat carrier temperatures  $t_0$ ,  $t_1$ , and  $t_2$  by the driving temperature differences  $\Delta T_0 = t_0 - T_0$  and  $\Delta T_1 = T_1 - t_1$  and  $\Delta T_2 = t_2 - T_2$  as shown in Fig. 7.

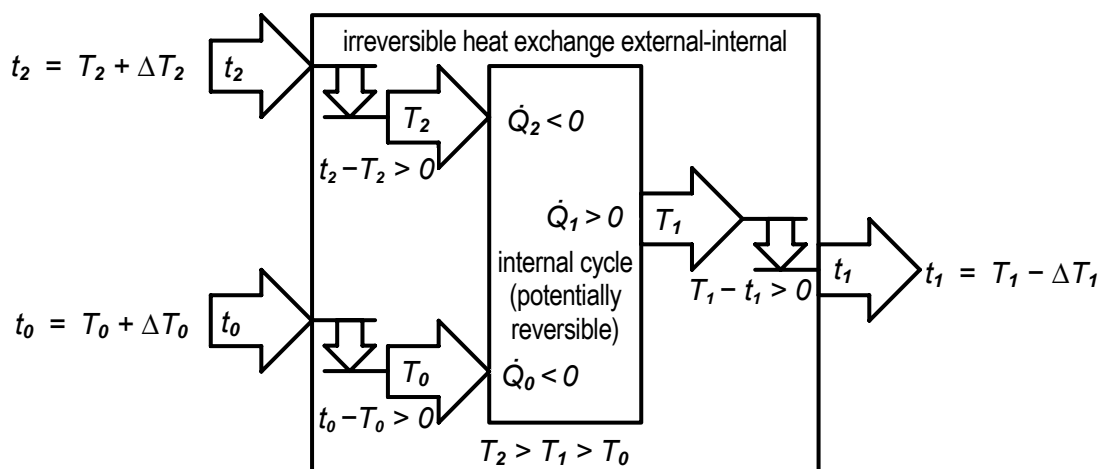


**Fig. 7: Endoreversible model for heat driven chillers.**

As a simplification,  $\Delta T_1$  represents a mean value for both, the temperature differences in absorber and condenser, which are slightly different in real machines as shown in Tab. 3<sup>19</sup>. Assuming the internal cycle being completely reversible the first and second law of thermodynamics for the endoreversible machine read:

$$\dot{Q}_0 + \dot{Q}_1 + \dot{Q}_2 = 0 \quad (2.26)$$

$$dS_{INT,REAL} \geq dS_{INT,ENDOREV} = \delta Q_0/T_0 + \delta Q_1/T_1 + \delta Q_2/T_2 = 0 \quad (2.27)$$

Hence results the cooling efficiency  $COP_{C,ENDOREV}$  of the endoreversible process as a more realistic upper limit for the efficiency  $COP_{C,REAL}$  of a real machine:

$$\begin{aligned} COP_{C,ENDOREV} &= (T_2 - T_1) / T_2 \cdot T_0 / (T_1 - T_0) \\ &= (t_2 - t_1 - \Delta T_2 - \Delta T_1) / (t_2 - \Delta T_2) \cdot (t_0 - \Delta T_0) / (t_1 - t_0 + \Delta T_1 + \Delta T_0) \end{aligned} \quad (2.28)$$

$$COP_{C,REAL} \leq COP_{C,ENDOREV} < COP_{C,REV} \quad (2.29)$$

For a reversible process, however, these internal temperatures  $T_0$ ,  $T_1$ , and  $T_2$  are identical to the saturation temperatures of the evaporation, condensation, and absorption processes at the respective temperature levels. Therefore, these variables are not independent but coupled by the property data of the refrigerant and the respective salt solution. For the basic single-effect cycle, this relation is expressed by the Dühring-equation (2.16) which reads for evaporator temperature  $T_E = T_0$ , absorber/condenser temperature  $T_A = T_C = T_1$ , and regenerator temperature  $T_G = T_2$ :

$$T_1 - T_0 = (T_2 - T_1) \cdot R_D(X_{SOL}) \quad (2.30)$$

Here the slope parameter  $R_D$  and the salt concentration  $X_{SOL}$  are dependent on the required shift in saturation temperatures from refrigerant to salt solution and therefore they are both given values if two of the temperatures are set. For full load operation of commercial chillers typically temperatures of both external heat carriers, chilled water and coolant, are given values, specified by climate conditions and system requirements as well as by locally applicable standards (e.g. ARI 560) as shown in Tab. 2. The required driving temperature consequently can be obtained from (2.30) assuming proper driving temperature differences between external and internal temperature levels as e.g. provided by Tab. 3. The endoreversible limit for the  $COP$  finally is determined by (2.28).

For an analytical solution, the parameter  $R_D$  can be expressed in dependence on the temperature levels  $T_0$  and  $T_1$  according to (2.14):

<sup>19</sup> In typical machines with a serial coolant interconnection from absorber to condenser the small discrepancies in external temperatures on the one hand and in driving temperature differences on the other hand partly compensate for each other, resulting in nearly identical mean internal temperatures in both components, absorber and condenser

$$R_D(\bar{X}_{SOL}) = T_0 / (T_1 - B_D(\bar{X}_{SOL})) \quad (2.31)$$

This reveals for the driving upper temperature and the efficiency of a single-effect chiller:

$$T_2 = (T_1^2 - B_D \cdot (T_1 - T_0)) / T_0 \quad (2.32)$$

$$COP_{C,ENDOREV} = T_0 \cdot (T_1 - B_D) / (T_1^2 - B_D \cdot (T_1 - T_0)) \quad (2.33)$$

As the Dühring intercept is a small number compared to the absolute temperatures  $B_D \ll T_1$  the approximation  $B_D = 0$  from (2.4) reduces (2.32) and (2.33) to simple relations that nevertheless reveal the main dependences between internal temperatures and efficiencies of single-effect chillers:

$$T_2 \approx T_1^2 / T_0 \quad (2.34)$$

$$COP_{C,ENDOREV} \approx T_0 / T_1 \approx R_D \quad (2.35)$$

Providing a more fundamental thermodynamic derivation, the latter relation (2.35) has already been employed by e.g. *Tozer & James (1997)* or *Tozer & Agnew (1999)*. Discussions of various simplified relations for estimating the efficiency of idealized single-effect chillers including (2.35) are found e.g. in *Hellmann (2002)* or *Ziegler (2005)*.

An evaluation of equations (2.32) and (2.33) for temperatures corresponding to ARI reference conditions for lithium bromide based single-effect chillers given in Tab. 2<sup>20</sup> finally produces the following results displayed in Tab. 4. Driving temperature differences between internal and external temperature levels given in Tab. 3 and the approximation  $B_D = -7.5 \text{ K}$  analogous to (2.5) have been used for this calculation. For convenience, the temperature differences from Tab. 3 have been interpreted as arithmetic means instead of logarithmic means<sup>21</sup>.

| Arithmetic mean temperatures and temperature differences | Mean external temperatures | Driving temperature differences | Mean internal temperatures |
|--|----------------------------|---------------------------------|----------------------------|
| Driving heat level                                       | $t_2 = 112.7 \text{ °C}$   | $\Delta T_2 = 20.0 \text{ K}$   | $T_2 = 92.7 \text{ °C}$    |
| Reject heat level  | $t_1 = 33.9 \text{ °C}$    | $\Delta T_1 = 10.0 \text{ K}$   | $T_1 = 43.9 \text{ °C}$    |
| Refrigeration level                                      | $t_0 = 9.5 \text{ °C}$     | $\Delta T_0 = 7.0 \text{ K}$    | $T_0 = 2.5 \text{ °C}$     |
| Endoreversible efficiency limit                          | $COP_{C,ENDOREV} = 0.887$  |                                 |                            |

**Tab. 4:** Example calculation utilizing the endoreversible model and approximate Dühring coefficients for evaluation of a typical single-effect chiller running at ARI standard conditions.

<sup>20</sup> As the ARI standard only defines the coolant mass flow while the temperature of the leaving coolant is dependent on the actual COP of the chiller. For convenience, however, for this calculation the leaving coolant temperature has been calculated ex ante assuming a “typical” COP of a real machine.

<sup>21</sup> This is an allowable approximation as the discrepancy between both definitions of the temperature difference is less than 1 K for this example, and this is still within the variations provided by Tab. 3 for the respective temperature differences.

A more accurate calculation with a computer program utilizing best-fit functions for lithium bromide property data instead of the simple approximation  $B_D = -7.5 K$  produced only slight deviations of less than  $0.5 K$  in driving temperatures ( $t_2 = 112.4^\circ\text{C}$ ,  $T_2 = 92.4^\circ\text{C}$ ) and a slightly different efficiency limit of  $0.882$ . A mean lithium bromide concentration of  $61\%$  was also obtained by this way.

For the endoreversible efficiency limits of double-effect chillers and more complex cycles, analogous calculations can be made; respective Dühring equations are e.g. provided by [Ziegler \(1997\)](#). Commercially available single-effect chillers actually realize  $80\%$  to  $85\%$  of the endoreversible  $COP$  derived above, this fact indicates the relevance of the endoreversible approach for absorption chillers. For this ratio of real to endoreversible efficiency [Ziegler \(1997\)](#) introduces the quality factor  $g = COP_{REAL} / COP_{ENDOREV}$  that can be directly calculated if the internal irreversibility generation  $\dot{S}_{INT} = dS_{INT} / dt$  is known:

$$g = COP_{REAL} / COP_{ENDOREV} = 1 - T_1 \cdot T_2 / (T_2 - T_1) \cdot \dot{S}_{INT} / \dot{Q}_2 \quad (2.36)$$

The endoreversible efficiency limit derived above for the basic cycle of about  $0.9$ , which is slightly dependent on salt concentration and on operating conditions, although variations are rather small, is a characteristic number of lithium bromide based absorption chillers. The value mainly reflects the ratio of the specific heat of vaporization of the refrigerant in the evaporator to the specific heat for boiling off the refrigerant in the regenerator. To boil off refrigerant vapor from salt solution in the regenerator additionally to the specific heat of vaporization the specific heat of solution has to be expended. As this additional specific heat of solution for common operating conditions of lithium bromide chillers typically comprises a tenth of the specific heat of vaporization, the heat input at the regenerator has to be at least  $10\%$  greater than the respective refrigeration produced in the evaporator – giving a  $COP$  limit of about  $0.9$ .

A more detailed deduction taking into account internal heat shift processes due to nonzero specific heat capacities of real working pairs is presented in appendix A.1. According to equation (7.26) in appendix A.1.3, it reveals that the endoreversible efficiency actually is the quotient of the specific heats of the phase changes at the same internal pressure level and corresponding saturation temperatures:

$$COP_{C,ENDOREV} = (\Delta h_{VAP})_{T1} / (\Delta h_{VAP} + \Delta h_{SOL})_{T2} \quad (2.37)$$

As all properties of an actual substance have to be thermodynamically consistent among each other, both deductions of the endoreversible efficiency, those based on temperatures and Dühring coefficients, (2.28), (2.33), and the latter, (2.37), based on specific heats should produce identical results. Slight deviations are possible, however, as (2.28) strictly follows

from the basic laws of thermodynamics while several approximations had to be employed in appendix A.1 to derive (2.37).

### 2.2.3 Internal loss mechanisms in single-effect cycles

The endoreversible efficiency – as expressed by (2.28), (2.33) or (2.37) – applies for machines without any internal losses or irreversibilities. In real machines, however, internal irreversibilities mainly result from the imperfection of the internal heat recovery or heat shift mechanisms. To avoid these irreversibilities, all internal mass flows would have to enter the next device or process step at the respective equilibrium temperature of the phase change process. Additional irreversibilities in real chillers result from pressure drops in the piping of the machine and the pumping and throttling of the liquid flows on their ways. However, these are relatively small effects for lithium bromide based chillers. Irreversibility might also be caused by the mixing of solutions of different concentrations. Anyway, this is no general issue as mixing only applies for some chiller designs;<sup>22</sup> if required mixing of different solution concentrations could be avoided.

#### Internal mass flows

In a single-effect cycle as shown in Fig. 2, five internal mass flows have to undergo a temperature change. These flows are also visualized in a Dühring chart (cf. Fig. 8 below), based on the respective saturation temperatures from the example calculation in Tab. 4.

The internal flows are:

1. Liquid refrigerant flow  $\dot{M}_{REFR}$  from condenser (C) to evaporator (E), requiring cooling  $\dot{M}_{REFR} \cdot c'_{REFR} \cdot (T_0 - T_1) < 0$  at gliding temperatures from  $T_1$  to  $T_0$ .
2. Refrigerant vapor flow  $\dot{M}_{REFR}$  from evaporator (E) to absorber (A), requiring heating  $\dot{M}_{REFR} \cdot c''_{REFR} \cdot (T_1 - T_0)$  at gliding temperatures from  $T_0$  to  $T_1$ .
3. Weak solution flow  $\dot{M}_{WEAK} = \dot{M}_{STRONG} + \dot{M}_{REFR}$  from absorber to regenerator, requiring heating  $\dot{M}_{WEAK} \cdot c'_{WEAK} \cdot (T_2 - T_1)$  at gliding temperatures from  $T_1$  to  $T_2$ .
4. Strong solution flow  $\dot{M}_{STRONG}$  from regenerator (G) to absorber (A), requiring cooling  $\dot{M}_{STRONG} \cdot c'_{STRONG} \cdot (T_1 - T_2) < 0$  at gliding temperatures from  $T_2$  to  $T_1$ .
5. Refrigerant vapor flow  $\dot{M}_{REFR}$  from regenerator (G) to condenser (C), requiring cooling  $\dot{M}_{REFR} \cdot c''_{REFR} \cdot (T_1 - T_2) < 0$  at gliding temperatures from  $T_2$  to  $T_1$ .

<sup>22</sup> Mixing of different concentrations generally occurs in regenerators employing simple pool boiler designs where entering weak solution is mixed with leaving strong solution. Additionally, it takes place in absorbers utilizing a solution recirculation to improve the wetting of the tube bundles (not too common). Further examples are advanced solution cycles of double-effect chillers, like unmatched parallel flow designs or reverse flow with partial bypass. However, mixing effects are rather small in most cases.



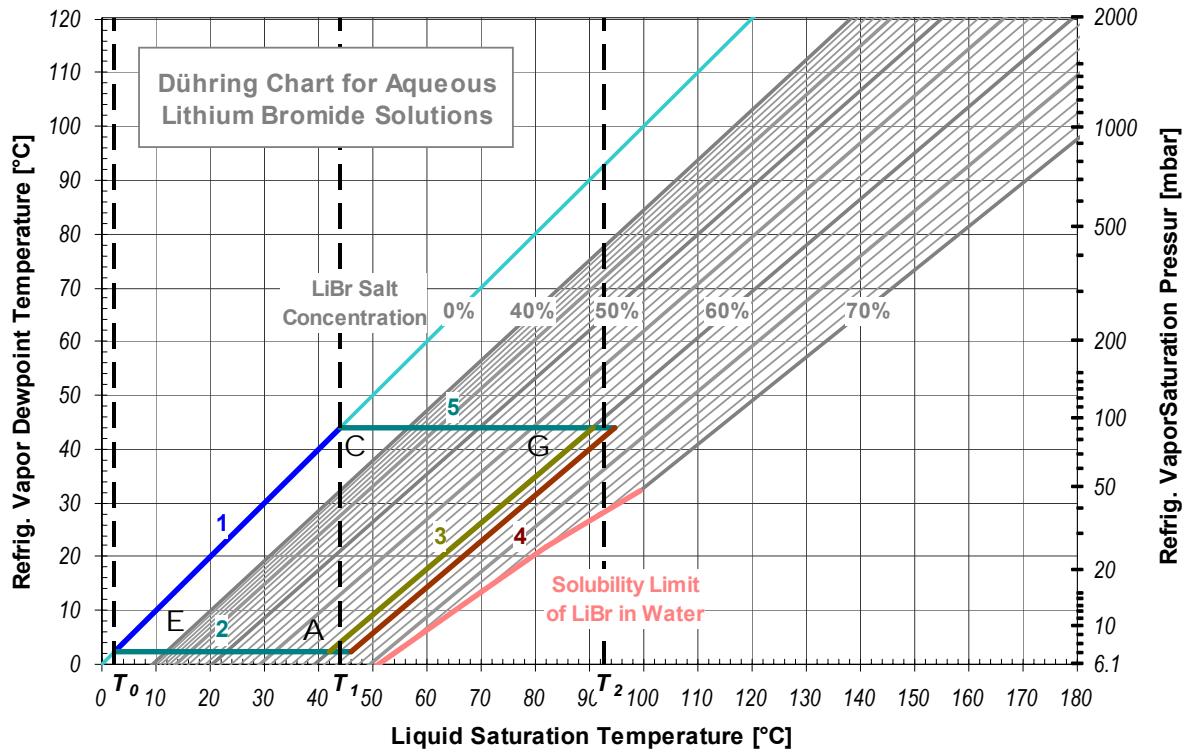


Fig. 8: Visualization of equilibrium states and internal mass flows of a sample single-effect chiller (cp. Tab. 4) in a Dühring chart.

In order to avoid or to minimize irreversibilities, a theoretical approach might suggest introducing at least one recuperative heat exchange between no. 1 and no. 2 and a second heat exchange between no. 3 to 5. Note, that the weak solution mass flow 3 equals the sum of strong solution flow 4 plus vapor flow no. 5. However, there is no technically proven and economically promising heat exchanger design for heating or cooling vapor flows (no. 2, no. 5) in water-based chillers at low absolute pressures and vapor densities without inducing significant parasitic pressure drops. This constraint finally imposes the practical technical limit for the thermal efficiency of water/lithium bromide based absorption chillers.

### Throttling loss

The first consequential implication hence is that the liquid refrigerant flow from condenser to evaporator (no. 1 in the above list) cannot be cooled to saturation temperature before entering the evaporator, as there is no suitable counterpart for an internal heat exchange. Besides, there is no substantial cooling by external heat exchange possible either, as another heat carrier at temperatures below chiller coolant temperature would be required. As a result, the refrigerant is de-superheated in the evaporator by flashing, producing additional refrigerant vapor that has to be absorbed in the absorber and subsequently to be boiled off again in the regenerator. Thus, the refrigeration capacity available externally, and as a result the thermal efficiency of the chiller, is reduced by the refrigeration consumed to pre-cool the refrigerant entering the evaporator. This loss in refrigeration capacity also referred to as

throttling loss  $\Delta\dot{Q}_{THROT}$  can be expressed as specific value  $\Delta q_{THROT}$  with respect to the circulating refrigerant flow  $\dot{M}_{REFR}$ :

$$\Delta q_{THROT} = \Delta\dot{Q}_{THROT} / \dot{M}_{REFR} = c'_{REFR} \cdot (T_1 - T_0) \quad (2.38)$$

The inability to heat up the vapor flow from evaporator to absorber (no. 2 in the above list) itself has no direct negative impact on the efficiency of the machine, at least what operation in chiller-mode is concerned. Yet, it slightly reduces the thermal load in the absorber, maybe saving some heat transfer surface. As well, the inability to cool the refrigerant vapor from regenerator to condenser (no. 5 in the above list) has no major negative impact in a direct way, as it just increases the thermal load in the condenser a bit, maybe causing a slight increase in heat transfer area.

### Mismatch and solution heat exchanger loss

After all, the only internal heat exchange that actually can be realized in single-effect chillers is between weak and strong solution (no. 3 and 4) from absorber to regenerator and back. Nevertheless, these already are the dominating internal heat flows, as the solution mass flow always is a multiple of the refrigerant flow rate. Heat exchangers between strong and weak solution as already shown in the flow schemes Fig. 2 and Fig. 3 above for single-effect and double-effect chillers are therefore incorporated in all commercially available machines.

Improper cooling of the solution flow regenerator-absorber (no. 4) would not directly reduce the efficiency of the chiller, but it would significantly increase the size of the absorber heat exchanger. Insufficient heating of the solution flow entering the regenerator (no. 3), however, does not only require additional heat exchange area in the regenerator, it directly reduces the *COP* as some extra heat is consumed to preheat the solution up to saturation temperature. The recuperative heat exchange between both solution flows would be perfect, if the weak solution would be heated up to the temperature of the strong solution leaving the regenerator, and the strong solution would be cooled down to the temperature of the weak solution leaving the absorber.

As already mentioned, the mass flow of the weak solution is the sum of the strong solution flow plus the refrigerant mass boiled off in the regenerator. According to an approximate relation provided by [Ziegler \(1997\)](#) this also applies for the heat capacities:

$$\dot{M}_{WEAK} \cdot c'_{WEAK} = \dot{M}_{STRONG} \cdot c'_{STRONG} + \dot{M}_{REFR} \cdot c'_{REFR} \quad (2.39)$$

Therefore, a mismatch  $\Delta\dot{Q}_{MISMATCH}$  in heat capacity flows always has to be balanced by expending extra driving heat in the regenerator – even if an ideal solution heat exchanger of infinite size would be installed.

$$\Delta\dot{Q}_{MISMATCH} = (\dot{M}_{WEAK} \cdot c'_{WEAK} - \dot{M}_{STRONG} \cdot c'_{STRONG}) \cdot (T_2 - T_1) \quad (2.40)$$

Employing (2.39) this also can be expressed as specific value  $\Delta q_{MISMATCH}$  with respect to the circulating refrigerant flow  $\dot{M}_{REFR}$ :

$$\Delta q_{MISMATCH} = \Delta\dot{Q}_{MISMATCH} / \dot{M}_{REFR} = c'_{REFR} \cdot (T_2 - T_1) \quad (2.41)$$

Finally, the solution heat exchanger in real machines between weak and strong solution flows (no. 3 and no. 4) is not perfect but requires a certain driving temperature difference. As the strong solution flow to be cooled down has a lower heat capacity than the weak solution flow to be heated up in this heat exchanger, there is a pinch point at the cold end. The heat exchanger loss  $\Delta\dot{Q}_{LOSS,SHX}$ , i.e. the amount of heat that cannot be transferred from the strong to weak solution consequently can be calculated from the terminal temperature difference  $TTD_{SHX}$  at the cold end of the solution heat exchanger and the heat capacity of the strong solution flow:

$$\Delta\dot{Q}_{LOSS,SHX} = \dot{M}_{STRONG} \cdot c'_{STRONG} \cdot TTD_{SHX} \quad (2.42)$$

Utilizing the definition (2.10) of the specific strong solution flow  $f_{STRONG} = \dot{M}_{STRONG} / \dot{M}_{REFR}$  the specific heat exchanger loss  $\Delta q_{LOSS,SHX}$  with respect to the circulating refrigerant can be written:

$$\Delta q_{LOSS,SHX} = \Delta\dot{Q}_{LOSS,SHX} / \dot{M}_{REFR} = c'_{STRONG} \cdot f_{STRONG} \cdot TTD_{SHX} \quad (2.43)$$

It has to be balanced by extra heat input at the regenerator, too.

### Thermal efficiency of real absorption chillers

Taking into account all these internal loss mechanisms, the maximum efficiency of a real water/lithium bromide based absorption chiller is:

$$COP_{C,REAL} = ((\Delta h_{VAP})_{T_0} - \Delta q_{THROT}) / ((\Delta h_{VAP} + \Delta h_{SOL})_{T_2} + \Delta q_{MISMATCH} + \Delta q_{LOSS,SHX}) \quad (2.44)$$

The efficiency of an actual machine will be slightly lower than this limit, as (2.44) does not account for e.g. external or internal heat losses due to imperfect thermal insulation of components and several minor internal irreversibilities.

While the throttling loss  $\Delta q_{THROT}$  and the mismatch  $\Delta q_{MISMATCH}$  can be directly calculated from the property data of the refrigerant once the internal the internal temperature levels  $T_0$ ,  $T_1$  and  $T_2$  are given, the solution heat exchanger loss  $\Delta q_{LOSS,SHX}$  is mainly dependent on technical and economical considerations and cannot be directly derived from thermodynamics. In actual machines, the specific solution circulation  $f_{STRONG}$  at full load operation ranges from at least 7 to about 30. Although the technical limit for the terminal temperature difference  $TTD_{SHX}$  in the solution heat exchanger is somewhere below 1 Kelvin, practical designs

realize values from at least 3 K to even 10 K and more at full load operation. This is mainly due to economical optimization. Besides, too effective cooling of the strong solution might induce crystallization in the solution heat exchanger, especially what low specific solution circulations  $f_{STRONG}$  are concerned<sup>23</sup>. Thus, there exists a practical lower limit for the product of  $f_{STRONG} \cdot TTD_{SHX}$  in (2.43).

For the mean temperature levels of the more or less typical example provided in Tab. 4 above, it reveals that the specific throttling loss  $\Delta q_{THROT}$  has a magnitude of about 7% of the specific heat of vaporization in the evaporator  $(\Delta h_{VAP})_{T0}$ . The magnitude of the specific mismatch  $\Delta q_{MISMATCH}$  is about 7% of the value of the specific heat for boiling off the refrigerant in the regenerator  $(\Delta h_{VAP} + \Delta h_{SOL})_{T2}$ . Regarding only these two loss mechanisms results in an efficiency limit of 0.79 which is, however, only 10% less than the endoreversible efficiency of an ideal chiller  $COP_{C,ENDOREV} = 0.882$  according to (2.28) or (2.37). The reason for this apparent discrepancy is, that both loss terms  $\Delta q_{THROT}$  and  $\Delta q_{MISMATCH}$  do not only reflect actual process irreversibilities; about a quarter of their values is no real loss from a thermodynamic point of view, but a compensation for the temperature dependency of the specific heat of vaporization. A more detailed discussion of this effect is given in appendix A.1.

For estimation of the specific heat exchanger loss  $\Delta q_{LOSS,SHX}$  we might assume a specific strong solution circulation  $f_{STRONG}$  of 14 and a terminal temperature difference  $TTD_{SHX}$  of 7, resulting in a heat exchanger loss in the same order of magnitude as the mismatch of about 7% of the heat for the phase change in the regenerator. A very ambitious design might be able to realize only halve this loss, however, in commercially available machines even higher values are common. After all this makes efficiency limits  $COP_{C,REAL}$  for real water / lithium bromide based single-effect chillers at typical operating conditions of about 0.74 to 0.79 according to (2.44). Actual machines reach slightly lower values due to additional internal loss mechanisms not included in (2.44), so actual efficiencies in the range of 0.70 to 0.75 at ARI standard conditions can be considered state of the art. According to (2.36), these numbers correspond with a thermodynamic quality factor  $g$  of 80% to 85%.

<sup>23</sup> This is because a small specific solution circulation rate  $f$  corresponds with a big difference in concentration  $\Delta X$  between strong and weak solution. For this case, the temperature of the weak solution entering the solution heat exchanger may already be below the solidification temperature of the strong solution in the counter flow. Therefore, the minimum approach temperature of the heat exchange process must not fall below a certain limit. The minimum design value, however, cannot be directly taken from property data on solidification temperatures, as some more effects like sudden temperature fluctuations due to control issues and inhomogeneous temperatures and flows within the heat exchanger also require their safety margins.

### 2.2.4 Efficiency of indirect-fired double-effect chillers

For hot water fired absorption chillers with driving heat input at a single temperature level, all considerations on efficiency limits of single-effect chillers presented above apply analogously. A double-effect cycle consists of two staggered single-effect cycles, where the low-temperature regenerator LTG at the intermediate temperature level is heated via an internal heat exchange by the condensation of the refrigerant boiled off in the high-temperature regenerator HTG at the highest temperature level. Assuming the same mean lithium bromide concentrations in both regenerators and neglecting the driving temperature difference  $\Delta T_{LTG}$  required for this internal heat exchange, from (2.14) and (2.15) the Dühring relation for a double-effect cycle can easily be derived:

$$T_1 - T_0 = (T_2 - T_1) \cdot R_D^2 / (1 + R_D) \quad (2.45)$$

This equation has the same form as the corresponding Dühring equation (2.30) for the basic single-effect cycle. The substitution of the Dühring slope  $R_D$  (2.31) gives again the internal driving temperature level  $T_2$ :

$$T_2 = \left[ T_1^3 - B_D \cdot (2 \cdot T_1 - T_0) \cdot (T_1 - T_0) + B_D^2 \cdot (T_1 - T_0) \right] / T_0^2 \quad (2.46)$$

The endoreversible limit for the *COP* of a double-effect cycle is again determined by the universal thermodynamic relation (2.28) for heat driven chillers.

Like for the basic single-effect cycle, the approximation  $B_D = 0$  from (2.4) reduces these lengthy expressions to simple relations:

$$T_2 \approx T_1^3 / T_0^2 \quad (2.47)$$

$$COP_{C,DE,ENDOREV} \approx T_0 / T_1 + (T_0 / T_1)^2 \approx R_D + R_D^2 \quad (2.48)$$

Using again external temperatures according to ARI standards (see Tab. 2), typical driving temperature differences (see Tab. 3) and an approximate Dühring intercept  $B_D = -7.5 \text{ K}$ , an calculation analogous to the single-effect case presented in Tab. 4 can be made up for the endoreversible double-effect chiller, too. From (2.28) and (2.46), an efficiency limit of  $COP_{C,DE,ENDOREV} = 1.65$  for the double-effect chiller can be estimated based on the mean internal temperatures  $T_0 = 2.5^\circ\text{C}$  and  $T_1 = 43.5^\circ\text{C}$  given in Tab. 4.

Respective formulations for throttling loss, mismatch and solution heat exchanger loss in double-effect chillers could be derived analogous to the single-effect case presented above. Without going into these details, the assumption of a thermodynamic quality factor  $g$  in the same range of about 80% to 85% for a double-effect chiller as derived for a single-effect cycle results in real efficiencies of about 1.3 to 1.4 according to (2.36). Actually, the increased complexity of the double-effect cycle and the additional internal heat exchange process

introduce some more non-idealities. Therefore, thermal efficiencies  $COP_{C,DE,REAL}$  in the range of 1.2 to 1.4 can be considered state of the art for indirect-fired double-effect chillers.

It has to be stated, however, that equations (2.45) to (2.48) given for double-effect chillers are less universal than the corresponding relations (2.30) to (2.32) for the basic single-effect cycle are. The basic assumption for setting up the endoreversible model of the single-effect cycle was that the major irreversibilities could be attributed to the nonideal heat exchange processes with nonzero driving temperature differences between external heat carriers and a nearly ideal internal cycle. The double-effect chiller violates this assumption as it introduces a major internal heat exchange to drive the low-temperature regenerator at the intermediate temperature level. This internal heat exchange typically takes driving temperature differences  $\Delta T_{LTG}$  of 10 K to 15 K under nominal operation (see Tab. 3); thus, it cannot be considered ideal or reversible. Strictly speaking, this internal irreversibility had to be considered explicitly in the quality factor according to (2.36) to pursue with the endoreversible modeling.

If we do not disregard the driving temperature difference  $\Delta T_{LTG}$  when setting up the Dühring relation, we find a shift in driving temperature  $T_2$  by  $\Delta T_{LTG}/R_D = \Delta T_{LTG} \cdot (T_1 - B_D)/T_0$  in comparison to equations (2.45) and (2.46):

$$T_1 - T_0 = \left[ (T_2 - \Delta T_{LTG}/R_D) - T_1 \right] \cdot R_D^2 / (1 + R_D) \quad (2.49)$$

$$T_2 = \Delta T_{LTG} \cdot (T_1 - B_D) / T_0 + \left[ T_1^3 - B_D \cdot (2 \cdot T_1 + T_0) \cdot (T_1 - T_0) + B_D^2 \cdot (T_1 - T_0) \right] / T_0^2 \quad (2.50)$$

With the assumption of 10 K driving temperature difference  $\Delta T_{LTG}$  and the same mean concentration in both regenerators, (2.50) can be evaluated for an analogous situation as given in Tab. 4. Actually, it is good practice in commercial chiller designs to keep all vessels at sub-atmospheric pressure to avoid extra cost due to pressure-vessel safety regulations. This limits temperatures in the low-temperature regenerator, as the internal condensation temperature  $T_{LTG} + \Delta T_{LTG}$  must not exceed 100°C. An example of typical mean temperatures in a double-effect absorption chiller at ARI conditions (see Tab. 2) is provided in Tab. 5<sup>24</sup> below.

<sup>24</sup> It should be noted that the mean internal temperatures listed in Tab. 5 deviate only slightly from the respective corresponding solution temperatures in the patent drawing of [Gupte \(2005\)](#) that is cited in Fig. 5 in 2.1.4 above.

| Arithmetic mean temperatures and temperature differences | Mean external temperatures                               | Driving temperature differences   | Mean internal temperatures              |
|--|--|-----------------------------------|---|
| Driving heat level                                       | $t_2 = 168.5 \text{ }^\circ\text{C}$                     | $\Delta T_2 = 20.0 \text{ K}$     | $T_2 = 148.5 \text{ }^\circ\text{C}$    |
| Internal heat exchange                                   | $T_{LTG} + \Delta T_{LTG} = 95.6 \text{ }^\circ\text{C}$ | $\Delta T_{LTG} = 10.0 \text{ K}$ | $T_{LTG} = 85.6 \text{ }^\circ\text{C}$ |
| Reject heat level  | $t_1 = 32.5 \text{ }^\circ\text{C}$                      | $\Delta T_1 = 9.0 \text{ K}$      | $T_1 = 41.5 \text{ }^\circ\text{C}$     |
| Refrigeration level                                      | $t_0 = 9.5 \text{ }^\circ\text{C}$                       | $\Delta T_0 = 6.0 \text{ K}$      | $T_0 = 3.5 \text{ }^\circ\text{C}$      |

*Tab. 5: Example calculation of mean internal and external temperatures in a typical double-effect chiller running at ARI standard conditions utilizing.*

Calculations based on an approximate Dühring intercept  $B_D = -7.5 \text{ K}$  as suggested above would reveal a mean internal driving temperature  $T_2$  of  $147^\circ\text{C}$  and a mean external driving temperature  $t_2$  of  $167^\circ\text{C}$  for the double-effect chiller in this example.

### 2.2.5 Triple-effect and quadruple-effect chillers

From theory it can be shown that combining an increasing number of basic single-effect cycles in a way that reject heat from one cycle provides driving heat for the next one creates an infinite series of multi-effect chillers, the double-effect cycle discussed above being just the first one in this line. With each additional stage, driving temperature and thermal efficiency are increased. However, more costly plant design due to increased complexity of the cycle, increased corrosivity of lithium bromide or similar salt solutions at elevated temperatures and regulatory and safety aspects for operation at respectively increased pressure levels results in a limited economic prospect.

Hence these cycles shall not be discussed in detail, but an estimation for internal driving temperatures and efficiencies can easily be derived employing the approximation  $B_D = 0$  from (2.4). Along the lines of (2.47) and (2.48) driving temperatures of the triple-effect cycle  $T_{2,TE}$  and the quadruple-effect cycle  $T_{2,QE}$  and endoreversible limits for the thermal efficiencies of the triple-effect chiller  $COP_{C,TE,ENDOREV}$  and of the quadruple-effect cycle  $COP_{C,QE,ENDOREV}$  can be approximated:

$$T_{2,TE} \approx T_1^4 / T_0^3 \quad (2.51)$$

$$\begin{aligned} COP_{C,TE,ENDOREV} &\approx T_0 / T_1 + (T_0 / T_1)^2 + (T_0 / T_1)^3 \\ &\approx R_D + R_D^2 + R_D^3 \end{aligned} \quad (2.52)$$

$$T_{2,QE} \approx T_1^5 / T_0^4 \quad (2.53)$$

$$\begin{aligned} COP_{C,QE,ENDOREV} &\approx T_0 / T_1 + (T_0 / T_1)^2 + (T_0 / T_1)^3 + (T_0 / T_1)^4 \\ &\approx R_D + R_D^2 + R_D^3 + R_D^4 \end{aligned} \quad (2.54)$$

An evaluation based on mean internal temperatures  $T_0$  and  $T_1$  of  $3.5^\circ\text{C}$  and  $40.5^\circ\text{C}$  – as used in the example above for a double-effect chiller at ARI conditions – estimates internal driving

temperatures for a triple-effect cycle of about  $190^{\circ}\text{C}$  and for a quadruple-effect cycle of about  $250^{\circ}\text{C}$ . Actual temperatures might be a little higher as the simple approximations (2.51) and (2.53) do not account for driving temperature differences in the internal heat exchange processes.

If we additionally assume that thermodynamic quality factors  $g$  of about 75% were feasible for realization of such complex cycles, we can estimate actual efficiencies  $COP_{REAL}$  of these multi-stage machines:

$$COP_{REAL} = g \cdot COP_{ENDOREV} \quad (2.55)$$

Thus, from (2.52), (2.54) and (2.55) we may expect thermal efficiencies of up to 1.7 for triple-effect chillers and efficiencies of up to 2.2 for quadruple-effect chillers.

## 2.2.6 Integrated multi-stage chillers

The thermal efficiency of multi-effect chillers that simultaneously receive driving heat input at different temperature levels like e.g. integrated single-effect/double-effect machines can easily be estimated from the superposition of the efficiencies of the individual cycles. If such a chiller receives the external heat input  $\dot{Q}_{2,DE}$  in the high-temperature regenerator of the double-effect cycle and the external heat input  $\dot{Q}_{2,SE}$  in the low-temperature regenerator of the single-effect cycle, then the efficiency  $COP_{C,SEDE}$  of the integrated chiller is about:

$$COP_{C,SEDE} \approx (COP_{C,SE} \cdot \dot{Q}_{2,SE} + COP_{C,DE} \cdot \dot{Q}_{2,DE}) / (\dot{Q}_{2,SE} + \dot{Q}_{2,DE}) \quad (2.56)$$

An exact calculation would have to take into account that both partial efficiencies  $COP_{C,SE}$  and  $COP_{C,DE}$  are dependent on the load of the chiller and thus are not independent from each other. For about balanced external heat input  $\dot{Q}_{2,SE} \approx \dot{Q}_{2,DE}$  and real cycle efficiencies of  $COP_{C,SE} \approx 0.7$  and  $COP_{C,DE} \approx 1.3$ , (2.56) yields a thermal efficiency of about  $COP_{C,SEDE} \approx 1$  for a SE/DE-chiller.



## 2.3 Flue gas fired absorption chillers

### 2.3.1 Terminology

The term “flue gas fired chiller” shall be used to denote all kinds of chillers that receive a major part of their driving heat by direct heat exchange from a hot flue gas stream. Of course, this applies for all kinds of exhaust-gas heat recovery from motor engines, gas turbines, high-temperature fuel cells, or industrial processes if the hot exhaust gas is directly utilized to heat a regenerator of an absorption chiller. However, this definition also includes the so-called direct-fired chillers equipped with gas or oil burners. Here a smaller portion of the driving heat of the chiller directly results from the radiation of the flame while the major part of the heat input is still gained by a convective heat transfer from the hot flue gas of the combustion process. Finally, there are co-fired chillers that alternatively or simultaneously can directly utilize two driving heat sources: a hot exhaust gas stream and a combustion process. On the other hand, the term flue gas fired chiller shall not comprise any indirect utilization of flue gas heat in an absorption chiller via an intermediate heat carrier like e.g. a hot water cycle, as this case is already covered by the term indirect-fired chiller.

### 2.3.2 Common design

From all kinds of flue gas fired chillers, only direct-fired chillers are available from series production. Meanwhile there are several installations of exhaust-fired and co-fired chillers and such machines are commercially available upon request from major suppliers, but there is not yet an optimized “standard design” for such machines. Actually, all these installations are based on slightly modified direct-fired chillers, e.g. as reported by *Pathakji et al. (2005)* or *Wagner et al. (2005)*.

Direct-fired chillers typically consist of two main components on two separate base frames installed side by side. The bigger one – covering about 60% of the total footprint of the plant – carries a steam-fired single-effect cycle like it is part of any double-effect chiller, the smaller frame – covering still about 40% of the total footprint – carries the direct-fired regenerator. The standard design of direct-fired regenerators is mainly determined by the request to be compatible with many kinds of fossil fuels: natural gas, town gas or liquid petrol gas as well as light fuel oil or even heavy fuel oil. Especially the utilization of heavy fuel oil imposes some boundary conditions on the design that are contrary to an optimized thermal efficiency and a compact and cost efficient design. Wide structures in all heat exchangers and high leaving flue gas temperatures are required to avoid clogging, sooting or corrosion due to aggressive condensate from the exhaust gas.

Hence, direct-fired regenerators are typically based on a two-pass design on the heating side, the first pass being a voluminous flame-tube, the second pass being a bunch of smoke

tubes placed above. Both passes are completely immersed in the boiling lithium bromide solution, which is contained itself in a big vacuum vessel. After all, this robust and proven but not yet very compact design comes along with certain disadvantages in terms of footprint and required space, high weight and big volume of expensive lithium bromide solution.



*Fig. 9: Examples for recently installed direct exhaust-fired double-effect chillers with voluminous smoke-tube regenerators covering about half the footprint of the total plant.*

*Left photograph from Pathakji et al. (2005), right photograph from Wagner et al. (2005).*

Current installations of absorption chillers for direct utilization of exhaust gas from gas engines, micro-turbines, or high-temperature fuel cells are mostly based on this regenerator design, too, except that there is no flame tube for these applications. One or two passes of horizontal tubes and completely immersed in boiling lithium bromide solution with the exhaust gas inside the tubes is the standard configuration (see also left sketch of Fig. 24 in 4.1.1 below). Two photographs of exhaust-fired absorption chillers employing such single-pass smoke-tube regenerators that have recently been installed in gas turbine based CCHP systems are shown in Fig. 9 above.

### 2.3.3 Thermal efficiency

The thermal efficiency  $COP_{FGF}$  of a flue gas fired chiller is the product of the cycle efficiency  $COP_{CYC}$  of the implemented absorption cycle and the efficiency  $\eta_{FGU}$  of the flue gas utilization in the machine.

$$COP_{FGF} = \eta_{FGU} \cdot COP_{CYC} \quad (2.57)$$

If the flue gas is only utilized in a single regenerator – as it is still state of the art in direct-fired chillers – then the cycle efficiency  $COP_{CYC}$  is identical to the  $COP$  of an indirect-fired chiller operating at the same internal temperatures. For the cycle efficiency  $COP_{CYC}$  of common direct-fired double-effect chillers in cooling mode, all considerations on real efficiencies of indirect-fired double-effect chillers presented in 2.2.4 above apply analogously, i.e.  $COP_{CYC} = COP_{C,DE,REAL}$ .

The efficiency of the flue gas utilization is the ratio of the used flue gas enthalpy  $H_{FG,USED}$  to the available flue gas enthalpy  $H_{FG,AVAIL}$ . Here the available flue gas enthalpy is defined as the energy that could be transferred if the flue gas would be cooled down from entering temperature  $T_{FG,ENTER}$  to ambient temperature  $T_{AMB}$  instead of its actual leaving stack temperature  $T_{FG,STACK}$ .

$$\begin{aligned}\eta_{FGU} &= H_{FG,USED} / H_{FG,AVAIL} \\ &= [h_{FG}(T_{FG,ENTER}) - h_{FG}(T_{FG,STACK})] / [h_{FG}(T_{FG,ENTER}) - h_{FG}(T_{AMB})]\end{aligned}\quad (2.58)$$

For direct-fired chillers, the flue gas utilization is ratio of the used flue gas enthalpy  $H_{FG,USED}$  to the actual calorific value of the fuel  $\Delta H_{CV,FUEL}$ , but the same formulation like (2.58) above can be used if the entering flue gas temperature  $T_{FG,ENTER}$  is replaced by the theoretical adiabatic flame temperature  $T_{FLAME}$ .

$$\begin{aligned}\eta_{FGU} &= H_{FG,USED} / \Delta H_{CV,FUEL} \\ &= [h_{FG}(T_{FLAME}) - h_{FG}(T_{FG,STACK})] / [h_{FG}(T_{FG,ENTER}) - h_{FG}(T_{AMB})]\end{aligned}\quad (2.59)$$

The adiabatic flame temperature  $T_{FLAME}$  is implicitly given for a specific fuel in dependence on the gravimetric calorific value  $\Delta h_{CV,FUEL}$ , the gravimetric stoichiometric air to fuel ratio  $AFR_{STOIC} = m_{AIR,STOIC} / m_{FUEL}$  for stoichiometric combustion and the excess air number  $\lambda_{EXC,AIR} = m_{AIR} / m_{AIR,STOIC}$  of the actual combustion process:

$$\Delta h_{CV,FUEL} = AFR_{STOIC} \cdot \lambda_{EXC,AIR} \cdot [h_{FG}(T_{FLAME}) - h_{FG}(T_{AMB})]\quad (2.60)$$

For natural gas, the adiabatic flame temperature  $T_{FLAME}$  is about  $2000^{\circ}\text{C}$  for stoichiometric combustion (i.e.  $\lambda_{AIR} = 1$ ) and about  $1500^{\circ}\text{C}$  for 50% excess air (i.e.  $\lambda_{AIR} = 1.5$ ). As  $\text{NO}_x$  emissions must not exceed certain limits in most countries due to environmental regulations, direct-fired chillers are typically operated with some excess air to reduce the actual flame temperature.

As the specific heat capacity of the flue gas  $c_{p,FG}$  is only slightly dependent on temperature below about  $1300^{\circ}\text{C}$ , assumption of a constant heat capacity may be used as first approximation for moderate entering flue gas temperatures and no condensation in the flue gas train ( $T_{FG,STACK} \geq 90^{\circ}\text{C}$ ). Thus, (2.58) can be simplified:

$$\eta_{FGU} \approx (T_{FG,ENTER} - T_{FG,STACK}) / (T_{FG,ENTER} - T_{AMB})\quad (2.61)$$

Within this work, however, computerized property data functions for air and natural gas combustion products based on the polynomial coefficients given by *Rhine & Tucker (1991)* were used for all calculations. By this way, for about 50% excess air,  $1500^{\circ}\text{C}$  adiabatic flame temperature and  $200^{\circ}\text{C}$  stack temperature from (2.59) about 90% flue gas utilization  $\eta_{FGU}$  are

obtained. Assuming state of the art efficiencies  $COP_{CYC} = COP_{C,DE,REAL}$  in the range of 1.2 to 1.4 for the double-effect absorption cycle, thermal efficiencies  $COP_{FGF}$  in the range of 1.1 to 1.3 can be derived from (2.57) for direct-fired chillers.

For utilization of exhaust gas from gas engines, micro turbines, or high temperature fuel cells with entering temperatures of about  $500^{\circ}\text{C}$  and similar boundary conditions, flue gas utilization drops to only 65%. The corresponding thermal efficiency with respect to the total flue-gas heat content  $COP_{FGF}$  of such an exhaust-fired double-effect chiller is only in the range of 0.8 to 0.9. Nevertheless, this is still better than the efficiency that would result for an exhaust-fired single-effect chiller, where the cycle efficiency  $COP_{CYC}$  itself would hardly exceed a value of 0.8.

## 3 Basic concepts for highly efficient flue gas fired chillers

### 3.1 General settings

The fundamental difference between indirect-fired chillers and flue gas fired chillers is that hot flue gas provides driving heat at gliding temperature, ranging from ambient temperature to several hundred degrees centigrade for exhaust gases or up to  $1500^{\circ}\text{C}$  and more in the case of direct firing. For maximum thermal efficiency, an endoreversible flue gas fired chiller therefore had to utilize this driving heat at gliding internal temperature or at numerous staggered internal temperatures from the flue gas entry temperature down to almost<sup>25</sup> ambient temperature.

Although driving heat input at gliding temperatures or at multiple temperature levels can only be realized to some extent in actual machines, there are general boundary conditions for the flue gas utilization in absorption machines.

#### 3.1.1 Terminal temperature difference for flue gas heat exchangers

Although a theoretical approach might suggest minimizing driving temperature differences to increase the efficiency of flue gas utilization in flue gas fired regenerators and other flue gas heat exchangers, typical designs use terminal temperature differences of  $15\text{ K}$  to  $50\text{ K}$  to ensure reasonable economics and acceptable pressure drops. In the following discussion, a terminal temperature difference of about  $30\text{ K}$  will be assumed as a minimum design limit.

#### 3.1.2 Lower temperature limit of flue gas utilization

Generally, the utilization of flue gas heat in at low temperatures where condensation of combustion products in the heat exchanger or in the flue gas duct downstream might occur is possible in case of appropriate material selection and plant design. However, this comes along with extra cost and design limitations not only for the heat exchangers but also for the total flue gas system downstream that after all might limit the application of such chiller technology.

In contrast to combustion products from heavy fuel oil or biomass, flue gas from combustion of natural gas or respective exhaust gas from gas-fuelled engines, turbines, or fuel cells is a quite “clean” substance. Its utilization is mainly limited by the possible condensation of water at temperatures below  $80^{\circ}\text{C}$ . As some additional temperature drop along the flue gas ducts has to be taken into account, only flue gas heat at temperatures above  $90^{\circ}\text{C}$  shall be

---

<sup>25</sup> The endoreversible concept already takes into account the requirement of a nonzero driving temperature difference for any external heat exchange.

accounted useful heat while flue gas heat at temperatures below  $90^{\circ}\text{C}$  shall always be assigned to the stack loss in the following discussion.

### 3.1.3 Upper internal temperature limit for driving heat input

From fundamental thermodynamics, it is obvious that utilization of flue gas heat is most efficient at the highest possible internal temperature level, just allowing for a minimum necessary temperature difference for the heat exchange from flue gas to internal cycle. Assuming at least  $30\text{ K}$  temperature difference as stated above, flue gas temperatures higher than  $230^{\circ}\text{C}$  would require a triple-effect chiller, flue gas temperatures higher than  $300^{\circ}\text{C}$  would even require a quadruple-effect chiller for maximum efficiency of heat utilization.

However, presently these complex high-temperature cycles are not commercially available and do not have a positive economic prospect, as they require a significantly more costly design than double-effect chillers. Therefore, in the following discussion only possibilities for efficient utilization of flue gas heat in single-effect and double-effect machines will be regarded. However, the basic concepts provided could also be applied to triple-effect chillers.

## 3.2 Cycle analysis

### 3.2.1 Flow scheme and equilibrium states

#### Dühring chart

The basic setting of equilibrium states and internal mass flows in a double-effect cycle is visualized in Fig. 10 in a Dühring chart; the set of mean internal temperatures from the sample calculation given in Tab. 5 in 2.2.4 above was employed as basis for this diagram. Actually, for finite solution circulation and nonzero concentration difference, these settings are dependent on the type of the solution cycle; therefore, a parallel-flow cycle is displayed in Fig. 10 as this is the most general case. In the following discussion, it will be assumed that the solution circulation is sufficiently high that there is approximately the same mean concentration in all absorbers and regenerators. Then small shifts in saturation temperatures depending on the actual solution cycle layout can be neglected.

The graph in Fig. 10 is also valid for integrated single-effect/double-effect chillers (cf. Fig. 4 in 2.1) assuming that the low-temperature regenerators of the single-effect and the double-effect cycle are operated at the same internal temperatures and concentrations. For thermodynamic considerations, this is equivalent to the integration of both low-temperature regenerators into a single device with heat input from two sources. Therefore, in the following discussion the term low-temperature regenerator shall address all regenerator units at this temperature level – no matter if they are actually integrated into a single device or not.

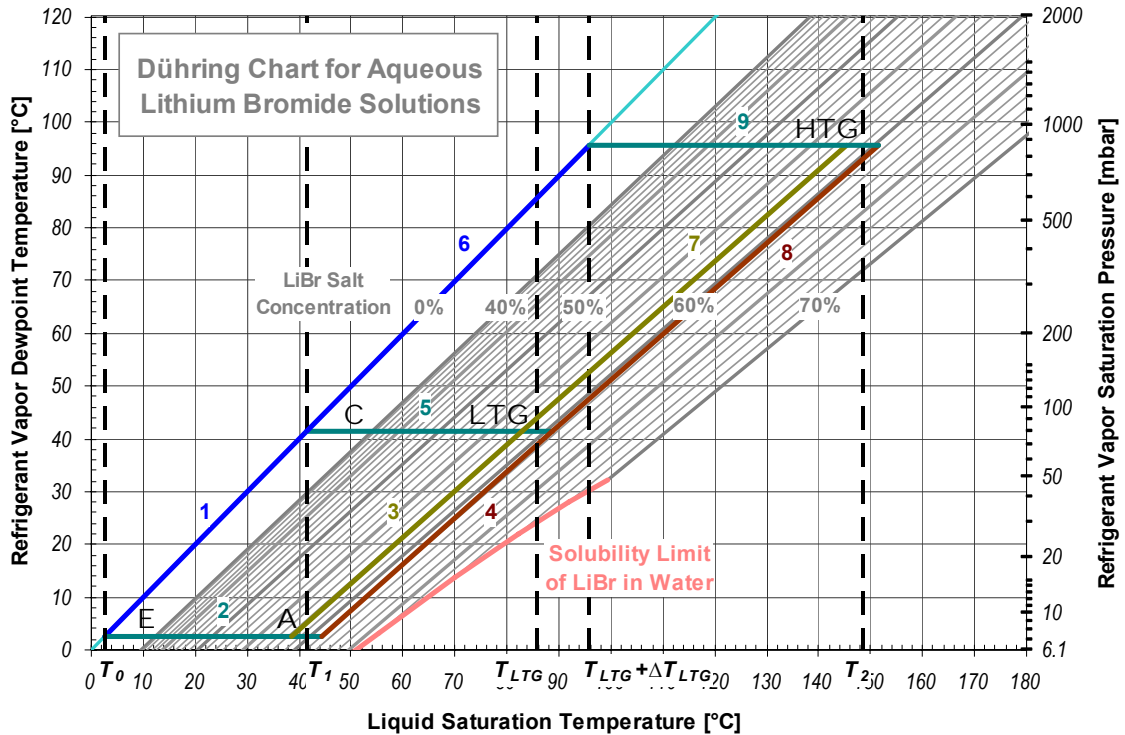


Fig. 10: Visualization of equilibrium states and internal mass flows of a sample double-effect chiller (cf. Tab. 5) in a Dühring chart.

### Refrigerant flows

In a DE or SE/DE chiller, the refrigerant flow from evaporator to absorber  $\dot{M}_{REFR}$  is the sum of the refrigerant being boiled off in the high-temperature regenerator  $\dot{M}_{REFR,HTG}$  and the refrigerant boiled off in the low-temperature regenerator(s)  $\dot{M}_{REFR,LTG}$ .

$$\dot{M}_{REFR} = \dot{M}_{REFR,HTG} + \dot{M}_{REFR,LTG} \quad (3.1)$$

For convenience, the fractions of the refrigerant boiled off in the individual stages shall be denoted as  $\gamma_{LTG}$  and  $\gamma_{HTG}$ :

$$\gamma_{HTG} = \dot{M}_{REFR,HTG} / \dot{M}_{REFR} \quad (3.2)$$

$$\gamma_{LTG} = \dot{M}_{REFR,LTG} / \dot{M}_{REFR} \quad (3.3)$$

$$\gamma_{HTG} + \gamma_{LTG} = 1 \quad (3.4)$$

In a double-effect chiller, in which the low-temperature regenerator receives only driving heat by the internal heat exchange and there is no extra input of external heat at this temperature level, about one-half of the total circulating refrigerant is boiled off in either of the regenerators, i.e.  $\gamma_{HTG} \approx \gamma_{LTG} \approx 0.5$ . The exact value of this ratio is dependent on the losses in both solution heat exchangers, however.

With extra heat input in the low-temperature regenerator in SE/DE machines, the refrigerant fraction from the low-temperature regenerator(s) becomes the dominant one  $\gamma_{LTG} > \gamma_{HTG}$ . For

about balanced external heat input  $\dot{Q}_{2,SE} \approx \dot{Q}_{2,DE}$  at both temperature stages, values of about  $\gamma_{LTG} \approx 0.7$  and  $\gamma_{HTG} \approx 0.3$  are to be expected.

For boiling off the circulating refrigerant flow  $\dot{M}_{REFR}$  in the machine, the specific heat input  $\Delta q_{HTG} = \gamma_{HTG} \cdot (\Delta h_{VAP} + \Delta h_{SOL})_{T2}$  is required in the high-temperature regenerator. Additionally, in the low-temperature regenerator the specific heat  $\Delta q_{LTG} = (1 - \gamma_{HTG}) \cdot (\Delta h_{VAP} + \Delta h_{SOL})_{TLTG}$  is required either from internal heat exchange or from external heat input.

### Series-flow and reverse-flow solution cycle

For a series-flow solution-cycle, all the weak solution leaving the absorber  $\dot{M}_{WEAK}$  is entering the high-temperature regenerator as  $\dot{M}_{WEAK,HTG}$  and all the strong solution leaving the low-temperature regenerator  $\dot{M}_{STRONG,LTG}$  is entering the absorber as  $\dot{M}_{STRONG}$ . The solution flow  $\dot{M}_{STRONG,HTG}$  leaving the high-temperature regenerator is entering the low-temperature regenerator as  $\dot{M}_{WEAK,LTG}$ :

$$\dot{M}_{WEAK,HTG} = \dot{M}_{WEAK} \quad (3.5)$$

$$\dot{M}_{STRONG,LTG} = \dot{M}_{STRONG} \quad (3.6)$$

$$\dot{M}_{STRONG,HTG} = \dot{M}_{WEAK,LTG} = \dot{M}_{WEAK} - \dot{M}_{REFR} \cdot \gamma_{HTG} = \dot{M}_{STRONG} + \dot{M}_{REFR} \cdot (1 - \gamma_{HTG}) \quad (3.7)$$

Corresponding equations for the – quite uncommon – reverse-flow solution cycle without bypass are as follows:

$$\dot{M}_{WEAK,LTG} = \dot{M}_{WEAK} \quad (3.8)$$

$$\dot{M}_{STRONG,HTG} = \dot{M}_{STRONG} \quad (3.9)$$

$$\dot{M}_{STRONG,LTG} = \dot{M}_{WEAK,HTG} = \dot{M}_{WEAK} - \dot{M}_{REFR} \cdot (1 - \gamma_{HTG}) = \dot{M}_{STRONG} + \dot{M}_{REFR} \cdot \gamma_{HTG} \quad (3.10)$$

As a result, the specific solution circulation in the high-temperature regenerator of a series-flow or reverse-flow chiller is higher than in the absorber. For the case of a series-flow cycle the specific weak solution flow entering the high-temperature regenerator  $f_{WEAK,HTG} = \dot{M}_{WEAK,HTG} / \dot{M}_{REFR,HTG}$  and the specific strong solution flow leaving the high-temperature regenerator  $f_{STRONG,HTG} = \dot{M}_{STRONG,HTG} / \dot{M}_{REFR,HTG}$  yield:

$$f_{WEAK,HTG} = f_{WEAK} / \gamma_{HTG} \quad (3.11)$$

$$f_{STRONG,HTG} = f_{STRONG} / \gamma_{HTG} + (1 - 1 / \gamma_{HTG}) \quad (3.12)$$

In the case of no external heat input in the low-temperature regenerator, the specific solution circulation in the high-temperature regenerator is about twice the specific circulation in the absorber:

$$\gamma_{HTG} \approx 0.5 \Rightarrow f_{WEAK,HTG} \approx 2 \cdot f_{WEAK} \quad (3.13)$$

$$\gamma_{HTG} \approx 0.5 \Rightarrow f_{STRONG,HTG} \approx 2 \cdot f_{STRONG} + 1 \quad (3.14)$$



According to (2.12) and (2.13), the concentration difference in the high-temperature regenerator is only half of the concentration difference in the absorber.

### Split solution flow

It has already been argued that a configuration of the solution cycle where solution flow is split and only a fraction of the total solution circulation passes the high-temperature regenerator is potentially advantageous as this design might result in a smaller high-temperature solution heat exchanger. The main constraints for the specific solution circulation in absorber and low-temperature solution heat exchanger – minimum required solution flow for proper wetting of the tube bundle and maximum possible strong solution concentration to avoid crystallization – do not apply for high-temperature regenerator and high-temperature solution heat exchanger<sup>26</sup>. Therefore, the specific solution circulation in the high-temperature regenerator  $f_{WEAK,HTG}$  can even be significantly lower than those in the absorber  $f_{WEAK}$  is. The following discussion, however, shall focus on the “symmetric” case characterized by identical specific solution circulations in absorber and high-temperature regenerator  $f_{WEAK,HTG} = f_{WEAK}$ ,  $f_{STRONG,HTG} = f_{STRONG}$ . The absolute mass flows are:

$$\dot{M}_{WEAK,HTG} = \dot{M}_{WEAK} \cdot \gamma_{HTG} \quad (3.15)$$

$$\dot{M}_{STRONG,HTG} = \dot{M}_{STRONG} \cdot \gamma_{HTG} \quad (3.16)$$

In the case of a parallel flow solution cycle the solution flow is split before entering the low-temperature regenerator, hence the solution flow in the low-temperature regenerator is:

$$\dot{M}_{WEAK,LTG} = \dot{M}_{WEAK} \cdot (1 - \gamma_{HTG}) \quad (3.17)$$

$$\dot{M}_{STRONG,LTG} = \dot{M}_{STRONG} \cdot (1 - \gamma_{HTG}) \quad (3.18)$$

On the other hand in the case of a reverse flow with bypass the solution flow is split after leaving the low-temperature regenerator, corresponding flows in the low-temperature regenerator are:

$$\dot{M}_{WEAK,LTG} = \dot{M}_{WEAK} \quad (3.19)$$

$$\dot{M}_{STRONG,LTG} = \dot{M}_{WEAK} - \dot{M}_{REFR} \cdot (1 - \gamma_{HTG}) \quad (3.20)$$

<sup>26</sup> Typically, no falling-film design is employed in high-temperature regenerators and solubility of lithium bromide in water is significantly better at higher temperatures.

### 3.2.2 Internal losses and internal heat recovery

#### Internal mass flows

Based on the definitions above, the internal loss mechanisms in a double-effect cycle can be analyzed. Following the approach in 2.2 for the analysis of the basic single-effect cycle (cf. Fig. 8), the heating and cooling demands of the nine internal mass flows in a double-effect chiller (Fig. 10) can be listed in an analogous way:

Liquid refrigerant flow  $\dot{M}_{REFR}$  from condenser (C) to evaporator (E), requiring cooling  $\dot{M}_{REFR} \cdot c'_{REFR} \cdot (T_0 - T_1) < 0$  at gliding temperatures from  $T_1$  to  $T_0$ .

Refrigerant vapor flow  $\dot{M}_{REFR}$  from evaporator (E) to absorber (A), requiring heating  $\dot{M}_{REFR} \cdot c''_{REFR} \cdot (T_1 - T_0)$  at gliding temperatures from  $T_0$  to  $T_1$ .

Weak solution flow  $\dot{M}_{WEAK} = \dot{M}_{STRONG} + \dot{M}_{REFR}$  from absorber (A) to low-temperature regenerator level (LTG), requiring heating  $\dot{M}_{WEAK} \cdot c'_{WEAK} \cdot (T_{LTG} - T_1)$  at gliding temperatures from  $T_1$  to  $T_{LTG}$ .

Strong solution flow  $\dot{M}_{STRONG}$  from low-temperature regenerator level (LTG) to absorber (A), requiring cooling  $\dot{M}_{STRONG} \cdot c'_{STRONG} \cdot (T_1 - T_{LTG}) < 0$  at gliding temperatures from  $T_{LTG}$  to  $T_1$ .

Refrigerant vapor flow  $\dot{M}_{REFR} \cdot (1 - \gamma_{HTG})$  from low-temperature regenerator (LTG) to condenser (C), requiring cooling  $\dot{M}_{REFR} \cdot (1 - \gamma_{HTG}) \cdot c''_{REFR} \cdot (T_1 - T_{LTG}) < 0$  at gliding temperatures from  $T_{LTG}$  to  $T_1$ .

Liquid refrigerant flow  $\dot{M}_{REFR} \cdot \gamma_{HTG}$  from condenser side of low-temperature regenerator to condenser (C), requiring cooling  $\dot{M}_{REFR} \cdot \gamma_{HTG} \cdot c'_{REFR} \cdot [T_1 - (T_{LTG} + \Delta T_{LTG})] < 0$  at gliding temperatures from  $T_{LTG} + \Delta T_{LTG}$  to  $T_1$ .

Weak solution flow  $\dot{M}_{WEAK,HTG} = \dot{M}_{STRONG,HTG} + \dot{M}_{REFR,HTG}$  from low-temperature regenerator level (LTG) to high-temperature regenerator (HTG), requiring heating  $\dot{M}_{WEAK,HTG} \cdot c'_{WEAK,HTG} \cdot (T_2 - T_{LTG})$  at gliding temperatures from  $T_{LTG}$  to  $T_2$ .

Strong solution flow  $\dot{M}_{STRONG,HTG}$  from high-temperature regenerator (HTG) to from low-temperature regenerator level (LTG), requiring cooling  $\dot{M}_{STRONG,HTG} \cdot c'_{STRONG,HTG} \cdot (T_{LTG} - T_2) < 0$  at gliding temperatures from  $T_2$  to  $T_{LTG}$ .

Refrigerant vapor flow  $\dot{M}_{REFR} \cdot \gamma_{HTG}$  from high-temperature regenerator (HTG) to from condenser side of low-temperature regenerator, requiring cooling  $\dot{M}_{REFR} \cdot \gamma_{HTG} \cdot c''_{REFR} \cdot [(T_{LTG} + \Delta T_{LTG}) - T_2] < 0$  at gliding temperatures from  $T_2$  to  $T_{LTG} + \Delta T_{LTG}$ .

The specific heating demands  $\Delta q_{WEAK,HT} = \Delta \dot{Q}_{WEAK,HT} / \dot{M}_{REFR}$  of the weak solution flow no. 7 in the temperature range  $T_{LTG}$  to  $T_2$  and  $\Delta q_{WEAK,LT} = \Delta \dot{Q}_{WEAK,LT} / \dot{M}_{REFR}$  of the weak solution flow no. 3 in the temperature range  $T_1$  to  $T_{LTG}$  can also be written as:

$$\Delta q_{WEAK,LT} = f_{WEAK} \cdot c'_{WEAK} \cdot (T_{LTG} - T_1) \quad (3.21)$$

$$\Delta q_{WEAK,HT} = \gamma_{HTG} \cdot f_{WEAK,HTG} \cdot c'_{WEAK,HTG} \cdot (T_2 - T_{LTG}) \quad (3.22)$$

For operation of the absorption cycle, both sensible heats (3.21) and (3.22) are required – either from internal heat exchange or from external heat input – in addition to the latent heats for evaporation of the refrigerant,  $\Delta q_{HTG} = \gamma_{HTG} \cdot (\Delta h_{VAP} + \Delta h_{SOL})_{T_2}$  at  $T_2$  and  $\Delta q_{LTG} = (1 - \gamma_{HTG}) \cdot (\Delta h_{VAP} + \Delta h_{SOL})_{T_{LTG}}$  at  $T_{LTG}$ . For a quite low specific solution circulation of only  $f_{WEAK,HTG} = 8$ , the sensible heating demand  $\Delta q_{WEAK,HT}$  in the temperature range  $T_{LTG}$  to  $T_2$  according to the sample calculation in Tab. 5 and Fig. 10 is already about 40% of the value of the required latent heat  $\Delta q_{HTG}$  at  $T_2$  in the high-temperature regenerator. At larger specific solution circulations,  $\Delta q_{WEAK,HT}$  may even exceed the value of  $\Delta q_{HTG}$ .

We can follow the line of argument given in 2.2.3 for the single-effect cycle that in a real machine there is no possibility for a heat exchange comprising the low-pressure vapor flows no. 2 and no. 5. Strictly speaking, this argumentation is not valid for the vapor flow no. 9 leaving the high-temperature regenerator, as this is almost<sup>27</sup> at ambient pressure. On the other hand, a heat exchanger for this internal vapor flow still would have higher specific costs than common liquid-liquid solution heat exchangers. As the heat not recovered from vapor flow no. 9 is not completely lost as waste heat but can still be utilized as driving heat in the low-temperature regenerator, a heat recovery from this vapor flow is not common in commercial designs.

Taking into account these restrictions, it is obvious from Fig. 10 that an optimized double-effect chiller had to implement two internal heat recovery processes: a low temperature heat recovery comprising flows no. 3, no. 4, and no. 6 and a high temperature heat recovery comprising flows no. 7, no. 8, and possibly no. 9. Common standard designs of commercial machines (cf. e.g. Fig. 3 in 2.1) only comprise a low-temperature solution heat exchanger between flows no. 3 and no. 4 and a high-temperature solution heat exchanger between flows no. 7 and no. 8, however.

It has to be noted however that – in contrast to the analogous discussion in 2.2.3 for single-effect cycles – the solution temperatures listed above for double-effect cycles are idealized approximations. Strictly speaking, the assumption that strong solution flow no. 4 enters the low-temperature heat exchanger at saturation temperature  $T_{LTG}$  is only valid for series flow cycles and the assumption that weak solution flow no. 7 enters the high-temperature heat exchanger at saturation temperature  $T_{LTG}$  is only valid for reverse flow cycles. Generally, both temperatures will be dependent on the effectiveness of the solution heat exchangers. Only if an ideal heat recovery is realized, the temperatures of the solution flows can be identical to the saturation temperatures displayed in Fig. 10.

<sup>27</sup> Typical design is heading for sub-atmospheric pressure in all vessels of a plant due to regulatory advantages in some countries (no classification as pressure vessel), economical optimization of the heat exchanger design might otherwise even result in slight overpressure.

In this ideal case, only the external heat input  $\Delta q_{HTG} = \gamma_{HTG} \cdot (\Delta h_{VAP} + \Delta h_{SOL})_{T_2}$  at internal temperature  $T_2$  would be required in the high temperature regenerator.

### Mismatch and solution heat exchanger losses

As already discussed in 2.2.3 for single-effect cycles, there is always a mismatch in the heat capacities of solution flows no. 3 no. 4. For DE and SE/DE cycles, the absolute mismatch  $\Delta \dot{Q}_{MISMATCH,LT}$  and the specific mismatch  $\Delta q_{MISMATCH,LT}$  in a low-temperature heat exchanger between these flows can be expressed on the lines of (2.40) and (2.41):

$$\Delta \dot{Q}_{MISMATCH,LT} = (\dot{M}_{WEAK} \cdot c'_{WEAK} - \dot{M}_{STRONG} \cdot c'_{STRONG}) \cdot (T_{LTG} - T_1) \quad (3.23)$$

$$\Delta q_{MISMATCH,LT} = \Delta \dot{Q}_{MISMATCH,LT} / \dot{M}_{REFR} = c'_{REFR} \cdot (T_{LTG} - T_1) \quad (3.24)$$

An analogous formulation is obtained for the specific mismatch in a high-temperature solution heat exchanger  $\Delta q_{MISMATCH,HT} = \Delta \dot{Q}_{MISMATCH,HT} / \dot{M}_{REFR}$  between flows no. 7 and no. 8:

$$\Delta q_{MISMATCH,HT} = \Delta \dot{Q}_{MISMATCH,HT} / \dot{M}_{REFR} = c'_{REFR} \cdot \gamma_{HTG} \cdot (T_2 - T_{LTG}) \quad (3.25)$$

In 2.2.3 it has already been argued that the magnitude of the specific mismatch in single-effect cycles  $\Delta q_{MISMATCH} = \Delta \dot{Q}_{MISMATCH} / \dot{M}_{REFR}$  is about 7% of the specific heat  $(\Delta h_{VAP} + \Delta h_{SOL})_G$  for boiling off the refrigerant in the regenerator of the single-effect cycle. This estimation is also valid for the mismatch  $\Delta q_{MISMATCH,LT}$  of the low-temperature heat exchange in double-effect cycles according to (3.24).

The respective formulation (3.25) for the high-temperature heat exchange shows a smaller value than (3.24) due to the extra factor  $\gamma_{HTG}$  being about 0.5 in DE-cycles and even less in SE/DE-machines. Partly, this extra factor is compensated, because the temperature difference  $T_2 - T_{LTG}$  in (3.25) is larger than  $T_{LTG} - T_1$  in (3.24), which is obvious from the geometric relations in Fig. 10 (cf. also Tab. 5 in 2.2.4 above). Nevertheless, in DE cycles the mismatch (3.25) in the high temperature heat exchange has an even greater impact on the efficiency of the absorption cycle than the low-temperature mismatch (3.24). It directly reduces the performance of the high-temperature regenerator unless it is otherwise compensated by extra heat input in the temperature range  $T_{LTG}$  to  $T_2$ .

Based on the temperatures of the sample calculation in Tab. 5 and Fig. 10, the mismatch  $\Delta q_{MISMATCH,HT}$  in the high temperature heat exchange is about 10% of the value of the latent heat  $\Delta q_{HTG}$  that is required at  $T_2$  in the high-temperature regenerator to boil off the refrigerant. This fraction  $\Delta q_{MISMATCH,HT} \approx 10\% \cdot \Delta q_{HTG}$  of the total heating demand  $\Delta q_{WEAK,HT} \geq 40\% \cdot \Delta q_{HTG}$  of the weak solution in the respective temperature range always requires external heat input as it cannot be covered by internal heat exchange.

For the losses in both solution heat exchangers in two-stage cycles, respective formulations on the lines of equations (2.42) and (2.43) provided for single-effect cycles in 2.2.3 can be obtained. Both loss terms are proportional to the solution flow rate and the terminal temperature difference in the respective heat exchanger. As discussed above, in the high-temperature solution heat exchanger, crystallization typically is no issue; therefore, the reduction of terminal temperature difference and thus the heat exchanger loss is only a question of economic feasibility. In this context, a split solution flow and thus a reduction of the solution flow in the high-temperature solution heat exchanger is advantageous.

### Refrigerant heat recovery

The mismatch  $\Delta q_{MISMATCH,LT}$  of the low-temperature heat exchange can be partly compensated by introducing an additional heat exchanger between the solution and the liquid refrigerant flow no. 6. To realize an ideal heat exchange, the weak solution flow no. 3 would have to be split into two partial flows. A first one,  $\dot{M}_{WEAK} \cdot [1 - c'_{REFR}/(c'_{WEAK} \cdot f_{WEAK})]$  with the same heat capacity as the strong solution flow no. 4 had to pass the low-temperature solution heat exchanger. The remaining weak solution  $\dot{M}_{WEAK} \cdot c'_{REFR}/(c'_{WEAK} \cdot f_{WEAK})$  had to enter the additional heat exchanger with the liquid refrigerant flow no. 6 connected in parallel<sup>28</sup> with the solution heat exchanger. This heat recovery reduces the mismatch  $\Delta q_{MISMATCH,LT}$  by the amount:

$$\Delta q_{REFR,LT} = \Delta \dot{Q}_{REFR,LT} / \dot{M}_{REFR} = \gamma_{HTG} \cdot c'_{REFR} \cdot (T_{LTG} + \Delta T_{LTG} - T_1) \quad (3.26)$$

Using (3.24), this can be written:

$$\Delta q_{REFR,LT} = \Delta q_{MISMATCH,LT} \cdot \gamma_{HTG} \cdot \left(1 + \frac{\Delta T_{LTG}}{T_{LTG} - T_1}\right) \approx \Delta q_{MISMATCH,LT} \cdot \gamma_{HTG} \quad (3.27)$$

The latter expression is a quite rough approximation, however. Thus, in a standard double-effect cycle with about  $\gamma_{HTG} \approx 0.5$ , the additional heat recovery from the liquid refrigerant flow no. 6 could reduce the mismatch of the low temperature heat exchange to about one-half its original value; a respective smaller effect is to be expected for SE/DE machines. In machines with reverse solution flow, a reduction of the mismatch results directly in an increased performance of the low-temperature regenerator as less heat is required for heating up the entering solution in this component. In machines with series flow or parallel flow layout, even a better performance of the high-temperature regenerator is to be expected, depending on the design on the other solution heat exchangers.

In 2.2.3 it has already been argued that the magnitude of the specific mismatch  $\Delta q_{MISMATCH} = \Delta \dot{Q}_{MISMATCH} / \dot{M}_{REFR}$  is about 7% of the specific heat for boiling off the refrigerant

<sup>28</sup> Respective heat exchanger configurations are e.g. shown in Fig. 20 and Fig. 21 discussed in 3.4.1 below.

in a regenerator. Hence, if the mismatch is reduced to one-half in a double-effect cycle with reverse flow, the thermal efficiency is expected to increase by at least 3%. About twice this increase was reported by *Shitara (2000)*, *Shitara et al. (2001)*, *Kashiwagi et al. (2002)*, and *Oka et al. (2003)* for the optimization of a series flow design (see also Fig. 20 in 3.4.1 below) in a Japanese development project.

### 3.3 Multi-stage utilization of flue gas enthalpy

#### 3.3.1 Basic considerations

##### Available flue gas heat at different temperature levels

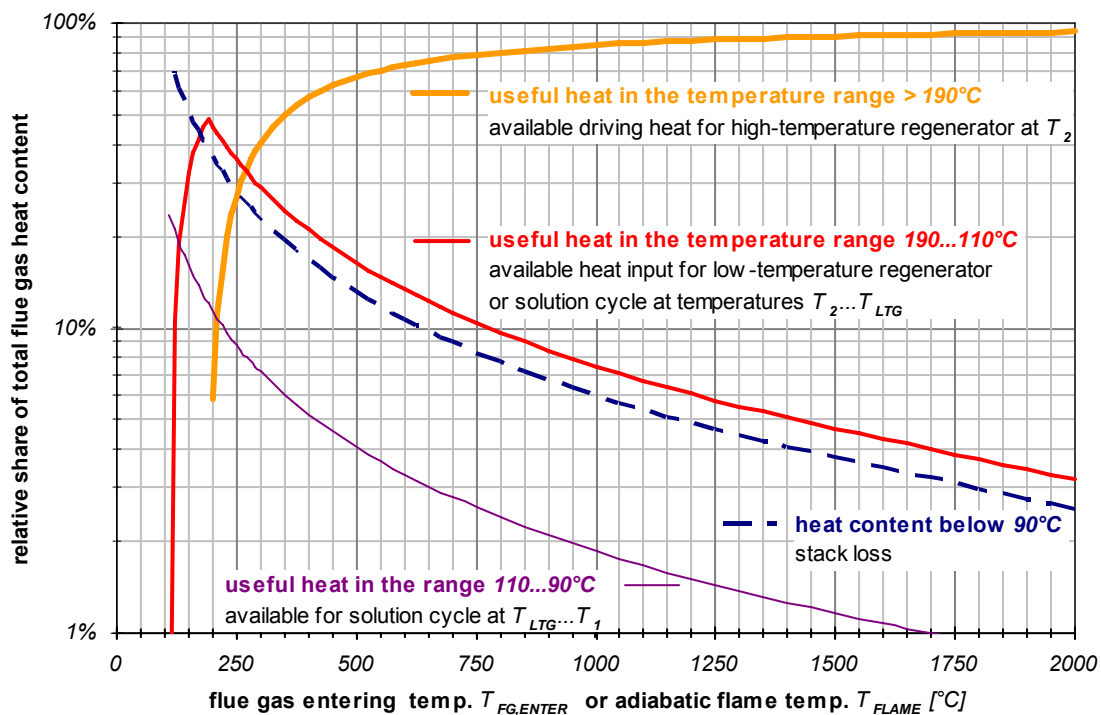


*Fig. 11: Relative share of useful flue gas heats in temperature ranges above 190°C, between 110°C and 190°C, and between 90°C and 110°C in dependence on the flue gas entering temperature in exhaust-fired chillers or the adiabatic flame temperature in direct-fired chillers respectively.*

As discussed in 2.3.3, the total combustion heat  $\Delta H_{CV,FUEL}$  in direct-fired chillers or the total exhaust gas enthalpy  $H_{FG,AVAIL}$  in exhaust-fired chillers are available at gliding temperatures. At typical operating conditions (cf. Fig. 10) and reasonable terminal temperature differences for economic heat exchanger design, it can be assumed that flue gas enthalpy at temperatures above about 190°C is available as driving heat for the high-temperature regenerator at internal temperature  $T_2$ . Additionally, the flue gas enthalpy in the temperature range of about 190...110°C can be utilized either in the low-temperature regenerator at internal temperature  $T_{LTG}$  or for preheating of weak solution in the range  $T_{LTG}...T_2$ . Flue gas enthalpy in the range of about 110...90°C can be utilized for preheating of weak solution in the range  $T_1...T_{LTG}$ . If condensation in the flue gas train has to be avoided, further cooling of the flue gas is not

suitable and thus the remaining flue gas enthalpy has necessarily to be assigned to stack loss. The relative shares of the useful flue gas enthalpy in these three temperature ranges and the percentage of not avoidable stack loss are displayed in Fig. 11 above in dependence of the exhaust gas entering temperature  $T_{FG,ENTER}$  or the adiabatic flame temperature  $T_{FLAME}$  respectively<sup>29</sup>.

### Flue gas utilization in the intermediate temperature range

Fig. 11 above shows that the useful flue gas enthalpy from the intermediate temperature range  $190...110^{\circ}\text{C}$  is only minor share of 10% or less of the total enthalpy at entering temperatures above  $800^{\circ}\text{C}$  like they are to be found downstream of a combustion process. On the other hand, for entering exhaust gas of  $300^{\circ}\text{C}$  and less the useful enthalpies from the both ranges  $>190^{\circ}\text{C}$  and  $190...110^{\circ}\text{C}$  are in the same order of magnitude. For entering temperatures of  $250^{\circ}\text{C}$  and less, the heat input from the intermediate range  $190...110^{\circ}\text{C}$  – to be utilized in a low-temperature regenerator at internal temperature  $T_{LTG}$  or for preheating of weak solution in the range  $T_{LTG}...T_2$  – becomes even the dominant one.

In 3.2.2 above it has already been shown that at least 40% of the heat  $\Delta q_{HTG}$  required for boiling off refrigerant in the high temperature regenerator is additionally required for heating up weak solution in the range  $T_{LTG}...T_2$ . While most of this heat  $\Delta q_{WEAK,HT}$  according to (3.22) is typically transferred to the weak solution from the counterflow of strong solution in the high-temperature solution heat exchanger, a smaller share  $\Delta q_{MISMATCH,HT} \approx 10\% \cdot \Delta q_{HTG}$  always requires additional external heat input, either in the high-temperature regenerator at  $T_2$  or in the solution cycle at  $T_{LTG}...T_2$ .

Compensating the mismatch  $\Delta q_{MISMATCH,HT}$  by means of external heat input in the solution cycle has the same effect on the performance of a chiller as an increase of the driving heat in the high-temperature regenerator by the same amount would have. Further input of external heat, however, mainly results in an increased superheating of the solution entering the low-temperature regenerator; thus, it has about the same effect as an increase of the driving heat input in the low-temperature regenerator would have<sup>30</sup>. Therefore, an ideal flue gas fired chiller would always have to utilize flue gas enthalpy in the range  $190...110^{\circ}\text{C}$  for preheating of weak solution to compensate for the mismatch. Only if the available flue gas enthalpy in this temperature range was larger than the amount required for this purpose, an idealized

<sup>29</sup> As simplification, specific enthalpy data for flue gas from stoichiometric combustion of natural gas have been employed as basis for the diagram.

<sup>30</sup> For series-flow solution cycles, additional heat input in the weak solution in the range  $T_{LTG}...T_2$  has exactly the same effect as additional heat input in the low-temperature regenerator would have. In parallel-flow and reverse-flow solution cycles, strictly speaking an infinitely large low-temperature solution heat exchanger would be required to make heat input in the solution cycle exactly as effective as heat input in a low-temperature regenerator.

design would additionally utilize the remaining share of flue gas heat in a low-temperature regenerator. Nevertheless, to limit the overall complexity of the cycle, practical designs might be aiming to realize only one of these both options of flue gas utilization.

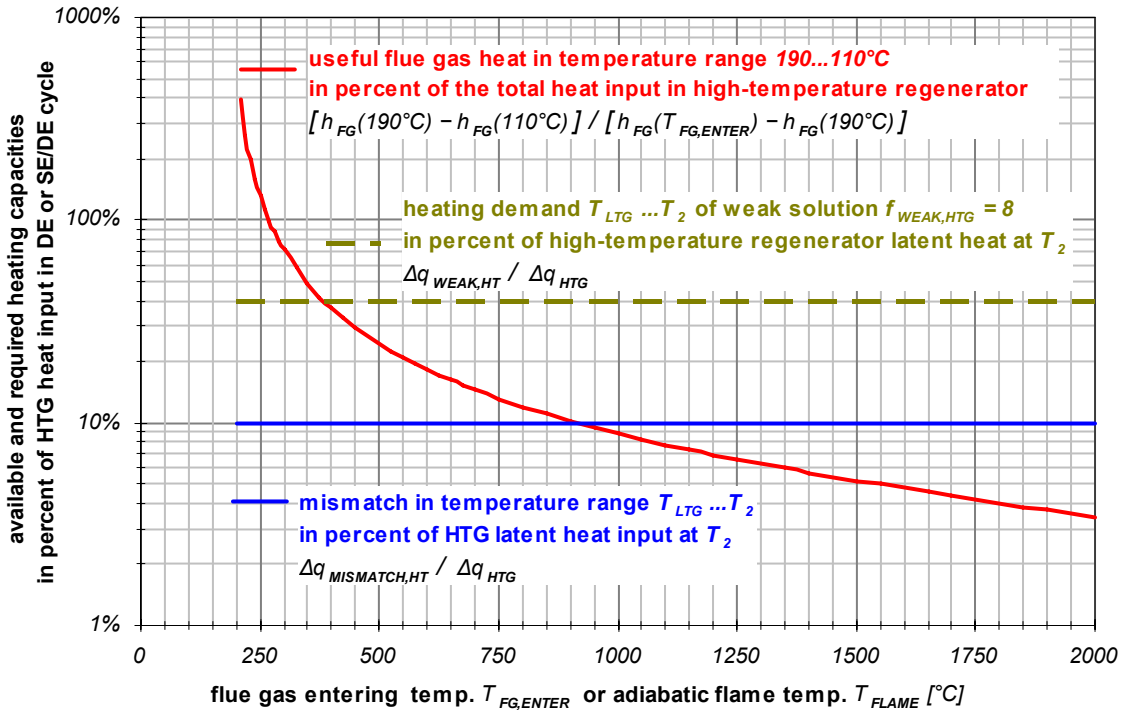


**Fig. 12: Comparison of available flue gas heat and heating demand in temperature range 110...190°C.** Available useful flue gas heat in temperature range between 110°C and 190°C in percent of the high-temperature regenerator heat input from flue gas heat above 190°C (red line) and required heating to compensate for the mismatch in the high-temperature heat exchange in percent of the latent heat input in the high-temperature regenerator (blue line). The total heating demand of the weak solution flow between temperatures  $T_{LTG}$  and  $T_2$  (assuming a specific circulation of  $f_{WEAK,HTG} = 8$ ) in percent of the latent heat input in the high-temperature regenerator (dashed yellow line) is shown for comparison.

Fig. 12 above visualizes the relative share of the available flue gas enthalpy in the intermediate temperature range 190...110°C in percent of the total heat input in the high-temperature regenerator as solid red line over exhaust gas entering temperature  $T_{FG,ENTER}$  or the adiabatic flame temperature  $T_{FLAME}$  respectively. For comparison, the relative share of required heat input in the solution cycle to compensate the mismatch (solid blue line) and the approximate lower limit for the total heating demand in the weak solution (assuming  $f_{WEAK,HTG} = 8$ ) are displayed (dashed yellow line).

Fig. 12 shows that for typical combustion temperatures of 1000°C and above, the flue gas enthalpy in the intermediate temperature range 190...110°C is already smaller than the heat that would be required to compensate fully the mismatch of the high-temperature solution heat exchange. Therefore, in direct-fired chillers, installation of a flue gas recuperator transferring heat to the solution cycle is the most promising option; it would outperform the application of a SE/DE-cycle concept with additional input of flue gas heat in a low-



temperature regenerator. It can also be concluded from Fig. 12 that for entering exhaust gas temperatures above about  $600^{\circ}\text{C}$  the installation of a flue gas recuperator is still more promising than exhaust gas utilization in a low temperature regenerator. At exhaust gas entering temperatures below about  $600^{\circ}\text{C}$ , the most promising solution will be mainly dependent on the complexity of the cycle-layout that is economically feasible and on the actual boundary conditions that have to be regarded in a special application.

Nevertheless, it can be concluded from Fig. 12 that even for exhaust gas entering temperatures as low as  $300^{\circ}\text{C}$  all enthalpy in the intermediate temperature range could be utilized in the solution cycle if desired. The dashed **yellow** line in the diagram just marks a lower limit for the weak solution heat capacity at values of  $f_{WEAK,HTG} = 8$  that can be realized in cycle layouts with a split solution flow. At least twice the value of  $\Delta q_{WEAK,HT}$  is to be expected in plain series-flow or reverse-flow cycles, even higher values are to be found if the solution circulation in the absorber is increased.

### Flue gas utilization in the low temperature range

Fig. 11 shows that in direct-fired chillers with typical adiabatic combustion temperatures of  $1000^{\circ}\text{C}$  and above, only a minor share of less than 2% of the total combustion heat is found in the usable low-temperature range of about  $110\dots 90^{\circ}\text{C}$ . Nevertheless, this heat could be utilized to compensate partly for the mismatch  $\Delta q_{MISMATCH,LT}$  in the low temperature heat exchange. In 3.2.2 it has already been argued that this mismatch  $\Delta q_{MISMATCH,LT}$  can at best be reduced to half its original value by utilization of the liquid refrigerant heat  $\Delta q_{REFR,LT}$ ; therefore there is still a theoretical possibility of further heat input from flue gas in this temperature range.

However, a real significance for flue gas utilization in the low-temperature range can be found at exhaust gas entering temperatures of  $500^{\circ}\text{C}$  and less in SE/DE-chillers. At decreasing temperature of the entering exhaust gas, on the one hand – according to Fig. 11 – the relative share of the flue gas enthalpy in the range  $110\dots 90^{\circ}\text{C}$  increases. On the other hand, according to (3.27), the relative share of the mismatch that can be compensated for by the utilization of the refrigerant heat decreases with decreasing values of  $\gamma_{HTG}$ .

### 3.3.2 Technical options for external heat input in absorption chillers

#### Heat input into multiple generators at different temperature levels

The most straightforward approach for utilization of driving heat at multiple temperature levels is the addition of a second low-temperature regenerator to a standard DE-cycle, thus resulting in a SE/DE machine. A cycle like this has e.g. been suggested by *Takahata et al. (1999)* for utilization of exhaust gas from a gas turbine (see Fig. 13).

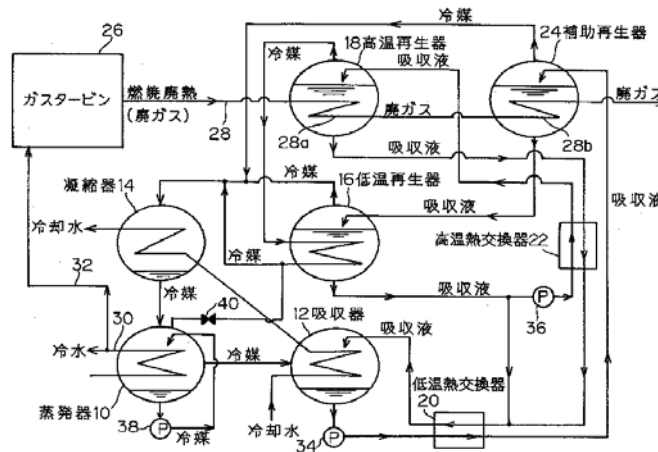


**Fig. 13: Flow scheme of a flue-gas fired SE/DE absorption chiller.**

Consecutive utilization of waste heat from the exhaust gas (28) of a gas turbine (26) in the high-temperature regenerator (18) and an additional low-temperature regenerator (24) of the chiller. Patent drawing from *Takahata et al. (1999)*.

The sophisticated solution cycle layout disclosed in the patent application by *Takahata et al. (1999)* is already optimized for maximum efficiency. A reverse cycle with split solution flow – the most diluted solution from the absorber (12) passing the exhaust-gas fired low temperature regenerator (28b) first – is shown in Fig. 13. This results in the lowest possible internal boiling temperature in the exhaust-gas fired low temperature regenerator and thus in the most efficient utilization of the flue gas enthalpy. As already discussed, the application of a split solution flow scheme with a partial bypass of the high-temperature regenerator reduces the size of the high-temperature solution heat exchanger (22) that is required to achieve a good heat exchanger efficiency.

As discussed above, staggered exhaust gas utilization in multiple regenerators is mainly a promising option for exhaust gas entering temperatures below 600°C. A comparison of different multistage absorption cycles by *Kren et al. (2002)* with respect to the potential for cold production from exhaust gas enthalpy in this temperature range is shown in Fig. 14.

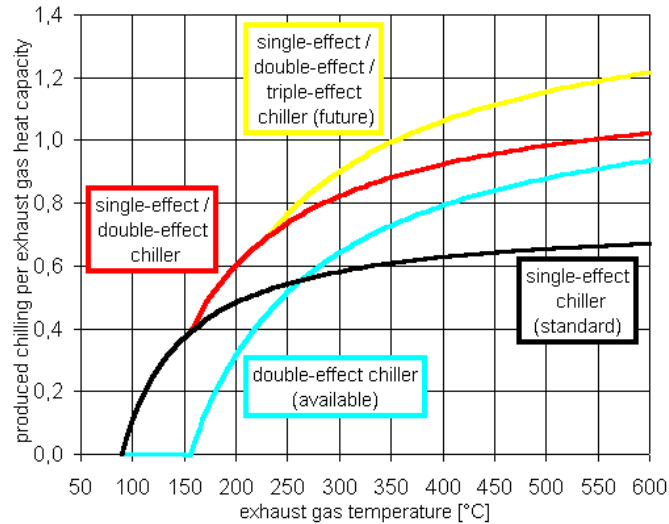


**Fig. 14: Cooling produced from exhaust gas waste heat per total exhaust gas heat capacity  $COP_{FGF}$  with reference to the exhaust gas entering temperature.**  
Comparison of different kinds of multistage cycles reported by *Kren et al. (2002)*.

The thermal efficiencies  $COP_{FGF}$  according to (2.56) and (2.57) displayed in this graph have been calculated based on typical cycle efficiencies and on maximum feasible flue gas utilization assuming very small terminal temperature differences in the respective heat exchangers. For comparison, also the forecasted efficiencies for – not yet available – single-effect/double-effect/triple-effect chillers with tri-stage exhaust gas utilization are shown in Fig. 14.

### External heat input into the solution cycle for preheating of weak solution

As discussed above, especially in direct-fired chillers utilization of flue gas enthalpy for preheating of weak solution is the most promising option for increasing the amount of cooling produced. Depending of the basic cycle layout, there are actually various possibilities for integration of a flue gas recuperator in the solution cycle. An overview compiled from a selection of flow schemes that have been investigated in the recent years is given below.

Two possibilities for integration of a flue gas recuperator in a quite rare series-flow layout with split solution flow and partial bypass of the high-temperature regenerator are shown in Fig. 15 below. In a Japanese patent by *Kurosawa et al. (1989)* the installation of the flue gas recuperator (66) parallel to the high-temperature solution heat exchanger (36) in the solution cycle (left sketch in Fig. 15) is denoted as prior art. The disclosed series connection (right sketch in Fig. 15) of low-temperature solution heat exchanger (42), flue gas recuperator (70), and high-temperature solution heat exchanger (36) is suggested to avoid difficulties in ensuring a stable flow rate in the recuperator solution line (62, 64) of the parallel arrangement (left sketch).

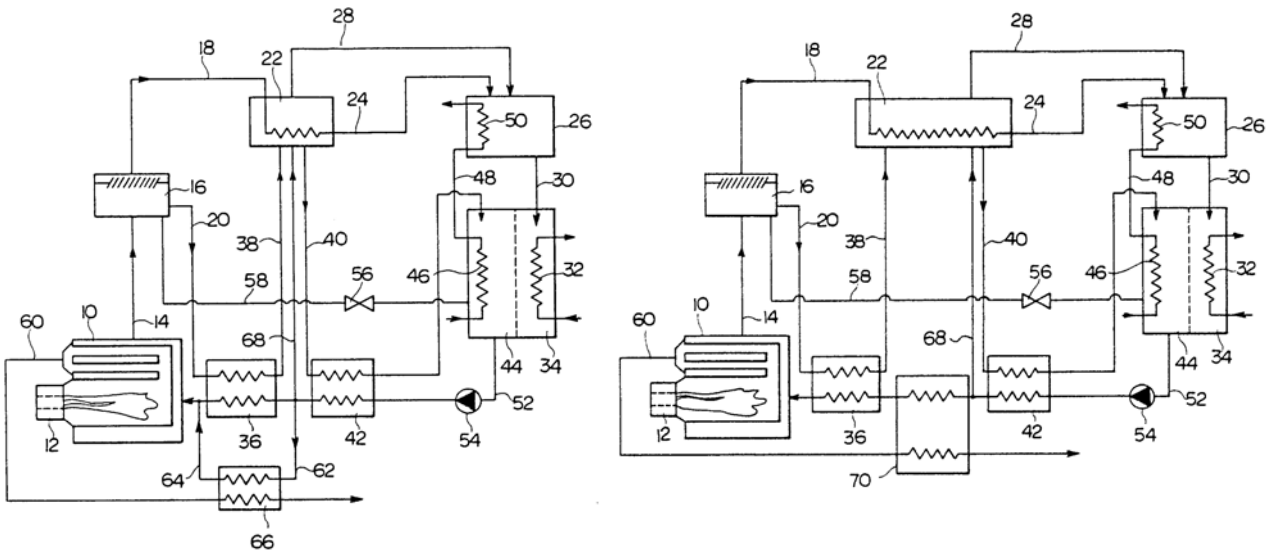


**Fig. 15: Flue gas utilization in direct-fired chiller with split/series-flow cycle layout.**

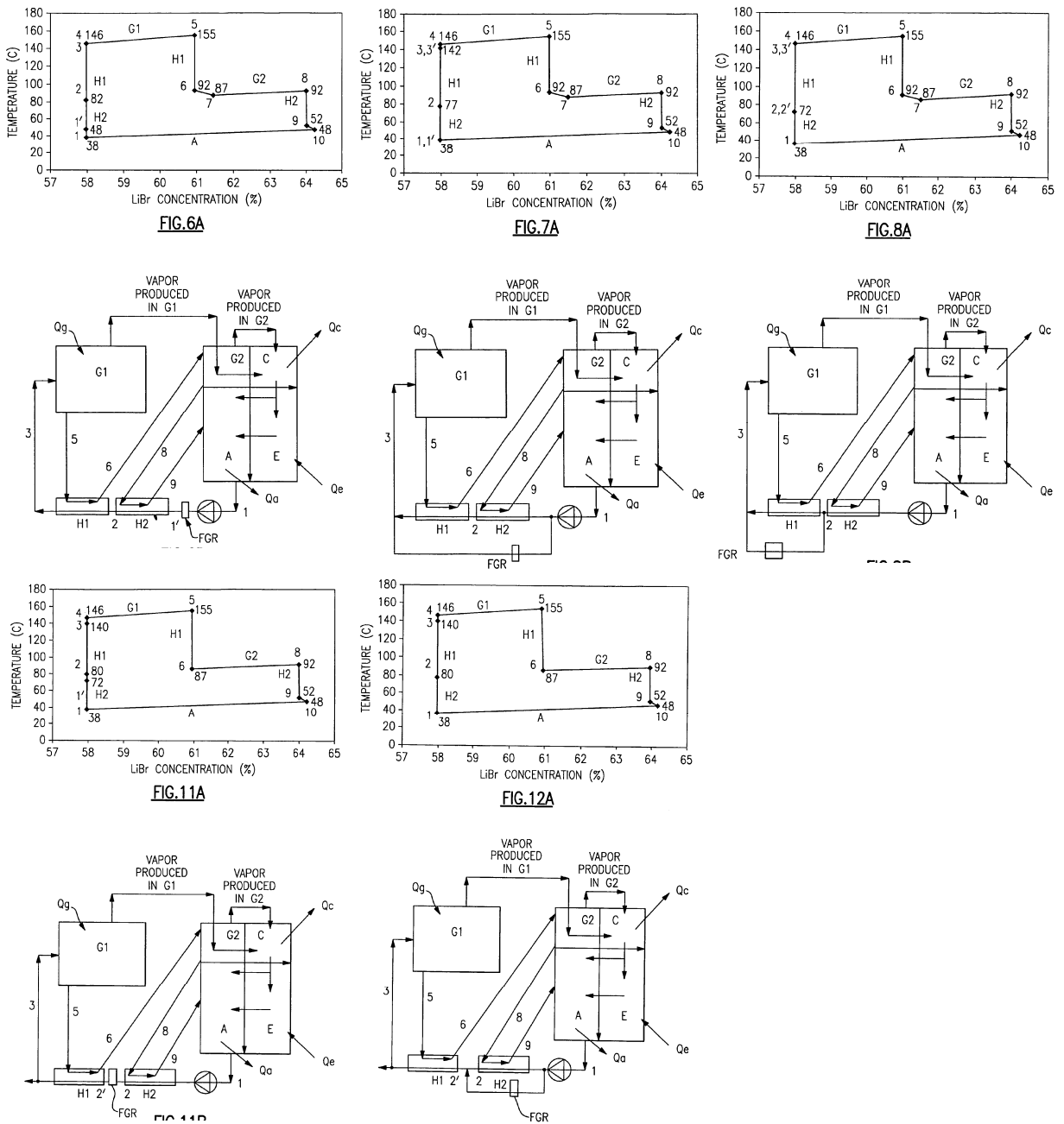
Utilization of the flue gas (60) leaving the direct-fired (12) high-temperature regenerator (10) for preheating of the weak solution flow in double-effect chillers comprising a split/series-flow cycle layout with partial bypass (68) of the high-temperature regenerator. Prior art (left sketch) with parallel installation of flue gas recuperator (66) and high-temperature solution heat exchanger (36) vs. series connection (right sketch) of low-temperature solution heat exchanger (42), flue gas recuperator (70), and high-temperature solution heat exchanger (36), as suggested in a Japanese patent granted to Yazaki. Patent drawings from *Kurosawa et al. (1989)*.

Fig. 16 below shows the results of a thermodynamic evaluation of even five different options for integration of a flue gas recuperator (“FGR”) in the common series-flow cycle without regenerator bypass that has been disclosed in two patents by *Gupte (2003, 2005)*. For each investigated case the temperature-concentration diagram of the solution cycle is displayed over the respective flow scheme in Fig. 16. No information is given on the boundary conditions that have been assumed for the comparison of the individual options, though.

Nevertheless, a comparison of the degree of subcooling of the weak solution entering the high-temperature regenerator (temperature difference between state points 4 and 3) in the temperature-concentration diagrams reveals that the highest efficiency is to be expected from the both cycles displayed in the upper left and the upper right position in Fig. 16. No subcooling of the entering weak solution at all is found for these two options, the flue gas recuperator placed in series between solution pump and low temperature regenerator (“H2”) – as shown in the upper left sketch – and the flue gas recuperator placed parallel to the high temperature solution heat exchanger (“H1”) – as shown in the upper right sketch. A principal difference between these two most efficient flow schemes is that the temperature of the weak solution entering the low-temperature solution heat exchanger is  $10\text{ K}$  higher in the upper left diagram (state point 1') than in the upper right diagram (state point 1).

Consequently, the series installation of the flue gas recuperator between solution pump and low-temperature heat exchanger (upper left sketch) has the operational advantage that the risk of crystallization in the low-temperature solution heat exchanger is almost completely

eliminated. On the other hand, the parallel installation of the flue gas recuperator (upper right sketch) has the economical advantage that a significantly smaller<sup>31</sup> low-temperature solution heat exchanger is required for the about the same overall efficiency of the chiller.



**Fig. 16: Thermodynamic evaluation of different options for integration of a flue gas recuperator in a series-flow double-effect cycle.**

Flue gas recuperator (“FGR”) installed either in parallel or in series with low-temperature solution heat exchanger (“H2”) and high-temperature solution heat exchanger (“H1”). Drawings from two U.S. patents by Gupte (2003, 2005) granted to Carrier.

Additionally, it has to be noted that the upper left flow scheme in Fig. 16 would most likely induce condensation in the flue gas under partial load operation; thus, suitable and poten-

<sup>31</sup> 4 K terminal temperature difference in the upper left diagram vs. 14 K terminal temperature difference in the upper right diagram – for the same absolute heat duty of the heat exchanger H2.

tially more expensive material is required for construction of the flue gas recuperator and the flue gas train downstream. On the other hand, the thermodynamically very promising parallel installation of the flue gas recuperator the (upper right flow scheme in Fig. 16) requires that a sufficient solution flow rate in the recuperator line is ensured under all operating conditions – otherwise blocking and crystallization at the liquid side of the recuperator might occur.

It has to be concluded that the thermodynamically most efficient flow scheme is not necessarily the most favorable one with respect to easy control and robust operation of the cycle under all circumstances,

According to *Cho et al. (2005)*, it has been shown in numerical parameter studies that a series installation (see Fig. 17 below) of a flue gas recuperator (“EGHX”) between low-temperature solution heat exchanger (“LSHX”) and high-temperature solution heat exchanger (“HSHX”) is already the most promising option resulting in the best chiller efficiency. Again, the boundary conditions that have been the basis for this finding are not available.

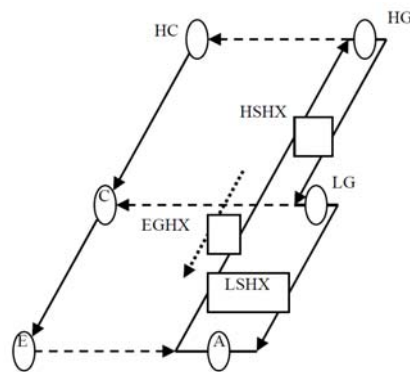


**Fig. 17:** Flow scheme (simplified Dühring chart) showing the integration of an exhaust gas recuperator (“EGHX”) in the weak solution line between low-temperature solution heat exchanger (“LSHX”) and high-temperature solution heat exchanger (“HSHX”) in a series-flow double-effect cycle, as suggested by *Cho et al. (2005)*.

It is evident, however, that the series installation of the flue gas recuperator at an intermediate temperature level – as shown in Fig. 17 and in the lower left sketch in Fig. 16 – is less prone to both issues, crystallization at the liquid side and condensation at the gas side of the recuperator, than the both flow schemes just discussed above. An increase of the  $COP_{FGF}$  by about 3% due to integration of a flue gas recuperator of moderate size according to Fig. 16 is expected by *Cho et al. (2005)* as result of a numerical study.

*Yoon et al. (2003)* reported on experimental investigations of the operating characteristics of a direct-fired chiller employing a parallel-flow solution cycle with and without additional flue gas recuperator installed. They suggested installing the flue gas recuperator in the weak solution line from the low-temperature solution heat exchanger (7) to the low-temperature regenerator (4) as shown in Fig. 18 below. For alternative utilization of flue gas enthalpy for

heating purposes, two damper valves at the recuperator enabled switching of the flue gas stream to a second heat exchanger coil (rightmost part of sketch below).

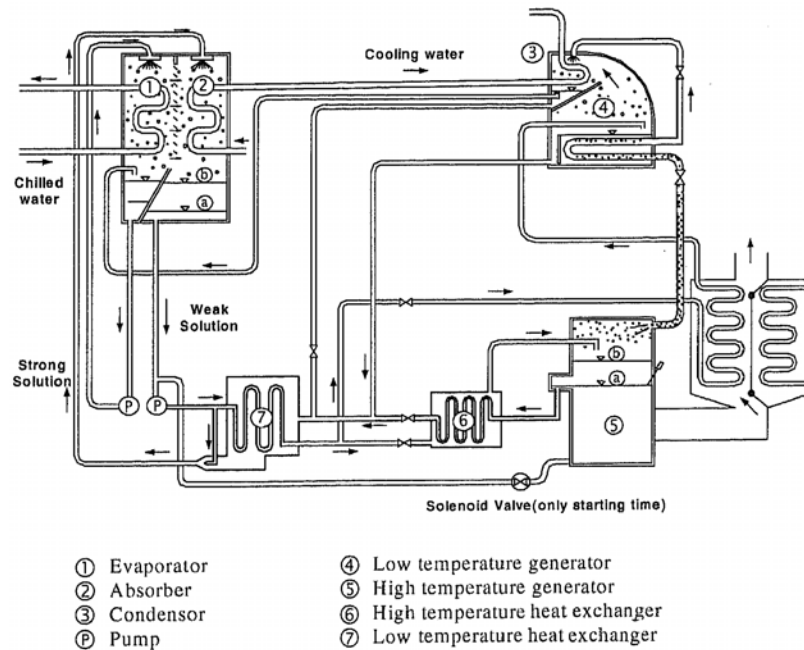


**Fig. 18:** Flow scheme of the modified parallel-flow double-effect chiller with additionally installed flue gas recuperator (rightmost device in drawing) that has been experimentally investigated by Yoon *et al.* (2003).

An increase of the  $COP_{FGF}$  by about 3% due to integration of the flue gas recuperator was experimentally proven. No information is provided by Yoon *et al.* (2003) however on the criteria for selection of the suggested position of the flue gas recuperator in the solution cycle.



### 3.4 Examples of recent developments

Below, selected developments of advanced direct-fired and exhaust-fired absorption chillers on which have been reported in the recent years are presented in short. Though no completeness is claimed for this compilation, the general trends in recent developments of flue gas fired absorption chillers can be shown.

#### 3.4.1 Advanced direct-fired absorption chillers

##### European consortium lead by Weir ENTROPIE S.A

A series of publications by *Schweigler et al. (1999)*, *Schweigler et al. (2000)*, *Kren et al. (2001)*, *Kren et al. (2002)* reports on development of an efficient natural gas fired double-effect chiller by Weir ENTROPIE S.A. and further project partners<sup>32</sup>. A refined parallel-flow solution cycle with two-stage flue gas utilization in a high-temperature regenerator and a flue gas recuperator and additional heat recovery from the liquid refrigerant flow between low temperature regenerator and condenser was employed. Various options for integration of these additional heat exchangers in the solution cycle – including the one shown in Fig. 19 below – were examined in a numerical study. The finally chosen design has not been disclosed, however. Laboratory testing of a prototype of the novel direct-fired regenerator developed within this project is reported in section 6 below.

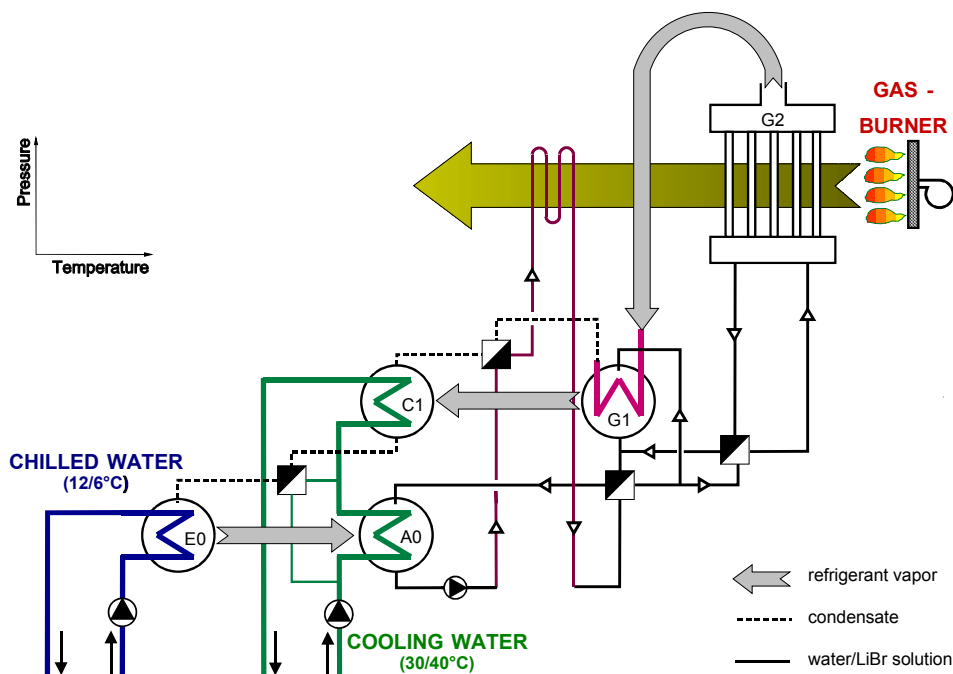


Fig. 19: Potential configuration of a direct-fired chiller with parallel-flow cycle and heat recovery from leaving flue gas and refrigerant condensate.

Cited from *Schweigler et al. (1999)*.

<sup>32</sup> "LiBr Absorption Chiller for Building Air Conditioning with Efficient Flexible Operation". Project partners: Weir ENTROPIE S.A (France), Gas Natural SDG S.A. (Spain), BG Technology Ltd. (UK), ZAE Bayern e.V. (Germany). Research funded in part by THE EUROPEAN COMMISSION in the framework of the Non Nuclear Energy Programme Joule III under Contract No.: JOE3 CT 97 0059



### Japanese consortium led by Tokyo Gas and Osaka Gas

A series of publications by *Shitara (2000)*, *Shitara (2000)*, *Shitara et al. (2001)*, *Kashiwagi et al. (2002)*, *Oka et al. (2003)* reports on development of an efficient gas fired double-effect chiller by a consortium of Japanese manufacturers and gas suppliers. The left sketch in Fig. 20 below shows the flow scheme that was finally chosen based on numerical studies. Based on a series-flow design, it comprises several refinements like a sophisticated three-stage absorber – not to be further discussed within this work – and a heat recovery from the liquid refrigerant flow. The refrigerant heat exchanger is installed parallel to the low-temperature solution heat exchanger in a bypass of the weak solution line. The reported impact of the individual modifications on the thermal efficiency is shown in the right diagram in Fig. 20.

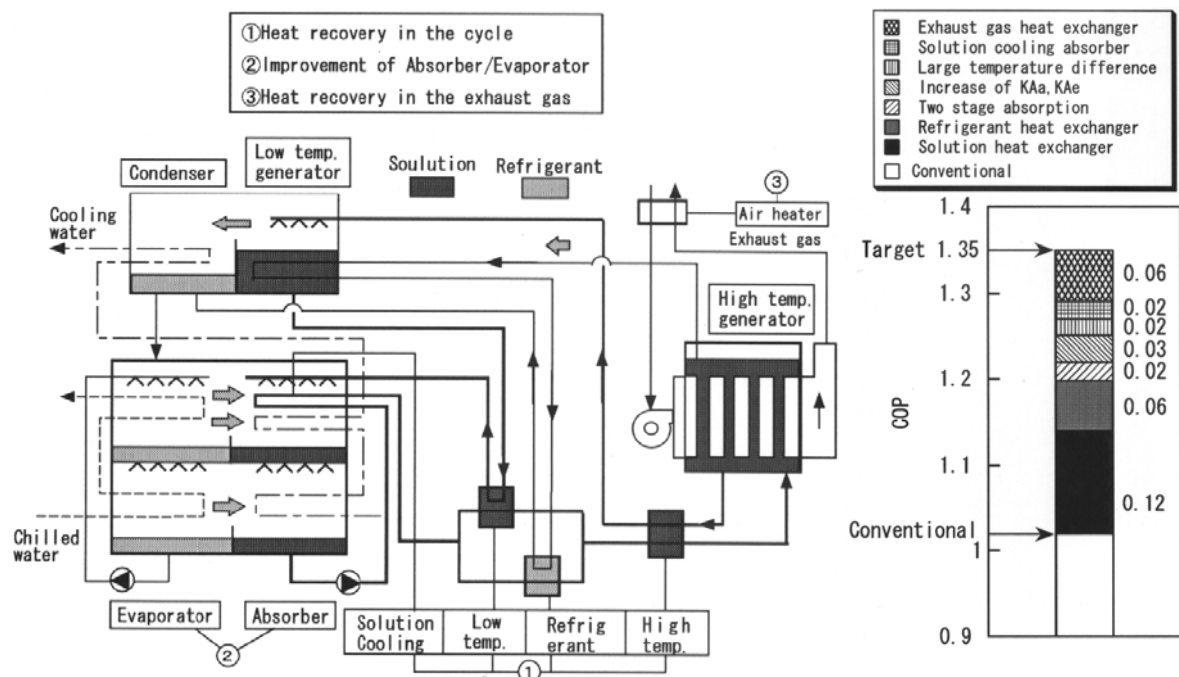


**Fig. 20: Advanced direct-fired chiller developed by Japanese consortium.**

Flow scheme comprising heat recovery from refrigerant condensate in a partial flow of weak solution parallel to the low-temperature solution heat exchanger and an exhaust gas heat exchanger serving as a combustion air preheater (left). Contributions of individual design improvements on COP increase (right). Cited from *Shitara et al. (2001)*.

Two-stage flue gas utilization was realized by means of a recuperative combustion air preheater. This single improvement already increased the efficiency by 6% compared to a standard design. The increased combustion temperature resulting from this flow scheme however required a special design of the high temperature regenerator to keep the  $\text{NO}_x$  emission within appropriate limits.

### Sanyo Electric

Fig. 21 below shows the flow scheme of an advanced direct-fired chiller – comprising even three-stage flue gas utilization in one high-temperature regenerator (1) and two flue gas recuperators (26, 27) as well as refrigerant heat recovery (11) – that has been disclosed in a

patent by [Yamazaki et al. \(2002\)](#) granted to Sanyo Electric. Like in the joint Japanese development discussed above, the solution cycle is based on a series-flow layout and the refrigerant heat exchanger (11) is installed in the weak solution line parallel to the low-temperature solution heat exchanger (9). The flue gas recuperators are installed in series, upstream (27) and downstream (26) of the high temperature solution heat exchanger (10). To prevent condensation of the flue gas under partial load operation or during startup, an additional bypass (14) for the weak solution at the low temperature recuperator (27) is installed, that is actively controlled by an automatic valve (28).

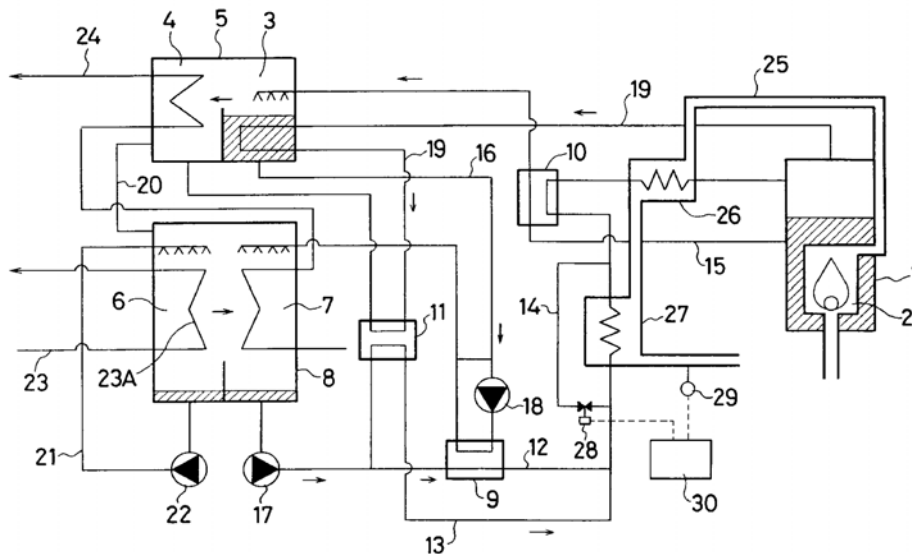


**Fig. 21: Flow scheme of a highly efficient direct-fired chiller from Sanyo Electric.**

Heat recovery (11) from refrigerant condensate (19) in a partial flow of weak solution (13) parallel to the low-temperature solution heat exchanger (9) and two flue gas recuperators passed by the weak solution before (27) and after (26) the high-temperature solution heat exchanger (10). Patent drawing from [Yamazaki et al. \(2002\)](#).

### 3.4.2 Novel exhaust-fired absorption chillers

#### Ebara Corporation

Several cycle layouts and heat exchanger designs for optimized SE/DE-chillers fired by exhaust from gas turbines are disclosed in two recent patents by [Inoue & Endo \(2004a, 2004b\)](#) granted to Ebara Corporation. The preferred embodiment displayed on the first page of [Inoue & Endo \(2004b\)](#) together with the corresponding Dühring chart for this cycle is shown in Fig. 22 below. Even four-stage flue gas utilization in a high-temperature regenerator (“GH”), a first flue gas recuperator (“XA”), a low-temperature regenerator (“GR”), and a second recuperator (“XB”) is suggested for this purpose; unlike in the direct-fired chiller concepts discussed above, no heat recovery from refrigerant condensate is considered. The embodiment presented in Fig. 22 below is based on a parallel-flow layout with both low temperature regenerators (“GL”, “GR”) connected in series, however. The both flue gas recuperators are connected to the weak solution line downstream of the low-temperature

solution heat exchanger (“XL”) and downstream of the high-temperature solution heat exchanger (“XH”) respectively.

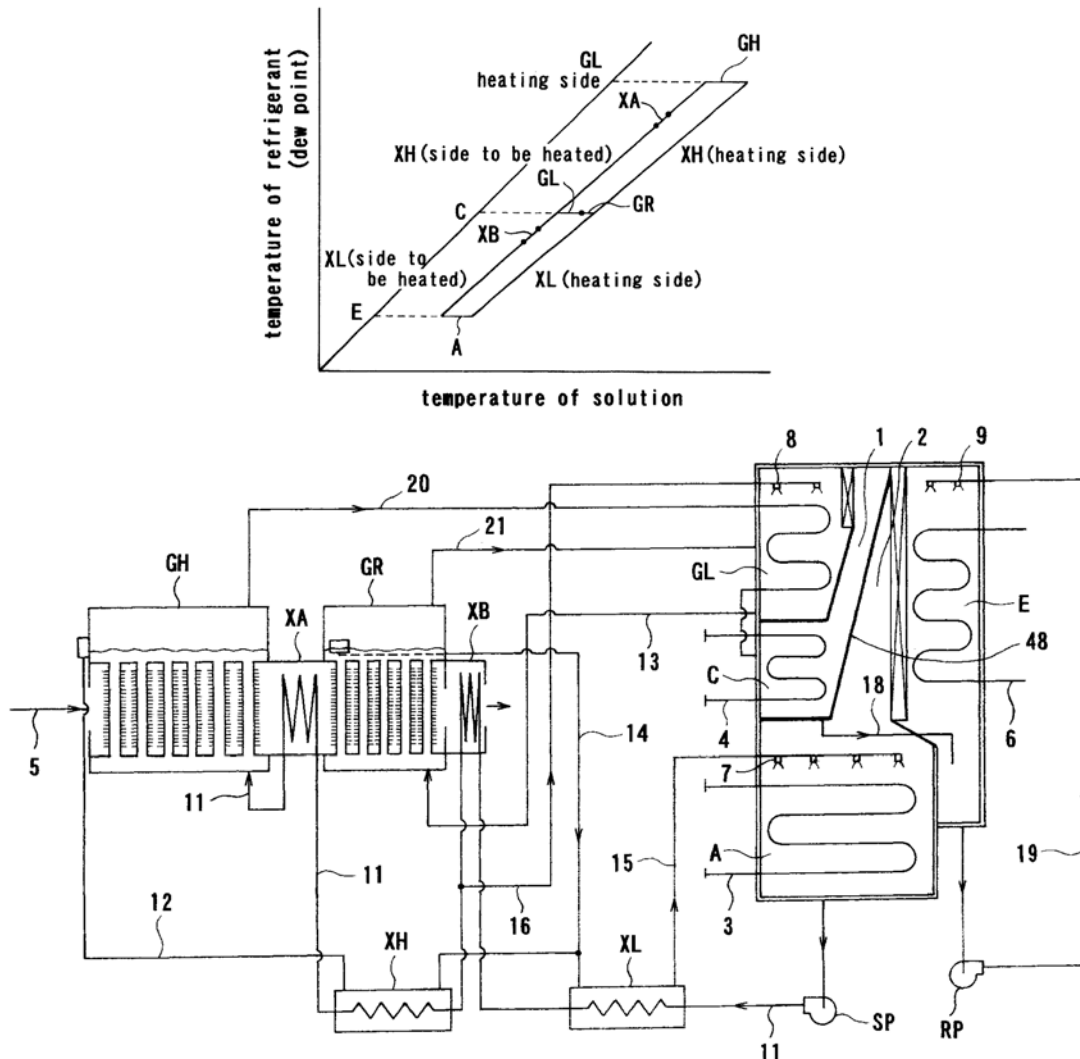


**Fig. 22: Exhaust-fired SE/DE-chiller with four-stage flue gas utilization.**

*Dühring chart (top) and flow scheme (below) of the cycle with two flue gas fired regenerators (“GH” and “GR”) and additional preheating of the weak solution in two flue gas recuperators (“XA” and “XB”). Patent drawings from Inoue & Endo (2004b).*

## ZAE Bayern

Fig. 23 below shows a flexible SE/DE-cycle concept with two-stage flue gas utilization especially suited for CCHP installations with variable ratios of simultaneous heating and cooling demand that has been described in a series of publications by [Kren et al. \(2004\)](#), [Paul \(2004\)](#), [Plura et al. \(2004\)](#), [Plura et al. \(2005\)](#), [Keil et al. \(2005\)](#). Unlike standard DE-cycles, the single low-temperature regenerator (“G1”) is not driven directly by the condensation of the refrigerant vapor from the high-temperature regenerator (“G2”) but by an external heat carrier loop. This loop collects the latent heat from condensation of the refrigerant in the additional condenser (“C2”) as well as flue gas enthalpy recovered in the flue gas recuperator (“EHX”).

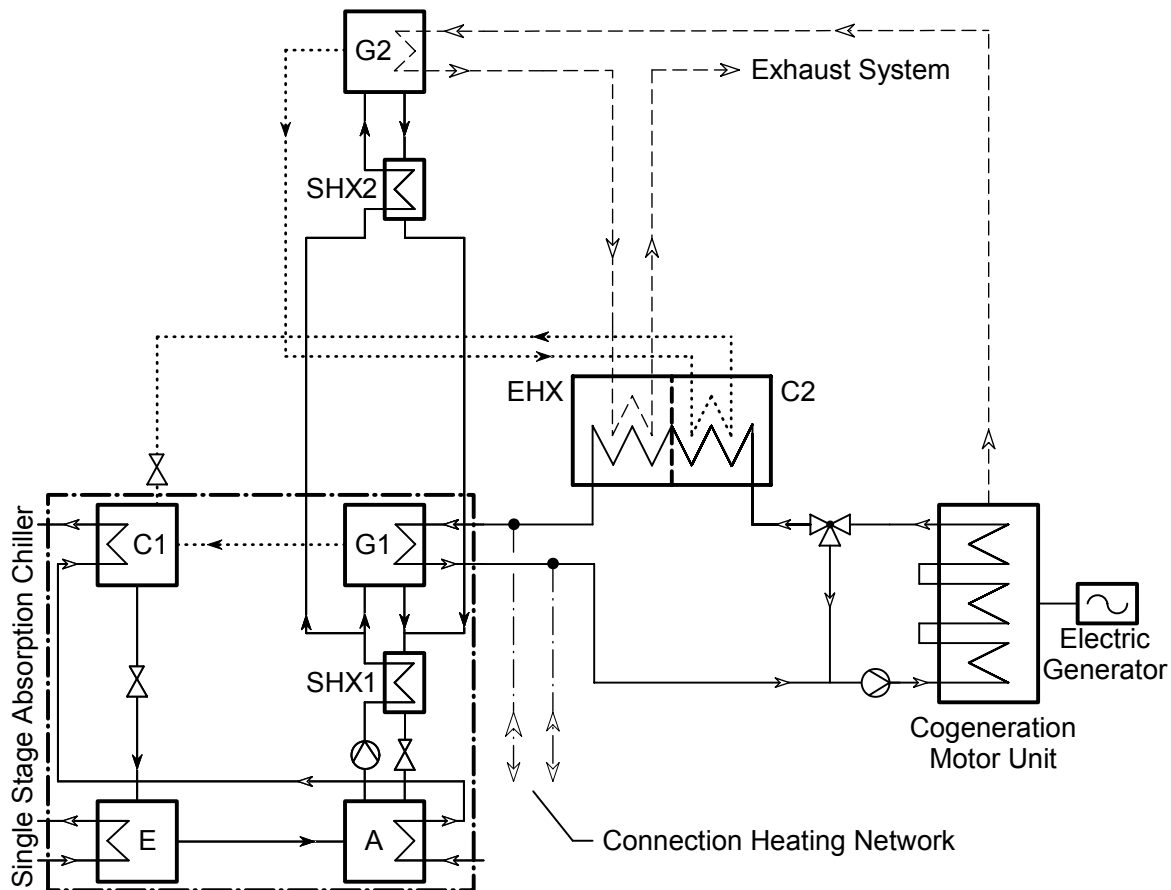


**Fig. 23: Flow scheme of a flexible SE/DE-chiller in a CCHP system with two-stage exhaust gas utilization.** Exhaust gas passes high-temperature regenerator (“G2”) and exhaust gas heat exchanger (“EHX”), which is connected to the low-temperature regenerator (“G1”) by an external water loop. Cited from *Plura et al. (2005)*.

If an internal combustion engine is employed as prime mover in the CCHP system – as shown in Fig. 23 above – the coupling loop of the SE/DE-chiller can be connected with the cooling water loop of the engine to collect its reject heat as additional driving heat for cold production. Finally, an interconnection between the heat carrier loop and the local heating network enables both extraction of heat for heating purposes as well as input of additional driving heat from external heat sources. Particularly, it is possible to transfer all flue gas heat to the heating network by means of the heat exchangers displayed in Fig. 23 above without any necessity to switch over the exhaust stream as e.g. shown in Fig. 18 in 3.3.2.

### **3.5 Conclusions for chiller design**

Several options for increasing the thermal efficiency of flue gas fired chillers have been discussed above. In direct-fired chillers, the integration of a heat recovery from refrigerant condensate and of one or two flue gas recuperators for preheating of weak solution downstream of the high-temperature regenerator is the most promising way. No general conclusion can be drawn concerning the most preferable flow scheme of the solution cycle incorporating these additional heat exchangers as the increasing complexity of the cycle and of its control – for preventing crystallization of the solution and condensation in the flue gas – have also to be considered. The most promising solution on terms of economic efficiency will presumably be dependent on the size of a chiller and on the field of application.

In exhaust-fired chillers, heat recovery from refrigerant condensate has a smaller effect on the overall efficiency. On the other hand, the significance of multi-stage flue gas utilization even increases at lower entering exhaust temperatures. Again, the most preferably flow scheme is dependent on the application needs and on the exhaust temperature.

Common to all options discussed so far is that in lieu of a single high-temperature regenerator – as e.g. found in the installations reported on by *Pathakji et al. (2005)* and *Wagner et al. (2005)* – a series of two to four heat exchangers has to be passed by the flue gas. Then the high-temperature regenerator is just the first heat exchanger – yet still the dominant one – in this line.

To ensure good economic prospects of such advanced chiller designs, however, it has to be ensured that neither the overall pressure drop in the flue gas nor size and the total cost of this series of heat exchangers are significantly larger than the respective numbers for a single flue-gas fired regenerator in a traditional design. This requires at first an optimization of the design of the high temperature regenerator in order to reduce both size and pressure drop at the flue gas side.

## 4 Fundamentals - Heat transfer and pressure drop in flue gas fired regenerators

### 4.1 Basic design considerations on flue gas fired regenerators

#### 4.1.1 Heat exchanger concepts

Fig. 24 shows two basic boiler designs that both can be applied to flue gas fired regenerators of absorption chillers. The drawing on the left represents the principal sketch of a shell boiler design given where horizontal smoke tubes are completely immersed in the boiling lithium bromide solution. The operation is characterized by pool boiling under conditions of free convection inside the vessel. The complete arrangement is enclosed by the outer pressure vessel shell. The drawing on the right represents the principal sketch of a tube boiler design where the lithium bromide solution flows through vertical boiling tubes crossing the pressure-less flue gas duct. The operation is characterized by flow boiling inside the boiling tubes. For the distribution of the liquid at the bottom of the boiling tubes and for the separation of liquid and vapor at the top there are two additional pressure vessels (header and bottom vessel in Fig. 24) required which are, however, much smaller in volume than the outer shell of a comparable shell boiler.

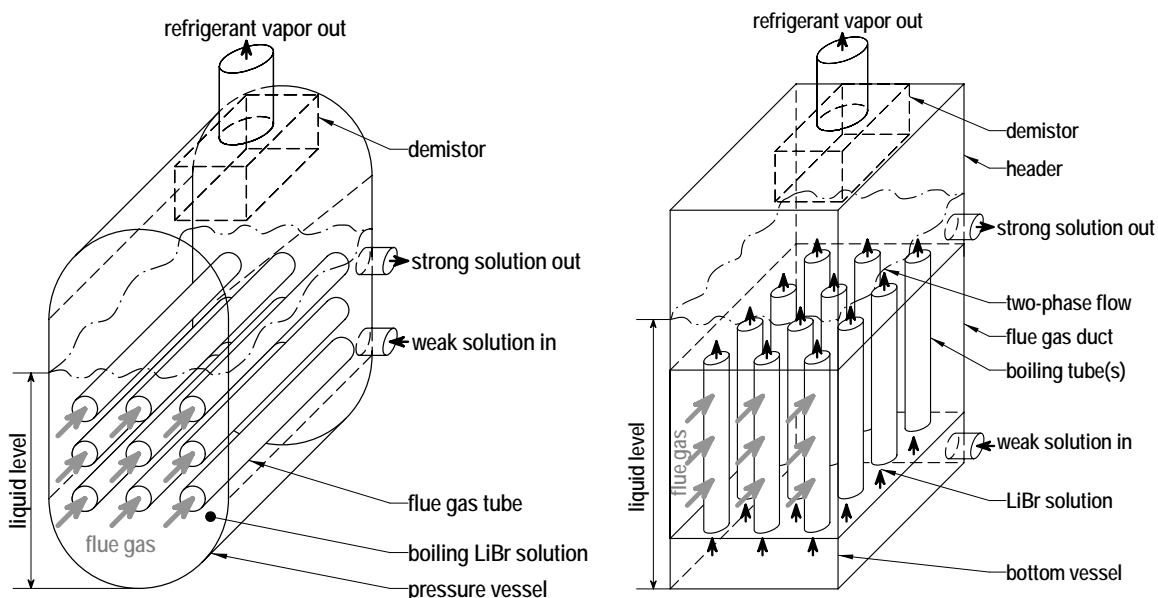


**Fig. 24: Principal sketch of two basic concepts of flue gas fired regenerators: Shell boiler with horizontal smoke tubes completely immersed in the boiling liquid (left) and tube boiler with liquid inside the vertical boiling tubes (right).**

As already discussed above, shell boilers employing smoke tubes (left sketch in Fig. 24) have effectively served as a kind of standard design for direct-fired regenerators of absorp-

tion chillers for several decades and they have also been applied to exhaust fired regenerators<sup>33</sup>. In the recent years, increasing interest in tube boiler designs (right sketch in Fig. 24) expresses e.g. in numerous newly filed patent applications<sup>34</sup>, in a Japanese joint R&D project for development of advanced chiller heaters<sup>35</sup>, or in US developments on advanced trigeneration systems<sup>36</sup>.

A folded hybrid design (cf. Fig. 25) integrating a single horizontal flame tube (furnace chamber) immersed in the boiling solution in the lower part of the regenerator and an upper section of boiling tubes with flue gas outside the tubes has been disclosed by *Furukawa (1988)*; Sanyo was granted a Japanese patent for this design. Such Sanyo-type regenerators have also been applied in great numbers of direct-fired absorption chillers from East-Asian production in the last decades (cf. e.g. *Shitara et al. (2001)*).

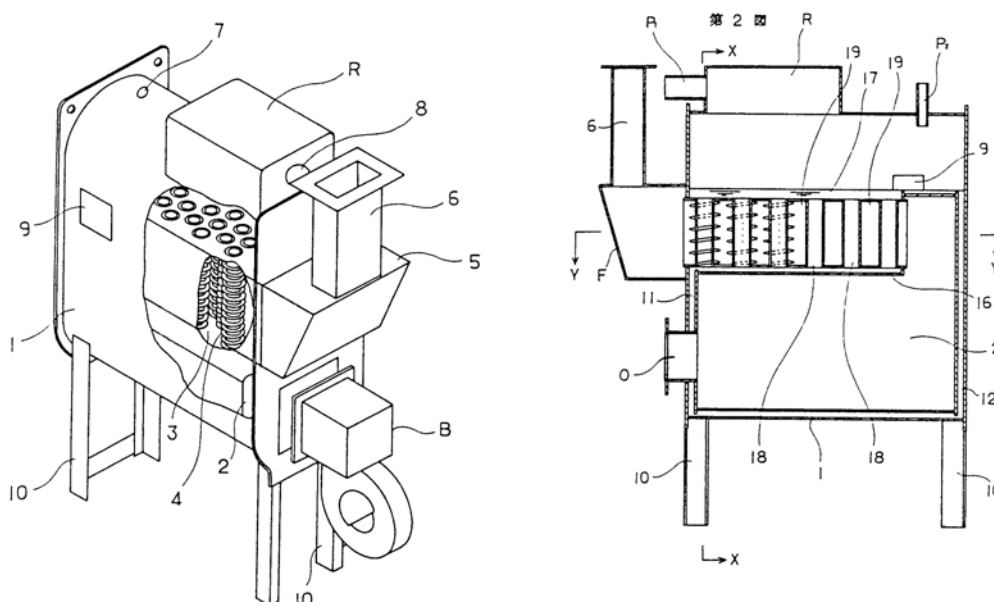


**Fig. 25: Folded hybrid design of a Sanyo-type direct-fired regenerator. Patent drawings from *Furukawa (1988)*.**

In tube-boilers, a certain flow velocity inside the tubes is needed to ensure proper heat transfer and to avoid a burnout. This can be achieved by a forced convection induced by an external circulation pump (see left sketch in Fig. 26) or – more conveniently – by a natural convection utilizing non-heated downcomer tubes (right sketch in Fig. 26). In the latter case, the difference in density between the liquid in the downcomer tubes and the two-phase-flow

<sup>33</sup> See e.g. photographs from *Pathakji et al. (2005)* and *Wagner et al. (2005)* cited in Fig. 9 in 2.3.2 above.

<sup>34</sup> See e.g. *Kori et al. (1997)* *Kouri et al. (1998)* *Inoue et al. (1999)*, *Kubota et al. (1999)*, *Nakamura et al. (2000)*, *Tucker et al. (2000)*, *Tucker et al. (2001)*, *Katayama et al. (2002)*, *Gupte (2003)*, *Inoue & Endo (2003)*, *Senba et al. (2003)*, *Gupte (2005)*.

<sup>35</sup> See e.g. *Shitara (2000)*, *Shitara et al. (2001)*, *Kashiwagi et al. (2002)*, *Oka et al. (2003)*, *Yabase et al. (2005)*

<sup>36</sup> See *Wagner et al. (2005)*

in the boiling tubes is employed as a driving force. Generally, the natural convection design can be used for boiling liquids at low pressures relative to the critical pressure of the liquid, as the specific volume of the vapor decreases at higher pressures. Therefore, regenerators of water/lithium bromide based absorption chillers operating at about atmospheric pressure in case of common double-effect cycles or maybe at 5...10 bar in case of future triple-effect cycles can be designed as natural convection boilers.

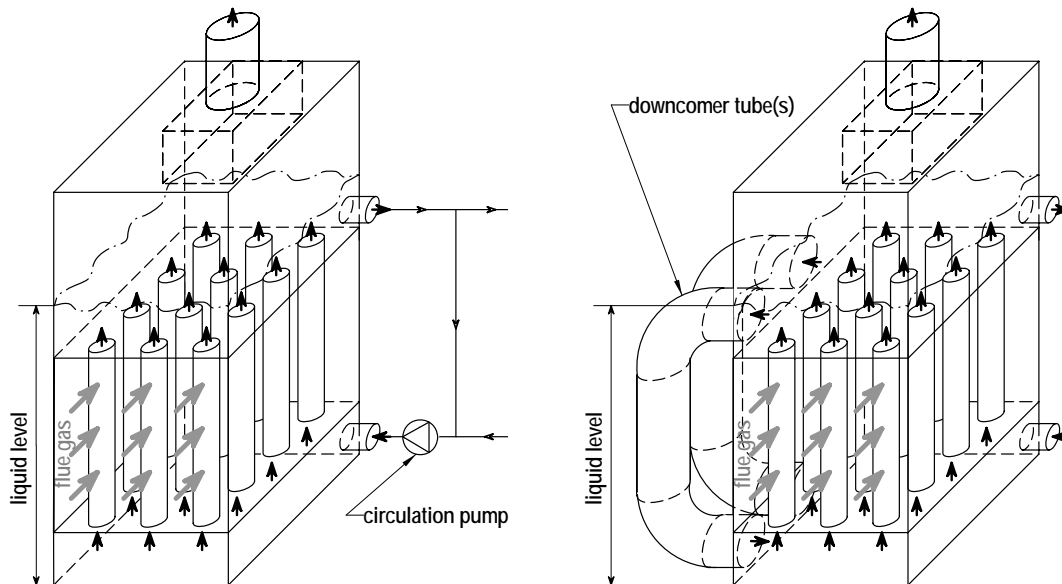


**Fig. 26: Principal sketch of tube boilers with forced convection and circulation pump (left) and with natural convection and downcomer tubes (right).**

For both types of circulation, the liquid is more or less in saturation in the header and enters the bottom vessel at about this temperature, too. Because of the higher pressure due to the additional liquid head at the bottom, there the liquid is subcooled with reference to the local pressure. Therefore, the liquid enters a boiling tube at the bottom as a subcooled single-phase flow that is first heated up in a lower pre-heat section in the tube without net vapor production. At a certain level, the flow reaches the local saturation temperature, which is still higher than saturation temperature in the header as there is still some additional pressure head at this position. In the upper boiling section of the tube, there subsequently is a two-phase flow with increasing vapor content along the flow direction.

To increase the heat transfer at the flue gas side, boiling tubes with outer fins can be used (see Fig. 27). Installation of a first section of plain boiling tubes followed by a second section of finned boiling tubes along the flow path of the flue gas can partly compensate for the drop in flue gas temperature resulting in inhomogeneous heat flux densities.



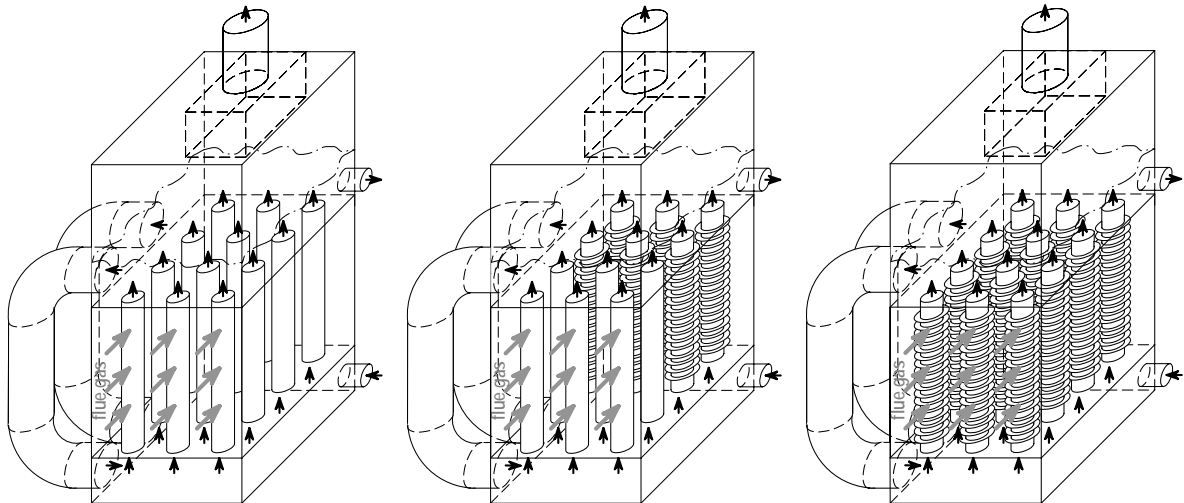


**Fig. 27: Principal sketch of natural convection boilers with plain and finned boiling tubes.**

Completely equipped with plain boiling tubes (left), equipped with a first section of plain boiling tubes followed by a second section of finned boiling tubes along the flue gas flow path (middle) and completely equipped with finned boiling tubes (right).

Both common boiler designs, shell boilers and tube boilers, have their advantages and disadvantages. While shell boilers come along with the less costly construction, tube boilers provide a more compact and flexible design with a lower liquid inventory.

#### 4.1.2 Typical heat transfer settings

For flue gas fired regenerators of both types shell boiler and tube boiler, three heat transfer zones have to be regarded (see Fig. 28):

1. Mainly convective heat transfer from the flue gas at local temperature  $T_G$  to the flue gas side of the tube wall at local temperature  $T_{W,G}$ .
2. Heat conduction across the tube wall from the flue gas side at temperature  $T_{W,G}$  to the liquid side at temperature  $T_{W,L}$ .
3. Mainly heat transfer at a nucleate boiling regime in the lithium bromide solution from the tube wall at temperature  $T_{W,L}$  to the liquid at local temperature  $T_L$ . The liquid is assumed to be close to its local saturation temperature  $T_{SAT}(\rho, X_{SOL})$  in dependence on the local pressure<sup>37</sup> and salt concentration.

The heat transfer coefficient  $\alpha_G$  of the convective heat transfer from the flue gas to the tube wall has an order of magnitude of  $10^2 \text{ W/m}^2\text{K}$ . Neglecting second order terms due to the curvature of the tube wall, heat conduction through the wall can be subsumed in another “virtual” heat transfer coefficient  $k_W = 2 \cdot \lambda_W / (d_O - d_I)$ . For steel tubes with reasonable wall thickness, this coefficient has an order of magnitude of  $10^4 \text{ W/m}^2\text{K}$ . The heat transfer in the

<sup>37</sup> Due to the hydrostatic head of the liquid, the local pressure is higher than the refrigerant vapor pressure above the liquid level.

liquid always is the superposition of a convective heat transfer and a boiling heat transfer. The boiling heat transfer coefficient is strongly dependent on the wall superheat at the liquid side relative to the local saturation temperature  $\Delta T_{SAT} = T_{W,L} - T_{SAT}$ . If this exceeds the characteristic threshold for the onset of nucleate boiling  $\Delta T_{SAT} > \Delta T_{ONB}$ , boiling heat transfer coefficient rises sharply and boiling heat transfer typically is the dominant mode at the liquid side. In this regime, the order of magnitude of the heat transfer coefficient at the liquid side  $\alpha_L$  is in the range of  $10^3 \text{ W/m}^2\text{K}$  to  $10^4 \text{ W/m}^2\text{K}$ .

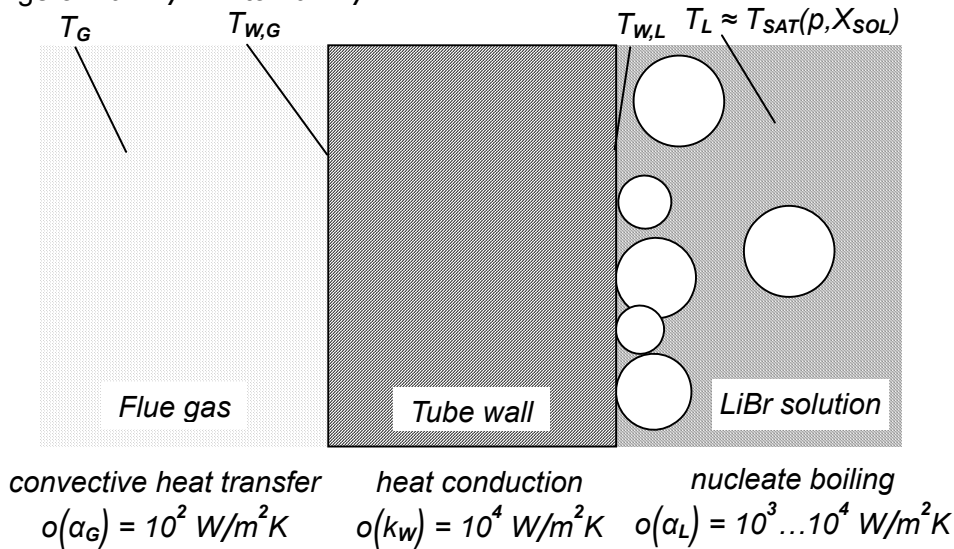


**Fig. 28:** Basic settings for heat transfer from flue gas to boiling lithium bromide solution in shell boilers and tube boilers.

As long as surface areas at gas side and liquid side are in the same order of magnitude, the overall heat transfer coefficient  $U$  is mainly determined by the heat transfer coefficient at the flue gas side  $\alpha_G$ , which is at least one order of magnitude smaller than both of the other values are<sup>38</sup>.

$$U = 1 / \left( 1 / \alpha_G + 1 / k_W + 1 / \alpha_L \right) \approx \alpha_G \quad (4.1)$$

The local heat flux density, i.e. the specific heat flux per area  $\dot{q} = \dot{Q} / A = U \cdot \Delta T$  is mainly determined by the local flue gas heat transfer coefficient  $\alpha_G$  and the local flue gas temperature  $T_G$ .

$$\dot{q} = U \cdot (T_G - T_{SAT}) \approx \alpha_G \cdot (T_G - T_{SAT}) \quad (4.2)$$

Hence, an optimized regenerator design must aim for high convective heat transfer coefficients at the flue gas side to achieve a high heat flux per area and hence to minimize the size of the heat exchanger. However, there are two more constraints to be considered.

<sup>38</sup> Application of highly finned heat exchanger surfaces allowing for an up to 20-fold increase of the gas-side surface area may partly compensate for this difference in heat transfer coefficients, but the flue gas side heat transfer will remain the limiting one.

First, there is a critical heat flux  $\dot{q}_{CRIT}$  where the boiling heat transfer coefficient at the liquid side  $\alpha_L$  dramatically decreases as a continuous vapor film starts to separate the liquid phase from the tube wall. As a result, tube wall temperatures  $T_{W,L}$  and  $T_{W,G}$  may increase by some hundred Kelvin and the heat exchanger is destroyed in a short time.

$$T_{W,L} = T_{SAT} + \Delta T_{SAT} = T_{SAT} + \dot{q} / \alpha_L \quad (4.3)$$

$$T_{W,G} = T_{W,L} + \dot{q} / k_W \quad (4.4)$$

This phenomenon called burnout is most likely to occur at hot spots in flue gas heated boilers next to the furnace or the exhaust gas intake. There local temperature differences between flue gas and boiling liquid  $\Delta T = T_G - T_{SAT}$  from several hundred Kelvin up to more than thousand Kelvin can be found.

Secondly, there is the problem that corrosivity of aqueous lithium bromide solutions significantly increases with temperature while all available corrosion inhibitors gradually lose their effect in the temperature range from 150°C to 200 °C. As a result, tube wall temperatures at the liquid side  $T_{W,L}$  should not permanently exceed 160...170°C under operation, at least as long as heat exchangers made from carbon steel are concerned. Even alloyed steel – being more costly – is not completely resistant against pitting corrosion in lithium bromide solution at elevated temperatures, too. Saturation temperature of the salt solution in a high-temperature regenerator already is in the range of 140...150°C (cf. Tab. 5) without taking into account the additional liquid head at the heat exchange surface. Therefore, the wall superheat  $\Delta T_{SAT}$  must be limited to only 15...20 K to avoid a slow degradation and destruction of the heat exchanger. According to (4.3) these limits in wall temperature  $T_{W,L} \leq T_{W,L,MAX}$  and wall superheat  $\Delta T_{SAT} \leq \Delta T_{SAT,MAX}$  set a second limit in the heat flux  $\dot{q} \leq \dot{q}_{MAX}$ :

$$T_{W,L} \leq T_{W,L,MAX} \Leftrightarrow \Delta T_{SAT} \leq \Delta T_{SAT,MAX} = T_{W,L,MAX} - T_{SAT} \Leftrightarrow \dot{q} \leq \dot{q}_{MAX} = \Delta T_{SAT,MAX} / \alpha_L \quad (4.5)$$

For high-temperature regenerators this limit from the wall temperature typically is much lower than the theoretical critical heat flux  $\dot{q}_{MAX} < \dot{q}_{CRIT}$ . Therefore, an optimized regenerator design must also aim for a high heat transfer coefficient at the liquid side  $\alpha_L$  to allow for a high heat flux in the heat exchanger. Especially in direct-fired regenerators, where flue gas temperature and local driving temperature difference  $\Delta T = T_G - T_{SAT}$  show large variations from furnace to stack, heat flux has to be deliberately balanced to get an efficient and reliable design.

## 4.2 General definitions for heat transfer and pressure drop calculations

### 4.2.1 Heat transfer coefficients at circular tubes

If the wall thickness of heat exchanger tubes is not some orders of magnitude smaller than the tube diameter, then there is a significant difference between inner and outer tube surface that has to be regarded for in heat transfer calculations. For boiling heat transfer e.g. the decisive parameter is the heat flux density at the liquid side of the tube wall  $\dot{q}_L = \dot{Q} / A_L$  being the quotient from the total heat flux through the tube wall  $\dot{Q}$  and the tube wall surface at the liquid side  $A_L$ .

Accordingly, the definition of an overall heat transfer coefficient (4.2) is dependent on the chosen surface and the simple equation (4.1) has to be extended. No matter on which side of the tube wall the liquid and the gas are the overall heat transfer coefficient  $U_I$  with respect to the tube inner surface  $A_I$  is:

$$\begin{aligned} U_I &= \dot{q}_I / \Delta T = \dot{Q} / A_I (T_G - T_{SAT}) = 1 / \left( \frac{A_I}{A_O} \cdot \frac{1}{\alpha_O} + \frac{1}{k_{W,I}} + \frac{1}{\alpha_I} \right) \\ &= 1 / \left[ \frac{d_I}{d_O} \alpha_O + \frac{d_I}{2} \cdot \ln \left( \frac{d_O}{d_I} \right) / \lambda_W + \frac{1}{\alpha_I} \right] \end{aligned} \quad (4.6)$$

The corresponding formulation for the overall heat transfer coefficient  $U_O$  with respect to the tube outer surface is:

$$\begin{aligned} U_O &= \dot{q}_O / \Delta T = \dot{Q} / A_O (T_G - T_{SAT}) = 1 / \left( \frac{1}{\alpha_O} + \frac{1}{k_{W,O}} + \frac{A_O}{A_I} \cdot \frac{1}{\alpha_I} \right) \\ &= 1 / \left[ \frac{1}{\alpha_O} + \frac{d_O}{2} \cdot \ln \left( \frac{d_O}{d_I} \right) / \lambda_W + \frac{d_O}{d_I} \alpha_I \right] \end{aligned} \quad (4.7)$$

In both formulations,  $\lambda_W$  is the thermal conductivity of the tube wall and  $\alpha_O$  and  $\alpha_I$  are the heat transfer coefficients at the outer and inner surface of the tube, respectively.

### 4.2.2 Dimensionless numbers and property data

A flow regime is mainly characterized by its dimensionless Reynolds number  $Re$ , which is given in dependence on the fluid velocity  $u$ , the kinematic viscosity of the fluid  $\nu$  and a characteristic length  $L$ , which is e.g. the inner diameter  $d_I$  for fluid flow in circular tubes.

$$Re = u \cdot L / \nu \quad (4.8)$$

The kinematic viscosity  $\nu$  is the quotient of the dynamic or absolute viscosity  $\mu$  and the fluid density  $\rho$ :

$$\nu = \mu / \rho \quad (4.9)$$

With this identity, the definition of the Reynolds number can alternatively be written as:

$$Re = u \cdot L \cdot \rho / \mu \quad (4.10)$$

Using the definition of a mass flux density or specific mass flow per cross section  $\dot{m}$  as the quotient of a mass flow  $\dot{M}$  and the area of the cross section  $A_{CS}$

$$\dot{m} = \dot{M} / A_{CS} = u \cdot \rho \quad (4.11)$$

A third alternative formulation of the Reynolds number can be given, that is especially convenient for fluids of variable density:

$$Re = \dot{m} \cdot L / \mu \quad (4.12)$$

Convective heat transfer is characterized by the dimensionless Nusselt number  $Nu$ , being a function of the convection heat transfer coefficient  $\alpha_{CV}$ , the thermal conductivity of the fluid  $\lambda$  and a characteristic length  $L$ , which is e.g. the inner diameter  $d_i$  for fluid flow in circular tubes:

$$Nu = \alpha_{CV} \cdot L / \lambda \quad (4.13)$$

In addition to the flow regime characterized by the Reynolds number  $Re$  and the thermal conductivity  $\lambda$  incorporated in definition (4.13), the convective heat transfer is also dependent on further physical properties of the fluid. These can be subsumed by the Prandtl number  $Pr$  that is the quotient of the kinematic viscosity  $\nu$  and the thermal diffusivity  $a$ :

$$Pr = \nu / a \quad (4.14)$$

The thermal diffusivity  $a$  can be calculated from thermal conductivity  $\lambda$ , density  $\rho$  and specific heat capacity  $c_P$  of the fluid:

$$a = \lambda / (\rho \cdot c_P) \quad (4.15)$$

From (4.9), (4.12) and (4.13) follows an alternative definition of the Prandtl number:

$$Pr = \mu \cdot c_P / \lambda \quad (4.16)$$

For air or flue gas from natural gas combustion, the Prandtl number is about  $Pr_{GAS} \approx 0.7$  and only weakly dependent on temperature. For liquids, the Prandtl number drops at rising temperatures. In aqueous lithium bromide solution, the Prandtl number additionally rises with increasing salt concentration. At atmospheric pressure, the Prandtl number of boiling water is about 2, the Prandtl number of boiling lithium bromide solution is about 7.

### 4.2.3 Reversible and non-reversible pressure drops

In a stagnant fluid, the pressure at each position is an isotropic thermodynamic variable. In moving fluids, however, the observed pressure forces are also dependent on the direction of the measurement. Nevertheless, the thermodynamically relevant static pressure is always the force per area that acts normal to the flow direction e.g. on a tube wall in tubular flows. Any variation in static pressure  $dp$  in flow direction  $x$  can be expressed by the sum of three different effects: the gravitational pressure drop  $dp_{GRAV}$ , the so-called “acceleration pressure drop”  $dp_{ACC}$ , and the frictional pressure drop  $dp_{FR}$ .

$$-dp = dp_{GRAV} + dp_{ACC} + dp_{FR} \quad (4.17)$$

Both, gravitational and acceleration pressure drop are reversible; the additional frictional pressure drop  $dp_{FR}$  that is found in viscous fluids is a non-reversible term. The gravitational pressure drop  $dp_{GRAV}$  in (4.17) is the well-known difference in the static head  $dp_{GRAV} = \rho \cdot g \cdot dh$ , being dependent on fluid density  $\rho$ , gravity  $g$ , and the displacement in height  $dh = \frac{dh}{dx} \cdot dx$ . It is of importance in liquid flows, but commonly neglected in calculations concerning gas flows. The acceleration pressure drop in (4.17) is:

$$dp_{ACC} = \rho \cdot u \cdot du = \dot{m} \cdot du = \dot{m} \cdot d\left(\frac{\dot{m}}{\rho}\right) \quad (4.18)$$

Equation (4.18) results from the conservation of momentum  $\frac{d}{dt}(dM \cdot u) = dp_{ACC} \cdot A_{CS}$  at variation of the velocity  $u$  of an infinitesimal fluid element of mass  $dM$  and cross section  $A_{CS}$  by means of insertion of definition (4.11), i.e.  $\dot{m} = \dot{M} / A_{CS} = u \cdot \rho$  and thus  $dM = A_{CS} \cdot \dot{m} \cdot dt$ . Here,  $\dot{M}$  is the absolute mass flow rate and  $\dot{m}$  is the specific mass flux per unit cross-sectional area. If the fluid velocity is decreased, i.e.  $du < 0$  in (4.18), this acceleration pressure drop  $dp_{ACC}$  becomes negative, being a kind of “deceleration pressure rise” (however, the latter term is no so common).

For incompressible ideal fluids without viscosity (i.e.  $dp_{FR} = 0$  and  $\rho = const.$ ) in ducts of variable diameter, equation (4.17) after insertion of (4.18) yields:  $-dp/\rho = g \cdot dh + u \cdot du$ ; an integration leads to Bernoulli’s well-known equation that requires little further explanation.

On the other hand, for variations in fluid density  $\rho$  – e.g. due to a heat exchange process – in flows inside ducts or tubes of constant diameter  $A_{CS} = const.$ , formulation (4.18) for the acceleration pressure drop simply yields:

$$dp_{ACC} = \dot{m}^2 \cdot d\left(\frac{1}{\rho}\right) \quad \text{for } A_{CS} = const. \text{ and thus } \dot{m} = const. \quad (4.19)$$

Hence if a fluid enters a heat exchanger duct or tube of constant cross section at density  $\rho_{IN}$  and leaves it at density  $\rho_{OUT}$ , the acceleration pressure drop or “deceleration pressure rise” respectively over this section is:

$$\Delta p_{ACC} = \dot{m}^2 \cdot \left( \frac{1}{\rho_{OUT}} - \frac{1}{\rho_{IN}} \right) \quad \text{for } \dot{m} = \text{const.} \quad (4.20)$$

### 4.3 Forced single phase flow inside circular tubes

A single-phase flow regime inside of tubes applies for both, flue gas flow inside the smoke tubes of a shell boiler and subcooled lithium bromide solution entering the bottom of the boiling tubes in a tube boiler (pre-heat section). Heat transfer and pressure drop relations are quoted with reference to the *VDI-Wärmeatlas*, 9<sup>th</sup> edition, *VDI-GVC (2002)*. An overview on heat transfer correlations is e.g. also provided by *Spang (2004)*.

#### 4.3.1 Definition of the Reynolds number

For circular tubes, the characteristic length is the inner diameter  $L = d_i$ . The Reynolds number is according to definitions (4.8), (4.10) and (4.12):

$$Re = u \cdot d_i / \nu = u \cdot d_i \cdot \rho / \mu = \dot{m} \cdot d_i / \mu \quad (4.21)$$

For Reynolds numbers  $Re \leq 2300$  pipe flow is always laminar, for  $Re > 10^4$  there is always turbulent flow. In the transition region  $2300 < Re < 10^4$  the flow regime is dependent on the boundary conditions at the tube inlet.

#### 4.3.2 Heat transfer

For flow inside of tubes, heat transfer coefficients are dependent on the position relative to the start of the heating or cooling of the flow. Especially for laminar flow, heat transfer is also dependent on the position relative to the tube inlet as the characteristic velocity profile builds up successively. For the definition of the Nusselt number the characteristic length is the inner diameter  $L = d_i$ .

$$Nu = \alpha_{CV} \cdot d_i / \lambda \quad (4.22)$$

#### Laminar flow

For laminar flow, the heat transfer can be calculated for the case of a constant wall temperature and for the case of a constant wall heat flux density. The case of a constant wall temperature is a reasonable approximation for flue gas flow inside of smoke tubes immersed in a saturated liquid. The case of constant heat flux is a reasonable approximation for lithium bromide solution entering heat exchanger tubes externally heated by flue gas.

For a simultaneously thermally and hydrodynamically developing laminar flow starting at tube inlet at position  $x = 0$  a local Nusselt number can be calculated at each position  $x$  downstream in dependence of Reynolds number  $Re$ , Prandtl number  $Pr$  and tube inner diameter  $d_i$ . Additionally a mean Nusselt number for the whole tube of the length  $l$  can be derived.

### Constant wall temperature in laminar flow

Local Nusselt number at position  $x$  downstream:

$$Nu_{T,LOC} = \left\{ 3.66^3 + 0.7^3 + \left[ 1.077 \left( Re \cdot Pr \cdot \frac{d_i}{x} \right)^{1/3} - 0.7 \right]^3 + \left[ \frac{1}{2} \cdot \left( \frac{2}{1} + 22Pr \right)^{1/6} \cdot \left( Re \cdot Pr \cdot \frac{d_i}{x} \right)^{1/2} \right]^3 \right\}^{1/3} \quad (4.23)$$

Mean Nusselt number for a tube of the length  $l$ :

$$Nu_{T,MN} = \left\{ 3.66^3 + 0.7^3 + \left[ 1.615 \cdot \left( Re \cdot Pr \cdot \frac{d_i}{l} \right)^{1/3} - 0.7 \right]^3 + \left[ \left( \frac{2}{1} + 22 \cdot Pr \right)^{1/6} \cdot \left( Re \cdot Pr \cdot \frac{d_i}{l} \right)^{1/2} \right]^3 \right\}^{1/3} \quad (4.24)$$

### Constant heat flux density in laminar flow

Local Nusselt number at position  $x$  downstream:

$$Nu_{Q,LOC} = \left\{ 4.364^3 + 1^3 + \left[ 1.302 \cdot \left( Re \cdot Pr \cdot \frac{d_i}{x} \right)^{1/3} - 1 \right]^3 + \left[ 0.462 \cdot Pr^{1/3} \cdot \left( Re \cdot \frac{d_i}{x} \right)^{1/2} \right]^3 \right\}^{1/3} \quad (4.25)$$

Mean Nusselt number for a tube of the length  $l$ :

$$Nu_{Q,MN} = \left\{ 4.364^3 + 0.6^3 + \left[ 1.953 \cdot \left( Re \cdot Pr \cdot \frac{d_i}{l} \right)^{1/3} - 0.6 \right]^3 + \left[ 0.924 \cdot Pr^{1/3} \cdot \left( Re \cdot \frac{d_i}{l} \right)^{1/2} \right]^3 \right\}^{1/3} \quad (4.26)$$

### Asymptotic values in laminar flow

For small values of  $Re \cdot \frac{d_i}{x}$  or  $Re \cdot \frac{d_i}{l}$ , i.e. for slow flow velocities and for tubes that are long compared to their inner diameter, the equations for local and mean Nusselt number both reduce to the same asymptotic value of  $Nu_T \approx 3.66$  for constant wall temperature or  $Nu_Q \approx 4.364$  for constant heat flux density, respectively.

### Turbulent flow

For turbulent flow there is no difference between constant wall temperature and constant heat flux density, however there is also a weak dependence on the position  $x$  relative to the tube inlet or on the tube length  $l$  respectively. Using the definition:

$$\xi = \left( 1.8 \cdot \log_{10}(Re) - 1.5 \right)^{-2} \quad (4.27)$$

The local Nusselt number at position  $x \geq d_i$  is:

$$Nu_{Loc} = \frac{\xi}{8} \cdot Re \cdot Pr \left/ \left[ 1 + 12.7 \cdot \left( \frac{\xi}{8} \right)^{1/2} \cdot \left( Pr^{2/3} - 1 \right) \right] \right. \cdot \left[ 1 + \frac{1}{3} \cdot \left( \frac{d_i}{x} \right)^{2/3} \right] \quad (4.28)$$

The mean Nusselt number for a tube of the length  $l$  is:

$$Nu_{MN} = \frac{\xi}{8} \cdot Re \cdot Pr \left/ \left[ 1 + 12.7 \cdot \left( \frac{\xi}{8} \right)^{1/2} \cdot \left( Pr^{2/3} - 1 \right) \right] \right. \cdot \left[ 1 + \left( \frac{d_i}{l} \right)^{2/3} \right] \quad (4.29)$$



For rough estimations [VDI-GVC \(2002\)](#) provide approximate formulas. For low Prandtl numbers in the range  $0.5 < Pr < 1.5$  (e.g. applicable for air or flue gas) the mean Nusselt number can be estimated:

$$Nu_{MN} \approx 0.0214 \cdot (Re^{0.8} - 100) \cdot Pr^{0.4} \cdot [1 + (d_f/l)^{2/3}] \quad (4.30)$$

An even more simple approximation is the though outdated still widely used so-called<sup>39</sup> Dittus and Boelter equation:

$$Nu_{MN} \approx 0.023 \cdot Re^{0.8} \cdot Pr^{0.4} \quad (4.31)$$

### Transition flow

In the transition region  $2300 < Re < 10^4$  the flow regime is dependent on the boundary conditions at the tube inlet and therefore an accurate prediction of the convective heat transfer from just  $Re$  and  $Pr$  is not possible. [VDI-GVC \(2002\)](#) provide an approximate interpolation formula for this region that allows for calculations without discontinuities at  $Re = 2300$  and  $Re = 10^4$ . Using the Nusselt numbers  $Nu_{LAM,2300} = Nu_{LAM}(Re=2300)$  calculated from (4.24) or (4.26) for laminar flow with a Reynolds number of 2300 and  $Nu_{TURB,10000} = Nu_{TURB}(Re=10^4)$  calculated from (4.28) for turbulent flow with a Reynolds number of  $10^4$  and the interpolation variable  $\gamma$ :

$$\gamma = (Re - 2300) / (10^4 - 2300), \quad 0 \leq \gamma \leq 1 \quad (4.32)$$

The Nusselt number for transient flow  $Nu_{TRANS}$  can be estimated:

$$Nu_{TRANS} = (1 - \gamma) \cdot Nu_{LAM,2300} + \gamma \cdot Nu_{TURB,10000} \quad (4.33)$$

This correlation has been shown to give reasonable approximations for mean Nusselt numbers of tubular flow.

### Effects of property variation with temperature

The correlations given above apply for fluids without a significant variation of properties along the temperature profile in the flow. Therefore, an additional correction factor may be necessary to account for this effect. For liquid flows with Nusselt number  $Nu_{TMN}$  calculated using property data at mean liquid temperature  $T_{MN}$ ,  $Pr_{TMN}$  being the Prandtl number at mean liquid temperature and  $Pr_{TW}$  being the Prandtl number at wall temperature  $T_w$  the corrected Nusselt number  $Nu_{LIQ}$  is:

$$Nu_{LIQ} = Nu_{TMN} \cdot (Pr_{TMN} / Pr_{TW})^{0.11} \quad (4.34)$$

<sup>39</sup> According to [Winterton \(1998\)](#), equation (4.31) although commonly referenced as “Dittus and Boelter equation” was actually introduced first by [McAdams \(1942\)](#). The original formulation given by [Dittus & Boelter \(1930\)](#) already had the form of (4.31), but used slightly different proportionality constants, which were additionally dependent on the flow direction (upward or downward flow).

The Nusselt number at mean liquid temperature  $Nu_{TMN}$  is calculated employing one of the correlations (4.23) to (4.33) given above depending on the general classification of the heat transfer.

For laminar gas flow according to *VDI-GVC (2002)* the influence of property data variation on the heat transfer coefficient is small enough that no correction is required; for turbulent gas flow, no clear recommendations are provided.

According to *Spang (2004)*, for turbulent gas flow inside tubes a correction in the form of

$$Nu_{GAS} = Nu_{TMN} \cdot (T_{G,MN} / T_{W,G})^N \quad (4.35)$$

can be applied where  $Nu_{TMN}$  is the Nusselt number calculated using property data at mean gas temperature  $T_{G,MN}$  and  $T_{W,G}$  is the wall temperature at the gas side. An exponent  $N = 0.36$  is given for turbulent flow while no correction, i.e.  $N = 0$  is utilized for laminar flow.

### 4.3.3 Frictional pressure drop

The frictional pressure drop  $\Delta p_{FR}$  for tubular flow is generally expressed in dependence of a friction factor. There are several definitions for the friction factor in literature, which differ only by factors of 2 or 4. Within this work a friction factor  $\zeta$  according to *VDI-GVC (2002)* will be used<sup>40</sup> that is implicitly defined by the following equation for frictional pressure drop  $\Delta p_{FR}$  in dependence on tube length  $l$ , inner diameter  $d_i$ , fluid density  $\rho$  and mean fluid velocity  $u$  or specific cross-sectional mass flow  $\dot{m}$ :

$$\Delta p_{FR} = \zeta \cdot l/d_i \cdot \rho u^2/2 = \zeta \cdot l/d_i \cdot \dot{m}^2/2\rho \quad (4.36)$$

#### Laminar flow

For laminar flow, the friction factor  $\zeta$  according to definition (4.36) can be expressed in dependence on the Reynolds number  $Re$ :

$$\zeta = 64/Re \quad (4.37)$$

#### Turbulent flow

For turbulent flow regime, the friction factor is also dependent on the roughness of the tube wall surface. The dimensionless parameter is the relative surface roughness  $\varepsilon = e/d_i$  being the quotient from the absolute mean roughness  $e$  and the inner diameter  $d_i$  of the tube.

According to *VDI-GVC (2002)*, for copper tubes evanescent absolute roughness  $e < 2 \mu m$  can be assumed whereas steel tubes show values of about  $e \approx 40 \mu m$  in new condition and

<sup>40</sup> Another widely used convention is to define a friction factor  $f = 1/4 \cdot \zeta$

up to 400  $\mu\text{m}$  in corroded state. The friction factor in dependence of Reynolds number  $d_i$  and relative roughness  $e/d_i$  is given by the implicit equation:

$$\zeta^{-1/2} = -2 \cdot \log_{10}(2.51 \cdot \zeta^{-1/2} / Re + (e/d_i) / 3.71) \quad (4.38)$$

For smooth tubes and moderate Reynolds numbers  $3\,000 \leq Re \leq 100\,000$  a simple explicit correlation for the friction factor can be used:

$$\zeta = 0.3164 \cdot Re^{-1/4} \quad (4.39)$$

### Transition flow

According to *VDI-GVC (2002)* in reasonable smooth tubes laminar flow can be found up to Reynolds numbers of  $Re = 8\,000$ ; with increasing roughness this threshold successively approaches  $Re = 2\,320$ . However interpolation formulas like (4.32), (4.33) for heat transfer, are not provided by *VDI-GVC (2002)*.

In the previous edition of the same reference work, *VDI-GVC (1997)*, some graphs on pressure drops in tubular flow of water and air had been given covering also the transition region  $2\,320 < Re < 10\,000$ . It shows that these graphs are basically compliant with the application of turbulent flow correlation (4.38) at Reynolds numbers greater than  $3\,000 \dots 4\,000$ . Below, either a correlation for turbulent flow or some interpolation between laminar and turbulent friction factors was used in these graphs.

For calculations within this work, an interpolation between laminar and turbulent friction factors has been performed in the region  $2\,350 < Re < 3\,500$  while correlation (4.38) was employed above.

### Inlet and outlet pressure drop

In addition to the reversible change in static pressure due to acceleration or deceleration, there are frictional pressure losses at the inlet and the outlet of each heat exchanger tube that starts or ends at a vessel or water box etc. The frictional pressure drops at the inlet ( $\Delta p_{IN}$ ) and at the outlet ( $\Delta p_{OUT}$ ) of a tube can be expressed by a formulation similar to (4.36) defining friction factors for inlet  $\zeta_{IN}$  and outlet  $\zeta_{OUT}$ :

$$\Delta p_{IN} + \Delta p_{OUT} = (\zeta_{IN} + \zeta_{OUT}) \cdot \rho u^2 / 2 = (\zeta_{IN} + \zeta_{OUT}) \cdot \dot{m}^2 / 2\rho \quad (4.40)$$

The friction factors  $\zeta_{IN}$  and  $\zeta_{OUT}$  are mainly dependent on the ratio of the fluid velocities before/after entering/leaving the tube and on the nature of the edges (sharpness, angle) at these positions but also on the Reynolds number of the tubular flow. Several graphs but no generally valid correlations for  $\zeta_{IN}$  and  $\zeta_{OUT}$  are provided by *VDI-GVC (2002)*. For typical

conditions at the inlet or outlet of heat exchanger tube bundles, however, it can be stated that these friction factors are most likely in the range of  $0.2 \dots 0.5$  each.

## 4.4 Forced convection flow across tube bundles

### 4.4.1 Definition of dimensionless numbers

The most common cases are tube bundles with symmetric staggered or in-line arrangement of the tubes. Fig. 29 shows a small staggered arrangement (left) and a small in-line arrangement (right) each comprising four rows of tubes  $N_{TB,LO} = 4$  (counted in longitudinal direction) consecutively passed by the fluid flow and three tubes per row  $N_{TB,TR} = 3$  (counted in transverse direction).

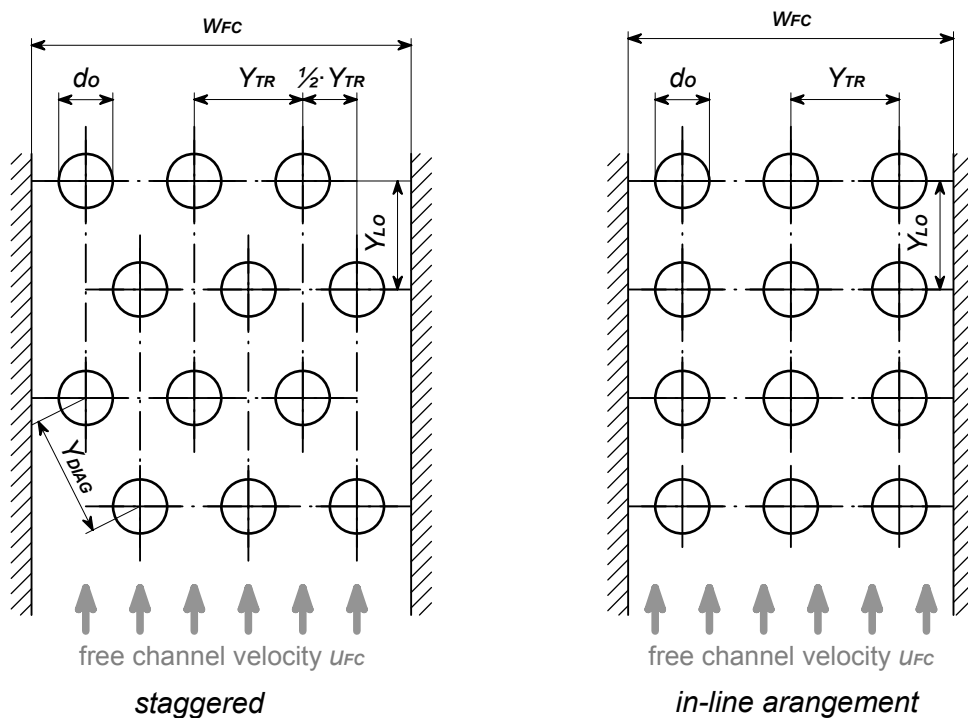


Fig. 29: Basic configuration of tube bundles with staggered (left) and in-line (right) arrangement. Definition of transverse and longitudinal tube pitch.

The transverse tube pitch  $Y_{TR}$  is defined as the center-to-center distance of two adjacent tubes normal to fluid flow. The longitudinal tube pitch  $Y_{LO}$  is defined as the distance between centers of successive rows in the mean flow direction. For staggered arrangements, only the symmetric arrangement will be considered with the tube centers of two successive rows shifted by half the transverse tube pitch. According to [Rhine & Tucker \(1991\)](#) both staggered and in-line tubes are frequently arranged so that  $Y_{LO} = Y_{TR}$ .

For heat transfer and pressure drop calculations the geometry of the tube arrangement is expressed by the transverse pitch ratio  $y_{TR} = Y_{TR}/d_o$  and the longitudinal pitch ratio

$y_{LO} = Y_{LO}/d_o$ . Also a diagonal tube pitch ratio  $y_{DIAG} = Y_{DIAG}/d_o$  can be defined; for symmetric staggered arrangements, it is calculated from transverse and longitudinal tube pitch ratio:

$$y_{DIAG} = Y_{DIAG}/d_o = \left( y_{TR}^2/4 + y_{LO}^2 \right)^{1/2} \quad (4.41)$$

A common definition of the Reynolds number is based on the outer diameter of the tubes  $d_o$  as characteristic length and the maximum fluid velocity  $u_{MAX}$  at the minimum cross flow area in the bundle  $A_{CS,MIN}$ .

$$Re_D = u_{MAX} \cdot d_o/\mu \quad (4.42)$$

Using the void ratio  $\psi_{MIN} = A_{CS,MIN}/A_{CS,FC}$  being the quotient of the minimum cross flow area  $A_{CS,MIN}$  and the cross sectional area of the free channel without tubes  $A_{CS,FC}$  the Reynolds number can also be written in dependence on the mass flux density  $\dot{m}_{FC} = u_{FC} \cdot \rho = \dot{M}/A_{CS,FC}$  in the free channel:

$$Re_D = \dot{m}_{FC}/\psi_{MIN} \cdot d_o/\mu \quad (4.43)$$

This definition of the Reynolds number using the outer diameter of the bare tube as characteristic length is also used for finned tubes (see Fig. 30). For calculation of the void ratio, however, the increased profile of the finned tube has to be regarded additionally.

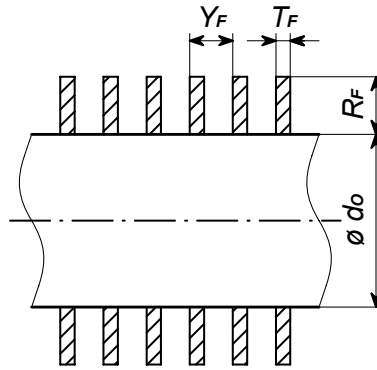


Fig. 30: Definition of fin height, fin thickness and fin pitch of tubes with outer circular fins.

Normal to fluid flow the cross sectional profile of a finned tube with bare tube outer diameter  $d_o$ , fin height  $R_F$ , fin thickness  $T_F$  and fin pitch  $Y_F$  is equivalent to the cross sectional profile of a plain tube of outer diameter  $d_{EFF} = \vartheta_{EFF} \cdot d_o$ , provided that:

$$\vartheta_{EFF} = d_{EFF}/d_o = 1 + 2 \cdot R_F/d_o \cdot T_F/Y_F \quad (4.44)$$

Introducing this effective profile factor  $\vartheta_{EFF}$  a consistent set of equations for calculation of the void ratio in arrangements of plain tubes as well as in arrangements of tubes with outer circular fins can be obtained. For plain tubes the effective profile factor is unity i.e.  $\vartheta_{EFF} = 1$ .

If there is only a single tube in each row  $N_{TB,TR} = 1$  the void ratio  $\psi_{MIN,1}$  is simply calculated from the width of the free channel  $w_{FC}$  and the outer diameter of the tubes  $d_o$  (cp. Fig. 29):

$$\psi_{MIN,1} = 1 - \partial_{EFF} \cdot d_o / w_{FC} \quad (4.45)$$

For wide tube-banks with a large number of tubes in each row  $N_{TB,TR} \rightarrow \infty$  the void ratio  $\psi_{MIN,\infty}$  can be expressed as a function of longitudinal and transversal pitch ratio.

For in-line arrangement as well as for staggered arrangement with sufficient longitudinal pitch  $y_{LO} / \partial_{EFF} \geq \frac{1}{2} \cdot (2 \cdot y_{TR} / \partial_{EFF} + 1)^{1/2}$  the minimum cross flow area is calculated as function of the transversal tube spacing and there is a simple relation for the minimum void ratio:

$$\psi_{MIN,\infty} = 1 - \partial_{EFF} / y_{TR} \quad (4.46)$$

Relation (4.46) is always valid for the frequent case  $y_{LO} = y_{TR}$  as the condition given above is always true for<sup>41</sup>  $y_{LO} / \partial_{EFF} = y_{TR} / \partial_{EFF} > 1$ . For staggered arrangement and small longitudinal pitch, the minimum cross flow area is dependent on the diagonal tube spacing and the void ratio is given:

$$\psi_{MIN,\infty} = (2 \cdot y_{DIAG} - \partial_{EFF}) / y_{TR} = [2 \cdot (y_{TR}^2 / 4 + y_{LO}^2)^{1/2} - \partial_{EFF}] / y_{TR} \quad (4.47)$$

for staggered arrangement and longitudinal pitch  $y_{LO} / \partial_{EFF} < \frac{1}{2} \cdot (2 \cdot y_{TR} / \partial_{EFF} + 1)^{1/2}$

The case of staggered arrangement in narrow tube banks with only a few tubes in each row  $o(N_{TB,TR}) = 1$  is not explicitly covered by [VDI-GVC \(2002\)](#). In this case, boundary effects have to be considered and the effective void ratio is also dependent on the actual channel width.

Therefore within this work for staggered tube banks with only few tubes in each row but sufficient longitudinal pitch the void ratio has been calculated analogous to (4.45) from the actual channel width:

$$\psi_{MIN,NA,ST} \approx 1 - N_{TB,TR} \cdot \partial_{EFF} \cdot d_o / w_{FC} \quad (4.48)$$

Assuming a width of the free channel of about  $w_{FC} \approx (N_{TB,TR} + \frac{1}{2}) \cdot y_{TR}$  this can also be written as a generalization of (4.46):

$$\psi_{MIN,NA,ST} \approx 1 - \partial_{EFF} / y_{TR} \cdot [N_{TB,TR} / (N_{TB,TR} + \frac{1}{2})] \quad (4.49)$$

The definition of the Reynolds number  $Re_D$  according to (4.42) and (4.43) based on the outer diameter of the bare tube and the maximum fluid velocity is used by [VDI-GVC \(2002\)](#) for three purposes. These are: Calculations of friction pressure drops across bundles of plain tubes, calculations of friction pressure drops across finned tubes, and heat transfer calcula-

<sup>41</sup> As neighboring tubes must not overlay, the condition  $y_{TR} / \partial_{EFF} > 1$  is always accomplished.

tions across bundles of finned tubes. It is also used for heat transfer in forced convection across plain tubes by literature sources like e.g. *Rhine & Tucker (1991)*.

*VDI-GVC (2002)*, however, provide an alternative definition of a Reynolds number  $Re_L$  based on half the perimeter of the tube as characteristic length  $L = \frac{\pi}{2} d_o$  and an average fluid velocity  $u_{AV}$  next to the outer tube wall. This average velocity  $u_{AV} = u_{FC} / \psi_{AV}$  is defined as the quotient of the fluid velocity in the free channel  $u_{FC} = \dot{m}_{FC} / \rho$  and an average void ratio  $\psi_{AV}$ . With this definition of  $L$  and  $u = u_{AV}$  from (4.8) follows:

$$Re_L = \frac{\dot{m}_{FC}}{\psi_{AV}} \cdot \frac{\pi}{2} \cdot \frac{d_o}{\mu} \quad (4.50)$$

If there is only a single tube in each row  $N_{TB,TR} = 1$ , the average void ratio  $\psi_{AV,1}$  is a function of the width of the free channel  $w_{FC}$  according to *VDI-GVC (2002)*:

$$\psi_{AV,1} = 1 - \frac{\pi}{4} \cdot \frac{d_o}{w_{FC}} \quad (4.51)$$

For wide tube-banks with a large number of tubes in each row  $N_{TB,TR} \rightarrow \infty$  the void ratio  $\psi_{AV,\infty}$  can be expressed as a function of the pitch ratio:

$$\psi_{AV,\infty} = 1 - \frac{\pi}{4} \cdot \frac{1}{y_{TR}} \quad \text{for } y_{LO} \geq 1 \quad (4.52)$$

$$\psi_{AV,\infty} = 1 - \frac{\pi}{4} \cdot \frac{1}{y_{LO} \cdot y_{TR}} \quad \text{for } y_{LO} < 1 \quad (4.53)$$

Again, the boundary effects in narrow staggered arrangements with only a few tubes in each row are not explicitly considered by *VDI-GVC (2002)*. Therefore, within this work for this case a formulation analogous to (4.49) assuming a free channel with  $w_{FC} \approx (N_{TB,TR} + \frac{1}{2}) \cdot Y_{TR}$  has been employed:

$$\psi_{AV,NA,ST} \approx 1 - \frac{\pi}{4} \cdot \frac{1}{y_{TR}} \cdot \left[ \frac{N_{TB,TR}}{N_{TB,TR} + \frac{1}{2}} \right] \Leftrightarrow y_{LO} \geq 1 \quad (4.54)$$

## 4.4.2 Heat transfer

### Flow across bundles of plain tubes

For convective heat transfer across plain tubes, *VDI-GVC (2002)* utilize half the perimeter of a tube  $L = \frac{\pi}{2} d_o$  as characteristic length for the definition of both, Reynolds number  $Re_L$  according to (4.50) and Nusselt number  $Nu_L$ :

$$Nu_L = \alpha_{cv} \cdot \frac{\pi}{2} \cdot \frac{d_o}{\lambda} \quad (4.55)$$

The mean Nusselt number of the tube bundle  $Nu_{L,MN}$  always comprises a laminar term  $Nu_{L,LAM}$  and a turbulent term  $Nu_{L,TURB}$ . The bundle geometry is considered by an arrangement factor  $f_A$ :

$$Nu_{L,MN} = f_A \cdot [0.3 + (Nu_{L,LAM}^2 + Nu_{L,TURB}^2)^{1/2}] \quad (4.56)$$

$$Nu_{L,LAM} = 0.664 \cdot Re_L^{1/2} \cdot Pr^{1/3} \quad (4.57)$$

$$Nu_{L,TURB} = 0.037 \cdot Re_L^{0.8} \cdot Pr \cdot [1 + 2.443 Re_L^{-0.1} (Pr^{2/3} - 1)]^{-1} \quad (4.58)$$

Correlation (4.56) is valid over the full range  $10 < Re_L < 10^6$  without the necessity to distinguish between different flow regimes.

For a single row of tubes  $N_{TB,LO} = 1$ , the arrangement factor is unity i.e.  $f_{A,1} = 1$ . For ten or more consecutive rows of tubes  $N_{TB,LO} \geq 10$  in a staggered arrangement, this factor is dependent on the transversal tube pitch:

$$f_{A,\infty} = 1 + 2 / (3 \cdot y_{TR}) \quad (4.59)$$

For in-line arrangements of ten or more rows of tubes  $N_{TB,LO} \geq 10$  [VDI-GVC \(2002\)](#) provide a more complex correlation valid for  $y_{TR} \geq 1.2$ :

$$f_{A,\infty} = 1 + 0.7 / \psi_{AV}^{1.5} \cdot (y_{TR}/y_{LO} - 0.3) \cdot (y_{TR}/y_{LO} - 0.7)^{-2} \quad (4.60)$$

For short tube bundles  $1 \leq N_{TB,LO} < 10$  [VDI-GVC \(2002\)](#) provide an interpolation formula:

$$f_{A,N} = 1/N_{TB,LO} + f_{A,\infty} \cdot (1 - 1/N_{TB,LO}) \quad (4.61)$$

Arrangement factors for individual rows within a bundle are not explicitly provided by [VDI-GVC \(2002\)](#). As long as no extra turbulator devices are positioned in the gas flow upstream of the tube bundle, on the first row of tubes the incident flow is laminar and only little increase in heat transfer can be expected. At all consecutive rows of tubes of the bundle the heat transfer is significantly increased by an additional turbulence in the incident flow caused by the preceding tube row.

For calculation of heat transfer at individual rows of tubes of a bundle, within this work the simple assumption of an arrangement factor  $f_A = f_{A,1} = 1$  at the first row and  $f_A = f_{A,\infty}$  at all consecutive rows has been made. This approximation is justified, as it is the only possible assumption that is completely consistent with (4.61), ensuring that row-by-row calculations will yield the same results as full-bundle calculations.

### Flow across bundles of finned tubes

For convective heat transfer across bundles of finned tubes [VDI-GVC \(2002\)](#) utilize the outer diameter of the bare tubes as characteristic length  $L = d_o$  for the definition of both, Reynolds number (4.42) and Nusselt number:

$$Nu_D = \alpha_{cv} \cdot d_o / \lambda \quad (4.62)$$



Here  $\alpha_{CV}$  is the mean convective heat transfer coefficient from the fluid outside the tube to the outer surface of the finned tube. The outer surface of a finned tube consists of the outer surface of the fins  $A_{FIN}$  and the remaining visible outer surface of the bare tube not covered by fins  $A_{BARE}$ . Typically, the total outer surface  $A_{TOT} = A_{BARE} + A_{FIN}$  of the finned tube is about ten times greater than the outer surface of the basic plain tube  $A_{PLAIN}$  without fins. This relative increase can be expressed by a surface-enhancement factor  $\beta_F$ :

$$\beta_F = A_{TOT} / A_{PLAIN} = (A_{BARE} + A_{FIN}) / A_{PLAIN} = 1 + 2 R_F (d_o + R_F + T_F) / Y_F d_o \quad (4.63)$$

*VDI-GVC (2002)* provide an approximation formula for the Nusselt number  $Nu_D$  in dependence of Reynolds number  $Re_D$ , Prandtl number  $Pr$ , surface enhancement  $\beta_F$ , and an additional arrangement constant  $C_A$ :

$$Nu_D = C_A \cdot Re_D^{0.6} \cdot \beta_F^{-0.15} \cdot Pr^{1/3} \quad (4.64)$$

Suggested values for the arrangement constant  $C_A$  are provided in dependence on arrangement and number of consecutive rows of tubes  $N_{TB,LO}$ :

| Number of consecutive tube rows | In-line arrangement | Staggered arrangement |
|---------------------------------|---------------------|-----------------------|
| $N_{TB,LO} = 1$                 | $C_A = 0.20$        |                       |
| $N_{TB,LO} = 2$                 | $C_A = 0.20$        | $C_A = 0.33$          |
| $N_{TB,LO} = 3$                 | $C_A = 0.20$        | $C_A = 0.36$          |
| $N_{TB,LO} \geq 4$              | $C_A = 0.22$        | $C_A = 0.38$          |

*Tab. 6: Arrangement constant  $C_A$  for heat transfer in fluid flow across finned tube bundles, in dependence on arrangement and number of consecutive rows of tubes  $N_{TB,LO}$ .*

According to *VDI-GVC (2002)*, correlation (4.64) is valid in the range  $10^3 < Re_L < 10^5$  and  $5 \leq \beta_F \leq 30$ . For the case  $N_{TB,LO} \geq 4$  a spread of  $\pm 10\%$  to  $\pm 25\%$  is given.

The convective heat transfer coefficient  $\alpha_{CV}$  according to (4.62) only accounts for the heat transfer to the outer surface of a finned tube, which actually consists mainly of the surface of the fins. The heat conductance through the fin body to the outer surface of the basic tube of diameter  $d_o$ , however, may impose another significant heat transfer resistance that has to be accounted for. In this case, the formulations (4.6) and (4.7) for the overall heat transfer coefficient would have to be extended by an additional term for the heat conductance through the fins. Therefore it is convenient to define a mean virtual heat transfer coefficient  $\alpha_{VIRT}$  with respect to the total outer surface  $A_{TOT}$  and a fin efficiency  $\eta_F = \alpha_{VIRT} / \alpha_{CV}$  in a way that analogous formulations to (4.6) and (4.7) are obtained for the overall heat transfer coefficients.

Then the overall heat transfer coefficient  $U_I$  with respect to the inner surface of the tube  $A_I$  is:

$$\begin{aligned} U_I &= \dot{q}_I / \Delta T = \dot{Q} / A_I (T_G - T_{SAT}) \\ &= 1 / \left[ d_I / (d_o \cdot (\beta_F \eta_F \alpha_{CV})) + d_I / 2 \cdot \ln(d_o / d_I) / \lambda_W + 1 / \alpha_I \right] \end{aligned} \quad (4.65)$$

The corresponding formulation for the overall heat transfer coefficient  $U_{TOT}$  with respect to the total outer surface  $A_{TOT}$  of the finned tube is:

$$\begin{aligned} U_{TOT} &= \dot{q}_{TOT} / \Delta T = \dot{Q} / A_{TOT} (T_G - T_{SAT}) \\ &= 1 / \left[ 1 / \eta_F \alpha_{CV} + \beta_F \cdot d_o / 2 \cdot \ln(d_o / d_I) / \lambda_W + \beta_F d_o / d_I \alpha_I \right] \end{aligned} \quad (4.66)$$

The fin efficiency  $\eta_F$  can be calculated according to [VDI-GVC \(2002\)](#) e.g. for circular fins from the geometry data (see Fig. 30), the convective heat transfer coefficient  $\alpha_{CV}$  and the thermal conductivity of the fin material  $\lambda_F$ :

$$\eta_F = \tanh(X) / X = \frac{1}{X} \cdot (e^X - e^{-X}) / (e^X + e^{-X}) \quad (4.67)$$

with the definition

$$X := \left( 2 \alpha_{CV} / \lambda_F T_F \right)^{1/2} \cdot R_F \cdot \left[ 1 + 0.35 \cdot \ln(1 + 2 R_F / d_o) \right]$$

### Effects of property variation with temperature

For liquid flows across tube bundles – liquid being outside the tubes – a correction factor analogous to (4.34) given for liquid flow inside tubes in 4.3.2 can be applied for heat transfer calculations to account for property variation with temperature. In this case, the exponent is dependent on the direction of the heat flux; liquid being heated up outside the tubes would result in an exponent of 0.25 instead of 0.11.

For gas flows across tube bundles, according to [VDI-GVC \(2002\)](#) a correction in the form of

$$NU_{GAS} = NU_{TMN} \cdot (T_{G,MN} / T_{W,G})^N \quad (4.68)$$

can be applied where  $NU_{TMN}$  is the Nusselt number calculated using property data at mean gas temperature  $T_{G,MN}$  and  $T_{W,G}$  is the wall temperature at the gas side. The same formulation (4.35) is also suggested by [Spang \(2004\)](#) for gas flow inside tubes.

According to [VDI-GVC \(2002\)](#) for bundles of plain tubes the exponent  $N$  in (4.68) is dependent on the kind of gas, for cooling of hot air a value of  $N = 0$  may be applicable, for cooling of nitrogen  $N = 0.12$  has been found. For finned tubes no information on correction terms are provided. [Spang \(2004\)](#) on the other hand gives an exponent of  $N = 0.12$  for both finned and plain tubes and all kinds of gas.

As contradictory information has been found in literature, within this work these corrections have been disregarded unless otherwise mentioned, assuming  $N = 0$  for both plain and finned tube bundles.

### 4.4.3 Frictional pressure drop

For pressure drop correlations regarding both plain and finned tube bundles, *VDI-GVC (2002)* utilize the Reynolds number definition (4.42) and (4.43) based on the tube outer diameter  $d_o$  and the maximum velocity  $u_{MAX} = \dot{m}_{FC} / \rho \cdot \psi_{MIN}$ . The friction factor  $\zeta$  is implicitly defined by the equation for frictional pressure drop  $\Delta p_{FR}$  in tube bundles:

$$\Delta p_{FR} = \zeta \cdot N_{RESIST} \cdot \rho \cdot u_{MAX}^2 / 2 = \zeta \cdot N_{RESIST} \cdot \dot{m}_{FC}^2 / (2 \cdot \rho \cdot \psi_{MIN}) \quad (4.69)$$

The additional parameter  $N_{RESIST}$  comprises the number of flow resistances in flow direction. For in-line arrangements and staggered arrangements with sufficient longitudinal tube pitch the number of resistances is equal to the number of rows of tubes  $N_{RESIST} = N_{TB,LO}$ . For staggered arrangements with small longitudinal pitch  $y_{LO}/\phi_{EFF} < 1/2 \cdot (2 \cdot y_{TR}/\phi_{EFF} + 1)^{1/2}$  and the minimum cross flow area being dependent on the diagonal tube spacing the number of resistances is  $N_{RESIST} = N_{TB,LO} - 1$ .

#### Plain tubes

The friction factor is always the sum of a laminar part and a turbulent part:

$$\zeta = \zeta_{LAM} + \zeta_{TURB} \quad (4.70)$$

The laminar part of the friction factor  $\zeta_{LAM}$  is a function of the Reynolds number  $Re_D$ , the dynamic viscosities of the fluid  $\mu_{TMN}$  at mean fluid temperature  $T_{MN}$  and  $\mu_W$  at wall temperature  $T_W$  next to the fluid and an arrangement factor  $f_{LAM}$  and a corrective exponent  $NL$ :

$$\zeta_{LAM} = Re_D^{-1} \cdot f_{LAM} \cdot (\mu_W / \mu_{TMN})^{NL} \quad (4.71)$$

The laminar arrangement factor for all in-line arrangements and for staggered arrangements with sufficient longitudinal pitch  $y_{LO} \geq 1/2 \cdot (2 \cdot y_{TR} + 1)^{1/2}$  is:

$$f_{LAM} = 280 \cdot \pi \cdot [(y_{LO}^{1/2} - 0.6)^2 + 0.75] / [(4 \cdot y_{LO} \cdot y_{TR} - \pi) \cdot y_{TR}^{1.6}] \quad (4.72)$$

For staggered arrangements with small longitudinal pitch, the factor  $f_{LAM}$  is also dependent on the diagonal tube pitch:

$$f_{LAM} = 280 \cdot \pi \cdot [(y_{LO}^{1/2} - 0.6)^2 + 0.75] / [(4 \cdot y_{LO} \cdot y_{TR} - \pi) \cdot y_{DIAG}^{1.6}] \quad (4.73)$$

for staggered arrangement,  $y_{LO} < 1/2 \cdot (2 \cdot y_{TR} + 1)^{1/2}$

The corrective exponent  $NL$  in (4.71) is dependent on the number of consecutive rows of tubes<sup>42</sup>  $N_{TB,LO}$ :

$$NL = 0.57 \cdot \left\{ \left[ \min(10, N_{TB,LO}) / 10 \right] / \left[ \left( 4 \cdot y_{LO} \cdot y_{TR} / \pi - 1 \right) \cdot Re_D \right] \right\}^{1/4} \quad (4.74)$$

The turbulent part of the friction factor  $\zeta_{TURB}$  is also dependent on an arrangement factor  $f_{TURB}$ , a Reynolds independent corrective term<sup>43</sup>  $\zeta_{CORR}$ , and two variable exponents:

$$\zeta_{TURB} = \left[ Re_D^{NRE} \cdot f_{TURB} \cdot \left( \mu_W / \mu_{TMN} \right)^{0.14} + \zeta_{CORR} \cdot \left( 1 / \min(10, N_{TB,LO}) - 1/10 \right) \right] \cdot (1 - e^{NT}) \quad (4.75)$$

For staggered arrangement the exponent of the Reynolds number is a constant value  $NRE = -0.25$ , for in-line arrangement it is dependent on the tube pitch  $NRE = -0.1 \cdot y_{TR} / y_{LO}$ .

For staggered arrangement the turbulent arrangement factor  $f_{TURB}$  is:

$$f_{TURB} = 2.5 + 1.2 / (y_{TR} - 0.85)^{1.08} + 0.4 \cdot (y_{LO} / y_{TR} - 1)^3 - 0.01 \cdot (y_{TR} / y_{LO} - 1)^3 \quad (4.76)$$

For in-line arrangement the turbulent arrangement factor  $f_{TURB}$  is:

$$f_{TURB} = \left[ 0.22 + 1.2 \left( 1 - 0.94 \frac{y_{LO}}{y_{TR}} \right)^{0.6} (y_{TR} - 0.85)^{-1.3} \right] \cdot 10^{0.47(y_{LO}/y_{TR} - 1.5)} + 0.03(y_{TR} - 1)(y_{LO} - 1) \quad (4.77)$$

The turbulent corrective term  $\zeta_{CORR}$  accounts for exit pressure drops in short tube bundles  $5 \leq N_{TB,LO} < 10$ . For in-line arrangements and for staggered arrangements with sufficient longitudinal pitch  $y_{LO} \geq \frac{1}{2} \cdot (2 \cdot y_{TR} + 1)^{1/2}$  the corrective term is:

$$\zeta_{CORR} = \frac{1}{y_{2TR}} \quad (4.78)$$

For staggered arrangements with small longitudinal pitch, the turbulent corrective term  $\zeta_{CORR}$  is also dependent on the diagonal tube pitch:

$$\zeta_{CORR} = \left[ 2 \cdot (y_{DIAG} - 1) / y_{TR} \cdot (y_{TR} - 1) \right]^2 \quad (4.79)$$

for staggered arrangement,  $y_{LO} < \frac{1}{2} \cdot (2 \cdot y_{TR} + 1)^{1/2}$

The turbulent exponent  $NT$  for staggered arrangement is:

$$NT = -(Re_D + 200) / 1000 \quad (4.80)$$

For in-line arrangement, the exponent yields:

$$NT = -(Re_D + 1000) / 2000 \quad (4.81)$$

<sup>42</sup> Note that  $\min(10, N_{TB,LO}) / 10 = 1$  for  $N_{TB,LO} \geq 10$

<sup>43</sup> Note that theoretically the factor  $1 / \min(10, N_{TB,LO}) - 1/10$  takes a value of  $9/10$  for a single tube row and successively drops to zero for ten and more rows of tubes. Validity range, however, for this corrective term is  $5 \leq N_{TB,LO} < 10$ . Therefore this factor actually drops from  $1/2$  for  $N_{TB,LO} = 5$  to zero for ten and more rows of tubes.

According to *VDI-GVC (2002)*, these pressure drop formulations for plain tube bundles are valid in the range  $1 \leq Re_D \leq 3 \cdot 10^5$  for at least five rows of tubes  $N_{TB,LO} \geq 5$ . For in-line arrangements they have been proven for  $1.25 \leq y_{TR} \leq 3.0$ ,  $1.2 \leq y_{LO} \leq 3.0$  and for staggered arrangements they have been proven for  $1.25 \leq y_{TR} \leq 3.0$ ,  $0.6 \leq y_{LO} \leq 3.0$ ,  $y_{DIAG} \geq 1.25$ .

### Finned tubes

For finned tubes in a staggered arrangement, the friction factor  $\zeta_{ST}$  according to *VDI-GVC (2002)* can be written in the form:

$$\zeta_{ST} = f_{N,ST} \cdot C_{RE,ST} \cdot Re_D^{NST} \cdot y_{TR}^{-0.55} \cdot y_{LO}^{-0.5} \cdot \left(1 - Y_F/d_o\right)^{1.8} \cdot \left(1 - R_F/d_o\right)^{-1.4} \quad (4.82)$$

For in-line arrangements with  $y_{LO} \approx y_{TR}$  the general form of the friction factor  $\zeta_{IN}$  is:

$$\zeta_{IN} = f_{N,IN} \cdot C_{RE,IN} \cdot Re_D^{NIN} \cdot y_{TR}^{-0.5} \cdot \left(Y_F/d_o\right)^{-0.7} \cdot \left(R_F/d_o\right)^{0.5} \quad (4.83)$$

In these formulations  $f_{N,ST}$  and  $f_{N,IN}$  are correction factors dependent on the number of consecutive rows of tubes accounting for inlet and exit pressure drops in short tube bundles. For tube bundles with at least five rows of tubes, these factors are unity. The applicable values for shorter bundles are listed in Tab. 7 below.

| Number of consecutive tube rows | Staggered arrangement | In-line arrangement |
|---------------------------------|-----------------------|---------------------|
| $N_{TB,LO} = 1$                 | $f_{N,ST} = 1.5$      | $f_{N,IN} = 2.2$    |
| $N_{TB,LO} = 2$                 | $f_{N,ST} = 1.25$     | $f_{N,IN} = 1.5$    |
| $N_{TB,LO} = 3$                 | $f_{N,ST} = 1.1$      | $f_{N,IN} = 1.15$   |
| $N_{TB,LO} = 4$                 | $f_{N,ST} = 1.02$     | $f_{N,IN} = 1.025$  |
| $N_{TB,LO} \geq 5$              | $f_{N,ST} = 1$        | $f_{N,IN} = 1$      |

**Tab. 7:** Correction factors  $f_{N,ST}$  and  $f_{N,IN}$  for friction pressure drop across finned tube bundles in dependence on arrangement and number of consecutive rows of tubes  $N_{TB,LO}$ .

The coefficients  $C_{RE,ST}$  and  $C_{RE,IN}$  as well as the exponents  $NST$  and  $NIN$  of the Reynolds number are dependent on the magnitude of the Reynolds number  $Re_D$ . For staggered arrangement, the values of the coefficients in (4.82) according to *VDI-GVC (2002)* are listed in Tab. 8:

| Reynolds number $Re_D$         | Coefficient $C_{RE,ST}$ | Exponent $NST$ |
|--------------------------------|-------------------------|----------------|
| $10^2 < Re_D < 10^3$           | 290                     | -0.7           |
| $10^3 < Re_D < 10^5$           | 13                      | -0.25          |
| $10^5 < Re_D < 1.4 \cdot 10^6$ | 0.74                    | 0              |

**Tab. 8:** Coefficient  $C_{RE,ST}$  and exponent  $NST$  for friction pressure drop across finned tube bundles with staggered arrangement in dependence of the magnitude of the Reynolds number  $Re_D$ .

For in-line arrangement, the values of the coefficients in (4.83) are listed in Tab. 9:

| Reynolds number $Re_D$                 | Coefficient $C_{RE,IN}$ | Exponent $NIN$ |
|--|-------------------------|----------------|
| $3 \cdot 10^3 < Re_D < 4 \cdot 10^4$   | 5.5                     | -0.3           |
| $4 \cdot 10^4 < Re_D < 1.4 \cdot 10^6$ | 0.23                    | 0              |

Tab. 9: Coefficient  $C_{RE,IN}$  and exponent  $NIN$  for friction pressure drop across finned tube bundles with in-line arrangement in dependence of the magnitude of the Reynolds number  $Re_D$ .

According to [VDI-GVC \(2002\)](#), these pressure drop formulations for finned tube bundles are valid for at least five rows  $N_{TB,LO} \geq 5$  and in the range  $3 \cdot 10^3 \leq Re_D \leq 1.4 \cdot 10^6$  for in-line arrangement or in the range  $10^2 \leq Re_D \leq 1.4 \cdot 10^6$  for staggered arrangement respectively. For in-line arrangements, they have been proven with a deviation of  $\pm 20\%$  for  $1.8 \leq y_{TR} \leq 2.45$ ,  $0.085 \leq Y_{F/d_0} \leq 0.2$ , and  $0.18 \leq R_{F/d_0} \leq 0.7$ . For staggered arrangements, they have been proven with a deviation of  $\pm 15\%$  for  $1.6 \leq y_{TR} \leq 2$ ,  $1.2 \leq y_{LO} \leq 2$ ,  $0.12 \leq Y_{F/d_0} \leq 0.28$ , and  $0.12 \leq R_{F/d_0} \leq 0.6$ .

## 4.5 Boiling heat transfer

### 4.5.1 Boiling regimes

#### Boiling regimes in pool boilers

As already indicated, boiling heat transfer is strongly dependent on heat flux density  $\dot{q}$  and wall superheat  $\Delta T_{SAT} = T_{W,L} - T_{SAT}$ . For small values of  $\dot{q}$  and  $\Delta T_{SAT}$ , there is no vapor generation within the liquid bulk or next to the wall, and all heat transfer takes place in a single-phase natural convection regime. If wall superheat and heat flux density exceed certain limits for the onset of nucleate boiling  $\Delta T_{SAT} > \Delta T_{ONB}$ ,  $\dot{q} > \dot{q}_{ONB}$ , vapor bubbles are generated at the heated surface and the heat transfer coefficient rises due to the agitation of the liquid by the vapor. If heat flux density exceeds a critical value  $\dot{q} > \dot{q}_{CRIT}$ , a continuous vapor film starts to separate the liquid phase from the tube wall and the heat transfer coefficient drops again.

For the design of flue gas fired boilers, mainly operation in the nucleate boiling regime is of interest and thus shall be discussed in the following. This also includes discussion of the operational limits of the nucleate boiling regime,  $\Delta T_{ONB}$  and  $\dot{q}_{CRIT}$ . Operation at heat duties exceeding  $\dot{q}_{CRIT}$  is not relevant, as this typically will lead to destruction of flue gas heated boilers. In contrast to this, low heat duties below  $\dot{q}_{ONB}$  are valid operating conditions that are likely to occur under transient part load operation; respective heat transfer correlations for this regime (natural convection in a single-phase liquid) are e.g. given by [VDI-GVC \(2002\)](#). For design purposes, however, these correlations may be neglected as the nucleate boiling

heat transfer correlations will always underestimate the heat transfer coefficient in this regime and thus inherently result in a safe design. For optimization purposes, operation below onset of nucleate boiling is of less interest anyway, as desirably high heat transfer coefficients are realized in the nucleate boiling regime.

### Boiling regimes in vertical tubes

As already discussed above for pool boiling, heat transfer during fluid flow in vertical tubes can also take place in two different regimes, viz. convection and nucleate boiling. Unlike pool boiling, however, the convective heat transfer inside boiling tubes cannot be neglected and may be even the dominant mode at design operation of tube boilers. One reason is that the onset of nucleate boiling can be suppressed by a high convective heat transfer. Another aspect is that the convective heat transfer resulting from the initial liquid flow is accelerated by the additional turbulence induced by the vapor bubbles in two-phase flow. On the other hand, nucleate boiling may also significantly increase the heat transfer to subcooled flows if a sufficient wall superheat is reached.

The increased turbulence in two-phase flow results in an increased convective heat transfer coefficient, higher than for liquid or vapor single-phase flow at the same mass flux. This increase is strongly dependent on the vapor fraction  $\dot{\chi} = \dot{M}_V / \dot{M}$  of the total mass flow  $\dot{M} = \dot{M}_L + \dot{M}_V$  in a tube. For a fluid flow in thermal equilibrium, this vapor fraction is identical to the thermodynamic equilibrium quality  $\dot{\chi}_{EQ}$  derived from the local specific enthalpy of the fluid  $h$ , the specific enthalpy of the liquid in saturation at local pressure  $h'$  and the specific heat of evaporation at local pressure  $\Delta h_{VAP}$ :

$$\dot{\chi}_{EQ} = (h - h') / \Delta h_{VAP} \quad (4.84)$$

For heated flows in boiling tubes the approximation  $\dot{\chi} \approx \dot{\chi}_{EQ}$  is still valid for a wide range of qualities of about  $0.1 < \dot{\chi}_{EQ} < 0.9$  and the vapor mass fraction at any cross section can be comfortably calculated from the mean fluid enthalpy at this position using (4.84). For low qualities  $\dot{\chi}_{EQ} \approx 0$  or slightly subcooled flows, however, there is an actual nonzero vapor fraction  $\dot{\chi} > \dot{\chi}_{EQ}$  in the flow as there are already vapor bubbles next to the wall while the core of the liquid stays subcooled.

With increasing quality in axial direction of a boiling tube, a number of different flow patterns and heat transfer modes can be identified. A more detailed introduction into this subject is e.g. given by [Corradini \(1998\)](#) or [Lienhard & Lienhard \(2003\)](#). Fig. 31 below visualizes the progression of flow patterns, heat transfer modes, wall temperature, and fluid temperature at a boiling tube with constant heat flux density.

In an actual configuration, however, not all of the regions “A” to “H” shown in Fig. 31 might be observed, as they are also dependent on operating conditions like the subcooling of the fluid entering the boiling tube, the heat flux density and the tube length.

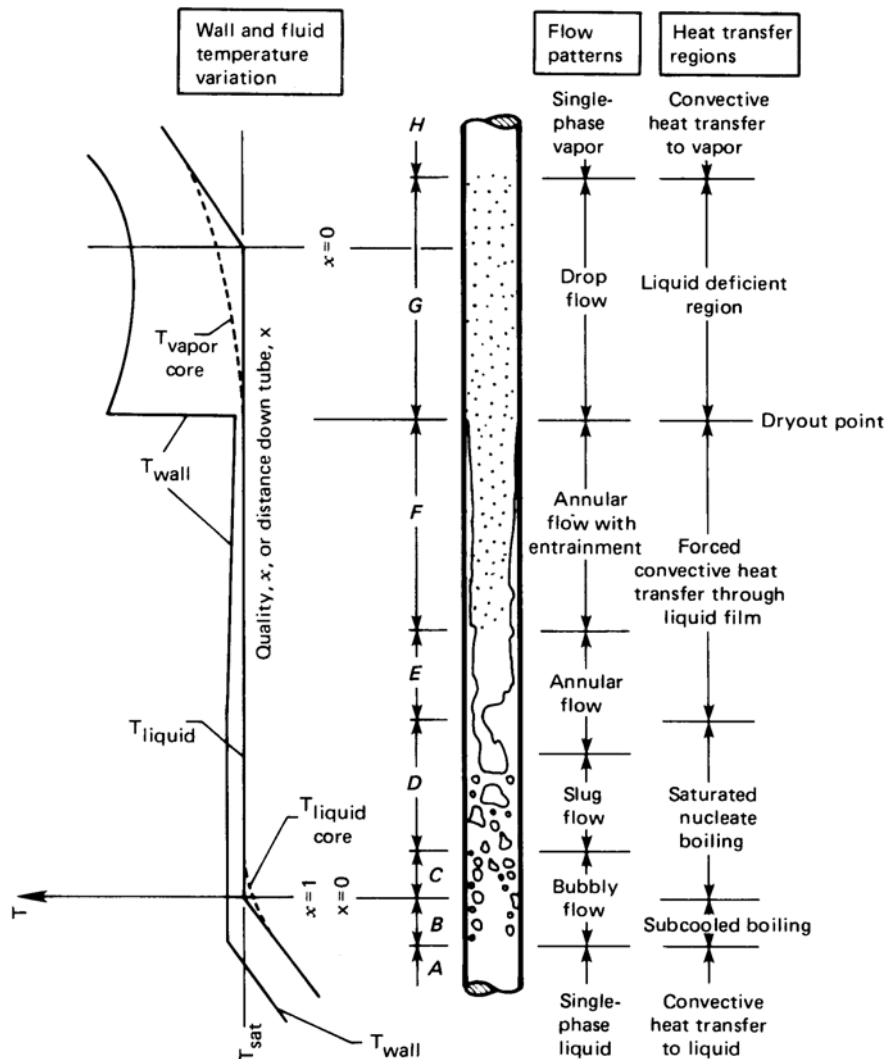


**Fig. 31: Development of a two-phase flow in a vertical tube with uniform wall heat flux (not to scale).** Flow pattern, dominant heat transfer mode and development of wall and fluid temperature along the boiling tube. Cited from Lienhard & Lienhard (2003) and Corradini (1998).

Fig. 32 below visualizes qualitatively these relations in a map with the position in the boiling tube in axial direction as abscissa and the heat flux density as ordinate. At low heat flux density, the regions “A”, “E” and “F” – as defined in Fig. 31 – might be dominant while at higher heat flux densities especially the regions “B”, “C” and “D” are of importance.

The maximum or critical heat flux in tube boiling is determined by two independent mechanisms and thus both have to be taken into account. At low vapor qualities and in the sub-



cooled region a burnout mechanism similar to that observed for pool boiling is found; the heater surface is covered by a stable vapor blanket and there is a transition to a film-boiling mode (cf. Fig. 32). For high vapor qualities the so-called dryout mechanism, a transition to the liquid deficient region “G” (cf. Fig. 31 and Fig. 32) is the limit.

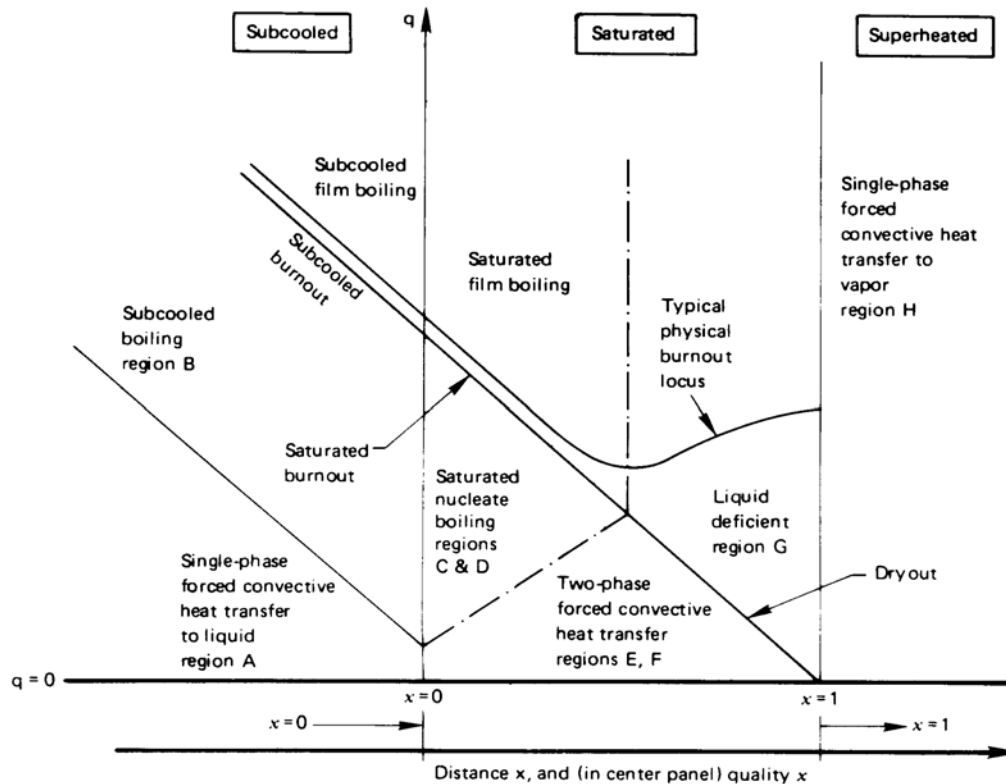


Fig. 32: The influence of heat flux on two-phase flow behavior. Cited from Lienhard & Lienhard (2003).

#### 4.5.2 Convective heat transfer in two-phase flows inside tubes

The convective heat transfer coefficient for two-phase flows  $\alpha_{2P}$  is mostly expressed as an enhancement of the liquid-only convection  $\alpha_{LO}$  by an enhancement factor  $F_{2P} = \alpha_{2P} / \alpha_{LO} = f(\dot{\chi}_{EQ})$  dependent on the local thermodynamic quality. It is based on a liquid-only heat transfer coefficient  $\alpha_{LO}$  calculated from  $Re_{LO}$  and  $Nu_{LO}$  according to the single-phase flow correlations given in 4.3 assuming that the total mass flow  $\dot{M} = \dot{M}_L + \dot{M}_V$  still was in saturated liquid state (i.e.  $\dot{\chi} = 0$ ) at local pressure. The enhancement factor is by convention calculated from the thermodynamic quality  $\dot{\chi}_{EQ}$  (rather than the actual vapor mass fraction  $\dot{\chi}$ ) and it is set to unity (i.e.  $\alpha_{2P} = \alpha_{LO}$ ) for all subcooled flows as well as for saturated flow at  $\dot{\chi}_{EQ} = 0$ . Numerous models – not to be repeated here – have been established in the past decades to calculate the enhancement factor  $F_{2P} = \alpha_{2P} / \alpha_{LO}$ ; an overview on this development is e.g. provided by Kandlikar (1990) or Steiner & Taborek (1992).

VDI-GVC (2002) suggest the quite sophisticated interpolation formula provided by Steiner & Taborek (1992) that has been experimentally proven for the full range of qualities

$0 < \dot{\chi}_{EQ} < 1$ . It is additionally based on a respective gas-only heat transfer coefficient  $\alpha_{GO}$  calculated from  $Re_{GO}$  and  $Nu_{GO}$  assuming that the total mass flow already was in saturated gaseous state ( $\dot{\chi} = 1$ ) at local pressure.

The enhancement factor then is calculated in dependence on  $\alpha_{LO}$ ,  $\alpha_{GO}$ ,  $\dot{\chi}_{EQ}$ , and the specific densities of liquid phase  $\rho'$  and vapor phase  $\rho''$  in saturation at local pressure:

$$F_{2P} = \alpha_{2P}/\alpha_{LO} = \left\{ (1-\dot{\chi}_{EQ})^{0.01} \cdot \left[ (1-\dot{\chi}_{EQ})^{1.5} + 1.9 \cdot \dot{\chi}_{EQ}^{0.6} \cdot (\rho'/\rho'')^{0.35} \right]^{-2.2} + \dot{\chi}_{EQ}^{0.01} \cdot \left[ \alpha_{GO}/\alpha_{LO} \cdot \left( 1 + 8 \cdot (1-\dot{\chi}_{EQ})^{0.7} \cdot (\rho'/\rho'')^{0.67} \right) \right]^{-2} \right\}^{-0.5} \quad (4.85)$$

The liquid-only and gas-only heat transfer coefficients  $\alpha_{LO}$  and  $\alpha_{GO}$  in this correlation (4.85) are assumed to be calculated using the respective equations (4.23), (4.25) or (4.28) provided by [VDI-GVC \(2002\)](#). For sufficiently low vapor qualities  $\dot{\chi}_{EQ} \leq 0.6$  which are commonly found in industrial applications like thermosiphon reboilers, [Steiner & Taborek \(1992\)](#) provide a more simple formulation:

$$F_{2P} = \alpha_{2P}/\alpha_{LO} = \left[ (1-\dot{\chi}_{EQ})^{1.5} + 1.9 \cdot \dot{\chi}_{EQ}^{0.6} \cdot (\rho'/\rho'')^{0.35} \right]^{1.1} \text{ for } \dot{\chi}_{EQ} \leq 0.6 \quad (4.86)$$

A similar formulation based on the quality  $\dot{\chi}_{EQ}$ , densities of liquid phase  $\rho'$  and vapor phase  $\rho''$ , and the Prandtl number of the liquid phase  $Pr'$  has been independently developed by [Liu & Winterton \(1991\)](#):

$$F_{2P} = \alpha_{2P}/\alpha_{LO} = \left[ 1 + \dot{\chi}_{EQ} \cdot Pr' \cdot (\rho'/\rho'' - 1) \right]^{0.35} \quad (4.87)$$

Another simple correlation was provided by [Kenning & Cooper \(1989\)](#) based on quality  $\dot{\chi}_{EQ}$ , densities of liquid phase  $\rho'$  and vapor phase  $\rho''$ , and dynamic viscosities of liquid phase  $\mu'$  and vapor phase  $\mu''$  (all properties taken in saturation at local pressure):

$$F_{2P} = \alpha_{2P}/\alpha_{LO} = 1 + 1.8 \cdot \left[ (\dot{\chi}_{EQ}/(1-\dot{\chi}_{EQ}))^{0.9} \cdot (\rho'/\rho'')^{0.5} \cdot (\mu'/\mu'')^{0.1} \right]^{0.87} \quad (4.88)$$

The expression inside the square brackets is known as the dimensionless Martinelli parameter, which is frequently used to characterize two-phase flows. It is however noted by [Kenning & Cooper \(1989\)](#) that this correlation (4.88) is mainly valid in the annular flow regime (cf. Fig. 31) and additional corrective terms might be required at small qualities  $\dot{\chi}_{EQ}$ . The latter correlations (4.87) and (4.88) both have been adjusted to experimental data by the respective authors using the Dittus-Boelter equation (4.31) for calculation of  $\alpha_{LO}$ .

Not surprisingly, all three correlations derived recently by a systematic regression of a high number of available experimental data deliver comparable results for common fluids and typical operating conditions. For boiling of water at atmospheric pressure, especially (4.86) by [Steiner & Taborek \(1992\)](#) and (4.87) by [Liu & Winterton \(1991\)](#) show reasonable agreement of  $\pm 30\%$  in the full range of  $\dot{\chi}_{EQ} = 0 \dots 0.15$ . Formulation (4.88) by

*Kenning & Cooper (1989)* is in good agreement with the previously mentioned correlations for small vapor qualities but produces significantly higher results than the others for  $\dot{\chi}_{EQ} > 0.07$ .

Things change, however, when these three correlations are applied to the boiling of aqueous lithium bromide solution showing a significantly higher Prandtl number than water. Strictly speaking, none of these formulations is defined in this case as the vapor phase is not saturated but superheated; therefore, properties of superheated vapor at saturation temperature and pressure of the salt solution have to be used. An evaluation of the correlations this way for 62wt.% lithium bromide solution boiling at atmospheric pressure reveals that now formulation (4.87) from *Liu & Winterton (1991)* with explicit dependency on the Prandtl number exceeds both other correlations by a factor of two at low vapor qualities. As all these correlations are based on data regression rather than on sound physical argumentations, results obtained for unusual fluids have generally to be taken with caution.

Altogether, for atmospheric boiling of water and vapor quality  $\dot{\chi}_{EQ} = 0.01$  enhancement factors of about 3 and for vapor quality  $\dot{\chi}_{EQ} = 0.1$  enhancement factors from 7 to 12 are obtained from the different formulations. For 62wt.% lithium bromide solution at atmospheric pressure and vapor quality  $\dot{\chi}_{EQ} = 0.01$  enhancement factors scatter between 3 and 7; for vapor quality  $\dot{\chi}_{EQ} = 0.1$  enhancement factors from 11 to 17 are obtained.

### 4.5.3 Onset of nucleate boiling in saturated and subcooled liquids

Due to capillary forces there is a significant overpressure inside microscopic gas bubbles in liquids  $\Delta p = p_{GAS} - p_{LIQUID} = \frac{2\sigma}{r_{BUB}}$  proportional to the surface tension of the liquid  $\sigma$  and inversely proportional to the bubble radius  $r_{BUB}$ . Therefore vapor bubbles will only grow if the surrounding liquid layer is superheated having at least a temperature  $T_{LIQUID} \geq T_{SAT}(p_{LIQUID} + \Delta p) > T_{SAT}(p_{LIQUID})$ .

As infinite local superheat would be required to create bubbles with zero diameters in the liquid bulk, bubble nucleation starts in microscopic cavities or crevices in the heating surface initially filled with gas. The availability of such nucleation sites is dependent on the surface roughness, i.e. the availability of crevices of a certain size, and the wetting behavior of the chosen wall-liquid combination. The worse the wetting the larger are the crevices that are not filled with liquid and thus can act as nucleation sites. As a simplification, it can be assumed that bubbles of a radius  $r_{BUB}$  are initially present in cavities of a radius  $r \approx r_{BUB}$  and that these bubbles can grow if the liquid temperature in a distance  $r_{BUB}$  from the heated surface is at least  $T_{LIQUID}(r_{BUB}) \geq T_{SAT}(p_{LIQUID} + \frac{2\sigma}{r_{BUB}})$ . A visualization of this criterion provided by *Kamil et al. (2005)* is shown in Fig. 33 below.

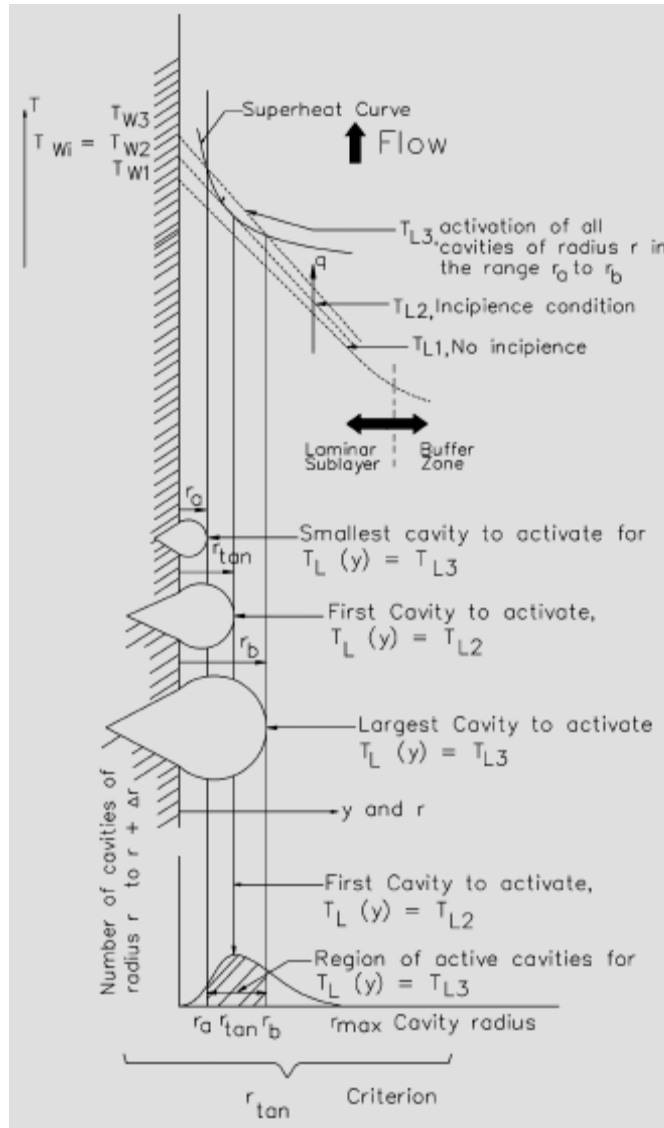


Fig. 33: Schematic visualization of incipience condition for onset of nucleate boiling assuming upward flow next to a heated surface. Cited from Kamil et al. (2005).

Employing the Clausius-Clapeyron equation (2.7) and the ideal gas law for estimating the saturation temperature inside the bubble finally reveals that a vapor bubble can grow if the surrounding liquid is at temperature  $T_{LIQUID} = T_{SAT}(\rho_{LIQUID}) + 2\sigma T_{SAT} \cdot (v' - v'') / r_{BUB} \Delta h_{VAP}$ , where  $v'$  and  $v''$  are the specific volumes of liquid and gas phase. To keep this excess temperature at a position with distance  $r_{BUB}$  to the heating surface in a liquid with thermal conductivity  $\lambda'$ , a minimum heat flux  $\dot{q}_{ONB}$  is required. Finally the required wall superheat for the onset of nucleate boiling in dependence of the initial bubble radius  $r_{BUB}$  is:

$$\Delta T_{SAT,ONB} = (T_W - T_{SAT})_{ONB} = \dot{q}_{ONB} \cdot r_{BUB} / \lambda' + 2\sigma T_{SAT} \cdot (v'' - v') / r_{BUB} \Delta h_{VAP} \quad (4.89)$$

The first term  $\dot{q}_{ONB} \cdot r_{BUB} / \lambda'$  is especially important for the calculation of the required wall superheat if the liquid in the bulk is still subcooled and therefore a significant heat flux density will take place even at small, zero or negative wall superheat. For saturated liquids, this first term is just small correction that may be disregarded. The wall superheat will find a minimum

(denoted ' $T_{W2}$ ' in Fig. 33) if initially bubbles of a critical radius  $r_{BUB} = r_{CRIT}$  (denoted ' $r_{TAN}$ ' in Fig. 33) can be formed:

$$r_{CRIT} = \left[ 2 \lambda' \sigma T_{SAT} \cdot (v'' - v') / \Delta h_{VAP} \dot{q}_{ONB} \right]^{1/2} \quad (4.90)$$

In this case, the minimum required wall superheat for nucleate boiling is only dependent on the heat flux density  $\dot{q}_{ONB}$ :

$$\Delta T_{SAT,ONB} = 2 \cdot \left[ 2 \sigma T_{SAT} \dot{q}_{ONB} \cdot (v'' - v') / \lambda' \Delta h_{VAP} \right]^{1/2} \quad (4.91)$$

For fluid flow inside tubes, wall superheat  $\Delta T_{SAT,ONB}$  and heat flux  $\dot{q}_{ONB}$  required for initiation of nucleate boiling are estimated by intersecting (4.89) or (4.91) with the equation for convective heat transfer in the liquid flow  $\dot{q}_{ONB} = \alpha_{CV} \cdot (T_W - \bar{T}_L)$ . Here  $\alpha_{CV}$  is the convective heat transfer coefficient for liquid flow inside tubes according to 4.3.2 and  $\bar{T}_L$  is the average liquid bulk temperature at this position in case of subcooled flows; for saturated flows, it is equal to the local saturation temperature  $\bar{T}_L = T_{SAT}$ .

Correlation (4.91) is especially applicable for liquids like water that generally show a bad wetting of solid surfaces. Then even gas bubbles with a radius greater than the critical radius  $r_{BUB} > r_{CRIT}$  might be available and the critical radius determined by (4.90) is the limit for the onset of nucleate boiling. [VDI-GVC \(2002\)](#) suggests application of equation (4.91) for subcooled flows "if nucleation sites of a radius  $r_{CRIT}$  according to (4.90) can be expected". For subcooled water flow inside tubes at pressures of 1 bar and above [VDI-GVC \(2002\)](#) also provide another empirical correlation that reasonably reproduces values obtained from (4.91). This confirms the practical relevance of this approach for the boiling of water and indicates the applicability of (4.91) for aqueous salt solutions – like e.g. lithium bromide solution – showing a higher surface tension and thus an even worse wetting behavior than water.

For saturated flows on the other hand [VDI-GVC \(2002\)](#) – following the argumentation of [Steiner & Taborek \(1992\)](#) – generally suggest another correlation, which is basically consistent with (4.89) in combination with the assumption of a quite small critical radius of only  $r_{CRIT} = 0.3 \mu m$ .

[Lienhard & Lienhard \(2003\)](#) finally suggest a correlation consistent with (4.91) for estimating the incipience of nucleate boiling for both saturated and subcooled flows. According to [Collier \(1981\)](#), on smooth metallic surfaces active nucleation sites up to  $0.5 \mu m$  can be found in case of organic fluids and refrigerants, and sites up to  $5 \mu m$  can be found for water. Even greater nucleation sites might be found e.g. on surfaces with deposits of corrosion products.

According to *VDI-GVC (2002)*, a mean surface roughness of  $5 \mu\text{m}$  can be expected for steel tubes covered by a magnetite (black iron oxide  $\text{Fe}_3\text{O}_4$ ) layer.

Therefore, it has to be stated that these correlations have to be used with some caution as contradictory information can be found in literature. Of course, the very strict assumption  $r_{\text{CRIT}} = 0.3 \mu\text{m}$  will lead to a safe design as that small nucleation sites will always be available.

Recent research showed that the wetting behavior of the chosen wall-liquid combination – expressed by the contact angle<sup>44</sup> – might have more influence on the onset of nucleate boiling than the actual surface roughness. Based on own measurements and literature data *Basu et al. (2002)* suppose a reduction factor as a function of the contact angle for the critical bubble radius obtained from the minimum superheat criterion (4.90). Their reduction factor is unity for contact angles  $\geq 90^\circ$  (bad wetting) and approaches zero for small contact angles (perfect wetting). This is compliant with the observation that equations (4.90) and (4.91) work fine for water (typical contact angles  $\approx 90^\circ$ ) while much smaller nucleation sites have to be assumed for organic refrigerants (contact angles  $10^\circ \dots 40^\circ$ ). The formulation of *Basu et al. (2002)*, however, has only been proven for atmospheric and higher pressures and for contact angles  $\leq 85^\circ$ . Therefore, their reduction factor applied on (4.90) is not necessarily the decisive limit for the initial bubble radius in the subatmospheric boiling of salt solutions, too.

#### 4.5.4 Nucleate pool boiling of saturated liquids

##### Heat transfer in nucleate boiling regime

Heat transfer in nucleate boiling regime is firstly dependent on the operating conditions namely pressure and heat flux density, secondly on the physical properties of the boiling fluid and thirdly on the properties of the heating surface namely roughness and thermal conductivity. It is well known that the heat transfer coefficient  $\alpha_B = \dot{q} / \Delta T_{\text{SAT}}$  shows an exponential dependency on the heat flux density  $\alpha_B \sim \dot{q}^N$  for a given experimental setup. According to *Lienhard & Lienhard (2003)*, the exponent  $N$  in this relation is dependent on the nucleation-site density function of the heater surface and therefore not easily predictable. For typically machined technical surfaces, however, experimentally found values scatter around  $N \approx 0.7$ . Therefore, in the nucleate boiling regime the surface heat flux rises sharply with increasing temperature difference  $\dot{q} \sim \Delta T_{\text{SAT}}^{3 \dots 4}$  while the wall superheat is only weakly dependent on the heat flux:

$$\Delta T_{\text{SAT}} \sim \dot{q}^{.1/4 \dots 1/3} \quad (4.92)$$

<sup>44</sup> The contact angle of a solid and a liquid surface is dependant on the specific surface energies of the solid wall and the solid-liquid interface as well as of the surface tension of the liquid. Liquids with a high surface tension (e.g. water) typically also show greater contact angles than liquids of low surface tension (e.g. organic fluids).

Although elaborate correlations for the dependence of boiling heat transfer coefficient on fluid properties are available, for common pure substances like e.g. water it is more convenient and yet more accurate to use semi-empirical correlations based on measured heat transfer values at reference conditions. Tabulated data for a great number of pure substances are e.g. provided by *VDI-GVC (2002)*.

The normalized heat transfer coefficient  $\alpha_B/\alpha_{B,0}$  in dependence on the normalized roughness  $R_A/R_{A,0}$ , the normalized thermal effusivity  $b/b_0$  the reduced pressure<sup>45</sup>  $p^* = p/p_c$ , and the normalized heat flux density  $\dot{q}/\dot{q}_0$  is according to *VDI-GVC (2002)* given by:

$$\alpha_B/\alpha_{B,0} = (R_A/R_{A,0})^{0.133} \cdot (b/b_0)^{0.5} \cdot F(p^*) \cdot (\dot{q}/\dot{q}_0)^{N(p^*)} \quad (4.93)$$

In this correlation,  $R_A$  is the arithmetic average roughness of the heating surface according to ISO 4287/1 and  $b = (\lambda_W \cdot \rho_W \cdot c_W)^{1/2}$  is the thermal effusivity of the wall given by the square root of the product of thermal conductivity  $\lambda_W$  and thermal mass  $\rho_W \cdot c_W$ . Finally,  $\dot{q}$  is the heat flux density in the nucleate boiling regime  $\dot{q}_{ONB} < \dot{q} < \dot{q}_{CRIT}$ . Normalization values are the experimentally determined heat transfer coefficient  $\alpha_{B,0}(R_{A,0}, b_0, p_0^*, \dot{q}_0)$  and the respective reference conditions  $R_{A,0}, b_0, p_0^*$ , and  $\dot{q}_0$  (see Tab. 10). The factor  $F(p^*)$  and the exponent  $N(p^*)$  both are functions in dependence on the class of boiling substance and the reduced pressure  $p^* = p/p_c$ . *VDI-GVC (2002)* provide different empirical correlations for organic fluids, namely fluorocarbons, cryogenic fluids, and water. Aqueous salt solutions are not explicitly covered, although it could be argued that the correlations found for water should also be applicable to some extent for aqueous salt solutions<sup>46</sup>.

For water the factor  $F(p^*)$  and the exponent  $N(p^*)$  in dependence of the reduced pressure  $p^*$  are:

$$F(p^*) = 1.73 \cdot p^{*0.27} + (6.1 + 0.68/1-p^{*2}) \cdot p^{*2} \quad (4.94)$$

$$N(p^*) = 0.9 - 0.3 \cdot p^{*0.15} \quad (4.95)$$

Normalization values for (4.93) have been chosen with respect to more or less typical operating conditions for technical boiling processes and typically machined copper tubes as heater. A compilation of all normalization values for nucleate boiling of water is provided by Tab. 10:

<sup>45</sup> i.e. the quotient of the boiling pressure  $p$  and the pressure at the critical point of the boiling substance  $p_c$

<sup>46</sup> At least with respect to properties like polarity, surface tension, density, and specific heat of evaporation aqueous solutions of salts like lithium bromide show even higher values than pure water, and this is an explicit difference in behavior to most organic fluids. Therefore, correlations found for water are expected to be better applicable for salt solutions than those found for organic fluids are.



| Normalization values for pool boiling         |                    |   |        |
|---|--------------------|---|--------|
| reduced pressure                              | $p_0^* = p/p_c$    | [-]                                     | 0.1    |
| heat flux density                             | $\dot{q}_0$        | [kW/m <sup>2</sup> ]                    | 20     |
| arithmetic mean surface roughness             | $R_{A,0}$          | [μm]                                    | 0.4    |
| wall thermal effusivity (copper)              | $b_0$              | [kW s <sup>1/2</sup> /m <sup>2</sup> K] | 35.35  |
| boiling of water at normalization conditions: |                    |   |        |
| pressure at critical point                    | $p_{c,H2O}$        | [bar]                                   | 220.64 |
| boiling heat transfer coefficient             | $\alpha_{B,0,H2O}$ | [kW/m <sup>2</sup> K]                   | 5.6    |

**Tab. 10:** Normalization values for saturated pool boiling correlation with respect to more or less typical operating conditions for technical boiling processes and typically machined copper tubes as heater.

For flue gas heated water boilers as well as for flue gas fired regenerators of absorption chillers the heating surface typically is a tube wall made of steel and covered by a magnetite layer (black iron oxide  $Fe_3O_4$ ). Typical values of surface roughness and thermal effusivity for this kind of walls according to [VDI-GVC \(2002\)](#) are listed in Tab. 11:

| Properties of steel tubes in water boilers |       |   |      |
|--|-------|---|------|
| surface roughness (magnetite layer)        | $R_A$ | [μm]                                    | 5    |
| thermal effusivity (carbon steel St 35.8)  | $b_0$ | [kW s <sup>1/2</sup> /m <sup>2</sup> K] | 13.4 |
| thermal effusivity (stainless steel)       | $b_0$ | [kW s <sup>1/2</sup> /m <sup>2</sup> K] | 7.73 |

**Tab. 11:** Surface roughness and thermal effusivity of steel tubes in water boilers.

The calculation method summarized above is also called Gorenflo method after the author of the respective chapter in [VDI-GVC \(2002\)](#).

Another important semi-empirical correlation is the frequently cited and easy-to-use formulation of [Cooper \(1984\)](#). The nucleate boiling heat transfer coefficient  $\alpha_B$  is calculated in dependence on the heat flux  $\dot{q}$ , the reduced pressure  $p^*$ , the surface roughness  $R_p$ , the molar mass of the fluid  $M$ , and a heater-dependent constant  $C_H$  being 1.7 for copper tubes and unity for all other heaters:

$$\alpha_B = C_H \cdot 55 \text{ W/m}^2\text{K} \cdot \left(\frac{M}{\text{g}\cdot\text{mol}^{-1}}\right)^{-0.5} \cdot p^{*0.12-0.2\cdot\log_{10}(R_p/1\mu\text{m})} \cdot \left(-\log_{10}(p^*)\right)^{-0.55} \cdot \left(\frac{\dot{q}}{\text{W}\cdot\text{m}^{-2}}\right)^{0.67} \quad (4.96)$$

For unknown surfaces, a roughness of  $R_p = 1\mu\text{m}$  is assumed which further simplifies the correlation as the logarithm in the exponent becomes zero.

Actually, formulation (4.96) of [Cooper \(1984\)](#) is not far away from the more sophisticated Gorenflo formulation (4.93) published in [VDI-GVC \(2002\)](#). The heater factor  $C_H = 1.7$  for copper tubes in (4.96) mainly reflects the difference between copper and steel heaters



introduced by the factor  $(b/b_0)^{0.25}$  in (4.93)<sup>47</sup>. The base constant  $55 \text{ W/m}^2\text{K}$  in (4.96) is adjusted to experimental data with special respect to the boiling of water. The single dependency on the molar mass of the fluid  $M$  has been chosen by [Cooper \(1984\)](#) to simplify the usage of his formulation; he argues that for many typical fluids several properties being relevant for the boiling heat transfer are linked in a characteristic way with the molar mass. Therefore, this molar mass dependency is equivalent but yet easier to evaluate than more sophisticated functions of various liquid and vapor properties that could be derived from physical modeling.

A significant discrepancy between both formulations, however, is the way the influence of the surface roughness is handled. In apparent contradiction to [VDI-GVC \(2002\)](#), [Cooper \(1984\)](#) refers to literature data suggesting a significantly increasing impact of the surface roughness on the heat transfer coefficient at low reduced pressures. Therefore, heat transfer coefficients predicted from (4.96) for rough surfaces and small reduced pressures significantly exceed values obtained from (4.93). Although it has to be stated that the correlation (4.96) of [Cooper \(1984\)](#) generally predicts higher values for the boiling heat transfer coefficient of water than the later and more sophisticated Gorenflo formulation (4.93) in [VDI-GVC \(2002\)](#).

Recently, [Estiot et al. \(2005\)](#) performed a literature survey on comparative studies on the atmospheric and subatmospheric boiling of aqueous lithium bromide solutions and pure water. They also conducted their own measurements of the nucleate boiling heat transfer coefficient of water under various subatmospheric pressures. They compared their own findings with the boiling heat transfer coefficients reported by [Minchenko & Firsova \(1969\)](#), [Charters et al. \(1982\)](#), [Kamoshida & Isshiki \(1994\)](#), [Varma et al. \(1994\)](#), [Furukawa et al. \(1995\)](#), [Wu et al. \(1998\)](#) and with the theoretical predictions from correlation (4.96) of [Cooper \(1984\)](#) and (4.93) of [VDI-GVC \(2002\)](#). As the original data had been obtained for different heater surfaces and for different ranges in pressure and heat flux, the data from each study were fitted with expressions of the type<sup>48</sup>  $\alpha_B = C_H \cdot \text{const.} \cdot p^{*EXP} \cdot (\dot{q}/\text{W}\cdot\text{m}^{-2})^N$  assuming the same material dependent heater constants  $C_H$  as given by [Cooper \(1984\)](#). The resulting regression functions were normalized to a copper heater surface and compared at a mean<sup>49</sup> heat flux density of  $50 \text{ kW/m}^2$ .

<sup>47</sup> In the latter case, factors of 2.1 for copper relative to stainless steel and of 1.6 for copper relative to carbon steel are obtained using the property data provided in Tab. 10 and Tab. 11.

<sup>48</sup> At low pressures, this type of equation is basically compliant with the correlation (4.96) of [Cooper \(1984\)](#) as the additional factor  $(-\log_{10}(p^*))^{-0.55}$  in (4.96) mainly contributes at high pressures  $p^* = 0.1 \dots 1$ .

<sup>49</sup> With respect to all available data in these five studies.

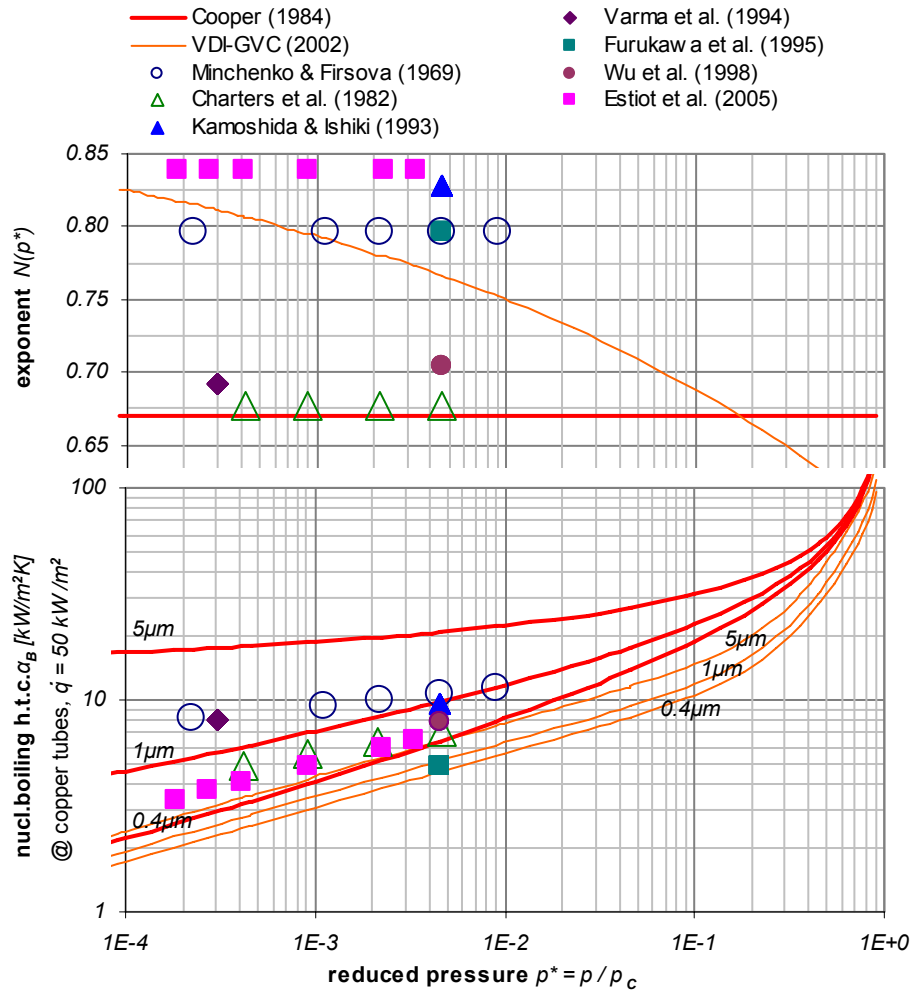


**Fig. 34: Nucleate boiling heat transfer coefficients  $\alpha_B$  and exponents  $N$  for water.**

Comparison of the correlations provided by *Cooper (1984)* and *VDI-GVC (2002)* with fits of experimental data of several authors in dependence on the reduced pressure. Singular points are marked for experimental data sets comprising only measurements at a single boiling pressure. Diagram based on data from *Estiot et al. (2005)*.

The exponents  $N$  obtained from the different data sets and theoretical correlations and the variation of the boiling heat transfer coefficient  $\alpha_B$  over the reduced pressure  $p^*$  are shown in Fig. 34 above.

It shows that the exponents  $N$  obtained by fitting these sets of experimental data scatter between 0.65 and 0.85 and give little evidence for preference of either of the correlations of *Cooper (1984)* and *VDI-GVC (2002)*. The experimentally determined heat transfer coefficients however always exceed the predictions according to (4.93) from *VDI-GVC (2002)* and show significantly better accordance<sup>50</sup> with (4.96) of *Cooper (1984)*. No conclusions concerning the dependence of the heat transfer coefficient on the roughness of the heater surface

<sup>50</sup> This preference for the Cooper correlation would be even emphasized if all boiling heat transfer coefficients were normalized to a stainless steel heater surface before comparison. Also the alternative comparison of heat transfer coefficients at a heat flux of  $20 \text{ kW/m}^2$  – as used as a reference condition by *VDI-GVC (2002)* – leads to an even stronger preference for the correlation of *Cooper (1984)*.

can be drawn from these experimental data as all authors characterized their heaters as “clean” or “polished” without providing any numerical roughness parameters. Finally, these experimental data suggest an even weaker dependency of the heat transfer coefficient on the reduced pressure than it is assumed by both correlations (4.93) and (4.96).

Of course this selective comparison with only seven sources of experimental data, *Minchenko & Firsova (1969)*, *Charters et al. (1982)*, *Kamoshida & Isshiki (1994)*, *Varma et al. (1994)*, *Furukawa et al. (1995)*, *Wu et al. (1998)*, *Estiot et al. (2005)*, gives no final evidence to either prove or disprove any of the correlations (4.93) and (4.96). Besides, some of these sources provide little information on the accuracy of measuring. Although it can be speculated that the correlation from *VDI-GVC (2002)* – being an almost authoritative reference guide for design of thermal systems – intentionally underpredicts boiling heat transfer coefficients in some cases, mainly heading for intrinsically safe designs rather than for the best accordance with all experimental data.

### Critical heat flux density

For saturated and slightly subcooled liquids, the critical heat flux density  $\dot{q}_{CRIT}$  for the departure from nucleate boiling is according to *VDI-GVC (2002)*:

$$\dot{q}_{CRIT} = 0.13 \cdot \Delta h_{VAP} \cdot (\rho'')^{1/2} \cdot [\sigma \cdot (\rho' - \rho'') \cdot g]^{1/4} \quad (4.97)$$

It is dependent on the specific heat of evaporation  $\Delta h_{VAP}$ , densities of liquid phase  $\rho'$  and of vapor phase  $\rho''$ , surface tension  $\sigma$  and gravity  $g$ : For pool boiling of subcooled liquids, the critical heat flux increases nearly linear with the subcooling. Thus (4.97) also provides a save estimation for the allowed heat flux density in subcooled state.

For the boiling of water at atmospheric pressure from (4.97) a critical heat flux of about  $1 \text{ MW/m}^2$  is obtained. From the properties of aqueous lithium bromide solutions boiling at the same pressure and the density of the respective superheated water vapor an even higher heat flux is calculated. As (4.97) has not explicitly been proven for aqueous salt solutions, however, the significance of this increase in the critical heat flux predicted by (4.97) might be questioned and thus disregarded to obtain a safe design.

### Effect of enhanced heater surfaces or heating by tube bundles

If the boiling liquid is heated by a tube bundle with several layers of heating tubes in vertical direction, the agitation of the liquid by the rising bubbles will induce an additional convective heat transfer. Thus, the total boiling heat transfer coefficient in tube bundles may be two or three times higher than calculated for a singular heater. The application of finned heater surfaces will also lead to an increased heat transfer coefficient due to convection along the fins. Especially for organic fluids showing good wetting behavior and thus a lack of nucleation

sites, the application of finned or appropriately machined surfaces can also lead to a significant increase in heat transfer. In any case, however, the pool boiling correlations presented above estimate a reliable lower limit for the heat transfer coefficient that will always result in a safe design.

#### 4.5.5 Nucleate boiling in upward tube flow

Based on the evaluation of experimental data on nucleate boiling dominated heat transfer in upward flow of water in tubes from own measurements and from literature, *Cooper (1989)* concluded that the pool boiling correlation (4.96) suggested in *Cooper (1984)* acts also as a sound estimation for nucleate boiling heat transfer in tubular flow. Due to the absence of systematic data on the variation of the surface roughness and due to the significant scatter of all available experimental data, *Cooper (1989)* suggests to evaluate (4.96) for unknown surface finish (i.e.  $R_p = 1\mu m$ ) and to introduce an additional reduction factor of 0.7 for a conservative prediction.

It is however noted by *Cooper (1989)* that the heat transfer coefficient for flow boiling is actually dependent on the surface finish, too. It is also reported by *Kenning & Cooper (1989)* that the nucleate boiling heat transfer coefficient in tubular flow increased after the inside of the tube was treated with fine emery paper although the measured surface roughness was decreased by this measure. By *Steiner & Taborek (1992)* it is stated that with surface roughness between 0.1 and  $5\mu m$  similar dependencies for flow boiling as for pool boiling have been found, although only incomplete data on this subject are available.

*VDI-GVC (2002)* suggest a more sophisticated semi-empirical correlation described in detail by *Steiner & Taborek (1992)* for the calculation of nucleate flow boiling heat transfer. It is based on the Gorenflo correlation (4.93) for pool boiling with an additional factor for the dependency on the tube diameter. A different pressure dependency function and a fluid property dependent corrective factor are however introduced; also, different normalization conditions are employed. Finally, the normalized heat transfer coefficient  $\alpha_B/\alpha_{B,0}$  is given in dependence on a fluid property constant  $C_F$ , the normalized roughness  $R_A/R_{A,0}$ , the normalized inner diameter  $d_I/d_{I,0}$ , the reduced pressure<sup>51</sup>  $p^* = p/p_c$ , the normalized heat flux density  $\dot{q}/\dot{q}_0$  and an exponent dependent on the reduced pressure  $N(p^*)$ :

$$\alpha_B/\alpha_{B,0} = C_F \cdot (R_A/R_{A,0})^{0.133} \cdot (d_I/d_{I,0})^{-0.4} \cdot [2.816 \cdot p^{*0.45} + (3.4 + 1.7/1 - p^{*7}) \cdot p^{*3.7}] \cdot (\dot{q}/\dot{q}_0)^{N(p^*)} \quad (4.98)$$

<sup>51</sup> i.e. the quotient of the boiling pressure  $p$  and the pressure at the critical point  $p_c$  of the boiling substance

In correlation (4.98), again  $R_A$  is the arithmetic average roughness of the heating surface according to ISO 4287/1. For all non-cryogenic liquids the exponent  $N(p^*)$  in dependence of the reduced pressure  $p^*$  is:

$$N(p^*) = 0.8 - 0.1 \cdot 10^{(0.76 \cdot P^*)} \quad (4.99)$$

The fluid property constant  $C_F$  is weakly dependent on the molar mass, for common fluids like water, tabulated values are available, otherwise an approximation formula is provided by [VDI-GVC \(2002\)](#). The normalization value of the heat transfer coefficient  $\alpha_{B,0}$ , is the pool boiling heat transfer coefficient according to (4.93) at the heat flux density  $\dot{q}_0$  and the roughness  $R_{A,0}$ ; for common fluids like water, again tabulated values are available. Normalization values for tube-boiling correlation (4.98) as provided in Tab. 12 below are, however, different to those given in Tab. 10 above for pool-boiling correlation (4.93). The reason is that correlations are normalized to different values of roughness  $R_{A,0}$  and heat flux density  $\dot{q}_0$ .

| Normalization values for nucleate boiling in vertical tubes |                     |                       |             |
|---|---------------------|-----------------------|-------------|
| reduced pressure  | $p_0^* = p/p_c$     | [-]                   | 0.1         |
| arithmetic mean surface roughness                           | $R_{A,0}$           | [ $\mu\text{m}$ ]     | 1.0         |
| tube inner diameter   | $d_{i,0}$           | [mm]                  | 10          |
| <b>boiling of water at normalization conditions:</b>        |                     |                       |             |
| normal heat flux density                                    | $\dot{q}_{0,H_2O}$  | [kW/m <sup>2</sup> ]  | 150         |
| pressure at critical point                                  | $p_{c,H_2O}$        | [bar]                 | 220.64      |
| fluid property constant                                     | $C_{F,H_2O}$        | [-]                   | 0.75 ± 0.26 |
| boiling heat transfer coefficient                           | $\alpha_{B,0,H_2O}$ | [kW/m <sup>2</sup> K] | 25.58       |

Tab. 12: Normalization values for nucleate boiling in vertical tubes.

Remarkably, at normalization conditions (cf. Tab. 12) the reduction factor  $C_{F,H_2O} = 0.75$  for the boiling heat transfer coefficient of water in tubes relative to pool boiling according to [Steiner & Taborek \(1992\)](#) is quite close to the reduction factor of about 0.7 suggested by [Cooper \(1989\)](#). In absolute numbers, however, the flow boiling correlation (4.98) of [Steiner & Taborek \(1992\)](#) predicts significantly lower heat transfer coefficients for the boiling of water at atmospheric and subatmospheric pressures than the suggestion of [Cooper \(1989\)](#).

A comparison of calculated heat transfer coefficients in dependence on the reduced pressure assuming tube inner diameter  $d_i = 10\text{mm}$  and heat flux  $\dot{q} = 150\text{ kW/m}^2$  in accordance with the normalization conditions of [Steiner & Taborek \(1992\)](#) listed in Tab. 12 is shown in Fig. 35.

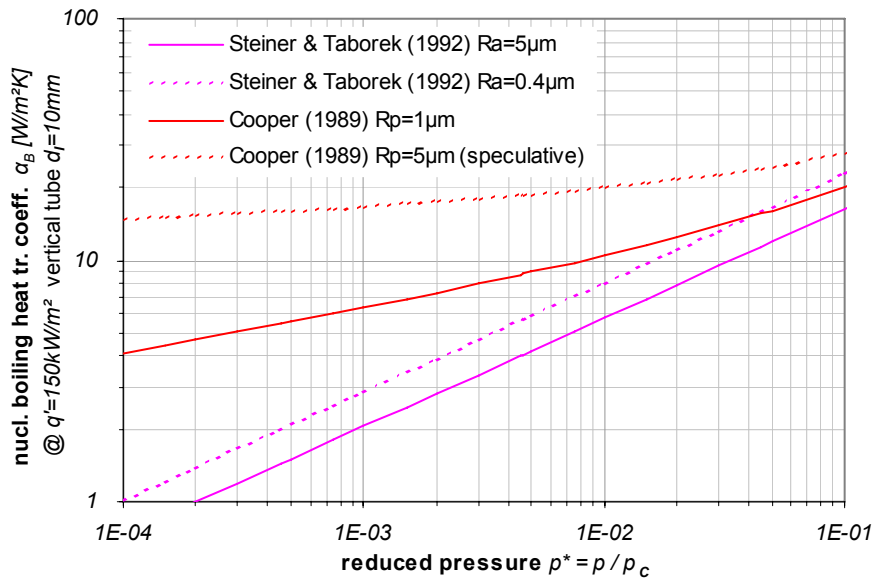


**Fig. 35: Boiling heat transfer coefficients  $\alpha_B$  for water in vertical tubes as predicted by the correlations of Cooper (1989) and Steiner & Taborek (1992) in dependence of the reduced pressure.**

Comparison shown for tube inner diameter  $d_i = 10\text{mm}$  and heat flux  $\dot{q} = 150\text{ kW/m}^2$  in accordance with the normalization conditions of Steiner & Taborek (1992) as listed in Tab. 12. Values obtained for surface roughness  $R_p = 5\mu\text{m}$  from correlation according to Cooper (1984) and Cooper (1989) are somewhat speculative however as application of the Cooper correlation to flow boiling has not explicitly been proven for roughness other than  $R_p = 1\mu\text{m}$ .

The difference between both correlations is strengthened at subatmospheric pressures and at increased surface roughness. The latter case is however somewhat speculative as application of the Cooper correlation to flow boiling according to Cooper (1989) has not explicitly been proven for roughness other than  $R_p = 1\mu\text{m}$ . Presently there is little evidence which of these proven semi-empirical correlations might be best applicable for the boiling of water and similar fluids at subatmospheric pressures and rough heater surfaces like steel covered with a magnetite layer. Even Steiner & Taborek (1992) who based their correlation on a remarkably comprehensive data bank containing over 13,000 data points do not quote a single source of experimental values that would meet all of these criteria at once.

#### 4.5.6 Calculation of overall heat transfer in flow boiling

If the wall superheat is sufficiently high for the onset of nucleate boiling (4.89) both mechanisms convection and nucleate boiling will contribute to the total flow boiling heat transfer coefficient  $\alpha_{FB}$ . It is generally accepted that these mechanisms are not simply additive and the resulting heat transfer coefficient is less than the arithmetic sum of both contributions  $\alpha_{FB} < \alpha_{CV} + \alpha_B$ . The actual nature of the interaction of both heat transfer mechanisms, however, has not been satisfactorily explained so far and remains subject to emotional public discussions amongst scholars; cf. e.g. the series of arguments and counter-arguments by Webb (2003a), Thome (2003), and Webb (2003b).

For saturated fluids where the same driving temperature difference  $\Delta T_{SAT}$  is valid for both mechanisms the overall flow boiling heat transfer coefficient  $\alpha_{FB}$  is mostly correlated in a purely empirical way:

$$\alpha_{FB} = \left( S_B \cdot \alpha_B^N + S_{CV} \cdot \alpha_{CV}^N \right)^{1/N} \quad (4.100)$$

Here  $N$  is an empirically determined exponent and  $S_B$  and  $S_{CV}$  are empirically determined functions to account for the suppression of the nucleate boiling by the convective flow or for the suppression of the convective heat transfer by the nucleate boiling process. In case of subcooled flow boiling the overall heat transfer coefficient is not well defined, however an analogous formulation for the heat flux can still be given.

The most simple approach on this way was outlined in a series of two articles by [Kenning & Cooper \(1989\)](#) and [Cooper \(1989\)](#). They stated that a great number of experimental flow boiling data for water is described well if no suppression or interaction mechanism is considered at all (i.e.  $S_B = S_{CV} = 1$ ) and just the larger of the two coefficients is taken (i.e.  $N = \infty$ ). Correlation (4.88) was suggested for calculation of the heat transfer coefficient in the convective regime and the Cooper pool boiling correlation (4.96) with an additional flow-independent reduction factor of 0.7 was suggested for calculations in the nucleate boiling regime. Formally this also could be interpreted as the choice of a constant suppression factor  $S_B = 0.7$  if the bare pool boiling correlation is taken as basis.

A more sophisticated and frequently cited general correlation for saturated and subcooled flow boiling was suggested by [Liu & Winterton \(1991\)](#); in saturated flows it is basically compliant with (4.100) using  $N=2$  and  $S_{CV}=1$ .

$$\dot{q}_{FB} = \left\{ \left[ S_B \cdot \alpha_{B,POOL} \cdot (T_{W,L} - T_{SAT}) \right]^2 + \left[ F_{2P} \cdot \alpha_{LO} \cdot (T_{W,L} - \bar{T}_L) \right]^2 \right\}^{1/2} \quad (4.101)$$

Here  $\alpha_{B,POOL}$  is the coefficient according to the Cooper pool boiling correlation (4.96),  $\alpha_{LO}$  is the liquid-only convective heat transfer coefficient calculated from the Dittus-Boelter equation (4.31),  $F_{2P} = \alpha_{2P} / \alpha_{LO}$  is the two-phase enhancement factor according to (4.87) in case of saturated flow or unity  $F_{2P} = 1$  for subcooled flow.  $\bar{T}_F$  is the local mean fluid temperature over the tube cross-section and by definition identical to the saturation temperature  $T_{SAT}$  in saturated flows. A flow-dependent suppression factor  $S_B$  is imposed on the nucleate boiling term:

$$S_B = \left( 1 + 0.055 \cdot F_{2P}^{0.1} \cdot Re_{LO}^{0.16} \right)^{-1} \quad (4.102)$$

A number of flow boiling models of similar form have been proposed by various authors, an overview is e.g. provided by [Kandlikar \(1990\)](#) or [Steiner & Taborek \(1992\)](#). Although such models have been successfully used to describe experimental boiling data, the assumption



of a suppression of the nucleate boiling rather than the convective heat transfer is completely arbitrary. This has been most explicitly demonstrated by *Wadekar (1993)* who set up an alternative semi-empirical model using arithmetic addition (i.e.  $N=1$ ), no flow-dependent suppression of the nucleate boiling term (i.e. constant value  $S_B = 0.7$  imposed on Cooper pool boiling correlation) and a boiling-dependent suppression of the convective heat transfer  $S_{CV} = f(\text{bubble parameters, mass flux, quality, pressure})$ . Although sound physical argumentation is provided by *Wadekar (1993)* to back his approach, it has gained little popularity, as the resulting formulations are less suitable for practical calculations.

Presently, the semi-empirical formulation based on the widest experimental data bank is the asymptotic model of *Steiner & Taborek (1992)* also suggested by *VDI-GVC (2002)* for saturated flow boiling. It employs no formal suppression factors at all (i.e.  $S_B = S_{CV} = 1$ ) and uses an exponent  $N=3$ . However, for calculation of the nucleate boiling heat transfer coefficient  $\alpha_B$  no general pool boiling correlation but an especially tailored tube-boiling correlation (4.98) is suggested that already includes a kind of constant or flow-independent suppression factor. Subcooled flow boiling is not explicitly discussed by *Steiner & Taborek (1992)* while another calculation method not directly based on *Steiner & Taborek (1992)* is suggested by *VDI-GVC (2002)* in this case.

As the greater exponent used by *Steiner & Taborek (1992)* and the additional suppression factor employed by *Liu & Winterton (1991)* partly compensate for each other, both models deliver similar results at typical operating conditions. The approach of *Steiner & Taborek (1992)* might generally be more promising as it is based on the wider experimental database and it does not introduce a suppression factor with little physical reason. On the other hand, the model of *Liu & Winterton (1991)* also explicitly covers subcooled flow boiling and allows for a direct calculation of the wall temperature in dependence of the heat flux, as there is an analytic solution of the equations.

### 4.5.7 Boiling of aqueous salt solutions

The semi-empirical correlations (pool boiling) and (4.98) (nucleate boiling in vertical tubes) provided by *VDI-GVC (2002)* extrapolate the nucleate boiling heat transfer coefficient for any pressure, heat flux density and geometric conditions from a single normalization value. Therefore, for each fluid the boiling heat transfer coefficient has to be determined – e.g. by experiment – at least at a single operational state prior to the application of these correlations. A list of suitable normalization data is provided by *VDI-GVC (2002)* for a number of common pure substances like e.g. water. For aqueous salt solutions like e.g. lithium bromide solution, however, no respective values are available.



For different pure substances, the boiling heat transfer coefficients at similar operating conditions are different due to differences in various property data (specific densities of liquid and vapor, surface tension, specific heat of evaporation, etc.), which are relevant in the process of nucleate boiling. *VDI-GVC (2002)* provide a quite complex semi-empirical correlation<sup>52</sup> – not cited here – that takes into account such dependencies and allows estimating the nucleate boiling heat transfer coefficient from a set of property data values. This correlation has been proven to reproduce experimentally determined heat transfer coefficients for a number of pure substances – mainly fluorocarbons and other organic fluids – with suitable accuracy.

For boiling of binary mixtures, additionally an attenuation of the heat transfer due to a depletion of the more volatile component in the liquid bulk next to a forming bubble has to be considered. This local shift in concentration results in a corresponding shift in saturation temperature that consumes some of the driving temperature difference. Therefore, a lower effective nucleate boiling heat transfer coefficient will be observed. *VDI-GVC (2002)* provide respective correlations – also not cited here – to calculate this attenuation for mixtures of volatile components, e.g. mixtures of organic refrigerants. For aqueous salt solutions with evanescent volatility of the salt fraction, however, the correlations provided by *VDI-GVC (2002)* are not applicable. Therefore, a calculation of the nucleate boiling heat transfer coefficient in lithium bromide solutions is not possible based on the *VDI-GVC (2002)* framework.

An applicable correlation<sup>53</sup> was provided by *Rant (1977)* estimating the boiling heat transfer coefficient  $\alpha_B$  of a fluid relative to the heat transfer coefficient  $\alpha_{B,H_2O}$  for the boiling of water at the same pressure  $p$  and heat flux density  $\dot{q}$  based on the respective ratios of seven fluid properties. This correlation had been proven by *Rant (1977)* for several aqueous solutions of inorganic salts and of sugar; it had explicitly been tested for lithium bromide solutions up to 40% salt content boiling at atmospheric pressure. The boiling heat transfer thus is a function of the specific densities of liquid  $\rho'$  and vapor  $\rho''$ , dynamic viscosity  $\mu'$ , thermal conductivity  $\lambda'$  and specific heat capacity  $c'$  in the liquid phase and surface tension  $\sigma$  and specific heat of evaporation  $\Delta h_{VAP}$  of the aqueous solution. Normalization values are the respective properties  $\rho'_{H_2O}$ ,  $\rho''_{H_2O}$ ,  $\mu'_{H_2O}$ ,  $\lambda'_{H_2O}$ ,  $c'_{H_2O}$ ,  $\sigma_{H_2O}$ ,  $\Delta h_{VAP,H_2O}$  of water at the same saturation pressure:

$$\alpha_B = \alpha_{B,H_2O} \cdot \frac{\rho'}{\rho'_{H_2O}} \cdot \left( \frac{\rho''}{\rho''_{H_2O}} \cdot \frac{\mu'}{\mu'_{H_2O}} \right)^{-0.25} \cdot \left( \frac{\lambda'}{\lambda'_{H_2O}} \cdot \frac{c'}{c'_{H_2O}} \right)^{0.5} \cdot \left( \frac{\sigma}{\sigma_{H_2O}} \cdot \frac{\Delta h_{VAP}}{\Delta h_{VAP,H_2O}} \right)^{-0.5} \quad (4.103)$$

<sup>52</sup> cf. Hab (11)-(12) in *VDI-GVC (2002)*

<sup>53</sup> cf. (5.17) in *Rant (1977)*

For lithium bromide solution with 60wt.% salt content, an attenuation of the nucleate boiling heat transfer coefficient of about 50% compared to pure water at the same saturation pressure is obtained from (4.103).

As already discussed in 4.5.4, a comprehensive literature survey on boiling heat transfer of aqueous lithium bromide solutions has recently been performed by *Estiot et al. (2005)*. They evaluated experimental data from *Minchenko & Firsova (1969)*, *Charters et al. (1982)*, *Lee et al. (1991)*, *Varma et al. (1994)*, *Kamoshida & Isshiki (1994)*, *Furukawa et al. (1995)*, *Wu et al. (1998)* and the theoretical correlation and experimental data from *Rant (1977)*. Except for *Lee et al. (1991)*, all above-mentioned authors measured boiling heat transfer coefficients for both, pure water and aqueous lithium bromide solution, in the same experimental setup. A comparison of attenuation factors  $(\alpha_{B,SOL}/\alpha_{B,H_2O})_{P,Q}$  for the boiling of lithium bromide derived from these experimental data and calculated from (4.103) after *Rant (1977)* has been given by *Estiot et al. (2005)*. An overview on experimental and theoretical attenuation factors  $(\alpha_{B,SOL}/\alpha_{B,H_2O})_{P,Q}$  obtained this way for boiling at atmospheric pressure (left diagram) and at low pressures of 67...137 mbar (right diagram) is provided in Fig. 36 below.

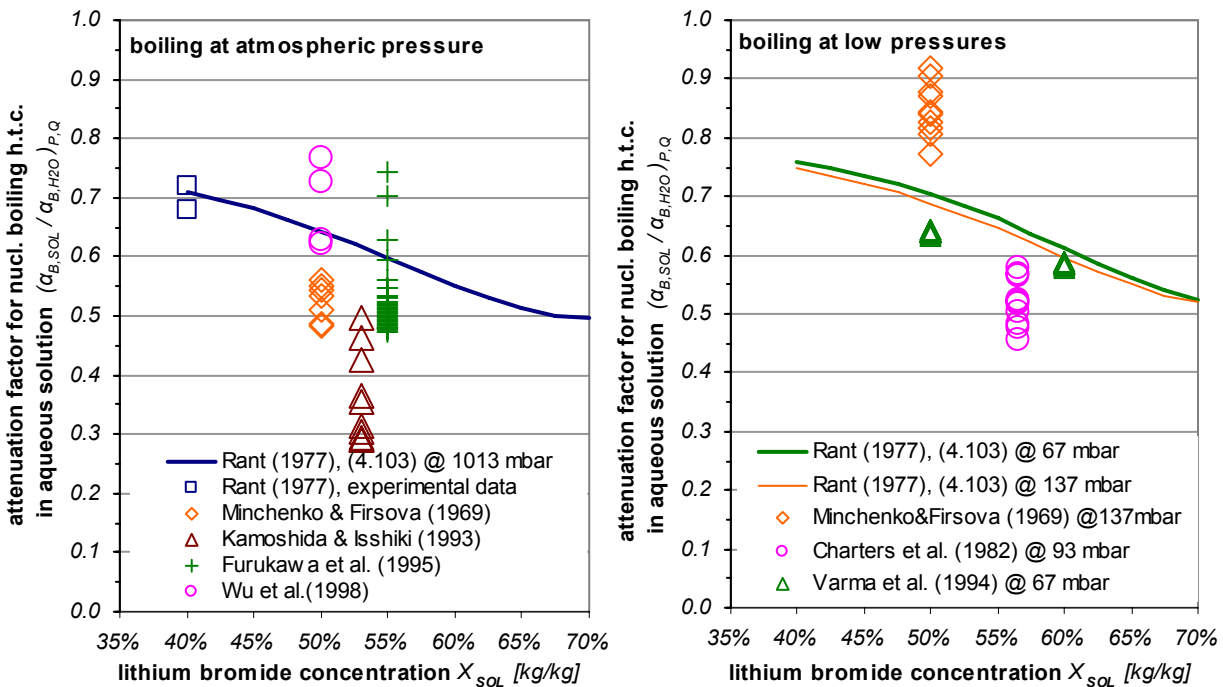


**Fig. 36: Relative nucleate boiling heat transfer coefficient of aqueous lithium bromide solution in relation to pure water at the same saturation pressure and heat flux density.**  
 Comparison of theoretical prediction from *Rant (1977)* and experimental findings of various authors. Diagrams based on data from *Estiot et al. (2005)*.

In both diagrams, solid lines denote the evaluation of (4.103) as function of the lithium bromide concentration  $X_{SOL}$  for different saturation pressures. Comparison of the thick blue line in the left diagram (1013 mbar) and the thin orange (137 mbar) and the thick green lines (67 mbar) in the right diagram exhibits an only weak pressure dependency of the correlation

after *Rant (1977)*. Individual symbols denote experimental values from various authors at different heat flux and solution concentration.

All data points in Fig. 36 are quotients of the boiling heat transfer coefficients of lithium bromide and of water that were determined by the same author in the same experimental configuration under similar experimental conditions – appropriate interpolations of the experimental data for water were employed where necessary. It shows that these experimental attenuation factors scatter significantly around the theoretical curves; values range from about 0.3 to 0.8 at atmospheric pressure and from about 0.4 to 0.9 at lower pressures. Basically, the distribution of the experimental data points in Fig. 36 backs up the prediction by (4.103) after *Rant (1977)* that the factor  $(\alpha_{B,SOL}/\alpha_{B,H2O})_{P,Q}$  should decrease with increasing salt concentration in the range 40...60wt.%. However, no significant evidence for a specific correlation between  $(\alpha_{B,SOL}/\alpha_{B,H2O})_{P,Q}$  and  $X_{SOL}$  can be obtained from the data; correlation (4.103) is neither proved nor disproved by the experimental data.

Finally, it has to be stated that presently no proven correlation for the boiling heat transfer coefficient of aqueous lithium bromide solutions at atmospheric and sub-atmospheric pressures is available. However, the attenuation factor (4.103) after *Rant (1977)* is basically compliant with experimental findings and incorporates the negative correlation of salt concentration and heat transfer coefficient that is generally expected to be found for a salt solution. Therefore, the attenuation factor (4.103) has been employed within this work as basis for all further calculations and evaluations of nucleate boiling heat transfer in lithium bromide solutions presented below.

## **4.6 Natural-convection boilers with vertical boiling tubes**

### **4.6.1 Common fields of application**

In the recent years increasing interest in tube boiler type regenerators of absorption chillers documents in numerous newly filed patent applications and granted patents – cf. e.g. *Kori et al. (1997)*, *Kouri et al. (1998)*, *Inoue et al. (1999)*, *Kubota et al. (1999)*, *Nakamura et al. (2000)*, *Tucker et al. (2000)*, *Tucker et al. (2001)*, *Katayama et al. (2002)*, *Gupte (2003)*, *Inoue & Endo (2003)*, *Senba et al. (2003)*, *Gupte (2005)*. Although virtually no publications in western languages on design and operation of these regenerators can be found in literature. As a major part of recent R&D efforts in this field was actually located in Japan, it might be speculated about publications available in East Asian languages. Another obvious reason for this discrepancy is, of course, that most of these recent developments are related to commercial chiller manufacturers and thus design details are not likely to be published.

Apart from absorption chiller business where shell boilers with smoke tubes can still be considered the “classic design”, tube boilers with self-circulation have a long tradition in two further fields of application. These are on the one hand steam boilers for operation of steam turbines in power stations, and on the other hand concentration or evaporation of liquid solutions in chemical or food industry, e.g. sugar production. For application of tube boilers with self-circulation, in both contexts publications can be found. Process parameters in both traditional applications are, however, quite different to those in a flue-gas fired regenerator of an absorption chiller. Therefore, these findings cannot be directly applied to absorption chillers. Finally, there are – a little bit apart from popular applications – a smaller number of reports on laboratory experiments with electrically heated tube boilers at moderate or low boiling pressures.

### **4.6.2 General aspects of modeling of natural-convection boilers**

The general problem of modeling natural-convection boilers is to find a self-consistent solution that predicts heat flux and mass flow in each boiling tube and the circulation in the downcomer in a way that pressure drops and buoyancy forces are exactly balanced. This implies that gravimetric and volumetric vapor fraction and the relative speed of the vapor phase are determined at any position within the boiling tubes. Suitable correlations are required to calculate local heat transfer and pressure drop in dependence of the local conditions of the two-phase flow.

At least the following effects have to be adequately covered:

- Downcomer tubes, presumably single-phase liquid flow:
  - Entering pressure drop (change in cross section)
  - Frictional pressure drop
  - Pressure change along flow due to liquid head
  - Leaving pressure drop (change in cross section)
- Boiling tubes, first subcooled section, mostly single-phase liquid flow:
  - Entering pressure drop (change in cross section)
  - Frictional pressure drop in liquid flow
  - Pressure change along flow due to liquid head
  - Decreasing saturation temperature and increasing fluid temperature along liquid flow
  - Convective heat transfer in single-phase flow
  - Subcooled boiling
- Boiling tubes, consequent saturated section, two-phase flow:
  - Different flow velocity of liquid and vapor phase
  - Frictional pressure drop in two-phase flow (greater than in single-phase flow, dependent on vapor content)
  - Acceleration pressure drop due to volume increase
  - Pressure change along flow due to decreasing liquid head
  - Decreasing fluid temperature in saturation due to decreasing pressure, possibly retarded due to concentration of less volatile component
  - Convective heat transfer in two-phase flow
  - Nucleate boiling heat transfer
  - Additional vapor generation by flashing at decreasing pressure head
  - Leaving pressure drop (change in cross section, additional pressure drops in header where applicable)

With all these effects integrated in a numerical modeling, the problem can be solved by an iterative algorithm. According to [Arneeth \(1999\)](#), there presently exists no simple calculation approach for natural-convection boilers providing sufficient accuracy. Even rather complex numerical models show certain deviations from measured data and fail for some operational states.

### 4.6.3 Steam boilers for power generation

The history of water tube boilers as steam generators can be traced back to the historic patent of *Babcock & Wilcox (1867)* on "Improvement in steam generators" which was the basis for the success of both, the Babcock & Wilcox Company and the so-called Babcock & Wilcox boilers. Allowing for higher steam pressures than shell boilers, water tube boilers have established in the following as standard design for generation of mechanical and – later on – electrical power. In the first half of the 20<sup>th</sup> century, water tube boilers also successively replaced other boiler designs in marine applications due to their lower specific weight.

Water boilers in power plants are typically equipped with boiling tubes of several meters in length and are operated at steam pressures above *100 bar* and at relatively high heat flux densities. Compared to boilers at atmospheric pressure, this results in high nucleate boiling heat transfer coefficients – increasing with pressure as given by (4.98) – but significantly reduced buoyancy forces as the difference in the specific densities of vapor and liquid ( $\rho'' - \rho'$ ) decreases at increasing pressure. A comparison of some important parameters for the boiling of water at *100 bar*, the boiling of water at *1 bar* and the boiling of 62% lithium bromide solution at *900 mbar* is given in Tab. 13.

| Important parameters for design of tube boilers at high and low absolute pressure  | Water boiling @ 100 bar  | Water boiling @ 1 bar   | LiBr solution 62wt.% boiling @ 900 mbar |
|--|--------------------------|-------------------------|---|
| Ratio of specific volumes of vapor and liquid at boiling point $v'' : v'$  | 12 : 1                   | 1600 : 1                | 3700 : 1                                |
| Increase in saturation temperature caused by additional liquid head of 1 m   | 0.05 K                   | 2.5 K                   | 5.5 K                                   |
| Estimated nucleate boiling heat transfer coefficient $\alpha_B$ according to ( 4.98 ) in vertical tubes $d_i = 20 \text{ mm}$ @ $100 \text{ kW/m}^2$ | 24.8 kW/m <sup>2</sup> K | 2.6 kW/m <sup>2</sup> K |   |

*Tab. 13: Comparison of important parameters for design of tube boilers at high and low absolute pressure.*

Therefore, significant vapor mass fraction  $\dot{\chi}$  is required to induce a permanent natural convection at high pressures. On the other hand, the additional liquid head at the bottom of the boiling tubes causes only a minor subcooling in such steam boilers.

Thus, design issues and operational behavior of conventional steam boilers and flue gas fired regenerators of absorption chillers are likely to be quite different.

### 4.6.4 Steam-heated thermosiphon reboilers

#### Typical designs and recent investigations

Natural convection boilers for concentration or evaporation of liquids widely used in chemical or food industry, on the other hand are quite close to regenerators of absorption chillers what boiling parameters are concerned, as they are operated at moderate pressures up to some bars, too. Even sub-atmospheric boiling and concentration of aqueous salt solutions are not uncommon tasks in this field of application. However, an important difference is that boilers in chemical or food industry typically are steam-fired themselves for exact control of the process temperature. Therefore, heat transfer intentionally takes place in constant-wall-temperature-mode rather than in constant-heat-flux-mode and process parameters at all boiling tubes are quite similar.

A prominent example of a steam-fired natural convection boiler with vertical boiling tubes is the Robert evaporator, introduced into sugar industry in the 19<sup>th</sup> century and widely used up to the present. This type of boiler comprises a central downcomer tube surrounded by the boiling tubes, both directly attached to a bottom and a header vessel. The simple design without any additional bends or interconnections is well suited for highly viscous fluids. According to *Rant (1977)*, the cross section of the downcomer tube in a Robert evaporator is typically chosen at least half of the total cross section of all boiling tubes.

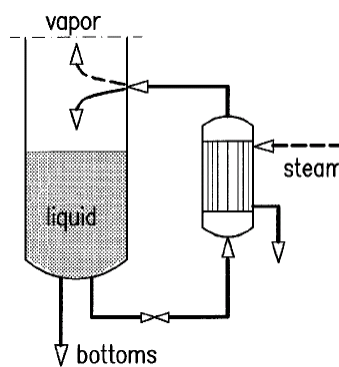


*Fig. 37: Standard setup of a steam-heated vertical thermosiphon reboiler. Cited from Arneith & Stichlmair (2001).*

Even more common are boiler designs as shown in Fig. 37 with a steam-heated bundle of boiling tubes apart from the main vessel, which serves as both liquid sump and downcomer tube. As indicated in Fig. 37, the liquid level in the main vessel of these steam-fired boilers is typically chosen below<sup>54</sup> the upper end of the boiling tubes. Typical design data of steam-fired natural convection boilers according to *Arneith (1999)* are listed in Tab. 14:

<sup>54</sup> For steam-fired boilers, the driving liquid head or submergence level is an important optimization parameter. For flue gas fired boilers, on the other hand, the boiling tubes have to be completely wetted even at the startup to prevent damage.



| Design data of steam-fired natural convection boilers |              |  |
|---|--------------|--|
| Tube length   | $l$          | 1...4 m  |
| Tube inner diameter                                   | $d_i$        | 15...50 mm   |
| Temperature difference steam (outside) – fluid        | $\Delta T$   | 10...40 K  |
| Vapor mass fraction in boiling tubes                  | $\dot{\chi}$ | 2...15% (aqueous)<br>5...30% (organic)   |
| Mean overall heat transfer coefficient                | $U$          | 2...4 kW/m <sup>2</sup> K (aqueous, clean surfaces)<br>1...2 kW/m <sup>2</sup> K (aqueous, fouling)<br>1...2 kW/m <sup>2</sup> K (organic, clean surfaces)<br>0.5...1.2 kW/m <sup>2</sup> K (organic, fouling) |

Tab. 14: Typical design and operation data of steam-fired natural convection boilers according to Arneth (1999).

The boiler design outlined in Fig. 37 has been subject to numerous investigations. In steam-heated boilers, parameters in all boiling tubes presumably are nearly identical; therefore, most laboratory experiments have effectively been conducted at single-tube boilers (cf. left sketch in Fig. 38).

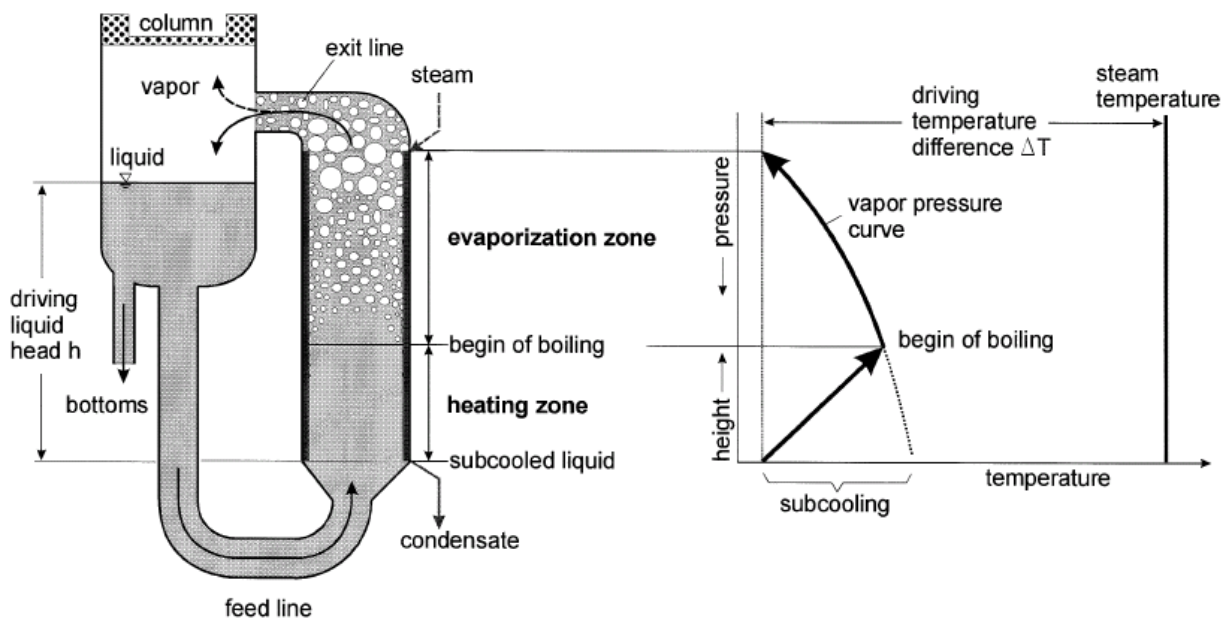


Fig. 38: Schematic of a vertical thermosiphon reboiler with a single boiling tube (left) and characteristic temperature profile inside the boiling tube (right).

Cited from Arneth & Stichlmair (2001).

Comprehensive studies on this system have already been published by late Prof. Kirschbaum (1900-1970) in e.g. Kirschbaum (1954), Kirschbaum (1955), Kirschbaum (1961), Kirschbaum (1962). This author performed numerous measurements on detailed pressure and temperature profiles during the atmospheric and sub-atmospheric boiling of water and aqueous solutions of salt and sugar. He varied tube length, tube diameter, and driving liquid head and found characteristic pressure-temperature profiles inside the boiling tubes in the



shape of Fig. 38. In *Kirschbaum (1955)*, he presents first attempts to find a simple dimensionless correlation to predict the mean heat transfer coefficient in thermosiphon reboilers. In later publications, *Nagel (1962)* and *Nagel & Kirschbaum (1963)* already showed that these boilers basically can be modeled assuming a heating zone with subcooled boiling and a consecutive evaporation zone with saturated flow boiling. A summary on the history of research on thermosiphon reboilers is provided by *Dialer (1983)*.

Recently, these investigations have been continued in a series of works by *Dialer (1983)*, *Kaiser (1988)*, *Arneith (1999)*, *Arneith & Stichlmair (2001)*, *Baars (2003)*. These authors still employed single-tube boilers for their own measurements on the boiling of water, organic fluids and mixtures of organic fluids and water. *Dialer (1983)*, *Kaiser (1988)* and *Arneith (1999)* refined the two-zone modeling approach of *Nagel & Kirschbaum (1963)* employing more recent correlations for heat transfer and pressure drop in two-phase flow regimes. These recent authors presented computerized calculation routines to determine a self-consistent solution for given external conditions, thus obtaining the initially unknown internal circulation rate in the tubes as an output. *Dialer (1983)* and *Kaiser (1988)* also provided approximation formulas for the mean overall heat transfer coefficient.

### Operational characteristics and modeling

*Kirschbaum (1962)* had already reported on flow instabilities and oscillations observed in the experimental setup at certain operating conditions. This behavior was also observed by e.g. *Dialer (1983)* and *Arneith (1999)*; phenomenological explanations are given by *Dialer (1983)*. A comprehensive experimental and theoretical study on instable operational states to be found in a thermosiphon reboiler with a single boiling tube has been provided by *Baars (2003)*. In this most simple design, already seven different operational modes two stationary ones and five transient ones are reported. Periodic variations of the mass flux are observed during density wave oscillations; even flow reversal occurs during U-tube oscillations.

Heat transfer modeling in these works listed above, however, has been performed based on assumption of stationary operation. *Nagel (1962)* mainly investigated the boiling of 93wt.% aqueous ethanol solution and reported entering liquid flow velocities in the boiling tube in the order of magnitude of  $0.1 \text{ m/s}$  and exit velocities of the two-phase flow of about  $10 \text{ m/s}$ . He found that heat transfer in the subcooled heating zone at slow flow velocities shows a nucleate boiling characteristic for sufficient wall superheat ( $\Delta T_{SAT} > 17 \text{ K}$  in his setup) while heat transfer in the saturated boiling zone is dominated by the enhanced convection due to the vapor content (cf. Fig. 39).

Copper Tube, Length 1.5m, Inner Diameter 40mm, Outer Diameter 48mm

|   |           |                |
|---|-----------|----------------|
|   | (Below ↓) | (Right →)      |
| Boiling fluid (inside of tube):             | Water     | 93wt.% Ethanol |
| Saturation temperature in headspace:        | 50°C      | 40.1°C         |
| Outside steam condensation temperature:     | 100°C     | (Variation)    |
| Relative driving liquid head (submergence): | 80%       | 40%, 60%, 70%  |

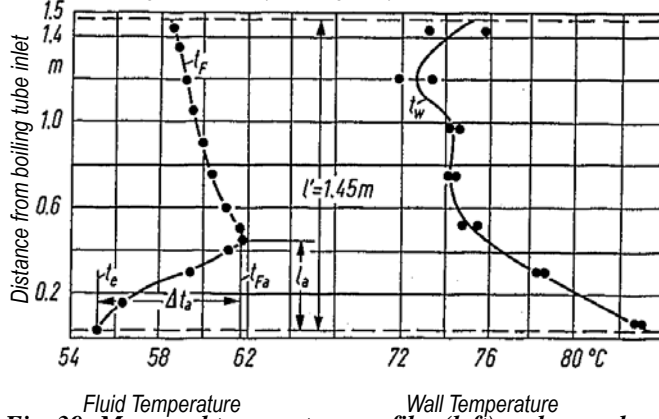


Fig. 39: Measured temperature profiles (left) and mean heat transfer coefficients in heating and evaporation zone (right). Visualization of experimental data by Nagel (1962) and Nagel & Kirschbaum (1963).

Nagel (1962) also proposed a semi-empirical physically based flow-boiling model that showed reasonable agreement with all his experimentally determined heat transfer coefficients in heating and evaporation zone for the boiling of water and 93wt.% aqueous ethanol solution.

Dialer (1983) and Kaiser (1988) investigated the boiling of water and of various binary mixtures using the same experimental setup. Dialer (1983) mainly focused on single component fluids and provided both, a very detailed simulation model for heat transfer and pressure drop distinguishing between various flow regimes and heat transfer modes, and a simple semi-empirical approximate correlation for the overall heat transfer coefficient. Kaiser (1988) then continued this work and extended the detailed model and the approximation formula to binary liquid mixtures. Both authors reported mean overall heat transfer coefficients in the range of 2...5 kW/m<sup>2</sup>·K at different operational states.

Arneth (1999) refined and simplified the model of Dialer (1983) and thus was finally able to achieve even better agreement of predicted values with own measurements and numerous literature data on various fluids and geometric parameters. In the model of Arneth (1999), in the heating zone (cf. left sketch in Fig. 38), only convective heat transfer in a single-phase flow according to the simple Dittus-Boelter equation (4.31) is considered and subcooled nucleate boiling is disregarded. In the evaporation zone the correlations (4.87), (4.101) and (4.102) according to Liu & Winterton (1991) are employed, evaluated once in the middle of the zone at mean process parameters. It has to be stated, however, that this simplified model has only been proven to reproduce correctly the overall heat transfer coefficient and the mass flow; it is not necessarily able to predict further internal system parameters like the

actual length of the heating zone or respective temperature gradients of fluid and tube wall, too.

According to [Arneth & Stichlmair \(2001\)](#) the circulation rate in thermosiphon reboilers first increases sharply with driving temperature difference and heat flux at then reaches a maximum between  $\Delta T = 20 \dots 30$  K; at higher loads the flow rate slightly decreases. These relations are visualized in Fig. 40 for boiling of water at atmospheric pressure. The reason is that at small loads the increasing density difference between downcomer and boiling tube accelerates the circulation with increasing vapor content while at higher loads the pressure drop at the boiling tube exit becomes dominant and limits the mass flow rate. For the same reason, increased boiling pressures and larger tube diameters result in higher mass flow densities, too.

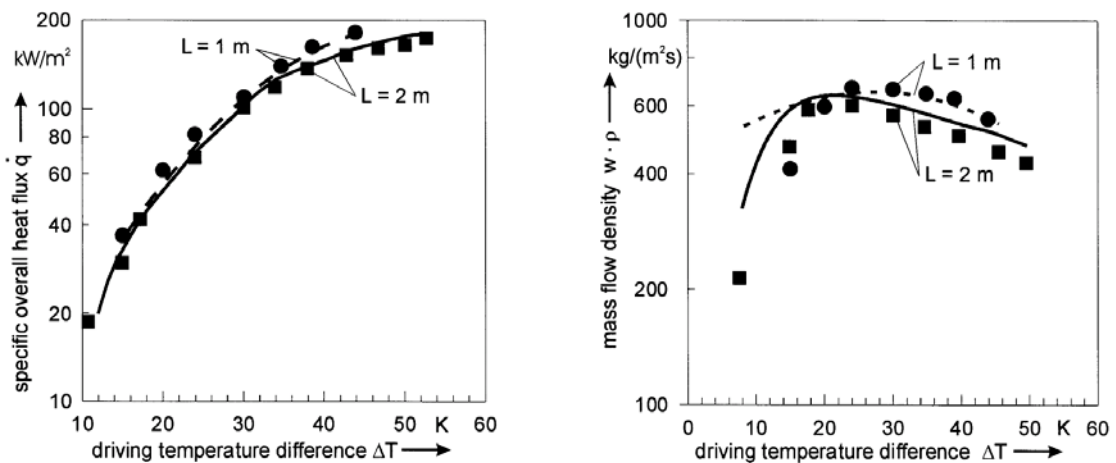


**Fig. 40:** Specific overall heat flux and boiling tube mass flux density in dependence on the total driving temperature difference in a thermosiphon reboiler for the boiling of water at atmospheric pressure. Visualization of experimental data and simulation results obtained by [Arneth \(1999\)](#) and [Arneth & Stichlmair \(2001\)](#) for tube inner and outer diameter  $d_i = 25$  mm and  $d_o = 28$  mm and different tube lengths.

According to the investigations of [Arneth \(1999\)](#), mass flux densities in boiling tubes are mostly in the range of  $200 \dots 900$  kg/s·m<sup>2</sup>, however, values around  $100$  kg/s·m<sup>2</sup> are found for low subatmospheric pressures in the range of  $0.1 \dots 0.2$  bar. This is compliant with the findings of [Nagel \(1962\)](#) and [Nagel & Kirschbaum \(1963\)](#) who also reported mass flux densities in the order of magnitude of  $100$  kg/s·m<sup>2</sup> for operation in this pressure range.

In all studies, general observation was that best overall heat transfer coefficients are obtained for driving liquid heads less than boiling tube length. Reduction of the liquid head results in lower liquid velocity at the boiling tube inlet and – together with the smaller pressure head at the tube bottom – also in a shorter heating zone. In steam-heated reboilers, an enlargement of the evaporation zone typically results in greater overall heat transfer coefficients. [Arneth & Stichlmair \(2001\)](#) stated that thermosiphon reboilers operated at ambient or higher pressured show best performance at driving liquid heads of  $80 \dots 100\%$  of

the pipe length while reboilers operated in vacuum conditions work best with liquid heads between 50% and 70% of the pipe length. They also found that at atmospheric pressure the length of the heating zone is typically 20...50% of the total tube length. It increases significantly with decreasing pressure. At very low boiling pressures, the length of the heating zone approaches 90% of tube length or even more.

#### 4.6.5 Laboratory experiments with unconventional designs

##### Electrically heated boiling tube with uniform heat flux at atmospheric pressure

A smaller number of laboratory experiments deals with electrically heated boiling tubes providing a uniform heat flux at moderate boiling pressures. This kind of system is quite close flue gas fired regenerator, if boiling tube geometry and operating pressure are in the same range. A series of publications by *Ali & Alam (1991)*, *Kamil et al. (1995)*, *Kamil et al. (2005)*, and *Shamsuzzoha et al. (2005)* deals with atmospheric boiling experiments using the same setup of a single vertical tube thermosiphon reboiler employing a 1.9 m long 25.56 mm inner diameter stainless steel boiling tube. Amongst several organic fluids, the boiling of water was studied in dependence on heat flux and driving liquid head (submergence); detailed temperature profiles of the tube wall were reported (cf. Fig. 41).

Unfortunately, these authors did not compare their experimental findings with predictions from established flow-boiling models. Neither did they provide the respective mass flow rates corresponding with the published temperature profiles; therefore, it is not easily possible to evaluate their experimental in a more detailed way. However, it clearly shows from all their measurements – including measurements with organic fluids not reproduced in Fig. 41 – that at high driving liquid heads the wall temperature locally achieves a maximum somewhere around the transition from the heating zone to the evaporation zone. At this position the heat transfer coefficient is worse than estimated for nucleate flow boiling according to *Cooper (1989)* from (4.96) with reduction factor 0.7 but better than calculated for nucleate boiling only from (4.98) according to *Steiner & Taborek (1992)*.

Unfortunately, no clear information on the corresponding liquid temperature and state of subcooling or saturation at this point is given. Nevertheless, it is evident from the experimental data of *Ali & Alam (1991)*, *Kamil et al. (1995)*, *Kamil et al. (2005)*, and *Shamsuzzoha et al. (2005)* that in tube boilers operating in uniform heat flux mode the most critical position is a wall temperature maximum somewhere at the end of the heating zone. In a lithium bromide filled boiler, the most severe corrosion attack is to be expected right there.

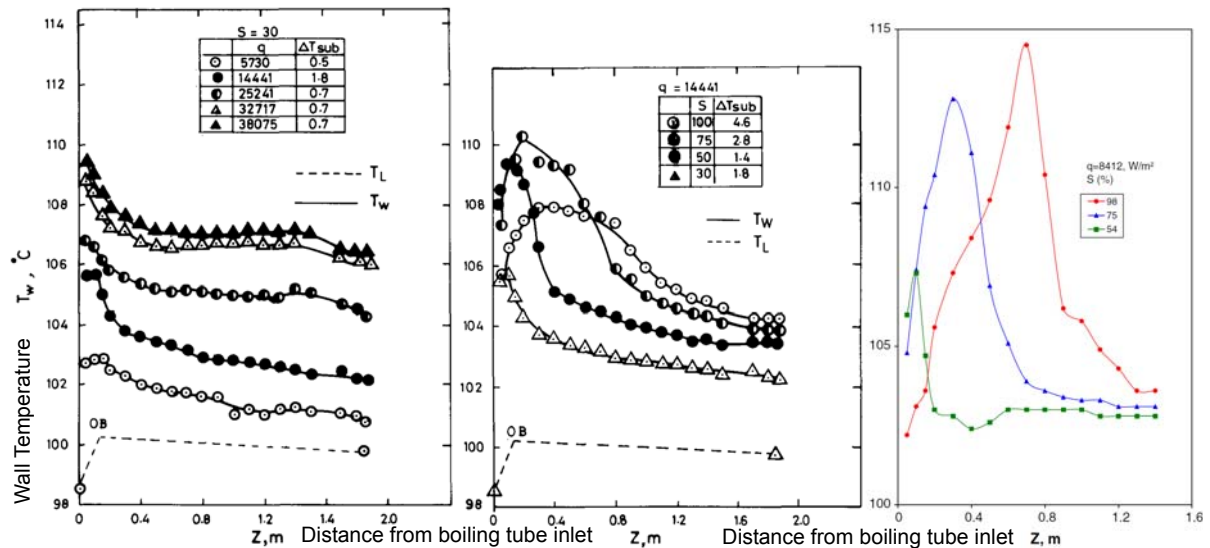


**Fig. 41: Measured wall temperature profiles during the atmospheric boiling of water in an electrically heated vertical thermosiphon reboiler with tube length  $l = 1.9$  m and inner diameter  $d_i = 25.25$  mm.**

Left diagram: Variation of heat flux  $q$  from  $5\,730$   $\text{W/m}^2$  to  $38\,075$   $\text{W/m}^2$  at 30% relative driving liquid head.

Middle/right diagram: Variation of submergence/relative driving liquid head  $S$  [%] at constant heat flux

$14\,441$   $\text{W/m}^2$  (middle diagram) and  $8\,412$   $\text{W/m}^2$  (right diagram). Cited from *Kamil et al. (1995)* (left and middle diagram) and from *Shamsuzzoha et al. (2005)* (right diagram).

### Small-scale direct-fired regenerator with axial flue gas flow

Laboratory testing of small direct-fired regenerator with five vertical boiling tubes and thermosiphon operating at heat duties up to  $25$  kW was reported by *Jung & Park (1998)*. Due to the small scale of this prototype, the design was different to conventional tube boilers with flue gas crossflow. *Jung & Park (1998)* employed a cylindrical surface-flame burner that was embedded in the bottom solution reservoir with upward flue gas flow axial to the five boiling tubes. Thus, the lithium bromide solution presumably entered the boiling tubes already in saturated state and the heat flux decreased along the boiling tubes together with the decreasing flue gas temperature. Only little data are provided; the boiling tubes were about  $1$  m in length and  $20$  mm in diameter, the setup was operated at about ambient pressure and  $93$  °C condensation temperature, the solution concentration was varied between  $56\text{...}60\text{w.}\%$ .

*Jung & Park (1998)* found that in their setup the natural circulation worked at driving liquid heads up to  $60\text{...}70$  cm below the upper end of the boiling tubes. Assuming a tube length of about  $1$  m this observation would be in-line with the findings of other researchers on the boiling of other aqueous fluids. The circulation rate  $\dot{M}$  measured by *Jung & Park (1998)* was basically compliant with a square root function of heat duty  $\dot{Q}$  and the difference of actual and minimum driving liquid head  $h - h_{MIN}$ .

$$\dot{M} \sim [\dot{Q} \cdot (h - h_{MIN})]^{1/2} \quad (4.104)$$

Although from their published data no real significance for this exponent  $\frac{1}{2}$  can be found. The mass flux density in the boiling tubes presumably was only in the order of magnitude of  $100 \text{ kg/s}\cdot\text{m}^2$  and thus much lower than in other atmospheric boiling experiments. A reason might be the axial flue gas flow in the design of *Jurng & Park (1998)* resulting in decreasing heat flux density along each boiling tube.

## 5 Optimized flue gas heat exchanger design

### 5.1 General settings

#### 5.1.1 Definition of the optimization problem

As required size and cost of a flue gas fired regenerator for given external conditions are mainly determined by the heat transfer at the flue gas side, one major target of a design optimization is to achieve a high heat transfer coefficient in the flue gas. Generally, for any heat exchanger geometry this heat transfer coefficient can reach almost any desired value if only the velocity of the gas flow is increased accordingly. The price is a significant increase in the friction pressure drop. Allowed pressure drop in the flue gas flow, however, in most cases is strictly limited. Therefore the optimization target – more precisely – is to achieve the best average heat flux density along the total heat exchanger for a given pressure drop.

Especially for high flue gas entering temperatures, the maximum acceptable local heat flux density at the solution side of the regenerator will impose a first constraint on this optimization. Additionally geometrical limitations, reasonable ratios of length, width, and height of the heat exchanger have to be considered. Further constraints result from manufacturing costs; the number and total length of all weld seams required as well as potentially increased welding effort due to small tube diameter or small tube spacing have to be taken into account.

#### 5.1.2 Considered types of heat exchangers

In the following discussion – already outlined in *Kren et al. (2005a)*, *Kren et al. (2005b)*, *Kren et al. (2006a)*, and *Kren et al. (2006b)* – three basic designs<sup>55</sup> for flue gas fired boilers will be considered:

- Gas flow inside plain circular tubes with boiling outside the tubes (i.e. standard pool boiler design, cf. left sketch in Fig. 24)
- Gas flow across plain tubes with boiling inside the tubes (cf. left sketch in Fig. 27)
- Gas flow across finned tubes with boiling inside the tubes (cf. right sketch in Fig. 27)
- As an acceptable approximation for each type of heat exchanger, the heat transfer at the flue gas side shall be assumed independent from the heat transfer at the liquid side.

---

<sup>55</sup> Actually, there is another design subtype that might be of interest: Flue gas flow inside tubes with fins or turbulators at the flue gas side. However, there is no standard for turbulators inside tubes, nor are there general correlations for heat transfer and pressure drop available in textbooks like *VDI-GVC (2002)* for such configurations.



### 5.1.3 Free parameters for design optimization

Once the total flue gas mass flow together with the entering and the desired leaving flue gas temperature are specified, only two free variables are left in a shell boiler design with flue gas flow inside tubes (cf. left sketch in Fig. 24). These variables are the tube inner diameter  $d_i$  and the specific mass flux with reference to the tube cross-section  $\dot{m} = u \cdot \rho$  being the invariant product of local velocity  $u$  and density  $\rho$  of the flue gas. The required number of parallel tubes then is a function of the total mass flow and the cross section of a single tube. The total tube length  $l$  is calculated accordingly as function of the heat transfer coefficient, as the inner surface of each single tube must be sufficiently large to ensure cooling of the flue gas from entering to the desired leaving temperature. If this total length has to be divided into a multiplicity of consecutive passes (e.g. a total length of  $8\text{ m}$  would presumably be broken into two passes of  $4\text{ m}$  each), mainly additional pressure drop is generated along with only little increase in heat transfer coefficient. Therefore, the smallest number of passes will always give the best results in terms of heat transfer and pressure drop. Variations in tube spacing and bundle arrangement do not directly affect heat transfer and pressure drop at the flue gas side and thus they will be disregarded.

For crossflow over tube bundles (cf. Fig. 27), analogously the tube outer diameter  $d_o$  and the invariant specific mass flux with reference to the cross section of the free channel  $\dot{m} = u_{FC} \cdot \rho$  can be identified as design parameters (cf. Fig. 29). The required number of consecutive rows of tubes downstream is calculated again in dependence on the heat transfer coefficient in a way that the desired leaving temperature is reached. Additional parameters are the configuration and geometry of the tube bank, staggered or in-line arrangement, and longitudinal  $Y_{LO}$  and transversal tube pitch  $Y_{TR}$  as shown in Fig. 29.

In finned tube banks, finally fin height  $R_F$ , fin pitch  $Y_F$  and fin thickness  $T_F$  as shown in Fig. 30 and the resulting enhancement  $\beta_F$  of the outer surface compared to a plain tubes are additional design parameters.



## 5.2 Theoretical analysis: Fundamental relations for optimization of heat exchanger design

### 5.2.1 Basic assumptions

It is not possible at all to derive analytical solutions for the optimization problem outlined above, taking into account temperature dependencies of the property data, interferences between heat transfer at flue gas and liquid sides, and all boundary effects. A numerical approach will not lead to simple results either, as optimum design will still be dependent on the selected flue gas temperatures. Employing some simplifications and approximations, makes it possible, however, to reveal some elementary proportional correlations and dependencies.

The following assumptions shall be employed for all designs:

1. Flue gas mass flow, thermal duty, and physical size of the heat exchanger are sufficiently large; therefore, boundary effects that would have to be taken into account in small heat exchangers can be disregarded.
2. Regardless of the pressure drop, the mean absolute pressure in the flue gas shall be the same for all designs
3. Entering and leaving flue gas temperature are fixed for the comparison of different heat exchanger designs; temperature at the liquid side is also fixed and constant at the whole heat exchanger.
4. With the same mean flue gas temperature and pressure also the mean values of all property data of flue gas like specific heat capacity  $c_p$ , dynamic viscosity  $\mu$ , thermal conductivity  $\lambda$ , density  $\rho$ , and Prandtl number  $Pr$ , shall be the same for all alternative designs.
5. Variations of all property data are so reasonably small that calculations of heat transfer and pressure drop can be based on a set of mean property data values for the total heat exchanger and the same set of mean property data values can be employed for all alternative designs. Effects due to the local variation of properties along the heat exchanger may be neglected.
6. The mean heat flux density that specifies the size of the required heat exchanger surface is directly proportional to the mean heat transfer coefficient at the flue gas side  $\dot{q} \sim \alpha_G$ . Influences from heat transfer resistances attributed to the tube wall and the liquid side are negligible.

The latter two assumptions no. 5 and no. 6 need further discussion. Actually, no. 5 is not completely true for large temperature variations in the flue gas that are found in this application. Nevertheless, according to *VDI-GVC (2002)* for all the discussed heat exchanger types it is suitable to perform heat transfer calculations with property data taken at the mean fluid temperature. To account for large temperature differences between flue gas and liquid side, additional correction factors (4.35), (4.68) discussed in 4.3.2 and 4.4.2 might have to be considered. At least for laminar gas flow inside tubes this correction can completely be neglected (exponent  $N = 0$ ), for gas flow across tube bundles it is only a minor effect (either  $N = 0$  or  $N = 0.12$ ). Only for turbulent gas flow inside tubes, according to *Spang (2004)* an

exponent  $N = 0.36$  has to be used that might result in a significantly increased convective heat transfer coefficient at large temperature differences. In any case, however, these correction factors (4.35), (4.68) are constant values as soon as all temperatures are set.

The last assumption no. 6 stating  $\dot{q} \sim \alpha_G$  is always fulfilled if it is assumed that the heat transfer resistances attributed to the tube wall and the liquid side can completely be neglected – as suggested in (4.1), (4.2) – and thus  $U \approx \alpha_G$ . However, this very simple approximation assuming zero wall superheat  $\Delta T_{SAT} \approx 0$  is not always applicable and may introduce some error especially at small temperature differences between flue gas and liquid side. On the other hand, the heat transfer at the liquid side typically takes place in a nucleate boiling regime, according to (4.92) characterized by a rather constant wall superheat  $\Delta T_{SAT} \sim \dot{q}^{-1/4 \dots 1/3}$  with only weak dependence on the heat flux (exponent  $1/4 \dots 1/3$ ). Therefore, it is a reasonable approximation to assume that the total temperature difference between mean liquid boiling temperature<sup>56</sup> and the tube wall at the flue gas side is a non-zero but constant value for all possible boiler designs. This again leads to a proportional relation of flue gas side heat transfer coefficient and surface heat flux  $\dot{q} \sim \alpha_G$ .

In the following discussion a constant wall temperature at the gas side  $T_{W,G} = const.$  will be assumed. Then, the heat transfer  $\dot{q} = \alpha_G \cdot LMTD_G$  is only dependent on the gas side heat transfer coefficient  $\alpha = \alpha_G$  and the temperature difference between gas and wall temperature  $LMTD_G$ . For comparison of different designs at given temperature conditions,  $LMTD_G$  is a fixed value.

As properties are considered invariant for the optimization problem also the simplified proportional relations  $\alpha \sim Nu/L$ ,  $\dot{q} \sim Nu/L$  and  $Re \sim \dot{m} \cdot L$  are obtained from (4.12) and (4.13) with  $L$  being the respective characteristic length are valid for all heat exchangers.

The optimization problem is to identify the configuration with the greatest heat transfer coefficient  $\alpha$  for each allowed frictional pressure drop  $\Delta p_{FR}$  along the total heat exchanger.

<sup>56</sup> Of course, the local saturation temperature in the heat exchanger shows some variation in dependence of the local liquid head; thus, the mean boiling temperature is a few Kelvin higher than the saturation temperature at the liquid level above.

## 5.2.2 Relations between geometric and operational parameters

### Fluid flow inside circular tubes

With invariant property data from (4.21), (4.22) and (4.36) the relations

$$Re \sim \dot{m} \cdot d_i \quad (5.1)$$

$$\alpha \sim Nu/d_i \quad (5.2)$$

$$\Delta p_{FR} \sim \zeta \cdot l/d_i \cdot \dot{m}^2 \sim \zeta \cdot l \cdot d_i^{-3} \cdot Re^2 \quad (5.3)$$

are obtained. The required length of each individual tube  $l$  is dependent on the tube diameter  $d_i$  and the mass flux density  $\dot{m}$ . For fixed entering and leaving temperature, the absolute heat flux through the inner surface of each single tube  $\dot{Q}_1$  is proportional to the absolute mass flow in a single tube  $\dot{Q}_1 \sim \dot{m} \cdot d_i^2$ . On the other hand it is also proportional to the product of heat transfer coefficient and tube surface  $\dot{Q}_1 \sim \alpha \cdot l \cdot d_i$ .

Therefore, the tube length  $l$  is proportional

$$l \sim \dot{m} \cdot d_i / \alpha \sim \dot{m} \cdot d_i^2 / Nu \sim Re \cdot d_i / Nu \quad (5.4)$$

and thus the frictional pressure drop  $\Delta p_{FR}$  yields

$$\Delta p_{FR} \sim \zeta \cdot \dot{m}^3 / \alpha \sim \zeta \cdot d_i^{-2} \cdot Re^3 / Nu \quad (5.5)$$

This formulation (5.5), however, does only account for the frictional pressure drops within the tubes, which actually are the dominant ones in many heat exchangers. If the additional frictional pressure drops at the inlet and outlet of the tubes have to be taken into account, from (4.40) another relation with slightly different dependencies can be obtained:

$$\Delta p_{IN} + \Delta p_{OUT} \sim (\zeta_{IN} + \zeta_{OUT}) \cdot \dot{m}^2 \sim (\zeta_{IN} + \zeta_{OUT}) \cdot d_i^{-2} \cdot Re^2 \quad (5.6)$$

The value of the sum of the friction factors for inlet and outlet  $(\zeta_{IN} + \zeta_{OUT})$  is strongly dependent on the shape of flue gas channel and tube ends and the number of passes in the heat exchanger and thus it cannot be covered by a general relation.

### Fluid flow across tube bundles

For tube bundles, there are two different definitions of Reynolds and Nusselt numbers, (4.43) vs. (4.50), (4.55) vs. (4.62). These Reynolds number definitions show a slightly different dependence on the tube pitch as different definitions of the void ratio are employed. Simple relations can be obtained again assuming identical tube pitch ratios for all configurations and constant fin efficiency for finned tube bundles:

$$Re \sim \dot{m}_{FC} \cdot d_o \quad (5.7)$$

$$\alpha \sim Nu/d_o \quad (5.8)$$

The relation for the pressure drop is according to (4.69)

$$\Delta p_{FR} \sim \zeta \cdot N_{RESIST} \cdot \dot{m}_{FC}^2 \sim \zeta \cdot N_{TB,LO} \cdot \dot{m}_{FC}^2 \sim \zeta \cdot N_{TB,LO} \cdot d_o^{-2} \cdot Re^2 \quad (5.9)$$

as  $N_{RESIST} \sim N_{TB,LO}$  is either exactly valid or a reasonable approximation for most cases. Assuming again fixed entering and leaving temperatures, the absolute heat flux in a heat exchanger is on the one hand proportional to flue gas channel cross section  $A_{FC}$  and mass flux density  $\dot{Q} \sim \dot{m}_{FC} \cdot A_{FC}$ . On the other hand it is proportional to the product of heat transfer coefficient, number of rows of tubes, number of tubes per row, and available surface per tube  $\dot{Q} \sim \alpha \cdot N_{TB,LO} \cdot N_{TB,TR} \cdot l \cdot d_o \cdot \beta_F$ . The surface enhancement factor  $\beta_F$  is unity for plain tubes. It is a reasonable assumption that the length of the individual tube  $l$  is identical to the channel height; the channel width thus is  $A_{FC}/l$ , and the number of tubes per row with tube pitch  $y_{TR} \cdot d_o$  is approximately  $N_{TB,TR} \sim (A_{FC}/l) / (y_{TR} \cdot d_o)$  for sufficiently big arrangements. Putting it all together, a relation for the number of rows of tubes can be obtained:

$$\begin{aligned} N_{TB,LO} &\sim \dot{m}_{FC} \cdot A_{FC} / (\alpha \cdot N_{TB,TR} \cdot l \cdot d_o \cdot \beta_F) \\ &\sim \dot{m}_{FC} \cdot A_{FC} / [\alpha \cdot (A_{FC}/l) / (y_{TR} \cdot d_o) \cdot l \cdot d_o \cdot \beta_F] \\ &\sim \dot{m}_{FC} \cdot y_{TR} / (\alpha \cdot \beta_F) \\ &\sim \dot{m}_{FC} / \alpha \sim Re / Nu \quad \text{assuming } y_{TR} = const., \beta_F = const. \end{aligned} \quad (5.10)$$

Constant tube pitch ratios  $y_{TR} = const.$ , constant fin geometry relative to the tube diameter  $Y_F/d_o = const.$ ,  $R_F/d_o = const.$  and thus constant surface enhancement factor  $\beta_F = const.$  can be assumed to obtain more simple relations. Analogous to (5.5), the pressure drop for fluid flow inside tubes finally is:

$$\Delta p_{FR} \sim \zeta \cdot \dot{m}_{FC}^3 / \alpha \sim \zeta \cdot d_o^{-2} \cdot Re^3 / Nu \quad (5.11)$$

In contrast to (5.5) for fluid flow inside tubes, no additional formulations for entering and leaving pressure drops are required for tube bundles with at least five consecutive rows of tubes at the flue gas side.

The length of the tube bundle in longitudinal direction  $l_{LO}$  is the product of the number of rows of tubes and the tube pitch  $l_{LO} = N_{TB,LO} \cdot Y_{LO} = N_{TB,LO} \cdot y_{LO} \cdot d_o$ ; a simple relation can be given again at constant tube pitch ratio  $y_{LO} = const.$ :

$$l_{LO} \sim \dot{m}_{FC} \cdot d_o / \alpha \sim \dot{m}_{FC} \cdot d_o^2 / Nu \sim Re \cdot d_o / Nu \quad (5.12)$$

### 5.2.3 Formal optimization approach

Employing the respective tube diameter – inner diameter for flow inside tubes, outer diameter for cross flow – and the respective definitions for the cross sectional mass flux, identical relations for heat transfer coefficient and pressure drop in all configurations can be used:

$$Re \sim \dot{m} \cdot d \quad (5.13)$$

$$\alpha \sim Nu \cdot d^{-1} \quad (5.14)$$

$$\Delta p_{FR} \sim \zeta \cdot d^{-2} \cdot Re^3 \cdot Nu^{-1} \quad (5.15)$$

The same relation is also found for the required tube length  $l$  in flow direction or the required bundle length  $l_{LO}$  in case of flow across tube bundles:

$$l \sim \dot{m} \cdot d / \alpha \sim Re / \alpha \sim \dot{m} \cdot d^2 / Nu \sim Re \cdot d / Nu \quad (5.16)$$

A further simplification of these relations for easy comparison is possible if Nusselt number and friction factor can be expressed by power-law relations in dependence on the Reynolds number and a fixed exponent:

$$Nu \sim Re^{NNU} \quad (5.17)$$

$$\zeta \sim Re^{NZ} \quad (5.18)$$

Thus, heat transfer coefficient and pressure drop relation can be written:

$$\alpha \sim d^{-1} \cdot Re^{NNU} \quad (5.19)$$

$$\Delta p_{FR} \sim d^{-2} \cdot Re^{3+NZ-NNU} \quad (5.20)$$

In addition, the relations for both geometry factors – tube length  $l$  for flow inside tubes and number of rows of tubes  $N_{TB,LO}$  for cross flow – can be simplified:

$$l \sim d \cdot Re^{1-NNU} \quad (5.21)$$

$$N_{TB,LO} \sim Re^{1-NNU} \quad (5.22)$$

For each design, the optimization problem can be subdivided into two tasks: 1.) find the optimum Reynolds number and 2.) find the optimum tube diameter. Once a Reynolds number has been selected, from (5.19) to (5.21) follows a fixed relation between heat transfer coefficient, pressure drop, diameter, and length:

$$\alpha \sim \Delta p_{FR}^{1/2} \sim d^{-1} \sim l^{-1} \text{ for } Re = \text{const.} \quad (5.23)$$

Thus, for each design the quotient of convective heat transfer coefficient and square root of frictional pressure drop is only a function of the Reynolds number:

$$\frac{\alpha}{\Delta p_{FR}^{1/2}} \sim Re^{3/2 \cdot NNU - 1/2 \cdot NZ - 3/2} \quad (5.24)$$

The largest possible heat transfer coefficient at a given allowed pressure drop or the minimum required pressure drop for a requested heat transfer coefficient will be found at the maximum value of this expression (5.24).

If the exponent in (5.24) is positive, i.e.  $3/2 \cdot NNU - 1/2 \cdot NZ - 3/2 > 0$ , the optimum configuration is to be looked for at high Reynolds numbers, if the exponent is negative, i.e.  $3/2 \cdot NNU - 1/2 \cdot NZ - 3/2 < 0$ , low Reynolds numbers are preferable.

### 5.2.4 Welding effort

The effort for welding of the heat exchanger tubes to the tubesheets is one of the main factors that determine the total welding cost of the flue gas fired regenerator. A major parameter for the welding effort is the total length of the weld seams  $l_{WS}$  that is twice the circumferential length of a heat exchanger tube times the total number of tubes  $l_{WS} = 2 \cdot \pi \cdot d \cdot N_{TB}$ . The required number of tubes  $N_{TB}$  is the quotient of the total required surface area  $A$  and the surface area  $\pi \cdot d \cdot l_{TB}$  of a single tube with length  $l_{TB}$ . For comparison of different designs at given temperature conditions, the total required surface area  $A$  is proportional the inverse heat transfer coefficient  $\alpha^{-1}$ , hence:

$$l_{WS} \sim \alpha^{-1} \cdot l_{TB}^{-1} \quad (5.25)$$

If plain tubes and finned tubes are to be compared, an "effective" heat transfer coefficient  $\alpha \cdot \eta_F \cdot \beta_F$  based on the outer surface of bare tubes has to be used in (5.25) instead of  $\alpha$  in order to account for surface enhancement  $\beta_F$  and fin efficiency  $\eta_F$ . If smoke tubes with a significant wall thickness are used, the "effective" heat transfer coefficient  $\alpha \cdot A_I/A_O$  calculated with reference to the outer surface of the smoke tubes has to be employed in (5.25) instead of the actual  $\alpha$  of the heat transfer at the inner surface.

For optimization of designs with flue gas flow across bundles of boiling tubes, the tube length  $l_{TB}$  can be considered a constant value as it is constrained by the height of the unit; typical

values are in the range  $1 \dots 1.5 \text{ m}$ . In smoke tube designs, the length of an individual tube  $l_{TB}$  is the quotient of the total required length in flow direction  $l$  and the number of passes  $N_P$ . Thus, the length of the weld seams is:

$$l_{WS} \sim N_P \cdot \alpha^{-1} \cdot l^{-1} \quad (5.26)$$

Of course, the minimum length of the weld seams is obtained at a single pass of smoke tubes  $N_P = 1$  and thus  $l_{TB} = l$ .

Another factor with relevance for the welding cost is the total number of weld seams  $N_{WS}$  that is twice the number of tubes  $N_{WS} = 2 \cdot N_{TB}$ , hence:

$$N_{WS} \sim d^{-1} \cdot \alpha^{-1} \cdot l_{TB}^{-1} \sim d^{-1} \cdot l_{WS} \quad (5.27)$$

$$N_{WS} \sim N_P \cdot d^{-1} \cdot \alpha^{-1} \cdot l^{-1} \sim d^{-1} \cdot l_{WS} \quad (5.28)$$

If the tube diameter is varied at constant Reynolds number, the parameters  $d$ ,  $\alpha$ , and  $l$  are linked according to (5.23); consequently relations (5.26) and (5.28) for tubular flow yield:

$$l_{WS} \sim N_P \quad \text{for } Re = \text{const.} \quad (5.29)$$

$$N_{WS} \sim N_P \cdot d^{-1} \quad \text{for } Re = \text{const.} \quad (5.30)$$

According to (5.29), at a fixed Reynolds number the length of the weld seams is not affected by variations of the tube diameter as long as the number of passes is not changed. However, the absolute number of weld seams increases in smoke tube boilers according to (5.30) if the tube diameter is reduced to achieve larger heat transfer coefficients.

For crossflow on tube banks, only diameter and heat transfer coefficient are linked by (5.23) while the tube length  $l_{TB}$  is only dependent on geometric constraints; evaluation of (5.25) and (5.27) thus results:

$$l_{WS} \sim d \cdot l_{TB}^{-1} \quad \text{for } Re = \text{const.} \quad (5.31)$$

$$N_{WS} \sim l_{TB}^{-1} \quad \text{for } Re = \text{const.} \quad (5.32)$$

It shows from (5.32) that in tube boiler designs the number tubes and consequently the number of weld seams are independent from variations in the tube diameter at a fixed Reynolds number and a chosen tube length. According to (5.31) the length of the weld seams even decreases if the tube diameter is reduced to achieve larger heat transfer coefficients.

Finally, it shows for all designs that both the length of the weld seams and the number of the weld seams decrease if the Reynolds number is increased at constant tube diameter. For

crossflow on tube banks, this directly results from (5.25) and (5.27) if it can be assumed that  $\alpha$  increases at increasing Reynolds number while the tube length  $l_{TB}$  remains unchanged. For tubular flow, the same result can be obtained from an insertion of the relation  $Re \sim \alpha \cdot l$  according to (5.16) into (5.26) and (5.28) if additionally the number of passes  $N_p$  remains unchanged.

## 5.2.5 Power-law relations for different configurations and regimes

For simplification, only flow inside smooth tubes and flow across staggered arrangements have been considered. Variation of tube pitch ratios and fin geometry is also not included; tube bundles are assumed to have a large number of rows of tubes and a large number of tubes per row. The respective values for  $NNU$  and  $NZ$  have been extracted from the correlations given in 4.3 and 4.4 as described below in detail.

### Fluid flow inside circular tubes

Correlations for the Nusselt number and friction factor are dependent on the flow regime. Flow characteristics in the transition region  $2300 < Re < 10^4$  are not completely predictable, therefore an optimum can be looked for either in the laminar regime  $Re < 2300$  or in the turbulent regime  $Re \geq 10^4$ .

#### Laminar flow regime

For the laminar friction factor, from (4.37) the simple relation  $\zeta \sim Re^{-1}$  can be obtained, i.e.  $NZ = -1$ . The mean Nusselt number at constant wall temperature in a circular tube of finite length is given by the rather complex correlation (4.24). It shows, however, that for small values of  $Re \cdot Pr \cdot d_i/l \sim \dot{m} \cdot d_i^2/l$ , i.e. for slow flow velocities, small diameter tubes and long tubes compared to the tube diameter the Nusselt number approaches a constant value  $Nu = const.$ , i.e.  $NNU = 0$ .

Even for high values of  $Re \cdot Pr \cdot d_i/l$  the Nusselt number is only weakly dependent on the Reynolds number never exceeding the asymptotic limit  $Nu \sim (Re \cdot d_i/l)^{1/2}$ . For fixed leaving temperature, the tube length has to be chosen appropriately as given by (5.4). This results in the asymptotic relation  $Nu \sim Nu^{1/2}$  and thus again  $Nu = const.$ , i.e.  $NNU = 0$ .

#### Turbulent flow regime

For turbulent flow of fluids with low Prandtl numbers (e.g. air or flue gas) in reasonable long tubes, from the approximations (4.30) or (4.31) a main dependency of the Nusselt number on the Reynolds number  $Nu \sim Re^{0.8}$  can be extracted. However, this is an oversimplification and the resulting value  $NNU \approx 0.8$  is only good for rough estimations.

A rather complex dependence of the turbulent friction factor on the Reynolds number and the surface roughness is given by (4.38). However, increased roughness implies increased



pressure drop without increasing the heat transfer coefficient, too. Therefore, an optimization must be heading for minimized roughness. For smooth tubes and moderate Reynolds numbers  $3000 \leq Re \leq 100\,000$  from (4.39) again a simple relation for the friction factor  $\zeta \sim Re^{-1/4}$  can be derived, i.e.  $NZ = -0.25$ .

### Additional frictional pressure drops at tube inlet and outlet

According to (5.20) the frictional pressured drop inside tubes follows the relation  $\Delta p_{FR} \sim d^{-2} \cdot Re^{3+NZ-NNU}$ . From the above given values of  $NNU$  and  $NZ$  it shows that the exponent on the Reynolds number is  $3+NZ-NNU = 2$  in laminar flow and  $3+NZ-NNU \approx 1.95$  in turbulent flow respectively. An exponent on the Reynolds number with the value of 2 results also from (5.6) for the inlet and outlet pressure drop if the sum of the inlet and outlet friction factors in  $\Delta p_{IN} + \Delta p_{OUT} \sim (\zeta_{IN} + \zeta_{OUT}) \cdot d_i^{-2} \cdot Re^2$  is nearly constant  $\zeta_{IN} + \zeta_{OUT} \approx const.$

Thus, as long as the shape of the tube inlet and outlet and the number of passes are not varied, both pressure drop terms follow about the same proportional dependency  $\sim d^{-2} \cdot Re^2$ . In this case, the inlet and outlet pressure drops  $\Delta p_{IN} + \Delta p_{OUT}$  could be considered by a constant factor on the frictional pressure drop  $\Delta p_{FR}$  for tubular flow. The relations (5.19) to (5.24) derived above and all conclusions drawn from these relations remain valid.

### Fluid flow across tube bundles

For sufficiently big arrangements of finned tubes, from (4.64) a simple relation for the Nusselt number  $Nu \sim Re^{0.6}$  can be isolated. For plain tubes according to (4.56), (4.57), and (4.58), there is a rather complex dependency for the Nusselt number and the respective exponent  $NNU$  on the Reynolds number varies from about 0.5 at low Reynolds numbers and laminar flow to about 0.8 for high Reynolds numbers and turbulent flow.

For the friction factor of finned arrangements from (4.82) and Tab. 8 the relations  $\zeta \sim Re^{-0.75}$  for laminar flow at  $10^2 \leq Re \leq 10^3$ , and  $\zeta \sim Re^{-0.25}$  for turbulent flow at  $10^3 \leq Re \leq 10^5$  can be obtained. For plain tubes the dependencies according to (4.70), (4.71), and (4.75) again are more complex. However, for the limiting cases of low and high Reynolds numbers exponents  $NZ$  of about  $-1$  and  $-0.25$  can be extracted.

## 5.2.6 Overview and discussion of the resulting relations

Tab. 15 gives an overview on exponents  $NNU$  and  $NZ$  and according approximate relations for heat transfer coefficient, pressure drop, tube length, and number of rows of tubes for different configurations and flow regimes.

For all cases listed in Tab. 15 the exponent  $3/2 \cdot NNU - 1/2 \cdot NZ - 3/2$  in (5.24) is negative. Therefore, optimized configurations in terms of high heat transfer coefficient, low pressure drop, and small surface area have to be looked for at low Reynolds numbers rather than at

high Reynolds numbers. However, some constraints have to be considered. First, in practical designs there is a lower limit for the flue gas mass flux density as the total cross section of the flue gas channel is limited. Second, there is a lower limit for the tube diameter as for reasonable corrosion durability in hot salt solution a certain thickness of tube walls of about 2...3 mm is required. Besides, for easy welding also a minimum wall thickness and a minimum tube diameter are required. Therefore, tube outer diameters significantly below 10 mm or tube inner diameters significantly below 5 mm are not of much relevance for such boiler designs. Consequently, there always is a practical lower limit for the Reynolds number. Additionally, relation (5.23) suggested that any heat transfer coefficient could be achieved at any Reynolds number if only the tube diameter was chosen small enough. In practice, this is also limited by the feasible range of diameters.

| Configuration & flow regime     | NNU           | NZ              | 3/2·NNU<br>-1/2·NZ<br>-3/2 | $\alpha$  | $\Delta p_{FR}$  | $l, N_{TB,LO}$                                   |
|---------------------------------|---------------|-----------------|----------------------------|---|--|--|
| <b>flow inside tubes</b>        |               |                 |                            |   |  |  |
| lam., $Re \leq 2300$            | 0             | -1              | -1                         | $\sim d_i^{-1}$<br>$\sim d_i^{-1} \cdot Re^0$   | $\sim \dot{m}^2$<br>$\sim d_i^{-2} \cdot Re^2$   | $l \sim \dot{m} \cdot d_i^2$                     |
| turb., $10^4 \leq Re \leq 10^5$ | $\approx 0.8$ | -0.25           | $\approx -0.175$           | $\left( \begin{array}{l} \sim \dot{m}^{0.8} \cdot d_i^{-0.2} \\ \sim d_i^{-1} \cdot Re^{0.8} \end{array} \right)$ | $\left( \begin{array}{l} \sim \dot{m}^{1.95} \cdot d_i^{-0.05} \\ \sim d_i^{-2} \cdot Re^{1.95} \end{array} \right)$ | $(l \sim \dot{m}^{0.2} \cdot d_i^{1.2})$         |
| <b>flow across plain tubes</b>  |               |                 |                            |   |  |  |
| lam., low Re                    | $\approx 0.5$ | $\approx -1$    | $\approx -0.25$            | $\left( \begin{array}{l} \sim \dot{m}^{0.5} \cdot d_o^{-0.5} \\ \sim d_o^{-1} \cdot Re^{0.5} \end{array} \right)$ | $\left( \begin{array}{l} \sim \dot{m}^{1.5} \cdot d_o^{-0.5} \\ \sim d_o^{-2} \cdot Re^{1.5} \end{array} \right)$    | $(N_{TB,LO} \sim \dot{m}^{0.5} \cdot d_o^{0.5})$ |
| turb., high Re                  | $\approx 0.8$ | $\approx -0.25$ | $\approx -0.175$           | $\left( \begin{array}{l} \sim \dot{m}^{0.8} \cdot d_o^{-0.2} \\ \sim d_o^{-1} \cdot Re^{0.8} \end{array} \right)$ | $\left( \begin{array}{l} \sim \dot{m}^{1.95} \cdot d_o^{-0.05} \\ \sim d_o^{-2} \cdot Re^{1.95} \end{array} \right)$ | $(N_{TB,LO} \sim \dot{m}^{0.2} \cdot d_o^{0.3})$ |
| <b>flow across finned tubes</b> |               |                 |                            |   |  |  |
| lam., $10^2 \leq Re \leq 10^3$  | 0.6           | -0.75           | -0.225                     | $\sim \dot{m}^{0.6} \cdot d_o^{-0.4}$<br>$\sim d_o^{-1} \cdot Re^{0.6}$   | $\sim \dot{m}^{1.7} \cdot d_o^{-0.3}$<br>$\sim d_o^{-2} \cdot Re^{1.65}$   | $N_{TB,LO} \sim \dot{m}^{0.4} \cdot d_o^{0.4}$   |
| turb., $10^3 \leq Re \leq 10^5$ | 0.6           | -0.25           | -0.475                     | $\sim \dot{m}^{0.6} \cdot d_o^{-0.4}$<br>$\sim d_o^{-1} \cdot Re^{0.6}$   | $\sim \dot{m}^{2.15} \cdot d_o^{0.15}$<br>$\sim d_o^{-2} \cdot Re^{2.15}$  | $N_{TB,LO} \sim \dot{m}^{0.4} \cdot d_o^{0.4}$   |

**Tab. 15: Approximate relations for heat transfer and pressure drop.**  
Formulations in parentheses are only rough estimations, however.

On the other hand, it has already been shown in 5.2.4 that both length and number of the required weld seams for welding the tubes into the tube sheets increase for decreasing Reynolds numbers. For crossflow on tube banks, this might be partially compensated for as a reduction of the tube diameter reduces the length of the weld seams in these configurations; in tubular flow designs smaller tube diameters even may further increase the number

of weld seams. However, the welding effort is also dependent on the length of the tubes and the number of passes, therefore no final conclusion on the most economical design can be given on the basis on these basic relations.

Additional constraints result from relations (5.21) and (5.22), as  $NNU < 1$  and thus the exponent on the Reynolds number are positive in both cases. For tubular flow, according to (5.21) the tube length reduces with decreasing Reynolds number and decreasing tube diameter. However, a lower limit for the tube length results from the fact that the tubes have to be installed in a boiler vessel that has to keep reasonable proportions of length vs. width vs. height. For cross flow in tube bundles, according to (5.22) the number of rows of tubes reduces with decreasing Reynolds number. The relations in Tab. 15, however, have been obtained for large number of rows of tubes. For less than about five consecutive rows, lower heat transfer coefficients and higher pressure drops are obtained from the respective correlations listed in 4.4. These boundary effects also provide an effective lower limit for the Reynolds number. Besides the ratio between the number of tubes counted in longitudinal direction and vs. transversal direction with respect to the gas flow,  $N_{TB,LO}$  vs.  $N_{TB,TR}$  has also to keep reasonable proportions.

Finally, the validity range of the individual relations listed in Tab. 15 has to be taken into account. This is especially important for turbulent flow inside tubes as heat transfer and pressure drop are not completely predictable in the range  $2\,300 < Re < 10\,000$ . Therefore the optimum design for tubular flow is either exactly  $Re = 10\,000$  comprising the lowest possible Reynolds number in turbulent flow regime or the combination of the smallest possible tube diameter and the lowest acceptable flow density in laminar flow regime. Which one is the best choice is dependent on the actual boundary conditions.

### 5.3 Numerical determination of promising configurations

To identify preferable heat exchanger designs taking into account all the additional constraints discussed above, a numerical parameter study for real boundary conditions has been performed.

#### 5.3.1 Method

It has been shown in general for all considered designs in 5.2 that for variation of tube diameter and gas flow rate at given temperatures the quotient of mean convective heat transfer coefficient and square root of frictional pressure drop  $\alpha/\Delta p_{FR}^{1/2}$  at the flue gas side is just a function of the Reynolds number of the flue gas. It has also been shown that this quotient increases at decreasing Reynolds numbers for all designs employing approximate relations for laminar and turbulent flow regime. Therefore, the configuration with the lowest Reynolds number is the most preferable one as long as all design parameters show reasonable values and all boundary conditions are sufficiently fulfilled.

To identify the optimal heat exchanger design for given boundary conditions, the minimum possible Reynolds number has to be determined for each design and the values  $\alpha/\Delta p_{FR}^{1/2}$  obtained at this points have to be compared. The design with the highest value then will grant the best possible heat transfer coefficient at an allowed pressure drop or alternatively the lowest possible pressure drop at a required heat transfer coefficient. This procedure is outlined below for more or less typical conditions in flue gas fired regenerators of double-effect absorption chillers, considering either direct firing or firing by exhaust gas of motor engines. Tube diameter and mass flux density have been varied for all three configurations: flue gas flow inside tubes, flue gas flow across plain tube bundles, and flue gas flow across finned tube bundles. For flue gas flow across tube bundles, variation of the tube pitch ratio has been considered as additional parameter assuming identical tube pitch in longitudinal and transversal direction.

Calculations have been based on the heat transfer and pressure drop correlations according to *VDI-GVC (2002)* (summarized in 4.3 and 4.4) utilizing property data for flue gas from stoichiometric combustion of natural gas according to *Rhine & Tucker (1991)*. A constant tube wall temperature at the flue gas side of  $T_{w,G} = 170^\circ\text{C}$  has been assumed. As a simplification, only mean values of all numbers for the total heat exchanger have been calculated utilizing property data at the mean flue gas temperature. Yet, for turbulent flue gas flow inside tubes, the correction factor (4.35) with exponent  $N = 0.36$  according to *Spang (2004)* was employed.

### 5.3.2 Basic assumptions

Tab. 16 summarizes the general assumptions and boundary conditions employed for the comparison of the different heat exchanger designs. For regenerators fired by motor engine exhaust gas an entering exhaust gas temperature of  $500^{\circ}\text{C}$  and a leaving exhaust gas temperature of  $200^{\circ}\text{C}$  were assumed<sup>57</sup>. A maximum allowed pressure drop in the exhaust gas of  $10\dots 15\text{ mbar}$  was assumed as design limit for the high-temperature regenerator.

| General assumptions and boundary conditions for comparison of different designs | Regenerator fired by motor engine exhaust gas           | Direct-fired regenerator                          |
|---|---|---|
| Entering flue gas temperature   | $500^{\circ}\text{C}$                                   | $1000^{\circ}\text{C}$<br>(after furnace chamber) |
| Leaving flue gas temperature  | $200^{\circ}\text{C}$                                   | $200^{\circ}\text{C}$                             |
| Mean flue gas temperature in heat exchanger                                     | $350^{\circ}\text{C}$                                   | $600^{\circ}\text{C}$                             |
| Tube wall temperature (flue gas side) $T_{w,G}$                                 | $170^{\circ}\text{C}$                                   | $170^{\circ}\text{C}$                             |
| Log. mean temp. diff. (flue gas side) $LMTD_G$                                  | $125.1\text{ K}$  | $240.9\text{ K}$                                  |
| Max. allowed pressure drop at flue gas side (preferred design values)           | $10\dots 15\text{ mbar}$<br>( $5\dots 10\text{ mbar}$ ) | $5\text{ mbar}$<br>( $0.2\dots 5\text{ mbar}$ )   |

*Tab. 16: General assumptions and boundary conditions for comparison of different heat exchanger designs.*

In direct-fired regenerators, the heat transfer in the furnace chamber and/or the first section of the heat exchanger is dominated by radiation, dependent on the type of the burner. Therefore, only convective heat transfer at flue gas temperatures below  $1000^{\circ}\text{C}$  has been considered for the comparison of different heat exchanger concepts. In conventional flame-tube/smoke tube designs, this is about the temperature of the flue gas entering the smoke tubes. If the burner is equipped with a fan, the pressure drop on the flue gas side of the regenerator is only limited by the size of the fan. Standard burners, however, only allow for some  $\text{mbar}$  backpressure, therefore  $5\text{ mbar}$  pressure drop in the heat exchanger was assumed as design limit. For operation of atmospheric burners without fans, only pressure drops in the range of  $20\dots 50\text{ Pa}$  are acceptable.

For flue gas flow inside tubes, inlet and outlet pressure drops have been considered only in a simplified way without taking into account the dependency on e.g. the number of passes. For flue gas flow across tube bundles, however, entering and leaving pressure drop are already considered by the correlations used.

<sup>57</sup> These are more or less representative example values for utilization of exhaust gas of motor engines or gas turbines; actually available exhaust gas temperatures may vary from about  $400^{\circ}\text{C}$  to  $600^{\circ}\text{C}$  depending on the selected engine.

Tab. 17 provides the variation of all design parameters taken into consideration for the optimization of the individual designs. For heat exchanger designs with flue gas flow inside tubes, a variation range of the tube inner diameter from at least 5 mm to about 150 mm was assumed feasible without difficulties. For flue gas flow across bundles of plain or finned tubes, a variation of the tube outer diameter from 10 mm to 100 mm was investigated. Assuming a wall thickness of about 2.5 mm for regenerator tubes, effectively the same lower limit for the tube outer diameter was set for comparison of all designs.

| Parameter variation for different designs  |                                    | Flue gas flow inside tubes                             | Flue gas flow across plain tube bundle                   | Flue gas flow across finned tube bundle                  |
|--|------------------------------------|--|--|--|
| <b>Tube geometry</b>   |                                    |  |  |  |
| Tube inner diameter  | $d_i$                              | 5...150 mm   |  |  |
| Tube outer diameter  | $d_o$                              |  | 10...100 mm  | 10...100 mm  |
| Tube wall thickness  | $(d_o - d_i) / 2$                  | 2.5 mm   |  |  |
| <b>Bundle geometry</b>   |                                    |  |  |  |
| Tube pitch ratios  | $y_{TR} = y_{LO}$                  |  | 1.4, 1.6   | 1.6, 2.0   |
| <b>Fin geometry</b>  |                                    |  |  |  |
| Fin pitch ratio  | $y_F = Y_F / d_o$                  |  |  | 0.15   |
| Fin thickness ratio  | $t_F = T_F / d_o$                  |  |  | 0.02   |
| Fin thermal conductivity <sup>58</sup>   | $\lambda_F$                        |  |  | 300 W/m·K  |
| Surf. enhancement factor   | $\beta_F = A_{TOT} / A_{PLAIN}$    |  | 1  | 6.3, 11.1  |
| <b>Overall heat exchanger size</b>   |                                    |  |  |  |
| Capacity per total cross section of all smoke tubes in each pass (Optional: very small cap.) | $\dot{Q} / A_{CS}$                 | $\geq 1 \text{ MW/m}^2$<br>$(\geq 400 \text{ kW/m}^2)$ |  |  |
| Capacity per free cross section of the flue gas channel (Optional: very small cap.)          | $\dot{Q} / A_{FC}$                 |  | $\geq 500 \text{ kW/m}^2$<br>$(\geq 200 \text{ kW/m}^2)$ | $\geq 500 \text{ kW/m}^2$<br>$(\geq 200 \text{ kW/m}^2)$ |
| Tb. length in flow direction   | $l$                                | 0.3...15 m   |  |  |
| Tube rows in flow direction  | $N_{TB,LO}$                        |  | $\geq 5$   | $\geq 5$   |
| Bundle length in flow dir.   | $N_{TB,LO} \cdot y_{LO} \cdot d_o$ |  | $\leq 3 \text{ m}$                                       | $\leq 3 \text{ m}$                                       |

Tab. 17: Parameter variation considered for comparison of different designs.

For plain tube bundles, tube pitch ratios from 1.4 to 1.6 and for finned bundles, values of 1.6 and 2.0 were selected. In the latter case, the fin height was chosen accordingly in a way that fins of neighboring tubes just would not overlap. As the heat transfer and pressure drop

<sup>58</sup> Assuming technical copper as fin material.

correlations provided by *VDI-GVC (2002)* have a limited range of validity, an independent variation of the fin pitch was not possible. Therefore, only a fin pitch ratio of *0.15* and resulting surface enhancement factors of *6.3* and *11.1* have been considered.

No general limits for the heat exchanger dimensions can be given either in absolute or in specific numbers that are valid for the full range of possible capacities. Nevertheless, for big units a compact design might be much more crucial than for smaller ones as e.g. the inner dimensions of a standard container (*5.9 m x 2.3 m x 2.4 m*) provide some “natural” limit. In the following calculations for flue gas inside tubes, a minimum tube length of *0.3 m* and a maximum tube length of *15 m* (e.g. three consecutive passes of *5 m* tubes each) were assumed as limits. However, short tubes of one meter or less mainly are an option for small capacities (e.g. *10...50 kW*) while individual tube lengths of more than three meters are of interest if at least some hundred kilowatts heat duty are transferred in a single device.

For tube bundles, a maximum length in flow direction of *3 m* and a minimum length of five consecutive rows<sup>59</sup> were considered. It has been shown above in 5.2 that low Reynolds numbers and thus low mass flux densities in the flue gas may be advantageous. On the other hand, the total cross section of flue gas channels or vessels will always be limited in practical designs; even for big units cross-sectional areas of more than *2...3 m<sup>2</sup>* might be hard to integrate. For pool boilers with immersed tube bundle, the total inner cross section of all smoke tubes will hardly cover more than half of the cross section of the vessel, and even less, if tubes of small diameter and significant wall thickness are employed. Therefore, a minimum heat duty of *1 MW/m<sup>2</sup>* tubes inner cross section was chosen as lower limit for the mass flux density inside tubes in medium sized units. As an option, for small capacities (e.g. *10...50 kW*) also specific heat duties down to *400 kW/m<sup>2</sup>* have been investigated. For flue gas flow across tube bundles, minimum heat duties of *500 kW/m<sup>2</sup>* with reference to the total cross section of a free channel and optionally *200 kW/m<sup>2</sup>* for small capacities have been assumed. Yet, these values are slightly more strict limitations than the latter ones for the conventional design of gas flow inside tubes.

---

<sup>59</sup> Very “short” tube bundles with only a couple of consecutive rows do not only show a lower heat transfer coefficient (because of the reduced turbulence) and a higher friction factor (because entering and leaving pressure drops become more dominant) than “long” bundles, they also lead to quite unconventional geometry of the regenerator.

### 5.3.3 Calculation results for exhaust-fired regenerators

According to the specifications in Tab. 16, in all diagrams below it is assumed that exhaust gas enters a heat exchanger at  $500^{\circ}\text{C}$  and leaves the heat exchanger again at  $200^{\circ}\text{C}$ , while the wall temperature at the gas side is  $170^{\circ}\text{C}$ . The required length of the tubes (in case of gas flow inside tubes) or the required number of consecutive rows of tubes (in case of gas flow across tube banks) were calculated accordingly. For exhaust gas flow across tube banks, however, the number of consecutive rows of tubes was always rounded up to yield the smallest integer number of rows of tubes that resulted in a leaving flue gas temperature of  $200^{\circ}\text{C}$  or less.

#### Variation of tube diameter and Reynolds number

Fig. 42 shows the mean convective heat transfer coefficient (bold orange lines) and the frictional pressure drop (thin blue lines) in dependence on tube diameter and Reynolds number at the flue gas side for boiler designs with gas flow inside tubes. The approximate values of heat transfer coefficient and pressure drop in the transition region  $2\,300 < Re < 10\,000$  obtained from interpolation formulas are shown as dashed lines.

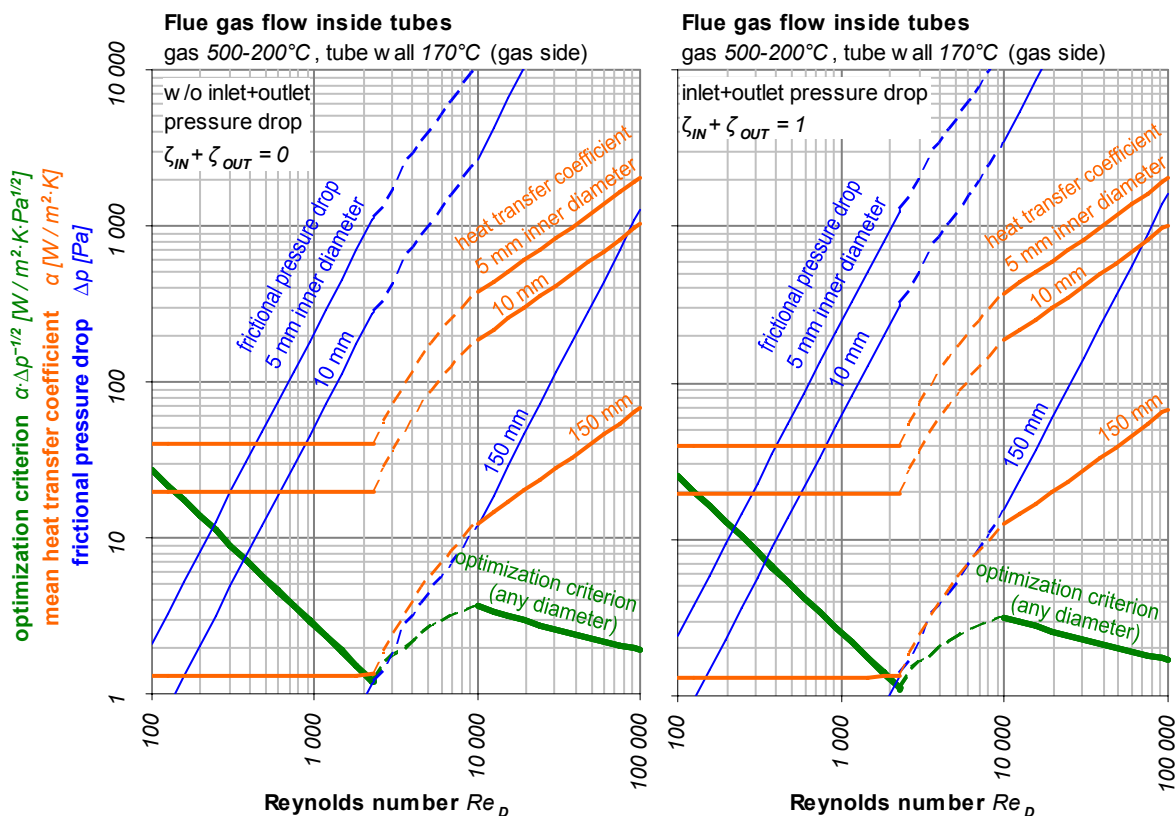


**Fig. 42: Mean convective heat transfer coefficient and frictional pressure drop at the flue gas side of boilers with gas flow inside tubes as functions of inner diameter and Reynolds number.**

Mean heat transfer coefficients as bold orange lines, frictional pressure drops as thin blue lines, and quotient of heat transfer coefficient and square root of the pressure drop (“optimization criterion”) as extra bold green lines over the Reynolds number. Dashed lines denote interpolations for the transition region  $2300 < Re < 10000$ . Numerical results without taking into account inlet and outlet pressure drops (left graph) and with assumption of constant friction factors for inlet and outlet (right graph).



In the left diagram, only the frictional pressure drop inside the tubes was taken into account, while in the right diagram, additional inlet and outlet pressure drops have been considered. In the latter case, inlet and outlet friction factors of about  $\zeta_{IN} + \zeta_{OUT} = 1$  were assumed; this order of magnitude can be expected in bundles with 1...3 passes – depending on the actual geometry and shape of the tube ends. A comparison of the both graphs in Fig. 42 shows that inlet and outlet pressure drops are only a minor share of the total frictional pressure drop in the gas flow. Therefore, the variation of the number of passes has not been investigated further as additional influencing variable. In all other diagrams for tubular flow designs given below, the approximation  $\zeta_{IN} + \zeta_{OUT} = 1$  was employed.

Instead of the approximate relations (5.17) and (5.18) for heat transfer and pressure drop, which were employed for the formal deduction of (5.24), best available correlations according to *VDI-GVC (2002)* have been employed for generation of the graphs in Fig. 42. Yet, it shows that the quotient of heat transfer coefficient and square root of the frictional pressure drop (extrabold **green** line) remains a function of the Reynolds number only  $\frac{\alpha}{\Delta p_{FR}}^{1/2} = f(Re)$  without extra dependency on the tube diameter. As anticipated (cf. Tab. 15), the slope of this line is negative in both the laminar and the fully turbulent regime.

In the transition region  $2\,300 < Re < 10\,000$ , in both diagrams in Fig. 42 the dashed green line has a positive slope resulting in a local maximum at  $Re = 10\,000$ . It has to be noted however, that the position where a maximum of the quotient  $\frac{\alpha}{\Delta p_{FR}}^{1/2}$  can be found depends on the employed interpolation formulas for the region  $2\,300 < Re < 10\,000$ . Strictly speaking, it only can be concluded that the quotient  $\frac{\alpha}{\Delta p_{FR}}^{1/2}$  has to show a local maximum at some Reynolds number in the range  $2\,300 < Re \leq 10\,000$ .

Respective graphs for gas flow across tube banks, showing again the heat transfer coefficient (bold **orange** lines) and the frictional pressure drop (thin **blue** lines) in dependence on tube diameter and Reynolds number are given in Fig. 43. The left diagram shows the results obtained for bundles of plain tubes, the right diagram provides the values for bundles of finned tubes; in both cases staggered arrangement and the same tube pitch ratios  $y_{TR} = y_{LO} = 1.6$  were assumed. For finned tube bundles, the limited thermal conductivity of the fins has already been taken into account in this calculation; therefore, the mean virtual heat transfer coefficient  $\eta_F \cdot \alpha$  incorporating realistic fin efficiency<sup>60</sup> is displayed in the right diagram in Fig. 43.

<sup>60</sup> Calculations showed however that for the assumed copper fins with relative thickness  $T_F/d_o = 0.02$  the fin efficiency  $\eta_F$  was at least 70% at all calculated data points. At realistic operational states (see discussion below), the fin efficiency even exceeded 80%. Therefore, it can be concluded that at least for the application of copper fins the fin efficiency has only a minor impact on the heat transfer. Thus, the variation of the fin thickness was not investigated as additional free parameter.

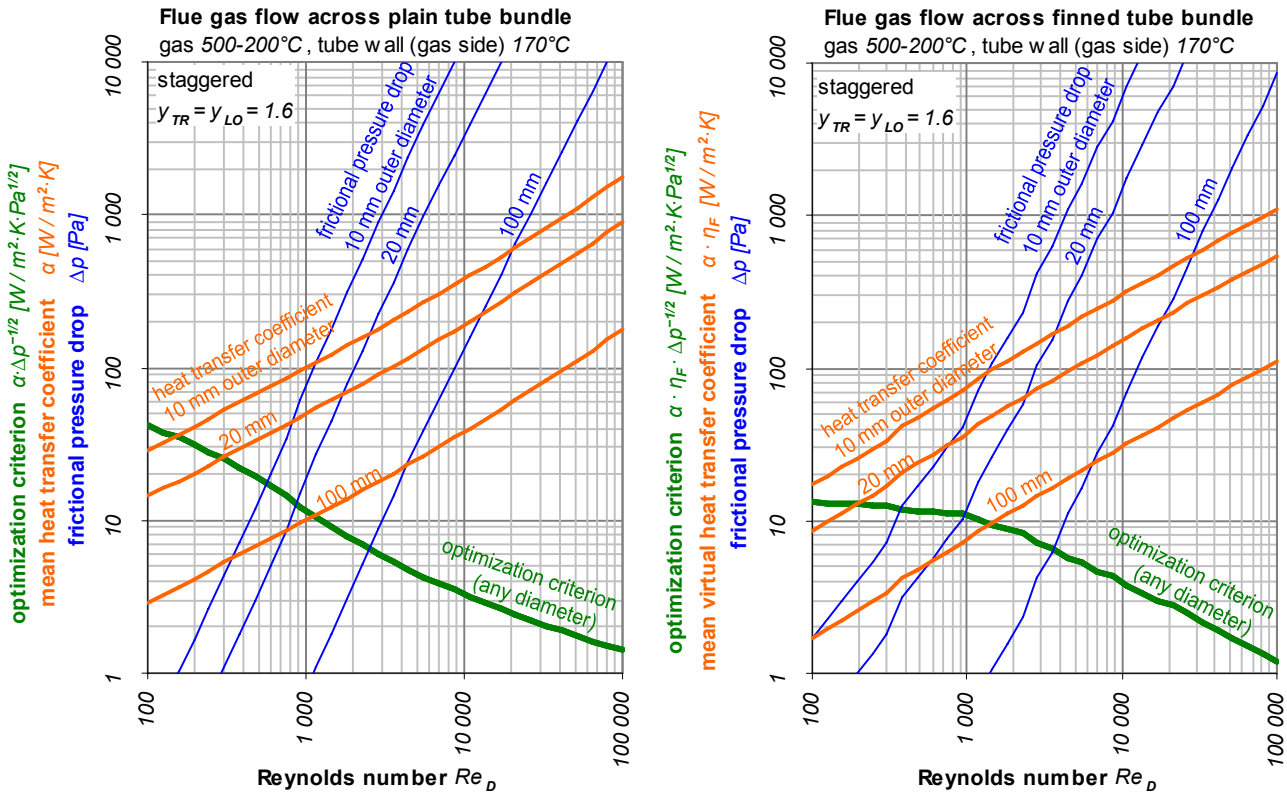


Fig. 43: Mean convective heat transfer coefficient and frictional pressure drop at the flue gas side of boilers with gas flow across tube banks as functions of outer diameter and Reynolds number.

Mean heat transfer coefficients as bold orange lines, frictional pressure drops as thin blue lines, and quotient of heat transfer coefficient and square root of the pressure drop (“optimization criterion”) as extra bold green lines over the Reynolds number. Numerical results for banks of plain tubes (left graph) and for banks of finned tubes (right graph).

In the right diagram in Fig. 43, the frictional pressure drops for selected tube diameter (thin blue lines) show a slightly “wavy” shape at smaller Reynolds numbers. The reason is that for the determination of the pressure drop at each data point the required number of rows of tubes to reach the desired flue gas outlet temperature was rounded up to obtain an integer number of rows of tubes. This produces some nonlinearity in the pressure drop vs. the Reynolds number relation, which becomes significant and visible at short bundles with only a few consecutive rows of tubes.

Fig. 43 confirms that also for cross flow on tube banks the quotient of heat transfer coefficient and square root of the frictional pressure drop (extra bold green line) remains a function of the Reynolds number only without extra dependency on the tube diameter. As anticipated (cf. Tab. 15), the slope of this line is not constant but always negative over the full range of Reynolds numbers.

A comparison of the extra bold green lines (“optimization criterion”) in the diagrams of Fig. 42 and Fig. 43 reveals that quite similar values for the ratio of heat transfer coefficient and square root of the pressure drop of  $3 \dots 4 \text{ W/m}^2 \text{ K} \cdot \text{Pa}^{1/2}$  are found around  $Re = 10\,000$  for all configurations. While this ratio drops again for tubular flow at Reynolds numbers below

10 000, it shows a quite similar behavior for both for gas flow across plain and finned bundles in the region  $1000 \leq Re \leq 10\,000$  reaching a value of about  $10 \text{ W/m}^2\text{K}\cdot\text{Pa}^{1/2}$  at  $Re = 1000$ . At even lower Reynolds numbers in the range  $100 \leq Re \leq 1000$  the highest values for the ratio of heat transfer coefficient and square root of the pressure drop are found for cross flow on plain tube bundles.

### Application of all boundary conditions

Out of all the boundary conditions for the parameter variation listed in Tab. 16 and Tab. 17, only the minimum and maximum tube diameters have been considered so far in the graphs in Fig. 42 and Fig. 43 above. The full set of constraints on the feasible range of Reynolds numbers and heat transfer coefficients in tubular flow arrangements – maximum allowed pressure drop, minimum and maximum tube lengths, and minimum specific capacity per cross section – given in Tab. 16 and Tab. 17 is visualized in the left diagram in Fig. 44 below.

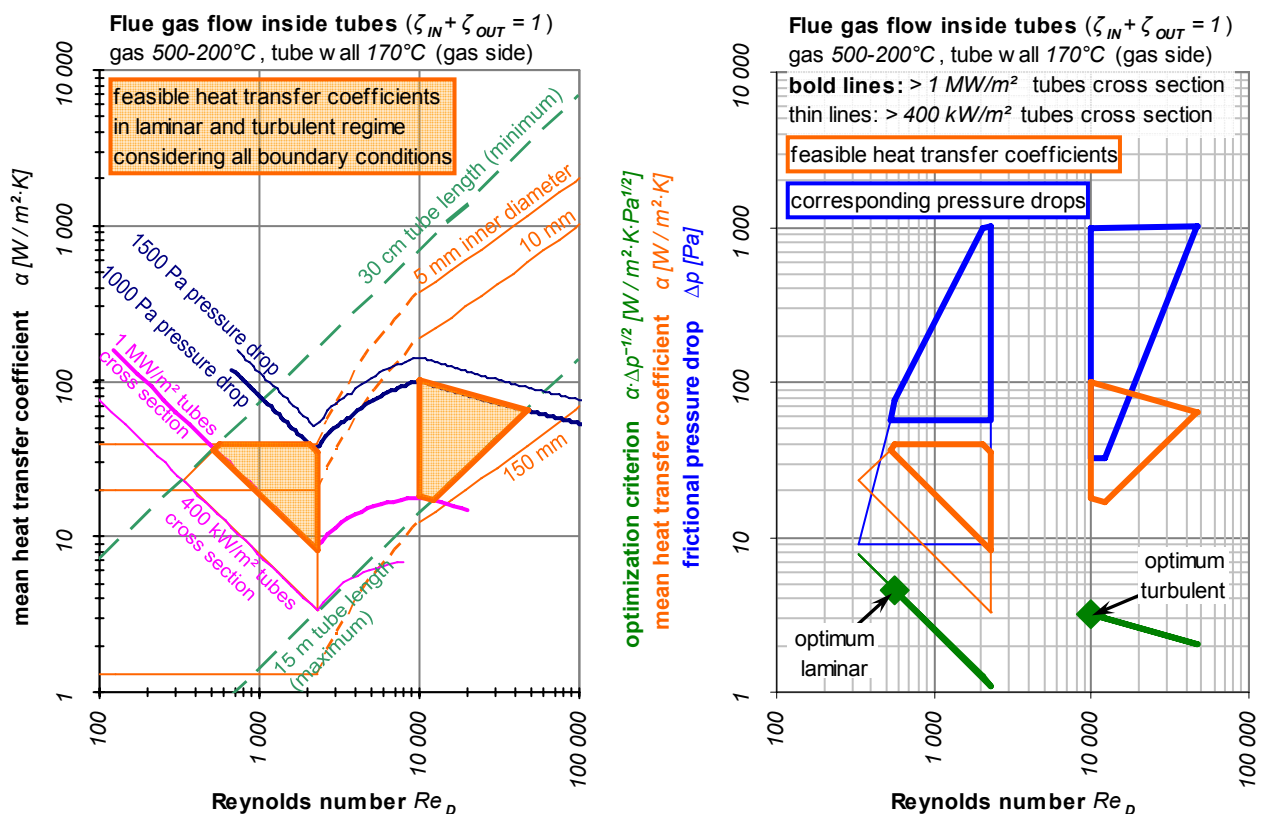


**Fig. 44: Feasible Reynolds numbers, heat transfer coefficients and pressure drops at the flue gas side of boilers with gas flow inside tubes.**

The left diagram visualizes the limitations on heat transfer coefficient and Reynolds number from the individual boundary conditions listed in Tab. 16 and Tab. 17. The right diagram displays the resulting ranges of feasible heat transfer coefficients (orange-bordered areas) and pressure drops (blue-bordered areas) together with the corresponding values of the “optimization criterion” (green lines) in the fully laminar and the fully turbulent region.

The remaining ranges of feasible heat transfer coefficients (orange-bordered areas) and pressure drops (blue-bordered areas) in fully laminar and fully turbulent regime are marked in the right diagram in Fig. 44. Thick borderlines denote the range of configurations with

specific capacities  $\dot{Q}/A_{cs} \geq 1 \text{ MW/m}^2$  while thin borderlines mark additional configurations with  $\dot{Q}/A_{cs} \geq 400 \text{ kW/m}^2$ , which are still an option for smaller units. For all possible configurations, the quotient of heat transfer coefficient and square root of the pressure drop is again shown in **green**. In both fully developed flow regimes, **green** squares indicate the optimum configurations where highest heat transfer coefficients and lowest pressure drops can be achieved.

It finally shows from the right diagram in Fig. 44, that in heat exchanger designs with flue gas flow inside the boiler tubes mean heat transfer coefficients up to approx.  $100 \text{ W/m}^2\text{K}$  can be realized at the quoted boundary conditions.

The corresponding diagrams on boundary conditions and feasible design values for heat exchangers with flue gas flow across tube banks of staggered arrangement are provided in Fig. 45. The upper diagrams in Fig. 45 show the results for banks of plain tubes while the lower two diagrams provide the numerical results for finned banks. Again, the left diagrams visualize the constraints on heat transfer coefficients and Reynolds numbers resulting from the individual boundary conditions given in Tab. 16 and Tab. 17; the right diagrams show the range of feasible heat transfer coefficients (**orange**-bordered areas), pressure drops (**blue**-bordered areas), and corresponding values of the “optimization criterion” (**green** lines).

Instead of a minimum tube length (cf. left diagram in Fig. 44), a minimum number of rows of tubes  $N_{TB,LO} \geq 5$  was employed as respective boundary condition (cf. Tab. 17) for tube banks. Actually, this only affected finned tube bundles in this example (cf. lower left diagram in Fig. 45) as for plain tube bundles anyway much larger numbers of rows of tubes were obtained from the other boundary conditions. Configurations with the same number of rows of tubes show up as vertical lines of constant Reynolds number in the lower left diagram in Fig. 45 – as to be expected regarding (5.22).

It finally shows that for staggered arrangement and tube pitch ratios  $y_{TR} = y_{LO} = 1.6$  in both cases, gas flow across plain and finned tube banks, mean heat transfer coefficients up to approx.  $200 \text{ W/m}^2\text{K}$  can be realized. This is twice value obtained for gas flow inside tubes (cf. Fig. 44).

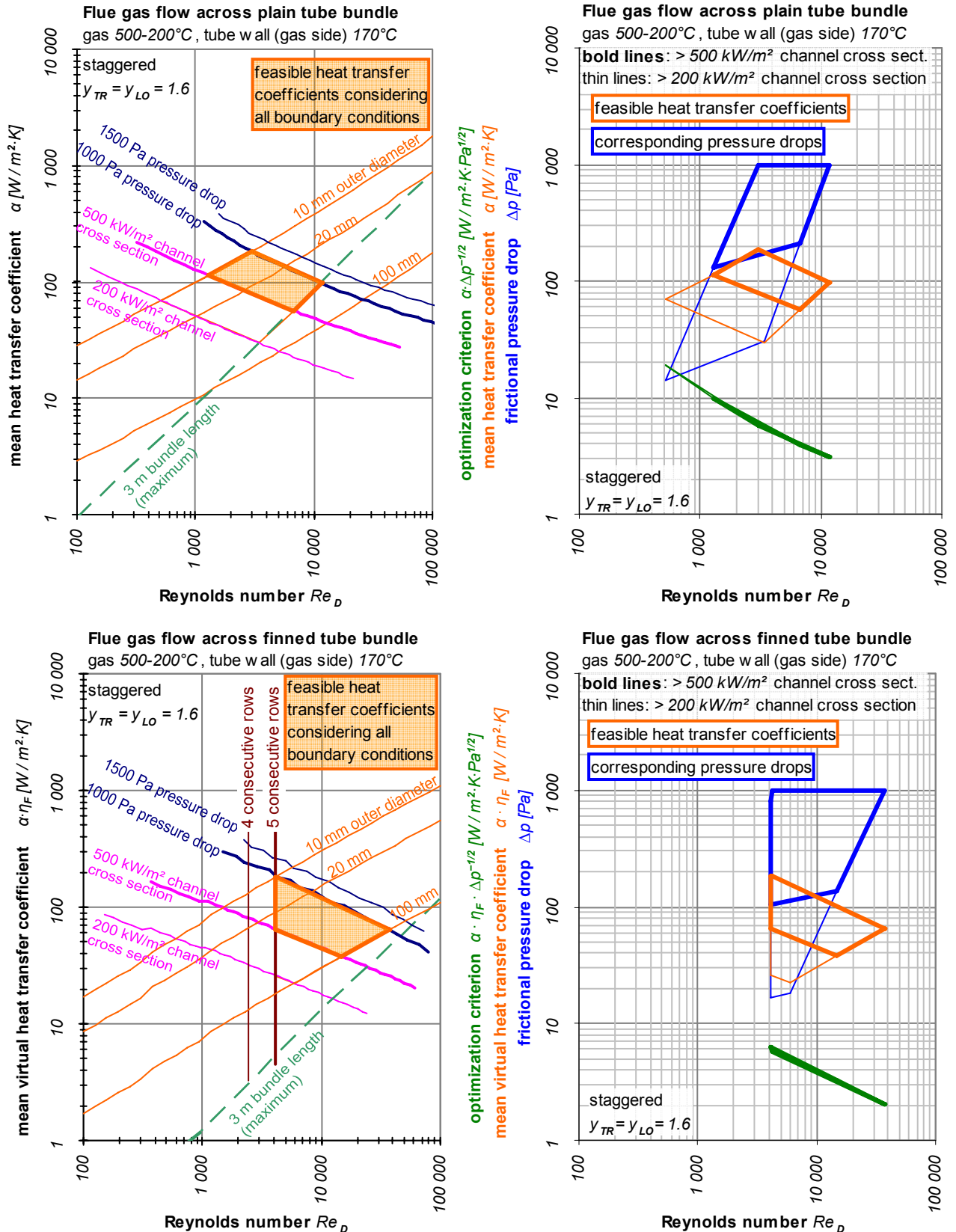


**Fig. 45: Feasible Reynolds numbers, heat transfer coefficients and pressure drops at the flue gas side of boilers with gas flow across plain (upper two diagrams) and finned (bottom two diagrams) tube bundles.** The left diagrams visualize the limitations on heat transfer coefficient and Reynolds number from the individual boundary conditions listed in Tab. 16 and Tab. 17. The right diagrams display the resulting ranges of feasible heat transfer coefficients (orange-bordered areas) and pressure drops (blue-bordered areas) together with the corresponding values of the “optimization criterion” (green lines).

### Normalization to outer surface of bare tubes

In the discussion above, feasible heat transfer coefficients  $\alpha$  in different kinds of heat exchangers have been compared that always had been defined based on the actual surface of the heat exchanger in contact with flue gas. This is the inner surface of the smoke tubes in pool boiler designs, the outer surface of the boiling tubes in designs with flue gas flow across plain tube bundles, and the total outer surface of the finned tubes in finned tube bundles.

Although physically sound, this approach does not lead to a fair comparison in terms of economics. In small diameter smoke tubes the wall thickness cannot be disregarded, therefore the actual size and weight of the heat exchanger as well as the length of the welding seams are rather related with the outer tube diameter and thus with the outer tube surface than with the inner diameter and surface. In finned tube bundles after all, size and weight of the heat exchanger and the length of the welding seams mainly scale with the outer surface of the bare tubes; the specific cost of the additional fin surface are much smaller than those of the bare tubes.

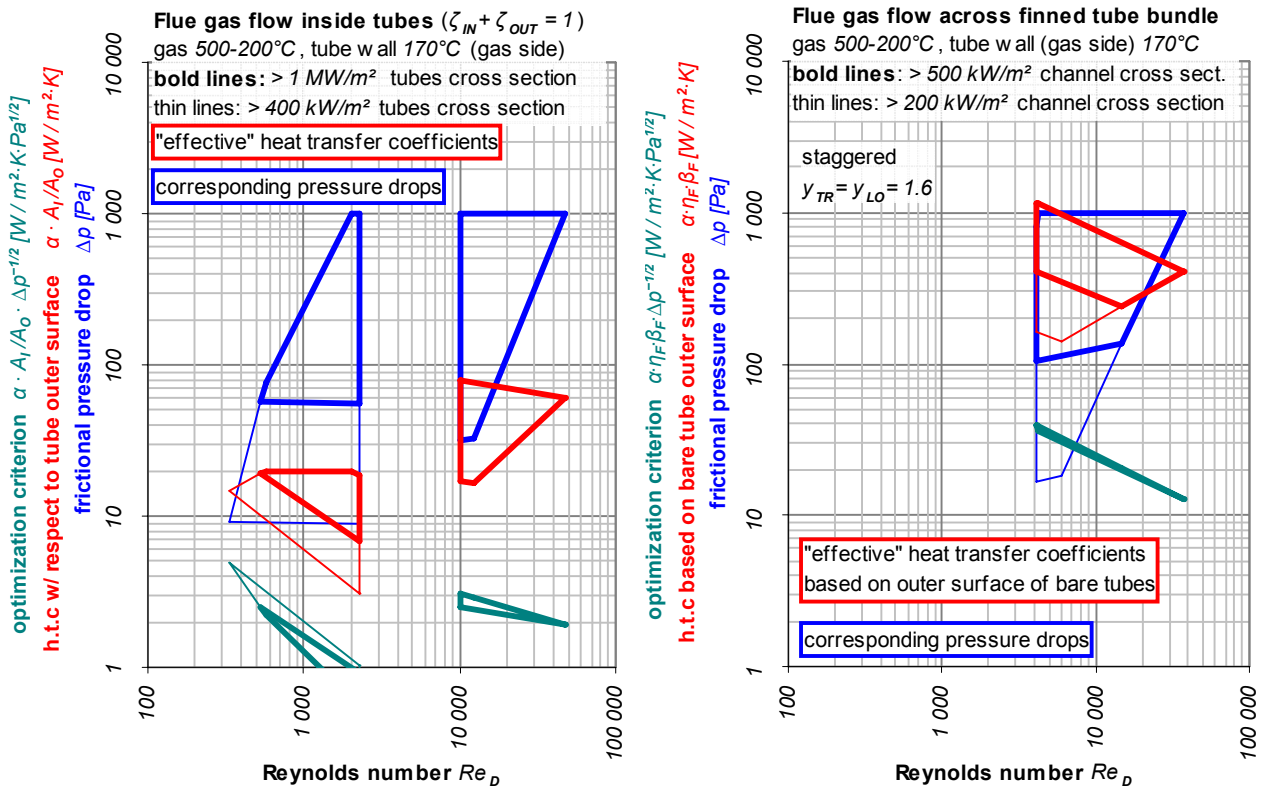


**Fig. 46:** Feasible “effective” heat transfer coefficients and corresponding pressure drops in dependence on the Reynolds number for gas flow inside tubes (left) and for gas flow across finned bundles (right). Feasible “effective” heat transfer coefficients calculated with respect to the outer surface of bare tubes as red-bordered areas, corresponding values for pressure drops as blue-bordered areas, quotients of “effective” heat transfer coefficient and square root of the pressure drop as teal-bordered areas.



This fact has been accounted for in Fig. 46, where “effective” heat transfer coefficients with respect to the outer surface of bare tubes are displayed (**red**-bordered areas) for both<sup>61</sup> heat exchangers with gas flow inside tubes (left diagram) and flue gas flow across finned tube bundles (right diagram). Hence, for tubular flow designs, the values of the expression<sup>62</sup>  $\alpha \cdot A_I/A_O = \alpha \cdot d_I/d_O$  have been plotted in Fig. 46 assuming a wall thickness of 2.5 mm (cf. Tab. 17); for finned tube bundles, the product of heat transfer coefficient, fin efficiency, and surface enhancement  $\alpha \cdot \eta_F \cdot \beta_F$  is plotted respectively. Finally, the values for the quotient of the respective “effective” heat transfer coefficient and the square root of the pressure drop are shown as **teal**-bordered areas in Fig. 46. As it can be seen in the left diagram, the resulting expression  $\alpha \cdot A_I/A_O \cdot \Delta p_{FR}^{-1/2}$  for gas flow inside tubes is no function of the Reynolds number only, however.

A comparison between the feasible heat transfer coefficients in tubular flow designs shown in Fig. 44 above and the range of “effective” heat transfer coefficients given in the left diagram in Fig. 46 reveals that the maximum heat transfer coefficient at  $Re = 10000$  drops only by 20% if the finite wall thickness is taken into account. Although at small tube diameters, which are most preferable in the fully laminar regime, the heat transfer coefficient is cut-half if it has to be related to the larger outer surface of the smoke tubes. Additionally, the values of the “optimization criterion” in the fully laminar regime drop below those in the fully turbulent regime if they are related to the outer surface area determining the actual size of the heat exchanger (cf. left diagram in Fig. 46). Hence, it can be concluded that laminar flow designs are no competitive option if a certain wall thickness is required for corrosion durability. For comparison with other heat exchanger types, a maximum “effective” heat transfer coefficient of about  $80 \text{ W/m}^2\text{K}$  with respect to the actual outer surface area of the heat exchanger tubes is a comparative figure that can be quoted for tubular flow designs.

A more detailed investigation of the impact of variations in the wall thickness is skipped here for brevity. It just shall be stated that the right diagram in Fig. 44 already shows the “effective” heat transfer coefficients for nearly zero wall thickness and that for tube walls in the range 0...2.5 mm all resulting values will be somewhere in between the limits set by the right diagram in Fig. 44 and the left diagram in Fig. 46.

For finned tube bundles, respective comparison of the lower right diagram in Fig. 45 (virtual heat transfer coefficients  $\alpha \cdot \eta_F$  related to the total outer surface) and the right diagram in Fig.

<sup>61</sup> Of course, the results for flue gas flow across plain tube bundles given in Fig. 45 are already based on the outer surface of plain tubes.

<sup>62</sup> This term is just a comparative figure with respect to economics (the outer surface area mainly determines size, weight, and cost of the heat exchanger); no physical meaning should be attributed to the expression  $\alpha \cdot A_I/A_O$  itself though.

46 (“effective” heat transfer coefficients  $\alpha \cdot \eta_F \cdot \beta_F$  based on the outer surface of bare tubes) just shows a shift by a constant offset in the logarithmic scale. Thanks to an approx. six-fold surface enhancement by the fins, “effective” heat transfer coefficients greater than  $1000 \text{ W/m}^2\text{K}$  can be achieved.

### Variation of bundle geometry

The theoretical analysis in 5.2 focused on generally valid relations between main variables in all kinds of heat exchangers subject to the discussion. Therefore, the additional impact of variations in tube arrangement and tube pitch ratios in tube banks in cross-flow was excluded from the discussion in 5.2 – assuming that that these parameters can be optimized more or less independently. Nevertheless, this approach has still to be justified by additional calculations.

Fig. 47 shows feasible heat transfer coefficients (**orange**-bordered areas), pressure drops (**blue**-bordered areas) and corresponding values of the “optimization criterion” (**green** lines) for flue gas flow across bundles of plain tubes at different arrangements and tube pitch ratios. The upper two diagrams visualize the numerical results for staggered arrangements – which also have been the basis for the theoretical discussion in 5.2 – and the lower two diagrams provide the comparative results for in-line arrangements. In both cases, the right diagram gives the result for tube pitch ratios  $y_{TR} = y_{LO} = 1.6$  (also assumed in Fig. 43 to Fig. 46 above) and the left diagram shows the respective results for somewhat smaller tube pitch ratios  $y_{TR} = y_{LO} = 1.4$ .

If can be seen from Fig. 47 that in both arrangements the quotient of heat transfer coefficient and square root of the pressure drop (“optimization criterion” in **green**) is almost unaffected by variation of the tube pitch ratios in this range. In addition, no significant change in the maximum feasible heat transfer coefficient due to variation of the tube pitch ratio can be seen. Comparison of staggered arrangement (upper diagrams) and in-line arrangement (lower diagrams) reveals that in-line arrangement might be a little more beneficial in bundles of plain tubes (little higher maximum feasible heat transfer coefficients, little lower minimum feasible pressure drops, slightly greater values of the “optimization criterion”).



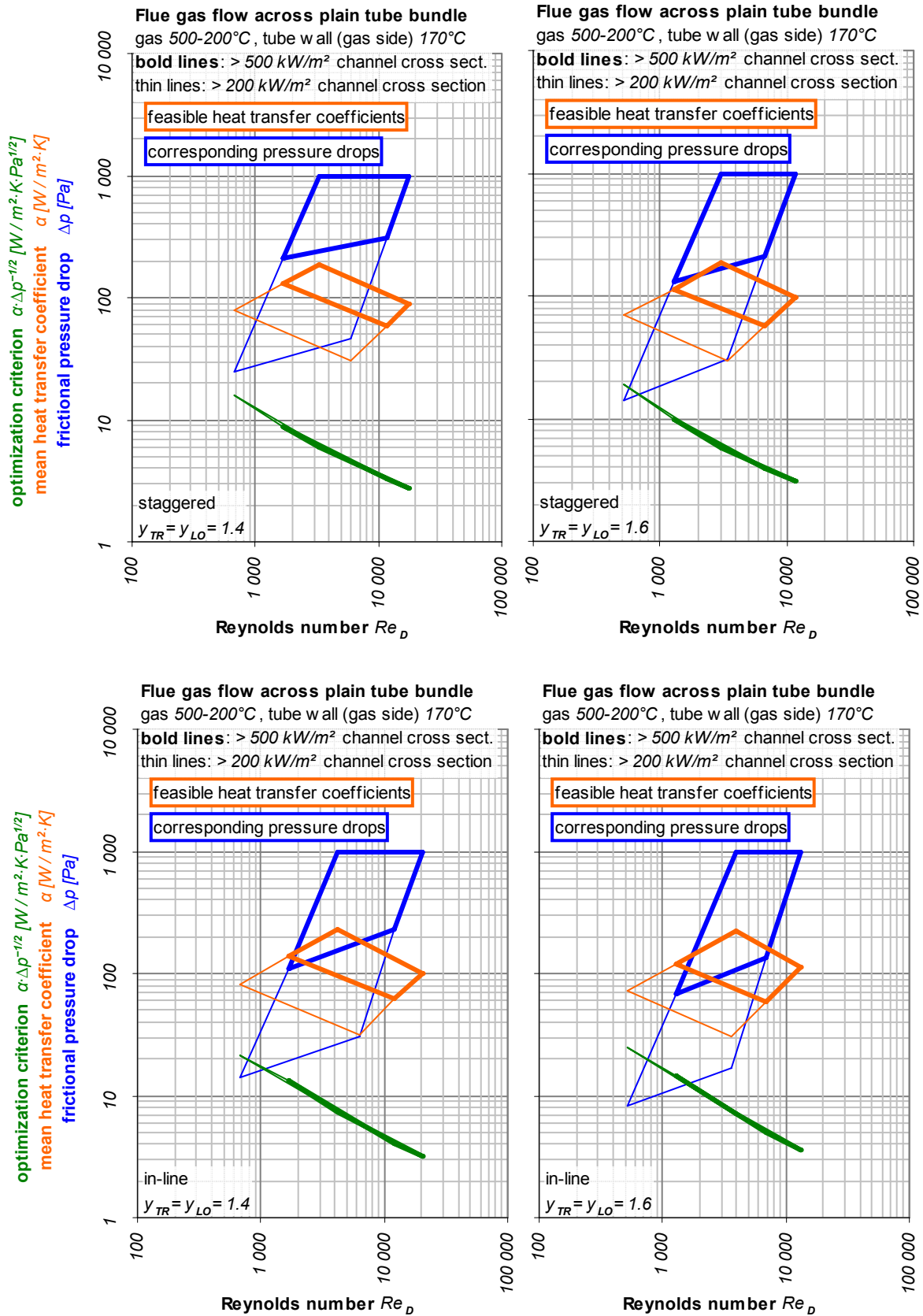


**Fig. 47: Variation of tube arrangement and tube pitch ratio for flue gas flow across plain tube bundles.** Feasible heat transfer coefficients (orange-bordered areas), pressure drops (blue-bordered areas) and corresponding values of the “optimization criterion” (green lines) for tube bundles with staggered arrangement (upper two diagrams) and in-line arrangement (lower two diagrams) respectively at two different tube pitch ratios (left vs. right diagrams).

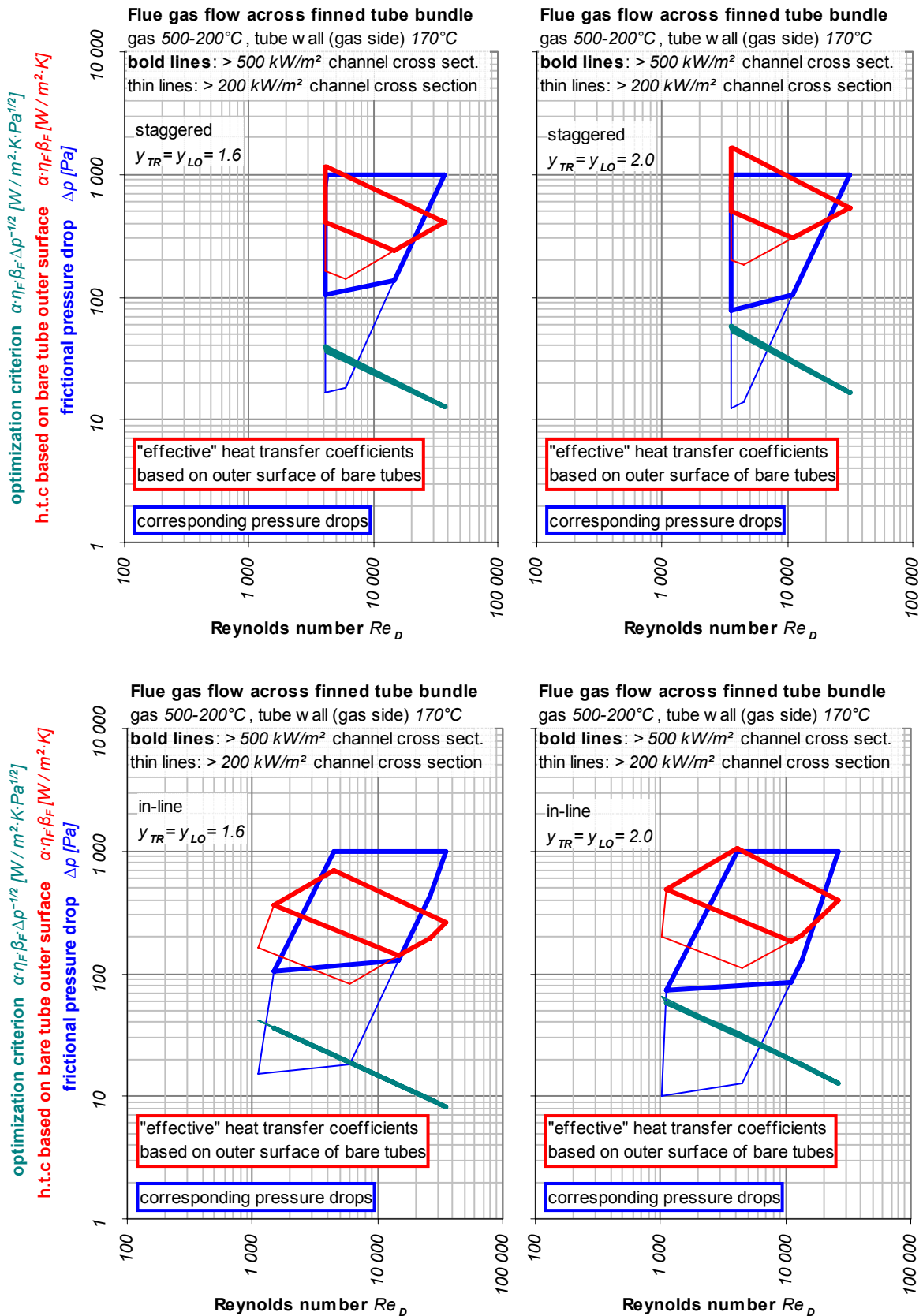


**Fig. 48: Variation of tube arrangement and tube pitch ratio for flue gas flow across finned tube bundles.** Feasible “effective” heat transfer coefficients based on outer surface of bare tubes (red-bordered areas), pressure drops (blue-bordered areas) and corresponding values of the “optimization criterion” (teal lines) for finned tube bundles with staggered arrangement (upper two diagrams) and in-line arrangement (lower two diagrams) respectively at two different tube pitch ratios (left vs. right diagrams).

An analogous comparison of the impact of different arrangements and tube pitch ratios in finned bundles is provided in Fig. 48. The economically relevant “effective” heat transfer coefficients based on outer surface of bare tubes (red-bordered areas) and corresponding values of the “optimization criterion” (teal lines) are displayed for this purpose. Again, the two upper diagrams show results for staggered arrangements and the two lower diagrams refer to in-line arrangements. Unlike the respective comparison for plain tube bundles, however in Fig. 48 finned bundles with tube pitch ratios of  $y_{TR} = y_{LO} = 1.6$  (left diagrams) and  $y_{TR} = y_{LO} = 2.0$  (right diagrams) have been compared.

In contrast to plain bundles, for finned bundles staggered arrangements are more advantageous (higher maximum feasible heat transfer coefficients). As the larger tube pitch allows for a greater fin height and thus a higher surface enhancement (cf. respective numbers in Tab. 17), the greater “effective” heat transfer coefficients (red-bordered areas) are found at the larger tube pitch ratio. Fig. 48 shows that in finned tube bundles both staggered and in-line arrangements enable “effective” heat transfer coefficients  $\alpha \cdot \eta_F \cdot \beta_F > 1000 \text{ W/m}^2\text{K}$ . It has to be noted however, that such large values might already be beyond the “optimum” design, especially what the first rows of tubes in contact with the entering hot exhaust gas are concerned. Therefore, a more in-depth evaluation taking into consideration the applied tube material, corrosion inhibitors, and exact operating conditions would be required here to identify the actual “optimum” within the feasible range of designs (red-bordered areas) shown in Fig. 48. Variation of the size of the fins along the bundle or combination of a plain and a finned section (cf. center sketch in Fig. 27) might also be promising solutions that are worth further investigation.

#### 5.3.4 Calculation results for direct-fired regenerators

For direct-fired regenerators it was assumed that flue gas enters the heat exchanger section after the furnace chamber at  $1000^\circ\text{C}$  and leaves the heat exchanger again at  $200^\circ\text{C}$ ; additionally the maximum allowed pressure drop at the flue gas side was limited to  $5 \text{ mbar}$  only (cf. specifications in Tab. 16).

Except for these altered boundary conditions, the calculations for direct-fired regenerators (presented below) follow the scheme already outlined above in 5.3.3 for the case of exhaust-fired regenerators; therefore, discussion will be kept brief. However, it can be stated generally that for direct-fired regenerators the same basic findings are obtained as for exhaust-fired regenerators discussed above in 5.3.3.

### Flue gas flow inside tubes

The feasible heat transfer coefficients and corresponding pressure drops in the fully laminar and in the fully turbulent regime of heat exchangers with flue gas flow inside tubes are shown in Fig. 49. The left diagram provides the flue gas side heat transfer coefficients (orange-bordered areas) and the right diagram gives the “effective” heat transfer coefficients calculated with respect to the actual outer surface of the tubes (red-bordered areas) assuming a wall thickness of 2.5 mm (cf. Tab. 17). Again, for tube walls in the range 0...2.5 mm all resulting values will be somewhere in between the limits set by the two diagrams in Fig. 49.

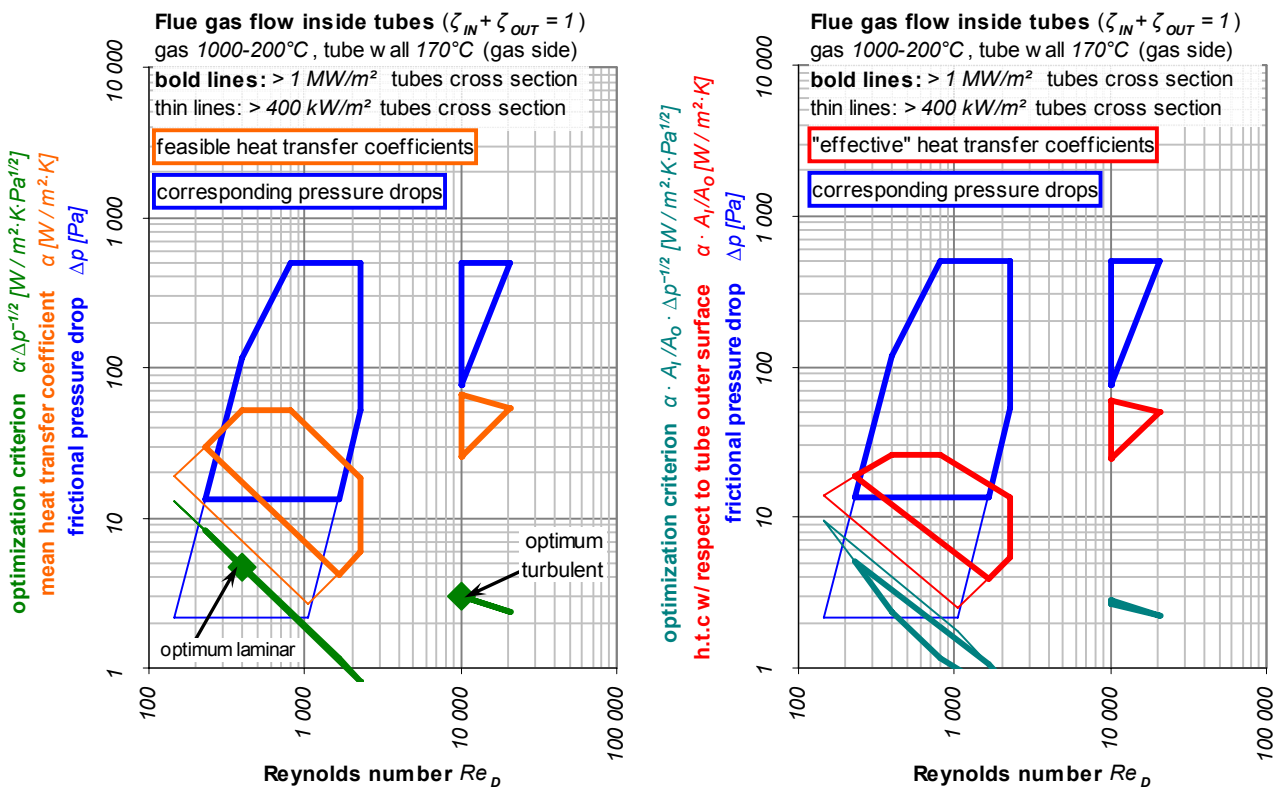


**Fig. 49:** Ranges of feasible heat transfer coefficients and pressure drops in the fully laminar and the fully turbulent region for heat exchangers with gas flow inside tubes.

Feasible heat transfer coefficients as orange-bordered areas, pressure drops as blue-bordered areas, corresponding values of the “optimization criterion” as green lines in the left diagram. Respective “effective” heat transfer coefficients calculated with respect to the outer surface of the tubes for the same configuration as red-bordered areas, quotients of “effective” heat transfer coefficient and square root of the pressure drop as teal-bordered areas in the right diagram.

As already found for exhaust-fired regenerators, largest heat transfer coefficients can be realized in turbulent flow at  $Re = 10000$  while laminar flow designs suffer significantly from the chosen wall thickness. Nevertheless, the laminar flow region is an option if an atmospheric burner has to be employed and thus pressure drop is limited to only 20...50 Pa.

### Flue gas flow across tube bundles

Fig. 50 and Fig. 51 above visualize the numerical results on feasible heat transfer coefficients and pressure drops in cross flow on plain and finned tube banks respectively with additional variation of arrangement and tube pitch ratios.

All the diagrams in Fig. 50 and Fig. 51 are analogous to those for exhaust-fired regenerators (Fig. 47 and Fig. 48 in 5.3.3) and thus require little additional explanation. For plain tube bundles (Fig. 50), again the feasible heat transfer coefficients (**orange**-bordered areas) and the corresponding values of the “optimization criterion” (**green** lines) are almost unaffected by a variation of the tube pitch ratio (left vs. right diagrams); again, slightly larger numbers are obtained for in-line arrangements (lower diagrams) than for staggered arrangements (upper two diagrams in Fig. 50). For finned tube bundles (Fig. 51), again the larger “effective” heat transfer coefficients based on outer surface of bare tubes (**red**-bordered areas) are possible at staggered arrangements (upper diagrams) and at larger tube pitch ratios (right diagrams in Fig. 51) respectively. Pressure drops below  $50 \text{ Pa}$  and thus the application of atmospheric burners is possible for any of the heat exchanger configurations in Fig. 50 and Fig. 51.

Although Fig. 51 shows that “effective” heat transfer coefficients  $\alpha \cdot \eta_F \cdot \beta_F$  of about  $1000 \text{ W/m}^2\text{K}$  can be achieved with finned tube bundles, it has to be stated that such large heat transfer coefficients are not desirable in direct-fired regenerators. As already discussed for exhaust-fired regenerators in 5.3.3 above, variation of the size of the fins along the bundle or combination of a plain and a finned section (cf. Fig. 27) might be more promising solutions.

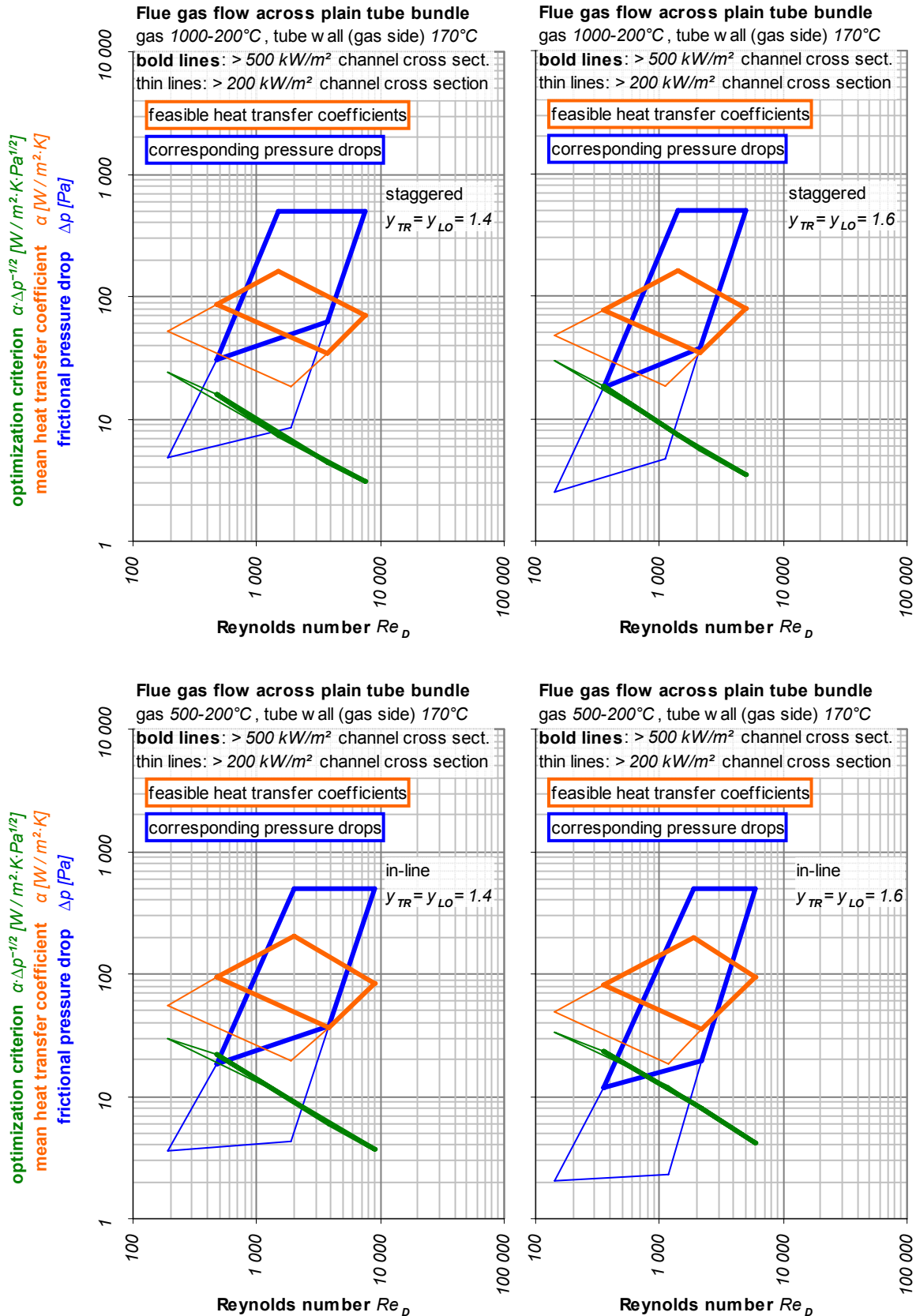


**Fig. 50: Variation of tube arrangement and tube pitch ratio for flue gas flow across plain tube bundles.** Feasible heat transfer coefficients (orange-bordered areas), pressure drops (blue-bordered areas) and corresponding values of the “optimization criterion” (green lines) for tube bundles with staggered arrangement (upper two diagrams) and in-line arrangement (lower two diagrams) respectively at two different tube pitch ratios (left vs. right diagrams).

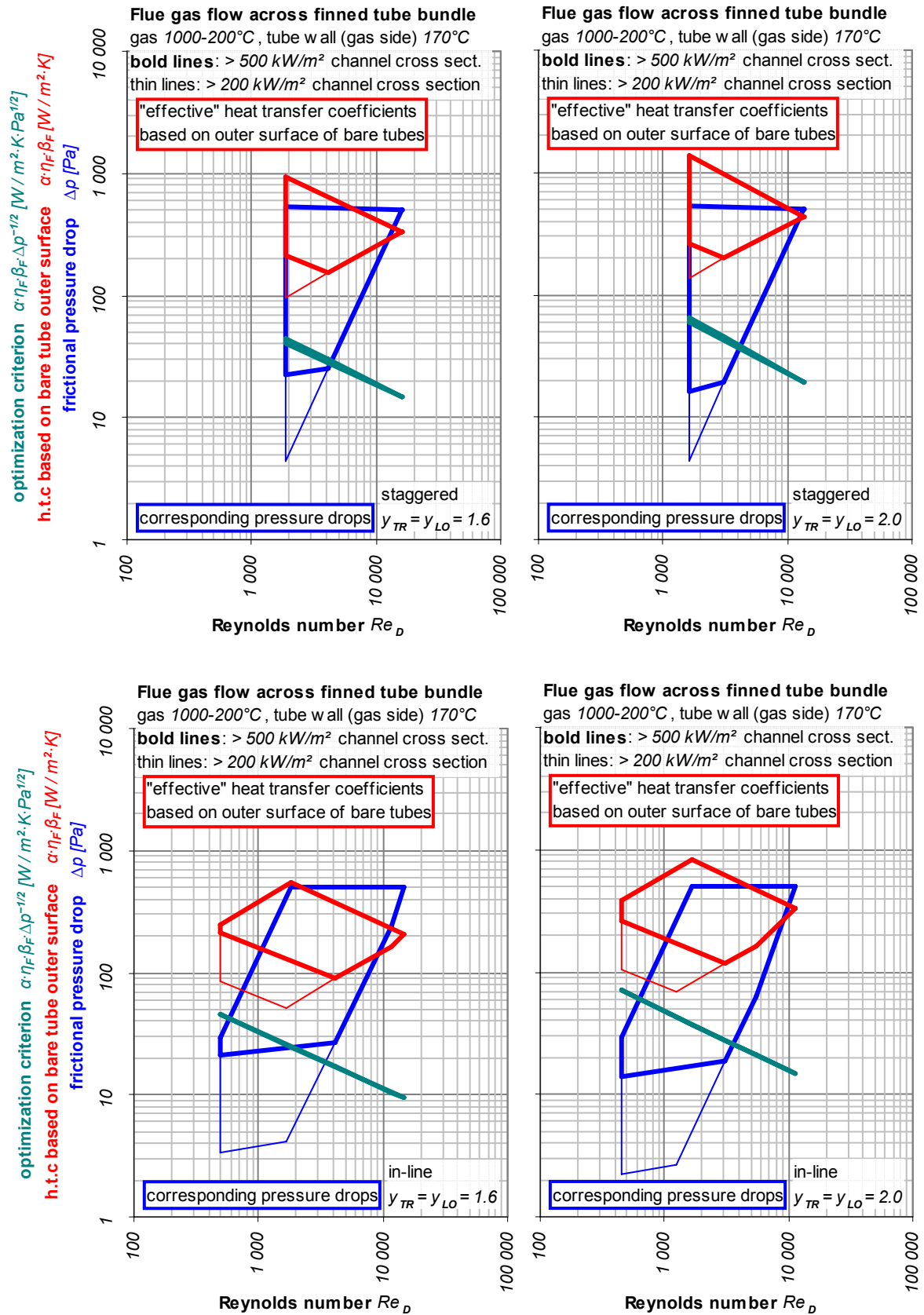


**Fig. 51: Variation of tube arrangement and tube pitch ratio for flue gas flow across finned tube bundles.** Feasible “effective” heat transfer coefficients based on outer surface of bare tubes (red-bordered areas), pressure drops (blue-bordered areas) and corresponding values of the “optimization criterion” (teal lines) for finned tube bundles with staggered arrangement (upper two diagrams) and in-line arrangement (lower two diagrams) respectively at two different tube pitch ratios (left vs. right diagrams).



### 5.3.5 Comparison and discussion of the numerical results

#### Design data for largest heat transfer coefficients

| Design data for largest heat transfer coefficients $\alpha$ in exhaust-fired regenerators    |   |   | Smoke tubes | Bank of plain tubes in crossflow |       |         |       | Bank of finned tubes |       |
|--|---|---|-------------|----------------------------------|-------|---------|-------|----------------------|-------|
| Tube pitch ratios  | $y_{TR} = y_{LO}$   | [-]                                     |             | 1.4                              |       | 1.6     |       | 1.6                  |       |
| Tube arrangement   | stag. / in-line   |   |             | in-line                          | stag. | in-line | stag. | in-line              | stag. |
| <b>Operational data</b>  |   |   |             |                                  |       |         |       |                      |       |
| Mass flux density  | $\dot{m}$ or $\dot{m}_{FC}$   | [kg/s·m <sup>2</sup> ]                  | 15.7        | 3.5                              | 2.7   | 4.3     | 3.3   | 4.2                  | 4.0   |
| Reynolds number  | $Re_D$  | [-]                                     | 10 000      | 4 180                            | 3 282 | 3 901   | 3 025 | 4 444                | 4 204 |
| <b>Performance data</b>  |   |   |             |                                  |       |         |       |                      |       |
| Pressure drop  | $\Delta p_{FR}$   | [Pa]                                    | 1 000       | 1 000                            | 1 000 | 1 000   | 1 000 | 1 000                | 1 000 |
| Heat transf. coeff.  | $\alpha$ or $\eta_F \cdot \alpha$   | [W/m <sup>2</sup> K]                    | 101         | 232                              | 188   | 222     | 185   | 110                  | 183   |
| “Effective” HTC (bare tb. outer surf.)   | $\alpha \cdot A_i/A_o$ or $\alpha$ or $\alpha \cdot \eta_F \cdot \beta_F$   | [W/m <sup>2</sup> K]                    | 80          | 232                              | 188   | 222     | 185   | 693                  | 1 148 |
| Optimization. crit.  | $\alpha / \Delta p_{FR}^{1/2}$  | [W/m <sup>2</sup> K Pa <sup>1/2</sup> ] | 3.2         | 7.4                              | 6.0   | 7.0     | 5.9   | 3.5                  | 5.8   |
| “Effective” optimization criterion (based on bare tube outer surface for all configurations) | $A_i/A_o \cdot \alpha / \Delta p_{FR}^{1/2}$ or $\alpha / \Delta p_{FR}^{1/2}$ or $\eta_F \cdot \beta_F \cdot \alpha / \Delta p_{FR}^{1/2}$ | [W/m <sup>2</sup> K Pa <sup>1/2</sup> ] | 2.5         | 7.4                              | 6.0   | 7.0     | 5.9   | 21.9                 | 36.3  |
| <b>Geometry data</b>   |   |   |             |                                  |       |         |       |                      |       |
| Tube inner diameter  | $d_i$   | [mm]                                    | 18.5        |                                  |       |         |       |                      |       |
| Tube outer diameter  | $d_o$   | [mm]                                    | 23.5        | 10.0                             | 10.0  | 10.0    | 10.0  | 10.0                 | 10.0  |
| Surf. enhancement  | $\beta_F$   | [-]                                     |             |                                  |       |         |       | 6.3                  | 6.3   |
| <b>Heat exchanger size</b>   |   |   |             |                                  |       |         |       |                      |       |
| Tb. length in flow dir.  | $l$   | [m]                                     | 2.1         |                                  |       |         |       |                      |       |
| Tube rows in flow dir.   | $N_{TB,LO}$   | [-]                                     |             | 19                               | 19    | 28      | 26    | 9                    | 6     |
| Bundle length  | $N_{TB,LO} \cdot y_{LO} \cdot d_o$  | [m]                                     |             | 0.27                             | 0.27  | 0.45    | 0.42  | 0.14                 | 0.10  |
| Capacity per cross section (tubes)   | $\dot{Q} / A_{CS}$  | [kW/m <sup>2</sup> ]                    | 5 586       |                                  |       |         |       |                      |       |
| Capacity per cross section (channel)   | $\dot{Q} / A_{FC}$  | [kW/m <sup>2</sup> ]                    |             | 1 237                            | 971   | 1 516   | 1 175 | 1 496                | 1 416 |

**Tab. 18:** Comparison of design data of the heat exchanger configurations yielding the largest feasible heat transfer coefficient in regenerators fired by exhaust gas under the boundary conditions of Tab. 16 and Tab. 17 for different basic regenerator designs (cf. Fig. 44 - Fig. 48 in 5.3.3).

Tab. 18 and Tab. 19 below summarize the design data of the heat exchanger configurations that showed the largest heat transfer coefficients in the diagrams in Fig. 44 to Fig. 51. The comparison includes smoke tube designs with flue gas flow inside tubes and boiling tube



designs with flue gas flow across tube bundles of different arrangements and tube pitch ratios. Although the results for large tube pitch ratios  $y_{TR} = y_{LO} = 2.0$  in finned bundles that had been shown in the diagrams above have been skipped in Tab. 18 and Tab. 19 as these configurations anyway resulted in too large heat transfer coefficients (see discussion above).

| Design data for largest heat transfer coefficients $\alpha$ in direct-fired regenerators     |   |   | Smoke tubes | Bank of plain tubes in crossflow |       |         |       | Bank of finned tubes |       |
|--|---|---|-------------|----------------------------------|-------|---------|-------|----------------------|-------|
| Tube pitch ratios  | $y_{TR} = y_{LO}$   | [-]                                     |             | 1.4                              |       | 1.6     |       | 1.6                  |       |
| Tube arrangement   | stag. / in-line   |   |             | in-line                          | stag. | in-line | stag. | in-line              | stag. |
| <b>Operational data</b>  |   |   |             |                                  |       |         |       |                      |       |
| Mass flux density  | $\dot{m}$ or $\dot{m}_{FC}$   | [kg/s·m <sup>2</sup> ]                  | 8.6         | 2.1                              | 1.6   | 2.6     | 2.0   | 2.2                  | 2.2   |
| Reynolds number  | $Re_D$  | [-]                                     | 10 000      | 1 979                            | 1 509 | 1 873   | 1 414 | 1 842                | 1 856 |
| <b>Performance data</b>  |   |   |             |                                  |       |         |       |                      |       |
| Pressure drop  | $\Delta p_{FR}$   | [Pa]                                    | 500         | 500                              | 500   | 500     | 500   | 500                  | 500   |
| Heat transf. coeff.  | $A$ or $\eta_F \cdot \alpha$  | [W/m <sup>2</sup> K]                    | 66          | 204                              | 163   | 196     | 162   | 88                   | 151   |
| “Effective” HTC (bare tb. outer surf.)   | $\alpha \cdot A_I / A_O$ or $\alpha$ or $\alpha \cdot \eta_F \cdot \beta_F$   | [W/m <sup>2</sup> K]                    | 60          | 204                              | 163   | 196     | 185   | 551                  | 948   |
| Optimization. crit.  | $\alpha / \Delta p_{FR}^{1/2}$  | [W/m <sup>2</sup> K Pa <sup>1/2</sup> ] | 3.0         | 9.1                              | 7.3   | 8.8     | 7.2   | 3.9                  | 6.5   |
| “Effective” optimization criterion (based on bare tube outer surface for all configurations) | $A_I / A_O \cdot \alpha / \Delta p_{FR}^{1/2}$ or $\alpha / \Delta p_{FR}^{1/2}$ or $\eta_F \cdot \beta_F \cdot \alpha / \Delta p_{FR}^{1/2}$ | [W/m <sup>2</sup> K Pa <sup>1/2</sup> ] | 2.7         | 9.1                              | 7.3   | 8.8     | 7.2   | 24.6                 | 41.0  |
| <b>Geometry data</b>   |   |   |             |                                  |       |         |       |                      |       |
| Tube inner diameter  | $d_I$   | [mm]                                    | 42.6        |                                  |       |         |       |                      |       |
| Tube outer diameter  | $d_O$   | [mm]                                    | 47.6        | 10.0                             | 10.0  | 10.0    | 10.0  | 10.0                 | 10.0  |
| Surf. enhancement  | $\beta_F$   | [-]                                     |             |                                  |       |         |       | 6.3                  | 6.3   |
| <b>Heat exchanger size</b>   |   |   |             |                                  |       |         |       |                      |       |
| Tb. length in flow dir.  | $l$   | [m]                                     | 5.8         |                                  |       |         |       |                      |       |
| Tube rows in flow dir.   | $N_{TB,LO}$   | [-]                                     |             | 20                               | 19    | 29      | 26    | 9                    | 6     |
| Bundle length  | $N_{TB,LO} \cdot y_{LO} \cdot d_O$  | [m]                                     |             | 0.28                             | 0.27  | 0.46    | 0.42  | 0.14                 | 0.10  |
| Capacity per cross section (tubes)   | $\dot{Q} / A_{CS}$  | [kW/m <sup>2</sup> ]                    | 8 724       |                                  |       |         |       |                      |       |
| Capacity per cross section (channel)   | $\dot{Q} / A_{FC}$  | [kW/m <sup>2</sup> ]                    |             | 2 103                            | 1 604 | 2 612   | 1 973 | 2 226                | 2 244 |

**Tab. 19:** Comparison of design data of the heat exchanger configurations yielding the largest feasible heat transfer coefficient in direct-fired regenerators under the boundary conditions of Tab. 16 and Tab. 17 for different basic regenerator designs (cf. Fig. 49 - Fig. 51 in 5.3.4).

For exhaust-fired regenerators, the comparison of the heat exchanger configurations yielding the largest heat transfer coefficients under the boundary conditions of Tab. 16 and Tab. 17 for different basic heat exchanger types is given in Tab. 18; the respective comparison for direct-fired regenerators is given in Tab. 19.

Comparison of the “effective” heat transfer coefficients (based on bare tube outer surface) in both tables reveals that banks of plain tubes in crossflow yield about three times larger values than smoke tubes in direct-fired regenerators (cf. Tab. 19) and still a more than two-fold increase in exhaust-fired regenerators (cf. Tab. 18). Thus, more than half of the required tube outer surface area is saved in boiling tube designs compared to smoke tube designs. An even more than three-fold increase of the mean heat transfer coefficients based on bare tube outer surface could be achieved by application of tube banks combining a plain and a finned section (cf. center sketch of Fig. 27 in 4.1.1 above).

### Heat exchanger dimensions

As already discussed above, operation at  $Re = 10\,000$  is most preferable for tubular flow designs in both cases; however, rather different values for the optimum tube diameter and mass flux density were obtained. For exhaust-fired regenerators equipped with smoke tubes (cf. Tab. 18), an optimum inner diameter of  $19\text{ mm}$  and a required total tube length of  $l = 2.1\text{ m}$  were found. For direct-fired regenerators (cf. Tab. 19) about  $43\text{ mm}$  inner diameter and a total length of  $l = 5.8\text{ m}$  (e.g. two passes of  $l_{TB} = 2.9\text{ m}$  or three passes of  $l_{TB} = 1.9\text{ m}$  tubes) were obtained as best configuration. These findings are mainly dependent on the maximum pressure drop  $\Delta p_{FR}$  that is assumed as boundary condition. If this parameter is varied, tube length  $l$  and inner diameter  $d_i$  follow the relation  $d_i \sim l \sim \Delta p_{FR}^{-1/2}$  according to (5.23) while the quotient  $\frac{\alpha}{\Delta p_{FR}^{1/2}}$  is invariant at  $Re = 10\,000$ .

For all designs with gas flow across tube bundles it shows that the smallest possible tube diameter ( $d_o = 10\text{ mm}$  according to the boundary conditions given in Tab. 17) already is the most preferable configuration. The bundle length is mainly dependent on the tube pitch ratio and the type of tubes. For plain tubes, at tube pitch ratios  $y_{TR} = y_{LO} = 1.6$  bundles with 26...29 consecutive rows of tubes were obtained, at the smaller tube pitch ratios  $y_{TR} = y_{LO} = 1.4$  the bundle length reduces to 19...20 rows, and for finned tubes only 6...9 rows are required. In all cases the length of the bundle  $N_{TB,LO} \cdot y_{LO} \cdot d_o$  can be less than half a meter and thus significantly shorter than a respective smoke tube design even if the total tube length would be broken up into two or three passes. The highest values for the capacity per cross section of the flue gas channel  $\dot{Q}/A_{Fc}$  – being a main parameter for the compactness of larger units – are found for plain tubes with large tube pitch ratios and in-line arrangement, the lowest ones for small tube pitch ratios and staggered arrangement. On the

other hand, the largest heat transfer coefficients and thus smallest surface areas in plain tube bundles can be realized with in-line arrangement and small tube pitch ratios. Actually, it is dependent on the special application whether the configuration yielding the smallest surface area (i.e. smallest tube pitch ratios) or the configuration yielding the smallest cross sectional area (i.e. larger tube pitch ratios) is the most suitable one.

The capacity per cross section of the smoke tubes  $\dot{Q}/A_{CS}$  in tubular flow designs is about four times higher than the respective values for  $\dot{Q}/A_{FC}$  in designs with crossflow on tube banks. However, it has to be considered that the total cross section of a heat exchanger equipped with smoke tubes is about twice the inner cross sectional area of the tubes; therefore, the effective capacity per cross section in tubular flow designs is only about twice the value of tube banks. If the total length of the smoke tubes is divided into two or three passes then the cross section of the heat exchanger increases by another factor of two or three and similar values for the capacity per cross section are obtained for all kinds of designs – smoke tubes and boiling tubes.

Nevertheless, in large units with heat duties  $\dot{Q}$  of several megawatts, smoke tube designs might have some advantage due to the higher capacity per cross section especially if only a single pass of smoke tubes would be installed. Of course, designs employing crossflow on tube banks also allow for higher values of  $\dot{Q}/A_{FC}$  than those given in Tab. 18 and Tab. 19 if only tube diameters or tube pitch ratios are increased. Consequently, this would result in heat transfer coefficients smaller than the “optimum values” provided in these tables; in this case, the advantage of the significantly higher heat transfer coefficients in boiling tube designs compared to smoke tube designs might be lost. Hence, this numerical evaluation would have to be restarted with altered boundary conditions to determine again the most promising design.

It finally can be stated that for heat duties of about two megawatts and less, regenerator designs employing flue gas flow across bundles of boiling tubes generally result in higher heat transfer coefficients, smaller required surface areas, and more compact heat exchangers.

### **Welding effort**

It has already been discussed in 5.2.4 that the total length and the number of the weld seams to mount the tubes into the tube sheets are main factors for the welding cost. According to (5.25) for given heat duty and temperature conditions, the total length of the weld seams is inverse-proportional to the product of the length of an individual tube and the heat transfer coefficient based on the outer tube surface. It was shown above that according to Tab. 18 and Tab. 19 plain tube bundles enable about three times larger effective heat transfer

coefficients than smoke tubes and even larger values are found in finned bundles. Thus, at least three times the tube length would be required in smoke tube designs to keep the same length of weld seams.

For flue gas flow inside smoke tubes, Tab. 18 and Tab. 19 quote a tube length of  $l = 2.1 \text{ m}$  in exhaust-fired regenerators and a length of  $l = 5.8 \text{ m}$  in direct-fired regenerators if there is only a single pass in the flue gas. In crossflow designs, boiling tubes with lengths  $l_{TB}$  in the range  $0.5 \dots 1.5 \text{ m}$  are feasible. Thus, in exhaust-fired regenerators, crossflow designs will most likely result in a shorter total length of weld seams than tubular flow designs. In direct-fired regenerators, a smoke tube design might result in a shorter total length of the weld seams than a plain tube bundle if only a single pass of smoke tubes is installed. Designs with two or more passes of smoke tubes will most likely result in a greater total length of the weld seams than a respective bundle of plain tubes in crossflow. The shortest total length of the weld seams can be realized by application of tube bundles that are partially or fully equipped with finned tubes.

The absolute number of weld seams is according to (5.27) inverse-proportional to the product of the tube diameter, the length of an individual tube, and the heat transfer coefficient based on the outer tube surface. Compared to relation (5.25) for the total length of the weld seams that has been employed above, the inverse tube diameter is an additional factor in relation (5.27) for the total number of weld seams. In the configurations with largest heat transfer coefficients listed in Tab. 18 and Tab. 19, however, the outer diameter in smoke tube designs is larger by a factor of about two in exhaust-fired regenerators and by a factor of almost five in direct-fired regenerators compared to crossflow designs. Especially what direct-fired regenerators are concerned, this additional factor favoring smoke tube designs can hardly be compensated by the larger heat transfer coefficient in crossflow designs, even if two or three passes of smoke tubes have to be installed. In exhaust-fired regenerators, boiling tube designs with tube bundles partially or fully equipped with finned tubes yield about the same absolute number of weld seams as smoke tube designs.

Actually, no final conclusion on the welding effort for different boiler designs can be drawn from on general relations between specific numbers, as the length of an individual tube  $l_{TB}$ , which is a major influencing variable, is dependent on limitations concerning the length and the height of the boiler unit. The general trend is, however, that crossflow on tube banks enables a short total length of the weld seams especially in exhaust-fired regenerators and if finned tubes are employed. Tubular flow yields a small total number of weld seams, especially in direct-fired regenerators and if the tube length is not limited by geometric constraints and thus a single pass of smoke tubes can be employed. Typically, crossflow designs

partially or fully equipped with finned tubes will yield the shortest total length of weld seams out of all possible configurations; additionally they will require a total number of weld seams that at least exceeds not much the respective value required in a smoke tube design at the same conditions.

## **5.4 Conclusions for regenerator design**

It shows that regenerator designs with flue gas flow across tube bundles generally allow for higher heat transfer coefficients at the same pressure drop at the flue gas side than all standard designs with flue gas flow inside tubes. The largest heat transfer coefficients based on the outer surface of bare tubes could be realized with finned tube bundles in crossflow; however, the combination of a first section of plain tubes and a consequent section of finned tubes is more promising as it avoids too large heat flux at the flue gas inlet side of the heat exchanger.

For pool boiler designs with flue gas flow inside tubes, in most cases a flue gas Reynolds number close to 10 000 is the best choice as it allows for the best relation between heat transfer coefficient and pressure drop. Only if an atmospheric burner were to be employed in a small direct-fired regenerator, laminar flue gas flow at Reynolds numbers below 1000 would be advantageous. In tube boiler designs with flue gas crossflow, Reynolds numbers in the intermediate range 500...5000 are found to be most promising.

In most cases, regenerators with flue gas crossflow on bundles of boiling tubes will not only require the smaller surface area than smoke tube designs, but they will also result in smaller and more compact units and require a shorter total length of weld seams for mounting the tubes into the tubesheets. Combinations of plain and finned tubes generally outperform simple plain tube bundles; in-line arrangement is preferable in banks of plain tubes while staggered arrangement yields the better results in banks of finned tubes.

Compared to smoke tube designs, heat exchangers employing cross flow on boiling tubes are very short but they typically occupy a larger cross sectional area normal to the flue gas flow direction. This results in quite compact and almost cubical dimensions of a tube boiler type regenerator at smaller heat duties, although it might create an issue at heat duties of several Megawatts when a cross sectional area of several square meters would be required. Therefore, pool boiler designs with smoke tubes are the more promising option for very large heat duties, while tube boiler designs are typically the best solution in small and medium sized regenerators up to about 2 MW.

As a further optimization in pool boiler designs with more than one pass of smoke tubes, tube diameter and mass flux density could be varied from pass to pass to balance the heat flux

density. The best configuration would realize  $Re = 10\,000$  in each pass with decreasing tube diameters. In designs with flue gas flow across tube bundles, tube diameter, tube pitch ratios, and fin geometry could even be adjusted for each row for this purpose.

## 6 Laboratory testing of a direct-fired regenerator prototype

Within the joint European R&D project *LiBrAC*<sup>63</sup>, a semi-industrial prototype of a direct-fired regenerator, employing a novel tube-boiler design, was tested in the laboratories at ZAE Bayern. An overview of the work conducted in this project and the results has already been given in the publications of *Schweigler et al. (1999)*, *Schweigler et al. (2000)*, *Kren et al. (2001)*, *Kren et al. (2002)*, *Kren et al. (2006a)*, and *Kren et al. (2006b)*; the final report by *Scharfe et al. (2000)* is classified confidential, however. A brief overview of the additional cycle refinements investigated in this project has already been provided in 3.4.1.

Measuring equipment was installed at the regenerator prototype during this test series to monitor the operational behavior and to verify the successful functioning of the design. An evaluation of the recorded data, with respect to heat transfer characteristics, pressure drop, and natural convection flow in this kind of regenerator, is given below in 6.4.

### 6.1 Heat exchanger design

The regenerator prototype was designed by Weir ENTROPIE S.A and BG Technology Ltd. (BGT) under the direction of BGT. Although full details are only contained in confidential project reports by *Clark et al. (1999a)*, *Clark et al. (1999b)* and *Clark (2000)*, which are not publicly available, the basic design has also been disclosed in two patent applications by *Tucker et al. (2000)* and *Tucker et al. (2001)*. A sketch of the prototype is given in Fig. 52 below. The regenerator was fired by a low-radiation surface-flame burner and equipped with an additional flue-gas recuperator, downstream. The regenerator itself was comprised of 2 non-heated thermosiphon tubes and 44 boiling tubes arranged in 11 staggered rows. To equalize the heat load, the first section of seven rows of tubes, next to the burner, was equipped with plain steel tubes, while the remaining four downstream rows were equipped with finned tubes. The boiling tubes were about 1 m in length and about 1 inch in diameter; the entire apparatus was about 2 m in height. The design details are the intellectual property of the industrial partners and the exact dimensions cannot be disclosed, however, a complete set of the original drawings was available for the evaluation of all the measurement data and calculation of the dimensionless values presented below..

---

<sup>63</sup> "LiBr Absorption Chiller for Building Air Conditioning with Efficient Flexible Operation". Project partners: Weir ENTROPIE S.A (France), Gas Natural SDG S.A. (Spain), BG Technology Ltd. (UK), ZAE Bayern e.V. (Germany). Research funded in part by THE EUROPEAN COMMISSION in the framework of the Non Nuclear Energy Programme Joule III under Contract No. JOE3 CT 97 0059.

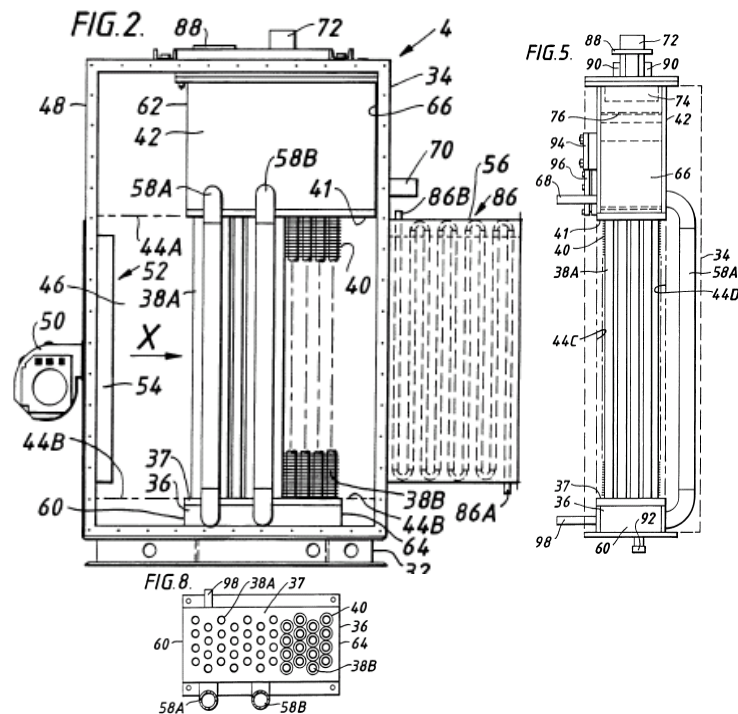


Fig. 52: Patent drawing of the direct-fired regenerator prototype as disclosed by Tucker et al. (2000) and Tucker et al. (2001). No. 56 denotes the additional flue gas recuperator (“economizer”) mounted downstream of the main regenerator.

The prototype was rated for a maximum burner duty of 350 kW, with reference to the gross calorific value of natural gas, which is about 315 kW, with reference to the net calorific value. The basic design was intentionally highly scalable. This was achieved by the variation of the number of boiling tubes in each row and the respective variation of the number of downcomer tubes, leaving all other design parameters unchanged. Therefore, the testing of this relatively small prototype, with only four boiling tubes in each row, was considered to be representative of the full range of capacities between 300 and 1500 kW. A quite expensive metal fiber premix burner, from ACOTECH, operated in low-radiation mode was employed in the regenerator prototype due to its easy availability. However, it is foreseen that more cost-effective ceramic burners will be found for application in such regenerators.

Fig. 52 also shows the flue gas recuperator (“economizer”, no. 56 in the drawing) that was mounted downstream of the main regenerator to optimize the thermal efficiency and flue gas utilization. Although physically connected to the regenerator, this device had a separate solution cycle and will not be a subject of the discussion below.

## 6.2 Test rig and experimental setup

### 6.2.1 Overview

To save the effort of erecting a complete industrial sized double-effect absorption chiller in the lab, the regenerator prototype was integrated in a special test rig (left photograph in Fig. 53), which enabled the simulation of representative operating conditions. Later, an additional



evaporator/absorber prototype and a solution heat exchanger were added to the test rig (right photograph in Fig. 53) and the complete system was operated as a kind of non-standard single-effect absorption chiller. The test rig in the ZAE Bayern laboratories has been described in detail by *Dantele (1999)* and *Eberl (2000)*.

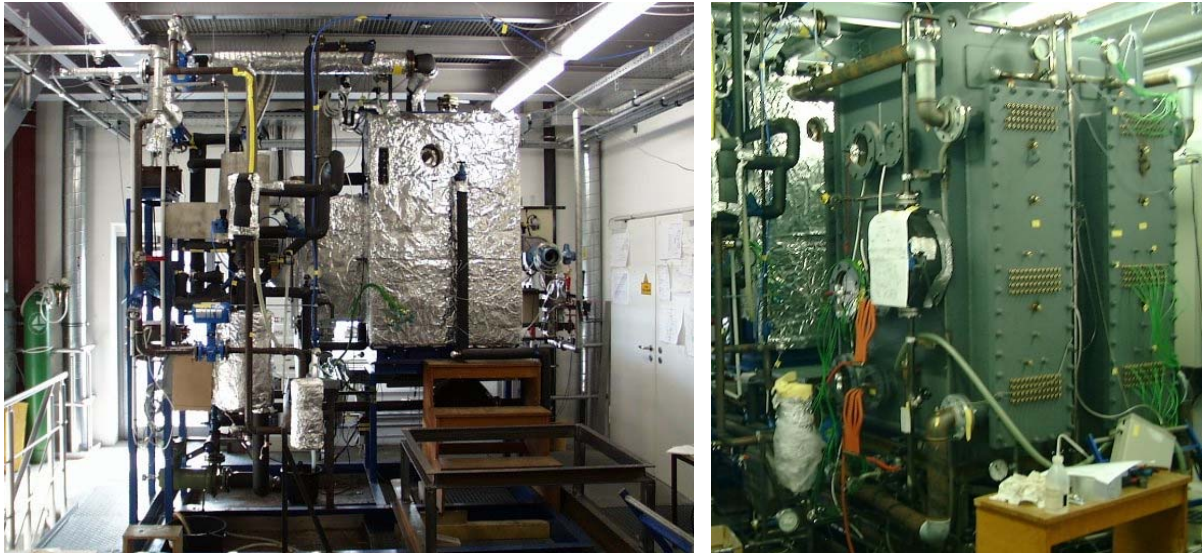
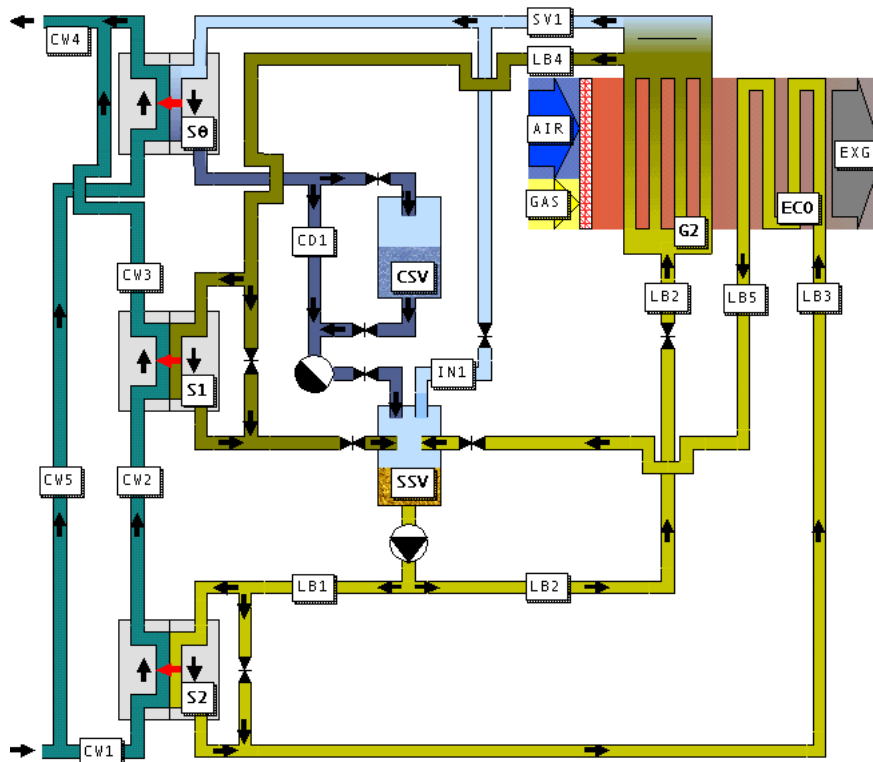


**Fig. 53:** Photograph of the regenerator test station before (left) and after (right) the installation of the evaporator/absorber unit.



| Components and Piping |                            |
|-----------------------|----------------------------|
| G2                    | (Re-)Generator             |
| ECO                   | Economizer                 |
| S0...2                | Simulation heat exchangers |
| CSV                   | Condensate storage vessel  |
| SSV                   | Solution storage vessel    |
| CW1...5               | Cooling water              |
| LB1...5               | LiBr solution              |
| SV1                   | Saturated vapor            |
| CD1                   | Condensate                 |
| IN1                   | Incond. gases              |
| GAS                   | Natural gas in             |
| AIR                   | Combustion air in          |
| EXG                   | Exhaust gas out            |

**Fig. 54:** Flow scheme of the initial regenerator test rig in the lab before the installation of the evaporator/absorber unit. Drawing taken from *Dantele (1999)*.

The flow scheme of the initial test rig as described by *Dantele (1999)* is shown in Fig. 54. As several changes and extensions were made to the piping and the instrumentation during

experimental phase, no valid single P&ID of the whole test rig can be provided. However, the configuration of all the piping and additional installations next to the regenerator, which are of relevance for the evaluation of the prototype, is shown in Fig. 55.

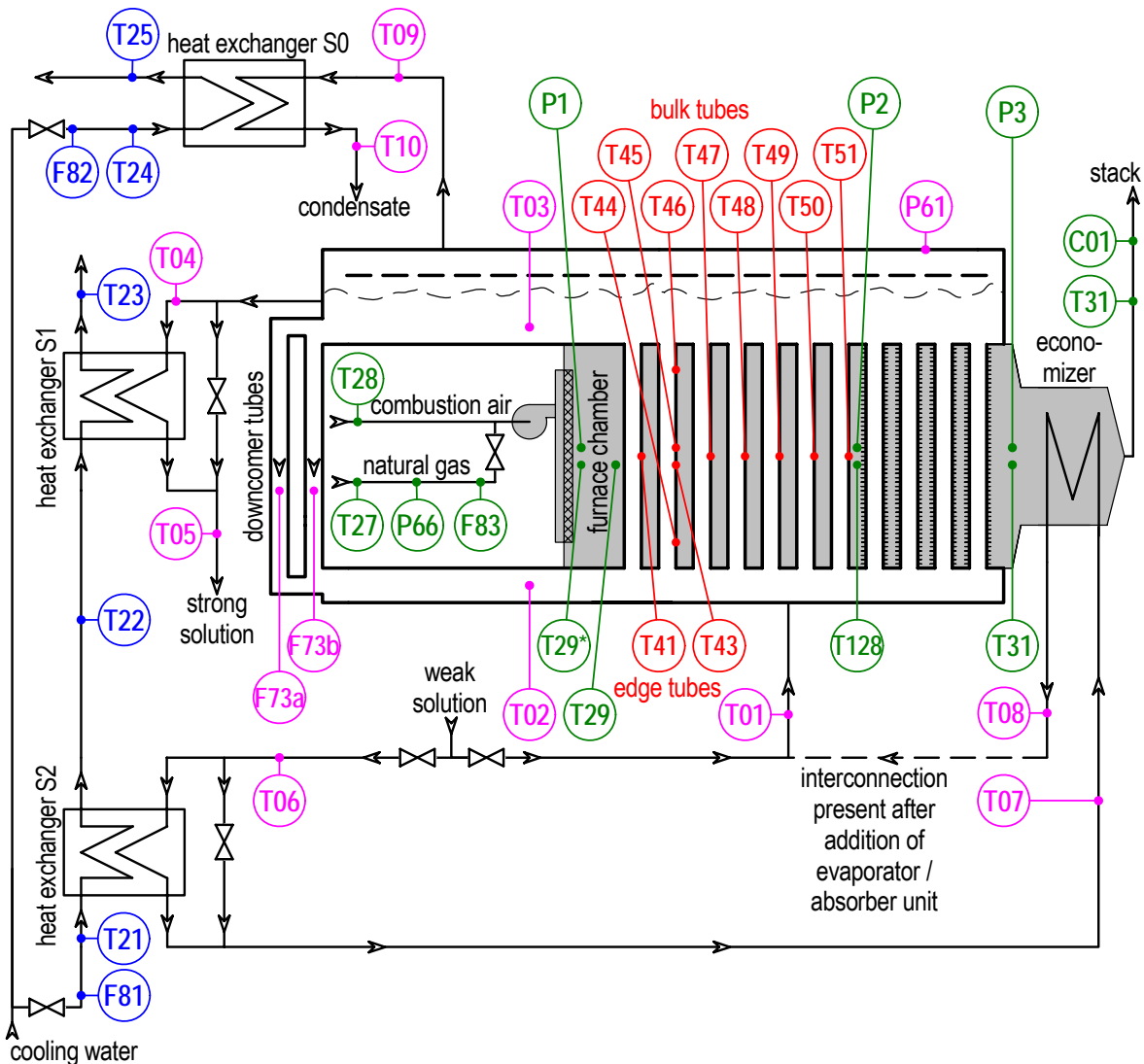


Fig. 55: Simplified P&ID showing a subset of measuring points at regenerator prototype and test rig that has been used for the evaluations presented below.

Measuring points in the internal cycle ( $T01-T10$ ,  $P61$ ,  $F73a/b$ ) are displayed in magenta, points in the external cooling water lines ( $T21-T25$ ,  $F81-F82$ ) are displayed in blue, measurements in the gas/air/flue-gas train ( $T27-T32$ ,  $T128$ ,  $P1-P3$ ,  $P66$ ,  $F83$ ,  $C01$ ) are given in green, and the measured tube wall temperatures ( $T41-T51$ ) are shown in red. For the complete enthalpy balance of the test rig after the addition of the evaporator/absorber unit, four additional temperatures and two additional flows were employed in the cooling water lines (cf. Tab. 21). These are not shown in this simplified drawing.

## 6.2.2 Instrumentation

During the laboratory experiments, the initial measuring instrumentation was gradually refined and extended. In the end, more than 150 measuring points were installed. In contrast, only a subset of these measuring points was employed for the evaluation of the heat transfer and pressure drop in the regenerator, as presented below. Hence, the simplified P&ID in Fig. 55 shows just this selection of measuring points next to the regenerator prototype. Measuring

points in the internal cycle are displayed in **magenta**, points in the external cooling water lines are displayed in **blue**, measurements in the gas/air/flue-gas train are given in **green**, and the measured boiling tube wall temperatures are shown in **red**. More details about the sensors employed and the estimated accuracies of the readings at the individual locations are listed in Tab. 20 for the internal cycle and the tube wall temperatures, in Tab. 21 for the cooling water lines, and in Tab. 22 for the system gas/air/flue gas.

### Temperature Measurements

Only Pt100 platinum resistance thermometers and 4-wire measuring technology were employed for temperature measurements in the internal refrigerant and absorbent solution cycle and in the external cooling water lines. All the thermometers were individually calibrated, in a temperature calibration bath, before installation. In the case of the internal cycle, all the thermometers were installed in thermowells, whereas for the cooling water lines, some thermometers were directly immersed in the water without the application of thermowells.

To observe the wall temperatures of the boiling tubes, the regenerator prototype was supplied with mineral-insulated type K thermocouples welded to the backsides<sup>64</sup> (i.e., not facing the burner) of selected plain boiling tubes (cf. Fig. 55). In the first two rows, probes were welded not only to one tube in the middle of the row (bulk-tubes) but also to one of the outer tubes (edge-tubes), next to the wall of the flue gas duct. Unfortunately, the thermocouple at the bulk tube in the first row of tubes was damaged on welding and failed soon after commissioning. Therefore, there is no measuring point shown at this position in Fig. 55 and Tab. 20. At each position, thermocouples were placed on the boiling tubes at half-height. Two additional probes were installed at the top and bottom of a bulk tube in the second row of tubes (see (see Fig. 55)). At the finned tubes, it was not possible to install temperature probes at the wall due to the small fin pitch.

Either resistance thermometers or mineral-insulated thermocouples were employed for temperature measurements in combustion air, natural gas, and flue gas. The measurements were taken with direct contact to the gas stream; except for the case of the natural gas line, when a thermowell was employed.

---

<sup>64</sup> The reason for this positioning was that, especially at the first row of tubes next to the furnace chamber, a smaller deviation of the measured values from the true wall temperatures was expected for probes not facing the significant radiation impact of the burner.

| List of selected measuring points for the internal cycle and boiling tube walls |                                       | Sensor                | Installation | Deviation (estimated) | Comment   |
|---|---------------------------------------|-----------------------|--------------|-----------------------|---|
| <b>Internal Cycle Temperatures</b>  |                                       |                       |              |                       |   |
| T01   | weak LiBr-sol. regenerator in         | Pt100 4-w.            | thermowell   | < 0.2 K               |   |
| T02   | LiBr-sol. regenerator bottom          | Pt100 4-w.            | thermowell   | (< 0.2 K)             | local temperature at probe, not equal mean temperature in bottom vessel |
| T03   | LiBr-sol. regenerator top             | Pt100 4-w.            | thermowell   | (< 0.2 K)             | local temperature, assumed superheated                                  |
| T04   | strong LiBr-sol. regenerator out      | Pt100 4-w.            | thermowell   | < 0.2 K               | assumed nearly saturation temp.   |
| T05   | strong LiBr-sol. HX S1 out            | Pt100 4-w.            | thermowell   | < 0.2 K               |   |
| T06   | weak LiBr-sol. HX S2 in               | Pt100 4-w.            | thermowell   | < 0.2 K               |   |
| T07   | weak LiBr-sol. economizer in          | Pt100 4-w.            | thermowell   | < 0.2 K               |   |
| T08   | weak LiBr-sol. economizer out         | Pt100 4-w.            | thermowell   | < 0.2 K               |   |
| T09   | refrig. vapor regenerator out         | Pt100 4-w.            | thermowell   | < 2 K                 |   |
| T10   | condensate HX S0 out                  | Pt100 4-w.            | thermowell   | < 0.2 K               |   |
| <b>Internal Cycle Pressures</b>   |                                       |                       |              |                       |   |
| P61   | vapor pressure in regenerator         | abs. press. transm.   | after siphon | < 10 mbar             | assumed sat. pressure   |
| <b>Internal Cycle Flows</b>   |                                       |                       |              |                       |   |
| F73a<br>F73b  | flow rate in a single downcomer tube  | ultrasonic flow meter | clamp-on     | < 10 cm/s             | alternatively installed at either of the both tubes                     |
| <b>Boiling Tube Outer Wall Temperatures</b>                                     |                                       |                       |              |                       |   |
| T41   | 1 <sup>st</sup> row edge-tube, middle | TC type-K             | welded       | < 3 K                 | backside, half-height   |
| T43   | 2 <sup>nd</sup> row edge-tube, middle | TC type-K             | welded       | < 3 K                 | backside, half-height   |
| T44   | 2 <sup>nd</sup> row bulk-tube, bottom | TC type-K             | welded       | < 3 K                 | ca. 20 cm from bottom   |
| T45   | 2 <sup>nd</sup> row bulk-tube, middle | TC type-K             | welded       | < 3 K                 | backside, half-height   |
| T46   | 2 <sup>nd</sup> row bulk-tube, top    | TC type-K             | welded       | < 3 K                 | ca. 20 cm from top  |
| T47   | 3 <sup>rd</sup> row bulk-tube, middle | TC type-K             | welded       | < 3 K                 | backside, half-height   |
| T48   | 4 <sup>th</sup> row bulk-tube, middle | TC type-K             | welded       | < 3 K                 | backside, half-height   |
| T49   | 5 <sup>th</sup> row bulk-tube, middle | TC type-K             | welded       | < 3 K                 | backside, half-height   |
| T50   | 6 <sup>th</sup> row bulk-tube, middle | TC type-K             | welded       | < 3 K                 | backside, half-height   |
| T51   | 7 <sup>th</sup> row bulk-tube, middle | TC type-K             | welded       | < 3 K                 | backside, half-height   |

Tab. 20: Subset of the measuring points in the internal cycle and at the boiling tube walls.

| List of selected measuring points in the external cooling water loops |                                  | Sensor            | Installation      | Deviation (estimated) | Comment              |
|---|----------------------------------|-------------------|-------------------|-----------------------|----------------------|
| <b>External Temperatures in Cooling Water</b>                         |                                  |                   |                   |                       |                      |
| T21   | cooling water HX S2 in           | Pt100 4-w.        | thermowell        | < 0.2 K               |                      |
| T22   | cooling water HX S2 out / S1 in  | Pt100 4-w.        | thermowell        | < 0.2 K               |                      |
| T23   | cooling water HX S1 out          | Pt100 4-w.        | thermowell        | < 0.2 K               |                      |
| T24   | cooling water HX S0 in           | Pt100 4-w.        | thermowell        | < 0.2 K               |                      |
| T25   | cooling water HX S0 out          | Pt100 4-w.        | thermowell        | < 0.2 K               |                      |
| T231  | cooling water evaporator in      | Pt100 4-w.        | immersed          | < 0.2 K               | not shown in Fig. 55 |
| T243  | cooling water evaporator out     | Pt100 4-w.        | immersed          | < 0.2 K               | not shown in Fig. 55 |
| T244  | cooling water absorber in        | Pt100 4-w.        | immersed          | < 0.2 K               | not shown in Fig. 55 |
| T256  | cooling water absorber out       | Pt100 4-w.        | immersed          | < 0.2 K               | not shown in Fig. 55 |
| <b>External Flows in Cooling Water Lines</b>                          |                                  |                   |                   |                       |                      |
| F81   | cooling water in HX S1 and HX S2 | magneto-inductive | in-line (flanged) | < 2%                  |                      |
| F82   | cooling water entering HX S0     | magneto-inductive | in-line (flanged) | < 2%                  |                      |
| F315  | cooling water in evaporator      | magneto-inductive | in-line (flanged) | < 2%                  | not shown in Fig. 55 |
| F316  | cooling water in absorber        | magneto-inductive | in-line (flanged) | < 2%                  | not shown in Fig. 55 |

**Tab. 21:** *Subset of the measuring points in the external cooling water loops.*

However, it must be mentioned that in hot gas streams, at temperatures above about 500°C and in the presence of radiative heat transfer, such standard contact-thermometers are not well suited and may result in huge deviations of the measured values. A further problem is the typically inhomogeneous temperature profile over the total cross section of a flue gas duct, which introduces an additional measuring uncertainty. Therefore, the estimated measurement deviations in the hot flue gas, listed in Tab. 22, are significantly greater than the thermometer accuracy itself.

To determine the magnitude of the temperature variation over the cross section, the positioning of the temperature probes in the flue gas between plain and finned tubes (T128) and downstream of the finned tubes (T31) was varied during some experiments at different operational states. The maximum temperature variation at each of the probes found this way has been used as estimation for the measuring uncertainties at these points.



| List of selected measuring points in natural gas / combustion air / flue gas |   | Sensor                   | Installation | Deviation (estimated)      | Comment  |
|--|---|--------------------------|--------------|----------------------------|--|
| <b>External Temperatures Gas/Air/Flue Gas</b>                                |   |                          |              |                            |  |
| T27  | natural gas entering burner   | Pt100 4-w.               | thermowell   | $< 0.2 K$                  |  |
| T28  | ambient air entering burner   | Pt100 4-w.               | direct       | $< 0.2 K$                  |  |
| T29  | flue gas in furnace chamber   | TC type-K                | direct       | $\approx 500 K$            | huge measuring error   |
| T29*   | flue gas in furnace chamber   | suction pyrometer        | temporary    | $< 200 K$                  | not permanently installed, experiments at a few burner duties        |
| T128   | flue gas between plain and finned tube bank   | TC type-K                | direct       | $\approx 50 K$             | inhomogeneous temperature profile, significant measuring uncertainty |
| T31  | flue gas leaving regenerator  | Pt100 4-w.               | direct       | $\approx 7 K$              | inhomogeneous temperature profile, some measuring uncertainty        |
| T32  | flue gas leaving economizer   | Pt100 4-w.               | direct       | $\approx 10 K$             | significant thermal loss   |
| <b>External Pressures Gas/Air/Flue Gas</b>                                   |   |                          |              |                            |  |
| P66  | natural gas at flow meter   | abs. press. transm.      | direct       | $< 1 mbar$                 |  |
| P1   | flue gas in furnace chamber   | diff. press. transm.     | temporary    | $< 1 Pa$ (rel. to ambient) | not permanently installed, experiments at a few burner duties        |
| P2   | flue gas between plain and finned tube bank   | diff. press. transm.     | temporary    | $< 1 Pa$ (rel. to ambient) | not permanently installed, experiments at a few burner duties        |
| P3   | flue gas leaving regenerator  | diff. press. transm.     | temporary    | $< 1 Pa$ (rel. to ambient) | not permanently installed, experiments at a few burner duties        |
| <b>Flows &amp; Composition Gas/Air/Flue Gas</b>                              |   |                          |              |                            |  |
| F83  | consumed natural gas  | gas meter (bellows-type) | in-line      | $< 2\%$                    | standard gas meter   |
| C01  | flue gas composition (excess air calculated from measured concentration of $CO_2$ ) | flue gas analyzer        | temporary    | $< 5\%$ excess air         | not permanently installed, experiments at a few burner duties        |

Tab. 22: Subset of the measuring points in the natural gas / combustion air / flue gas system.

Contact thermometers are not well suited for the measurement of elevated gas temperatures, under conditions of a non-zero radiation balance. Consequently, thermocouple T29 can only provide a rough estimate of the flue gas temperature in the furnace chamber while under operation ( $> 1000^\circ C$ ) in the direct vicinity of the much cooler boiling tubes ( $\approx 200^\circ C$ ).

Therefore, the actual gas temperature in the furnace chamber was also checked at a few burner duties by means of a suction pyrometer ( $T_{29}^*$ ) experiment, as described by *Atkinson (1956)* and *Atkinson & Hargreaves (1958)*.

### **Pressure Measurements**

Absolute pressure transmitters with a current output were employed for pressure measurements in the internal refrigerant and absorbent solution cycle ( $P_{61}$ ) and in the natural gas line ( $P_{66}$ ). Both sensors were individually calibrated with a pressure calibrator before installation.

The overpressure relative to ambient in the furnace chamber ( $P_1$ ), in the tube bundle between the plain and finned tubes ( $P_2$ ), and at the flue gas exit of the regenerator ( $P_3$ ) was determined by a differential pressure transmitter at a number of operational states with different burner duties. During steady operation of the plant, the positive port of the sensor was consecutively connected to these three measurement points.

### **Flow Measurements**

An ultrasonic flow meter was clamped on, to measure the circulation of the lithium bromide solution in the downcomer tubes, without interfering with the process and without introducing additional pressure drops. The flow meter could be installed at either of the downcomer tubes ( $F_{73a}$ ,  $F_{73b}$ ). The position of the ultrasonic flow meter was changed several times during the experiments. However, no significant difference was found in the measured flow rates at both downcomer tubes.

Magneto inductive flow meters were employed in the external cooling water loops. The gas consumption of the burner was measured by a standard bellows-type gas meter.

### **Flue Gas Composition**

At some operational states with different burner duties, the excess combustion air was determined by means of a flue gas analyzer that automatically calculated the value from the measured  $CO_2$  concentration in the flue gas. As the flue gas analyzer was not suited to the continuous online monitoring of the combustion process, the characteristic function of the excess air resulting from the chosen burner settings was fitted to its dependence on the burner duty. The correlation thus obtained was employed for the calculation of the excess air at all the operational states where no measured value was available.

## 6.3 Evaluation of measured data

### 6.3.1 Data recording and selection of stationary operational states

During the operation of the test rig, all measurement data were recorded by means of several Keithley 7001 scanners, Keithley 2001 multimeters, and a multipurpose DAQ card attached to a PC computer, running a data acquisition and visualization program written in National Instruments Labview. A complete data set was stored every 15 to 30 seconds.

Stationary operational states were extracted, after recording all the data from a days lab operation, for further evaluation. Using a Visual Basic macro in Excel, periods of at least 10 minutes duration, with a minimum variation in all the process variables, were identified and the mean value of each variable within this time slot was computed. For reference purposes, the mean values employed as raw data for all further evaluations are listed in Tab. 23 and Tab. 24 in appendix A.3.

### 6.3.2 Calculation of process variables from measured data

All the required process variables can be calculated easily from the set of measurement points given in Fig. 55 or in Tab. 20 to Tab. 22. In addition, due to an intentional redundancy of the measuring points, a number of process variables can be obtained in different ways from different sets of measured variables. Significant uncertainties have to be accounted for in some of the measured values. However, different methods of calculation will result in different values of the calculated process variables and in different uncertainties, which have to be attributed to these values.

The calculation procedure that was eventually employed, for the evaluation of the measured data, is outlined below. It was chosen so that consistent enthalpy balances were obtained and experimental uncertainty in the calculated variables was minimized.

#### Measurement uncertainty and error propagation

Unless otherwise noted, the uncertainty in all the process variables was determined, in conjunction with the calculation of the values, from error propagation by a simplified numerical procedure. For the multiplication or division of variables,  $X$  and  $Y$ , with uncertainties  $\Delta X$  and  $\Delta Y$ , the uncertainty  $\Delta Z$  of the result,  $Z$ , was estimated by the addition of the relative uncertainties at each data point:

$$Z = X \cdot Y \Leftrightarrow \frac{\Delta Z}{Z} = \frac{\Delta X}{X} + \frac{\Delta Y}{Y} \quad (6.1)$$

For the addition or subtraction of variables,  $X$  and  $Y$ , the resulting uncertainty,  $\Delta Z$ , was estimated by the arithmetic addition of the absolute values of the contributions  $\Delta X$  and  $\Delta Y$ ,



instead of a geometric addition. This procedure is compliant with the assumption of independent systematic measuring errors, yielding an upper limit for the uncertainty.

$$Z = X \pm Y \Leftrightarrow \Delta Z = \Delta X + \Delta Y \quad (6.2)$$

For functional dependencies  $Z = f(X, Y)$  that are more complex, a simplified numerical calculation scheme was employed to determine the error propagation. The difference quotients,  $\Delta Z_x / \Delta X$ ,  $\Delta Z_y / \Delta Y$ , were employed instead of the partial derivations,  $\partial Z / \partial X$ ,  $\partial Z / \partial Y$ . Also, the arithmetic addition of the absolute values of the contributions from different variables was always performed, instead of geometric addition:

$$\begin{aligned} Z = f(X, Y) \Leftrightarrow \Delta Z &= \text{Abs}(\Delta Z_x) + \text{Abs}(\Delta Z_y) \\ \text{whereby } \Delta Z_x &= [f(X+\Delta X, Y) - f(X-\Delta X, Y)] / 2 \\ \Delta Z_y &= [f(X, Y+\Delta Y) - f(X, Y-\Delta Y)] / 2 \end{aligned} \quad (6.3)$$

As further simplifications, specific heat capacities of fluids and specific liquid densities were assumed to be temperature invariant for error propagation calculations. Additionally, marginal contributions to the resulting uncertainty, where  $\text{Abs}(\Delta Z_x) \ll \text{Abs}(\Delta Z_y)$ , were neglected in favor of the dominant ones, where applicable<sup>65</sup>.

### External heat loads

The heat loads at the three simulation test rig heat exchangers were calculated from enthalpy balances, based on temperatures and flow rates measured in the external cooling water lines (cf. Fig. 55 and Tab. 21):

$$\dot{Q}_{S0} = F_{82} \cdot \rho_{H_2O}(T_{24}) \cdot [h'_{H_2O}(T_{25}) - h'_{H_2O}(T_{24})]$$

$$\dot{Q}_{S1} = F_{81} \cdot \rho_{H_2O}(T_{21}) \cdot [h'_{H_2O}(T_{23}) - h'_{H_2O}(T_{22})]$$

$$\dot{Q}_{S2} = F_{81} \cdot \rho_{H_2O}(T_{21}) \cdot [h'_{H_2O}(T_{22}) - h'_{H_2O}(T_{21})]$$

Additionally, the heat loads at absorber  $\dot{Q}_A$  and evaporator  $\dot{Q}_E$  were calculated from the respective measuring points listed in Tab. 21 for operational states after the addition of the evaporator/absorber unit to the test rig:

$$\dot{Q}_A = F_{316} \cdot \rho_{H_2O}(T_{244}) \cdot [h'_{H_2O}(T_{256}) - h'_{H_2O}(T_{244})] \quad (6.4)$$

$$\dot{Q}_E = F_{315} \cdot \rho_{H_2O}(T_{231}) \cdot [h'_{H_2O}(T_{243}) - h'_{H_2O}(T_{231})] \leq 0 \quad (6.5)$$

<sup>65</sup> E.g., solution temperature measuring uncertainties (cf. Tab. 20), which were at least one order of magnitude smaller than those in the flue gas, were disregarded when determining the uncertainties of the driving temperature differences.

### Internal cycle data

The refrigerant mass flow was calculated from an enthalpy balance at the heat exchanger, S0, functioning as a condenser, based on the external heat load,  $\dot{Q}_{S0}$ , and the measured pressure and temperatures in the internal cycle (cf. Fig. 55 and Tab. 20):

$$\dot{M}_{REFR} = \dot{Q}_{S0} / [h''_{REFR}(T09, P61) - h'_{REFR}(T10)]$$

The strong solution concentration was calculated from the regenerator pressure and solution outlet temperature assuming a state of equilibrium:

$$X_{STRONG} = X_{SAT}(P61, T04)$$

The uncertainty for the solution concentration was not estimated; the rather weak dependence of the specific heat capacity and the specific density on small variations in the salt concentration was neglected in error propagation calculations.

The strong solution mass flow leaving the regenerator was calculated from an enthalpy balance at the heat exchanger, S1, which acted to cool the solution:

$$\dot{M}_{STRONG} = \dot{Q}_{S1} / [h'_{STRONG}(X_{STRONG}, T04) - h'_{STRONG}(X_{STRONG}, T05)]$$

The weak solution mass flow entering the regenerator and the corresponding weak solution concentration was calculated by mass balance:

$$\begin{aligned} \dot{M}_{WEAK} &= \dot{M}_{STRONG} + \dot{M}_{REFR} \\ X_{WEAK} &= X_{STRONG} \cdot \dot{M}_{STRONG} / \dot{M}_{WEAK} \end{aligned}$$

The solution concentration in heat exchanger S2 and the economizer was identical to the weak solution concentration. Solution mass flow in this loop was calculated from an enthalpy balance at heat exchanger S2. Finally, the heat load at the economizer was calculated from an enthalpy balance in the solution cycle:

$$\begin{aligned} \dot{M}_{ECO} &= \dot{Q}_{S2} / [h'_{WEAK}(X_{WEAK}, T06) - h'_{WEAK}(X_{WEAK}, T07)] \\ \dot{Q}_{ECO} &= \dot{M}_{ECO} \cdot [h'_{WEAK}(X_{WEAK}, T07) - h'_{WEAK}(X_{WEAK}, T08)] \end{aligned}$$

The mean boiling temperature of the solution in the regenerator boiling tubes,  $T_{SAT,MN}$ , was estimated from the saturation conditions of the exiting strong solution and the additional liquid head,  $\Delta\rho_{HH}$ , at half height, assuming the boiling tubes were completely filled with liquid solution at concentration  $X_{STRONG}$ .

$$T_{SAT,MN} = T_{SAT}(X_{STRONG}, P61 + \Delta\rho_{HH}) \quad (6.6)$$

The uncertainty of the solution outlet temperature,  $T04$ , was assumed to be the dominant contribution to the uncertainty of the mean boiling temperature. Therefore, additional uncertainties in the differential pressure head at half height were neglected.

### Gas / air / flue gas side data

The natural gas mass flow was calculated from the gas meter reading, pressure, and temperature of the gas. The burner duty was calculated from the gas flow and the calorific value of the natural gas,  $\Delta h_{CV,GAS}$ , according to gas analysis data from the supplier.

$$\dot{M}_{GAS} = F83 \cdot \rho_{GAS}(P66, T27) \quad (6.7)$$

$$\dot{Q}_{GAS} = \dot{M}_{GAS} \cdot \Delta h_{CV,GAS} \quad (6.8)$$

A function fit was determined for the characteristic dependence of the excess air coefficient on the burner duty,  $\lambda_{EXCAIR}(\dot{Q}_{GAS})$ . Together with the stoichiometric air/gas-ratio,  $AFR_{STOIC,GAS}$ , from gas analysis data, the calculation of the combustion air and flue gas mass flow became possible:

$$\dot{M}_{AIR} = \dot{M}_{GAS} \cdot AFR_{STOIC,GAS} \cdot \lambda_{EXC.AIR}(\dot{Q}_{GAS}) \quad (6.9)$$

$$\dot{M}_{FG} = \dot{M}_{GAS} + \dot{M}_{AIR} \quad (6.10)$$

The theoretical adiabatic flame temperature of the combustion process was obtained from an enthalpy balance according to (2.60) for an ambient air temperature  $T_{AMB} = T28$ :

$$T_{FLAME} = f(AFR_{STOIC,GAS}, \Delta h_{CV,GAS}, \lambda_{EXC.AIR}(\dot{Q}_{GAS}), T28)$$

### Regenerator heat flux

The total heat flux at the regenerator  $\dot{Q}_G$  was calculated from an enthalpy balance with respect to all the heat loads detected in the external cooling water lines and the economizer heat duty:

$$\dot{Q}_G = \dot{Q}_{S0} + \dot{Q}_{S1} + \dot{Q}_{S2} + \dot{Q}_A + \dot{Q}_E - \dot{Q}_{ECO} \quad (6.11)$$

The total heat input to the regenerator was given from the enthalpy balance at the flue gas side:

$$\dot{Q}_{G,FG} = \dot{M}_{FG} \cdot [h_{FG}(T_{FLAME}) - h_{FG}(T31)] \quad (6.12)$$

The difference between the two values was attributed to thermal losses to the ambient in the regenerator:

$$\dot{Q}_{G,LOSS} = \dot{Q}_{G,FG} - \dot{Q}_G \quad (6.13)$$

It was assumed that the major share of these regenerator losses had to be attributed to the hot sections next to the burner and furnace chamber and only a minor share was attributed to the final section, equipped with finned tubes. Therefore, the heat flux at the finned section of the regenerator was estimated from the flue gas mass flow and the flue gas temperatures upstream and downstream of the finned section:

$$\dot{Q}_{FS} = \dot{M}_{FG} \cdot [h_{FG}(T128) - h_{FG}(T31)] \quad (6.14)$$

The remaining heat flux was attributed to the section of plain tubes:

$$\dot{Q}_{PS} = \dot{Q}_G - \dot{Q}_{FS} = \dot{Q}_{G,FG} - \dot{Q}_{G,LOSS} - \dot{Q}_{FS} \quad (6.15)$$

The total heat flux at the regenerator can be divided into two portions, one for actually generating the refrigerant vapor  $\dot{Q}_{G,VAP}$ , and the other just needed for preheating the solution entering the regenerator  $\dot{Q}_{G,HEAT}$ . In a complete absorption cycle (instead of a regenerator test rig), the term  $\dot{Q}_{G,HEAT}$  would reflect the unbalanced portion of mismatch and solution heat exchanger loss that has to be compensated for by extra heat input in the regenerator.

$$\dot{Q}_G = \dot{Q}_{G,VAP} + \dot{Q}_{G,HEAT}$$

The heat attributed solely to the generation of refrigerant vapor  $\dot{Q}_{G,VAP}$  was calculated from an enthalpy balance at the temperature  $T04$  of the exiting weak solution:

$$\dot{Q}_{G,VAP} = \dot{M}_{REFR} \cdot h''_{REFR}(T04, P61) + \dot{M}_{STRONG} \cdot h'_{STRONG}(T04) - \dot{M}_{WEAK} \cdot h'_{WEAK}(T04)$$

Admittedly, this simplified balance does not reflect the actual thermodynamic process in the regenerator, but it is compliant with the definitions of mismatch and solution heat exchanger loss (2.40), (2.42), (3.23) - (3.25) that have been employed so far in this work. The difference between the two heat fluxes was finally attributed to the preheating of the solution entering the regenerator:

$$\dot{Q}_{G,HEAT} = \dot{Q}_G - \dot{Q}_{G,VAP}$$

### 6.3.3 Range of experimental data from stationary states

20 stationary operational states were identified from all the measurements taken during the operation of the test rig, seven of which were recorded prior to completion of the measurement instrumentation (states no. 1-7 in Tab. 23 in appendix A.3). Fig. 56, below, provides an overview of the heat fluxes and mass flows over the gas burner duty at these states, in comparison to the respective design values of the regenerator prototype. Experimental data from the 13 measurements recorded with full instrumentation (states no. 8-20 in Tab. 23 and Tab. 24 in appendix A.3) are displayed as filled symbols. The additional data for the 7 measurements without full instrumentation are shown as empty symbols; these are not included in the further evaluations presented below. The respective design values are shown as enlarged symbols at the rated burner duty of 315 kW.

It shows that experimental data are available in the range of burner duties,  $\dot{Q}_{GAS}$ , from about 85 kW to 255 kW proving a turndown ratio of at least 3:1. The rated duty of 315 kW could not be achieved during the tests. This was caused by the installation of an inadequate fan at the prototypes gas burner. Consequently, the heat flux in the regenerator,  $\dot{Q}_G$ , (orange diamonds in the left diagram) did not reach its design value.

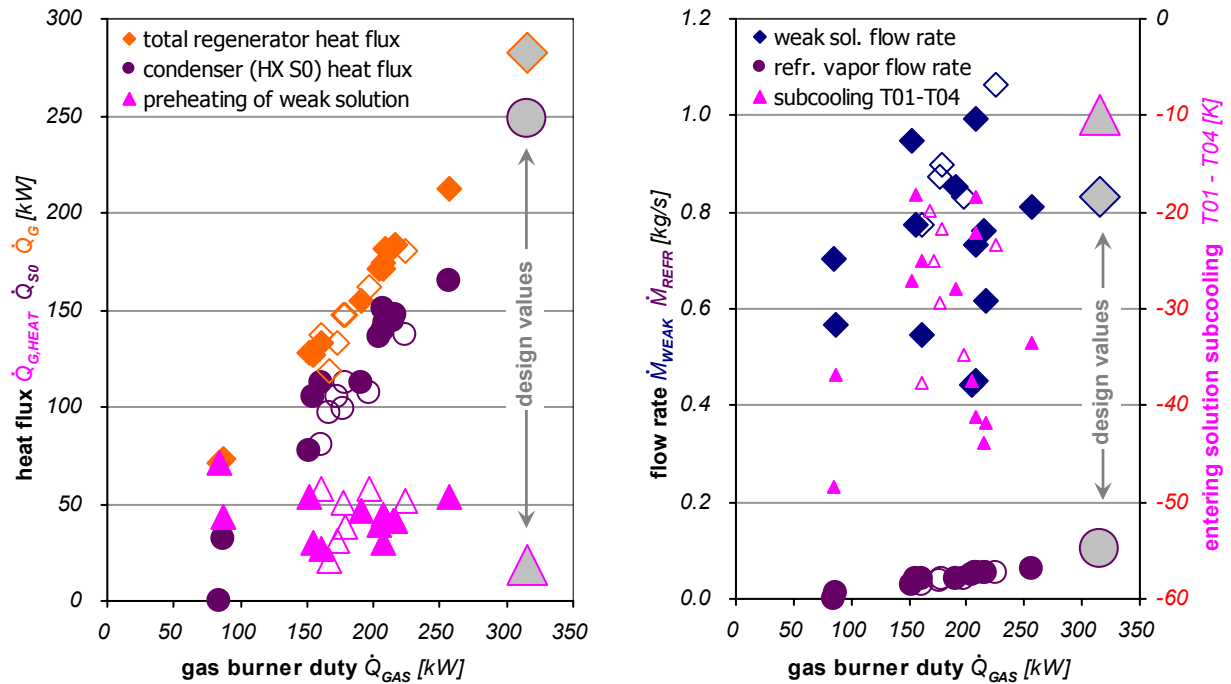


*Fig. 56: Range of available experimental data from 13 stationary operational states with full measurement instrumentation installed (filled symbols) and 7 additional stationary states recorded prior to completion of the instrumentation (empty symbols), compared to the design values of the regenerator prototype at full load operation (enlarged symbols).*

While the mass flow of the entering weak solution,  $\dot{M}_{WEAK}$ , (blue diamonds in the diagram on the right) could be varied around its design value in the test rig, the subcooling of the entering solution relative to the saturated leaving solution,  $T_{01} - T_{04}$ , (small magenta triangles in the right diagram) showed significantly larger absolute values in the experiments. This was due to the limitations of the test rig, which did not have a real solution heat exchanger but instead required the cooling of the solution in the heat exchanger HX S1, to prevent cavitation in the solution pump below the solution storage vessel SSV (cf. Fig. 54). Consequently, the heat flux,  $\dot{Q}_{G,HEAT}$ , required for preheating the entering solution (magenta triangles in left diagram) was always slightly higher in the test rig than was foreseen for the design point operation of the regenerator prototype.

Due to the lower burner duty and the higher share of the heat flux required for preheating the solution in the test rig, both the heat flux,  $\dot{Q}_{S0}$ , in condenser S0 and the refrigerant vapor mass flow,  $\dot{M}_{REFR}$ , (violet circles in the respective diagrams) only reached about two-thirds of their respective design values. Also, as can be seen in the left diagram of Fig. 56, one stationary state at minimum burner duty was recorded with the regenerator merely functioning as a solution heater, without net vapor generation and thus zero condenser heat flux. Operational states without net vapor generation are found in actual machines during the startup phase.

Overall, it can be stated that the prototype was operated in the test rig at a wide range of typical part load conditions found in double-effect cycles that are not fully optimized, characterized by a significant and load-independent loss term,  $\dot{Q}_{G,HEAT}$ , (magenta triangles in left diagram of Fig. 56) over the full range of burner duties.

### 6.3.4 Estimation of radiative heat transfer

#### Enthalpy balances

Although a low-radiation burner was employed in the regenerator prototype, a significant share,  $\dot{Q}_{RAD}$ , of the total heat flux in the first section,  $\dot{Q}_{PS}$  according to (6.15), still resulted from radiation. Only the remaining portion,  $\dot{Q}_{CV,PS}$ , can be attributed to convective heat transfer.

$$\dot{Q}_{PS} = \dot{Q}_{RAD} + \dot{Q}_{CV,PS} \quad (6.16)$$

The total radiative heat flux to the tubes,  $\dot{Q}_{RAD}$ , consists of the following contributions:

- Burner surface radiation, which was intentionally low at high-fire, but increased at low-fire when the flame approached the metal burner matrix
- Radiation from the hot walls of the flue gas duct and especially from the walls of the furnace chamber section
- Gas radiation from the furnace chamber, which was especially significant at high-fire operation, with small excess air values and high combustion temperatures
- Gas radiation within the bundle of tubes (flue gas in the space between neighboring tubes). This contribution was neglected as it had only a minor effect compared to the three other heat fluxes.

In the chosen staggered tube arrangement, only the first two rows of tubes were facing the radiation from the burner and furnace chamber. Due to this radiation, the temperature of the flue gas hitting the first row of tubes,  $T_{FG,PS,ENTER}$ , was already lower than the theoretical adiabatic flame temperature,  $T_{FLAME}$ , even if there were no thermal losses to the ambient. If thermal losses have to be accounted for, the temperature of the flue gas hitting the first row of tubes,  $T_{FG,PS,ENTER}$ , is also dependent on the amount of thermal losses attributable to the furnace chamber.

Actually, it can be argued that the major part of all the thermal losses to the ambient in the regenerator prototype,  $\dot{Q}_{G,LOSS}$ , was from the hot furnace chamber and burner section. The reason was that the structure and thickness of the furnace chamber insulation were the same as in the tube sections of the regenerator, although the flue gas temperatures varied significantly; the front plate where the burner was mounted was not insulated at all. Therefore, it was assumed for simplification of the evaluation of the experimental data that the thermal losses,  $\dot{Q}_{G,LOSS}$  according to (6.13), in the regenerator could be completely attributed to the furnace chamber. In this case, the entering flue gas temperature,  $T_{FG,PS,ENTER}$ , the

radiation heat flux,  $\dot{Q}_{RAD}$ , and the thermal losses,  $\dot{Q}_{G,LOSS}$ , are linked by a simple enthalpy balance:

$$\dot{Q}_{RAD} + \dot{Q}_{G,LOSS} = \dot{M}_{FG} \cdot [h_{FG}(T_{FLAME}) - h_{FG}(T_{FG,PS,ENTER})] \quad (6.17)$$

With the same assumption, the heat flux from convective heat transfer in the plain tubes section  $\dot{Q}_{CV,PS}$  is obtained analogous to (6.14) from the entering flue gas temperature  $T_{FG,PS,ENTER}$  and the temperature between the plain and finned section  $T_{128}$ :

$$\dot{Q}_{CV,PS} = \dot{M}_{FG} \cdot [h_{FG}(T_{FG,PS,ENTER}) - h_{FG}(T_{128})] \quad (6.18)$$

In addition, for a complete evaluation of the regenerator heat transfer, at least one of the three variables, radiation heat flux,  $\dot{Q}_{RAD}$ , convective heat transfer,  $\dot{Q}_{CV,PS}$ , and flue gas temperature,  $T_{FG,PS,ENTER}$ , has to be determined. Subsequently, the other two can be calculated from (6.17) and (6.18).

### Different approaches for determining the radiation heat flux

In fact, none of the three variables, radiation heat flux  $\dot{Q}_{RAD}$ , convective heat transfer  $\dot{Q}_{CV,PS}$ , and flue gas temperature  $T_{FG,PS,ENTER}$  quoted above can easily be determined with good accuracy. Fig. 57, below, shows a comparison of the results from different approaches for the estimation of the dependence of the radiative heat transfer,  $\dot{Q}_{RAD}$ , on the burner duty,  $\dot{Q}_{GAS}$ .

Results from initial design calculations made by *Clark et al. (1999a)* based on the specifications of the burner manufacturer are displayed as **magenta** squares in Fig. 57. They found that load dependent variations in burner surface radiation and in gas radiation should nearly compensate for each other, resulting in a radiative heat transfer  $\dot{Q}_{RAD} \approx 30 \text{ kW}$ , which is almost independent of the burner duty.

The **red** circles in Fig. 57 denote the values of  $\dot{Q}_{RAD}$  that were obtained from (6.17), if the readings of thermocouple  $T_{29}$  were employed for the estimation of the actual temperature of the entering flue gas, i.e.,  $T_{FG,PS,ENTER} \approx T_{29}$ . Thermocouple  $T_{29}$  was mounted in the furnace chamber quite close to the first tube. However, as a result of the unbalanced radiation exchange between the thermocouple at temperature  $T_{29}$  and the significantly cooler boiling tubes, it has to be assumed that the measured values are smaller than the actual gas temperature at this position, i.e.,  $T_{29} < T_{FG,PS,ENTER}$ . Consequently, the radiative heat transfer calculated from  $T_{29}$  is too high and the values denoted by the **red** circles in Fig. 57 have to be interpreted as upper limits for  $\dot{Q}_{RAD}$ . In contrast to the calculations by *Clark et al. (1999a)* (**magenta** squares), the evaluation of the temperature measurement  $T_{29}$  (**red** circles) suggests a nearly proportional dependence of the radiative heat flux on the burner duty with about 30% radiation.

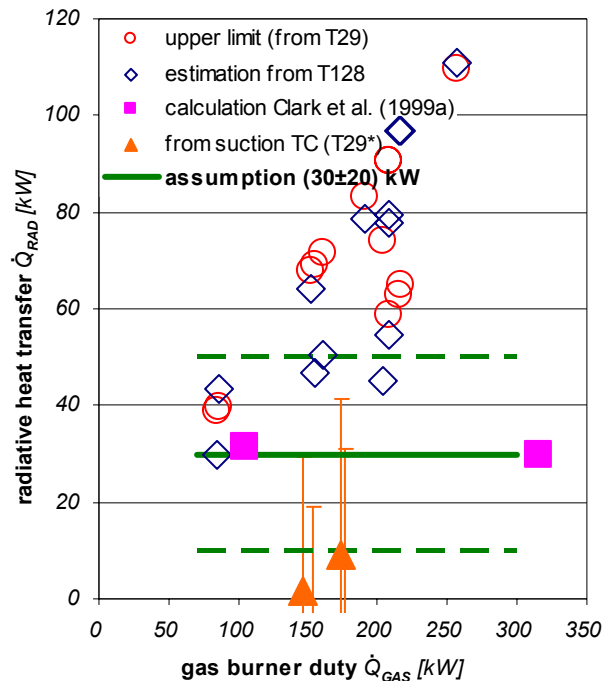


**Fig. 57: Different approaches to the estimation of the radiative heat transfer over the gas burner duty.** Upper limit from readings of thermometer T29 appear as **red** circles, rough estimation from a convective heat transfer calculation based on temperature T128 appear as **blue** diamonds, results from suction thermocouple experiments appear as **orange** triangles with error bars, calculations by Clark et al. (1999a) based on burner specifications appear as **magenta** squares. The final assumption for radiative heat transfer that was employed for further evaluations is shown as a solid **green** line.

As the radiation values calculated from T29 (**red** circles in Fig. 57) showed a significant deviation from the theoretical prediction (**magenta** squares in Fig. 57), the radiative heat transfer was additionally estimated by means of two other independent methods (**blue** diamonds and **orange** triangles in Fig. 57). A rough estimation of the radiative heat transfer (**blue** diamonds in Fig. 57) was obtained from the measured flue gas temperature T128 between the plain and finned tubes, assuming that the convective heat transfer in the plain tubes section,  $\dot{Q}_{CV,PS}$ , was completely compliant with the respective correlations from VDI-GVC (2002). Then, the dependence of the entering flue gas temperature,  $T_{FG,PS,ENTER}$ , on  $\dot{Q}_{CV,PS}$  and T128 could be calculated from (6.18). Additionally, experiments with a suction pyrometer setup, as described by Atkinson (1956) and Atkinson & Hargreaves (1958) were conducted to determine the flue gas temperature in the furnace chamber T29\*. The resulting radiation values are displayed as **orange** triangles with error bars. Both methods are described below in greater detail.

### Backward heat transfer calculation

A stepwise backward-calculation was performed along the section of plain tubes starting with the flue gas temperature T128 downstream of the 7<sup>th</sup> row, to determine the **blue** diamonds shown in Fig. 57, a stepwise backward-calculation has been performed along the section of plain tubes starting with the flue gas temperature T128 downstream of the 7<sup>th</sup> row. At each



row of tubes,  $J = 7 \dots 1$ , self-consistent solutions were numerically derived for the heat flux,  $\dot{Q}_{CV,J}$ , and the flue gas temperatures upstream ( $T_{FG,J}$ ) and downstream ( $T_{FG,J+1}$ ) of row  $J$ :

$$\dot{Q}_{CV,J} = \dot{M}_{FG} \cdot [h_{FG}(T_{FG,J}) - h_{FG}(T_{FG,J+1})] = U_{O,J} \cdot A_{O,ROW} \cdot LMTD_J \quad (6.19)$$

At the last row of plain tubes  $J = 7$ , the downstream temperature  $T_{FG,J+1}$  was set  $T_{FG,8} := T_{128}$ ; for all consecutive iterations concerning rows  $J = 6 \dots 1$ , the flue gas temperature  $T_{FG,J}$  determined in the preceding calculation step was used as new downstream temperature  $T_{FG,J+1}$ . The referred surface area in (6.19) is the gas side surface of the four boiling tubes in a single row  $A_{O,ROW} = \frac{1}{7} \cdot A_{PS,G}$  being one seventh of the total gas side surface in the section of plain tubes. The logarithmic mean temperature difference  $LMTD_J$  at each row  $J$  was calculated based on the applicable flue gas temperatures and the assumed mean boiling temperature  $T_{SAT,MN}$  according to (6.6).

$$LMTD_J = LMTD(T_{FG,J+1} - T_{SAT,MN}, T_{FG,J} - T_{SAT,MN}) \quad (6.20)$$

The overall heat transfer coefficient  $U_{O,J}$  in each row  $J$  was calculated on the lines of (4.7) based on the conductivity of the tube wall and on the local heat transfer coefficients  $\alpha_{O,J}$  at the outer side (flue gas) and  $\alpha_{I,J}$  at the inner side (liquid). The correlations (4.55) - (4.61) listed in 4.4.2 for convective heat transfer in tube bundles according to *VDI-GVC (2002)* have been employed for calculation of the convective heat transfer coefficients  $\alpha_{O,J} = \alpha_{CV,J}$  at the gas side. The boiling correlation (4.96) of *Cooper (1984)* assuming unknown surface finish ( $R_p = 1 \mu m$ ) and the attenuation factor (4.103) according to *Rant (1977)* were used to calculate the heat transfer  $\alpha_{I,J} = \alpha_{B,J}$  at the liquid side of each tube row.

Finally, consistent values for total convective heat flux  $\dot{Q}_{CV,PS}$

$$\dot{Q}_{CV,PS} = \sum_J \dot{Q}_{CV,J} \quad (6.21)$$

and entering flue gas temperature  $T_{FG,PS,ENTER} = T_{FG,8}$  at the section of plain tubes were obtained that enabled an estimation of the radiative heat flux  $\dot{Q}_{RAD}$  displayed as **blue** diamonds in Fig. 57. It has to be stated however that this kind of estimation goes along with a significant uncertainty as small variations in the flue gas temperature  $T_{128}$  or in the assumed convective heat transfer coefficients  $\alpha_{O,J} = \alpha_{CV,J}$  result in large changes of the calculated temperature  $T_{FG,PS,ENTER}$ .

It shows that the radiation estimated from the leaving flue gas temperature  $T_{128}$  (**blue** diamonds in Fig. 57) is basically compliant with the values calculated as upper limit from the readings of thermometer  $T_{29}$  (**red** circles in Fig. 57). On the other hand, it is in apparent contradiction to the initial design calculations made by *Clark et al. (1999a)* based on specifications of the burner manufacturer (displayed as **magenta** squares in Fig. 57).

### Suction pyrometer experiments

In order to resolve this issue, additional experiments employing a suction pyrometer setup according to *Atkinson (1956)* and *Atkinson & Hargreaves (1958)* have been conducted. This method uses a thermocouple probe that is mounted inside a small tube, which itself is connected to the furnace chamber. A small stream of hot flue gas is sucked through the tube by means of a vacuum pump. During the experiment, this flue gas flow is varied and the minimum and the maximum temperature readings are recorded. High flow speed of the flue gas inside the tube ensures good thermal coupling with the thermometer. Therefore in all experiments the maximum readings  $T_{29}^{**}$  of this thermocouple inside the suction tube have already been higher than the readings from thermocouple  $T_{29}$  in the furnace chamber. However, the maximum readings  $T_{29}^{**}$  are still lower than the true flue gas temperature as the thermal coupling is imperfect and the temperature of the thermometer tip is reduced by heat conduction and radiation effects. To compensate for this deviation, an empirical correction formula is provided by *Atkinson (1956)* and *Atkinson & Hargreaves (1958)* that finally estimates the true flue gas temperature  $T_{29}^*$  from the minimum and maximum thermometer reading.

Altogether four experiments with the suction pyrometer at two different burner duties have been conducted. Taking the corrected temperatures as estimation for the entering flue gas temperatures  $T_{FG,PS,ENTER} \approx T_{29}^*$ , radiation values  $\dot{Q}_{RAD}$  were calculated from (6.17) that are displayed as **orange** triangles in Fig. 57. In two of these experiments the corrected temperatures from the suction pyrometer  $T_{29}^*$  were only slightly lower than the estimated adiabatic flame temperatures  $T_{FLAME}$  at these operational states. Consequently, (6.17) yielded quite low radiative heat fluxes  $\dot{Q}_{RAD} < 10 \text{ kW}$ . During the other two experiments, the corrected flue gas temperatures  $T_{29}^*$  were even slightly higher than the estimated adiabatic flame temperatures and thus no radiation heat flux could be calculated at all. Therefore, only two **orange** triangles are shown in Fig. 57. The upper ends of the four **orange** error bars in Fig. 57 visualize the radiation values that would have been obtained if the uncorrected maximum thermometer readings were used for estimating the entering flue gas temperatures i.e.  $T_{FG,PS,ENTER} \approx T_{29}^{**}$ .

After all, it has to be stated that the suction pyrometer experiments could not prove the existence of significantly higher radiative heat flux values than proposed by the initial calculations of *Clark et al. (1999a)*. However, there is also some uncertainty in the values obtained from the suction pyrometer, especially what the correct application of the empirical correction formula is concerned. The temperature values  $T_{29}^*$  thus obtained obviously underestimate the radiative heat flux that always must have been present in this environment. Another source of error is the installation position of the suction pyrometer, which was

during the experiments flanged to the furnace chamber quite close to the burner and with some distance to the first tube row<sup>66</sup>. Therefore, it must be taken into consideration that the flue gas temperature at the suction pyrometer might generally be higher than the temperature of the gas entering the plain tubes section.

### Assumed radiation heat flux

As no clear evidence for the magnitude of the radiative heat could be derived from the experimental data, the design values from *Clark et al. (1999a)* have been employed as basis for all further evaluations of measurement data. Thus a constant radiative heat flux  $\dot{Q}_{RAD} = 30 \text{ kW}$  was assumed at all burner duties  $\dot{Q}_{GAS} \geq 70 \text{ kW}$  (solid green line in Fig. 57). To account for the certain discrepancies, an uncertainty of  $\pm 20 \text{ kW}$  (dashed green lines in Fig. 57) was attributed to this estimation. The entering flue gas temperatures  $T_{FG,PS,ENTER}$  employed in all further evaluations presented below have been calculated from (6.17) in accordance with the assumption  $\dot{Q}_{RAD} = 30 \text{ kW}$ .

### 6.3.5 Determination of specific numbers

A specific weak solution circulation  $f_{WEAK}$  for the regenerator prototype in the test rig was calculated from refrigerant mass flow and weak solution mass flow:

$$f_{WEAK} = \dot{M}_{WEAK} / \dot{M}_{REFR}$$

This definition is basically compliant with the definition of the specific solution circulation in a double-effect absorption chiller employing a parallel-flow design and thus  $f_{WEAK,HTG} \approx f_{WEAK}$ .

A mean cross-sectional vapor flux  $\dot{m}_{REFR,CS}$  and a mean cross-sectional weak solution flux  $\dot{m}_{WEAK,CS}$  can be defined with reference to the total cross section  $A_{CS,L}$  of all boiling tubes at the liquid side:

$$\dot{m}_{REFR,CS} = \dot{M}_{REFR} / A_{CS,L}$$

$$\dot{m}_{WEAK,CS} = \dot{M}_{WEAK} / A_{CS,L}$$

This specific cross-sectional vapor flux  $\dot{m}_{REFR,CS}$  has a direct physical relevance, as it is the mean value of the actual mass flux of the vapor leaving the boiling tubes at the upper ends. The specific cross-sectional weak solution flux  $\dot{m}_{WEAK,CS}$  is not directly related to any physical value in a natural convection boiler where the total upward mass flow in the boiling tubes is larger than the entering mass flow due to the internal recirculation. Here  $\dot{m}_{WEAK,CS}$  can be interpreted as an easy to determine lower limit for the hard to determine actual mass flux in the boiling tubes.

<sup>66</sup> At this position, a sight glass initially had been present; the respective cut out in the furnace chamber wall enabled the installation of the suction tube.

The mean surface heat flux  $\dot{q}_{MN,L}$  at the solution side of the regenerator boiling tubes was calculated from the quotient of the total regenerator heat flux  $\dot{Q}_G$  and the total surface at the liquid side of all boiling tubes  $A_L$ :

$$\dot{q}_{MN,L} = \dot{Q}_G / A_L$$

Respectively, mean surface heat fluxes  $\dot{q}_{PS,G}$  and  $\dot{q}_{FS,G}$  at the gas side of the regenerator boiling tubes in the plain and finned sections were calculated:

$$\dot{q}_{PS,G} = \dot{Q}_{PS} / A_{PS,G}$$

$$\dot{q}_{FS,G} = \dot{Q}_{FS} / A_{FS,G}$$

Here,  $\dot{Q}_{PS}$  and  $\dot{Q}_{FS}$  are total the heat fluxes in the plain and finned section according to (6.14) and (6.15);  $A_{PS,G}$  and  $A_{FS,G}$  are the applicable gas side surfaces of all tubes in the respective sections.

At the section of plain tubes, additionally the share of the surface heat flux resulting from convective heat transfer in the flue gas  $\dot{Q}_{CV,PS}$  was calculated:

$$\dot{q}_{CV,PS,G} = \dot{Q}_{CV,PS} / A_{PS,G}$$

In Fig. 58 below, an overview on characteristic specific numbers of the stationary operational states with full measurement data available is provided. Additionally, the design values for the regenerator prototype at full load operation are shown for comparison.

In the left diagram, the specific cross-sectional mass flux of entering weak solution  $\dot{m}_{WEAK,CS}$ , the specific solution circulation  $f_{WEAK}$ , and the relative share of the total heat flux required for preheating the entering solution  $\dot{Q}_{G,HEAT} / \dot{Q}_G$  are shown over the mean surface heat flux  $\dot{q}_{MN,L}$  at the solution side of the boiling tubes. In the right diagram, the mean surface heat flux  $\dot{q}_{MN,L}$ , the specific solution circulation  $f_{WEAK}$ , and the share of preheating  $\dot{Q}_{G,HEAT} / \dot{Q}_G$  are shown over the specific cross sectional mass flux of refrigerant vapor  $\dot{m}_{REFR,CS}$ .

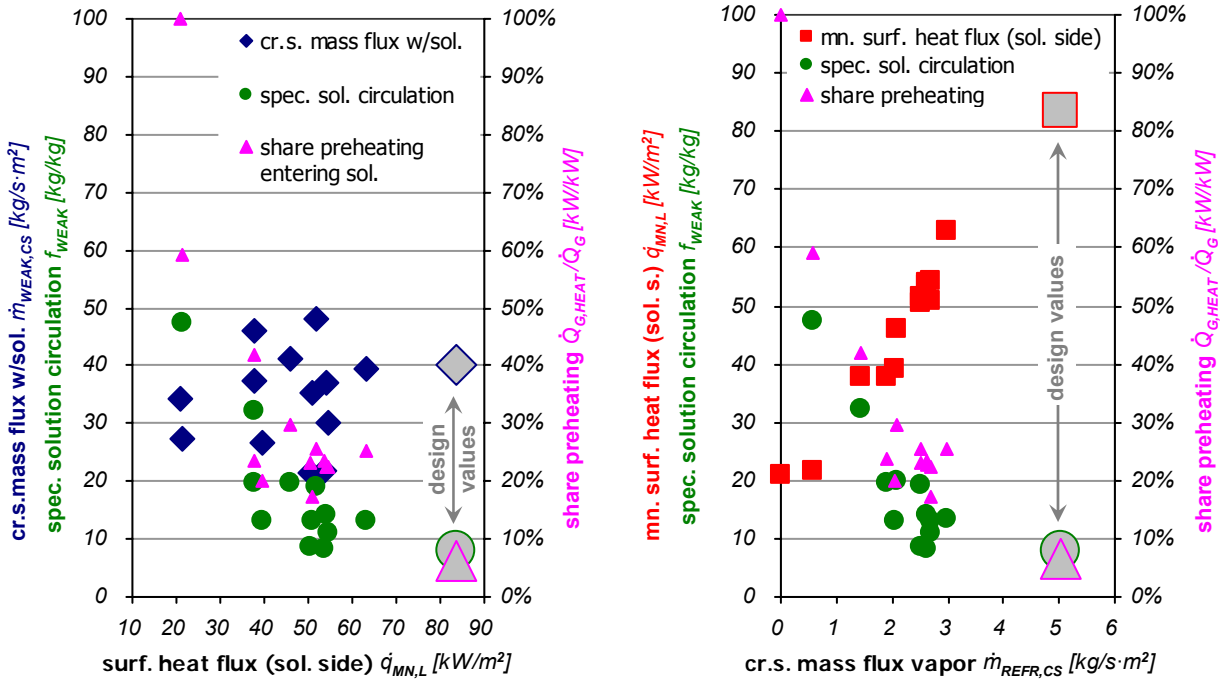


**Fig. 58:** Range of available experimental data from stationary operational states in terms of specific numbers. Mass flux of entering solution with reference to the cross sectional area (blue diamonds), specific solution circulation (green circles), mean surface heat flux at the solution side (red squares), and share of the total heat flux required for preheating entering solution (small magenta triangles) over the surface heat flux (left diagram) and the mass flux of refrigerant vapor (right diagram).

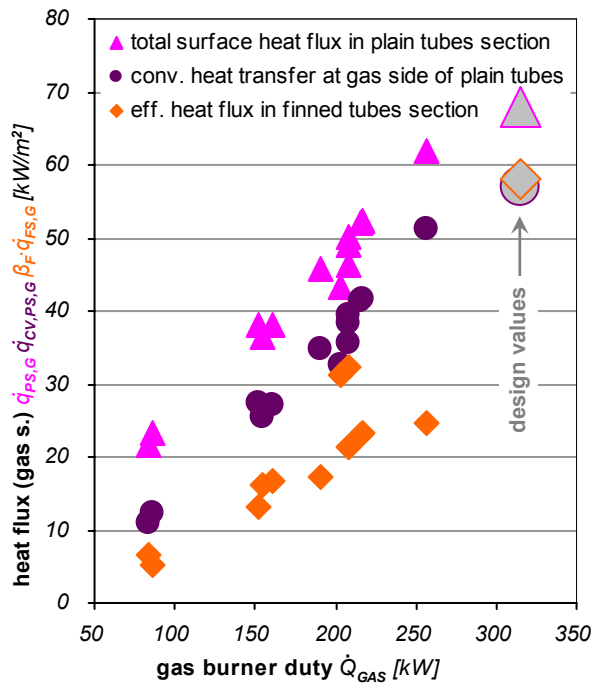


**Fig. 59:** Range of experimental heat fluxes at the gas side of the regenerator in comparison with the design values at full load operation.

Mean heat flux at the outer side of all plain boiling tubes (magenta triangles) and the share of this heat flux attributed to convective heat transfer at the gas side (violet circles). For the section of finned tubes, the mean heat flux with respect to the outer surface of plain tubes without fins is shown (orange diamonds).

The specific heat fluxes at the gas side of the boiling tubes in dependence on the burner duty  $\dot{Q}_{GAS}$  are shown in Fig. 59 above. For the section of plain tubes the mean heat flux  $\dot{q}_{PS,G}$  and the heat flux attributed to convective heat transfer only  $\dot{q}_{CV,PS,G}$  are given. For the section of finned tubes, the “effective” heat flux  $\beta_F \cdot \dot{q}_{FS,G}$  with respect to the outer surface of plain tubes without fins is provided to obtain comparable numbers. The surface enhancement factor of the finned tubes  $\beta_F$  was calculated according to (4.63) from the fin geometry data of the prototype provided by *Clark et al. (1999a)*.

With respect to the significant scatter of the data points, it has to be noted however that these experimental data have been obtained at different settings of the gas burner concerning the dependency of the excess air coefficient on the burner duty  $\lambda_{EXCAIR}(\dot{Q}_{GAS})$ . Therefore, the heat fluxes due to convective heat transfer  $\dot{q}_{CV,PS}$ , and  $\beta_F \cdot \dot{q}_{FS,G}$  in Fig. 59 are not exclusively functions of the burner duty that is employed as abscissa in this diagram.

The three diagrams in Fig. 58 and Fig. 59 repeat information already provided by Fig. 56 in 6.3.3 above in specific rather than absolute numbers. Therefore, the same conclusions on the range of available data and on the operational characteristics of the test rig already provided for Fig. 56 in 6.3.3 above apply as well for Fig. 58 and Fig. 59.

Additionally, Fig. 59 comprises information on the surface heat flux in the two sections of the heat exchanger. It shows that the heat exchanger intentionally was designed for similar surface heat flux with reference to the bare tube bodies in the plain and the finned section (enlarged symbols in Fig. 59). During the test series, however, the effective surface heat flux  $\beta_F \cdot \dot{q}_{FS,G}$  in the finned section (**orange diamonds**) was significantly smaller than the convective heat flux  $\dot{q}_{CV,PS}$  at the plain tubes (**violet circles**). The reason for this obvious mismatch is – once again – that due to the too small fan of the burner prototype the heat exchanger only could be operated under part load at reduced flue gas flow rates.

## 6.4 Experimental results

### 6.4.1 Flue gas side heat transfer

#### Main influencing variables and experimental uncertainties

As already discussed above, significant uncertainties have to be attributed to the experimental determination of flue gas temperatures in the test rig (cf. Tab. 22). These uncertainties have to be considered in the calculation of heat transfer coefficients at the flue gas side from the experimental data. Additionally uncertainties in determination of the excess air coefficient  $\lambda_{EXC.AIR}$ , the gas burner duty  $\dot{Q}_{GAS}$ , and the total regenerator heat transfer rate  $\dot{Q}_G$  have to be regarded. As already discussed in 6.3.2 above, minor contributions from measuring uncertainties in solution temperatures (cf. Tab. 20) being at least one order of magnitude smaller than those in the flue gas were disregarded for determination of the error propagation. An overview on main influencing variables including the uncertainties is provided in Fig. 60 below.

The upper left diagram shows the excess air coefficients  $\lambda_{EXC.AIR}$  and the resultant adiabatic flame temperatures  $T_{FLAME}$  with the respective uncertainties. The uncertainty of the excess air coefficient was also the main source of error in the determination of the flue gas mass flow rate  $\dot{M}_{FG}$  according to (6.7)-(6.10). The flue gas mass flow rate  $\dot{M}_{FG}$  itself is no independent influencing variable and thus it is not additionally shown in Fig. 60.

The upper right diagram displays the assumed temperature of the flue gas entering the section of plain tubes  $T_{FG,PS,ENTER}$  vs. the total heat transfer rate of the regenerator  $\dot{Q}_G$  and the respective uncertainties. For comparison, additionally the readings of thermometer  $T_{29}$  mounted in front of the plain tubes section are given. The huge uncertainties in the entering temperature  $T_{FG,PS,ENTER}$  result from significant contributions in three influencing variables: excess air coefficient  $\lambda_{EXC.AIR}$ , regenerator heat transfer rate  $\dot{Q}_G$ , and assumed radiative heat transfer  $\dot{Q}_{RAD} = (30 \pm 20) kW$ .

The lower left diagram shows measured values and uncertainties of the temperatures of flue gas entering the finned section  $T_{128}$  and leaving the regenerator  $T_{31}$  vs. the total heat transfer rate of the regenerator  $\dot{Q}_G$ .

The leaving flue gas temperature  $T_{31}$  was always close to the leaving strong solution temperature  $T_{04}$ , which itself varied considerably between different operational states. Therefore, only the difference  $T_{31} - T_{04}$  between leaving flue gas temperature and leaving solution temperature vs. the total heat transfer rate is displayed in the lower right diagram. Finally, for comparison the difference  $T_{SAT,MN} - T_{04}$  between the assumed mean solution boiling temperature  $T_{SAT,MN}$  from (6.6) and the leaving solution temperature  $T_{04}$  is given in

this diagram. For definition of the driving temperature differences and overall heat transfer coefficients in the regenerator, this mean solution boiling temperature  $T_{SAT,MN}$  was employed.

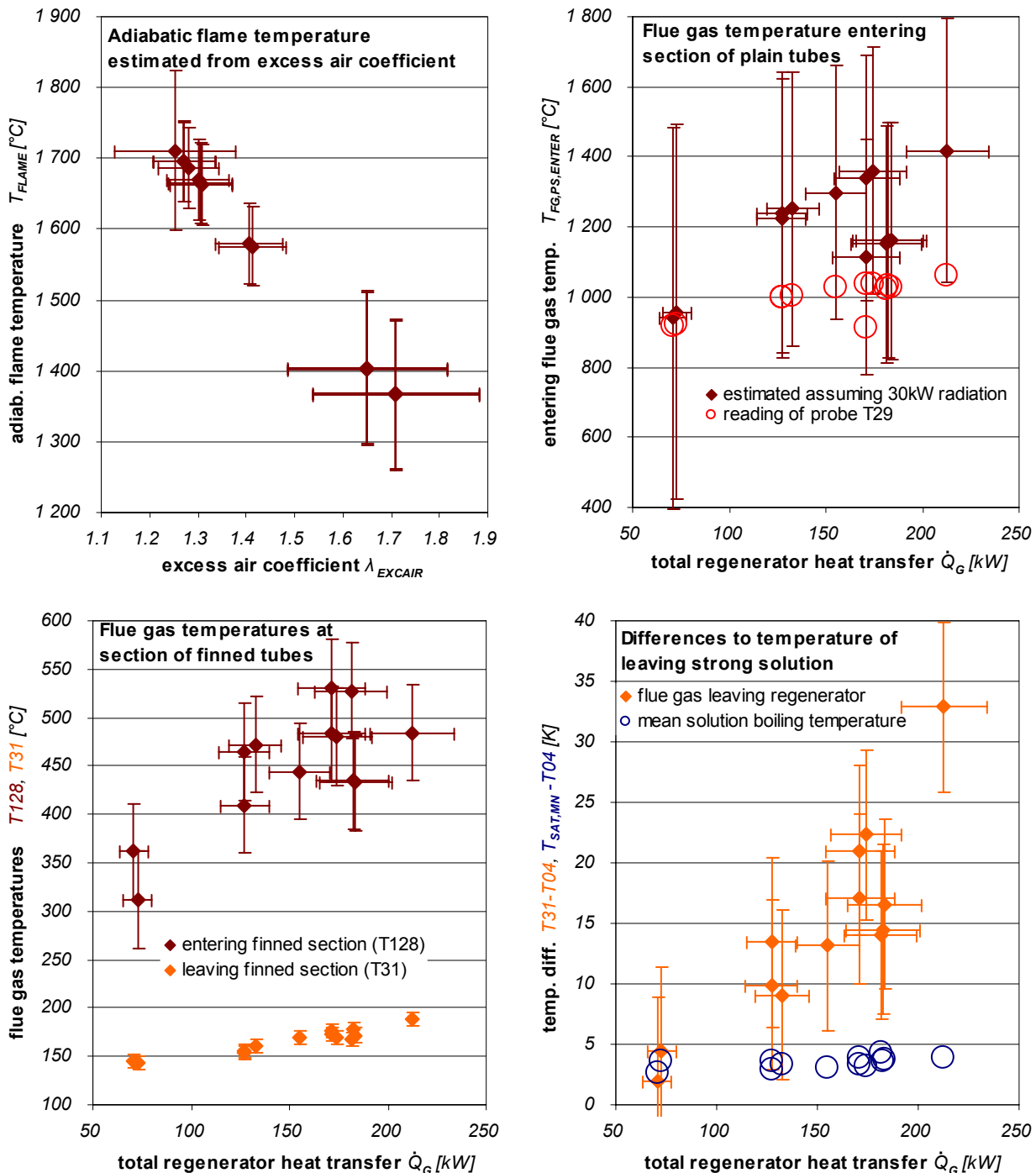


**Fig. 60: Main influencing variables for determination of experimental heat transfer coefficients at the flue gas side of the regenerator prototype and assumed experimental uncertainties for these variables.** Adiabatic flame temperature calculated from excess air coefficient (upper left diagram). Estimated temperature of flue gas entering the section of plain tubes vs. total regenerator heat transfer rate (upper right diagram). Measured temperatures of flue gas entering and leaving the section of finned tubes (lower left diagram). Temperature difference between leaving flue gas and leaving strong solution (lower right diagram).

It shows that the uncertainty attributed to the leaving flue gas temperature  $T_{31}$  is still larger than the estimated offset  $T_{SAT,MN} - T_{04}$  in the saturation temperature. Therefore, minor



uncertainties in the determination of the true mean boiling temperature resulting from the uncertain additional pressure head at half height of the boiling tubes  $\Delta\rho_{HH}$  could be disregarded. The uncertainties in the flue gas side temperatures are dominant for the determination of driving temperature differences between flue gas and boiling solution.

### Heat flux and overall heat transfer coefficients

Overall heat transfer coefficients  $U_{PS,G}$  and  $U_{FS,G}$  for the plain and finned section were calculated from the heat fluxes  $\dot{q}_{CV,PS,G}$  and  $\dot{q}_{FS,G}$  attributed to convective heat transfer in both sections and from the temperatures  $T_{FG,PS,ENTER}$ ,  $T_{128}$  and  $T_{31}$  in the flue gas and the mean solution boiling temperature  $T_{SAT,MN}$ .

$$U_{PS,G} = \dot{q}_{CV,PS,G} / \text{LMTD}(T_{FG,PS,ENTER} - T_{SAT,MN}, T_{128} - T_{SAT,MN})$$

$$U_{FS,G} = \dot{q}_{FS,G} / \text{LMTD}(T_{128} - T_{SAT,MN}, T_{31} - T_{SAT,MN})$$

The obtained values of the heat transfer coefficients over the surface heat fluxes are displayed in Fig. 61 for the section of plain tubes (left diagram) and the section of finned tubes (right diagram). For better comparison of the actual heat exchanger performance in both sections, all values are shown with respect to the outer surface of bare tubes; thus an “effective” heat transfer coefficient  $U_{FS,G} \cdot \beta_F$  already incorporating the surface enhancement by the fins over an “effective” heat flux  $\dot{q}_{FS,G} \cdot \beta_F$  is displayed for the finned section (right diagram).

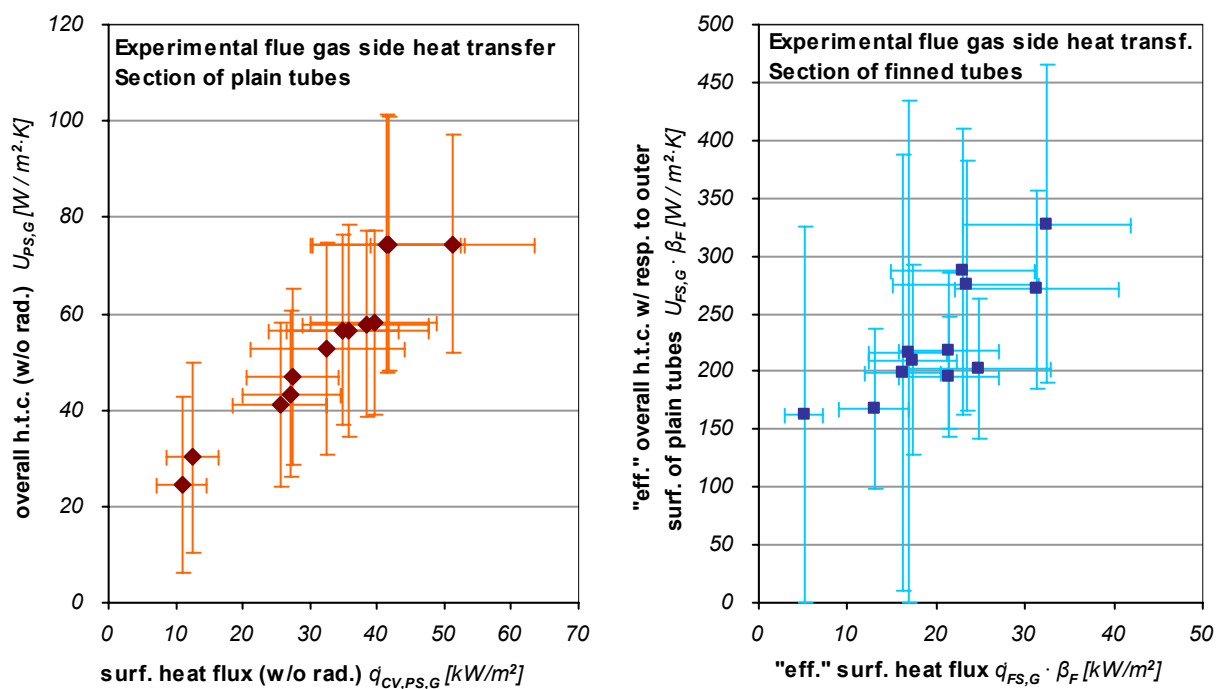


**Fig. 61: Overall heat transfer coefficients vs. heat flux at plain (left) and finned (right) sections of the regenerator with respect to the outer surface of plain tubes.**

For the section of plain tubes (left), only the heat flux attributed to convective heat transfer in the flue gas is considered. For the section of finned tubes (right), the values have been multiplied by the surface enhancement factor to obtain comparable numbers with respect to the tube surface without fins.

One set of measurement data at small heat duty had to be skipped for the calculation of the heat transfer coefficient in the finned section (right diagram in Fig. 61) as the measured leaving flue gas temperature  $T_{31}$  was already lower than the estimated mean boiling temperature  $T_{SAT,MN}$ . Two more data points at small heat duties had to be attributed uncertainties of  $\pm 100\%$  as the uncertainty in the determination of the leaving flue gas temperature  $T_{31}$  was already greater than the temperature difference  $T_{31} - T_{SAT,MN}$  between flue gas and solution itself.

### Convective heat transfer

According to Fig. 58 in 6.3.5 above, the mean surface heat flux at the liquid side varied around  $40 \text{ kW/m}^2$  during the test series. A mean boiling heat transfer coefficient  $\alpha_l = \alpha_B \approx 3 \text{ kW/m}^2\text{K}$  at the liquid side is obtained for this heat flux from the boiling correlation (4.96) of [Cooper \(1984\)](#) assuming unknown surface finish ( $R_p = 1 \mu\text{m}$ ) and the attenuation factor (4.103) according to [Rant \(1977\)](#). This value is at least one order of magnitude larger than the effective overall heat transfer coefficients displayed in Fig. 61; thus it can be concluded that the heat transfer at the liquid side has only a minor impact on the determination of the gas side heat transfer coefficients from the measured data. Therefore an approximate mean heat transfer coefficient of  $\alpha_l = 3 \text{ kW/m}^2\text{K}$  at the liquid side was assumed for evaluation of data from all operational states.

Convective heat transfer coefficients  $\alpha_{CV,PS}$ , and  $\alpha_{CV,FS}$ , at the flue gas side were calculated from the overall heat transfer coefficients  $U_{PS,G}$  and  $U_{FS,G}$  by means of (4.7) and (4.66). The according fin efficiency  $\eta_F$  in the finned section was calculated by means of (4.67). The respective Nusselt numbers,  $Nu_L$  according to (4.55) in the plain section and  $Nu_D$  according to (4.62) in the finned section, were calculated from the gas-side heat transfer coefficients and the respective thermal conductivities of the flue gas at the mean flue gas temperatures in both sections.

These heat transfer coefficients and Nusselt numbers are shown in Fig. 62 below in dependence of the respective Reynolds numbers in the flue gas. The applicable Reynolds numbers,  $Re_L$  according to (4.50) in the plain section and  $Re_D$  according to (4.43) in the finned section, were calculated from the flue gas mass flow  $\dot{M}_{FG}$  and the respective viscosities of the flue gas at the mean flue gas temperatures in both sections. Both Reynolds numbers were calculated from gas flow velocities based of the actual bundle width according to (4.49) and (4.54) rather than on the tube pitch only.

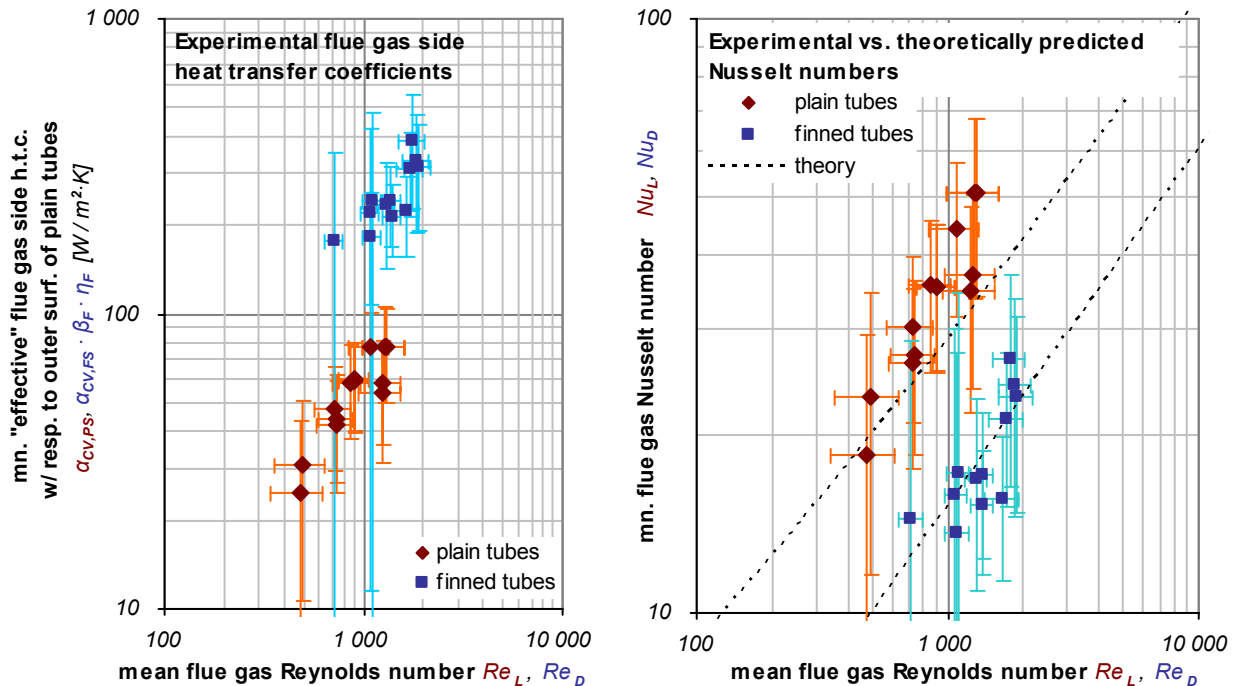


**Fig. 62:** Effective flue gas side heat transfer coefficients with respect to the surface of plain tubes (left) and flue gas side Nusselt numbers (right) vs. the mean flue gas Reynolds numbers in plain and finned section. Data points for the section of plain tubes are denoted as **brown** diamonds, values for the section of finned tubes are displayed as **blue** squares.

The left diagram in Fig. 62 shows the heat transfer coefficients at the gas side over the Reynolds number. For better comparison, “effective” heat transfer coefficients  $\alpha_{CV,FS} \cdot \beta_F \cdot \eta_F$  with respect to the outer surface of plain tubes – already incorporating the enhancement by the fins – are displayed for the finned section. The right diagram in Fig. 62 shows the experimentally found Nusselt numbers at the plain and finned sections in comparison with the theoretically predicted relations between Nusselt and Reynolds numbers according to *VDI-GVC (2002)* as outlined in 4.4.2. Dotted lines indicate the results from evaluation of correlations (4.56) to (4.61) for the plain section and from correlation (4.64) for the finned section respectively at mean Prandtl numbers<sup>67</sup> for both sections.

### Deviation of experimental values from theoretical predictions

As it can already be seen in the right diagram in Fig. 62 above, the Nusselt numbers experimentally found for the finned section scatter around the theoretical curve. In the plain section, the experimental values are slightly underpredicted by the theoretical correlations from *VDI-GVC (2002)*. A more detailed comparison of experimental and theoretical Nusselt numbers is provided in Fig. 63 below. The upper left diagram in Fig. 63 shows the experimentally found Nusselt numbers from Fig. 62 for plain and finned section over the corre-

<sup>67</sup> As flue gas temperatures and excess air ratios showed some variation over the experimental data points, slightly different Prandtl numbers would be found for different data points. However, these variations are reasonably small and would have had only a minor impact on the Nusselt numbers in this case

sponding theoretically predicted Nusselt numbers. It shows that all experimental values for finned tubes (**blue** squares) fall within an interval of  $\pm 30\%$  around the theoretical values. On the other hand, the experimental Nusselt numbers for plain tubes (**brown** diamonds) exceed this interval especially at larger values.

The upper right diagram in Fig. 63 provides a comparison of the experimental Nusselt numbers with theoretical predictions utilizing the additional correction factor (4.68) for temperature dependency of property data. An exponent  $N = 0.12$  as suggested by *Spang (2004)* has been applied in this case, yielding 2...4% larger Nusselt numbers for the section of finned tubes and 10...13% larger Nusselt numbers for the section of plain tubes compared to the prior calculation without the correction (4.68). While no significant change in the accordance of experimental and theoretical values due to the application of (4.68) is found for the finned tubes section (empty vs. filled **blue** squares), the agreement of both values is improved for the section of plain tubes (empty vs. filled **brown** diamonds). In the upper right diagram in Fig. 63 only two data points exceed the interval of  $\pm 30\%$  around the theoretical values.

No error bars are provided in the two upper diagrams in Fig. 63; this is on the one hand to improve the readability and on the other hand because orthogonal error bars would be misleading in this graph. It also has to be stated that the orthogonal error bars shown in the left diagram in Fig. 62 (Nusselt numbers vs. Reynolds numbers) cannot truly reflect the significance of the correlation between experimental and theoretical Nusselt numbers either. In both cases, the reason is that the uncertainties determined for the experimental Reynolds numbers and for the experimental Nusselt numbers are not independent from each other as both numbers were calculated from common influencing variables like flue gas mass flow and various flue gas temperatures (see overview in Fig. 60).

Therefore, the actual uncertainty of the experimental data in Fig. 62 is smaller than the range denoted by the orthogonal error bars shown in the diagrams<sup>68</sup>. The same argumentation holds for the two upper diagrams in Fig. 63, as the shown theoretical Nusselt numbers are calculated from experimental Reynolds numbers and temperature-dependent Prandtl numbers at each data point.

---

<sup>68</sup> The actual relation between experimentally determined Nusselt numbers and Reynolds numbers would have to be visualized by means of inclined error bars instead of orthogonal error bars. For readability reasons however this approach was not pursued.

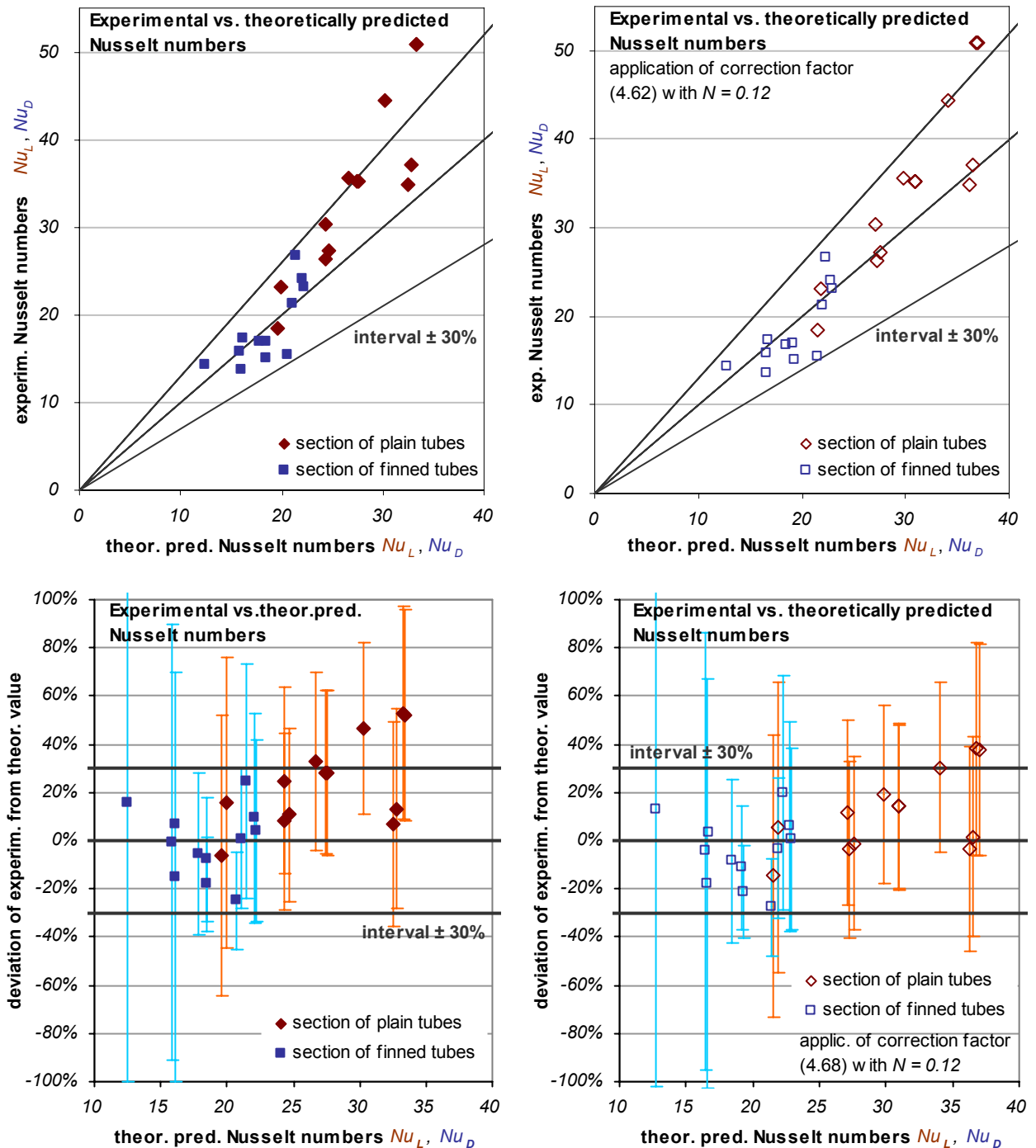


**Fig. 63: Experimentally found vs. theoretically predicted Nusselt numbers (top two diagrams) and relative deviation of experimental from theoretical values (bottom two diagrams).**

Calculation based on *VDI-GVC (2002)* without (left two diagrams, filled symbols) and with (right two diagrams, empty symbols) application of correction factor (4.68) with exponent  $N = 0.12$  for temperature dependency of property data.

The partial correlation of uncertainties derived from error propagation was taken into account in the bottom two diagrams in Fig. 63 where the relative deviation of experimental from theoretical Nusselt numbers  $(Nu_{EXPERIMENTAL} - Nu_{THEORETICAL}) / Nu_{THEORETICAL}$  is shown. For this expression, the error propagation again yields a single error bar that subsumes the

uncertainties of both, the determination of the experimental Nusselt numbers and the determination of the experimental Reynolds numbers from the measured data.

A comparison of the lower left diagram in Fig. 63 (filled symbols) which was obtained without application of correction (4.68) and the lower right diagram (empty symbols) where correction factor (4.68) with exponent  $N = 0.12$  was taken into account reveals that this additional factor slightly improves the accordance of experimental and theoretical values in the plain section (**brown** diamonds). In the right diagram, the deviation of the experimental Nusselt numbers from the theoretical Nusselt numbers is always smaller than the measuring uncertainty (**orange** error bars) while in the left diagram without application of (4.68) three data points are out of this range. In addition, the virtual dependency of the deviation from the Nusselt number is weaker in the right diagram with correction factor.

Concerning the section of plain tubes (**blue** squares) however the accordance of experimental and theoretical values is slightly worse if the correction factor (4.68) with exponent  $N = 0.12$  is applied. In the right diagram (empty **blue** squares), the deviation exceeds the measuring uncertainty (**light blue** error bars) at two data points but only at one data point in the left diagram (filled **blue** squares) without factor (4.68).

Altogether, it can be stated that the correction factor apparently improves concordance of experimental and theoretical values. However, these findings have to be taken with some care as relatively large uncertainties have to be attributed to the experimental values and scatter of the data is significant.

## 6.4.2 Flue gas side pressure drop

At nine operational states, measurements of the overpressure in furnace chamber ( $P1$ ) and at the flue gas exit of the regenerator ( $P3$ ) are available; from these data a pressure drop  $\Delta p = P1 - P3$  across the total heat exchanger was calculated. At five states, additionally the overpressure in the tube bundle between plain and finned tubes ( $P2$ ) was measured; respective pressure drops  $\Delta p = P1 - P2$  across the plain tubes and  $\Delta p = P2 - P3$  across the finned tubes were obtained. For reference, the measured pressure differences are shown in Fig. 77 in appendix A.4.

As density and hence velocity of the flue gas vary along the heat exchanger, the measured differences in the static pressure  $\Delta p$  are according to (4.17) a sum<sup>69</sup>  $\Delta p = \Delta p_{FR} + \Delta p_{ACC}$  of a frictional pressure drop  $\Delta p_{FR}$  and a so-called “acceleration pressure drop”  $\Delta p_{ACC}$ . According to (4.18), the acceleration pressure drop  $\Delta p_{ACC}$  is negative for “deceleration” of the fluid at decreasing temperatures and hence increasing fluid densities. This “deceleration pressure

<sup>69</sup> The additional gravitational pressure drop term in (4.17) yields zero, as the flow was horizontal.

rise”  $\Delta p_{ACC} < 0$  was taken into account for the determination of all frictional pressure drops  $\Delta p_{FR} = \Delta p - \Delta p_{ACC}$  from measured pressure differences. It shows that for the section of finned tubes  $\Delta p_{ACC}$  is only a minor correction in the range of 1...2% of the measured pressure difference  $\Delta p$  and could have been neglected. In the section of plain tubes, however the “deceleration pressure rise” due to the cooling of the flue gas was in the range of 8...16% of the measured pressure difference  $\Delta p$ . After all, an uncertainty of  $\pm 3 \text{ Pa}$  was attributed to the determined frictional pressure drops  $\Delta p_{FR}$ .

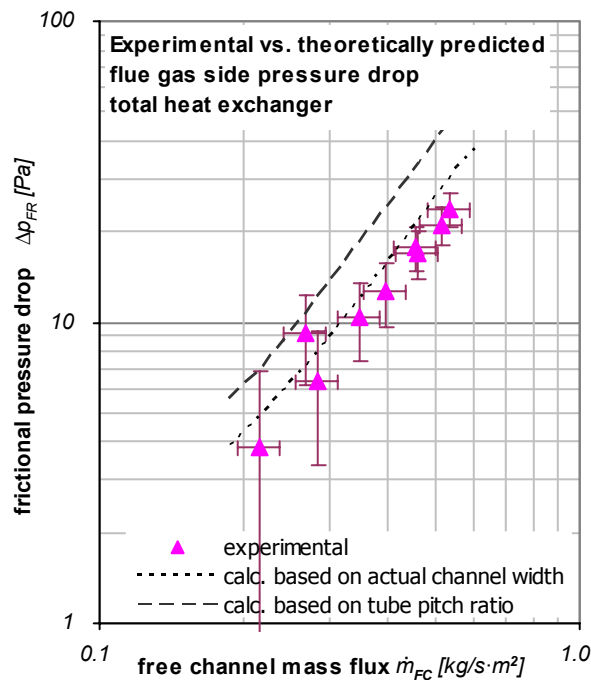


Fig. 64: Experimentally found and theoretically predicted pressure drop at the flue gas side of the regenerator vs. the free-channel mass flux.

Fig. 64 above shows the experimentally determined frictional pressure drops across the total heat exchanger  $\Delta p_{FR}$  over the free channel mass flux  $\dot{m}_{FC}$ . Unlike in the situation discussed in 6.4.1 above, here the displayed orthogonal error bars truly reflect the uncertainty of the measurement, as both errors are independent from each other. Additionally, in the diagram in Fig. 64 theoretically predicted frictional pressure drops are shown that have been calculated according to *VDI-GVC (2002)* from flue gas mass flows and temperatures<sup>70</sup> by means of the correlations (4.69) to (4.83).

As discussed in 4.4.1, no clear information is provided in *VDI-GVC (2002)* how to determine the applicable void ratio  $\psi_{MIN}$  in narrow staggered arrangements. Therefore two different

<sup>70</sup> Actually different values for flue gas temperatures, excess air ratios, and resulting flue gas properties are found at the individual operational states where experimental pressure drop measurements are available. Therefore, the pressure drops are not simply functions of the flue gas mass flux. To obtain smooth curves in the diagrams, the relevant variables have been fitted in dependence of the flue gas mass flow and the thus obtained relations were actually employed for the calculation of the “theoretical curves” shown in the diagrams. See appendix A.4 for details.



theoretical pressure drop relations are displayed in Fig. 64, one for a calculation of the void ratio according to (4.46) based on the tube pitch ratio only and another for the calculation of the void ratio based on the channel width according to (4.49). Fig. 64 shows clearly that the calculation based on the channel width (dotted line) is in reasonable accordance with the experimental data, deviations are within the marked measuring uncertainties. The larger pressure drops obtained from a calculation based on the tube pitch ratio only (dashed line) significantly exceed all but two of the experimental data points. Therefore, only the determination of void ratios and resulting Reynolds numbers according to (4.49) and (4.54) respectively was employed for the evaluation of all gas-side heat transfer and pressure drop values in this experimental setup.

A comparison of the experimentally determined frictional pressure drops across the individual sections of the heat exchanger with theoretical predictions is provided in the upper two diagrams in Fig. 65 below. The data points from all five operational states where additional measurements of the overpressure at position  $P2$  were available and thus evaluations for both individual sections were possible show good accordance with the theoretical predictions. Especially the measured frictional pressure drops across the section of finned tubes (upper right diagram) match almost perfectly the theoretical curve. In the section of plain tubes (upper left diagram), all experimental values were slightly smaller than the theoretical curve, however all deviations are still within the range of measuring uncertainty.

The lower two diagrams in Fig. 65 provide a comparison of the friction factors in the flue gas determined from the experimental data with the theoretical predictions from (4.70) to (4.78) for the section of plain tubes and (4.82) for the section of finned tubes. It shows again that the data points for the section of finned tubes (**blue** squares in the lower right diagram) nicely fit the predicted curve over the Reynolds numbers.

The friction factors determined from the extremely low measured pressure drops across the section of plain tubes (**brown** diamonds in the lower left diagram) however fail to reproduce the predicted shape of the curve. However, this is not significant as all deviations are still smaller than the measuring uncertainties.



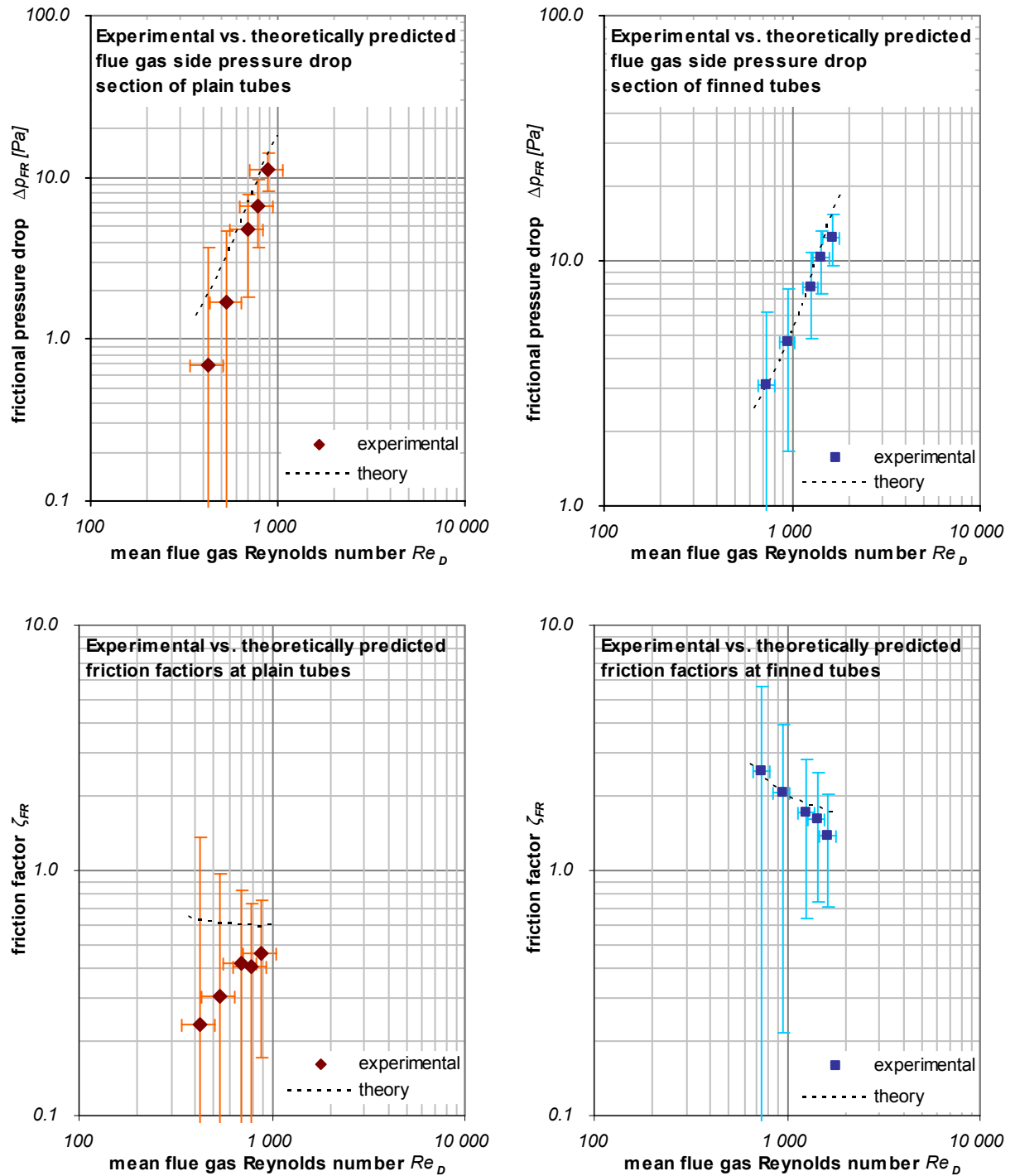


**Fig. 65:** Experimental and predicted frictional pressure drops (upper two diagrams) and friction factors (bottom two diagrams) for the flue gas flow across the section of plain tubes (left two diagrams) and across the section of finned tubes (right two diagrams) vs. the mean Reynolds numbers in the respective sections.

Finally, Fig. 66 below provides a comparison of experimentally found vs. theoretically predicted pressure drops at all data points. It shows that only two data points obtained for the section of plain tubes (**brown** diamonds) exceed the interval of  $\pm 30\%$  around the theoretical values at very small pressure drops.

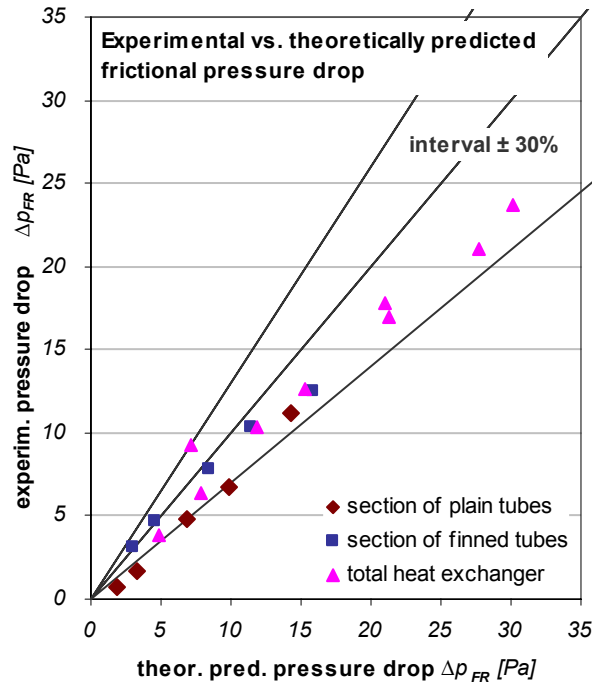


Fig. 66: Experimentally found vs. theoretically predicted pressure drops in the flue gas.

### 6.4.3 Natural convection in thermosyphon tubes

The velocity of the solution flow in the downcomer tubes  $u_{DOWNCOMER}$  was directly measured by means of an ultrasonic flow meter, which was clamped on one of the two tubes. Thus, only one of the two measurement points *F73a* and *F73b* shown in Fig. 55 was active at a time. Switching the position of the flow meter never revealed significant differences in the velocities in both tubes, neither had different velocities been expected as both tubes were installed close to each other. Therefore, no effort was taken to distinguish between measurement data from *F73a* and *F73b*.

From the density of the solution in the header at temperature  $T_{03}$  and concentration  $X_{STRONG}$ , the cross sectional area of both downcomer tubes, and the measured velocity  $u_{DOWNCOMER}$  in these tubes, the absolute mass flow  $\dot{M}_{DOWNCOMER}$  was obtained. The net upward mass flow in all boiling tubes  $\dot{M}$  thus was the sum of the downcomer flow  $\dot{M}_{DOWNCOMER}$  and the entering weak solution flow  $\dot{M}_{WEAK}$ .

$$\dot{M} = \dot{M}_{DOWNCOMER} + \dot{M}_{WEAK} \quad (6.22)$$

The mean cross sectional mass flux in the boiling tubes with reference to the cross section of all tubes at the liquid side  $A_{CS,L}$  was thus calculated:

$$\dot{m}_{CS} = \dot{M} / A_{CS,L} \quad (6.23)$$

Assuming ideal mixing of the solution from the regenerator inlet (mass flow  $\dot{M}_{WEAK}$  at temperature  $T_{01}$  and concentration  $X_{WEAK}$ ) and the solution from the downcomer tubes (mass flow  $\dot{M}_{DOWNCOMER}$  at temperature  $T_{03}$  and concentration  $X_{STRONG}$ ) in the bottom vessel of the regenerator, a homogenous temperature  $T$  and concentration  $X$  would be found there. These parameters could be calculated from the salt balance and the enthalpy balance at the point of mixing:

$$\dot{M} \cdot X = \dot{M}_{DOWNCOMER} \cdot X_{STRONG} + \dot{M}_{WEAK} \cdot X_{WEAK} \quad (6.24)$$

$$\dot{M} \cdot h'_{BOTTOM}(T,X) = \dot{M}_{DOWNCOMER} \cdot h'_{STRONG}(T_{03},X_{STRONG}) + \dot{M}_{WEAK} \cdot h'_{WEAK}(T_{01},X_{WEAK}) \quad (6.25)$$

As no ideal mixing of the solution in the bottom vessel can be assumed, the values  $T$  and  $X$  obtained from (6.22) to (6.25) on the basis of the measured flow rate  $F_{73a/b}$  have to be interpreted as the expected mean values of temperature and concentration in this vessel. Therefore, some deviation between the readings from temperature probe  $T_{02}$  at the bottom vessel and the calculated mean temperature  $T$  is to be expected.

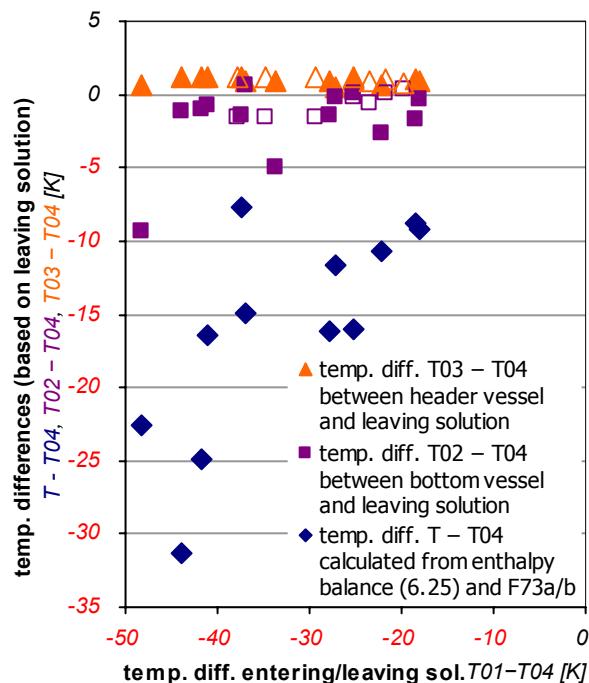


**Fig. 67: Measured and calculated differences in the solution temperature in the regenerator prototype.**

Measured temperature differences between header vessel and leaving solution (orange triangles) and between bottom vessel and leaving solution (violet squares) vs. the subcooling of the entering solution in comparison to the temperature difference  $T - T_{04}$  (blue diamonds) calculated from enthalpy balance (6.25). Empty symbols denote additional data points from operational states with incomplete measuring instrumentation that have not been included in the evaluation presented below.

A comparison provided in Fig. 67 above however reveals significant differences between the measured and the calculated temperature in the bottom vessel. For better visibility, the measured temperatures in the header vessel (**orange** triangles) and in the bottom vessel (**violet** squares) and the calculated mean temperature at this position (**blue** diamonds) are displayed as temperature differences relative to the measured solution outlet temperature  $T_{02}$  over the subcooling of the entering solution. Fig. 67 reveals that the measured subcooling  $T_{02} - T_{04}$  exhibited significantly smaller absolute values than the calculated temperature difference  $T - T_{04}$  according to measured flow rate  $F_{73a/b}$  and enthalpy balance (6.25). Therefore, it has to be stated that the measured downcomer velocities  $F_{73a/b}$  might not be consistent with the temperature measurements  $T_{01}/T_{02}/T_{03}$  at the regenerator prototype.

If, on the other hand, the measured temperature  $T_{02}$  in the bottom vessel was assumed to be close to the true mixing temperature at this vessel, the downcomer flow rate  $\dot{M}_{DOWNCOMER}$  could alternatively be calculated from mass and enthalpy balances (6.22) to (6.25) based on the assumption  $T := T_{02}$ . In this case, significantly higher values for the downcomer velocity  $u_{DOWNCOMER}$  are would be obtained than originally measured at  $F_{73a/b}$ .

Fig. 68 below shows the velocity in the downcomer tubes  $u_{DOWNCOMER}$  over four different possible influencing variables, mean surface heat flux  $\dot{q}_{MN,L}$  (upper left diagram), mean cross-sectional vapor flux  $\dot{m}_{REFR,CS}$  (upper right diagram), specific solution circulation  $f_{WEAK}$  (bottom left diagram), and specific cross-sectional mass flux of weak solution  $\dot{m}_{WEAK,CS}$  (bottom right diagram). The actually measured values ( $F_{73a/b}$ ) are displayed as filled **blue** triangles, values that would be obtained from mass and enthalpy balances (6.22) to (6.25) based on temperature measurements  $T_{01}/T_{02}/T_{03}$  are provided as empty **magenta** diamonds for comparison.

It shows that the measured velocities  $F_{73a/b}$  (filled **blue** triangles) scatter around only  $10 \text{ cm/s}$  and exhibit no significant dependency from any of these potential influencing variables. The upper right diagram reveals that the convection flow even keeps this value at zero net vapor generation in the boiling tubes. It has to be noted, however, that these – unexpectedly low – measured flow rates are in the same order of magnitude as the absolute measuring uncertainty of the ultrasonic flow meter (cf. Tab. 20). On the other hand, the flow rates (empty **magenta** diamonds) calculated from measured temperatures  $T_{01}/T_{02}/T_{03}$  by means of (6.22) to (6.25) are about one order of magnitude larger than the readings of  $F_{73a/b}$  – the difference between both data sets significantly exceeds the measuring uncertainty of the ultrasonic flow meter.

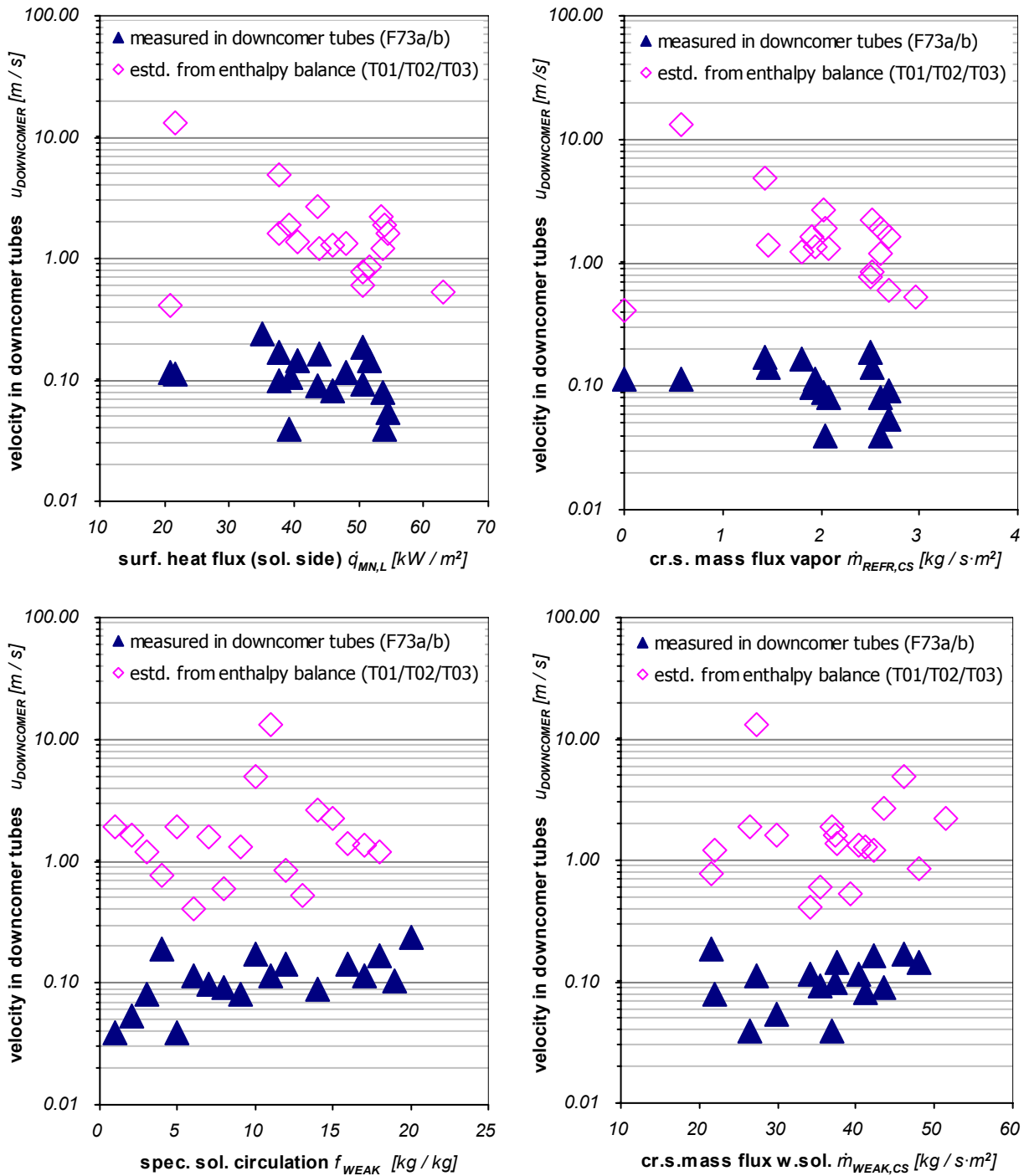


**Fig. 68: Velocity of natural convection flow in downcomer tubes in dependence of various possible influencing variables.**

Values measured in downcomer tubes by means of an ultrasonic flow meter F73a/b shown as filled **blue** triangles, significantly higher values that could be estimated from enthalpy balance (6.22) to (6.25) based on temperature measurements T01/T02/T03 displayed as empty **magenta** diamonds.

Fig. 69 below finally displays the mean specific mass flux in the boiling tubes  $\dot{m}_{CS}$  that can be obtained from either the measured downcomer velocity F73a/b (**blue** triangles) or the enthalpy balance based on T01/T02/T03 (**magenta** diamonds). Again, both results differ by about one order of magnitude. According to the calculation based on the downcomer velocity, the boiling tubes mass flux (**blue** triangles) varied between 40...100 kg/s·m<sup>2</sup> without any

significant dependency on the heat flux. This behavior is not really compliant with literature data (see detailed discussions in 4.6.4 and 4.6.5); for similar boiling tube geometries rather  $100 \dots 600 \text{ kg/s}\cdot\text{m}^2$  with significant dependency on the heat flux have been reported.

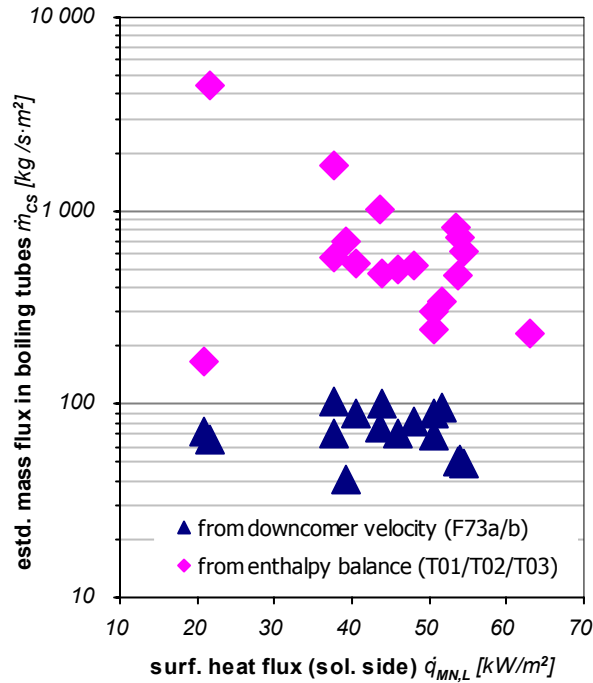


**Fig. 69:** Estimated cross-sectional mass flux in boiling tubes vs. surface heat flux at the solution side. Values calculated from the measured velocity in the downcomer tubes shown as blue triangles and values calculated from an enthalpy balance displayed as magenta diamonds.

On a first glance, the data points obtained from the enthalpy balance  $T01/T02/T03$  (magenta diamonds) show better compliance with literature data; all but two scatter in the range of  $200 \dots 1\,000 \text{ kg/s}\cdot\text{m}^2$ . Two data points however significantly exceed this range exhibiting values of about  $2\,000 \text{ kg/s}\cdot\text{m}^2$  or even  $4\,500 \text{ kg/s}\cdot\text{m}^2$  which are not expected to be found in this setup. Therefore, it has to be concluded that presumably none of the two data series displayed in Fig. 69 represents the actual upward mass flux in the boiling tubes.

All evaluations presented above have been performed assuming an uniform upward flow direction inside all boiling tubes like it is common practice for steam-heated thermosiphon reboilers where conditions in all tubes are quite similar. Actually, there is no real evidence for validity of this assumption in this setup; neither was the installed instrumentation able to deliver detailed insight into the flow directions in individual tubes. Therefore, it can only be speculated here about downward flow in some of the boiling tubes that would nicely explain the apparent discrepancy discussed above between the measured velocities  $F73a/b$  in the downcomer tubes, the enthalpy balance  $T01/T02/T03$ , and the prior findings in literature on typical mass fluxes.

### 6.4.4 Solution side heat transfer

#### Tube wall temperatures

The test rig was operated at various different pressure levels in the regenerator and different concentrations of the strong solution; accordingly, different saturation temperatures of the leaving strong solution can be attributed to the recorded operational states. For the evaluation of the measurement data, it was assumed<sup>71</sup> that the leaving solution was in saturation and thus the measured temperature  $T_{04}$  was identical to the saturation temperature.

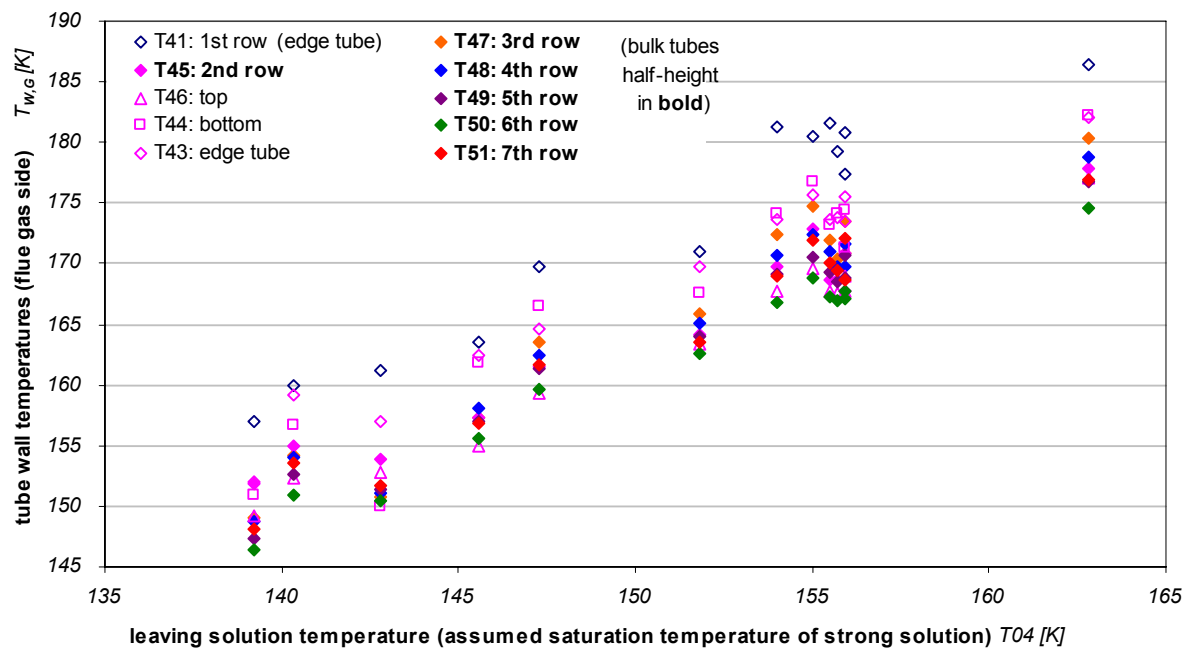


*Fig. 70: Measured tube wall temperatures at the flue gas side vs. the measured temperature of the leaving strong solution.*

A plot of the measured tube wall temperatures  $T_{41}$  to  $T_{51}$  at different positions in the bundle over the temperature  $T_{04}$  of the leaving solution is given in Fig. 70. Measured temperatures at the tube walls are ranging from about  $146^{\circ}\text{C}$  to about  $186^{\circ}\text{C}$  – mainly dependent on the solution temperature and the location of the probe. This behavior is as expected for boiling dominated heat transfer, where wall temperatures mainly follow the local saturation temperatures. To eliminate the dominant influence from variations in the solution temperature for the discussion of further influencing variables, only temperature differences between tube walls and leaving solution are displayed in the following diagrams.

Fig. 71 below shows the temperature differences between the tube wall  $T_{w,G}$  at the locations of the individual probes and the leaving solution  $T_{04}$  over the mean surface heat flux  $\dot{q}_{MN,L}$ . This temperature differences ranges from about  $7\text{ K}$  to about  $27\text{ K}$ , exhibiting only a weak

<sup>71</sup> This assumption is backed up by the fact that the leaving solution had to pass a non-heated “leveling chamber” behind two weirs before finally entering the outlet pipe where the temperature probe was installed.

dependency on the mean heat flux  $\dot{q}_{MN,L}$  and a even more significant dependency on the position of the temperature probe.

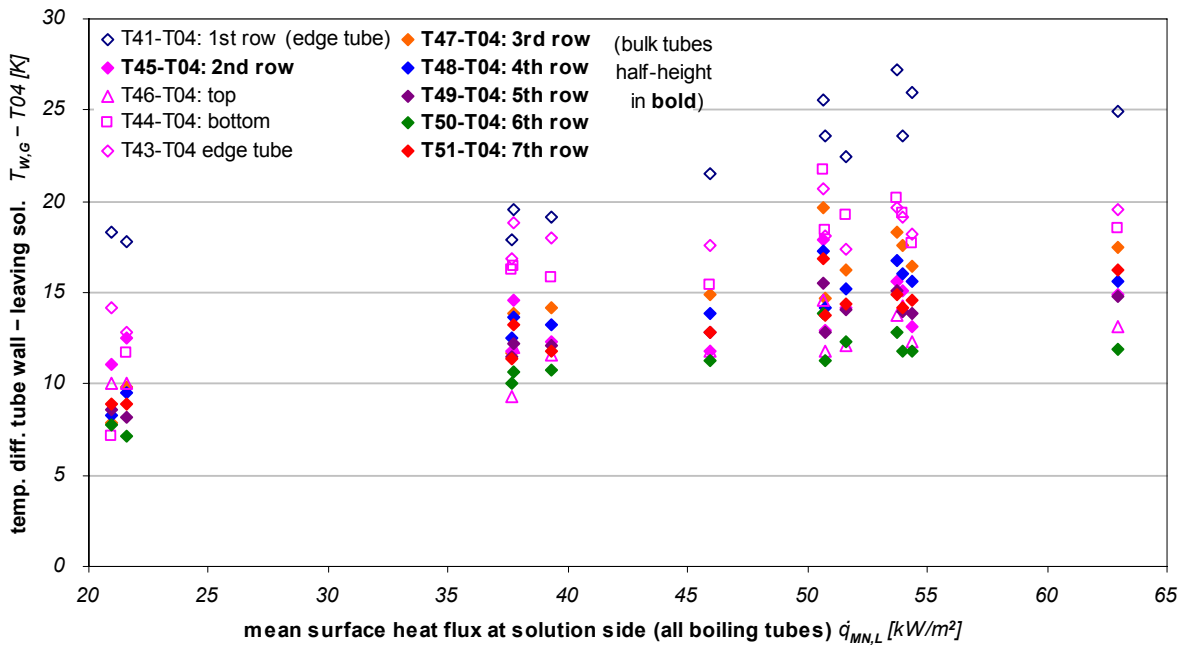


*Fig. 71: Temperature differences between measuring points at the boiling tube walls (gas side) and the leaving solution temperature vs. the mean heat flux at the solution side of all boiling tubes.*

A weak dependency of the wall temperatures on the heat flux can be interpreted as characteristic feature of a nucleate boiling dominated heat transfer – see relation (4.92) in 4.5.4. The significant dependency on the position of the respective thermocouple can be attributed to, on the one hand, the different local surface heat flux and, on the other hand, to the differences in the local saturation temperature due to a different local liquid head.

The dependency of the temperature difference between tube wall and leaving solution on the location of the individual probes is visualized in Fig. 72 below; the upper two diagrams show the height profile at a bulk tube in the 2<sup>nd</sup> row, the bottom two diagrams show profiles in longitudinal direction from the 1<sup>st</sup> to the 7<sup>th</sup> row of tubes at half-height. Simplistic information on the transversal profile is also contained in the bottom two diagrams as data points from both a bulk tube and an edge tube in the 2<sup>nd</sup> row are shown.



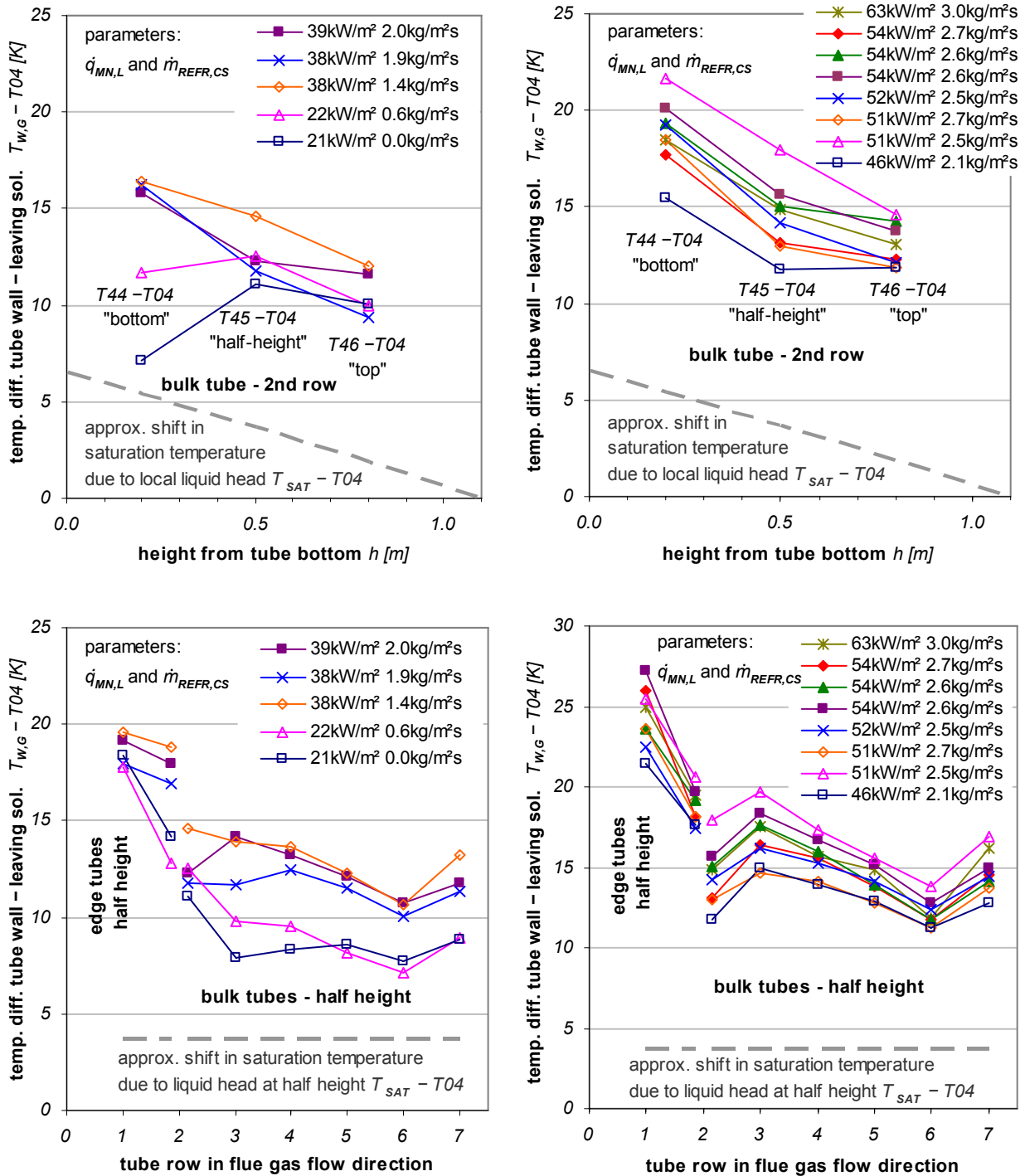


**Fig. 72: Temperature difference between boiling tube wall (gas side) and leaving solution temperature in dependence of the location of the wall temperature measurement.**  
 Temperature profile along a bulk tube in the 2<sup>nd</sup> row of tubes (upper two diagrams) and temperature profile across the different rows of tubes in flow direction (lower two diagrams). In all diagrams the mean surface heat flux at the solution side and the mean cross-sectional vapor flux are given as parameters.

In all diagrams in Fig. 72, the mean heat flux at the liquid side of all tubes and the mean cross-sectional vapor flux in all tubes are given as parameters. The left two diagrams show data from operational states at low heat fluxes with  $\dot{q}_{MN,L}$  in the range 20...40  $\text{kW/m}^2$ , the right two diagrams subsume the states at high heat fluxes with  $\dot{q}_{MN,L}$  being in the range

45...65 kW/m<sup>2</sup>. Dashed lines visualize the approximate<sup>72</sup> shift in saturation temperature at the actual height of the measuring location relative to the saturation temperature *T04* at the liquid level above<sup>73</sup> the tubes.

The upper two diagrams in Fig. 72 show that in all but one recorded state (empty **blue** squares in the upper right diagram) the temperature of the tube wall decreases from the measuring location *T45* at half-height to the position of probe *T46* in the upper third of the boiling tube. In all but two states (empty **blue** squares and empty **magenta** triangles in the upper left diagram), the wall temperature also decreases from *T44* in the lower third of the tube to *T45* at half-height. Both exceptions from this general behavior correspond with very small vapor fluxes and highly subcooled solution entering the regenerator at the bottom. At all other states the wall temperatures mostly follow the estimated gradient in the saturation temperature at a nearly constant temperature difference, which is an indication for the dominance of a nucleate boiling regime at constant heat flux inside the tubes.

It has to be stated however that the recording of wall temperatures at only three different positions along a boiling tube cannot give full evidence on the actual shape of the temperature profile. Therefore, the potential existence of a local maximum in the wall temperature as reported by other authors – cf. Fig. 41 in 4.6.5 – that might exceed all measured temperatures shown in Fig. 72 is not finally disproved by these experiments.

The profiles at half-height shown in the bottom two diagrams in Fig. 72 reveal that in all but one operational state the wall temperature was higher at the edge tube than at the bulk tube in the 2<sup>nd</sup> row<sup>74</sup>. Increased heat flux at the edge tubes due to radiation from the uncooled walls of furnace chamber or due to increased convective heat transfer at the edges of the bundle are possible explanations that could be given for this observation.

As flue gas temperatures gradually drop from row of tubes to tube row, also tube wall temperatures could be expected to decrease in longitudinal direction. However, the respec-

---

<sup>72</sup> Calculation has been performed based on the static liquid head assuming the tubes completely filled with strong solution. Effects from pressure drop due to fluid movement and evaporation and from density variation in the fluid due to vapor generation have been neglected. This approach is justified as only small velocities in the downcomer tubes have been measured (see Fig. 68 in 6.4.3) and thus the frictional pressure drop in this part is small compared to the static pressure difference. Therefore, the effects from pressure drop and density variation in the boiling tubes nearly compensate for each other over the full length of each tube. Nevertheless, the actual local pressure in the liquid at the height of the probes can either be a little lower or a little higher than the value estimated from the static liquid head.

<sup>73</sup> The boiling liquid in the header vessel above the tubes actually was heavily agitated; therefore, no well-defined liquid-level could be determined during operation. In the diagrams a static liquid level 10 cm above the upper end of the boiling tubes was assumed, which is basically compliant with the configuration of internal weirs and the position of the solution outlet pipe.

<sup>74</sup> Unfortunately, the probe installed at a bulk tube in the 1<sup>st</sup> row had a failure and thus the respective transversal profiles in the 1<sup>st</sup> row could not be recorded.

tive wall temperature profiles shown in the bottom two diagrams in Fig. 72 do not follow this trend in general. Monotonically decreasing wall temperatures are only found from the 1<sup>st</sup> to the 2<sup>nd</sup> row and – in all but two recorded states – from the 3<sup>rd</sup> to the 6<sup>th</sup> row; both exceptions are found at low heat fluxes (cf. bottom left diagram in Fig. 72). On the other hand increasing wall temperatures from the 6<sup>th</sup> to the 7<sup>th</sup> row of tubes are found for all operational states. Additionally, increasing wall temperatures are found from the 2<sup>nd</sup> to the 3<sup>rd</sup> row in all but three recorded states, again these exceptions are found at low heat fluxes.

Both, changes in the turbulence of the flue gas flow and changes in the flow inside the tubes (i.e. changing flow direction) between two consecutive rows are possible explanations for increasing tube wall temperatures in longitudinal direction; however, no final conclusions can be drawn from these data. Concerning the temperature increase from the 6<sup>th</sup> to the 7<sup>th</sup> row of tubes found at all operational states, it has to be noted that the temperature probe at the backside of the tube in the 7<sup>th</sup> row was already facing the fins of the 8<sup>th</sup> tube row. Thus, it is quite likely that increased turbulence in the flue gas flow was found downstream of the 7<sup>th</sup> row compared to all preceding rows of plain tubes.

### **Estimation of local heat flux and saturation temperature difference**

Fig. 73 below shows the difference between measured wall temperature and estimated local saturation temperature  $T_{SAT}$  over the estimated local heat flux at the solution side  $\dot{q}_L$  for all available data points. The local saturation temperatures  $T_{SAT}$  at the height of the individual wall temperature probes were estimated – in the same way as shown in Fig. 72 above – from the hydrostatic head assuming the boiling tubes were completely filled with strong solution. Effects from pressure drop due to fluid movement and evaporation and from density variation in the fluid due to vapor generation have again been neglected in the calculation of the local saturation temperature itself. However, the full range of the possible variation of the local saturation temperature<sup>75</sup> due to these effects has been considered as an additional independent uncertainty for the calculation of the error bars shown in Fig. 73.

---

<sup>75</sup> An upper limit for the maximum possible variation of the local pressure in the boiling tubes is set by the range from the vapor pressure at the liquid level in the header vessel *P61* to the static pressure in the bottom vessel assuming the downcomer tubes completely filled with non-moving liquid.

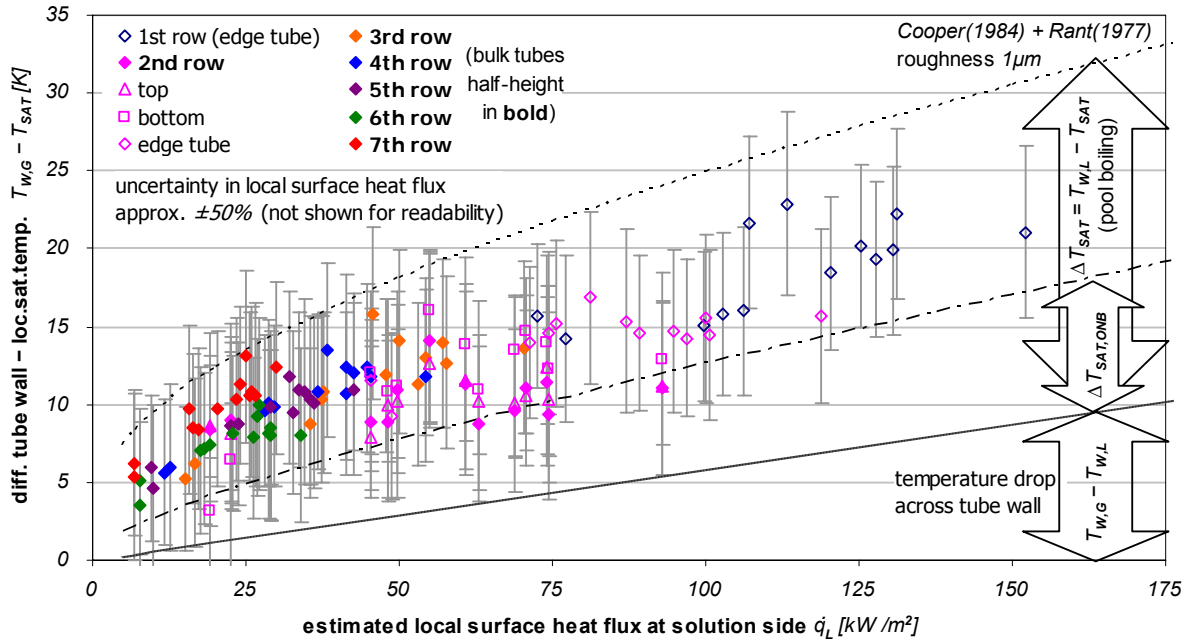


**Fig. 73: Temperature difference between measured tube wall temperatures (gas side) and estimated local saturation temperatures vs. the estimated local surface heat flux at each position.**

For comparison the expected temperature drop across the tube walls, the required superheat for the onset of nucleate boiling, and the estimated wall superheat for nucleate boiling according to the Cooper correlation are shown.

The local heat flux  $\dot{q}_L$  at each position is the sum of the local heat flux due to convective heat transfer  $\dot{q}_{CV,LOC,L}$  and the local heat flux due to radiation  $\dot{q}_{RAD,LOC,L}$ .

$$\dot{q}_L = \dot{q}_{CV,LOC,L} + \dot{q}_{RAD,LOC,L} \quad (6.26)$$

The local convective heat flux  $\dot{q}_{CV,LOC,L}$  at the individual temperature probes was assumed only dependent on the tube row position. Both contributions in (6.26) have been estimated in a simplified way – as outlined below – from the total convective heat transfer in the section of plain tubes  $\dot{Q}_{CV,PS}$  and the total heat transfer by radiation  $\dot{Q}_{RAD}$ .

The estimation of the local convective heat transfer was based on the calculation scheme (6.18) to (6.21) already presented in 6.3.4. However, the convective heat transfer  $\dot{Q}_{CV,J}$  at the individual tube rows  $J$  was assumed compliant with the total convective heat transfer in the section of plain tubes  $\dot{Q}_{CV,PS}$  and the entering flue gas temperature  $T_{FG,PS,ENTER}$  that resulted from the assumption  $\dot{Q}_{RAD} = 30 \text{ kW}$ . Therefore, for each recorded operational state an empirical correction factor  $f_{CV,CORR}$  for the convective heat transfer in the flue gas was determined as quotient of the experimentally found Nusselt number  $NU_{EXPERIMENTAL}$  and the theoretically calculated Nusselt number  $NU_{THEORETICAL}$  (cf. Fig. 62 and Fig. 63 in 6.4.1) for the section of plain tubes:

$$f_{CV,CORR} = NU_{EXPERIMENTAL} / NU_{THEORETICAL} \quad (6.27)$$

The correction factor  $f_{CV,CORR}$  varied in the range  $0.9...1.5$  according to the deviation shown as filled **brown** diamonds in the left diagram of Fig. 63 in 6.4.1. Utilizing this additional factor, consistent profiles of flue gas temperatures  $T_{FG,J}$  and convective heat fluxes  $\dot{Q}_{CV,J}$  at each row of tubes  $J = 1...7$  were calculated by an iterative procedure on the lines of (6.19) - (6.20). Again, correlations (4.55) - (4.96) listed in 4.4.2 for convective heat transfer in tube bundles according to *VDI-GVC (2002)* have been employed to obtain theoretical Nusselt numbers  $NU_{THEORETICAL,J}$  at each individual tube row. Then the empirical correction factor  $f_{CV,CORR}$  obtained for the total plain section from (6.27) was applied to the theoretical Nusselt numbers

$$NU_{CONSISTENT,J} = f_{CV,CORR} \cdot NU_{THEORETICAL,J} \quad (6.28)$$

at each tube row<sup>76</sup> for calculation of consistent convective heat transfer coefficients  $\alpha_{O,J} = \alpha_{CV,CONSISTENT,J}$  at the gas side. At the liquid side of each tube row, again the boiling correlation (4.96) of *Cooper (1984)* assuming unknown surface finish ( $R_p = 1\mu m$ ) and the attenuation factor (4.103) according to *Rant (1977)* were used to calculate the heat transfer  $\alpha_{I,J} = \alpha_{B,J}$ .

Actually, the local heat flux to the boiling tubes at the gas side shows variations in circumferential direction and the thermal conductivity of steel tubes in this direction is too low to fully equalize the heat flux at the solution side. Variations in the convective heat transfer result on the one hand from a dependence of the local Nusselt number from the circumferential position and on the other hand from a significant drop in the flue gas temperatures across each row of tubes in the section of plain tubes. Nevertheless, effects from local variations in the Nusselt number are not covered by the heat transfer correlations given in *VDI-GVC (2002)* that have been successfully employed so far to model the convective heat transfer at the flue gas side. Therefore, these additional details have been disregarded for the more simplified estimation of the local heat flux.

The variation of the flue gas temperature was considered in the determination of the local convective heat flux  $\dot{q}_{CV,LOC,L}$  in a simplified way. It was assumed that the heat flux at the positions of the temperature probes at the backside of the tubes of row  $J$  was about the mean over the heat flux  $\dot{Q}_{CV,J}$  in the total row  $J$  and  $\dot{Q}_{CV,J+1}$  the successive row  $J+1$ . With  $A_{ROW,L}$  being the surface of a single row at the liquid side the local convective heat flux  $\dot{q}_{CV,LOC,L}$  at all probes at the backside of tubes in row  $J$  finally was calculated:

$$\dot{q}_{CV,LOC,L} = (\dot{Q}_{CV,J} + \dot{Q}_{CV,J+1}) / 2 \cdot A_{ROW,L} \quad (6.29)$$

Quite sophisticated calculations concerning the entire radiation balance in the furnace chamber and the in front section of the regenerator would have been required for a determi-

<sup>76</sup> This simplified approach resulted in a difference of a few percent between both sides of the equal sign in (6.21) that finally was neglected.

nation of the actual radiation heat flux  $\dot{q}_{RAD,LOC,L}$  at the positions of the wall temperature measurements. In spite of the required effort, important input parameters concerning the behavior of the flat matrix burner and the insulation material of the furnace chamber were not easily available. Therefore again a simple estimation was employed. The following assumptions were made:

1. It was assumed that significant radiative heat transfer only affected the 1<sup>st</sup> and the 2<sup>nd</sup> tube row.
2. For these two rows, it was assumed that radiation affected the front sides of all tubes and additionally the backsides of the four edge tubes.
3. Arbitrarily it was assumed that radiative heat flux in the first row was about twice the radiative heat flux in the 2<sup>nd</sup> row.
4. Finally, it was assumed that within a row of tubes radiative heat flux was equal at all front sides but only about half this value at the backsides of the edge tubes.

These assumptions produce the result that about  $1/30$  of the total radiative heat transfer  $\dot{Q}_{RAD} \approx 30 \text{ kW}$ , i.e. about  $1 \text{ kW}$ , has to be attributed to the backside of the edge tube in the 2<sup>nd</sup> row where temperature probe  $T_{43}$  was located. About twice this value can be attributed to the backside of the edge tube in the 1<sup>st</sup> row where  $T_{43}$  was located. At all the other locations of wall temperature measurements, no significant heat flux from radiation is expected, i.e.  $\dot{q}_{RAD,LOC,L} = 0$ . The major share of the radiative heat transfer ( $\approx 16 \text{ kW}$ ) was assumed to take place at the front side of the first row of tubes where no thermocouples were installed.

Uncertainties of about  $\pm 50\%$  have to be attributed to the local surface heat fluxes  $\dot{q}_L = \dot{q}_{CV,LOC,L} + \dot{q}_{RAD,LOC,L}$  shown in Fig. 73, although no respective error bars are displayed there for better readability.

For comparison, Fig. 73 also visualizes the temperature drop across the tube wall  $T_{W,G} - T_{W,L} = \dot{q}_L / k_{W,L}$  estimated from the local surface heat flux and the minimum wall superheat for nucleate boiling  $\Delta T_{SAT,ONB}$  according to (4.91). Additionally the wall superheat  $\Delta T_{SAT} = T_{W,L} - T_{SAT}$  for nucleate pool boiling at a standard surface roughness of  $1 \mu\text{m}$  according to the boiling correlation (4.96) of [Cooper \(1984\)](#) and the attenuation factor (4.103) after [Rant \(1977\)](#) is displayed.

As expected, the correlation of wall temperatures and surface heat flux in Fig. 73 – taking into account local variations of saturation temperature and heat flux – is better than the one in Fig. 71 above that did not yet account for these effects. Additionally, Fig. 73 shows that the temperature drop across the tube wall  $T_{W,G} - T_{W,L}$  has already the same order of magnitude as the wall superheat  $\Delta T_{SAT} = T_{W,L} - T_{SAT}$  and thus cannot be neglected at all in the evaluations. The experimentally found wall superheats scatter mostly between the theoretical

values obtained for the onset of nucleated boiling  $\Delta T_{SAT,ONB}$  and for nucleate boiling according to (4.96) of Cooper (1984) and (4.103) after Rant (1977). It has to be stated, however, that due to the significant uncertainty of about  $\pm 50\%$  in the estimation of the local surface heat fluxes  $\dot{q}_L$  an additional uncertainty of  $\pm 0.5 \cdot \dot{q}_L / k_{W,L}$  has to be attributed to the determination of the wall superheat  $\Delta T_{SAT} = T_{W,G} - T_{SAT} - \dot{q}_L / k_{W,L}$ . This has been accounted for in Fig. 74 below where the surface heat flux  $\dot{q}_L$  is displayed vs. the wall superheat  $\Delta T_{SAT}$  (“Nukiyama plot”).

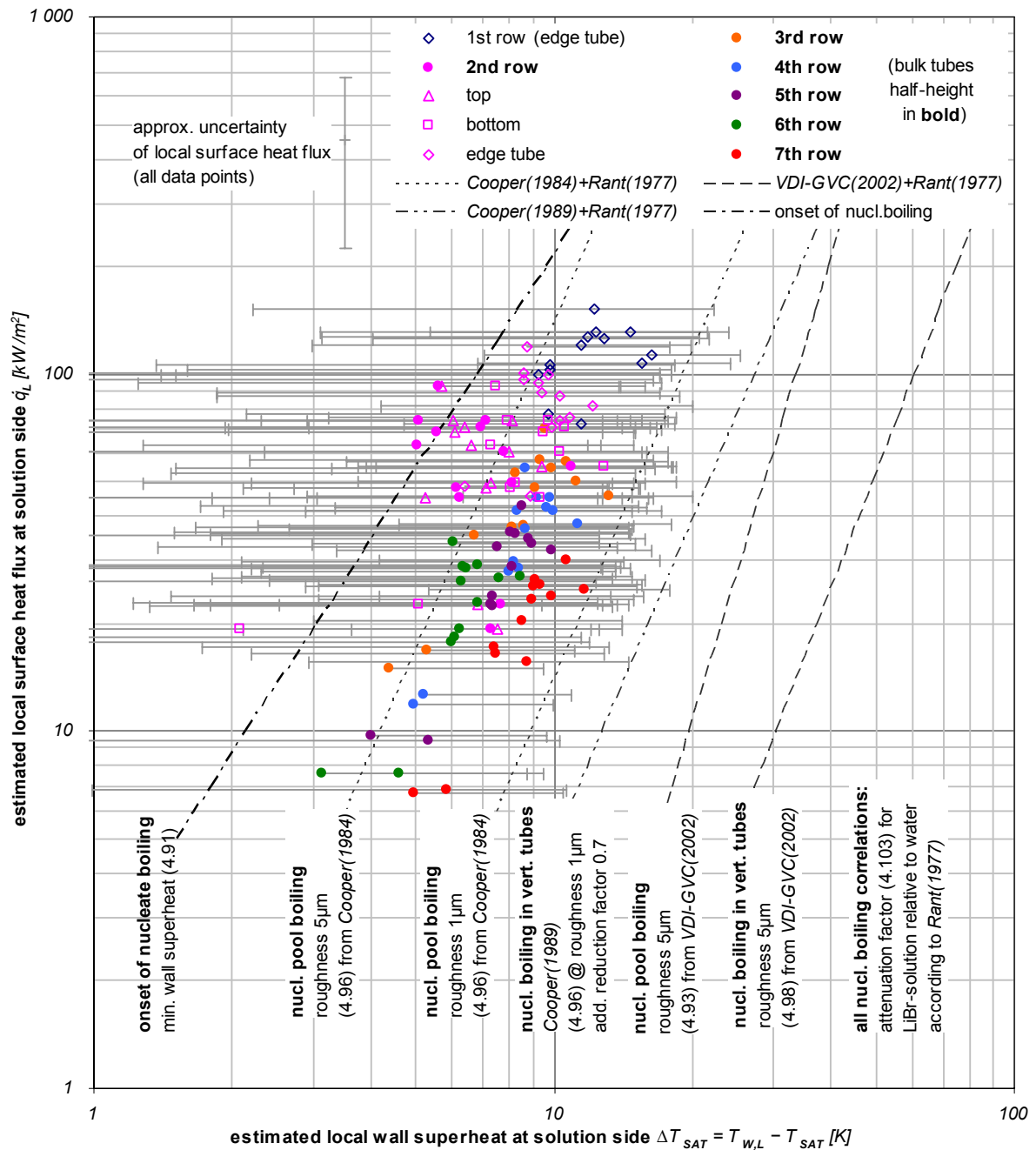


Fig. 74: Local heat flux vs. wall superheat at liquid side (Nukiyama-plot). Experimental values in comparison with various boiling correlations.



Again, minimum wall superheat for nucleate boiling  $\Delta T_{SAT,ONB}$  according to (4.91) is displayed for comparison. Additionally, theoretical values from the pool boiling correlation (4.96) of [Cooper \(1984\)](#) and the Gorenflo correlation (4.93) from [VDI-GVC \(2002\)](#) as well as from the flow boiling correlations of [Cooper \(1989\)](#) and (4.98) from [Steiner & Taborek \(1992\)](#) and [VDI-GVC \(2002\)](#) are shown in Fig. 74.

Taking into account the significant uncertainties in the experimental values, the following conclusions can be drawn from a comparison of theoretical curves and experimental data points in Fig. 74:

1. As experimental wall superheats are rather small, there is no clear evidence for the general existence of a nucleate boiling regime at all data points. Neither is there clear disprove for the dominance of a nucleate boiling heat transfer at any data point. Nevertheless, experimental data suggest the existence of nucleate boiling as the great majority of data points show sufficient wall superheat  $\Delta T_{SAT} > \Delta T_{SAT,ONB}$ .
2. Both nucleate boiling correlations (4.93) and (4.98) given in [VDI-GVC \(2002\)](#) significantly overestimate the experimental values for the wall superheat. The dominant heat transfer mechanism in this experiment cannot be described by any of these formulas.
3. The boiling correlation (4.96) of [Cooper \(1984\)](#) evaluated for standard surface roughness of  $1\mu m$  provides an upper limit for the range of experimentally found wall superheats. For all but a few data points, the predicted values lie within the range of experimental uncertainty.
4. An evaluation of the boiling correlation (4.96) of [Cooper \(1984\)](#) at the increased surface roughness of  $5\mu m$  results in a slightly better agreement with experimental data, the application of a reduction factor for flow boiling suggested by [Cooper \(1989\)](#) has the opposite effect. However, no real significance for the preference of either of those correlations can be claimed due to the rather large systematic uncertainties.

Most experimental data points lie in between the results from correlation (4.96) of [Cooper \(1984\)](#) evaluated for standard surface roughness of  $1\mu m$  and the respective evaluation for increased surface roughness of  $5\mu m$ . This actually suggests the application of the reduction factor for flow boiling according to [Cooper \(1989\)](#) on the boiling correlation at  $5\mu m$  surface roughness; nevertheless, [Cooper \(1989\)](#) always employed the pool boiling correlation at  $1\mu m$  surface roughness as basis for his flow boiling correlation. Again, it has to be stated that experimental uncertainties in Fig. 74 are too large to claim any significance for such considerations. Finally, it is to be mentioned that the single data point in Fig. 74 (2<sup>nd</sup> row, bulk tube, bottom: empty magenta square) exhibiting only about 2 K wall superheat at  $20\text{ kW/m}^2$  – in contradiction to all other data – results from an operational state with large subcooling of the solution entering the bottom vessel (cf. Fig. 72 and discussion above). The lower wall temperature measured at this position is an indication for the presence of significantly subcooled solution in the bottom of the boiling tube at this operational state; thus, it should not be interpreted as a measuring error.



## Boiling heat transfer coefficients

Fig. 75 below shows the boiling heat transfer coefficients  $\alpha_L = \dot{q}_L / \Delta T_{SAT}$  that can be calculated from the wall superheats shown above over the estimated surface heat flux  $\dot{q}_L$ . No more error bars are given for better readability<sup>77</sup>; again, the theoretical results from the nucleate boiling correlations discussed above are shown for comparison.

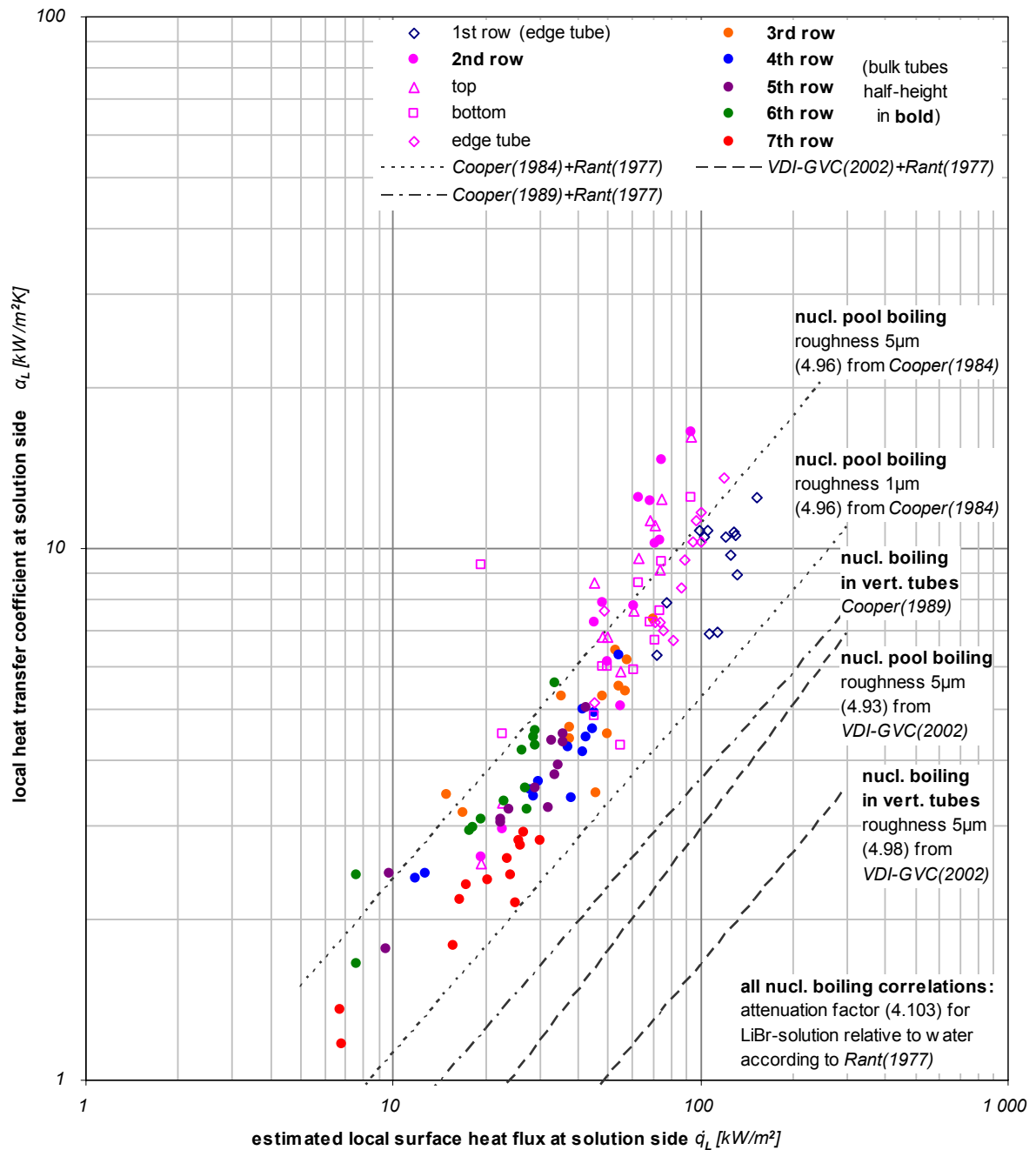


Fig. 75: Boiling heat transfer coefficients vs. heat flux. Comparison of experimental values with various nucleate boiling correlations.

<sup>77</sup> Note that inclined error bars would be required to reflect the actual interdependence of the uncertainties of measured values in such  $\alpha_L$  vs.  $\Delta T_{SAT}$  plots, because the displayed heat transfer coefficients (abscissa) are functions of the measured heat flux (ordinate) itself. Therefore, the much better suited Nukiyama plot – Fig. 74 – was employed for the discussion of experimental uncertainties.

Experimental heat transfer coefficients at the solution side range from about  $1.5 \text{ kW/m}^2 \cdot \text{K}$  to  $15 \text{ kW/m}^2 \cdot \text{K}$ . As already discussed above, the majority of all data points lies between the theoretical curves from the nucleate pool boiling correlation of [Cooper \(1984\)](#) evaluated for  $1 \mu\text{m}$  and  $5 \mu\text{m}$  surface roughness. In contrast, the nucleate boiling correlation for vertical tubes (4.98) according to [Steiner & Taborek \(1992\)](#) and [VDI-GVC \(2002\)](#) is exceeded by a factor of about five. The single data point (2<sup>nd</sup> row, bulk tube, bottom: empty magenta square) at about  $20 \text{ kW/m}^2$  that exceeds the other experimental data by a factor of about three originates from an operational state with large subcooling of the solution entering the bottom vessel (cf. Fig. 72, Fig. 74, and discussion above). No nucleate-boiling dominated heat transfer regime – probably no nucleate boiling at all – is expected to be found at this location at this operational state; therefore a boiling heat transfer coefficient is not well defined<sup>78</sup> at this data point and the value displayed in Fig. 75 is not expected to meet any of the theoretical nucleate boiling correlations.

Fig. 76 below finally compares all experimental boiling heat transfer coefficients at measuring locations at half-height of the boiling tubes with a series of calculations for enhanced convective heat transfer in two-phase flow. As already discussed in 6.4.3, no clear information on the mass flow and the state of the solution entering the boiling tubes can be obtained from the experimental data, findings are contradictory in part and not always compliant with literature. Therefore, a parameter variation has been performed in Fig. 76 to determine the range of possible heat transfer coefficients that might be found in a convective boiling regime.

In the simulation, the specific mass flow in the boiling tubes  $\dot{m}_{CS}$  was varied in the range of  $100 \dots 1000 \text{ kg/s} \cdot \text{m}^2$ , which covers at least the full range of values that has been reported in literature for different configurations. Typically, the solution is expected to enter the boiling tubes at about its saturation temperature in the header vessel, where no additional liquid head is present (in the bottom vessel, solution of this temperature is already subcooled due to the local shift in saturation temperatures), or at slightly lower temperatures if significantly subcooled weak solution is entering the bottom vessel. According to Fig. 67, the measured temperature difference  $T_{02} - T_{04}$  between bottom vessel and saturation temperature at liquid level varied in the range of about  $+1 \dots -10 \text{ K}$ . Therefore, alternative calculations assuming either  $0 \text{ K}$  or  $10 \text{ K}$  additional subcooling of the solution entering the boiling tubes have been performed, thus covering the full range of the found variation.

---

<sup>78</sup> Actually, some literature sources define an “enhanced” boiling heat transfer coefficient at subcooled boiling states to account for the increased convective heat transfer. However, this approach shall not be followed here.

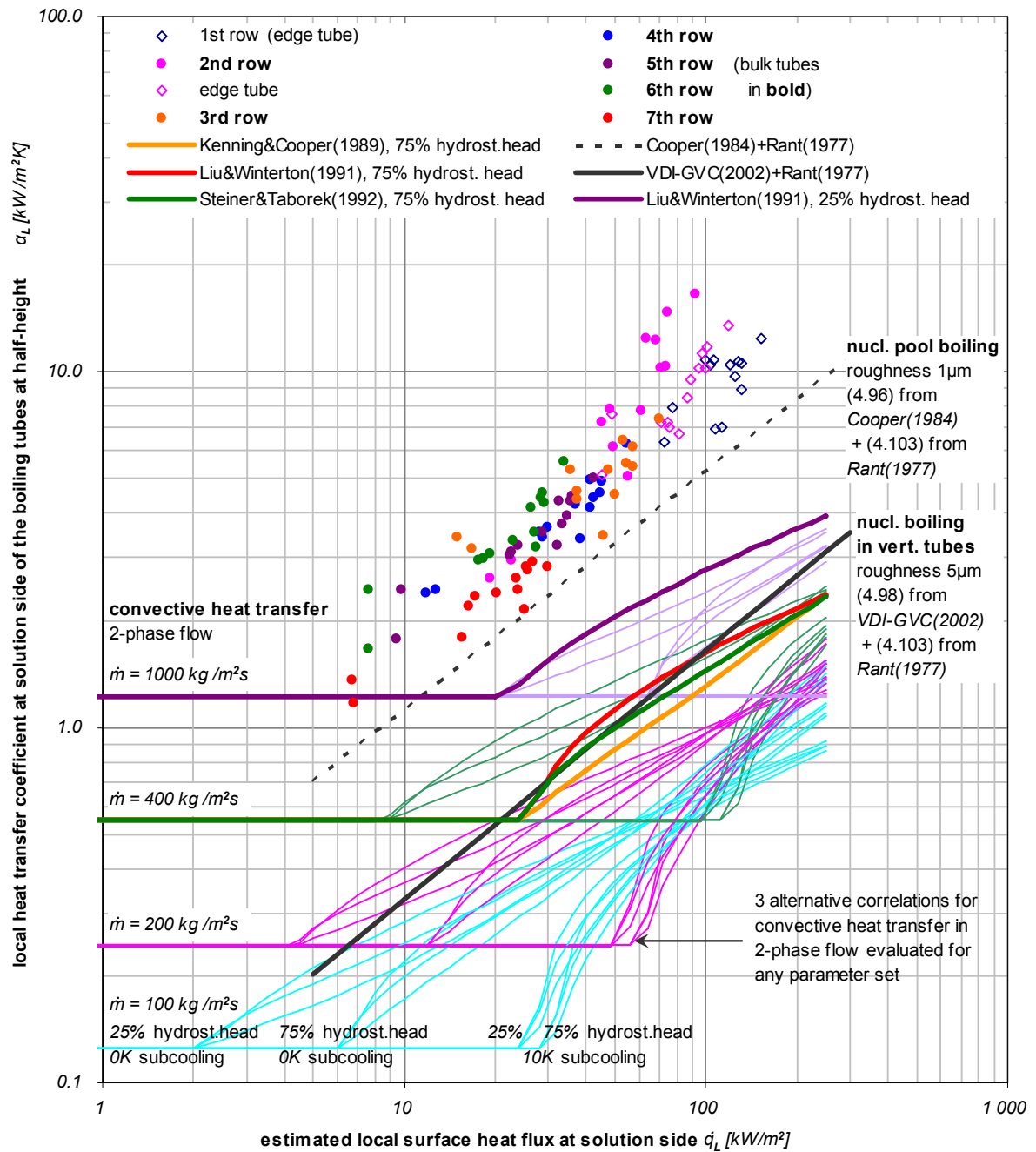


Fig. 76: Boiling heat transfer coefficients vs. heat flux. Comparison of experimental values with various calculations for convective heat transfer in a two-phase flow regime (convective flow boiling).

Finally, the actual hydrostatic heads at half-height in the individual boiling tubes are additional influencing variables that are basically unknown. During operation of a thermosiphon boiler, the hydrostatic heads in the bottom vessel and in the subcooled bottom sections of the boiling tubes have to be a little lower than in the static case (all tubes filled completely with non-moving liquid). The reason is that a driving force for the liquid motion must be present that overcomes (small) frictional pressure drops in the 1-phase flow regimes (downward flow in the downcomer tubes, upward flow in the bottom section of the boiling tubes). In the topmost section of the boiling tubes, on the other hand, the pressure has to be even higher

under operation as a significant exit pressure drop (two-phase flow regime) has to be accounted for. In the two-phase flow section of the boiling tubes, the local pressure at a measuring point can be either smaller or larger than in the static case – dependent on the position and the operational state of the boiler. A reduction of the hydrostatic head results in an increased vapor fraction of the flow and thus in larger enhancement of the convective heat transfer in two-phase flow. Therefore, alternative calculations have been performed assuming the hydrostatic head at half-height being either 75% or only 25% of its value in a tube filled completely with non-moving strong solution.

As a final variation, all three correlations for the enhancement factor  $F_{2P}$  in two-phase flow discussed in 4.5.2, i.e. (4.86) from *Steiner & Taborek (1992)*, (4.87) from *Liu & Winterton (1991)*, and (4.88) from *Kenning & Cooper (1989)* have alternatively been employed. In each case, the vapor quality  $\dot{\chi}_{EQ}$  at half-height has been calculated in dependence on the surface heat flux  $\dot{q}_L$  and the cross-sectional mass flux  $\dot{m}_{CS}$  by an enthalpy balance.

As result of the parameter study, a set of 48 curves<sup>79</sup> – not to be discussed in detail – are displayed as solid colored lines in Fig. 76 for the convective heat transfer coefficient at half-height over the surface heat flux in the boiling tube. The influence of the variation of hydrostatic head and initial subcooling is marked for the curves at  $100 \text{ kg/s}\cdot\text{m}^2$  (solid **light blue** lines). The largest convective heat transfer coefficients are found for the smallest hydrostatic head and without additional subcooling as these conditions result in the largest vapor mass fraction. The influence of the different two-phase flow correlations is marked for the case  $\dot{m}_{CS} = 100 \text{ kg/s}\cdot\text{m}^2$ , 75% hydrostatic head at half-height,  $0 \text{ K}$  additional subcooling of the entering solution by means of three different thick lines. The results from (4.86) after *Steiner & Taborek (1992)* are displayed as solid thick **green** line, (4.87) after *Liu & Winterton (1991)* is visualized as solid thick **red** line, and (4.88) from *Kenning & Cooper (1989)* is shown as solid thick **yellow** line; the largest numbers are produced by correlation (4.87) after *Liu & Winterton (1991)*. The largest convective heat transfer coefficients at all in this parameter study – shown as solid thick **violet** line – were obtained for the application of the latter correlation on the above mentioned parameter set ( $\dot{m}_{CS} = 100 \text{ kg/s}\cdot\text{m}^2$ , 75% hydrostatic head at half-height,  $0 \text{ K}$  additional subcooling of the entering solution). For comparison, also the results from the nucleate pool boiling correlation of *Cooper (1984)* (dotted **black** line) and from the nucleate boiling correlation for vertical tubes according to *Steiner & Taborek (1992)* and *VDI-GVC (2002)* (solid thick **black** line) that have already been discussed above are displayed in Fig. 76.

<sup>79</sup> 4 different mass flows x 2 different hydrostatic heads at half height x 2 different degrees of subcooling in the bottom vessel x 3 alternative correlations = 48 cases

It shows that – except for a single data point at very small heat flux – all experimentally found heat transfer coefficients exceed the values obtained for convective heat transfer in two-phase flow in the parameter study. Thus, in a convective flow boiling dominated regime at mass fluxes up to  $1000 \text{ kg/s}\cdot\text{m}^2$ , significantly lower heat transfer coefficients would have been observed at half-height than those experimentally found or those predicted by the Cooper boiling correlation (dotted **black** line). On the other hand – as already discussed in 6.4.3 above – existence of significantly larger mass fluxes than  $1000 \text{ kg/s}\cdot\text{m}^2$  is neither to be expected from theory nor suggested by the experimental findings. Therefore, it can be concluded that there is little evidence for the dominance of a convective flow-boiling regime. The experimental data are best described by the nucleate boiling correlation (4.96) of [Cooper \(1984\)](#).

## 7 Conclusion and outlook

### 7.1 Conclusions from this work

This work focused on water/lithium bromide based absorption chillers that utilized a hot flue gas stream as the main driving energy. A characteristic feature, with thermodynamic as well as technical implications, was that the driving heat was available on a gliding temperature level. Consequently, the evaluation of flue gas fired chillers had to go beyond the “classical” model of a nearly ideal thermodynamic process between three temperature levels, which has successfully been applied on steam-fired and hot water fired machines.

It has been shown, in this work, that multi-stage flue gas utilization is a key step towards the increased efficiency of direct-fired and exhaust-fired absorption chillers, being the subject of numerous recent development efforts. An overview of the major current trends has been presented, based on an extensive literature survey.

There is a great variety of promising flow schemes possible for such advanced machines, depending on the application and boundary conditions, for instance, the available flue gas temperature. Quite complex cycles, requiring sophisticated control strategies, may be an option for large capacities, though less efficient, but simpler and more robust, flow schemes are likely to be the most economical solution for small and medium sized units. Therefore, this work has intentionally discussed and rated the potential and applicability of various thermodynamic concepts for increasing the thermal efficiency on a more general basis. Nevertheless, the ultimate identification of the best solution for a particular application will always remain subject to an individual numerical study.

A general conclusion is that advanced flue gas fired chillers, with increased efficiency compared to the standard designs available, require a series of two to four heat exchangers in the flue gas train, in place of the conventional high-temperature regenerator. A significant increase in the respective pressure drop or in the size and cost of the plant is not acceptable; therefore, the development of suitable compact and efficient flue-gas fired regenerators is a key issue for the economics of such thermodynamically advanced machines.

While the flue gas fired high-temperature regenerator is the first and main flue gas heat exchanger in such machines, consecutive stages of flue gas utilization can consist of flue gas recuperators, connected to the internal solution cycle or by the direct or indirect heating of a low-temperature regenerator in the absorption cycle. It could be shown that, for flue gas entry temperatures above  $600^{\circ}\text{C}$ , suitably placed flue gas recuperators are the most promising option. In the case where an exhaust gas of only  $300^{\circ}\text{C}$  or less was available, two

exhaust-fired regenerators of about the same capacity would be required for maximum efficiency. In the intermediate temperature range from 300 to 600°C, where most applications for exhaust gas in CHP environments are to be found, the input of additional flue gas heat into the solution cycle or into a low temperature regenerator are equivalent options, from a thermodynamic point of view. The best solution is again dependent on the requirements of the particular application.

A literature review revealed that although numerous works are published every year dealing with falling film absorption, only limited information, considering design issues for high-temperature regenerators of absorption chillers, was found in the open literature in western languages. While proven correlations for the prediction of the flue gas side heat transfer and pressure drop can be found in textbooks and reference works, data on boiling heat transfer at the solution side are still incomplete or contradictory. Thus far, standard correlations, derived for the boiling of pure substances or for organic refrigerant mixtures, have not been proven for lithium bromide brine. No reliable information is available for the prediction of wall superheat and the circulation rate in natural convection boilers incorporating a lithium bromide solution.

Based on the available correlations for heat transfer and pressure drop at the flue gas side, promising heat exchanger configurations, in terms of size, pressure drop, and the effort involved in manufacturing, have been identified in this work. In general, valid relations between the heat transfer coefficient and pressure drop for the comparison of different heat exchanger concepts were deduced and applied in a numerical parameter study at typical boundary conditions. It was shown that the basic design of a liquid-tube boiler with flue gas crossflow outside the bank of vertical boiling tubes is advantageous to the, ever dominant, conventional pool boiler design with tubular flue gas flow inside the smoke tubes. In the latter case, the optimum relation between the heat transfer coefficient and pressure drop at the flue gas side was already achieved at Reynolds numbers of around 10 000. Larger heat transfer coefficients and even smaller pressure drops could be realized at the same time in crossflow configurations at Reynolds numbers in the range from 500 to 5000. The use of boiling tubes, equipped with outer fins, in the downstream section of the heat exchanger enabled a further increase of the mean heat transfer coefficient and a reduction in the size and weight of the heat exchanger.

A semi-industrial prototype of such a direct-fired regenerator with vertical boiling tubes was tested in the laboratory. To increase the flow velocity and heat transfer inside the tubes, the novel prototype was designed like a natural convection boiler with additional unheated downcomer tubes. To enhance external heat transfer, a section of the downstream boiling

tubes was equipped with external circular fins. The appropriate operation of the novel design was successfully proven. Experimental results from laboratory testing were presented in this work.

The flue gas side heat transfer coefficients and pressure drops measured showed good agreement with theoretical predictions, based on correlations provided in standard engineering references. The heat transfer coefficients established at the solution side showed reasonable agreement with the boiling correlation of *Cooper (1984)*, but significantly exceeded the values obtained from the correlations suggested in *VDI-GVC (2002)*. The small flow velocities measured in the downcomer tubes were neither compliant with an enthalpy balance over the solution temperatures measured nor with literature data from steam-fired thermosiphon reboilers at similar operating conditions. Therefore, it could be speculated that downward solution flow occurred inside some of the boiling tubes. However, the limited measuring instrumentation available at the semi-industrial prototype could not provide any further insight on solution circulation inside the regenerator.

## **7.2 Unresolved issues and further work**

This work attempted to outline the development of flue gas fired absorption chillers with an improved efficiency of the conversion of flue gas enthalpy into useful refrigeration. Due to the fundamental nature of the study, its results can be extended to other related technical topics. The next step would be the extension of the discussion to the class of so-called chiller-heaters, i.e., integrated machines capable of the alternative, or even simultaneous, production of chilled and hot water. A flow scheme for such a flexible SE/DE-chiller, developed at ZAE Bayern, allowing a smooth switchover from the heating to cooling mode in CCHP systems, has already been quoted as an example. The thermal and economic optimization of such bimodal systems is an appropriate subject for future work.

So far, this work only discussed the optimization of the design of flue gas fired high-temperature regenerators of double-effect absorption chillers; high-temperature regenerators of triple-effect chillers could be handled in the same way, yet different numerical results might be obtained. However, the framework presented could also be adapted to the comparison and optimization of flue gas recuperators, if a sufficiently large velocity is chosen at the liquid side, such that the overall heat transfer is again dominated by the gas side. If direct exhaust-fired low-temperature regenerators are considered, all conclusions concerning the flue gas side still hold true. However, a different boiling behavior of lithium bromide solution at a lower saturation pressure might result in additional design optimization constraints; further work is required to clarify this point.



The experimental investigations presented in this work were conducted at a semi-industrial sized prototype of a direct-fired regenerator that had been prepared for and partly equipped with measuring instrumentation during fabrication, as a number of sensor positions would no longer be accessible after the completion of manufacture. The instrumentation was intentionally optimized to cause minimum interference in the operation of the regenerator, rather than for the most accurate possible observation of individual physical phenomena. Therefore, all observations could be related to the actual operational behavior of a “real” regenerator, rather than to artifacts that may have resulted from (over-)simplified geometry in lab experiments, with only a single row of tubes or, in the most extreme case, just a single boiling tube. Of course, the disadvantage of the chosen approach is that uncertainties in the measurements are significantly larger than would be expected in a “classical” laboratory heat transfer experiment, built around the requirements of the exact measurement of a selected phenomenon.

As a consequence, the experimental findings have to be treated with great care and should be verified by further investigations before the final conclusions are drawn. The largest uncertainties in the present study result from the unknown radiation balance in the short furnace chamber between the burner and the first row of tubes. In the actual geometric conditions of this compact direct-fired prototype, the exact measurement of the flue gas temperatures in front of the heat exchanger was scarcely possible. An accurate theoretical calculation of the flue gas temperatures would require detailed information on the radiation characteristics of the surface burner employed and of the insulation material of the walls of the furnace chamber. Therefore, a more promising approach would be the investigation of a similar heat exchanger in an exhaust-fired application, without a direct view of the flame. Generally, experiments under the conditions of typical CCHP applications, with initial exhaust gas temperatures of  $600^{\circ}\text{C}$  or less, would greatly reduce the radiation impact and allow for more accurate studies of convective and boiling heat transfer phenomena.

Additionally, further experiments should be equipped with a larger number of wall temperature probes at a greater variety of positions. This empirical approach should give more accurate information on the local distribution of the surface heat flux, which would also help to reduce the uncertainties in the evaluation of the boiling heat transfer.

Within this work, only correlations for the mean convective heat transfer at single rows of tubes have been employed. In reality, the turbulence of the flue gas flow and thus the local Nusselt number might show a tangential variation around each boiling tube. Additionally, significant inhomogeneities in the velocity and temperature of the flue gas normal to the principal flow direction might be found, due to boundary effects in narrow and short tube

bundles like the one investigated in this work. Therefore, an extension of the theoretical model of the convective heat transfer at the flue gas side, the introduction of angle-dependent correction factors for the Nusselt numbers, or maybe even a numerical CFD-calculation of the flue gas side heat transfer might be further steps to be considered.

Finally, further work is required to gain more insight into the internal solution circulation. Obviously, the popular assumption of equal conditions in each boiling tube, employed in the modeling of steam-fired thermosiphon reboilers, is not applicable for direct-fired regenerators. The determination of the mean flow velocity in the downcomer tubes was shown to be insufficient to set up a consistent model for internal mass flows and enthalpy balances. A more accurate recording of the variations and, possibly, oscillations in the down-flow rates might be a first step towards an improved understanding of these. Additional measuring installations will be required to detect the flow rates, or at least the flow directions, inside the boiling tubes. In fact, measuring the flow rates inside the tubes, without disturbing the original flow rates, is quite difficult in real heat exchanger geometry. The installation of a number of additional thermometers at the inlet and outlet of the individual tubes in the bottom and header vessel could be a feasible option to at least determine the local flow direction.

# Appendix

## A.1 Endoreversible efficiency and loss mechanisms

### A.1.1 Endoreversible efficiency according to internal temperatures

In 2.2, it is shown that for absorption chillers it is a favorable approach to separate the heat exchange between the external heat carriers and the internal refrigeration cycle accounting for the main irreversibility of the system from the discussion of the efficiency of the refrigeration process. Actually, the remaining internal refrigeration cycle of lithium bromide based absorption chillers works close enough to the efficiency of a reversible thermodynamic process that it is worth discussing its individual loss mechanisms in detail.

Defining mean temperatures  $t_0$ ,  $t_1$ ,  $t_2$  in the external heat carrier loops for refrigeration, reject heat and driving heat, respective internal saturation temperatures  $T_0$  (evaporator),  $T_1$  (absorber and condenser), and  $T_2$  (regenerator), and appropriate driving temperature differences  $\Delta T_0$ ,  $\Delta T_1$ , and  $\Delta T_2$ , the reversible efficiency of the internal cycle reads according to (2.28):

$$\begin{aligned} COP_{C,ENDOREV} &= (T_2 - T_1) / T_2 \cdot T_0 / (T_1 - T_0) \\ &= (t_2 - t_1 - \Delta T_2 - \Delta T_1) / (t_2 - \Delta T_2) \cdot (t_0 - \Delta T_0) / (t_1 - t_0 + \Delta T_1 + \Delta T_0) \end{aligned} \quad (7.1)$$

Utilizing the Dühring-relations for the shift in saturation temperature at constant vapor pressure from evaporator to absorber and from condenser to regenerator as a function of the Dühring intercept  $B_D$  and the slope parameter  $R_D$  according to (2.14) and (2.15) provided in 2.1.2:

$$T_0 = (T_1 - B_D(X_{SOL})) \cdot R_D(X_{SOL}) \quad (7.2)$$

$$T_1 = (T_2 - B_D(X_{SOL})) \cdot R_D(X_{SOL}) \quad (7.3)$$

It has already been shown in 2.2 that the endoreversible efficiency can be directly calculated if two of the three temperature levels are set and if the required property data are available to determine the Dühring intercept  $B_D$ . If the lower temperatures  $T_0$  (evaporator) and  $T_1$  (absorber and condenser) are given, the efficiency is according to (2.33):

$$COP_{C,ENDOREV} = T_0 \cdot (T_1 - B_D) / (T_1^2 - B_D \cdot (T_1 - T_0)) \quad (7.4)$$

This is the efficiency of an ideal heat driven chiller based on a real working pair assuming that at least the internal refrigeration process is operating without any irreversibilities. This would require ideal internal heat exchange processes and possibly ideal internal heat pumps to ensure that all media flows enter a phase change process already at the respective equilibrium temperature. Additionally the endoreversible efficiency requires that no irreversi-

bilities result from pumping and throttling of liquid flows between different pressure levels, i.e. an ideal recovery of mechanical work had to be performed. However, for water based chillers with relatively small differences between system pressures of different components these irreversibilities are small compared to those attributed to improper heat recovery. Therefore, they will not be discussed any further.

### A.1.2 Endoreversible efficiency assuming an ideal working pair

All the common irreversibilities in absorption chillers resulting from process media entering in a subcooled or superheated state scale down if the specific heats of the media are reduced. Therefore, preferable working pairs for absorption machines are characterized by specific heat capacities for liquid and vapor phase that are small compared to the specific heat of vaporization. A working pair could be considered as ideal if the specific heats would vanish completely; then no internal heat exchange at all would be required to realize an endoreversible absorption chiller.

The endoreversible efficiency of the basic single-effect cycle then simply is the ratio of the specific heat of vaporization  $\Delta h_{VAP}$  in the evaporator to the sum of specific heat of vaporization plus specific heat of solution  $\Delta h_{VAP} + \Delta h_{SOL}$  in the regenerator:

$$COP_{C,ENDOREV} = \Delta h_{VAP} / (\Delta h_{VAP} + \Delta h_{SOL}) \quad (7.5)$$

For substances with marginal heat capacity, making the additional assumption of negligible specific volume of the liquid phase the specific heat of vaporization is no longer dependent on saturation temperature and pressure. Then expression (7.5) is a characteristic constant for a given salt concentration. This value gets closer to its maximum of unity if the specific heat of solution is small compared to the specific heat of vaporization.

As different kinds of property data of the same substance are always thermodynamically consistent, this formula for the efficiency based on the specific heats of evaporation and solution (7.5) and the previously given formulas (7.1) to (7.4) based on the Dühring coefficients have to return similar values for a chosen working pair. For water / lithium bromide, the specific heat of solution is typically about one tenth of the specific heat of vaporization, resulting in an endoreversible efficiency of about 0.9 according to (7.5). Roughly, this same value was obtained from the sample calculation Tab. 4 in 2.2 based on saturation temperatures and Dühring-coefficients.

Although the equation (7.5) is popular due to its simplicity, it has to be noted that it was derived assuming theoretical substances without heat capacity and only represents an approximation for actual working pairs. In contrast (7.1) is universal and the relations (7.2) and (7.3) according to Dühring are the best available to characterize the shift in saturation

temperature for salt solutions. Therefore, there still is a slight but systematical deviation of the results obtained by equation (7.5) from the true efficiencies obtained from (7.2) and (7.3).

### A.1.3 Endoreversible efficiency for real working pairs

For real working pairs with non-negligible heat capacities all internal mass flows require heating or cooling to avoid internal irreversibilities. For a single-effect cycle operating at the internal temperatures  $T_0 < T_1 < T_2$ , the following seven flows are affected (see also Fig. 8 in 2.2):

1. Liquid refrigerant flow  $\dot{M}_{REFR}$  from condenser (C) to evaporator (E), requiring cooling  $\dot{M}_{REFR} \cdot c'_{REFR} \cdot (T_0 - T_1) < 0$  at gliding temperatures from  $T_1$  to  $T_0$ .
2. Refrigerant vapor flow  $\dot{M}_{REFR}$  from evaporator (E) to absorber (A), requiring heating  $\dot{M}_{REFR} \cdot c''_{REFR} \cdot (T_1 - T_0)$  at gliding temperatures from  $T_0$  to  $T_1$ .
3. Weak solution flow  $\dot{M}_{WEAK} = \dot{M}_{STRONG} + \dot{M}_{REFR}$  from absorber to regenerator, requiring heating  $\dot{M}_{WEAK} \cdot c'_{WEAK} \cdot (T_2 - T_1)$  at gliding temperatures from  $T_1$  to  $T_2$ .
4. Strong solution flow  $\dot{M}_{STRONG}$  from regenerator (G) to absorber (A), requiring cooling  $\dot{M}_{STRONG} \cdot c'_{STRONG} \cdot (T_1 - T_2) < 0$  at gliding temperatures from  $T_2$  to  $T_1$ .
5. Refrigerant vapor flow  $\dot{M}_{REFR}$  from regenerator (G) to condenser (C), requiring cooling  $\dot{M}_{REFR} \cdot c''_{REFR} \cdot (T_1 - T_2) < 0$  at gliding temperatures from  $T_2$  to  $T_1$ .

Neglecting technical constraints, an endoreversible machine would have to realize a first ideal recuperative heat exchange between the flows no. 1 and 2 and a second one between the flows no. 3 to 5. However, there remains a mismatch between the absolute heat capacities of the flows to be cooled and the flows to be heated in each heat exchange as for real fluids the specific heat capacity in the vapor phase  $c''$  is lower than the one  $c'$  in the liquid phase. Consequently, some additional cooling is required at gliding temperatures from  $T_1$  to  $T_0$  and some additional heating is required at gliding temperatures from  $T_1$  to  $T_2$ .

Assuming the specific heat capacities being independent from temperature the additionally required specific cooling  $\Delta q_{10,ER} = \Delta \dot{Q}_{10,ER} / \dot{M}_{REFR}$  of flow no. 1 is:

$$\Delta q_{10,ER} = \Delta \dot{Q}_{10,ER} / \dot{M}_{REFR} = (c'_{REFR} - c''_{REFR}) \cdot (T_1 - T_0) \quad (7.6)$$

Employing an approximate relation provided by [Ziegler \(1997\)](#) for the heat capacities of weak and strong solution:

$$\dot{M}_{WEAK} \cdot c'_{WEAK} = \dot{M}_{STRONG} \cdot c'_{STRONG} + \dot{M}_{REFR} \cdot c'_{REFR} \quad (7.7)$$

The additionally required specific heating of flow no. 3  $\Delta q_{12,ER}$  with reference to the refrigerant circulation  $\dot{M}_{REFR}$  is:

$$\Delta q_{12,ER} = \Delta \dot{Q}_{12,ER} / \dot{M}_{REFR} = (c'_{REFR} - c''_{REFR}) \cdot (T_2 - T_1) \quad (7.8)$$

A closer look on the individual terms reveals that because the specific heat capacity  $c_{REFR}''$  of the vapor phase is about half of those of the liquid phase  $c_{REFR}'$ , roughly half of the cooling required for the condensate entering the evaporator can be gained from the vapor leaving the evaporator. Analogously the vapor leaving the regenerator delivers about half of the additional heating required for the solution. The remaining cooling demand  $\Delta q_{10,ER}$  from  $T_1$  to  $T_0$  and the remaining extra heating demand  $\Delta q_{12,ER}$  from  $T_2$  to  $T_1$  both have a magnitude of about 4% of the respective heats of evaporation  $(\Delta h_{VAP})_{T_0}$  in the evaporator and  $(\Delta h_{VAP} + \Delta h_{SOL})_{T_2}$  in the regenerator.

Assuming an endoreversible chiller, heating and cooling of internal flows at gliding temperatures had to be provided by respective reversibly operating heat pumps. Nevertheless, to drive these heat pumps input of additional heat at the driving temperature level  $T_2$  or a respective consumption of some of the produced refrigeration at  $T_0$  is required. Using the entropic mean temperatures of the temperature glides which are, however, close to the arithmetic means according to (2.21):

$$\bar{T}_{10} = (T_1 - T_0) / \ln(T_1 / T_0) \approx (T_0 + T_1) / 2 \quad (7.9)$$

$$\bar{T}_{12} = (T_2 - T_1) / \ln(T_2 / T_1) \approx (T_1 + T_2) / 2 \quad (7.10)$$

We can assume that the cooling  $\dot{Q}_{10,ER}$  at a temperature  $\bar{T}_{10}$  is performed by an ideal heat pump<sup>80</sup> releasing heat at temperature  $T_1$  and consuming “driving refrigeration”  $\Delta \dot{Q}_{0,ER}$  at temperature  $T_0$ . We also assume that the heating  $\dot{Q}_{12,ER}$  at a temperature  $\bar{T}_{12}$  is performed by an ideal heat pump absorbing heat at temperature  $T_1$  and consuming driving heat  $\Delta \dot{Q}_{2,ER}$  at temperature  $T_2$ . According to the first and second law of thermodynamics given in (2.26) and (2.27), the ideal thermal efficiencies  $COP_{10,0} = \Delta \dot{Q}_{10,ER} / \Delta \dot{Q}_{0,ER} = \Delta q_{10,ER} / \Delta q_{0,ER}$  and  $COP_{12,2} = \Delta \dot{Q}_{12,ER} / \Delta \dot{Q}_{2,ER} = \Delta q_{12,ER} / \Delta q_{2,ER}$  of these reversible heat pumps are in the order of two:

$$COP_{10,0} = (T_1 - T_0) / T_0 \cdot \bar{T}_{10} / (T_1 - \bar{T}_{10}) \approx 2 + (T_1 - T_0) / T_0 \approx 2 \quad (7.11)$$

$$COP_{12,2} = (T_2 - T_1) / T_2 \cdot \bar{T}_{12} / (\bar{T}_{12} - T_1) \approx 2 - (T_2 - T_1) / T_2 \approx 2 \quad (7.12)$$

Therefore the final loss of refrigeration  $\Delta q_{0,ER}$  and the additionally required heat input  $\Delta q_{2,ER}$  both reduce to about half of the respective cooling and heating demands  $\Delta q_{10,ER}$  and  $\Delta q_{12,ER}$  at gliding temperatures or to only a quarter of the respective terms without the vapor-liquid heat exchange. For typical water / lithium bromide based single-effect chillers both loss terms have a magnitude of about 2% of the respective heats of evaporation  $(\Delta h_{VAP})_{T_0}$  in the evaporator and  $(\Delta h_{VAP} + \Delta h_{SOL})_{T_2}$  in the regenerator.

<sup>80</sup> A heat pump like this, absorbing heat at an intermediate temperature level and rejecting heat simultaneously at a lower and at a higher temperature level, is also called “heat transformer” or “heat pump type 2”

$$\Delta q_{0,ER} = (C'_{REFR} - C''_{REFR}) \cdot (T_1 - T_0) / COP_{10,0} \quad (7.13)$$

$$\begin{aligned} \Delta q_{0,ER} &\approx (C'_{REFR} - C''_{REFR}) \cdot (T_1 - T_0) / 2 \\ &\approx C'_{REFR} \cdot (T_1 - T_0) / 4 \\ &\approx 2\% \cdot (\Delta h_{VAP})_{T_0} \text{ (for water/lithium bromide)} \end{aligned} \quad (7.14)$$

$$\Delta q_{2,ER} = (C'_{REFR} - C''_{REFR}) \cdot (T_2 - T_1) / COP_{12,2} \quad (7.15)$$

$$\begin{aligned} \Delta q_{2,ER} &\approx (C'_{REFR} - C''_{REFR}) \cdot (T_2 - T_1) / 2 \\ &\approx C'_{REFR} \cdot (T_2 - T_1) / 4 \\ &\approx 2\% \cdot (\Delta h_{VAP} + \Delta h_{SOL})_{T_2} \text{ (for water/lithium bromide)} \end{aligned} \quad (7.16)$$

Thus, we can write for the endoreversible efficiency of an idealized chiller utilizing a real working pair:

$$COP_{C,ENDOREV} = ((\Delta h_{VAP})_{T_0} - \Delta q_{0,ER}) / ((\Delta h_{VAP} + \Delta h_{SOL})_{T_2} + \Delta q_{2,ER}) \quad (7.17)$$

Using the definitions ( 7.13 ) and ( 7.15 ) for both loss terms, the endoreversible efficiency finally is:

$$COP_{C,ENDOREV} = \frac{(\Delta h_{VAP})_{T_0} - (C'_{REFR} - C''_{REFR}) \cdot (T_1 - T_0) / COP_{10,0}}{(\Delta h_{VAP} + \Delta h_{SOL})_{T_2} + (C'_{REFR} - C''_{REFR}) \cdot (T_2 - T_1) / COP_{12,2}} \quad (7.18)$$

Regarding water/lithium bromide, both loss terms together reduce the efficiency by about 4%. Combining the approximations ( 7.14 ) and ( 7.16 ) with ( 7.17 ) leads to the estimation:

$$\begin{aligned} COP_{C,ENDOREV} &\approx ((\Delta h_{VAP})_{T_0} \cdot 98\%) / ((\Delta h_{VAP} + \Delta h_{SOL})_{T_2} \cdot 102\%) \\ &\approx (\Delta h_{VAP})_{T_0} / (\Delta h_{VAP} + \Delta h_{SOL})_{T_2} \cdot 96\% \end{aligned} \quad (7.19)$$

Relations ( 7.17 ) to ( 7.19 ) demonstrate that, as a consequence from the thermodynamic properties of the real working pair, even in a theoretical ideal absorption chiller the effective usable refrigeration would be less than the heat of vaporization of the circulating refrigerant at evaporator temperature. Additionally the consumed driving heat had to be greater than the heat required to boil off the circulating refrigerant at regenerator temperature.

Instead of providing the heating  $\Delta q_{12,ER}$  required at gliding temperatures from  $T_1$  to  $T_2$  by a heat pump driven by heat at regeneration temperature  $T_2$ , a less intuitive but thermodynamically equivalent approach would be driving this ideal heat pump by cooling at evaporator temperature  $T_0$ . The ideal thermal efficiency  $COP_{12,0} = \Delta q_{12,ER} / \Delta q'_{0,ER}$  of a reversible heat pump absorbing heat at temperature  $T_1$ , releasing heat  $\Delta q_{12,ER}$  at temperature  $\tilde{T}_{12}$  and consuming driving refrigeration  $\Delta q'_{0,ER}$  at temperature  $T_0$  is:

$$COP_{12,0} = (T_1 - T_0) / T_0 \cdot \bar{T}_{12} / (\bar{T}_{12} - T_1) \quad (7.20)$$

As for this case both internal heat pumps consume some refrigeration at  $T_0$  there is no additional driving heat consumption  $\Delta q'_{2,ER} = 0$  at  $T_2$  while the total loss of refrigeration  $\Delta q'_{0,ER}$  is:

$$\Delta q'_{0,ER} = (c'_{REFR} - c''_{REFR}) \cdot (T_1 - T_0) / COP_{10,0} + (c'_{REFR} - c''_{REFR}) \cdot (T_2 - T_1) / COP_{12,0} \quad (7.21)$$

To evaluate this lengthy expression, we can employ the approximate relation  $T_2 \approx T_1^2 / T_0$  according to (2.34) between internal temperatures; by insertion of the definitions of the efficiencies (7.11), (7.20) and of the entropic mean temperatures (7.9), (7.10), we find:

$$\Delta q'_{0,ER} = (c'_{REFR} - c''_{REFR}) \cdot (T_1 - T_0) \quad (7.22)$$

The endoreversible efficiency therefore can be expressed by a relation even more simple than the equivalent formulation (7.17):

$$\begin{aligned} COP_{C,ENDOREV} &= [(\Delta h_{VAP})_{T_0} - \Delta q'_{0,ER}] / (\Delta h_{VAP} + \Delta h_{SOL})_{T_2} \\ &= [(\Delta h_{VAP})_{T_0} - (c'_{REFR} - c''_{REFR}) \cdot (T_1 - T_0)] / (\Delta h_{VAP} + \Delta h_{SOL})_{T_2} \end{aligned} \quad (7.23)$$

This can be further simplified using Planck's formula for the dependencies of the specific heat of vaporization on temperature and pressure as e.g. provided by [Ziegler \(1997\)](#):

$$d(\Delta h_{VAP}) = (c''_{REFR} - c'_{REFR}) \cdot dT - v'_{REFR} \cdot dp \quad (7.24)$$

For this purpose, the pressure related term  $v'_{REFR} \cdot dp$  shall be neglected as at the relatively low pressure differences in water based chillers it is at least two orders of magnitude smaller than the temperature related term  $(c''_{REFR} - c'_{REFR}) \cdot dT$ . If specific heat capacities are additionally considered independent from temperature and pressure, (7.24) can be simplified to:

$$(\Delta h_{VAP})_{T_0} - (\Delta h_{VAP})_{T_1} = (c'_{REFR} - c''_{REFR}) \cdot (T_1 - T_0) \quad (7.25)$$

Finally, from (7.23) and (7.25) we obtain the endoreversible efficiency of a single-effect chiller being the quotient of the specific heats of the phase change processes at the internal condensation pressure and the corresponding saturation temperatures:

$$COP_{C,ENDOREV} = (\Delta h_{VAP})_{T_1} / (\Delta h_{VAP} + \Delta h_{SOL})_{T_2} \quad (7.26)$$

This equation (7.26) has again the same form as the corresponding equation (7.5) derived for ideal working pairs, however, as for real working pairs the heat of vaporization is dependent on pressures or temperatures these parameters must be specified in addition to the salt concentration. Note that the endoreversible efficiency for cooling is calculated taking the specific heat of vaporization at the same saturation pressure as the regeneration process although the refrigeration is actually produced at a lower saturation pressure in the evaporator.



As all properties of an actual substance have to be thermodynamically consistent among each other, both deductions of the endoreversible efficiency, those based on temperatures and Dühring coefficients, (7.1), (7.4), and the latter, (7.17), (7.26), based on specific heats should produce identical results. Slight deviations are possible, however, as (7.1) strictly follows from the basic laws of thermodynamics while several approximations had to be employed to derive (7.26). For the example of a more or less typical single-effect chiller running at ARI standard conditions presented in Tab. 4 in 2.2, mean internal temperatures  $T_0 = 2.5 \text{ °C}$ ,  $T_1 = 43.9 \text{ °C}$ , and  $T_2 = 92.4 \text{ °C}$  and a corresponding  $COP_{C,ENDOREV} = 0.882$  were derived using (7.4) and computerized property data for the Dühring coefficients. Only a slightly different value of  $COP_{C,ENDOREV} = 0.887$  can be obtained employing the convenient approximation  $B_D = 7.5 \text{ K}$  instead of more sophisticated property data functions. The same value of  $COP_{C,ENDOREV} = 0.887$  resulted also from evaluating (7.26) using computerized property data for all specific heats.

### A.1.4 Efficiency limits for real water/lithium bromide chillers

Efficiency of real absorption chillers is limited by some more constraints: First, of course, there are no ideal internal heat pumps to cool down the condensate and to heat up the solution at gliding temperatures, and secondly, all internal heat exchange processes require a nonzero driving temperature difference. However, for chillers utilizing water as a refrigerant, there is another principle difference to the ideal machine outlined above in A.1.3. Due to the low absolute pressure and the low density of the refrigerant vapor at the internal operating conditions there are no economically promising heat exchanger designs to heat or cool such internal vapor flows without introducing significant pressure drops. As a consequence in a real single-effect chiller based on water/lithium bromide there is only one internal heat exchange process, namely between weak and strong solution flow (no. 3 and no. 4 in the list above in A.1.3).

As there is no heat exchange possible against a corresponding vapor flow and there is no internal heat pump available as assumed for the ideal machine, the entire refrigerant entering the evaporator (flow no. 1) has to be cooled down to the respective saturation temperature consuming refrigeration at temperature  $T_0$ . In actual machines, this is realized by isenthalpic throttling the condensate when entering the evaporator vessel, thus cooling itself by flashing. The specific refrigeration loss due to this throttling  $\Delta q_{THROT}$  consequently is:

$$\Delta q_{THROT} = \Delta \dot{Q}_{THROT} / \dot{M}_{REFR} = c'_{REFR} \cdot (T_1 - T_0) \quad (7.27)$$

Basically, the same argumentation holds true for heating up the weak solution flow (no. 3) to regenerator temperature  $T_2$ . Without a heat exchange incorporating the respective vapor flow (no. 5) and without an internal heat pump the mismatch  $\Delta \dot{Q}_{MISMATCH}$  between heat capacities

of weak and strong solution flows (no. 3 and no. 4) can only be balanced by consuming extra driving heat.

$$\Delta\dot{Q}_{MISMATCH} = (\dot{M}_{WEAK} \cdot c'_{WEAK} - \dot{M}_{STRONG} \cdot c'_{STRONG}) \cdot (T_2 - T_1) \quad (7.28)$$

Using again the approximation (7.7) provided by [Ziegler \(1997\)](#) the specific heat demand  $\Delta q_{MISMATCH}$  to balance this mismatch can be written:

$$\Delta q_{MISMATCH} = \Delta\dot{Q}_{MISMATCH} / \dot{M}_{REFR} = c'_{REFR} \cdot (T_2 - T_1) \quad (7.29)$$

Finally, the solution heat exchanger between weak and strong solution flows (no. 3 and no. 4) requires a certain driving temperature difference in real machines. As the strong solution flow to be cooled down has a lower heat capacity than the weak solution flow to be heated up in this heat exchanger, there is a pinch at the cold end. The heat exchanger loss  $\Delta\dot{Q}_{LOSS,SHX}$ , i.e. the amount of heat that cannot be transferred from the strong to weak solution consequently can be calculated from the terminal temperature difference  $TTD_{SHX}$  or minimum approach temperature at the cold end of the solution heat exchanger and the heat capacity of the strong solution flow:

$$\Delta\dot{Q}_{LOSS,SHX} = \dot{M}_{STRONG} \cdot c'_{STRONG} \cdot TTD_{SHX} \quad (7.30)$$

Utilizing the definition (2.10) of the specific strong solution flow  $f_{STRONG} = \dot{M}_{STRONG} / \dot{M}_{REFR}$  the specific heat exchanger loss  $\Delta q_{LOSS,SHX}$  can be written:

$$\Delta q_{LOSS,SHX} = \Delta\dot{Q}_{LOSS,SHX} / \dot{M}_{REFR} = f_{STRONG} \cdot c'_{STRONG} \cdot TTD_{SHX} \quad (7.31)$$

This loss also has to be balanced by an extra input of driving heat at regenerator temperature  $T_2$ . Although the technical limit for the terminal temperature difference  $TTD_{SHX}$  in the solution heat exchanger is somewhere below *1 Kelvin*, practical designs realize values from at least *3 K* to even *10 K* and more at full load operation. This is mainly due to economical optimization. Besides too effective cooling of the strong solution might induce crystallization in the solution heat exchanger, especially what low specific solution circulations  $f_{STRONG}$  are concerned<sup>81</sup>. Typical specific solution flow rates range from about *7* to *30* for full load operation.

Taking into account all these internal loss mechanisms, the maximum efficiency of a real water/lithium bromide based absorption chiller is:

<sup>81</sup> This is because a small specific solution circulation rate  $f$  corresponds with a big difference in concentration  $\Delta X$  between strong and weak solution. For this case, the temperature of the weak solution entering the solution heat exchanger may already be below the solidification temperature of the strong solution in the counter flow. Therefore, the minimum approach temperature of the heat exchange process must not fall below a certain limit. The minimum design value, however, must not be directly taken from property data on solidification temperatures, as some more effects like sudden temperature fluctuations due to control issues and inhomogeneous temperatures and flows within the heat exchanger also require their safety margins.

$$COP_{C,REAL} = [(\Delta h_{VAP})_{T_0} - \Delta q_{THROT}] / [(\Delta h_{VAP} + \Delta h_{SOL})_{T_2} + \Delta q_{MISMATCH} + \Delta q_{LOSS,SHX}] \quad (7.32)$$

Using the definitions (7.27) and (7.29), this can be written as:

$$COP_{C,REAL} = [(\Delta h_{VAP})_{T_0} - C'_{REFR} \cdot (T_1 - T_0)] / [(\Delta h_{VAP} + \Delta h_{SOL})_{T_2} + C'_{REFR} \cdot (T_2 - T_1) + \Delta q_{LOSS,SHX}] \quad (7.33)$$

Employing the approximation (7.25) we obtain an alternative formulation for the efficiency from (7.33) equivalent to those given by [Ziegler \(1997\)](#) based on the specific heats of vaporization at the same saturation pressure:

$$COP_{C,REAL} = ((\Delta h_{VAP})_{T_1} - C''_{REFR} \cdot (T_1 - T_0)) / ((\Delta h_{VAP} + \Delta h_{SOL})_{T_2} + C'_{REFR} \cdot (T_2 - T_1) + \Delta q_{LOSS,SHX}) \quad (7.34)$$

A comparison of the previously derived efficiency formulations for an endoreversible chiller (7.17) and (7.18) and the corresponding relations for a real chiller (7.32) and (7.33) given above reveals an identical structure. For the real chiller just the formal loss terms  $\Delta q_{0,ER}$  and  $\Delta q_{2,ER}$  are replaced by the actual throttling loss  $\Delta q_{THROT}$  in the numerator and the actual sum of mismatch  $\Delta q_{MISMATCH}$  and solution heat exchanger loss  $\Delta q_{LOSS,SHX}$  in the denominator. A comparison of (7.14) with (7.27) and of (7.16) with (7.29) shows that throttling loss and mismatch are about four times as big as their respective counterparts  $\Delta q_{0,ER}$  and  $\Delta q_{2,ER}$  in the endoreversible case while the solution heat exchanger loss is an additional loss term for the real chiller.

The fundamental difference between the actual loss terms of the real chiller and the formal loss terms  $\Delta q_{0,ER}$  and  $\Delta q_{2,ER}$  in the formulation for the endoreversible chiller is, however, that  $\Delta q_{0,ER}$  and  $\Delta q_{2,ER}$  do not represent any irreversibilities. They are a kind of artifacts due to the temperature dependency of the specific heat of vaporization as it has been demonstrated by the transformation of (7.17) to the alternative formulation (7.26) that does no longer incorporate such loss terms. As a consequence also about one quarter of the heats attributed to both actual loss terms,  $\Delta q_{THROT}$  and  $\Delta q_{MISMATCH}$ , is no real loss from a thermodynamic point of view, as it does not reflect an internal irreversibility. This effect becomes more explicit if demonstrated in actual numbers: For typical operating conditions of a water/lithium bromide single-effect chiller as given in Tab. 4 in 2.2, the throttling loss  $\Delta q_{THROT}$  consumes about 7% of the refrigeration  $(\Delta h_{VAP})_{T_0}$  that would result from evaporating the entire refrigerant at  $T_0$ . Additionally the mismatch  $\Delta q_{MISMATCH}$  increases the driving heat demand by about 7% of the heat  $(\Delta h_{VAP} + \Delta h_{SOL})_{T_2}$  required to boil off the refrigerant at  $T_2$ . If the solution heat exchanger loss  $\Delta q_{LOSS,SHX}$  is assumed to be zero, then from (7.32) results a maximum efficiency  $COP_{C,REAL}$  for the real chiller of 0.79 which is, however, only 10% less than the endoreversible efficiency of an ideal chiller  $COP_{C,ENDOREV} = 0.882$  that was derived in A.1.3 using (7.4).

The solution heat exchanger loss  $\Delta q_{LOSS,SHX}$  is mainly dependent on technical and economical considerations and cannot be directly derived from thermodynamics. However, a comparison of the formulations for the mismatch (7.29) and for the heat exchanger loss (7.31) reveals, that both terms are in the same order of magnitude. A typical value for the specific solution circulation  $f_{STRONG}$  in (7.31) is 15 and for the example design from in Tab. 4 in 2.2 an economical design for the solution heat exchanger might be around  $TTD_{SHX} = 7 \text{ K}$ . The temperature difference  $(T_2 - T_1)$  in the corresponding formulation (7.29) is about 50 K and the specific heat capacity of the refrigerant water  $c'_{REFR}$  is about twice the value obtained for lithium bromide solution  $c'_{STRONG}$ . Multiplying all these numbers finally leads to similar values from both formulas; at least as far as water/lithium bromide as working pair is concerned. An advanced design might further reduce the solution heat exchanger loss to about half value of the mismatch by reducing  $f_{STRONG}$  and  $TTD_{SHX}$ . This optimization is limited yet because a very small  $TTD_{SHX}$  cannot be realized together with a low specific solution flow  $f_{STRONG}$  without the risk of crystallization of the lithium bromide solution. On the other hand, the heat exchanger loss might also be two or three times as big as the mismatch, if higher values for  $f_{STRONG}$  and  $TTD_{SHX}$  are chosen in a chiller design.

Putting all together in (7.32) the efficiency limit for the real chiller  $COP_{C,REAL}$  reduces from 0.79, which was calculated above assuming zero heat exchanger loss, to about 0.74 if the heat exchanger loss has the same value as the mismatch or to about 0.76 for ambitious designs where the heat exchanger loss is only half this value. Actual machines might realize slightly lower efficiencies at the same operating conditions, as the limiting equation (7.32) does not account for e.g. external or internal heat losses due to imperfect thermal insulation of components and several minor internal irreversibilities. Therefore, actual efficiencies in the range of 0.70 to 0.75 at ARI standard conditions can be considered state of the art.

## **A.2 The “square-root criterion” revised**

A major issue at the design of an absorption machine is to determine the optimum size of each heat exchanger in a way that the total manufacturing cost are minimized for a given power rating and given temperature conditions in all external heat carrier loops. If a basic cycle layout defining the number of major components and the piping effort has already been chosen, the required total surface of all heat exchangers is the main optimization parameter. Generally the required size of each heat exchanger can be minimized at a given heat load, if the driving temperature difference at this heat exchanger is increased by a variation of internal saturation pressures and salt concentration. As each two main components in an absorption machine are either linked by a common internal pressure level or a common internal salt concentration, a variation of this common internal variable will at the same time increase the driving temperature difference in one of these components and reduce the driving temperature difference in the other one. The challenge therefore is to find the optimum value of the internal variable in a way that the sum of the sizes of both linked components finds its minimum.

It has already been shown in literature by [Riesch \(1991\)](#), [Ziegler \(1997\)](#), [Schweigler \(1999\)](#), and [Cerkvenik et al. \(2001\)](#) that an analytical expression called “square-root criterion” can be derived for the ratio of the heat exchanger surfaces of all main components as a solution of this optimization problem. Of course, this mathematically derived surface distribution may be constrained in reality by concentration or pressure limits to avoid crystallization or freezing in the machine. As already discussed by [Schweigler \(1999\)](#), the “square-root criterion” typically fails to predict the optimum size of evaporator and absorber in cycles where relatively high driving temperature is available while it is quite useful for design of machines utilizing low-grade driving heat.

It has to be stated however that the formulation of this optimum surface distribution initially derived by [Riesch \(1991\)](#) and consequently adopted by the other authors was based on a simplified linear modeling of absorption machines. Therefore, their correlation that is intentionally not repeated here may lead to significant calculation errors. An alternative derivation of a more generally valid formulation is presented below.

### **A.2.1 Basic assumptions**

Firstly, it is assumed that external heat carrier temperatures at each main component, being an evaporator, absorber, regenerator, or condenser, are already given. Secondly, it is also assumed that given heat duties at each component are independent from small variations by

some Kelvin in internal saturation temperatures<sup>82</sup>. Thirdly, it is assumed that specific solution circulation is invariant and sufficiently high so that Dühring slope parameters for strong and weak solution  $R_D(X_{STRONG}) \approx R_D(X_{WEAK})$  do not differ too much from each other and that the slope  $R_D$  does not vary significantly at small variations in salt concentration. Fourthly, it is assumed that in each component major part of the heat is transferred by phase change at respective saturation temperatures and that either ideal counterflow of external and internal fluid or perfect mixing of the internal fluid are found. Finally, it has to be assumed that the overall heat transfer coefficient in each component is constant and independent on heat flux density.

The same assumptions – amongst others – were also required by *Riesch (1991)*. Only the first one can always be made true; second to fourth ones are reasonable approximations under typical conditions. The final assumption is to some extent valid for falling film heat exchangers, it does not hold true for pool-boiler type regenerators operated in nucleate-boiling mode, however.

With the assumptions above, for each component  $I$  the general heat transfer equation correlating the initially given heat duty  $\dot{Q}_I$  and the initially given heat transfer coefficient  $U_I$  with the surface  $A_I$  and driving temperature difference  $LMTD_I$  to be optimized reads:

$$\dot{Q}_I = U_I \cdot A_I \cdot LMTD_I \quad (7.35)$$

For ideal counterflow, ideal co-flow, or ideal mixing of either of the fluids, the logarithmic mean temperature difference  $LMTD_I$  yields from the terminal temperature differences at the hot end  $TTD_{H,I}$  and at the cold end  $TTD_{C,I}$  of each heat exchanger:

$$LMTD_I = \frac{TTD_{H,I} - TTD_{C,I}}{\ln\left(\frac{TTD_{H,I}}{TTD_{C,I}}\right)} \quad (7.36)$$

The terminal temperature differences  $TTD_{H,I}$  and  $TTD_{C,I}$  result accordingly from the entering or leaving temperatures of the external heat carriers at the hot  $t_{EXT,H,I}$  and cold end  $t_{EXT,C,I}$  and the respective internal saturation temperatures at hot  $T_{SAT,H,I}$  and cold end  $T_{SAT,C,I}$ :

$$TTD_{H,I} = |t_{EXT,H,I} - T_{SAT,H,I}| \quad (7.37)$$

$$TTD_{C,I} = |t_{EXT,C,I} - T_{SAT,C,I}| \quad (7.38)$$

For components like condensers and evaporators internal saturation temperature at hot and cold end are identical  $T_{SAT,H,I} = T_{SAT,C,I}$ , of course. This can also be assumed as an approxi-

<sup>82</sup> Note that strictly speaking, heat loads at individual components are not independent from temperature variations as specific heats of evaporation and loss terms like throttling loss and mismatch are sensitive to variations in the saturation temperatures in the cycle. However, these are small effects.

mation for devices with ideal mixing of the internal fluid. Absolute values have been chosen in the formulations (7.37) and (7.38) to yield positive numbers for all heat duties and temperature differences.

Below the definition of the slope parameter  $R_D(X_{SOL}) = 1/A_D(X_{SOL}) = \Delta T_{SAT,REFR}/\Delta T_{SAT,SOL}$  as the inverse Dühring gradient being  $R_D = 1$  for pure refrigerant and  $R_D < 1$  for lithium bromide solution is employed. Each main component  $I$  is attributed a mean slope parameter  $R_{D,I}$  that is unity for evaporators and condensers and that is the respective value in dependence on the mean salt concentration in absorbers and regenerators. Now it is assumed that in two main components  $I, J$  at the same vapor pressure like e.g. evaporator and absorber the saturation temperature in the refrigerant is varied by  $dT_{SAT}$  and that e.g. component  $I$  is the evaporator and component  $J$  is the absorber. Then the saturation temperature  $T_{SAT,H,I} = T_{SAT,C,I}$  in evaporator  $I$  will change by  $dT_{SAT,H,I} = dT_{SAT,C,I} = dT_{SAT}$  and saturation temperatures in the solution in the linked absorber  $J$  will change by  $dT_{SAT,H,J} = dT_{SAT,C,J} = dT_{SAT}/R_{D,J}$ .

Using the definitions and assumptions above, this can be written in a general form valid for any pair of components linked by a joint saturation pressure:

$$dT_{SAT,H,I} \cdot R_{D,I} = dT_{SAT,C,I} \cdot R_{D,I} = dT_{SAT,H,J} \cdot R_{D,J} = dT_{SAT,C,J} \cdot R_{D,J} = dT_{SAT} \quad (7.39)$$

As an approximation, this equation also holds true for two components operating at linked salt concentrations like absorber and regenerator for joint variation of the salt concentration with the assumption  $R_{D,I} = R_{D,J} = const.$  Some error is introduced here, however, as  $R_D$  is actually not completely invariant to variations of the salt concentration.

## A.2.2 Optimization approach

In the following, a pair of main heat exchangers sharing either the same saturation pressure or the same salt concentration will be considered. If the linked saturation temperatures are varied according to (7.39), the driving temperature differences  $LMTD_I, LMTD_J$  will be functions of this variation and so will be the required surface areas  $A_I = \dot{Q}_I/(U_I \cdot LMTD_I), A_J = \dot{Q}_J/(U_J \cdot LMTD_J)$ . At the optimum configuration, the sum of both areas  $A_I + A_J$  will find a minimum and thus:

$$\frac{d}{dT_{SAT}}(A_I + A_J) = 0 \quad (7.40)$$

This approach can even be made a little more general if different specific prices  $p_I = P_I/A_I, p_J = P_J/A_J$  are attributed to the heat exchanger surfaces of the components and the minimum price for the pair is looked for:

$$\frac{d}{dT_{SAT}}(P_I + P_J) = \frac{d}{dT_{SAT}}(p_I \cdot A_I + p_J \cdot A_J) = 0 \quad (7.41)$$

As  $p_i, p_j, U_i, U_j, \dot{Q}_i, \dot{Q}_j$  are considered invariant, the criterion finally reads:

$$\frac{p_i \cdot \dot{Q}_i}{U_i} \cdot \frac{d}{dT_{SAT}} \left( \frac{1}{LMTD_i} \right) = \frac{-p_j \cdot \dot{Q}_j}{U_j} \cdot \frac{d}{dT_{SAT}} \left( \frac{1}{LMTD_j} \right) \quad (7.42)$$

The derivatives  $\frac{d}{dT_{SAT}} \left( \frac{1}{LMTD_i} \right)$  and  $\frac{d}{dT_{SAT}} \left( \frac{1}{LMTD_j} \right)$  formally are

$$\frac{d}{dT_{SAT}} \left( \frac{1}{LMTD_i} \right) = \frac{\partial}{\partial TTD_{H,i}} \left( \frac{1}{LMTD_i} \right) \cdot \frac{\partial}{\partial T_{SAT}} TTD_{H,i} + \frac{\partial}{\partial TTD_{C,i}} \left( \frac{1}{LMTD_i} \right) \cdot \frac{\partial}{\partial T_{SAT}} TTD_{C,i} \quad (7.43)$$

and a respective formulation for component  $J$ . Assuming that component  $I$  is absorbing heat from the external carrier like e.g. an evaporator and component  $J$  is releasing heat to the external carrier like e.g. an absorber, the partial derivatives with respect to  $\partial T_{SAT}$  are according (7.37) to (7.39) yield:

$$\frac{\partial}{\partial T_{SAT}} TTD_{H,i} = \frac{\partial}{\partial T_{SAT}} TTD_{C,i} = -\frac{1}{R_{D,i}} \quad (7.44)$$

$$\frac{\partial}{\partial T_{SAT}} TTD_{H,j} = \frac{\partial}{\partial T_{SAT}} TTD_{C,j} = -\frac{1}{R_{D,j}} \quad (7.45)$$

Thus, (7.43) can be simplified:

$$\frac{d}{dT_{SAT}} \left( \frac{1}{LMTD_i} \right) = -\frac{1}{R_{D,i}} \cdot \left[ \frac{\partial}{\partial TTD_{H,i}} \left( \frac{1}{LMTD_i} \right) + \frac{\partial}{\partial TTD_{C,i}} \left( \frac{1}{LMTD_i} \right) \right] \quad (7.46)$$

$$\frac{d}{dT_{SAT}} \left( \frac{1}{LMTD_j} \right) = \frac{1}{R_{D,j}} \cdot \left[ \frac{\partial}{\partial TTD_{H,j}} \left( \frac{1}{LMTD_j} \right) + \frac{\partial}{\partial TTD_{C,j}} \left( \frac{1}{LMTD_j} \right) \right] \quad (7.47)$$

The sums of the remaining partial derivatives yield simple expressions

$$\frac{\partial}{\partial TTD_{H,i}} \left( \frac{1}{LMTD_i} \right) + \frac{\partial}{\partial TTD_{C,i}} \left( \frac{1}{LMTD_i} \right) = \frac{-1}{TTD_{H,i} \cdot TTD_{C,i}} \quad (7.48)$$

and a respective formulation for component  $J$ . The derivatives with respect to  $dT_{SAT}$  finally are:

$$\frac{d}{dT_{SAT}} \left( \frac{1}{LMTD_i} \right) = \frac{1}{R_{D,i} \cdot TTD_{H,i} \cdot TTD_{C,i}} \quad (7.49)$$

$$\frac{d}{dT_{SAT}} \left( \frac{1}{LMTD_j} \right) = \frac{-1}{R_{D,j} \cdot TTD_{H,j} \cdot TTD_{C,j}} \quad (7.50)$$

The optimization criterion (7.42) now can be evaluated:

$$\frac{p_i \cdot \dot{Q}_i}{U_i \cdot R_{D,i} \cdot TTD_{H,i} \cdot TTD_{C,i}} = \frac{p_j \cdot \dot{Q}_j}{U_j \cdot R_{D,j} \cdot TTD_{H,j} \cdot TTD_{C,j}} \quad (7.51)$$

To eliminate the products of terminal temperature differences, geometric mean temperatures differences  $GMTD$  and counterflow-ideality factors  $z$  are defined:

$$GMTD_i = (TTD_{H,i} \cdot TTD_{C,i})^{1/2} \quad \text{and respectively for component } J \quad (7.52)$$



$$z_I = LMTD_I / GMTD_I \quad \text{and respectively for component } J \quad (7.53)$$

A counterflow-ideality factor  $z_I$  will become unity if all temperature differences at a heat exchanger are identical  $TTD_{H,I} = TTD_{C,I} = LMTD_I = GMTD_I$ .

Thus, the optimization criterion (7.51) can be rewritten:

$$\frac{p_I \cdot \dot{Q}_I \cdot z_I^2}{U_I \cdot R_{D,I} \cdot LMTD_I^2} = \frac{p_J \cdot \dot{Q}_J \cdot z_J^2}{U_J \cdot R_{D,J} \cdot LMTD_J^2} \quad (7.54)$$

To obtain a criterion for the ratio of heat transfer surfaces rather than the ratio of driving temperature differences,  $LMTD_I$  and  $LMTD_J$  can be substituted according to (7.35):

$$\frac{p_I \cdot A_I^2 \cdot U_I \cdot z_I^2}{\dot{Q}_I \cdot R_{D,I}} = \frac{p_J \cdot A_J^2 \cdot U_J \cdot z_J^2}{\dot{Q}_J \cdot R_{D,J}} \quad (7.55)$$

The optimum ratio of heat transfer surfaces of a pair of main heat exchangers  $I, J$  sharing either the same saturation pressure or the same salt concentration finally is:

$$\frac{A_I}{A_J} = \frac{1/z_I \cdot (\dot{Q}_I / p_I \cdot U_I \cdot R_{D,I})^{1/2}}{1/z_J \cdot (\dot{Q}_J / p_J \cdot U_J \cdot R_{D,J})^{1/2}} \quad (7.56)$$

If simply the minimum total surface is looked for both price factors  $p_I, p_J$  can be set unity and the respective ratio can be omitted.

### A.2.3 Discussion

An equation very similar to (7.56) was called “square-root criterion” by [Riesch \(1991\)](#), [Ziegler \(1997\)](#), [Schweigler \(1999\)](#), and [Cerkvenik et al. \(2001\)](#). [Riesch \(1991\)](#) introduced an alternative definition of the counterflow-ideality factors  $z$ , which was consecutively assumed by [Schweigler \(1999\)](#) and [Cerkvenik et al. \(2001\)](#), although [Schweigler \(1999\)](#) already pointed out that their definition could lead to problems. [Ziegler \(1997\)](#) focused on the discussion of systems with ideal counterflow  $TTD_{H,I} \approx TTD_{C,I} \approx LMTD_I$  and thus avoided the introduction of counterflow-ideality factors.

Formulation (7.56) being derived above employing the definitions (7.52) and (7.53) is the most accurate formulation of the “square-root criterion” so far. In contrast to the earlier derivation by [Riesch \(1991\)](#), no additional hidden assumptions or approximations have been used. Results obtained from (7.56) are mostly consistent with findings from numerical optimizations of absorption chillers.

Relation (7.56) has been derived so far only for two components  $I, J$  sharing either the same saturation pressure or the same salt concentration. As in a simple single-effect cycle it could

be applied consecutively to the respective pairs evaporator-absorber, absorber-regenerator, and regenerator-condenser, it can be concluded that (7.56) is generally valid for any ratio of heat transfer surfaces in a single-effect machine, even for non-neighboring components like evaporator and regenerator.

### A.3 Raw data from stationary operational states

During operation of the test rig, all measurement data from permanently installed sensors listed in Tab. 20 - Tab. 22 have been recorded by means of several Keithley 7001 scanners, Keithley 2001 multimeters, and a multipurpose DAQ card attached to a PC computer. By means of a data acquisition and visualization program written in National Instruments Labview every 15 to 30 seconds a complete data set was stored.

From all data recorded during a day of lab operation, stationary operational states were extracted afterwards for further evaluation. By means of a Visual Basic macro in Excel, periods of at least 10 minutes duration with a minimum variation in all process variables were identified and the mean value of each variable within this time slot was computed. The mean values obtained this way for 20 stationary operational states are listed in chronological order in Tab. 23 and Tab. 24 below.

With the exception of the six variables  $F81^*$ ,  $F82^*$ ,  $\dot{Q}_E$ ,  $\dot{Q}_A$ ,  $C01$ ,  $\Delta C01$ , all data provided in Tab. 23 and Tab. 24 correspond directly with the respective sensors listed in Tab. 20 - Tab. 22. For the both flows  $F81$  and  $F82$ , the measured volumetric flow rates have already been converted to gravimetric flow rates  $F81^*$  and  $F82^*$  by the data acquisition program prior to calculation of the mean values of the variables at the operational states:

$$F81^* = F81 \cdot \rho'_{H2O}(T21) \quad (7.57)$$

$$F82^* = F81 \cdot \rho'_{H2O}(T21) \quad (7.58)$$

Similarly, equations (6.4) and (6.5) for the determination of evaporator and absorber heat loads  $\dot{Q}_E$  and  $\dot{Q}_A$  from  $T231$ ,  $T243$ ,  $T244$ ,  $T256$ ,  $F315$ ,  $F316$  have already been evaluated by the data acquisition program prior to calculation of the mean values. Therefore, only the mean values for the resulting variables  $\dot{Q}_E$  and  $\dot{Q}_A$  are given in Tab. 23 and Tab. 24.

During the series of experiments, the settings of the gas burner have been adjusted several times. Afterwards, the excess combustion air was determined at different burner duties by means of a flue gas analyzer that automatically calculated this value from the measured  $CO_2$  concentration in the flue gas. As the flue gas analyzer was not suited for continuous online monitoring of the combustion process, the characteristic function of the excess air resulting from the chosen burner settings was fitted in dependency on the burner duty. The variable  $C01$  in Tab. 23 and Tab. 24 shows the excess combustion air values obtained this way from the applicable correlations at the individual states. The estimated uncertainties attributed to these values are given in the corresponding values of  $\Delta C01$  in Tab. 23 and Tab. 24 below.

| State No.      |        | 1      | 2      | 3      | 4      | 5      | 6      | 7      | 8      | 9      | 10     |
|----------------|--------|--------|--------|--------|--------|--------|--------|--------|--------|--------|--------|
| T01            | [°C]   | 135.1  | 134.4  | 130.7  | 123.3  | 116.2  | 123.4  | 132.8  | 122.3  | 125.1  | 102.3  |
| T02            | [°C]   | 155.3  | 159.3  | 158.5  | 156.6  | 152.3  | 146.3  | 154.6  | 151.0  | 144.7  | 139.9  |
| T03            | [°C]   | 155.7  | 160.7  | 161.2  | 159.4  | 155.0  | 147.8  | 155.6  | 156.9  | 147.9  | 140.1  |
| T04            | [°C]   | 154.9  | 159.5  | 160.1  | 158.2  | 153.9  | 146.9  | 154.6  | 155.9  | 147.3  | 139.2  |
| T05            | [°C]   | 134.0  | 136.3  | 130.6  | 126.8  | 125.0  | 129.0  | 135.8  | 131.1  | 129.2  | 117.1  |
| T06            | [°C]   | 135.2  | 134.4  | 130.6  | 123.2  | 116.0  | 123.4  | 132.8  | 125.2  | 132.4  | 102.8  |
| T07            | [°C]   | 57.1   | 71.4   | 50.0   | 81.9   | 76.3   | 59.8   | 79.5   | 87.9   | 53.6   | 65.1   |
| T08            | [°C]   | 125.2  | 113.1  | 120.4  | 101.9  | 87.4   | 97.7   | 109.2  | 104.6  | 126.1  | 71.2   |
| T09            | [°C]   | 153.7  | 158.1  | 158.8  | 156.5  | 152.4  | 145.8  | 153.5  | 153.9  | 145.5  | 134.6  |
| T10            | [°C]   | 70.0   | 32.6   | 30.3   | 28.1   | 26.5   | 27.6   | 21.6   | 20.5   | 22.9   | 21.3   |
| T21            | [°C]   | 28.0   | 27.2   | 28.6   | 26.0   | 26.3   | 20.3   | 20.6   | 20.3   | 20.2   | 20.2   |
| T22            | [°C]   | 48.0   | 52.4   | 37.8   | 38.7   | 44.7   | 41.2   | 39.3   | 46.2   | 26.7   | 36.8   |
| T23            | [°C]   | 110.1  | 116.0  | 94.4   | 83.5   | 83.3   | 101.2  | 100.2  | 89.1   | 56.3   | 60.1   |
| T24            | [°C]   | 28.1   | 27.3   | 28.7   | 26.1   | 26.3   | 20.4   | 20.7   | 20.3   | 20.2   | 20.1   |
| T25            | [°C]   | 97.4   | 90.8   | 86.0   | 83.1   | 45.4   | 89.1   | 78.0   | 52.6   | 83.4   | 87.9   |
| T26            | [°C]   | 22.9   | 21.5   | 22.5   | 21.1   | 21.0   | 17.4   | 17.9   | 15.6   | 17.6   | 18.1   |
| T27            | [°C]   | 27.5   | 25.5   | 27.5   | 25.4   | 24.9   | 19.9   | 21.2   | 22.4   | 24.0   | 21.8   |
| T28            | [°C]   | 1051.6 | 1053.1 | 1051.2 | 1086.5 | 1080.5 | 1119.5 | 1041.5 | 1060.4 | 1037.8 | 923.8  |
| T29            | [°C]   | 27.8   | 26.0   | 27.1   | 21.2   | 21.6   | 15.0   | 87.1   | 89.9   | 78.0   | 64.6   |
| T30            | [°C]   | 159.5  | 165.0  | 165.3  | 165.0  | 156.6  | 157.4  | 160.7  | 188.8  | 169.6  | 143.6  |
| T31            | [°C]   | 71.7   | 74.4   | 66.7   | 80.1   | 72.7   | 59.8   | 78.9   | 86.3   | 69.3   | 61.0   |
| T41            | [°C]   | 179.4  | 183.8  | 184.3  | 186.9  | 178.5  | 177.1  | 175.8  | 180.8  | 169.7  | 157.0  |
| T43            | [°C]   | 173.2  | 177.9  | 178.7  | 178.8  | 172.6  | 168.4  | 173.2  | 175.4  | 164.7  | 152.0  |
| T44            | [°C]   | 172.8  | 176.2  | 176.2  | 176.1  | 171.0  | 167.6  | 174.1  | 174.4  | 166.5  | 150.9  |
| T45            | [°C]   | 170.9  | 174.5  | 175.1  | 176.0  | 170.5  | 164.9  | 169.9  | 170.8  | 161.5  | 151.8  |
| T46            | [°C]   | 168.4  | 172.0  | 173.0  | 169.8  | 166.1  | 160.2  | 166.4  | 169.0  | 159.4  | 149.2  |
| T47            | [°C]   | 172.8  | 176.6  | 177.3  | 178.0  | 172.0  | 167.5  | 172.7  | 173.4  | 163.5  | 149.1  |
| T48            | [°C]   | 171.2  | 175.6  | 176.2  | 176.5  | 170.7  | 166.3  | 171.3  | 171.6  | 162.5  | 148.7  |
| T49            | [°C]   | 170.8  | 174.8  | 175.8  | 174.8  | 168.4  | 164.8  | 171.0  | 170.8  | 161.3  | 147.4  |
| T50            | [°C]   | 168.7  | 172.5  | 173.5  | 172.5  | 166.9  | 162.3  | 168.7  | 167.8  | 159.6  | 146.4  |
| T51            | [°C]   | 169.5  | 173.5  | 174.6  | 173.8  | 168.2  | 164.0  | 170.2  | 172.1  | 161.7  | 148.1  |
| T128           | [°C]   | n/a    | n/a    | n/a    | n/a    | n/a    | n/a    | n/a    | 484.4  | 480.4  | 312.0  |
| P61            | [mbar] | 991.3  | 898.0  | 896.0  | 854.7  | 783.4  | 962.7  | 742.3  | 799.4  | 931.5  | 779.9  |
| P66            | [mbar] | 966.5  | 969.3  | 961.3  | 959.7  | 959.3  | 968.4  | 975.5  | 968.5  | 972.5  | 962.1  |
| F73            | [m/s]  | 0.2389 | 0.1055 | 0.1647 | 0.1138 | 0.1419 | n/a    | 0.0901 | n/a    | 0.1427 | 0.1132 |
| F81*           | [kg/s] | 0.0784 | 0.0932 | 0.2005 | 0.2562 | 0.2595 | 0.1506 | 0.1213 | 0.2005 | 0.2869 | 0.2650 |
| F82*           | [kg/s] | 0.3343 | 0.3936 | 0.4141 | 0.4483 | 1.0132 | 0.4776 | 0.4688 | 1.2253 | 0.5251 | 0.1114 |
| F83            | [l/s]  | 5.2955 | 5.4113 | 5.5020 | 6.0917 | 4.9930 | 6.7966 | 5.3593 | 7.7092 | 6.2722 | 2.6383 |
| C01            | [-]    | 1.30   | 1.29   | 1.29   | 1.28   | 1.30   | 1.27   | 1.29   | 1.25   | 1.27   | 1.41   |
| ΔC01           | [%]    | 15%    | 15%    | 15%    | 15%    | 15%    | 15%    | 10%    | 10%    | 5%     | 5%     |
| Q <sub>E</sub> | [kW]   | n/a    | n/a    | n/a    | n/a    | n/a    | n/a    | n/a    | n/a    | n/a    | n/a    |
| Q <sub>A</sub> | [kW]   | n/a    | n/a    | n/a    | n/a    | n/a    | n/a    | n/a    | n/a    | n/a    | n/a    |

Tab. 23: Raw data from stationary operational states no. 1-10 (mean values of measured variables).

| State No.      |        | 11     | 12     | 13     | 14     | 15     | 16     | 17     | 18     | 19     | 20     |
|----------------|--------|--------|--------|--------|--------|--------|--------|--------|--------|--------|--------|
| T01            | [°C]   | 113.2  | 128.0  | 137.3  | 127.4  | 94.5   | 126.7  | 117.6  | 112.9  | 113.7  | 119.0  |
| T02            | [°C]   | 140.1  | 154.4  | 154.0  | 145.2  | 133.5  | 151.9  | 153.6  | 153.3  | 154.6  | 161.7  |
| T03            | [°C]   | 140.9  | 156.9  | 156.7  | 146.4  | 143.4  | 152.8  | 156.3  | 155.3  | 156.7  | 164.0  |
| T04            | [°C]   | 140.3  | 155.9  | 155.7  | 145.6  | 142.8  | 151.8  | 155.0  | 154.0  | 155.5  | 162.8  |
| T05            | [°C]   | 123.4  | 138.7  | 140.7  | 132.0  | 110.9  | 132.0  | 141.1  | 139.4  | 141.7  | 150.2  |
| T06            | [°C]   | 114.2  | 128.0  | 137.3  | 127.4  | 94.1   | 126.8  | 140.4  | 139.0  | 140.7  | 148.9  |
| T07            | [°C]   | 79.2   | 95.2   | 79.6   | 69.5   | 58.6   | 68.0   | 59.6   | 60.1   | 61.7   | 62.4   |
| T08            | [°C]   | 86.5   | 105.3  | 131.6  | 118.5  | 63.6   | 125.9  | 131.1  | 111.4  | 125.2  | 125.0  |
| T09            | [°C]   | 138.8  | 154.2  | 154.5  | 144.2  | 101.9  | 150.1  | 154.0  | 152.3  | 153.6  | 160.9  |
| T10            | [°C]   | 30.4   | 38.5   | 19.5   | 23.3   | 56.3   | 23.2   | 36.0   | 28.8   | 31.3   | 27.2   |
| T21            | [°C]   | 20.1   | 21.3   | 19.2   | 21.7   | 20.2   | 22.8   | 22.1   | 22.1   | 23.0   | 22.6   |
| T22            | [°C]   | 30.9   | 53.1   | 32.4   | 30.3   | 24.6   | 40.4   | 41.9   | 40.0   | 42.1   | 40.9   |
| T23            | [°C]   | 47.1   | 96.3   | 65.7   | 60.6   | 33.2   | 98.3   | 70.0   | 62.0   | 84.1   | 79.1   |
| T24            | [°C]   | 20.1   | 21.3   | 19.2   | 21.8   | 20.3   | 22.9   | 22.0   | 22.1   | 23.0   | 22.7   |
| T25            | [°C]   | 90.2   | 93.5   | 44.0   | 82.9   | 58.6   | 52.0   | 62.2   | 44.7   | 60.4   | 55.0   |
| T26            | [°C]   | 15.3   | 16.4   | 17.8   | 16.0   | 19.6   | 20.6   | 20.4   | 21.4   | 20.2   | 18.8   |
| T27            | [°C]   | 20.3   | 21.2   | 22.8   | 21.4   | 23.2   | 24.0   | 22.6   | 26.3   | 24.3   | 21.7   |
| T28            | [°C]   | 998.2  | 1026.7 | 1037.6 | 1001.4 | 919.3  | 1003.6 | 915.1  | 1021.6 | 1027.9 | 1034.9 |
| T29            | [°C]   | 79.1   | 93.4   | 89.9   | 77.3   | 57.6   | 78.8   | 79.6   | 69.7   | 75.9   | 75.0   |
| T30            | [°C]   | 153.7  | 169.1  | 172.7  | 155.5  | 144.7  | 160.9  | 176.1  | 168.1  | 172.0  | 177.3  |
| T31            | [°C]   | 73.4   | 95.0   | 89.3   | 78.3   | 56.7   | 78.9   | 78.5   | 69.4   | 75.4   | 74.5   |
| T41            | [°C]   | 159.9  | 177.4  | 179.3  | 163.5  | 161.2  | 171.0  | 180.5  | 181.2  | 181.5  | 186.4  |
| T43            | [°C]   | 159.1  | 173.5  | 173.8  | 162.4  | 157.0  | 169.8  | 175.7  | 173.7  | 173.7  | 182.0  |
| T44            | [°C]   | 156.7  | 171.4  | 174.2  | 161.8  | 149.9  | 167.6  | 176.7  | 174.1  | 173.2  | 182.2  |
| T45            | [°C]   | 154.9  | 167.7  | 168.7  | 157.3  | 153.9  | 164.1  | 172.9  | 169.7  | 168.6  | 177.9  |
| T46            | [°C]   | 152.3  | 167.7  | 167.5  | 154.9  | 152.8  | 163.4  | 169.6  | 167.8  | 167.8  | 177.1  |
| T47            | [°C]   | 154.2  | 170.8  | 170.4  | 157.2  | 150.7  | 165.9  | 174.7  | 172.4  | 171.9  | 180.4  |
| T48            | [°C]   | 154.0  | 169.8  | 169.8  | 158.0  | 151.1  | 165.1  | 172.3  | 170.7  | 171.1  | 178.9  |
| T49            | [°C]   | 152.6  | 168.8  | 168.5  | 157.0  | 151.4  | 163.9  | 170.6  | 169.2  | 169.3  | 176.8  |
| T50            | [°C]   | 150.9  | 167.1  | 166.9  | 155.6  | 150.5  | 162.5  | 168.9  | 166.8  | 167.3  | 174.6  |
| T51            | [°C]   | 153.6  | 168.7  | 169.4  | 156.9  | 151.7  | 163.6  | 171.9  | 169.0  | 170.1  | 177.0  |
| T128           | [°C]   | 409.6  | 444.4  | 483.1  | 464.6  | 361.5  | 472.2  | 531.4  | 527.9  | 432.5  | 435.3  |
| P61            | [mbar] | 779.9  | 1008.5 | 908.2  | 1005.9 | 1077.3 | 891.1  | 798.7  | 701.8  | 820.3  | 878.3  |
| P66            | [mbar] | 952.4  | 969.8  | 972.9  | 978.7  | 974.9  | 960.3  | 963.2  | 963.9  | 956.9  | 952.2  |
| F73            | [m/s]  | 0.1705 | 0.0815 | 0.0926 | 0.0984 | 0.1149 | 0.0396 | 0.1869 | 0.0798 | 0.0541 | 0.0391 |
| F81*           | [kg/s] | 0.4818 | 0.1553 | 0.1452 | 0.1666 | 1.3676 | 0.0834 | 0.0905 | 0.1211 | 0.0865 | 0.1064 |
| F82*           | [kg/s] | 0.2642 | 0.3722 | 1.4474 | 0.4111 | 0.0004 | 0.9244 | 0.8084 | 1.5175 | 0.9397 | 1.0700 |
| F83            | [l/s]  | 4.6477 | 5.7283 | 6.2713 | 4.6228 | 2.5450 | 4.9541 | 6.2583 | 6.4176 | 6.7033 | 6.6607 |
| C01            | [-]    | 1.31   | 1.28   | 1.27   | 1.30   | 1.41   | 1.30   | 1.71   | 1.71   | 1.65   | 1.65   |
| ΔC01           | [%]    | 5%     | 5%     | 5%     | 5%     | 5%     | 5%     | 10%    | 10%    | 10%    | 10%    |
| Q <sub>E</sub> | [kW]   | n/a    | n/a    | n/a    | n/a    | n/a    | n/a    | -118.9 | -135.7 | -130.8 | -124.5 |
| Q <sub>A</sub> | [kW]   | n/a    | n/a    | n/a    | n/a    | n/a    | n/a    | 145.3  | 162.4  | 153.8  | 146.2  |

Tab. 24: Raw data from stationary operational states no. 11-21 (mean values of measured variables).

## **A.4 Raw data from pressure drop measurements and employed interpolations for data evaluation**

At nine operational states of constant burner duty, measurements of the overpressure in furnace chamber ( $P1$ ) and at the flue gas exit of the regenerator ( $P3$ ) are available; from these data a pressure drop  $\Delta p = P1 - P3$  across the total heat exchanger was calculated. At five states, additionally the overpressure in the tube bundle between plain and finned tubes ( $P2$ ) was measured; respective pressure drops  $\Delta p = P1 - P2$  across the plain tubes and  $\Delta p = P2 - P3$  across the finned tubes were obtained. These experimentally determined pressure drops are shown in Fig. 77 below as empty symbols over the respective gas burner duties  $\dot{Q}_{GAS}$ .

Relevant influencing variables obtained at nine stationary operational states with identical burner settings (cf. no. 8...16 in Tab. 23 and Tab. 24 in appendix A.3) have been fitted in dependence on the gas burner duty  $\dot{Q}_{GAS}$ . This is shown in Fig. 77 for the flue gas mass flow  $\dot{M}_{FG}$  and the mean densities and viscosities of the flue gas in both sections  $\rho_{MN,PL}$ ,  $\rho_{MN,FI}$ ,  $\mu_{MN,PL}$ ,  $\mu_{MN,FI}$ , filled **black** circles denoting the data values at the nine stationary states and colored lines showing the fitted curves. Similar fits have been performed for the entering and leaving flue gas densities required for the determination of the acceleration pressure drop  $\Delta p_{ACC}$ . These interpolations have been employed for the evaluation of the experimental data points shown in Fig. 64 and Fig. 65 in 6.4.2.

Additionally, in Fig. 64 and Fig. 65 in 6.4.2 experimentally determined flue gas side pressure drops at individual operational states are compared to theoretical curves over flue gas mass flux (Fig. 64) and flue gas Reynolds number (Fig. 65). Actually, different values for flue gas temperatures and excess air ratios and consequently for the relevant flue gas properties like specific density and dynamic viscosity are found at the individual states where experimental pressure drop measurements are available. Therefore, the frictional pressure drops are not simply functions of the flue gas mass flux but incorporate additional dependencies on variations of the flue gas properties.

To obtain smooth curves for the theoretical flue gas pressure drop in the diagrams in Fig. 64 and Fig. 65 in 6.4.2, all relevant influencing variables have additionally been fitted in dependence of the flue gas mass flow. The thus obtained interpolations were actually employed for the calculation of the "theoretical curves" shown in the diagrams.

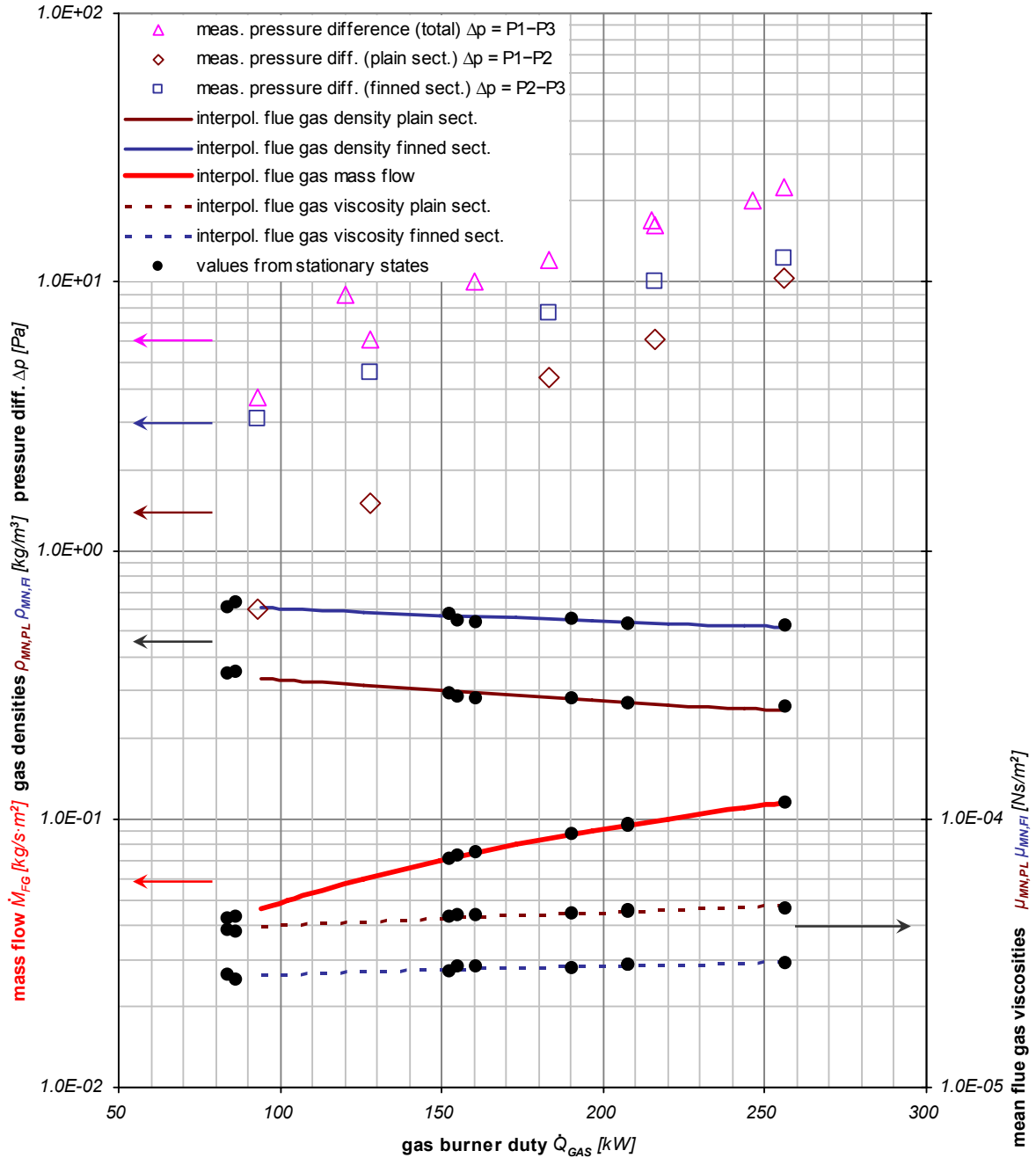
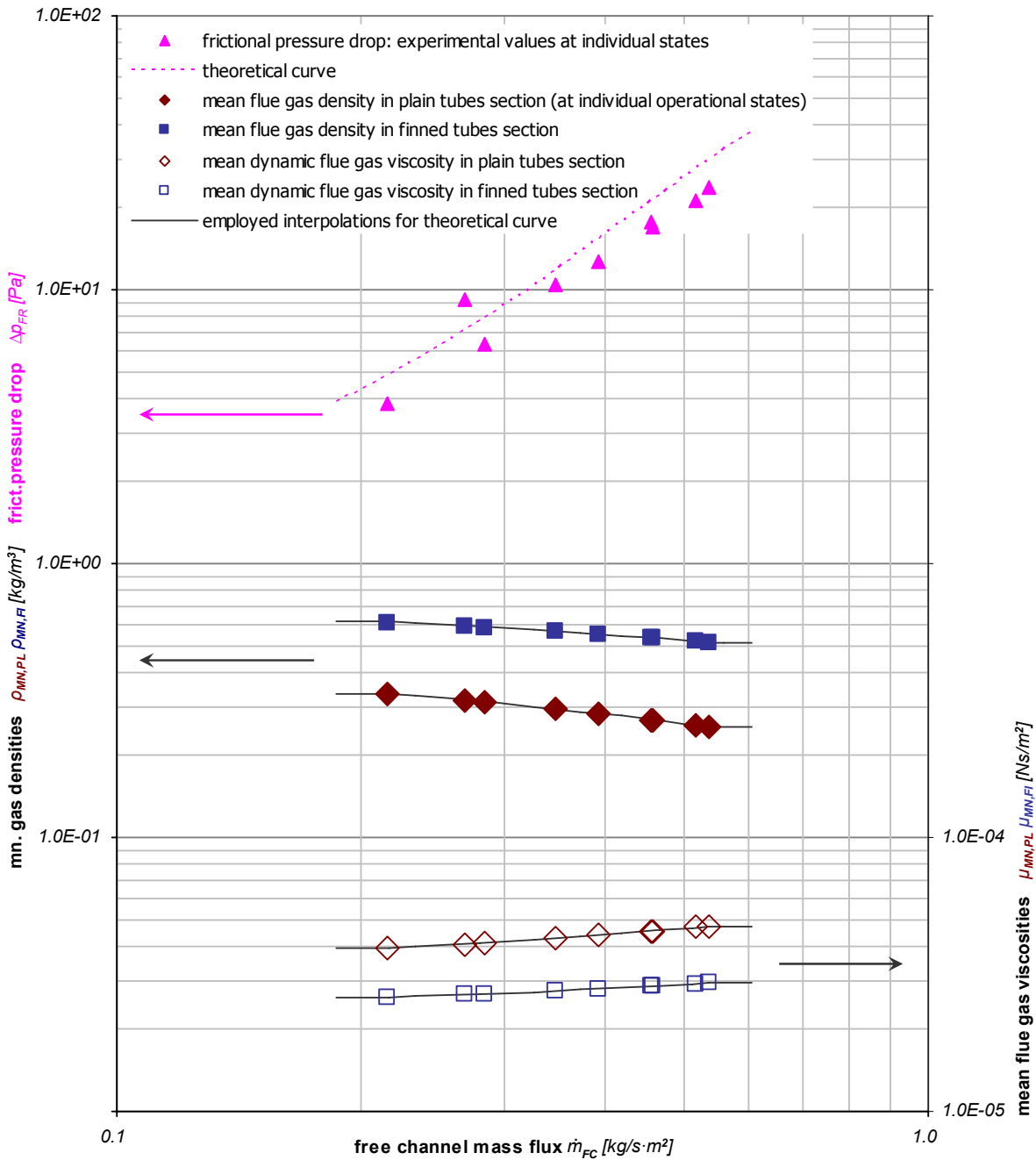


Fig. 77: Raw data from pressure drop measurements (empty symbols) and interpolations (colored lines) of data points from stationary operational states (filled black circles) that have been employed for evaluation.

This is demonstrated in Fig. 78 below for the calculation of the frictional flue gas pressure drop of the total heat exchanger  $\Delta p_{FR}$  (dotted magenta line) in dependence of the mass flux  $\dot{m}_{FC}$  (cf. corresponding diagram in Fig. 64 in 6.4.2). Additional influencing variables for this calculation are the mean flue gas densities in the sections of plain tubes  $\rho_{MN,PL}$  (filled brown diamonds) and finned tubes  $\rho_{MN,FI}$  (filled blue squares), and the respective mean dynamic viscosities in both sections,  $\mu_{MN,PL}$  (empty brown diamonds) and  $\mu_{MN,FI}$  (empty blue squares). Fig. 78 shows that these four properties exhibit only small variations over the full range of

experimental data. The employed interpolations (solid **black** lines) satisfactorily reproduce the property values determined at the individual operational states.



**Fig. 78:** Interpolation of flue gas properties between individual operational states for calculation of theoretical pressure drop curves.

The same interpolations of the flue gas properties have also been employed for calculation of the theoretical curves in the diagrams of Fig. 65 in 6.4.2.



# Literature

## List of referenced literature

Wherever available, the Digital Object Identifier (DOI) of a publication is provided as additional reference information. For convenience, the DOIs are embedded in hyperlinks using the DOI proxy server <http://dx.doi.org/>. At least the abstract of a referenced document will be publicly available there. The actual DOI of the document is always the right part of the given hyperlink following the expression ".../doi:". For more information on the DOI system, please see <http://www.doi.org/>.

- [1] **Abyaneh, M.H.J.; Saidi, M.H. (2005):** Simulation of direct fired double-effect LiBr-H<sub>2</sub>O absorption chillers. *Proceedings, International Sorption Heat Pump Conference, ISHPC 2005, June 22-24, 2005, Denver, CO*, Paper No. ISHPC-001-2005, electronically retrieved from: <http://www.enme.umd.edu/ceee/ishpc/content/ISHPC2005Proceedings.pdf>
- [2] **Alefeld, G. (1982):** Regeln für den Entwurf von mehrstufigen Absorbermaschinen. *Brennst.-Wärme-Kraft*, Volume 34, Issue 2, pp. 64-73.
- [3] **Alefeld, G. (1985):** *Multi-stage apparatus having working-fluid and absorption cycles, and method of operation thereof*. United States Patent, Patent. No.: US 4,531,374, electronically retrieved from: <http://v3.espacenet.com/origdoc?DB=EPODOC&IDX=US4531374>
- [4] **Alefeld, G.; Radermacher, R. (1993):** *Heat Conversion Systems*. CRC Press, Boca Raton, FL, table of contents and sample pages electronically available via Google Books: <http://books.google.com/books?vid=ISBN0849389283>
- [5] **Ali, H.; Alam, S.S. (1991):** Boiling incipience in a reboiler tube. *Industrial & Engineering Chemistry Research*, Volume 30, Issue 3, pp. 562 - 569, electronically accessible via Digital Object Identifier (DOI): <http://dx.doi.org/doi:10.1021/ie00051a018>
- [6] **ARI - Air-Conditioning and Refrigeration Institute (2000):** *ANSI/ARI Standard 560-2000, Standard for Absorption Water Chilling and Water Heating Packages*, Air-Conditioning and Refrigeration Institute, 4301 North Fairfax Drive, Suite 425, Arlington, Va. 22203, U.S.A., electronically retrieved from: <http://www.ari.org/std/individual/560-2000.pdf>
- [7] **Arneth, S. (1999):** *Dimensionierung und Betriebsverhalten von Naturumlaufverdampfern*. Thesis, Fakultät für Maschinenwesen, Technische Universität München. Hieronymus, Munich
- [8] **Arneth, S.; Stichlmair, J. (2001):** Characteristics of thermosiphon reboilers. *International Journal of Thermal Sciences*, Volume 40, Issue 4, pp. 385-391, electronically accessible via Digital Object Identifier (DOI): [http://dx.doi.org/doi:10.1016/S1290-0729\(01\)01231-5](http://dx.doi.org/doi:10.1016/S1290-0729(01)01231-5)
- [9] **Arun, M.B.; Maiya, M.P.; Murthy, S.S. (2001):** Performance comparison of double-effect parallel-flow and series flow water-lithium bromide absorption systems. *Applied Thermal Engineering*, Volume 21, Issue 12, pp. 1273-1279, electronically accessible via Digital Object Identifier (DOI): [http://dx.doi.org/doi:10.1016/S1359-4311\(01\)00005-9](http://dx.doi.org/doi:10.1016/S1359-4311(01)00005-9)
- [10] **Atkinson, P.G. (1956):** *The Measurement of Gas Stream Temperatures in Industrial Appliances*. Research Communication GC33, The Gas Council, London

- [11] **Atkinson, P.G.; Hargreaves, J.R. (1958):** *The Measurement of Gas Stream Temperatures in Industrial Appliances. II – A Suction Pyrometer for Temperatures above 1,100°C.* Research Communication GC57, The Gas Council, London
- [12] **Baars, A. (2003):** *Stationäre und instationäre Betriebszustände eines Naturumlauferdampfers.* Thesis, Fakultät Wissenschaftszentrum Weihenstephan für Ernährung, Landnutzung und Umwelt, Technische Universität München. Fortschritt-Berichte VDI, Reihe 3, Nr. 779, VDI-Verlag, Düsseldorf
- [13] **Babcock, G.H.; Wilcox, S. (1867):** *Improvement in steam generators.* United States Patent, Patent. No.: US 65,042, electronically retrieved from: <http://v3.espacenet.com/origdoc?DB=EPODOC&IDX=US65042>
- [14] **Basu, N.; Warriar, G.R.; Dhir, V. (2002):** Onset of Nucleate Boiling and Active Nucleation Site Density During Subcooled Flow Boiling. *Journal of Heat Transfer*, Volume 124, Issue 4, pp. 717-728, electronically accessible via Digital Object Identifier (DOI): <http://dx.doi.org/doi:10.1115/1.1471522>
- [15] **Cerkvenik, B.; Poredos, A.; Ziegler, F. (2001):** Influence of adsorption cycle limitations on the system performance. *International Journal of Refrigeration*, Volume 24, Issue 6, pp. 475-485, electronically accessible via Digital Object Identifier (DOI): [http://dx.doi.org/doi:10.1016/S0140-7007\(00\)00075-X](http://dx.doi.org/doi:10.1016/S0140-7007(00)00075-X)
- [16] **Charters, W.W.S.; Megler, V.R.; Chen, W.D.; Wang, Y.F. (1982):** Atmospheric and sub-atmospheric boiling of H<sub>2</sub>O and LiBr/H<sub>2</sub>O solutions. *International Journal of Refrigeration*, Volume 5, Issue 2, pp. 107-114, electronically accessible via Digital Object Identifier (DOI): [http://dx.doi.org/doi:10.1016/0140-7007\(82\)90085-8](http://dx.doi.org/doi:10.1016/0140-7007(82)90085-8)
- [17] **Cho, E.S.; Park, C.; Jeong, S. (2005):** Performance characteristics of exhaust gas heat exchangers for absorption chillers. *Proceedings, International Sorption Heat Pump Conference, ISHPC 2005, June 22-24, 2005, Denver, CO*, Paper No. ISHPC-088-2005, electronically retrieved from: <http://www.enme.umd.edu/ceee/ishpc/content/ISHPC2005Proceedings.pdf>
- [18] **Chua, H.T.; Toh, H.K.; Malek, A.; Ng, K.C.; Srinivasan, K. (2000a):** Improved thermodynamic property fields of LiBr-H<sub>2</sub>O solution. *International Journal of Refrigeration*, Volume 23, Issue 6, pp. 412-429, electronically accessible via Digital Object Identifier (DOI): [http://dx.doi.org/doi:10.1016/S0140-7007\(99\)00076-6](http://dx.doi.org/doi:10.1016/S0140-7007(99)00076-6)
- [19] **Chua, H.T.; Toh, H.K.; Malek, A.; Ng, K.C.; Srinivasan, K. (2000b):** General thermodynamic framework for understanding the behaviour of absorption chillers. *International Journal of Refrigeration*, Volume 23, Issue 7, pp. 491-507, electronically accessible via Digital Object Identifier (DOI): [http://dx.doi.org/doi:10.1016/S0140-7007\(99\)00077-8](http://dx.doi.org/doi:10.1016/S0140-7007(99)00077-8)
- [20] **Clark, D.A.; Lua, A.B., Sadler, J.D., Tucker, R.J. (1999a):** *LiBr Absorption Chiller for Building Air Conditioning with Efficient and Flexible Operation – EU Project JOE3-CT97-0059. Task 3 Report: LiBr Regenerator and Recuperator Design Details.* Confidential Internal Report R2808, BG Technology Ltd., Loughborough
- [21] **Clark, D.A.; Lua, A.B., Sadler, J.D. (1999b):** *LiBr Absorption Chiller for Building Air Conditioning with Efficient and Flexible Operation – EU Project JOE3-CT97-0059. Task 7 Report: Fabrication of a 350kW Prototype Regenerator and Recuperator.-Preliminary Tests Results Operating as a Water Heater.* Confidential Internal Report R3039, BG Technology Ltd., Loughborough

- [22] **Clark, D.A. (2000):** *LiBr Absorption Chiller for Building Air Conditioning with Efficient and Flexible Operation – EU Project JOE3-CT97-0059. Fabrication, commissioning and operation of a 350 kW Prototype Regenerator.* Confidential Periodic Report, BG Technology Ltd., Loughborough
- [23] **Collier, J.G. (1981):** *Convective Boiling and Condensation.* 2<sup>nd</sup> edition, New York, McGraw-Hill
- [24] **Cooper, M.G. (1984):** Heat Flow Rates in Saturated Nucleate Pool Boiling – A Wide-Ranging Examination Using Reduced Properties. *Advances in Heat Transfer*, Volume 16, pp. 157-239
- [25] **Cooper, M.G. (1989):** Flow boiling—the ‘apparently nucleate’ regime. *International Journal of Heat and Mass Transfer*, Volume 32, Issue 3, pp. 459-464, electronically accessible via Digital Object Identifier (DOI):  
[http://dx.doi.org/doi:10.1016/0017-9310\(89\)90133-6](http://dx.doi.org/doi:10.1016/0017-9310(89)90133-6)
- [26] **Corradini, M.L. (1998):** *Fundamentals of Multiphase Flow.* Department of Engineering Physics, University of Wisconsin, Madison, WI, electronic resource, retrieved from:  
<http://wins.engr.wisc.edu/teaching/mpfBook/>
- [27] **Dantele, T. (1999):** *Entwicklung und Versuchsbetrieb eines gasgefeuerten Austreibers für eine zweistufige Wasser-Lithiumbromid-Absorptionskälteanlage.* Diploma Thesis, Physik-Department der Technischen Universität München / Bayerisches Zentrum für Angewandte Energieforschung e.V. (ZAE Bayern), Garching
- [28] **Dialer, K. (1983):** *Die Wärmeübertragung beim Naturumlaufverdampfer.* Thesis, Eidgenössische Technische Hochschule Zürich, Diss. ETH Nr. 7407, Zürich
- [29] **Dittus, F.W.; Boelter, L.M.K. (1930):** Heat transfer in automobile radiators of the tubular type. *University of California Publications in Engineering*, Volume 2, pp. 443-461, republished as facsimile:  
**Dittus, F.W.; Boelter, L.M.K. (1985):** Heat transfer in automobile radiators of the tubular type. *International Communications in Heat and Mass Transfer*, Volume 12, Issue 1, pp. 3-22, electronically accessible via Digital Object Identifier (DOI):  
[http://dx.doi.org/doi:10.1016/0735-1933\(85\)90003-X](http://dx.doi.org/doi:10.1016/0735-1933(85)90003-X)
- [30] **Eberl, G. (2000):** *Planung und Auslegung eines Testaufbaus zur Bestimmung des Wärmeübergangs im Verdampfer/Absorber einer Absorptionskälteanlage.* Diploma Thesis, Fachhochschule München, Fachbereich 05 Versorgungstechnik, München / Bayerisches Zentrum für Angewandte Energieforschung e.V. (ZAE Bayern), Garching
- [31] **Edera, M.; Kojima, H. (2002):** Development of a new gas absorption chiller heater—advanced utilization of waste heat from gas-driven co-generation systems for air-conditioning. *Energy Conversion and Management*, Volume 43, Issues 9-12, pp. 1493-1501, electronically accessible via Digital Object Identifier (DOI):  
[http://dx.doi.org/doi:10.1016/S0196-8904\(02\)00031-6](http://dx.doi.org/doi:10.1016/S0196-8904(02)00031-6)
- [32] **Estiot, E.; Natzer, S.; Harm, M.; Kren, C.; Schweigler, C. (2005):** Heat Exchanger Development for Compact Water/LiBr Sorption Systems. *Proceedings, International Sorption Heat Pump Conference, ISHPC 2005, June 22-24, 2005, Denver, CO*, Paper No. ISHPC-070-2005, electronically retrieved from:  
<http://www.enme.umd.edu/ceee/ishpc/content/ISHPC2005Proceedings.pdf>
- [33] **Feuerecker, G.; Scharfe, J.; Greiter, I.; Frank, C.; Alefeld, G. (1994):** Measurement of thermophysical properties of LiBr-solutions at high temperatures and concentrations. *Proceedings of the International Absorption Heat Pump Conference, New Orleans, LA, January 19-21, 1994, AES – vol. 31, ASME*, pp. 493-499

- [34] **Furukawa, M. (1988):** *Direct firing generator*. Japanese Patent, Unexamined Publication No.: JP S63-294467 A, electronically retrieved from: <http://v3.espacenet.com/origdoc?DB=EPODOC&IDX=JP63294467>
- [35] **Furukawa, M.; Kaji, M.; Suyama, T.; Sekoguchi, K. (1995):** Enhancement of Pool Boiling Heat Transfer to Lithium Bromide Aqueous Solution. *Technology Reports of the Osaka University*, Volume 45, No. 2211, pp. 49-58
- [36] **Furutera, M.; Origane, T.; Sawada, T.; Kunugi, Y.; Kashiwagi, T.; Takei, T. (1996):** Advanced absorption heat pump cycles. *Proceedings, International Ab-Sorption Heat Pump Conference (Ab-Sorption 96), September 17-20, 1996, Montréal, Québec, Canada*, pp.109-119.
- [37] **Gommed, K.; Grossman, G. (1990):** Performance Analysis of Staged Absorption Heat Pumps: Water-Lithium Bromide Systems. *Proceedings, The 1990 Winter Meeting, Atlanta, GA, ASHRAE Transactions*, Volume 96, Part 1, Paper No. AT-90-30-6, pp. 1590-1598, abstract electronically accessible at ASHRAE bookstore: <http://resourcecenter.ashrae.org/store/ashrae/newstore.cgi?itemid=18565&view=item&categoryid=469>
- [38] **Grossman, G., Wilk, M., DeVault, R.C. (1994):** Simulation and performance analysis of triple-effect absorption cycles. *Proceedings of the ASHRAE Winter Meeting, New Orleans, LA, January 23 -26, 1994, ASHRAE Transactions*, Vol.100, Part 1, Paper No. 3781, pp. 452-462, abstract electronically accessible at ASHRAE bookstore: <http://resourcecenter.ashrae.org/store/ashrae/newstore.cgi?itemid=17713&view=item&categoryid=461>
- [39] **Gupte, N.S. (2003):** *Heat exchanger for high stage generator of absorption chiller*. United States Patent, Patent. No.: US 6,598,420 B2, electronically retrieved from: <http://v3.espacenet.com/origdoc?DB=EPODOC&IDX=US6598420>
- [40] **Gupte, N.S. (2005):** *Heat exchanger for high stage generator of absorption chiller*. United States Patent, Patent. No.: US 6,877,338 B2, electronically retrieved from: <http://v3.espacenet.com/origdoc?DB=EPODOC&IDX=US6877338>
- [41] **Hellmann, H.-M. (2002):** Carnot-COP for sorption heat pumps working between four temperature levels. *International Journal of Refrigeration*, Volume 25, Issue 1, pp. 66-74, electronically accessible via Digital Object Identifier (DOI): [http://dx.doi.org/doi:10.1016/S0140-7007\(01\)00008-1](http://dx.doi.org/doi:10.1016/S0140-7007(01)00008-1)
- [42] **Herold, K.E.; Radermacher, R.; Klein, S.A. (1996):** *Absorption Chillers and Heat Pumps*. CRC Press, Boca Raton, FL, table of contents and sample pages electronically available via Google Books: <http://books.google.com/books?vid=ISBN0849394279>
- [43] **IAPWS - International Association for the Properties of Water and Steam (1996):** *IAPWS-95. Release on the IAPWS Formulation 1995 for the Thermodynamic Properties of Ordinary Water Substance for General and Scientific Use*. IAPWS Secretariat, Electric Power Research Institute, Palo Alto, CA, electronically retrieved from: <http://www.iapws.org/relguide/IAPWS95.pdf>
- [44] **IAPWS - International Association for the Properties of Water and Steam (1997):** *IAPWS-IF97. Release on the IAPWS Industrial Formulation 1997 for the Thermodynamic Properties of Water and Steam*. IAPWS Secretariat, Electric Power Research Institute, Palo Alto, CA, electronically retrieved from: <http://www.iapws.org/relguide/IF97.pdf>



- [45] **Inoue, N.; Endo, T. (2003):** *Absorption chiller-heater and generator for use in such absorption chiller-heater.* European Patent Application, Pub. No.: EP 1 286 121 A2, electronically retrieved from:  
<http://v3.espacenet.com/origdoc?DB=EPODOC&IDX=EP1286121>
- [46] **Inoue, N.; Endo, T. (2004a):** *Absorption cold or hot water generating machine.* United States Patent, Patent No.: US 6,675,608 B2, electronically retrieved from:  
<http://v3.espacenet.com/origdoc?DB=EPODOC&IDX=US6675608>
- [47] **Inoue, N.; Endo, T. (2004b):** *Absorption chiller-heater and generator for use in such absorption chiller-heater.* United States Patent, Patent No.: US 6,694,772 B2, electronically retrieved from:  
<http://v3.espacenet.com/origdoc?DB=EPODOC&IDX=US6694772>
- [48] **Inoue, N.; Mochizuki, T.; Kera, M. (1999):** *High-temperature generator.* United States Patent, Patent No.: US 5,915,468, electronically retrieved from:  
<http://v3.espacenet.com/origdoc?DB=EPODOC&IDX=US5915468>
- [49] **Inoue, N.; Irie, T.; Saito, K.; Kawai, S. (2003):** Study on High Efficient Absorption Refrigerator Using Multi-effect Cycle -1st Report: Triple-effect Cycle-. *Trans. of the JSRAE*, Volume 20, No. 4, pp. 461-472
- [50] **Jurung, J.; Park, C.W. (1998):** On the performance of a desorber for absorption heat pumps with a thermosyphon and a surface-flame burner. *Applied Thermal Engineering*, Volume 18, Issues 3-4, pp. 73-83, electronically accessible via Digital Object Identifier (DOI): [http://dx.doi.org/doi:10.1016/S1359-4311\(97\)00073-2](http://dx.doi.org/doi:10.1016/S1359-4311(97)00073-2)
- [51] **Kaiser, E.P. (1988):** *Waermeuebertragung beim Sieden von binaeren Gemischen im Naturumlauferdampfer.* Thesis, Eidgenössische Technische Hochschule Zürich, Diss. ETH Nr. 8504, Zürich
- [52] **Kaita, Y. (2001):** Thermodynamic properties of lithium bromide-water solutions at high temperatures. *International Journal of Refrigeration*, Volume 24, Issue 5, pp. 374-390, electronically accessible via Digital Object Identifier (DOI):  
[http://dx.doi.org/doi:10.1016/S0140-7007\(00\)00039-6](http://dx.doi.org/doi:10.1016/S0140-7007(00)00039-6)
- [53] **Kaita, Y. (2002):** Simulation results of triple-effect absorption cycles. *International Journal of Refrigeration*, Volume 25, Issue 7, pp. 999-1007, electronically accessible via Digital Object Identifier (DOI): [http://dx.doi.org/doi:10.1016/S0140-7007\(01\)00100-1](http://dx.doi.org/doi:10.1016/S0140-7007(01)00100-1)
- [54] **Kamil, M.; Ali, H.; Alam, S.S. (1995):** Heat transfer to boiling liquids in a single vertical tube thermosiphon reboiler. *Experimental Thermal and Fluid Science*, Volume 10, Issue 1, pp. 44-53, electronically accessible via Digital Object Identifier (DOI):  
[http://dx.doi.org/doi:10.1016/0894-1777\(94\)00047-C](http://dx.doi.org/doi:10.1016/0894-1777(94)00047-C)
- [55] **Kamil, M.; Shamsuzzoha, M.; Alam, S.S. (2005):** Effect of submergence on boiling incipience in a vertical thermosiphon reboiler. *International Journal of Thermal Sciences*, Volume 44, Issue 1, pp. 75-87, electronically accessible via Digital Object Identifier (DOI): <http://dx.doi.org/doi:10.1016/j.ijthermalsci.2004.03.007>
- [56] **Kamoshida, J.; Isshiki, N. (1994):** Heat transfer to water and water/lithium halide salt solutions in nucleate pool boiling. *Proceedings of the International Absorption Heat Pump Conference, New Orleans, LA, January 19-21, 1994, AES – vol. 31, ASME*, pp. 501-507

- [57] **Kang, Y.T.; Kunugi, Y.; Kashiwagi, T. (2000):** Review of advanced absorption cycles: performance improvement and temperature lift enhancement. *International Journal of Refrigeration*, Volume 23, Issue 5, pp. 388-401, electronically accessible via Digital Object Identifier (DOI): [http://dx.doi.org/doi:10.1016/S0140-7007\(99\)00064-X](http://dx.doi.org/doi:10.1016/S0140-7007(99)00064-X)
- [58] **Kandlikar, S.G. (1990):** A General Correlation for Two-phase Flow Boiling Heat Transfer Inside Horizontal and Vertical Tubes. *Journal of Heat Transfer*, Volume 112, pp. 219-228, fulltext electronically available from the author: <http://www.rit.edu/~taleme/Papers/Journal%20Papers/J010.pdf>
- [59] **Kashiwagi, T.; Akisawa, A.; Yoshida, S.; Alam, C.A. (2002):** Heat driven sorption refrigerating and air conditioning cycle in Japan, *ISHPC'02 Proceedings of the International Sorption Heat Pump Conference, Shanghai, China, 24–27 September 2002*, pp. 50–62
- [60] **Katayama, M.; Origane, T.; Matsuda, K. (2002):** Absorption waste heat recovery system. United States Patent, Patent No.: US 6,460,338 B1, electronically retrieved from: <http://v3.espacenet.com/origdoc?DB=EPODOC&IDX=US6460338>
- [61] **Keil, C.; Plura, S.; Kren, C.; Schweigler, C. (2005):** Einsatzbeispiele angepasster Absorptions-Wärmepumpen mit Heizleistungen über 500 kW, *Proceedings, DKV-Tagungsbericht 2005, 32. Deutsche Kälte-Klima-Tagung, Würzburg, 16.-18. Nov, 2005*, Vol. 4, pp. 293-308, Deutscher Kälte- und Klimatechnischer Verein e.V. (DKV), Stuttgart.
- [62] **Kenning, D.B.R.; Cooper, M.G. (1989):** Saturated flow boiling of water in vertical tubes. *International Journal of Heat and Mass Transfer*, Volume 32, Issue 3, pp. 445-458, electronically accessible via Digital Object Identifier (DOI): [http://dx.doi.org/doi:10.1016/0017-9310\(89\)90132-4](http://dx.doi.org/doi:10.1016/0017-9310(89)90132-4)
- [63] **Kirschbaum, E. (1954):** Der Wärmeübergang im senkrechten Verdampferrohr. *Chemie Ingenieur Technik - CIT*, Volume 26, Issue 1, pp. 25 - 28, electronically accessible via Digital Object Identifier (DOI): <http://dx.doi.org/doi:10.1002/cite.330260107>
- [64] **Kirschbaum, E. (1955):** Der Wärmeübergang im senkrechten Verdampferrohr in dimensionsloser Darstellung. *Chemie Ingenieur Technik - CIT*, Volume 27, Issue 5, pp. 248 - 257, electronically accessible via Digital Object Identifier (DOI): <http://dx.doi.org/doi:10.1002/cite.330270503>
- [65] **Kirschbaum, E. (1961):** Der Verdampfungsvorgang bei Selbst-Umlauf im senkrechten Rohr. *Chemie Ingenieur Technik - CIT*, Volume 33, Issue 7, pp. 479 - 484, electronically accessible via Digital Object Identifier (DOI): <http://dx.doi.org/doi:10.1002/cite.330330703>
- [66] **Kirschbaum, E. (1962):** Einfluß des Rohrdurchmessers und der Rohrlänge auf die Leistung von Verdampfapparaten mit Selbstumlauf. *Chemie Ingenieur Technik - CIT*, Volume 34, Issue 3, pp. 183 - 192, electronically accessible via Digital Object Identifier (DOI): <http://dx.doi.org/doi:10.1002/cite.330340309>
- [67] **Kohler, J.A.; He, X. (1999):** Recovery of flue gas energy in a triple-effect absorption refrigeration system. United States Patent, Patent No.: US 6,003,331, electronically retrieved from: <http://v3.espacenet.com/origdoc?DB=EPODOC&IDX=US6003331>
- [68] **Kori, T.; Shidara, A.; Asakawa, M. (1997):** Regenerator for absorption type refrigerator. Japanese Patent, Unexamined Publication No.: JP H09-159306 A, electronically retrieved from: <http://v3.espacenet.com/origdoc?DB=EPODOC&IDX=JP9159306>

- [69] **Kouri, Y.; Morita, T.; Asakawa, M.; Arima, H.; Kubota, N. (1998):** *Absorption type refrigerator*. United States Patent, Patent No.: US 5,832,742, electronically retrieved from: <http://v3.espacenet.com/origdoc?DB=EPODOC&IDX=US5832742>
- [70] **Kren, C.; Dantele, T.; Schweigler, C.; Ziegler, F. (1999):** Entwicklung einer zweistufigen gasgefeuerten Absorptionskälteanlage, *Proceedings, DKV-Tagungsbericht 1999, 26. Deutsche Kälte-Klima-Tagung, Berlin, 16.-18. Nov. 1999*, Vol. II.1, pp. 173-186, Deutscher Kälte- und Klimatechnischer Verein e.V., Stuttgart.
- [71] **Kren, C.; Dantele, T.; Schweigler, C.; Ziegler, F.; Sadler, J.; Tucker, R.J.; Scharfe, J.; Larger, C.; Sahun, J. (2001):** An efficient LiBr absorption chiller for the European air conditioning market, *Proceedings, 2001 International Gas Research Conference (IGRC 2001), 5-8 November 2001, Amsterdam, The Netherlands*, Paper-No. RCO-07
- [72] **Kren, C.; Schweigler, C.; Storkenmaier, F. (2004):** *Multistage absorption refrigerating apparatus or heat pump and the use of the apparatus in an energy conversion system*. European Patent Application, Pub. No.: EP 1 391 665 A2, electronically retrieved from: <http://v3.espacenet.com/origdoc?DB=EPODOC&IDX=EP1391665>
- [73] **Kren, C.; Schweigler, C.; Ziegler, F. (2002):** Efficient LiBr Absorption Chillers for the European Air Conditioning Market, *ISHPC'02 Proceedings of the International Sorption Heat Pump Conference, Shanghai, China, 24–27 September 2002*, pp. 76–83
- [74] **Kren, C.; Schweigler, C.; Ziegler, F. (2005a):** Heat Transfer Characteristics in Flue Gas Fired Regenerators of Water/Lithium Bromide Absorption Chillers, *Proceedings, International Sorption Heat Pump Conference, ISHPC 2005, June 22-24, 2005, Denver, CO*, Paper No. ISHPC-072-2005, electronically retrieved from: <http://www.enme.umd.edu/ceee/ishpc/content/ISHPC2005Proceedings.pdf>
- [75] **Kren, C.; Schweigler, C.; Ziegler, F. (2005b):** Wärmeübertragung in rauchgasbeheizten Austreibern von mehrstufigen Absorptionskälteanlagen, *Proceedings, DKV-Tagungsbericht 2005, 32. Deutsche Kälte-Klima-Tagung, Würzburg, 16.-18. Nov. 2005*, Vol. II.1, pp. 319-334, Deutscher Kälte- und Klimatechnischer Verein e.V., Stuttgart.
- [76] **Kren, C.; Schweigler, C.; Ziegler, F. (2006a):** Heat transfer characteristics in flue gas fired regenerators of water/lithium bromide absorption chillers. *Proceedings of IMECE2006, 2006 ASME International Mechanical Engineering Congress and Exposition, November 5-10, 2006, Chicago, Illinois, USA*. Paper No. IMECE2006-15834.
- [77] **Kren, C.; Schweigler, C.; Ziegler, F. (2006b):** Wärmeübertragung in rauchgasbeheizten Naturumlauf-Austreibern mit stehenden Siederohren, *Proceedings, DKV-Tagungsbericht 2006, 33. Deutsche Kälte-Klima-Tagung, Dresden, 22.-24. Nov. 2006*, Vol. II.1, Deutscher Kälte- und Klimatechnischer Verein e.V., Stuttgart, Paper No. II.1.15.
- [78] **Kubota, N.; Shikanuma, H.; Izu, M. (1999):** *High-temperature regenerator*. Japanese Patent Application, Unexamined Publication No.: JP H11-211271 A, electronically retrieved from: <http://v3.espacenet.com/origdoc?DB=EPODOC&IDX=JP11211271>
- [79] **Kujak, S.; Schultz, K. (2000):** Demonstration of a Direct-fired Triple-effect Absorption Chiller. *Energy Engineering*, Volume 97, Issue 3, pp. 49-56
- [80] **Kurosawa, M.; Kannou, S.; Takemoto, S.; Oshima, M.; Hisatsuchi, T.; Sei, T. (1989):** *Double-effect absorption water cooler/heater*. Japanese Patent, Unexamined Publication No.: JP H01-244257 A, electronically retrieved from: <http://v3.espacenet.com/origdoc?DB=EPODOC&IDX=JP1244257>

- [81] **Lee, C. C.; Chuah, Y. K.; Lu, D. C.; Chao, H. Y. (1991):** Experimental investigation of pool boiling of lithium bromide solution on a vertical tube under subatmospheric pressures. *International Communications in Heat and Mass Transfer*, Volume 18, Issue 3, pp. 309-320, electronically accessible via Digital Object Identifier (DOI): [http://dx.doi.org/doi:10.1016/0735-1933\(91\)90018-Y](http://dx.doi.org/doi:10.1016/0735-1933(91)90018-Y)
- [82] **Lee, S.-F.; Sherif, S.A. (2001):** Second Law Analysis of Various Double-Effect Lithium Bromide/Water Absorption Chillers. *Proceedings, The 2001 Winter Meeting, Atlanta, GA, ASHRAE Transactions*, Volume 107, Part 1, Paper No. AT-01-9-5, pp. 664-673, abstract electronically accessible at ASHRAE bookstore: <http://resourcecenter.ashrae.org/store/ashrae/newstore.cgi?itemid=7173&view=item&categoryid=162>
- [83] **Lienhard, J.H.; Lienhard, J.H. (2003):** *A heat transfer textbook*. 3<sup>rd</sup> edition, Phlogiston Press, Cambridge, MA., also available as electronic resource, retrieved from: <http://web.mit.edu/lienhard/www/ahtt.html>
- [84] **Liu, Z.; Winterton, R.H.S. (1991):** A general correlation for saturated and subcooled flow boiling in tubes and annuli, based on a nucleate pool boiling equation. *International Journal of Heat and Mass Transfer*, Volume 34, Issue 11, pp. 2759-2766, electronically accessible via Digital Object Identifier (DOI): [http://dx.doi.org/doi:10.1016/0017-9310\(91\)90234-6](http://dx.doi.org/doi:10.1016/0017-9310(91)90234-6)
- [85] **McAdams, W.H. (1942):** *Heat Transmission*. 2<sup>nd</sup> edition, McGraw-Hill, New York
- [86] **Minchenko, F. P.; Firsova, E. V. (1969):** Heat transfer to water and water-lithium salt solutions in nucleate pool boiling. In: *Problems of Heat Transfer and Hydraulics of Two-Phase Media*, S. S. Kutateladze ed., Pergamon Press, Oxford, pp. 137-51
- [87] **Mori, A.; Watanabe, S.; Matsunaga, M.; Machizawa, K.; Minowa, R. (1984):** *Absorption type refrigeration system*. United States Patent, Patent No.: US 4,439,999, electronically retrieved from: <http://v3.espacenet.com/origdoc?DB=EPODOC&IDX=US4439999>
- [88] **Mori, K.; Oka, M.; Ohhashi, T. (2003):** Development of Triple-effect Absorption Chiller-heater, *Proceedings, 22nd World Gas Conference Tokyo 2003 (WGC2003), Tokyo, June 1-5, 2003*, WOC 7, TF7-C, electronically retrieved from: [http://www.igu.org/html/wgc2003/WGC\\_pdffiles/10626\\_1045222692\\_11599\\_1.pdf](http://www.igu.org/html/wgc2003/WGC_pdffiles/10626_1045222692_11599_1.pdf)
- [89] **Nagel, O. (1962):** *Beitrag zum Wärmeübergang in Umlaufverdampfern*. Thesis, Fakultät für Maschinenwesen, Technische Hochschule Karlsruhe, Karlsruhe
- [90] **Nagel, O.; Kirschbaum, E. (1963):** Zusammenhänge zwischen Wärmeübergang und Phasenänderung im Umlaufverdampfer. *Chemie Ingenieur Technik - CIT*, Volume 35, Issue 3, pp. 179 - 185, electronically accessible via Digital Object Identifier (DOI): <http://dx.doi.org/doi:10.1002/cite.330350311>
- [91] **Nakamura, M.; Shitara, A.; Arima, H.; Kanuma, H.; Furukawa, M.; Enomoto, E.; Yamada, T. (2000):** *High-temperature regenerator*. United States Patent, Patent. No.: US 6,145,338, electronically retrieved from: <http://v3.espacenet.com/origdoc?DB=EPODOC&IDX=US6145338>
- [92] **Oka, M.; Ohashi, T.; Ozawa, Y.; Yamazaki, S.; Miyake, S. (2003):** Development of a High Efficiency Absorption Chiller-Heater and a Compact Absorption Chiller-Heater, *Proceedings, 22nd World Gas Conference Tokyo 2003 (WGC2003), Tokyo, June 1-5, 2003*, WOC 6, electronically retrieved from: [http://www.igu.org/html/wgc2003/WGC\\_pdffiles/10153\\_1045125162\\_20177\\_1.pdf](http://www.igu.org/html/wgc2003/WGC_pdffiles/10153_1045125162_20177_1.pdf)



- [93] **Pathakji, N.; Dyer, J.; Berry, J.B.; Gabel, S. (2005):** Exhaust-driven absorption chiller-heater and reference designs advance the use of IES technology, *Proceedings, International Sorption Heat Pump Conference, ISHPC 2005, June 22-24, 2005, Denver, CO*, Paper No. ISHPC-096-2005, electronically retrieved from: <http://www.enme.umd.edu/ceee/ishpc/content/ISHPC2005Proceedings.pdf>
- [94] **Paul, U. (2004):** *Absorptionskälteanlagen für effiziente Kraft-Wärme-Kälte-Kopplung*, Diploma Thesis, Bayerisches Zentrum für Angewandte Energieforschung e.V. (ZAE Bayern), Garching, Otto-von-Guericke-Universität Magdeburg, Magdeburg.
- [95] **Plura, S.; Kren, C.; Paul, U.; Schweigler, C. (2004):** Absorptionskälteanlagen für effiziente Kraft-Wärme-Kälte-Kopplung, *Proceedings, DKV-Tagungsbericht 2004, 31. Deutsche Kälte-Klima-Tagung, Bremen, 17.-19. Nov. 2004*, Vol. II.1, pp. 127-144, Deutscher Kälte- und Klimatechnischer Verein e.V., Stuttgart.
- [96] **Plura, S.; Kren, C.; Schweigler, C. (2005):** System Concept for Efficient and Flexible Tri-Generation. *Proceedings, International Sorption Heat Pump Conference, ISHPC 2005, June 22-24, 2005, Denver, CO*, Paper No. ISHPC-071-2005, electronically retrieved from: <http://www.enme.umd.edu/ceee/ishpc/content/ISHPC2005Proceedings.pdf>
- [97] **Rant, Z. (1977):** *Verdampfen in Theorie und Praxis*. Verlag Sauerländer, Aarau, Frankfurt am Main
- [98] **Rhine, J.M.; Tucker, R.J. (1991):** *Modelling of gas-fired furnaces and boilers and other industrial heating processes*. British Gas plc., London, in association with McGraw-Hill, Maidenhead
- [99] **Riesch, P. (1991):** *Absorptionswärmehaube mit hohem Temperaturhub*. Thesis, Fakultät für Physik, Technische Universität München. Forschungsberichte des DKV Nr. 36, Deutscher Kälte- und Klimatechnischer Verein e.V. (DKV), Stuttgart
- [100] **Saito, K.; Igarashi, H.; Kawai, S. (1996):** Study on the effect of the difference of absorption cycles on the characteristics of double-effect absorption refrigerator. *Nippon Kikai Gakkai Ronbunshu, B Hen/Transactions of the Japan Society of Mechanical Engineers, Part B*, Volume 62, Issue 595, pp. 1193-1197
- [101] **Scharfe, J.; Sahun, J.; Tucker, R.J.; Ziegler, F. (2000):** *LiBr-Absorption Chiller for Building Air Conditioning with efficient and flexible operation*. Confidential Final Report to THE EUROPEAN COMMISSION, Contract No. JOE-CT97-0059, *Weir ENTROPIE S.A., Saint-Germain-en-Laye / Gas Natural SDG, S.A., Barcelona / BG Technology Ltd., Loughborough / ZAE Bayern e.V., Garching*
- [102] **Schweigler, C. (1999):** *Kälte aus Fernwärme. Konzept, Auslegung und Betrieb der Single-Effect/Double-Lift-Absorptionskälteanlage*. Thesis. Fortschritt-Berichte VDI, Reihe 19, Nr. 121, VDI-Verlag, Düsseldorf
- [103] **Schweigler, C.; Dantele, T.; Kren, C.; Ziegler, F.; Clark, D.; Fulachier, M.-H.; Sahun, J. (1999):** Development of a direct-fired partly air-cooled double-effect absorption chiller. *Proc. of the 29th International Congress of Refrigeration, 19.-24. September 1999, Sydney*
- [104] **Schweigler, C.; Dantele, T.; Kren, C.; Ziegler, F.; Clark, D.; Fulachier, M.-H.; Sahun, J. (2000):** Improvements in Absorption Li/Br Chiller for Air Conditioning, *Proceedings, 21st World Gas Conference, IGU Conference Nice 2000, WOC6*, Paper No. P-605.

- [105] **Senba, Y.; Ishikawa, K.; Miyake, S.; Oka, M.; Yamada, K.; Ozawa, Y. (2003):** *High-temperature regenerator and absorption cool and hot water machine*. Japanese Patent Application, Unexamined Publication No.: JP 2003-336931 A, electronically retrieved from: <http://v3.espacenet.com/origdoc?DB=EPODOC&IDX=JP2003336931>
- [106] **Shamsuzzoha, M.; Moonyoung Lee; Alam, S.S. (2005):** The determination of superheated layer thickness and wall superheat in vertical tube natural circulation reboiler. *Applied Thermal Engineering*, Volume 25, Issue 13, pp. 1961-1978, electronically accessible via Digital Object Identifier (DOI): <http://dx.doi.org/doi:10.1016/j.applthermaleng.2004.11.018>
- [107] **Shitara, A. (2000):** Improvement of the COP of the LiBr-Water Double-Effect Absorption Cycles, *Trans. of the JSRAE*, Volume 17, No. 3, pp. 257-268
- [108] **Shitara, A.; Matsubara, M.; Ohashi, T. (2001):** Development of a high efficiency absorption chiller-heater and a compact absorption chiller-heater, *Proceedings, 2001 International Gas Research Conference (IGRC 2001), 5-8 November 2001, Amsterdam, The Netherlands*, Paper-No. RCO-08
- [109] **Spang, B. (2002):** Thermodynamic and Transport Properties of Water and Steam. *The Chemical Engineers' Resource Page*, [www.cheresources.com](http://www.cheresources.com), Website, electronic resource, retrieved from: <http://www.cheresources.com/iapwsif97.shtml>
- [110] **Spang, B. (2004):** Correlations for Convective Heat Transfer. *The Chemical Engineers' Resource Page*, [www.cheresources.com](http://www.cheresources.com), Website, electronic resource, retrieved from: <http://www.cheresources.com/convection.shtml>
- [111] **Steiner, D.; Taborek, J. (1992):** Flow Boiling Heat Transfer in Vertical Tubes Correlated by an Asymptotic Model. *Heat Transfer Engineering*, Volume 13, Issue 2, pp. 43-69
- [112] **Takahata, S.; Ochi, T.; Saito, K. (1999):** *Waste heat utilized absorption type water cooling/heating machine refrigerating machine*. Japanese Patent Application (rejected), Unexamined Publication No.: JP H11-304274 A, electronically retrieved from: <http://v3.espacenet.com/origdoc?DB=EPODOC&IDX=JP11304274>
- [113] **Thome, J.R. (2003):** Discussion: "Commentary on Correlations for Convective Vaporization in Tubes", (Webb, Ralph. L., 2003, ASME J. of Heat Transfer, 125(1), pp. 184-185.). *Journal of Heat Transfer*, Volume 125, Issue 6, pp. 1206-7, electronically accessible via Digital Object Identifier (DOI): <http://dx.doi.org/doi:10.1115/1.1621895>
- [114] **Tozer, R.M.; James, R.W. (1997):** Fundamental thermodynamics of ideal absorption cycles. *International Journal of Refrigeration*, Volume 20, Issue 2, pp. 120-135, electronically accessible via Digital Object Identifier (DOI): [http://dx.doi.org/doi:10.1016/S0140-7007\(96\)00061-8](http://dx.doi.org/doi:10.1016/S0140-7007(96)00061-8)
- [115] **Tozer, R.M.; Agnew, B. (1999):** Optimisation of ideal absorption cycles with external irreversibilities. *Proc. of the International Sorption Heat Pump Conference (ISHPC 99), München, 24. - 26. März 1999*, pp.453-457.
- [116] **Tucker, R.J.; Clark, D.A.; Sadler, J.D.; Lua, A.B. (2000):** *An absorption chiller*. International Patent Application (PCT), Pub. No.: WO 00/68622, electronically retrieved from: <http://v3.espacenet.com/origdoc?DB=EPODOC&IDX=WO0068622>
- [117] **Tucker, R.J.; Clark, D.A.; Sadler, J.D.; Lua, A.B. (2001):** *A generator for an absorption chiller*. International Patent Application (PCT), Pub. No.: WO 01/11295 A1, electronically retrieved from: <http://v3.espacenet.com/origdoc?DB=EPODOC&IDX=WO0111295>

- [118] **TRANE (2003):** *Trane Horizon™ Absorption Series. Two-Stage Steam-Fired or Hot Water Absorption Water Chillers, 380-1650 Tons – 50-60 Hz. Built for Industrial and Commercial Applications.* Product catalog, Trane - A business of American Standard Companies Inc., Literature Order Number ABS-PRC004-EN, electronically retrieved from: <http://www.trane.com/Commercial/Equipment/PDF/1/ABSPRC004EN.pdf>
- [119] **Varma, H.K.; Mehrotra, R.K.; Agrawal, K.N.; Singh, S. (1994):** Heat transfer during pool boiling of LiBr-water solutions at subatmospheric pressures. *International Communications in Heat and Mass Transfer*, Volume 21, Issue 4, pp. 539-548, electronically accessible via Digital Object Identifier (DOI): [http://dx.doi.org/doi:10.1016/0735-1933\(94\)90053-1](http://dx.doi.org/doi:10.1016/0735-1933(94)90053-1)
- [120] **VDI-GVC - Verein Deutscher Ingenieure, VDI-Gesellschaft Verfahrenstechnik und Chemieingenieurwesen (eds.), (1997):** *VDI-Wärmeatlas. Berechnungsblätter für den Wärmeübergang.* 8<sup>th</sup> Edition, Springer-Verlag, Berlin, Heidelberg, New York
- [121] **VDI-GVC - Verein Deutscher Ingenieure, VDI-Gesellschaft Verfahrenstechnik und Chemieingenieurwesen (eds.), (2002):** *VDI-Wärmeatlas. Berechnungsblätter für den Wärmeübergang.* 9<sup>th</sup> Edition, Springer-Verlag, Berlin, Heidelberg, New York
- [122] **Wadekar, V.V. (1993):** A model for addition of convective and nucleate boiling heat transfer in flow boiling. *Institution of Chemical Engineers (IChemE) Symposium Series*, No. 129, Issue 1, pp. 181-187
- [123] **Wagner, T.C.; Jung, S.; Marler, M.E. (2005):** Development of a waste-heat-driven double-effect absorption chiller, *Proceedings, International Sorption Heat Pump Conference, ISHPC 2005, June 22-24, 2005, Denver, CO*, Paper No. ISHPC-100-2005, electronically retrieved from: <http://www.enme.umd.edu/ceee/ishpc/content/ISHPC2005Proceedings.pdf>
- [124] **Webb, R.L. (2003a):** Commentary on Correlations for Convective Vaporization in Tubes. *Journal of Heat Transfer*, Volume 125, No. 1, pp. 184-185, electronically retrieved from: [http://scitation.aip.org/journals/doc/JHTRAO-ft/vol\\_125/iss\\_1/184\\_1.html](http://scitation.aip.org/journals/doc/JHTRAO-ft/vol_125/iss_1/184_1.html)
- [125] **Webb, R.L. (2003b):** Closure to "Discussion: 'Commentary on Correlations for Convective Vaporization in Tubes,' (Webb, Ralph. L., 2003, ASME J. of Heat Transfer, 124(1), pp. 184–185.)". *Journal of Heat Transfer*, Volume 125, Issue 6, p. 1208, electronically accessible via Digital Object Identifier (DOI): <http://dx.doi.org/doi:10.1115/1.1621896>
- [126] **Winterton, R.H.S. (1998):** Where did the Dittus and Boelter equation come from? *International Journal of Heat and Mass Transfer*, Volume 41, Issue 4-5, pp. 809-810, electronically accessible via Digital Object Identifier (DOI): [http://dx.doi.org/doi:10.1016/S0017-9310\(97\)00177-4](http://dx.doi.org/doi:10.1016/S0017-9310(97)00177-4)
- [127] **Wu, W.-T.; Yang, Y.-M.; Maa, J.-R. (1998):** Effect of surfactant additive on pool boiling of concentrated lithium bromide solution. *International Communications in Heat and Mass Transfer*, Volume 25, Issue 8, pp. 1127-1134, electronically accessible via Digital Object Identifier (DOI): [http://dx.doi.org/doi:10.1016/S0735-1933\(98\)00103-1](http://dx.doi.org/doi:10.1016/S0735-1933(98)00103-1)
- [128] **Yabase, H.; Kawabata, K.; Yakushiji, F.; Takigawa, T. (2005):** Development of triple-effect absorption chiller-heater. *Proceedings, International Sorption Heat Pump Conference, ISHPC 2005, June 22-24, 2005, Denver, CO*, Paper No. ISHPC-048-2005, electronically retrieved from: <http://www.enme.umd.edu/ceee/ishpc/content/ISHPC2005Proceedings.pdf>

- [129] **Yamazaki, S.; Enomoto, E.; Kamada, Y.; Furukawa, M. (2002):** *Absorption refrigerator*. United States Patent, Patent No.: US 6,487,874 B2, electronically retrieved from: <http://v3.espacenet.com/origdoc?DB=EPODOC&IDX=US6487874>
- [130] **Yoon, J.-I.; Choi, K.-H.; Moon, C.-G.; Kim, Y.J.; Kwon, O.-K. (2003):** A study on the advanced performance of an absorption heater/chiller with a solution preheater using waste gas. *Applied Thermal Engineering*, Volume 23, Issue 6, pp. 757-767, electronically accessible via Digital Object Identifier (DOI): [http://dx.doi.org/doi:10.1016/S1359-4311\(03\)00003-6](http://dx.doi.org/doi:10.1016/S1359-4311(03)00003-6)
- [131] **Ziegler, F. (1997):** *Sorptionswärmepumpen*. Professorial Dissertation. Forschungsberichte des DKV Nr. 57, Deutscher Kälte- und Klimatechnischer Verein e.V. (DKV), Stuttgart.
- [132] **Ziegler, F. (2005):** Absorption Cycle Basics Revisited. *Proceedings, International Sorption Heat Pump Conference, ISHPC 2005, June 22-24, 2005, Denver, CO*, Paper No. ISHPC-082-2005, electronically retrieved from: <http://www.enme.umd.edu/ceee/ishpc/content/ISHPC2005Proceedings.pdf>

## Declaration of prior publication

Excerpts of this work have been published by the author prior to submission of the thesis in literature references [71]-[77].

## Christoph KREN

D-85375 Neufahrn bei Freising

E-Mail: [Christoph@Kren.de](mailto:Christoph@Kren.de)

Internet: <http://Christoph.Kren.de>



### o Persönliche Daten

Name, Vorname: Kren, Christoph  
Geboren am: 08.07.1971 in Murnau am Staffelsee  
Familienstand: verheiratet  
Staatsbürgerschaft: deutsch, österreichisch

### o Schulbildung

1978 – 1982 Grundschule in Murnau am Staffelsee  
1982 – 1991 Mathematisch-naturwissenschaftliches Staffelsee-Gymnasium in Murnau  
1991 Allgemeine Hochschulreife (Abitur)

### o Wehrdienst

1991 – 1992 12-monatiger Grundwehrdienst beim Gebirgsfernmeldelehrbataillon 8 in Murnau. Nach der Grundausbildung Einsatz als Materialbuchhalter im Stabsdienst.

### o Ausbildung

1992 – 1998 Studium der Technischen Physik mit Vertiefungsfach Elektrotechnik an der Technischen Universität München (TU München)  
1997 – 1998 Diplomarbeit am Bayerischen Zentrum für Angewandte Energieforschung e.V. (ZAE Bayern). Thema: *„Untersuchungen zu statischen und dynamischen Oberflächenspannungen wässriger LiBr-Lösungen mit höheren Alkoholen als Heat-Transfer-Additiven“*  
1998 Studienabschluss und Erwerb des akademischen Grades eines Diplom-Physikers (Univ.)

### o Berufliche Tätigkeit

1998 – 2006 Wissenschaftlicher Angestellter am Bayerischen Zentrum für Angewandte Energieforschung e.V. (ZAE Bayern), Abteilung „Technik für Energiesysteme und Erneuerbare Energien“, Arbeitsgruppe „Kältemaschinen und Wärmepumpen“.